

JYU DISSERTATIONS 500

Risto Ojajarvi

Competition and Interplay between Magnetism and Superconductivity



UNIVERSITY OF JYVÄSKYLÄ
FACULTY OF MATHEMATICS
AND SCIENCE

JYU DISSERTATIONS 500

Risto Ojajärvi

Competition and Interplay Between Magnetism and Superconductivity

Esitetään Jyväskylän yliopiston matemaattis-luonnontieteellisen tiedekunnan suostumuksella
julkisesti tarkastettavaksi huhtikuun 8. päivänä 2022 kello 12.

Academic dissertation to be publicly discussed, by permission of
the Faculty of Mathematics and Science of the University of Jyväskylä,
on April 8, 2022 at 12 o'clock noon.



JYVÄSKYLÄN YLIOPISTO
UNIVERSITY OF JYVÄSKYLÄ

JYVÄSKYLÄ 2022

Editors

Ilari Maasilta

Department of Physics, University of Jyväskylä

Timo Hautala

Open Science Centre, University of Jyväskylä

Copyright © 2022, by Author and University of Jyväskylä

ISBN 978-951-39-9060-2 (PDF)

URN:ISBN:978-951-39-9060-2

ISSN 2489-9003

Permanent link to the online version of this publication: <http://urn.fi/URN:ISBN:978-951-39-9060-2>

ABSTRACT

This dissertation is composed of nine publications and this introduction, which outlines the theories of superconductivity, magnetism and non-equilibrium physics that are applied in the publications. The publications can be divided into two bodies which share some common themes.

The publications of the first body deal with the physics of flat electronic bands, and in particular the superconducting and magnetic phase transitions on them. In the related part of the introduction part I present the basic theories of superconductivity and magnetism, and discuss the properties which make the flat bands prone to spontaneous symmetry breaking. We formulate the theory of electron-phonon superconductivity on a flat band model, and show how its predictions differ from those of a simpler BCS model. Of the materials which have flat bands, we are particularly interested in those based on graphene e.g., twisted bilayer graphene, for which we show that the conventional BCS theory of superconductivity based on the attractive electron-phonon interaction is compatible with the experimental observations. Flat bands are often enabled by some topological property. We classify the topological transitions on a system of rhombohedrally stacked honeycomb lattices.

The publications of the second body are about superconducting spintronics. One central theme in these publications is the magnetic proximity effect and its various application. We propose that a magnetically proximitized superconductor can be used as the functional unit of a new kind of thermoelectric radiation detector. A second theme is the effect of superconductivity on the spin pumping effect. This is studied in four publications, in which we predict e.g. a cooling effect due to precessing magnetization, a giant spin battery effect, and an antiferromagnetic coupling between two magnets mediated by spin supercurrent. A third theme is the Higgs mode i.e. the amplitude mode of the superconducting order parameter. The magnetic proximity effect enables a new coupling between a charge degree of freedom and the Higgs mode, which can be utilized to measure it electrically. We also study the magnon-Higgs coupling mediated by spin-orbit interaction. In the introductory part related to this body, I outline the Keldysh theory of non-equilibrium states and the quasiclassical theory of superconductivity, which have been heavily utilized in the publications.

Keywords: superconductivity, ferromagnetism, spintronics, quasiclassical formalism, non-equilibrium, flat bands

TIIVISTELMÄ (ABSTRACT IN FINNISH)

Tämä väitöskirja koostuu yhdeksästä julkaisusta sekä johdanto-osasta, joka käsittelee tutkimusten taustalla olevia suprajohtavuuden, magnetismin ja epätasapainotilojen teorioita. Väitöskirjaan sisällytetyt julkaisut voidaan jakaa kahteen kokonaisuuteen, joilla on joitain yhteisiä teemoja.

Ensimmäisen kokonaisuuden julkaisut käsittelevät litteiden elektronisten vöiden (tasovöiden) fysiikkaa, ja erityisesti niillä tapahtuvia magnetismin ja suprajohtavuuteen johtavia olomuodonmuutoksia. Ensimmäiseen kokonaisuuteen liittyvässä johdanto-osan luvussa esittelen suprajohtavuuden ja magnetismin teoreettisen perustan ja käsittelen tasovöiden erikoispiirteitä. Julkaisuissa muotoilemme elektroni-fononi-suprajohtavuuden teorian tasovyömallille, ja näytämme kuinka sen ennustukset eroavat BCS-mallin ennustuksista. Erityishuomion kohteena ovat hiilipohjaiset tasovyömateriaalit, esimerkiksi kierretty kaksitasografeeni, jolle näytämme että elektroni-fononi-vuorovaikutukseen perustuva suprajohtavuuden malli on yhteensopiva kokeellisten havaintojen kanssa. Tasovöiden taustalla vaikuttaa usein jokin topologinen ominaisuus. Tähän liittyen luokittelemme romboedrisesti ladotun hunajakennohilan topologisia transitoita.

Toisen kokonaisuuden julkaisut käsittelevät suprajohtavaa spintroniikkaa. Yhtenä kantavana teemana näissä töissä on magneettinen läheisyysilmiö ja sen sovellutukset. Näytämme että tätä ilmiötä voidaan käyttää uudenlaisen lämpösähköisen säteilyilmaisimen kehittämiseksi. Toinen keskeinen teema on suprajohteen järjestysparametriin dynamiikkaan liittyvä Higgsin moodi, jonka ennustamme kytkeytyvän magneettisen läheisyysilmiön kautta uusilla tavoilla, jotka mahdollistavat sen sähköisen havaitsemisen. Kolmas keskeinen teema ovat suprajohtavuuden vaikutukset prekessoivan magnetisaation aikaansaamaan spinpumpppaukseen. Tätä aihetta käsitellään eri näkökulmista neljässä julkaisussa, joissa ennustamme mm. spinpumpppauksen tuottaman jäähtytyksen, jättimäisen spinakku-ilmiön, spinsupravirran tuottaman kytkennän kahden prekessoivan magneetin välillä, sekä spin-rata-vuorovaikutuksen välittämän kytkennän magnonien, magneettisten värähtelyiden, sekä Higgsin moodin välillä. Esittelen johdanto-osassa näiden ilmiöiden kuvailuun käytettävän epätasapainotilojen Keldysh-teorian sekä suprajohtavuuden kvasiklassisen teorian.

Avainsanat: Suprajohtavuus, ferromagnetismi, spintroniikka, kvasiklassinen formalismi, epätasapainotila, tasovyö

Author

Risto Ojajärvi
Department of Physics
University of Jyväskylä
Finland

Supervisors

Professor Tero T. Heikkilä
Department of Physics
University of Jyväskylä
Finland

Doctor Mikhail Silaev
Department of Physics
University of Jyväskylä
Finland

Pre-examiners

Doctor Alexander Melnikov
Head of the Department of Physics of Superconductivity
Institute for Physics of Microstructures
Russian Academy of Sciences

Doctor Matti Silveri
Academy Research Fellow
Nano and Molecular Systems Research Unit
University of Oulu
Finland

Opponent

Professor Daniel Loss
Department of Physics
University of Basel
Switzerland

PREFACE

I started my PhD studies in the Nanoscience Center at the University of Jyväskylä in 2017 and finished this dissertation at the beginning of the year 2022. This dissertation would not have come to fruition without the support of many people, whom I now wish to thank.

I am deeply grateful for my supervisors Tero Heikkilä and Mikhail Silaev for all the guidance and encouragement during the years of my PhD studies and during the time when I was doing my master's thesis under Tero's supervision. I thank you for introducing me to this field of science and for giving me so many opportunities for exciting collaborations. It has been a joy to work with you, and this dissertation would simply not have been possible without both of you.

I thank Dr. F. Sebastian Bergeret and his research group for the hospitality during my research visit to San Sebastián. Those months in the Basque country and under Sebas's guidance were some of the most inspiring during the years of my PhD studies. I also wish to thank Dr. Pauli Virtanen, Dr. Timo Hyart, and Dr. Yao Lu; without your contributions, this thesis would not have been as successful. I thank my colleagues Dr. Faluke Aikebaier, Mr. Kalle Kansanen, Mr. Kurt Meier, Dr. Camillo Tassi, and Dr. Subrata Chakraborty for many useful discussions, and the co-authors Prof. I.J. Maasilta, Dr. E. Strambini, and Prof. F. Giazotto for the collaboration.

A special thanks goes to Dr. Teemu Peltonen for the countless discussions on physics and beyond during our shared time as PhD students. Those discussions were as beneficial for my studies as they were to yours, and were sorely missed after your graduation and during the various stages of the COVID-19 pandemic. I also thank my friends and colleagues in the Nanoscience Center and beyond. I acknowledge with gratitude the financial support from Jenny and Antti Wihuri Foundation.

Kaikkein eniten kiitän vaimoani Katria rakkaudesta, tuesta ja kärsivällisyydestä jatko-opintojeni aikana. Vanhemmilleni ja myös appivanhemmilleni olen kiitollinen kaikesta saamastamme tuesta. Tyttäreni Lyyliä ja Meeriä kiitän kaikesta siitä ilosta ja rakkaudesta, jonka he tuovat elämääni.

In Jyväskylä, 21st of February 2022

Risto Ojajärvi

LIST OF PUBLICATIONS

- I** R. Ojajärvi, T. Hyart, M.A. Silaev and T.T. Heikkilä. Competition of electron-phonon mediated superconductivity and Stoner magnetism on a flat band. *Physical Review B* **98**, 054515, DOI:[10.1103/PhysRevB.98.054515](https://doi.org/10.1103/PhysRevB.98.054515), 2018.
- II** T. Hyart, R. Ojajärvi and T.T. Heikkilä. Two topologically distinct Dirac-line semimetal phases and topological phase transitions in rhombohedrally stacked honeycomb lattices. *Journal of Low Temperature Physics* **191**, 35-48, DOI:[10.1007/s10909-017-1846-3](https://doi.org/10.1007/s10909-017-1846-3), 2018.
- III** T.T. Heikkilä, R. Ojajärvi, I.J. Maasilta, E. Strambini, F. Giazotto, and F.S. Bergeret. Thermoelectric radiation detector based on superconductor-ferromagnet systems. *Physical Review Applied* **10**, 034053, DOI:[10.1103/PhysRevApplied.10.034053](https://doi.org/10.1103/PhysRevApplied.10.034053), 2018.
- IV** T.J. Peltonen, R. Ojajärvi, and T.T. Heikkilä. Mean-field theory for superconductivity in twisted bilayer graphene. *Physical Review B* **98**, 220504(R), DOI:[10.1103/PhysRevB.98.220504](https://doi.org/10.1103/PhysRevB.98.220504), 2018.
- V** R. Ojajärvi, J. Manninen, T.T. Heikkilä and P. Virtanen. Nonlinear spin torque, pumping, and cooling in superconductor/ferromagnet systems. *Physical Review B* **101**, 115406, DOI:[10.1103/PhysRevB.101.115406](https://doi.org/10.1103/PhysRevB.101.115406), 2020.
- VI** M.A. Silaev, R. Ojajärvi and T.T. Heikkilä. Spin and charge currents driven by the Higgs mode in high-field superconductors. *Physical Review Research* **2**, 033416, DOI:[10.1103/PhysRevResearch.2.033416](https://doi.org/10.1103/PhysRevResearch.2.033416), 2020.
- VII** R. Ojajärvi, T.T. Heikkilä, P. Virtanen and M.A. Silaev. Giant enhancement to spin battery effect in superconductor/ferromagnetic insulator systems. *Physical Review B* **103**, 224524, DOI:[10.1103/PhysRevB.103.224524](https://doi.org/10.1103/PhysRevB.103.224524), 2021.
- VIII** R. Ojajärvi, F.S. Bergeret, M.A. Silaev and T.T. Heikkilä. Dynamics of two ferromagnetic insulators coupled by superconducting spin current. *arXiv preprint*, [arXiv:2107.09959](https://arxiv.org/abs/2107.09959) [cond-mat.supr-con], 2021.
- IX** Y. Lu, R. Ojajärvi, P. Virtanen, M.A. Silaev and T.T. Heikkilä. Coupling the Higgs mode and ferromagnetic resonance in spin-split superconductors with Rashba spin-orbit coupling. *arXiv preprint*, [arXiv:2108.06202](https://arxiv.org/abs/2108.06202) [cond-mat.supr-con], 2021.

LIST OF CODES

Publicly available numerical codes to which I have contributed.

<https://gitlab.jyu.fi/jyucmt/fi-sc-fi>

Codes for Publication **VIII**. Includes a solver for the spin susceptibility of dirty superconductor in the thin-film limit, and a solver for Usadel equation for thick FI/SC/FI structures.

<https://gitlab.jyu.fi/jyucmt/sssc-higgs-rashba>

Codes for Publication **IX**. Includes a solver for the Higgs-mode enhanced spin susceptibility of a dirty superconductor with Rashba spin-orbit coupling.

AUTHOR'S CONTRIBUTION

The research presented in this thesis was conducted by me in collaboration with the listed authors during the years 2017–2021 in University of Jyväskylä. The specific contributions for the individual publications are detailed below.

The initial form of Publication **I** was based on my master's thesis and my contribution was to develop the theory, do the numerical calculations and write the first version of the manuscript. For Publication **II**, I did the numerical and analytical calculations based on the tight-binding model. For Publication **III**, I derived the electron-phonon heat conductance and wrote a part of the manuscript. For Publication **IV**, I participated in developing the theory and in particular developed the model for the electron-electron interactions. For Publication **V**, I derived many of the analytical results, using the action derived by Pauli Virtanen, wrote the numerical codes and participated in writing the manuscript. For Publication **VI**, I made many of the calculations and participated in writing the manuscript. For Publication **VII**, I derived and wrote the numerical codes for the perturbation theory calculations and participated in writing of the manuscript. For Publication **VIII**, I did all the calculations and wrote most of the manuscript. For Publication **IX**, I wrote the numerical code and participated in writing the manuscript.

CONTENTS

Abstract

Tiivistelmä (Abstract in Finnish)

Preface

List of Publications

List of Codes

Author's Contribution

Contents

1	Introduction	13
2	Superconductivity and magnetism in equilibrium	16
2.1	Superconductivity	16
2.1.1	Bogoliubov-de Gennes equations	17
2.1.2	BCS theory for metals	19
2.1.3	Phonon-mediated superconductivity	20
2.1.4	Coulomb interaction	23
2.2	Simple models for magnetism	25
2.2.1	Heisenberg model	26
2.2.2	Stoner model	26
2.3	Superconductivity and magnetism on flat electronic bands	28
2.3.1	Flat bands in ABC graphite	28
2.3.2	Competition between magnetism and superconductivity	31
2.3.3	Magic-angle twisted bilayer graphene	34
3	Non-equilibrium superconductivity	38
3.1	Keldysh formalism	38
3.1.1	Keldysh contour	39
3.1.2	Real-time matrix structure	40
3.1.3	Full counting statistics	42
3.2	Quasiclassical theory of superconductivity	42
3.2.1	Eilenberger equation	43
3.2.2	Usadel equation	45
3.2.3	Spectral equation	46
3.2.4	Kinetic equation	47
3.2.5	Self-energies	48
3.2.6	Self-consistency equation	49
3.2.7	Observables	50
3.2.8	Quasiclassical symmetries	51
3.2.9	Boundary conditions	52
3.2.10	Parametrization of the spectral functions	53
4	Superconducting spintronics	55
4.1	Spin-splitting field in a superconductor	56

4.1.1	Magnetic proximity effect	58
4.1.2	Thermoelectric effects at the SC/FM interface	60
4.2	Magnetization dynamics and spin pumping.....	62
4.2.1	Landau-Lifschitz-Gilbert equation	62
4.2.2	Ferromagnetic resonance.....	63
4.2.3	Spin pumping in the normal state.....	64
4.2.4	Spin-transfer torque.....	66
4.3	Spin pumping in the superconducting state	67
4.3.1	Boundary condition to a ferromagnetic metal.....	69
4.3.2	Boundary condition to a ferromagnetic insulator	71
4.3.3	Spin supercurrent.....	72
4.4	Higgs mode.....	73
4.5	Spin-orbit coupling	75
5	Conclusions and summary	77
	Bibliography	79
	Publications	

1 INTRODUCTION

In 1959, Richard Feynman gave a lecture "There's Plenty of Room at the Bottom" at an American Physical Society meeting in Caltech in which he imagined the possibilities of manipulating and controlling matter at very small scales, all the way to the atomic scale.[1] Feynman's lecture has often been cited as the starting point of nanoscience. Although such attribution is historically incorrect,[2] the lecture still seems almost prophetic from today's perspective, and many of the advances Feynman called for have been achieved in last few decades.

Such improved control over the nanoscale fabrication processes and technologies like scanning tunnelling microscope, together with digital tools and rapidly increasing theoretical understanding of condensed matter systems, have given rise to a concept of designer materials, which are artificial materials tailored to have the desired functionalities. Possible functionalities that can be controlled not only encompass the mechanical and electrical properties of the materials, but also their quantum properties, such as susceptibility to certain phase transitions.[3, 4] On the atomic scale, we are of course bound to work with the elements of the periodic table and with the chemistry between them, there is no way around that. However, on the wide intermediate scale between the atomic and the macroscopic scales, which I refer here as nanoscale, there remains a large freedom in the ways the atoms or molecules can be organized. Different structures imply different functionalities to be exploited in technologies that promise more energy-efficient information processing or data storage units, sensors with improved sensitivity, or building blocks for the quantum computer.

This dissertation is situated in the realm of theoretical condensed matter physics. It can be roughly divided into two main topics which share some common themes. A central theme that runs through the whole dissertation is the phenomenology of superconductivity and magnetism, and their interplay on mesoscopic scale. As phases of electronic matter, superconductivity and ferromagnetism have some similarities. Both are macroscopic manifestations of quantum mechanical properties of matter and exhibit a special kind of coherence. For a superconductor, this coherence is in the quantum-mechanical phase of the Cooper pair wavefunction, whereas for a ferromagnet it is the spin directions of the individual electrons that are locked

together. In macroscopic materials there is not much interplay between the two states, as they are largely incompatible with one another; the (*s*-wave) superconducting state requires a symmetry between the spins, whereas the ferromagnetic state is based on breaking of that symmetry.

The first main topic of the dissertation is the phenomenology of flat electronic bands and phase transitions on them. The defining property of the flat band materials is the large degeneracy in the electronic spectrum, which makes them strongly correlated and prone to many kinds of phase transitions. One example of a flat-band system is the magic-angle twisted bilayer graphene (MATBG), which was first fabricated in 2018, and which was the first purely graphene-based system in which superconductivity was found in a repeatable fashion. MATBG is composed of two graphene sheets held together by van der Waals forces, and it is a prototypical example of a more general class of designer materials known as the van der Waals materials. materials.[5]

In the publications that are related to this topic, we e.g., consider the competition between superconductivity and magnetism of a flat band model, show that superconductivity in MATBG is compatible with the phonon-mechanism of superconductivity, and classify the topological transitions on graphite-like rhombohedral honeycomb lattices.

The second main topic of the dissertation is the interplay between magnetism and superconductivity in more perhaps more traditional kind of artificial materials which are composed of thin films of magnetic and superconducting materials. What makes such hybrid structures interesting is that in small length scales the boundaries between the superconducting and magnetic parts of the system become blurred by the so-called proximity effects. If a superconductor is placed in contact with a ferromagnet, Cooper pairs tend to spill out of the superconductor and induce some superconducting properties to the ferromagnet. At the same time, the magnetic correlations leak into the superconductor, which becomes magnetically polarized.

The proximity effects induce a plethora of secondary effects which are studied in this dissertation. In particular, I study their effect on spin transport. Together with my collaborators, we predict e.g., a cooling effect due to precessing magnetization, a giant spin battery effect, and dynamic effects related to antiferromagnetic coupling between two ferromagnetic insulators mediated by spin supercurrent. Two of the publications discuss the Higgs mode or the amplitude mode of the superconducting order parameter, which can be coupled to the charge degree of freedom by the magnetic proximity effect.

In this dissertation, I use mostly the natural units in which $\hbar = k_B = 1$. When relevant, for example when comparing to values in SI units, \hbar and k_B are restored to the equations.

Organization of the thesis

The dissertation is composed of two parts: the included publications, and this overview which serves as an introduction to the publications. In the overview, the focus is on the underlying theoretical framework and concepts, and on the connections

between the works. In the overview, the publications themselves are only shortly summarized, and some of the key results are highlighted.

The organization of the overview is as follows. Chapter 2 introduces the basic concepts of electron-phonon superconductivity and ferromagnetism in equilibrium. We apply these concepts to systems with flat electronic bands, focusing on two graphene-based systems: twisted bilayer graphene and rhombohedrally stacked multilayer graphene. As an example of topologically protected flat bands, we discuss the properties of rhombohedrally stacked multilayers.

We then shift the topic to the interplay between magnetism and superconductivity in conventional metals interfaced with magnetic materials. Chapter 3 introduces the theoretical tools used to describe non-equilibrium superconductivity: the Keldysh formalism for non-equilibrium states, and the quasiclassical theory of superconductivity. In Chapter 4 we introduce the field of spintronics and apply the tools of nonequilibrium superconductivity to superconducting spintronics.

2 SUPERCONDUCTIVITY AND MAGNETISM IN EQUILIBRIUM

2.1 Superconductivity

Superconductivity was discovered in 1911 by H. Kamerlingh Onnes. [6] Kamerlingh Onnes was a pioneer of low-temperature physics and had been the first to liquefy helium few years earlier. He used the liquid helium as a refrigerant for studying the electrical resistivity of metals at low temperatures, and noticed that the resistance of a mercury wire abruptly vanished at 4.2K. Kamerlingh Onnes realized the wire had passed to a new state of matter, and named the phenomenon *superconductivity*. Another effect which characterizes the superconducting state is the Meissner effect [7], which is the expulsion of magnetic fields from the bulk of the superconductor.

What is the common factor for these seemingly separate effects? A partial answer was given in 1935 when a set of phenomenological equations describing the electrodynamics of a superconductor were developed by brothers Fritz and Heinz London. [8] According to these equations a superconductor supports a *supercurrent*

$$\mathbf{j}_s = -D_s \mathbf{A}, \quad (1)$$

where D_s is the superfluid weight, a constant related to the density of the superconducting carriers, and \mathbf{A} is the vector potential¹. What distinguishes supercurrents from regular ohmic currents is that they are dissipationless and can exist even in equilibrium.²

It is easy to see that the supercurrent naturally explains the observed zero resistivity of superconductors. To see that the Meissner effect can also be explained in the same terms, we invoke Ampère's law $\nabla \times \mathbf{B} = \mu_0 \mathbf{j}_s$, where \mathbf{B} is the magnetic

¹ Eq. (1) is valid in the London gauge, in which $\nabla \cdot \mathbf{A} = 0$, $\mathbf{A} = 0$ in the superconductor bulk, and $\mathbf{n} \cdot \mathbf{A} = 0$, where \mathbf{n} is a surface normal of the superconductor.

² Dissipationless currents can also exist in the normal (non-superconducting) state, for example in rings with nonzero magnetic flux threaded through, but in the normal state they are very small because there is no phase coherence and different components of the current tend to cancel each other.

flux density and μ_0 is the vacuum permeability. Taking the curl from both sides, we find that the magnetic field obeys the equation

$$(\nabla^2 - \mu_0 D_s) \mathbf{B} = 0, \quad (2)$$

which means that magnetic fields are screened from the bulk of the superconductor with the characteristic scale $\lambda_L = 1/\sqrt{\mu_0 D_s}$ called the London penetration depth. The screening is due to the circulating surface supercurrents induced by the magnetic field.

Despite their success, the London equations offer little insight into the nature of the superconducting state or the supercurrent. In 1950 Ginzburg and Landau [9] proposed a phenomenological free energy model, in which the transition to the superconducting state occurs as a spontaneous breaking of the electromagnetic $U(1)$ gauge symmetry, and the supercurrent is given by the phase gradient of the order parameter. The existence of the supercurrent (1) is thus explained by the phase rigidity³ of the superconducting state quantified by superfluid weight D_s .

A satisfactory microscopic description of superconductivity in terms of a many-body wavefunction was finally given in 1957 by Bardeen, Cooper and Schrieffer [10]. This theory now known as the *BCS theory* forms the basis for our understanding of superconductivity. The key element of the BCS theory is the coupling between electrons and phonons, the vibrations of the atomic lattice. At low frequencies, the phonon system mediates a weak attractive interaction between the electrons. This attraction then leads to an instability of the electron system, and a new superconducting ground state with broken symmetry forms, as in the Ginzburg-Landau theory. The London equation (1) emerges from the BCS theory at the long-wavelength, low temperature limit.

2.1.1 Bogoliubov-de Gennes equations

To study the BCS theory in more detail, let us consider a Hamiltonian consisting of a single particle part H_0 and a local attractive interaction

$$H = \sum_{\sigma\sigma'} \int d\mathbf{x} \left[\psi_{\sigma}^{\dagger}(\mathbf{x}) H_0(\mathbf{x})_{\sigma\sigma'} \psi_{\sigma'}(\mathbf{x}) - V \psi_{\uparrow}^{\dagger}(\mathbf{x}) \psi_{\downarrow}^{\dagger}(\mathbf{x}) \psi_{\downarrow}(\mathbf{x}) \psi_{\uparrow}(\mathbf{x}) \right], \quad (3)$$

where $\psi_{\sigma}(\mathbf{x})$ is the field operator for electron with spin σ and $V > 0$ is the strength of the attractive interaction. This attractive interaction serves as a toy model for the attractive part of the electron-phonon interaction. Next comes the magic step: To diagonalize the Hamiltonian, we approximate the interaction term with a mean field in the particle-hole channel as

$$\lambda \psi_{\uparrow}^{\dagger}(\mathbf{x}) \psi_{\downarrow}^{\dagger}(\mathbf{x}) \psi_{\downarrow}(\mathbf{x}) \psi_{\uparrow}(\mathbf{x}) \approx \Delta(\mathbf{x})^* \psi_{\downarrow}(\mathbf{x}) \psi_{\uparrow}(\mathbf{x}) + \psi_{\uparrow}^{\dagger}(\mathbf{x}) \psi_{\downarrow}^{\dagger}(\mathbf{x}) \Delta(\mathbf{x}) - \frac{|\Delta(\mathbf{x})|^2}{V} \quad (4)$$

where $\Delta(\mathbf{x}) = \lambda \langle \psi_{\downarrow}(\mathbf{x}) \psi_{\uparrow}(\mathbf{x}) \rangle$ is the anomalous correlator, and the order parameter for the superconducting state. Since BCS theory formulated in terms of simplified

³ Phase rigidity is related to the energy cost of the order parameter phase gradient.

interactions and band structures does not accurately represent the normal state of any real material, we disregard the normal state Hartree-Fock mean-field terms which are not specific to the superconducting state.

The peculiar property of the superconducting mean-field is that the Hamiltonian does not conserve particle number, as it contains terms of the form $\psi_\mu\psi_\nu$ and $\psi_\mu^\dagger\psi_\nu^\dagger$. This reflects the fact that charge can be transported by the superconducting condensate. The charge conservation is not violated as long as the order parameter is calculated in a self-consistent way. To diagonalize the Hamiltonian we need to expand the space in which we are operating. We define a bi-spinor

$$\Psi(\mathbf{x}) = \left(\psi_\uparrow(\mathbf{x}) \quad \psi_\downarrow(\mathbf{x}) \quad -\psi_\downarrow^\dagger(\mathbf{x}) \quad \psi_\uparrow^\dagger(\mathbf{x}) \right)^\top, \quad (5)$$

in which the last two components are the time-reversed copies of the first two. We refer to this extra structure as the Nambu space, so that the above spinor is the outer product of Nambu and spin spaces. The mean-field Hamiltonian can be written as

$$H = \frac{1}{2} \int d\mathbf{x} \Psi^\dagger(\mathbf{x}) \underbrace{\begin{pmatrix} \hat{H}_0(\mathbf{x}) & \hat{\Delta}(\mathbf{x}) \\ \hat{\Delta}^\dagger(\mathbf{x}) & -\sigma_2 \hat{H}_0(\mathbf{x})^* \sigma_2 \end{pmatrix}}_{H_{\text{BdG}}} \Psi(\mathbf{x}), \quad (6)$$

where σ_i are the Pauli matrices in spin space. Correspondingly, the Pauli matrices in Nambu space are denoted by τ_j . We have chosen the structure of the time-reversed spinor in Eq. (5) so that the s -wave order parameter is proportional to unit matrix in spin space, $\hat{\Delta} = \Delta\sigma_0$. The factor of one-half in front of the Hamiltonian is due to double counting of the degrees of freedom in the Nambu spinor. This *particle-hole redundancy*⁴ is reflected in the relation

$$\Psi^\dagger(\mathbf{x}) = -[\sigma_2\tau_2\Psi(\mathbf{x})]^\top, \quad (7)$$

between the Nambu spinor creation and annihilation operators. The particle-hole redundancy also constrains the possible forms of the Bogoliubov-de Gennes (BdG) Hamiltonian H_{BdG} , so that it always has the symmetry

$$\sigma_2\tau_2 H_{\text{BdG}}(\mathbf{x}, \mathbf{x}')^* \sigma_2\tau_2 = -H_{\text{BdG}}(\mathbf{x}, \mathbf{x}'). \quad (8)$$

The normalized solutions $w_n(\mathbf{x})$ of the BdG Hamiltonian are found by solving the eigenvalue equation

$$\int d\mathbf{x}' H_{\text{BdG}}(\mathbf{x}, \mathbf{x}') w_n(\mathbf{x}') = E_n w_n(\mathbf{x}). \quad (9)$$

From a single solution $w_n(\mathbf{x})$, one can define a Bogoliubov operator for a quasiparticle excitation

$$\gamma_n = \mathcal{V}^{-1} \int d\mathbf{x} w_n^\dagger(\mathbf{x}) \Psi(\mathbf{x}), \quad (10)$$

⁴ Also known as charge conjugation symmetry. [11] The particle-hole redundancy is distinct from the particle-hole symmetry, which refers to the symmetry between the normal state electron and hole excitations. In ideal metals there is an approximate particle-hole symmetry at low energy.

which is a mixture of particle and hole excitations and has a non-integer charge. The particle-hole redundancy implies that given an eigenvector w_n , there is a particle-hole conjugated eigenvector $w_{\bar{n}} = \sigma_2 \tau_2 w_n^*$ with energy $E_{\bar{n}} = -E_n$. The associated annihilation and creation operators are related by $\gamma_n^\dagger = \gamma_{\bar{n}}$. One can use this to remove any reference to the negative-energy states. The inverse transformation from Nambu field operators to positive-energy Bogoliubov operators is

$$\Psi(\mathbf{x}) = \sum_{E_n > 0} [w_n(\mathbf{x})\gamma_n + w_{\bar{n}}(\mathbf{x})\gamma_n^\dagger]. \quad (11)$$

The Bogoliubov transformation to the quasiparticle basis gives a diagonal Hamiltonian

$$H = \sum_{E_n > 0} E_n \gamma_n^\dagger \gamma_n + \text{const.}, \quad (12)$$

where the restricted set of positive energy Bogoliubov creation/annihilation operators have the usual fermionic anticommutation relations $\{\gamma_n, \gamma_m^\dagger\} = \delta_{nm}$ and $\{\gamma_n, \gamma_m\} = 0$. Thus, the quasiparticle excitations obey Fermi-Dirac statistics. In thermal equilibrium, the expectation values are given by $\langle \gamma_n^\dagger \gamma_m \rangle = \delta_{nm} f(E_n)$, where $f(E)$ is the Fermi-Dirac distribution function.

When the eigenstates have been solved, the value of the order parameter can be determined from the *self-consistency equation*, i.e. the definition of Δ :

$$\begin{aligned} \Delta(\mathbf{x}) &= \lambda \langle \psi_\uparrow(\mathbf{x}) \psi_\downarrow(\mathbf{x}) \rangle = \frac{\lambda}{4} \langle \Psi^\dagger(\mathbf{x}) (\tau_1 - i\tau_2) \Psi(\mathbf{x}) \rangle \\ &= \frac{\lambda}{4} \sum_{E_n > 0} v_n^\dagger(\mathbf{x}) u_n(\mathbf{x}) \tanh\left(\frac{E_n}{2T}\right), \end{aligned} \quad (13)$$

where u_n and v_n are the electron and hole parts of the bispinor $w_n^\top = (u_n^\top \ v_n^\top)$.

The order parameter and the eigenstates depend on each other, and are usually solved by iteration: (1) The eigenstates for $H_{\text{BdG}}[\Delta]$ are solved with fixed Δ . (2) The eigenstates are substituted into the self-consistency equation and Δ is updated. One starts with some initial guess for Δ and repeats the steps (1) and (2) until Δ converges.

2.1.2 BCS theory for metals

The above is the general theory for any s -wave superconductor with local attractive interaction. In a translation-invariant and isotropic system with the normal state Hamiltonian $H_0 = \varepsilon_p - \mu$, and assuming that the value of Δ does not depend on position, the eigenstates are plane waves and the self-consistency equation becomes

$$\Delta = \lambda \int_{-\omega_D}^{\omega_D} d\varepsilon N(\varepsilon) \frac{\Delta}{\sqrt{\varepsilon^2 + |\Delta|^2}} \tanh\left(\frac{\sqrt{\varepsilon^2 + |\Delta|^2}}{2T}\right), \quad (14)$$

where $N(\varepsilon)$ is the density of states at energy ε relative to the chemical potential μ in the normal state. To regularize the theory, we have inserted a cutoff at the Debye frequency $\omega_D \ll \mu$, which is related to the typical phonon frequency. When

the Fermi energy is large compared to the Debye frequency, the density of states is almost constant within the cutoff, and we can approximate $N(\varepsilon) \approx N_0$ where N_0 is the density of states at Fermi energy, and define a dimensionless interaction constant $g = \lambda N_0$. Adding a cutoff is required due to the simplified interaction model. Below we see that a more detailed description of electron-phonon interaction provides a natural soft cutoff.

The simplest observables one can calculate from the BCS theory are Δ_0 , the order parameter at zero temperature, which determines the gap of the excitation spectrum, and the transition temperature

$$T_c = \omega_D \exp(-1/g), \quad (15)$$

where we have assumed weak coupling $g \ll 1$. In metals the zero-temperature gap is related to the transition temperature by the ratio $\Delta_0/T_c \approx 1.764$. This ratio is universal in the sense that it does not depend on the value of g or ω_D . However, it does depend on the interaction model and on the details of the electronic dispersion.

The BdG approach puts the emphasis on the diagonalization of the Hamiltonian and is suited for clean systems which are periodic or otherwise simple enough. We use the BdG approach in Publication **IV** to study superconductivity on twisted bilayer graphene. For inhomogeneous problems, non-equilibrium states, or disordered systems, it is better to use Green's function methods, which allow more varied approximation schemes.

2.1.3 Phonon-mediated superconductivity

Conventional *s*-wave superconductivity requires an attractive interaction between the electrons. In most of the superconductors this is provided by the phonon system which interacts with an electron and mediates a retarded response to the other electrons. In most of the included publications we do not focus on the interaction mechanism, but model the interaction with the simplified BCS interaction as above. In contrast to that, in Publication **I** we are interested in the frequency-dependence of the electron-phonon interaction. In Publications **I** and **IV** we also discuss the effect of Coulomb interaction on the superconducting state. In Publications **III** and **VII** we also consider the other major role the phonon system has; it acts as a heat bath for the electrons.

To give some background for the publications, let us now discuss the Eliashberg theory, which is a field-theoretical formulation of the electron-phonon superconductivity that goes beyond the instantaneous BCS interaction and describes all the above effects in a natural way.[12] A classic text which gives a good introduction to electron-phonon superconductivity is due to Schrieffer.[13] There is also a recent review on the contemporary formulations by Marsiglio.[14] In this section we concentrate on the equilibrium properties of electron-phonon superconductors. The electron-phonon energy relaxation is described in Sec. 3.2.5.

The Hamiltonian for the coupled electron-phonon system is

$$H = H_e + H_{e-e} + H_{ph} + H_{e-ph}, \quad (16)$$

where $H_{e/\text{ph}}$ are the Hamiltonians for free electrons and free phonons. H_{e-e} contains the Coulomb interaction between the electrons, and $H_{e-\text{ph}}$ is the interaction between the electrons and phonons. Let us at first disregard the Coulomb interaction and only consider the electron-phonon interaction, given by

$$H_{e-\text{ph}} = \sum_{\mathbf{p}, \mathbf{q}, s} (g_{\mathbf{p}\mathbf{q}} \varphi_{\mathbf{q}}^{\dagger} + g_{\mathbf{p}\mathbf{q}}^* \varphi_{-\mathbf{q}}) c_{\mathbf{p}-\mathbf{q}, s}^{\dagger} c_{\mathbf{p}, s}, \quad (17)$$

where $\varphi_{\mathbf{q}}^{\dagger}$ is the bosonic creation operator for a phonon with momentum \mathbf{q} , $c_{\mathbf{p}\sigma}^{\dagger}$ is the electron creation operator, and $g_{\mathbf{p}\mathbf{q}}$ is the electron-phonon coupling constant. In practice, there are multiple phonon branches which can contribute to the interactions between the electrons, but for simplicity, we consider here only a single branch.

The Green's function (GF) method allows for a natural description of the dynamic phonon-mediated interaction. In the superconducting state, we define the electronic GF as the matrix

$$\hat{G}(1, 2)_{\mu\nu} = -(\tau_3)_{\mu\mu} \langle \mathcal{T}_{\tau} \Psi_{\mu}(1) \Psi_{\nu}^{\dagger}(2) \rangle, \quad (18)$$

where the indices μ and ν indicate the Nambu-spin components. Correspondingly, the phonon propagator is defined as

$$D(1, 2) = -D \langle \mathcal{T}_{\tau} \varphi(1) \varphi^{\dagger}(2) \rangle, \quad (19)$$

where the condensed notation $1 = (\mathbf{x}_1, \tau_1)$ includes the space and imaginary time variables, \mathcal{T}_{τ} is the contour-ordering operator for the imaginary-time contour, and the operators are in the Heisenberg picture $\Psi^{(\dagger)}(1) = e^{H\tau_1} \Psi_S^{(\dagger)}(\mathbf{x}_1) e^{-H\tau_1}$. The conventional τ_3 Pauli matrix is introduced into the electronic GF in order to make the resulting equations more symmetric.

The electron and phonon GFs are determined from the Dyson equations

$$\hat{G}^{-1} = \hat{G}_0^{-1} - \hat{\Sigma}, \quad (20)$$

$$D^{-1} = D_0^{-1} - \Pi, \quad (21)$$

where Σ and Π are the electron and phonon self-energies, respectively. The free-electron and free-phonon propagators are $G_0 = [i\omega_n \tau_3 - \xi_{\mathbf{p}} \tau_0]^{-1}$, and $D_0(\mathbf{q}, i\nu_n) = -2\omega_{\mathbf{q}} / (\omega_{\mathbf{q}}^2 + \nu_n^2)$, where $\xi_{\mathbf{p}}$ and $\omega_{\mathbf{q}}$ are the electron and phonon dispersion relations, and ω_n and ν_n are fermionic and bosonic Matsubara frequencies, respectively. The self-energies can be defined as the sums of all the irreducible single-particle Feynman diagrams.

In a fully self-consistent theory, the phonon and electron self-energies depend on each other, but in Eliashberg theory one typically adopts a view that the phonon parameters which determine the propagator D_0 are to be obtained from experiment and we should not do any further renormalizations to them in the theory, as this would correspond to an overcounting of the diagrams. Thus the phonon propagator is assumed as given. Similarly, the electronic properties of the normal metal are assumed as given so that one only needs to consider the parts of the self-energy which depend on superconductivity. Modern variants of the Eliashberg theory often

take a different approach, aiming to solve the properties of the coupled system of electrons and phonons from the first principles.[14]

The lowest order contribution to the electronic self-energy is given by the Fock diagram which describes a virtual phonon emission from an electron and its subsequent absorption:

$$\hat{\Sigma}_{\text{e-ph}}(p) = \sum_{p'} g^2 D(p-p') \tau_3 \hat{G}(p') \tau_3 \quad (22)$$

This self-energy can be decomposed into four Nambu components Z , χ , $\text{Re } \phi$ and $\text{Im } \phi$ as

$$\hat{\Sigma}_{\text{e-ph}}(p) = i[1 - Z(p)]\omega_n \tau_3 + \chi(p)\tau_0 + i\hat{\phi}(p), \quad (23)$$

where $\hat{\phi}(p) = \text{Re } \phi(p)\tau_1 + \text{Im } \phi(p)\tau_2$. If there are no other self-energies to consider, the GF is

$$\begin{aligned} \hat{G}(\mathbf{p}, \omega_n) &= [i\omega_n \tau_3 - \xi_{\mathbf{p}} \tau_0 - \hat{\Sigma}_{\text{e-ph}}(\mathbf{p}, \omega_n)]^{-1} \\ &= \frac{[\xi_{\mathbf{p}} + \chi(\mathbf{p}, \omega_n)]\tau_0 - iZ(\mathbf{p}, \omega_n)\omega_n \tau_3 + i\hat{\phi}(\mathbf{p}, \omega_n)}{\Omega(\mathbf{p}, \omega_n)}, \end{aligned} \quad (24)$$

where $\Omega(\mathbf{p}, \omega_n) = [Z(\mathbf{p}, \omega_n)\omega_n]^2 + [\xi_{\mathbf{p}} + \chi(\mathbf{p}, \omega_n)]^2 + |\phi(\mathbf{p}, \omega_n)|^2$. The different components have different roles: Z renormalizes the quasiparticle weight, χ is a frequency and momentum dependent renormalization of the chemical potential, and ϕ is the superconducting order parameter. The usual notation Δ for the order parameter is reserved for the the renormalized quantity

$$\hat{\Delta}(\omega_n) \equiv \frac{\hat{\phi}(\omega_n)}{Z(\omega_n)}, \quad (25)$$

which is more closely related to the excitation gap than ϕ .

Substituting Eq. (24) into the electron-phonon self-energy (22), we obtain the *Eliashberg equations*,

$$\phi(\mathbf{p}, i\omega_n) = - \int \frac{d\mathbf{p}'}{(2\pi)^3} T \sum_m g_{\mathbf{p}-\mathbf{p}'}^2 D(\mathbf{p}-\mathbf{p}', i\omega_n - i\omega_m) \frac{\phi(\mathbf{p}', i\omega_m)}{\Omega(\mathbf{p}', i\omega_m)}, \quad (26)$$

$$Z(\mathbf{p}, i\omega_n) = 1 - \int \frac{d\mathbf{p}'}{(2\pi)^3} T \sum_m g_{\mathbf{p}-\mathbf{p}'}^2 D(\mathbf{p}-\mathbf{p}', i\omega_n - i\omega_m) \frac{\omega_m Z(\mathbf{p}', i\omega_m)}{\omega_n \Omega(\mathbf{p}', i\omega_m)}, \quad (27)$$

$$\chi(\mathbf{p}, i\omega_n) = + \int \frac{d\mathbf{p}'}{(2\pi)^3} T \sum_m g_{\mathbf{p}-\mathbf{p}'}^2 D(\mathbf{p}-\mathbf{p}', i\omega_n - i\omega_m) \frac{\xi_{\mathbf{p}'} + \chi(\mathbf{p}', i\omega_m)}{\Omega(\mathbf{p}', i\omega_m)}, \quad (28)$$

which are the set of self-consistency equations for the superconducting state. They can be regarded as a generalization of the self-consistency Eq. (13). For a metal with a large Fermi energy $\mu \gg \omega_D$ the equations can be simplified as before by noting that the self-energy is largely independent of $|\mathbf{p}|$ and we can carry out the $|\mathbf{p}|$ integral, so that only the properties of the Fermi surface matter.

The BCS model is recovered from the Eliashberg theory by approximating the interaction as a constant interaction which only exists at low energies

$$g^2 D(\omega_n, \omega_m) N_0 \rightarrow \lambda \theta(|\omega_n| - \omega_D) \theta(|\omega_m| - \omega_D).$$

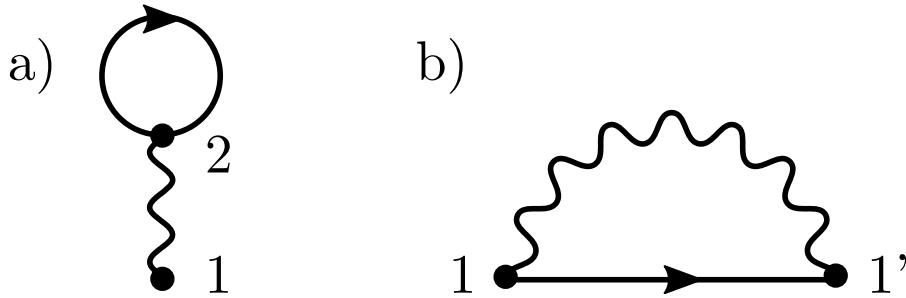


FIGURE 1 a) Hartree diagram. b) Fock diagram. The solid line is the electron propagator, and the wiggly line is the interaction.

χ vanishes in metals due to (approximate) electron-hole symmetry, but the quasi-particle renormalization Z does not vanish. For weak coupling $Z \approx 1 - g$, and the self-consistency equation becomes

$$\Delta = \frac{\phi}{Z} \approx \frac{g}{1+g} \sum_{|\omega| < \omega_D} \frac{\Delta}{\sqrt{\omega_n^2 + |\Delta|^2}}, \quad (29)$$

which is the BCS equation with a renormalized coupling.

The above is for a metallic system. In Sec. 2.3 and Publication I we formulate the Eliashberg theory for a flat band system, in which the Debye energy is larger than the bandwidth of the electronic band. Flat bands are generally very favorable to phase transitions, and we find that electron-phonon superconductivity is no exception.

2.1.4 Coulomb interaction

Surprisingly, even though the direct Coulomb interaction between the electrons is the strongest interaction in the system, it can be mostly disregarded in the theory of superconductivity. This is partially due to the general philosophy of the Eliashberg theory, which assumes that the normal state properties are already taken into account in the parameters of the single-particle Hamiltonian, and we are just studying the residual superconducting effects. The diagonal (in Nambu space) Coulomb self-energies are thus usually discarded, or considered as Fermi liquid effects. That the residual effects of Coulomb interaction on the superconducting state are small can be traced to the separation between the phonon and electron scales ω_D and E_F . Let us see how this goes in some detail.

For simplicity, instead of starting from the microscopic Coulomb interaction and describing the screening in detail, we model the screened Coulomb interaction with a local Hubbard interaction

$$H'_{e-e} = U \int d\mathbf{x} \psi_{\uparrow}^{\dagger}(\mathbf{x}) \psi_{\downarrow}^{\dagger}(\mathbf{x}) \psi_{\downarrow}(\mathbf{x}) \psi_{\uparrow}(\mathbf{x}), \quad (30)$$

where the Hubbard parameter $U > 0$ determines the strength of the interaction. The lowest order diagrams for the self-energy related to this interaction are the Hartree and Fock diagrams shown in Fig. 1. Together, they give the self-energy

$$\hat{\Sigma}_C = U \sum_p \left(\tau_3 \text{Tr}[\hat{G}(p)\tau_3] - \tau_3 \hat{G}(p)\tau_3 \right), \quad (31)$$

where the first term is called the Hartree term and the second one is called the Fock term. The Hartree term describes a classical interaction between the electrons and the local charge density. It is only relevant when we are interested in the capacitance of the system or when the electron distribution is inhomogeneous, as otherwise it can be included into the chemical potential. The Fock term on the other hand describes a quantum mechanical process of an emission and absorption of a virtual photon. Unlike the phonon-mediated interaction, the Coulomb interaction is practically instantaneous and does not have a high-energy cutoff. This is also reflected in the fact that the Coulomb self-energy does not depend on frequency.

Let us consider how the Coulomb interaction affects superconductivity. The Nambu off-diagonal component of the Fock diagram gives a correction to the order parameter

$$\phi_C = U \int \frac{d\mathbf{p}'}{(2\pi)^3} T \sum_{\omega_m} \frac{\phi(\mathbf{p}', i\omega_m)}{\Omega(\mathbf{p}', i\omega_m)}, \quad (32)$$

so that the full order parameter ϕ includes contributions from both electron-phonon and Coulomb interactions, $\phi(\omega_n) = \phi_{\text{ph}}(\omega_n) + \phi_C$. Here ϕ_{ph} is defined by Eq. (26) by using the full ϕ on the right hand side and ϕ_{ph} on the left hand side of that equation. Since the Coulomb interaction is repulsive, it does not by itself cause a superconducting instability in the s -wave channel, but it can modify and suppress the instability induced by the phonon-mediated attraction.

In order to write the superconducting problem as an effective theory for the low-energy modes, we integrate out the high-energy modes $|\xi_{\mathbf{p}}| > \omega_D$ and high frequencies $|\omega_n| > \omega_D$ from the self-consistency equation. For the electron-phonon interaction, there is a soft cutoff and the Matsubara sums can be truncated at Debye frequency ω_D without much effect. For the Coulomb interaction, one splits the Matsubara sum into low and high-energy parts (Fig. 2), and uses the fact that $\phi_{\text{ph}} \approx 0$ and $\phi_C \ll \sqrt{\omega_n^2 + \xi_{\mathbf{p}}^2}$ at high frequencies to obtain the equation

$$\phi_C = U \sum_{p \in \text{low}} \frac{\phi}{\Omega(\mathbf{p}, \omega_n)} + U \sum_{p \notin \text{low}} \frac{\phi_C}{\omega_n^2 + \xi_{\mathbf{p}}^2}. \quad (33)$$

This can be partially solved for ϕ_C as

$$\phi_C = \frac{U}{1 + U\chi_h} \sum_{p \in \text{low}} \frac{\phi(\omega_n)}{\Omega(\mathbf{p}, \omega_n)}, \quad (34)$$

where

$$\begin{aligned} \chi_h &= \sum_{p \notin \text{low}} \frac{1}{\omega_n^2 + \xi_{\mathbf{p}}^2} = 2 \int_{-D}^D d\varepsilon \int_{\omega_D}^{\infty} \frac{d\omega}{2\pi} \frac{N(\varepsilon)}{\omega^2 + \varepsilon^2} \\ &\approx \bar{N} \ln \left(\frac{D}{\omega_D} \right), \end{aligned} \quad (35)$$

and we have approximated the electronic dispersion as if it had a constant density of states \bar{N} for energies $|\varepsilon| < D$, and assumed that the bandwidth D is large compared to the Debye frequency ω_D . This term diverges logarithmically as the bandwidth increases, and is not very sensitive to details of the dispersion.

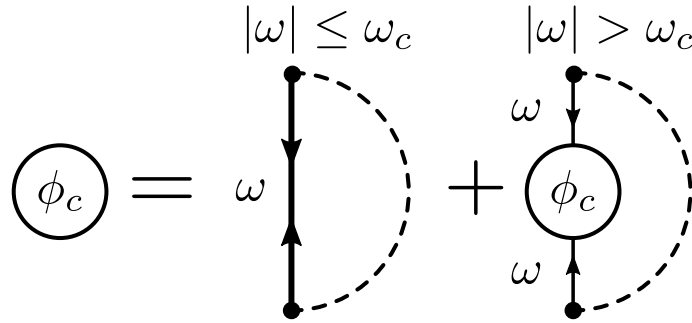


FIGURE 2 Self-energy diagram for the Coulomb pseudopotential effect. Dashed line is the Coulomb interaction, thin solid line with single arrow is the normal state propagator, thick solid line with double arrows is the anomalous propagator. At low energies the anomalous propagator is calculated self-consistently and includes the electron-phonon self-energy, whereas the high-energy propagator has been approximated with the lowest order contribution from the Coulomb self-energy.

After integrating out the high-energy bands and high Matsubara frequencies, we find a self-consistency equation which includes both interactions, and only refers to low Matsubara frequencies and low-energy bands

$$\phi(\mathbf{p}, i\omega_n) = - \int \frac{d\mathbf{p}'}{(2\pi)^3} T \sum_m \left[g_{\mathbf{p}-\mathbf{p}'}^2 D(\mathbf{p}-\mathbf{p}', i\omega_n - i\omega_m) - U^+ \right] \frac{\phi(\mathbf{p}', i\omega_m)}{\Omega(\mathbf{p}', i\omega_m)}. \quad (36)$$

The original Coulomb interaction has been replaced with a Coulomb pseudopotential $U^+ = U/(1 + U\chi_h)$, which approaches $1/\chi_h$ when $U \rightarrow \infty$. The physical picture for the Coulomb pseudopotential effect is that the high-energy pair correlations give a negative feedback for the low-energy pair correlations and try to suppress them.

In Sec. 2.3 we discuss Publications I and IV and consider the effect of the Coulomb pseudopotential on a flat band systems.

2.2 Simple models for magnetism

Let us now contrast superconductivity with another symmetry broken state; the ferromagnetic state. Both ferromagnetism and superconductivity are quantum mechanical phenomena in which a material obtains a macroscopic coherence. Unlike superconductivity, ferromagnetism occurs in common materials well above room temperature, and magnetic materials have been known since antiquity. The theoretical understanding of the microscopic origin of magnetism has only been acquired after the development of quantum mechanics.

Magnetization of a material occurs when the microscopic magnetic moments of the material become ordered. For a free electron, the magnetic moment is

$$\boldsymbol{\mu} = -\mu_B(\mathbf{L} + g\mathbf{S}), \quad (37)$$

where μ_B is the Bohr magneton, $g \approx 2$ is the electron g -factor, and \mathbf{L} and \mathbf{S} are the orbital and spin angular momentum, respectively. In many materials the

orbital contribution to magnetism can be disregarded, and here we only consider the magnetic moment due to spin. Because of the negative charge of an electron, its magnetic moment and spin point into opposite directions.

The magnetic moments in the materials can become ordered in different ways and the phenomenology of the magnetic materials is rich and varied. Let us introduce some simple classes of magnetic materials. In a *paramagnetic material*, unpaired spins of the material are randomized by thermal fluctuations and point into random direction, so that the total magnetic moment vanishes. If an external magnetic field is applied, there is an energy penalty of $E = g\mu_B \mathbf{B} \cdot \mathbf{S}$ which tends to align the individual electronic spins antiparallel to the magnetic field and the material obtains a total magnetic moment.

2.2.1 Heisenberg model

The material can also magnetize spontaneously due to interactions. This is exemplified by the Heisenberg model [15]

$$H = -J \sum_{\langle ij \rangle} \mathbf{S}_i \cdot \mathbf{S}_j, \quad (38)$$

where \mathbf{S}_i are the spin operators on some lattice and $\sum_{\langle ij \rangle}$ indicates the sum over pairs of nearest neighbours. The spin operators represent the spins of the unpaired valence electrons. If the exchange interaction J is positive, the energy is minimized when all the spins point in the same direction. The materials which have a ground state with this kind of arrangement are known as *ferromagnets*. The ferromagnetic state is a symmetry-broken state; in the absence of an external field, no single spin direction is preferred and the direction of the magnetization is picked spontaneously. At high temperatures the system is always in the non-symmetry-broken state. The temperature at which ferromagnetism vanishes is known as the *Curie temperature* (T_C). For $T > T_C$ the material is in the paramagnetic state, in which it can be magnetized by an external field, but has no intrinsic magnetization in the absence of such field.

If J is negative, the preferred arrangement can be more complicated. If the system is bipartite, i.e. can be divided into two interlocking lattices so that the nearest neighbours always belong to different lattices, then the ground state is *antiferromagnetic*; every other spin points in the up direction, and every other to the down direction. Again, “up“ is spontaneously chosen. In this case the total magnetic moment vanishes, but there still exists a magnetic order within the material. If the system is not bipartite, the configuration becomes frustrated, as one cannot simply minimize each term of the Hamiltonian individually to obtain the lowest energy configuration. In this case, the ground state can have a more complicated spin structure.

2.2.2 Stoner model

The Heisenberg model applies to insulating magnets with localized spins. In metals, the magnetism may also originate from the interactions between the delocalized

conduction electrons, described by the Stoner Hamiltonian [16]

$$H = \int d\mathbf{x} \left[\sum_{\sigma=\uparrow,\downarrow} \psi_{\sigma}^{\dagger}(\mathbf{x}) \left(-\frac{\nabla^2}{2m} - \mu \right) \psi_{\sigma}(\mathbf{x}) + U \psi_{\uparrow}^{\dagger}(\mathbf{x}) \psi_{\downarrow}^{\dagger}(\mathbf{x}) \psi_{\downarrow}(\mathbf{x}) \psi_{\uparrow}(\mathbf{x}) \right], \quad (39)$$

where ψ_{σ} are the field operators for the conduction electron with spin σ , and $U > 0$ is the repulsive Hubbard interaction. We assume that the number of electrons N is fixed. This model does not give a good description of magnetism in e.g. rare-earth metals, for which the magnetism originates from the localized $4f$ electrons. [17]

The Hamiltonian (39) is rotationally symmetric. The kinetic energy is minimized when the lowest energy states (in terms of the noninteracting dispersion) are filled equally for both spins. In the absence of interactions, $U = 0$, the ground state of the system is non-magnetic. However, when there are interactions, the spin symmetry can be spontaneously broken and the system can become spontaneously magnetized.

At the mean-field level, the energy contribution from interactions comes from the Hartree and Fock terms discussed above. The Hartree term only depends on the electron density and does not play a role here. In contrast, the Fock self-energy for an electron with spin σ depends only on the density of spin σ electrons. With repulsive U , the Fock energy is minimized when the system is fully polarized so that all the electrons have the same spin. However, such an arrangement increases the kinetic energy of the system, as the electrons have to occupy states with higher momentum. Thus, there is a competition between the kinetic energy and the Fock self-energy. If U is large enough to overcome the kinetic energy cost, there is an instability towards a magnetic state.

Let us calculate the critical interaction strength. In fact, we have already done all the heavy work when discussing the superconducting system. Here all we need to do is to identify the difference between up and down spin self-energies as the order parameter h (which we call the exchange field) and calculate its value self-consistently:

$$\begin{aligned} h &\equiv \frac{1}{4} \text{Tr}[\sigma_3 \hat{\Sigma}] = \frac{U}{4} \sum_{\omega, \mathbf{p}} \text{Tr}[\sigma_3 \hat{G}(\mathbf{p}, \omega)] \\ &= \frac{U}{4} \int_0^{\infty} d\varepsilon N(\varepsilon) [f_{\text{FD}}(\varepsilon - \mu - h) - f_{\text{FD}}(\varepsilon - \mu + h)], \end{aligned} \quad (40)$$

where μ is chosen so that the number of electrons is N . Taking $h \rightarrow 0$ gives a derivative of the Fermi-Dirac distribution at the chemical potential⁵ $\varepsilon = \mu$. At zero temperature it becomes a delta function and we obtain

$$1 = U\chi(T). \quad (41)$$

where $\chi(T) = \int d\varepsilon N(\varepsilon) df_{\text{FD}}/d\varepsilon$ is the spin susceptibility of the non-interacting system at temperature T . This is known as the *Stoner criterion*. At zero temperature, $\chi(0) = N(\varepsilon_{\text{F}})$. If the right-hand-side is larger than 1, the system is unstable against spontaneous magnetization.

⁵ Because of the spin rotation symmetry, the chemical potential does not change to linear order in h .

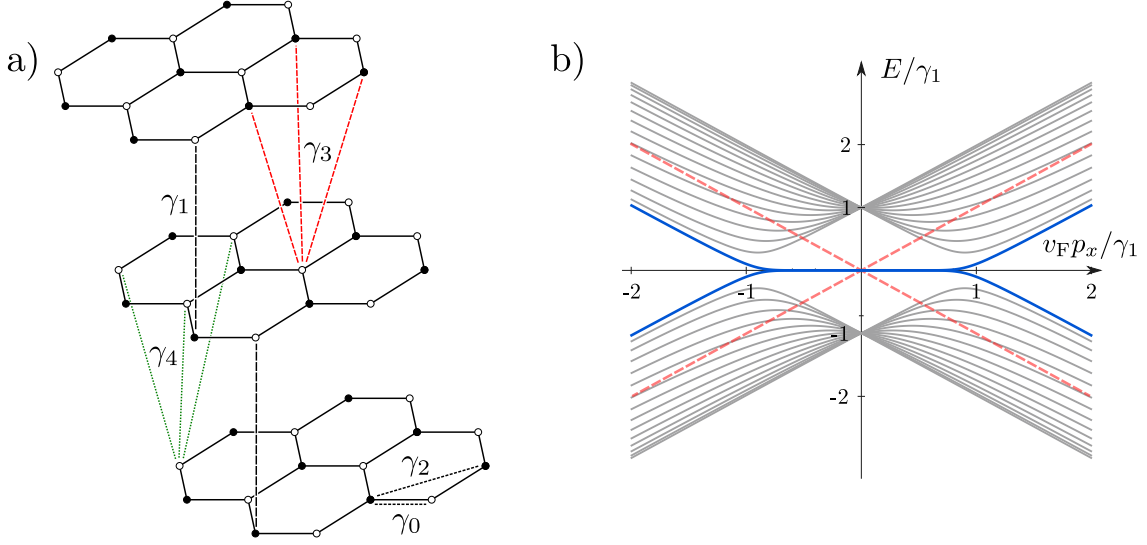


FIGURE 3 a) Structure of ABC graphite. γ_i are the tight-binding hopping parameters. b) Cross-section of the dispersion for 15-layer ABC graphene with chiral symmetry near the K point. Blue lines are the surface states and gray lines are the bulk states. The red dashed line is the Dirac dispersion of single graphene layer.

2.3 Superconductivity and magnetism on flat electronic bands

Since the initial discovery of superconductivity there has been a push for finding superconducting materials with high critical temperatures. In 1988 Bednorz and Müller discovered the first high- T_c superconductor which only requires liquid nitrogen, which has the boiling point of 77 K, as a coolant. In subsequent years, increasing the transition temperature up to room temperature has become the holy grail of superconductivity research. This goal may have been achieved in 2020 when room temperature superconductivity was reported in carbonaceous sulfur hydride.[18] The result has been called into question because the alleged superconducting transitions are anomalously sharp as a function of temperature, and their widths do not change with the applied magnetic field.[14] Even if the result is valid, it is of limited practical value, since it was only achieved in a diamond anvil cell under an extreme pressure of 267 GPa. The search for practical room-temperature superconductors continues.

In this section, I discuss how flat bands can lead to an increase in the critical temperature, and to an emergence of superconductivity in materials which are not usually superconducting at any temperature, and how such degeneracy can be engineered in graphene-based systems.

2.3.1 Flat bands in ABC graphite

Flat bands can be generated by a variety of mechanisms. A trivial flat band can be made by taking a set of identical atoms with strongly localized electronic states and arranging them in a lattice. If there is no coupling between the nearby localized states, the resulting system is an atomic insulator with dispersion relation $\varepsilon(\mathbf{p}) = \varepsilon_a$,

where ε_a is the localized state energy. This system does not support any currents and is arguably very boring.

Flat bands with more interesting properties can arise due to either topological reasons or from interactions. [19] As an example of topologically protected flat band, let us consider rhombohedral graphite (RHG), a naturally occurring metastable allotrope of graphite, in which N graphene layers are stacked in ABC order (Fig. 3a). The in-plane coupling between the carbon atoms is due to covalent bonds, whereas coupling between the layers is due to weaker van der Waals forces. This system has been studied in Publication II. The properties of RHG can be described with a tight-binding model which includes the in-layer nearest-neighbour hopping γ_0 , and hoppings γ_1 , γ_3 and γ_4 between the neighbouring sites in adjacent layers as shown in Fig. 3. Generally, the hopping strength depends strongly on the distance between the sites. The sites connected by γ_1 are directly on top of each other, whereas sites for γ_3 and γ_4 are offset in the in-plane direction. This implies a hierarchy $\gamma_0 \gg \gamma_1 \gg \gamma_3, \gamma_4$ between the hopping parameters. Below, for simplicity, we disregard the hoppings γ_2 , γ_3 and γ_4 .

The Hamiltonian for N rhombohedrally stacked graphene layers can be written in $2N \times 2N$ sublattice-layer space as a matrix[20, 21]

$$H(\mathbf{k}) = \begin{pmatrix} \hat{H}_0(\mathbf{k}) & \hat{H}_+(\mathbf{k}) & 0 & \cdots & 0 \\ \hat{H}_+(\mathbf{k})^\dagger & \hat{H}_0(\mathbf{k}) & \hat{H}_+(\mathbf{k}) & & \vdots \\ 0 & \hat{H}_+(\mathbf{k})^\dagger & \ddots & \ddots & 0 \\ \vdots & & \ddots & \ddots & \hat{H}_+(\mathbf{k}) \\ 0 & \cdots & 0 & \hat{H}_+(\mathbf{k})^\dagger & \hat{H}_0(\mathbf{k}) \end{pmatrix}. \quad (42)$$

The submatrices are

$$\hat{H}_0(\mathbf{k}) = -\gamma_0 \sum_i e^{i\delta_i \cdot \mathbf{k}} \hat{\sigma}_+ + \text{h.c.} \quad \text{and} \quad \hat{H}_+(\mathbf{k}) = \gamma_1 \sigma_-, \quad (43)$$

where $\mathbf{k} = (k_x, k_y)$ is the transverse momentum, $\sigma_\pm = (\sigma_x \pm i\sigma_y)/2$ are the sublattice ladder operators, and δ_i are the three nearest-neighbour vectors inside the layers. The dispersion for RHG with 15 layers (with $\gamma_1 \ll \gamma_0$ and $\gamma_3 = \gamma_4 = 0$) is shown in Fig. 3b. The surface states are at almost zero energy for $|\mathbf{k} - \mathbf{K}| < \gamma_1/v_F$.

For a fixed transverse momentum \mathbf{k} the above Hamiltonian coincides with the one-dimensional Su-Schrieffer-Heeger (SSH) model with an even number of sites.[22] The SSH model has two topological phases which can be distinguished by the bulk topological invariant. The corresponding bulk Hamiltonian is

$$H_{\text{bulk}}(\mathbf{k}, k_z) = \begin{pmatrix} 0 & \Phi(\mathbf{k}, k_z) \\ \Phi(\mathbf{k}, k_z)^* & 0 \end{pmatrix}, \quad \Phi(\mathbf{k}, k_z) = -\gamma_0 \sum_i e^{i\delta_i \cdot \mathbf{k}} - \gamma_1 e^{ik_z d}, \quad (44)$$

where d is the distance between the layers. This Hamiltonian has a chiral symmetry $H_{\text{bulk}}(\mathbf{k}, k_z) = -\hat{\sigma}_z H_{\text{bulk}}(\mathbf{k}, k_z) \hat{\sigma}_z$, which allows us to define the topological invariant, the winding number, as

$$W(\mathbf{k}) = -\frac{i}{2\pi} \int \frac{dz(k_z)}{z}, \quad z = \frac{\Phi(\mathbf{k}, k_z)}{|\Phi(\mathbf{k}, k_z)|}, \quad (45)$$

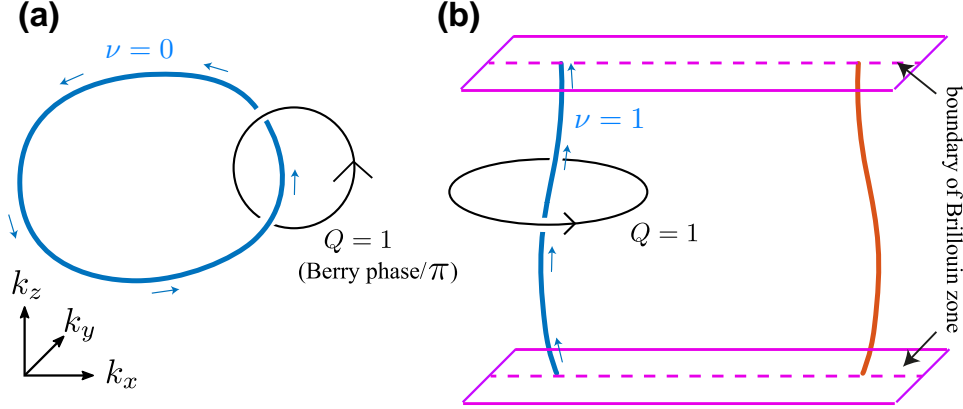


FIGURE 4 (a) Type A nodal lines (blue lines) are closed loops fully inside the Brillouin zone. (b) Type B nodal lines (blue and red lines) extend through the Brillouin zone. The nodal lines carry a topological charge defined with help of the Berry phase for a path around the Dirac line (black lines). Reprinted with permission from Publication **II**, Copyright 2018 Springer Science+Business Media, LLC, part of Springer Nature.

where the integration is from $k_z = 0$ to $k_z = 2\pi/d$. Depending on the transverse momentum, the winding number obtains the value 0 or 1. The bulk-boundary correspondence implies that the change in the winding number across an interface equals the number of zero-energy surface states. The winding number can only change when the gap closes at some point along the integration path. The gap-closing condition $\Phi(\mathbf{k}, k_z) = 0$ defines momentum-space curves known as Dirac nodal lines. The two topologically different regions and the surface states are bounded by the 2D projections of these curves. For $\gamma_1 < \gamma_0$ the surface flat bands occur for in-plane momentum close to K and K' points as shown in Fig. 3b.

In Publication **II** we show that one can distinguish between two types of nodal lines (Fig. 4). Type A nodal lines form loops within the Brillouin zone and can be shrunk continuously into a point, whereas the Type B nodal lines go around the Brillouin zone (which has the topology of a torus) and cannot be shrunk into a point. To destroy Type B lines, one has to bring two lines of opposite charge together so that they annihilate each other and transform into Type A lines. When $\gamma_1 < \gamma_0$ the K and K' points are surrounded by the projections of Type B nodal lines with opposite charge. At $\gamma_0 = \gamma_1$ the two nodal lines collide and for $\gamma_0 < \gamma_1 < 3\gamma_0$, the projection of a single Type A nodal line surrounds the Γ point. At $\gamma_1 = 3\gamma_0$ the Type A nodal line shrinks into a point, and for $\gamma_1 > 3\gamma_0$ the system becomes a 3D topological insulator and the surface flat bands occur at all momenta.[23]

With nonzero γ_2 and γ_4 the chiral symmetry is only approximate. However, as we show in Publication **II**, the nodal lines are topologically protected even if the system only has $SU(2)$ spin rotation symmetry, time-reversal symmetry and inversion symmetry. These assumptions are well met in graphene-based systems which have a low spin-orbit coupling. Breaking of the chiral symmetry modifies the dispersion of the surface states, which are no longer exactly flat in the thermodynamic limit

$N \rightarrow \infty$, but become approximately flat drumhead states bounded by the projected Dirac lines.

2.3.2 Competition between magnetism and superconductivity

The occurrence of flat bands can increase the superconducting transition temperature. To see why this happens, let us consider first metallic systems with constant density of states near the Fermi surface. As we see in Sec. 2.1.2, the superconducting critical temperature depends on the density of states at the Fermi energy, Debye energy and interaction strength as

$$T_c = \omega_D \exp\left(-\frac{1}{\lambda N_0}\right). \quad (46)$$

This is valid at the weak-coupling limit when the bandwidth is large compared to the Debye energy and to the emergent superconducting energy scale T_c . The above equation suggests that the critical temperature could be increased either by increasing the interaction strength, Debye energy, or the density of states.

Let us consider the third option, and modify the density of states. Instead of a constant density of states, we assume that we have a flat band so that the density of states has a delta-function form $N(\varepsilon) = \nu_{\text{FB}}\delta(\varepsilon - \varepsilon_0)$, where ν_{FB} is the degeneracy of the flat band. Now consider the BCS theory for such a system. When the chemical potential coincides with the degeneracy, $\mu = \varepsilon_0$, the BCS self-consistency Eq. (14) becomes [24]

$$\Delta = \lambda \nu_{\text{FB}} \tanh\left(\frac{\Delta}{2T}\right). \quad (47)$$

By expanding around $\Delta = 0$ we find the critical temperature $T_c = \lambda N_{\text{FB}}/2$. Instead of being exponentially small, the critical temperature scales linearly as a function of the interaction constant. This suggests that if we could take a material and perturb its electronic structure to create a flat band, there could be a large increase in the superconducting transition temperature. Alternatively, by engineering a flat band, superconductivity can emerge in materials which ordinarily would not be superconducting at any temperature.

In Publication I we study the phase transitions with a model Hamiltonian which approximates the RHG surface states. With chiral symmetry the surface states for N -layer graphene have the dispersion $\epsilon_p = \pm \varepsilon_0 |\tilde{p}|^N (1 - |\tilde{p}|^2)$ [21], where $\varepsilon_0 = v_F p_{\text{FB}}$, $\tilde{p} = \mathbf{p}/p_{\text{FB}}$, and $p_{\text{FB}} = \gamma_1/v_F$ is the momentum-space radius of the flat band. In the model we only consider the A sublattice on the bottom layer and B sublattice on the top layer, as the low-energy surface states are localized on those parts of the system, and neglect the interaction with the bulk. The dispersion of the surface states is roughly reproduced by taking the momentum space Hamiltonian to be

$$H = \varepsilon_0 \begin{pmatrix} 0 & \tilde{p}^N \\ \tilde{p}^N & 0 \end{pmatrix} \quad (48)$$

in the $|A, 1\rangle \oplus |B, N\rangle$ space.

To study the competition between symmetry-broken phases in this system, we assume that there are two interactions, the attractive electron-phonon interaction,

described within the dynamic Eliashberg model (Sec. 2.1.3), and the repulsive Coulomb interaction approximated with the Hubbard U interaction. In 2D systems controlled with nearby electric gates, the Hubbard U parameter which we include into the model can be related to the Coulomb interaction and to the Thomas-Fermi screening length, which is determined partially by the possible metallic gate electrodes near the system under consideration, and partially by the intrinsic properties of that system. [25].

If the electron-phonon interaction would be approximated with a static BCS interaction λ , the total interaction would be simply a sum $V = U - \lambda$, which would have a definite sign and only enable superconductivity when $V < 0$ or a magnetic state when $V > 0$, but there would be no competition between the two states on the mean-field level. However, due to the retardation of the electron-phonon interaction, there are two separate interaction channels. A low energy attractive channel enables a possible superconducting transition, and the repulsive channel with high-energy component enables the possible magnetic phases.

What would be the structure of the magnetic phase? The on-site interaction favors a locally ferromagnetic alignment on each of the surfaces, i.e. creates an exchange field on each of the surfaces with a relative angle θ between them. To determine this angle we note that the two exchange fields are coupled by the wavefunctions which extend from one surface to the another.

A similar situation occurs in the superconducting state with θ replaced by the relative phase φ between Δ s on the two surfaces. Comparing the magnetic free energy with the free energy of the superconducting state, one notices that the free energy for the antiparallel magnetization has the same structure as the superconducting state with $\varphi = 0$ phase difference. Correspondingly, the state with parallel magnetization coincides with the $\varphi = \pi$ superconducting state. In the superconducting state the Josephson energy fixes the phase difference to $\varphi = 0$. By analogy, the stable magnetization state is the one with antiparallel alignment between the surfaces. The situation is also analogous to an antiferromagnetic spin density wave in a system with a nesting property.[26]

For the antiparallel magnetic state, the Stoner criterion (41) can still be written as $U\chi(T) = 1$, but now with the susceptibility

$$\chi(T) = \int_{-\infty}^{\infty} d\varepsilon \frac{N(\varepsilon)}{\varepsilon} \tanh\left(\frac{\varepsilon}{2T}\right). \quad (49)$$

Because the magnetic structure is not fully uniform, this susceptibility differs from the (ferromagnetic) spin susceptibility in Eq. (41). For a flat band with density of states $N(\varepsilon) = \nu_{FB}\delta(\varepsilon)$, the transition temperature is $T_c = U\nu_{FB}/2$, which is linear in the interaction strength.

In addition to the low-energy flat band, there are high-energy bands which cannot be completely neglected since they give a logarithmic contribution to the susceptibility (49). As we see in Sec. 2.1.4, for the superconducting state the high-energy bands create the pseudopotential effect by screening the Coulomb repulsion at low energies. We can do a similar separation into high and low energy bands for the magnetic state, but the effect is opposite; the high-energy bands give a positive feedback and enhance the effective Coulomb interaction at low energies.

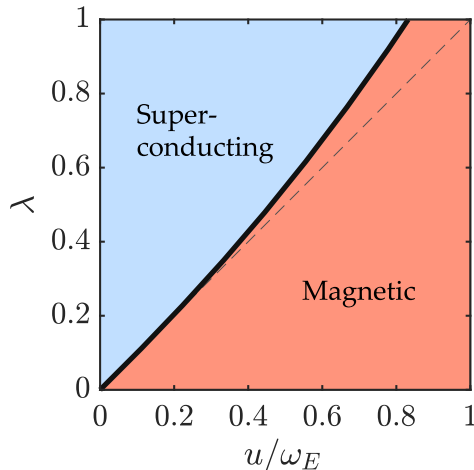


FIGURE 5 Mean-field phase diagram at $T = 0$ for rhombohedral graphite surface states, when the high-energy states are neglected ($\chi_h = 0$). The thin dashed line shows the phase boundary in the case of instantaneous interactions. The retardation effects modify the phase boundary. Reprinted with permission from Publication I, Copyright 2018 American Physical Society.

The high-energy bands can be included as a parameter

$$\chi_h = \int_{\Lambda}^D d\varepsilon \frac{N(\varepsilon)}{|\varepsilon|} \approx \bar{N} \log(D/\Lambda), \quad (50)$$

where Λ is the cutoff frequency between low and high energy bands, D is the bandwidth and \bar{N} is an average density of states. The effective interactions for the particle-particle ($-$) and particle-hole ($+$) channels are

$$V_{\pm} = U^{\pm} - g, \quad \text{where} \quad U^{\pm} = \frac{U}{1 \pm U\chi_h}. \quad (51)$$

For the particle-particle channel, the interaction strength diverges at $U\chi_h = 1$. This means the Stoner criterion is fulfilled already by the high-energy bands, and indicates that with the chosen cutoff Λ , the theory is not fully self-consistent and one needs to use a larger cutoff. In addition to the pseudopotential effect, the retardation also gives a frequency dependence for the electron-phonon interaction g , which modifies the quasiparticle weights through the self-energy component Z and has a minor effect on the phase diagram as shown in Fig. 5.

Recently, bilayer AB graphene and trilayer ABC graphene were found to exhibit superconductivity with maximum T_c 's of 30 mK and 50 mK, respectively, at carefully tuned gate voltages and displacement fields. [27, 28] Based on the above arguments, one expects that if a rhombohedrally stacked system with larger number of graphene layers can be fabricated, it will have a larger critical temperature [21]. In trilayer ABC graphene, the superconducting state occurs on the cusp of a magnetic transition. This observation is consistent with the above model, in which the magnetic and superconducting phases share no common interaction mechanism, but are enabled by the large degeneracy of the flat band.[28]

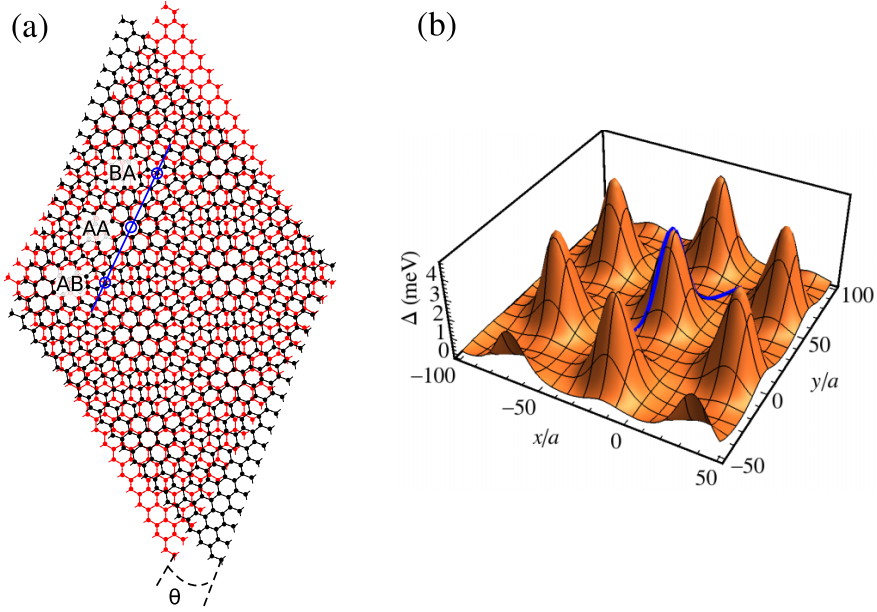


FIGURE 6 (a) Twisted bilayer graphene and its moiré superlattice. The upper layer is rotated by an angle θ relative to the lower layer. (b) Position dependence of the self-consistent Δ , shown here at $T = 0$ for the magic angle $\theta = 0.96^\circ$ and $\lambda = 5 \text{ eV a}^2$. In both figures also a line passing through high-symmetry points with AB, AA, and BA stacking is shown. Reprinted with permission from Publication IV, Copyright 2018 American Physical Society.

2.3.3 Magic-angle twisted bilayer graphene

The system which popularized the study of flat bands on a large scale is the magic-angle twisted bilayer graphene (MATBG), which was found in 2018 to host multiple superconducting and correlated insulator phases tunable simply with a gate voltage. [29, 30] It was the first purely graphene-based system that exhibits superconductivity in a reproducible manner.⁶

MATBG consists of two layers of graphene coupled by van der Waals forces, and twisted relative to each other so that the unit cells of the two graphene layers are at angle θ relative to each other (Fig. 6a). The two overlaid honeycomb lattices create a moiré pattern. The electronic structure of the individual graphene sheets is modified by the spatial modulation of the overlap between π orbitals of the two sheets. As a consequence of the moiré pattern with large unit cell $A_{\text{moiré}}$, the graphene Brillouin zone fragments into a much smaller superlattice Brillouin zone. At twist angle $\theta \approx 1.1^\circ$ the level repulsion between the bands flattens the Dirac cones of the lowest lying bands so that the Fermi velocity vanishes, creating an approximate flat

⁶ Indications of superconductivity with high transition temperature have been reported in highly oriented pyrolytic graphite (HOPG) samples since 1999.[31, 32] However, these samples are not as well controlled as MATBG systems, and have not received similar attention. The superconductivity in HOPG is related to the interfaces in the sample, and may share a common mechanism with MATBG. [33]

band state.

The experimental phase diagram of MATBG depends on the sample, but in the original experiments [29, 30] it was found that there were insulating correlated states at integer fillings $\nu = nA_{\text{moiré}} \in \{\pm 2, \pm 3\}$, where n is the number density of electrons relative to the charge neutral state, and superconducting domes around the insulating states (Fig. 7). This is reminiscent of the phase diagram of some high- T_c superconductors, in which the superconducting pairing is assumed to be mediated by spin or electronic fluctuations, so that the superconducting state and the correlated insulating state share a common mechanism and the insulating state functions as a precursor phase for the superconducting transition. In some theoretical works, the phase diagram was taken as an indication that also in MATBG the superconductivity might not be mediated by phonons, but by Coulomb interaction [34–43]. If superconductivity in MATBG were to share a similar mechanism with (some of) the high- T_c superconductors, this would be useful indeed, since the MATBG is much more easily controlled. For example, in high- T_c superconductors the electron density needs to be controlled by introducing impurity atoms, and each data point thus requires a fabrication of a new sample. In MATBG the electron density is tunable simply by gating, and the whole phase diagram can be explored in a single sample.

However, in later experiments with cleaner samples, the location of the superconducting state and the insulating states on the phase diagram do not seem to be correlated quite so closely [44], and the phase diagram is not so suggestive of the high- T_c physics anymore. Moreover, it can be argued that the phonon mechanism is sufficient to explain the superconducting state. In the phonon hypothesis, the only common factor for the superconducting and insulating states are the flat bands, which tend to make the system unstable in many different channels.

In Publication **IV**, we study arguably the simplest possibility for the superconducting state in MATBG, namely s -wave superconductivity enabled by an attractive local interaction, which we identify with the electron-phonon interaction. The normal state of TBG is described with a tight-binding model of Refs. [45, 46], which describes the two graphene layers at twist angle θ coupled by a hopping which depends on the distance between the sites. We solve the BdG Eqs. (9–13) for this model and find that even a relatively weak electron-phonon interaction can explain the superconducting T_c 's observed in the experiments, and the phonon hypothesis is consistent with the experimental observations. The phonon hypothesis is also supported by other works,[47, 48] and by experiments where the screening of Coulomb interaction is enhanced by using a thinner hBN layer between the gate and the sample. [49] The insulating state is not observed in such experiments, but superconductivity remains. The structure of the order parameter is still an open question, but there is some evidence that it may have nodes.[50] Since the local density of states varies significantly within the moiré unit cell, being largest at the sites with AA stacking and lowest at the sites with AB or BA stacking, the order parameter also has a significant position dependence within the moiré unit cell (Fig. 6b).

In general, the mean-field Δ is not a sufficient condition for superconductivity. A proper superconducting state should also support a finite supercurrent (Eq. (1)),

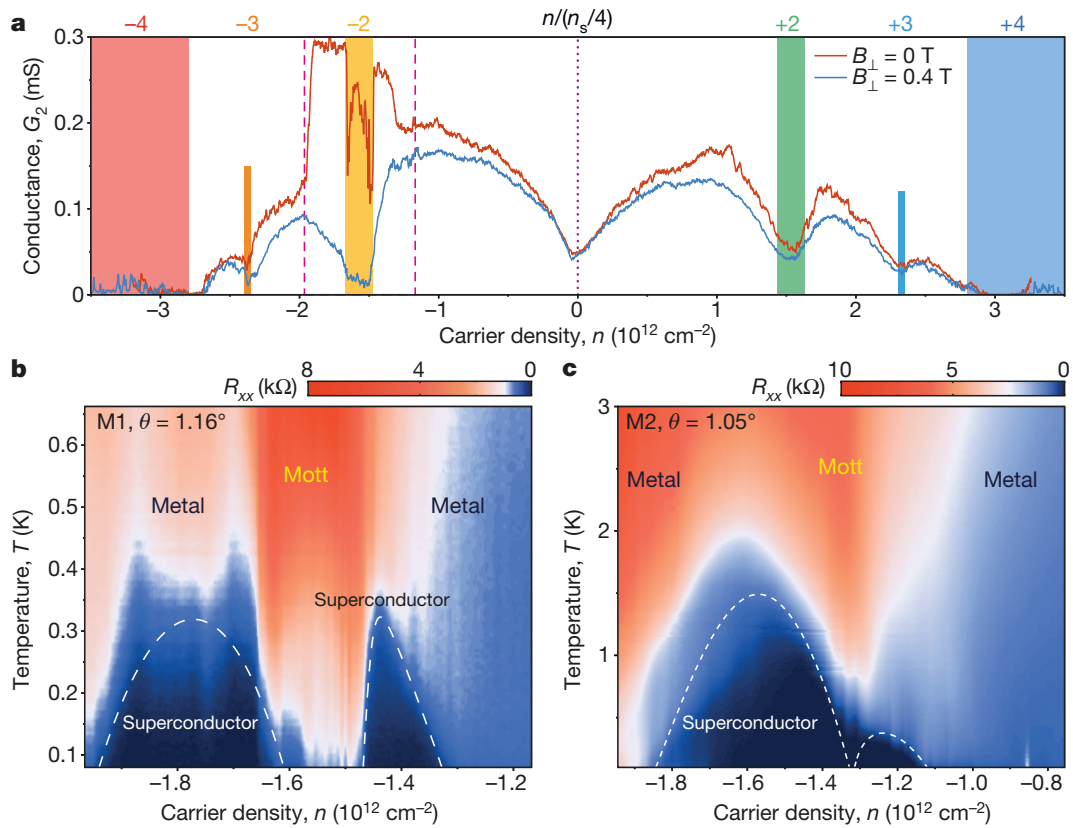


FIGURE 7 Gate-tunable superconductivity and insulating phases in MATBG as observed in Ref. [29]. (a) Two-terminal conductance as a function of the carrier density $n = CV_g/e$, where C and V_g are the gate capacitance and gate voltage, respectively. The upper axis shows the filling factor $\nu = n/(n_s/4)$. (b,c) Four-terminal resistance for two samples at densities close to $\nu = -2$ shows the correlated (Mott) insulator phase and the adjacent superconducting domes. Reprinted with permission from Ref. [29], Copyright 2018 Springer Nature.

which requires a nonzero superfluid weight i.e. phase rigidity. In conventional systems the superfluid weight can be related to the effective electron mass m_{eff} by the relation [51]

$$D_s = e^2 n_s / m_{\text{eff}}, \quad (52)$$

where n_s is the superfluid density. In flat band systems the effective mass diverges and this definition gives a vanishing superfluid weight. However, there can be other contributions to the superfluid weight which originate from the band geometry [52]. In particular, the superfluid weight for rhombohedral graphite surface states [21] and MATBG is finite [53]. For an in-depth discussion of superfluid weight in flat-band systems, see the recent review [54].

At finite temperatures and in two-dimensional systems the long-range order can also be destroyed by thermal fluctuations. Above the so-called Berezinskii-Kosterlitz-Thouless (BKT) transition temperature T_{BKT} the system becomes unstable against the creation of pairs of vortices, quantized topological defects in the order parameter texture, and as the number of vortices increases the phase coherence is lost. Cooper pairs may still exist in the system, but the resistance becomes finite. In the mean-field theory the order parameter is regarded as a static quantity, and the effect of such fluctuations is not captured. In two-dimensional superconductors, the observed resistance transition happens at the BKT temperature T_{BKT} , not at the mean-field critical temperature.

Two-dimensional charged superfluids such as thin-film superconductors constitute a special case of the BKT theory, which in its original form only concerns neutral superfluids and analogous systems.[55–57] In neutral superfluids the BKT transition happens because when the distance between a pair of vortices is large, the interaction energy between two vortices increases logarithmically as a function of distance. In contrast, in bulk superconductors the interaction energy between two vortices falls off exponentially as a function of distance, and there is no BKT transition. In thin-film superconductors the interaction strength is asymptotically inversely proportional to the distance, and thus Kosterlitz and Thouless initially suggested that they should not exhibit a BKT transition.[57]

However, as pointed out by Beasley, Mooij and Orlando,[58] the asymptotic form of the interaction energy used by Kosterlitz and Thouless only applies for distances larger than the Pearl penetration depth λ_{\perp} ,[59] the magnetic penetration depth for fields perpendicular to the film, which is inversely proportional to the film thickness. For thin films, λ_{\perp} can reach values that are of the order of centimeters.[60] For distances smaller than λ_{\perp} , the interaction energy between the vortices increases logarithmically just like in neutral superfluids. Thus, in principle there is no BKT phase transition in superconductors in the thermodynamic limit, but since the experiments are never done in the thermodynamic limit, the BKT transition in superconductors can be in practice be indistinguishable from a true phase transition and one can almost directly apply the methods of the original BKT theory in superconductors.[60] In the case of MATBG, this avenue has been pursued by the co-authors of Publication **IV**. [53]

3 NON-EQUILIBRIUM SUPERCONDUCTIVITY

Above we describe the equilibrium properties of superconducting and magnetic materials. However, many applications and experimental probes induce a non-equilibrium state. Here we are in particular interested in the non-equilibrium properties of superconductors, in which the density of states depends strongly on energy. This feature provides them with unique properties, but also complicates the theoretical description, forcing us to develop some rather heavy calculational machinery to calculate the responses to time-dependent fields.

We start by describing the general formal tools for the non-equilibrium situation. The idea here is not to develop the theory in full, but rather to trace out the path from basic quantum mechanics to the quasiclassical formalism of non-equilibrium superconductivity. The full details can be found in the review articles [61–63] and the textbooks [64–66].

3.1 Keldysh formalism

A rather general approach to non-equilibrium dynamics is to use the Keldysh formalism. It has some advantages over the alternatives such as Matsubara formalism: it allows to the description of transient effects and systems far away from thermal equilibrium. There is also no need for analytical continuation, even though the analytical structure of the response functions does sometimes show up in the theory. A feature unique to Keldysh theory is that it allows the calculation of full counting statistics, giving access to all cumulants of an observable. The main drawback of the Keldysh theory is that it doubles the matrix size of the Green's function, and can sometimes be cumbersome to use.

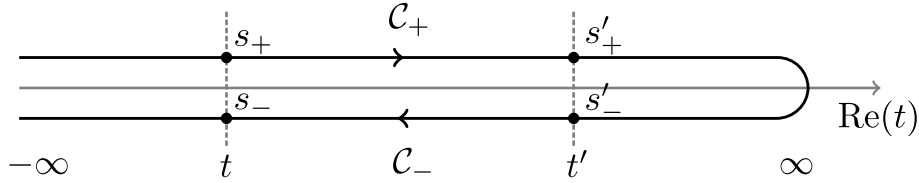


FIGURE 8 Keldysh contour. The contour-ordering operator orders the contour-time variables in the order $s_+ < s'_+ < s'_- < s_-$.

3.1.1 Keldysh contour

The time evolution of a quantum mechanical system is determined by its Hamiltonian \mathcal{H} . We assume that we can divide the Hamiltonian into three parts,

$$\mathcal{H} = H_0 + H^{\text{int}} + H'(t), \quad (53)$$

where H_0 is a time-independent single-particle Hamiltonian, which can be easily diagonalized and used to determine the basis states. H^{int} describes the interactions between the particles and is solvable only with approximations. The last part H' is explicitly time-dependent and describes the processes which induce the non-equilibrium state.

In the interaction picture the expectation value of an operator \hat{O} can be expressed as

$$O(t) = \langle U(t_0, t) \hat{O}(t) U(t, t_0) \rangle. \quad (54)$$

The time-evolution from some initial state is given by the Dyson expansion

$$U(t, t_0) = \mathcal{T} \left[e^{-i \int_{t_0}^t d\tau H^{\text{int}}(\tau) + H'(\tau)} \right], \quad (55)$$

with the time-ordering operator \mathcal{T} . The time-dependent operators $X(t)$ in the interaction picture are defined relative to the Schrödinger picture operator X_S as $X(t) = e^{iH_0 t} X_S e^{-iH_0 t}$. We assume that the system is coupled to a thermal bath with temperature T and take the initial time to be far away in the past, $t_0 \rightarrow -\infty$. The coupling to the thermal bath washes out any initial correlations, so that the expectation value is evaluated about the thermal equilibrium $\langle \cdot \rangle \equiv \mathcal{Z}^{-1} \text{Tr}[e^{-\beta H_0} \cdot]$, where $\beta = 1/T$ is the inverse temperature and $\mathcal{Z} = \text{Tr}[-\beta H_0]$ is the non-interacting partition function. In particular, we do not need to specify the initial state of the system at $t = t_0$.

We then define a *contour ordering operator* \mathcal{T}_C which orders the operators in an increasing order in the contour variable on a closed path \mathcal{C} (Fig. 8) on which t goes from $-\infty$ to ∞ on the forward branch \mathcal{C}_+ , and then back from ∞ to $-\infty$ on the backward branch \mathcal{C}_- . The expectation value can be concisely written as

$$O(t) = \langle \mathcal{T}_C [S_C \hat{O}(t)] \rangle, \quad (56)$$

where the S -matrix is defined as $S_C = \exp[-i \int_C d\tau H^{\text{int}}(\tau) + H'(\tau)]$. Similarly, we define the contour-ordered Green's function

$$G(1, 1') = \langle \mathcal{T}_C [S_C \psi(1) \psi^\dagger(1')] \rangle, \quad (57)$$

where the concise coordinate notation $1 = (\mathbf{x}_1, t_1)$ includes at least temporal and spatial coordinates and can include additional degrees of freedom (e.g. spin).

The above formal trick is useful because under the contour-ordering operator \mathcal{T}_c the operators can be treated as if they are numbers and the S -matrix can be expanded in Taylor series. It can then be shown that Wick's theorem generalizes for the contour-time operators, and any string of operators can be expressed as a sum of products of zeroth order GFs

$$G_0(1, 1') = \langle \mathcal{T}_c [\psi(1)\psi^\dagger(1')] \rangle, \quad (58)$$

and interaction vertices. The contour-ordering can thus be used to develop a perturbation theory, namely the Feynman diagram expansion.

3.1.2 Real-time matrix structure

Instead of contour-time, we are ultimately interested in the values of the observables in real time. To see how we get back to the real time, let us consider a simple example. Suppose that the interaction Hamiltonian is given by the one-body operator $H^{\text{int}} = V(\mathbf{x})\psi^\dagger(\mathbf{x})\psi(\mathbf{x})$ and that the time-dependent part vanishes, $H'(t) = 0$. Expanding the S -matrix in Eq. (57) to the first order in V gives

$$G(1, 1') = G_0(1, 1') + \int d\mathbf{x}_2 \int_c ds G_0(1, 2)V(2)G_0(2, 1') + \mathcal{O}(V^2). \quad (59)$$

We break the contour integrals into two real-time integrals

$$\int_c ds X(s) = \left(\int_{c_+} ds + \int_{c_-} ds \right) X(s) = \int_{-\infty}^{\infty} dt X(t, +) - \int_{-\infty}^{+\infty} dt X(t, -), \quad (60)$$

For a pair of real times t, t' , we get four different Green's functions depending on whether the two times reside on the forward (+) or backward (-) branch of the contour:

$$G^{++}(1, 1') = -i \langle \mathcal{T} [\psi(1)\psi^\dagger(1')] \rangle, \quad G^{+-}(1, 1') = \mp i \langle \psi^\dagger(1)\psi(1') \rangle, \quad (61)$$

$$G^{-+}(1, 1') = +i \langle \psi(1')\psi^\dagger(1) \rangle, \quad G^{--}(1, 1') = -i \langle \tilde{\mathcal{T}} [\psi(1)\psi^\dagger(1')] \rangle, \quad (62)$$

where ψ are now operators in the Heisenberg picture, and $\tilde{\mathcal{T}}$ is the anti-time-ordering operator, which orders the operators to the opposite order than \mathcal{T} . For G^{+-} the upper sign is for bosons, and the lower sign is for fermions. The four GFs can be collected in one matrix propagator with components $[\check{G}]_{\alpha\beta} = G^{\alpha\beta}$. In terms of the matrix propagator the above expansion can be written as

$$\check{G}(1, 1') = \check{G}_0(1, 1') + d\mathbf{x}_2 \int_{-\infty}^{\infty} dt_2 \int \check{G}_0(1, 2)\check{\tau}_3 V(2)\check{G}_0(2, 1'). \quad (63)$$

where $\check{\tau}_3$ is the third Pauli matrix.

To clarify the physical content of the matrix propagator, it is useful to transform to the Larkin-Ovchinnikov representation for fermions, in which the matrix structure

is rotated $\check{G} \rightarrow L\check{G}L^\dagger$ with $L = (\check{1} - i\check{\tau}_2)/\sqrt{2}$, and the matrix propagator obtains the trigonal structure:

$$\check{G} = \begin{pmatrix} G^R & G^K \\ 0 & G^A \end{pmatrix}, \quad (64)$$

where the retarded (R), advanced (A) and Keldysh (K) propagators can be defined as

$$G^R(1, 1') = -i\theta(t - t') \langle [\psi(1), \psi^\dagger(1')]_{\mp} \rangle, \quad (65)$$

$$G^A(1, 1') = i\theta(t' - t) \langle [\psi(1), \psi^\dagger(1')]_{\mp} \rangle, \quad (66)$$

$$G^K(1, 1') = -i \langle [\psi(1), \psi^\dagger(1')]_{\pm} \rangle, \quad (67)$$

with $[X, Y]_{\mp} = XY \mp YX$, where $-$ and $+$ signs are for bosons and fermions, respectively. By definition, the retarded and advanced functions are related by $G^A(1, 1') = G^R(1', 1)^*$ and Keldysh function is anti-hermitean: $G^K(1, 1') = -G^K(1', 1)^*$.

The Larkin-Ovchinnikov representation for the GF is useful since its components admit a clear physical interpretation. The retarded and advanced GFs encode spectral information; e.g. in equilibrium the density of states is given by $N(\varepsilon) = \mathcal{V}^{-1} \int_{\mathbf{x}} \text{Tr}[G^R(\mathbf{x}, \varepsilon) - G^A(\mathbf{x}, \varepsilon)]$. The Keldysh GF on the other hand encodes information about the distribution function. In equilibrium it is determined by the fluctuation-dissipation theorem:

$$G^K(\mathbf{x}, \varepsilon) = [G^R(\mathbf{x}, \varepsilon) - G^A(\mathbf{x}, \varepsilon)] \tanh\left(\frac{\varepsilon}{2T}\right), \quad (68)$$

where T is the bath temperature. In general, the Keldysh GF can be parametrized in terms of the distribution function F as $G^K = G^R \otimes F - F \otimes G^A$, where F is hermitean: $F(1, 1) = F(1', 1)^*$.

In the Larkin-Ovchinnikov representation the inverse GF and the self-energy share the same structure as the GF itself:

$$\check{G}^{-1} = \begin{pmatrix} (G^R)^{-1} & (G^{-1})^K \\ 0 & (G^A)^{-1} \end{pmatrix}, \quad \check{\Sigma} = \begin{pmatrix} \Sigma^R & \Sigma^K \\ 0 & \Sigma^A \end{pmatrix}. \quad (69)$$

The inverse is defined as $(X \otimes X^{-1})(1, 1') = \hat{1}\delta(1 - 1')$ where \otimes is a convolution product in space-time arguments. In terms of the distribution function F , the Keldysh part of the inverse propagator is $(G^{-1})^K = (G^R)^{-1} \otimes F - F \otimes (G^A)^{-1}$.

As in the equilibrium case, the matrix propagator obeys the Dyson equation

$$(\check{G}_0^{-1} - \check{\Sigma}) \otimes \check{G} = \delta(1 - 1')\check{1}, \quad (70)$$

where the zeroth order Green's function is

$$G_0^{R/A}(\mathbf{p}, \varepsilon) = \frac{1}{\varepsilon - H_{\mathbf{p}} \pm i\delta}. \quad (71)$$

Here $H_{\mathbf{p}}$ is the single-particle Hamiltonian. The self-energy Σ is defined as the difference between the bare and the dressed GFs, or equivalently as the sum of all the irreducible single particle diagrams which are obtained by expanding the S -matrix.[64]

Here we operate within the (self-consistent) mean-field approximation, and only include the Hartree-Fock skeleton diagrams which give the self-energy

$$\Sigma(k) = -V(0)\hat{\tau}_3 \text{Tr}[\hat{\tau}_3 G] + V(q) \text{Tr}[\hat{\tau}_3 G(k-q)\hat{\tau}_3], \quad (72)$$

for some two-body interaction V . This approximation closes the equations of motion, so that one only needs to solve the coupled equations for G and Σ .

It may seem that we use a sledgehammer to crack a nut in developing all this formalism to calculate things within the mean-field approximation, which reduces the problem to an effective single-particle problem. However, we occasionally want to step out of the linear response theory and then it is useful that the formalism does not get in the way.

3.1.3 Full counting statistics

For a stochastic transport process, e.g. electron transfer through a tunnel barrier, full counting statistics means that we not only calculate the average rate of the process, but instead consider the probability distribution related to that process and calculate all its cumulants. The Keldysh theory provides a practical method to obtain the generating function for the cumulants.[62]

In Keldysh formalism, a single time t maps onto two variables s_{\pm} on the contour, one on the forward branch and the other on the backward branch. All operators \hat{O} corresponding to physical fields can only depend on the real time and are defined symmetrically on the two branches: $\hat{O}(s_-) = \hat{O}(s_+)$. However, it is also possible to define operators \hat{A} which are antisymmetric on the contour: $\hat{A}(s_-) = -\hat{A}(s_+)$. The fields defined by such operators are called *counting fields* and can be used to develop the full counting statistics of an observable.

We use this technique in Publication **V**, in which we derive an Keldysh action for a tunnel junction between a nanomagnet with precessing magnetization and a spin-split superconductor. The full counting statistics for charge, spin and energy transfer over the junction are obtained as derivatives of the action with respect to the counting fields.

3.2 Quasiclassical theory of superconductivity

Many properties of metals can be described with the phenomenological Fermi liquid theory [67, 68]. A Fermi liquid is an interacting system with rather strong interactions, but due to phase space restrictions the quasiparticle excitations near Fermi surface cannot decay and the ground state resembles that of a Fermi gas. One then only needs to describe the residual interactions between the excitations. The dynamics of a Fermi liquid can be described with a fairly simple Boltzmann kinetic equation in terms of the distribution function $f_{p\sigma}(\mathbf{x})$.

The quasiclassical theory is a natural generalization of the Fermi liquid theory to the superconducting state. [69] Such a generalization is needed because for many

applications of interest, the full Gor'kov equations for the GFs are too cumbersome to solve. The quasiclassical theory is based on the observation that the typical interactions in metals do not depend strongly on momentum near the Fermi surface, and consequently the quasiparticle poles remain sharp in momentum space. This makes it possible to integrate the equations of motion over momentum. This procedure neglects some (inessential) information and results into a simpler set of equations of motion. The quasiclassical theory for equilibrium states was first obtained by Eilenberger [70]. The extension to non-equilibrium states was initially developed by Eliashberg, Larkin and Ovchinnikov [71, 72].

In the works included in this dissertation, we do not consider Fermi liquid interactions explicitly, apart from the attractive BCS interaction, which enables superconductivity. However, the philosophy of the Fermi liquid theory is present in the sense that we are only concerned on the excitations near the Fermi surface.

3.2.1 Eilenberger equation

The formal way of obtaining the quasiclassical equations of motion is sketched below. In the following we separate the order parameter matrix $\hat{\Delta}$ from other self-energy terms, which include contributions such as inelastic electron-phonon relaxation and impurity scattering. We begin by subtracting the left and right-handed versions of the Gor'kov–Dyson equations

$$\check{G} \otimes (\check{G}_0^{-1} - \hat{\Delta} - \check{\Sigma}) = 0, \quad \text{and} \quad (\check{G}_0^{-1} - \hat{\Delta} - \check{\Sigma}) \otimes \check{G} = 0, \quad (73)$$

with zeroth order GF

$$\check{G}_0^{-1}(t - t') = \begin{pmatrix} i\partial_t \hat{\tau}_3 + i\delta - \xi_p & 2i\delta F^{\text{eq}}(t) \\ 0 & i\partial_t \hat{\tau}_3 - i\delta - \xi_p \end{pmatrix} \delta(t - t'), \quad (74)$$

from each other, to obtain the equation

$$[\check{G}_0^{-1} - \hat{\Delta} - \check{\Sigma} \otimes \check{G}] = 0, \quad (75)$$

The infinitesimal $\delta > 0$ sets the analytical structure, and the infinitesimally small Keldysh part determines the distribution function $F^{\text{eq}}(\varepsilon) = \tanh(\varepsilon/2T)$, where T is the bath temperature. The self-energy contains the electron-electron and electron-phonon interactions and impurity scattering. We specify it in detail only for the diffusive case.

The next step of the process is the Wigner transform, in which internal and external length scales of the problem are separated. Here we do the Wigner transform in spatial coordinates but not in the temporal coordinates, because we are interested in periodic driving and the structure of the temporal Fourier transforms is better preserved this way. We define the center-of-mass coordinate $\mathbf{R} = (\mathbf{x}_1 + \mathbf{x}_2)/2$ and relative coordinate $\mathbf{r} = \mathbf{x}_1 - \mathbf{x}_2$. The Fourier transform with respect to the relative coordinate is

$$G(\mathbf{R}, \mathbf{p}) = \int d\mathbf{r} e^{i\mathbf{p}\cdot\mathbf{r}} G(\mathbf{R} + \mathbf{r}/2, \mathbf{R} - \mathbf{r}/2), \quad (76)$$

This is the mixed-coordinate representation of G . In mixed coordinates, the space-time convolution product of two two-coordinate functions is

$$(A \otimes B)(\mathbf{R}, \mathbf{p}) = e^{\frac{i}{2}(\nabla_{\mathbf{p}_1} \nabla_{\mathbf{R}_2} - \nabla_{\mathbf{p}_2} \nabla_{\mathbf{R}_1})} A(\mathbf{R}_1, \mathbf{p}_1) \circ B(\mathbf{R}_2, \mathbf{p}_2) \Big|_{\mathbf{p}_{1/2}=\mathbf{p}, \mathbf{R}_{1/2}=\mathbf{R}}, \quad (77)$$

where \circ is a time-convolution product. For functions with slow \mathbf{R} dependence (as compared to internal length scales, i.e. Fermi wavelength) the above exponential can be expanded in Taylor series for spatial gradients.

Applying the gradient expansion to the left-right subtracted Dyson equation (75) and retaining only the terms in the lowest non-vanishing order in gradients, one obtains a local equation of motion for $G(\mathbf{R}, \mathbf{p}, t, t')$. Integrating that equation over the momentum magnitude $|\mathbf{p}|$, we then obtain the Eilenberger equation for the quasiclassical propagator \check{g} [70]

$$v_F \hat{\mathbf{p}} \cdot \nabla \check{g} = [-i\varepsilon\tau_3 + \check{\Sigma} + \hat{\Delta} \circ \check{g}], \quad (78)$$

where $v_F = p_F/m$ is the Fermi velocity and the self-energy is restricted to the Fermi surface $\Sigma(\mathbf{p}) \approx \Sigma(p_F \hat{\mathbf{p}})$. The quasiclassical propagator is defined as

$$\check{g}(\mathbf{R}, \hat{\mathbf{p}}) = \frac{i}{\pi} \int \! \! \! \int d\xi_p \check{G}(\mathbf{R}, \mathbf{p}). \quad (79)$$

The slash over the integral indicates that the integration over $\xi_p = \frac{p^2}{2m} - \varepsilon_F$ is restricted to energies near the Fermi surface [61, 70]. To uniquely fix the solution, the Eilenberger equation is solved together with a normalization condition $\check{g} \circ \check{g} = \check{1}$. According to the Eilenberger equation, the quasiparticles move in straight lines in the direction $\hat{\mathbf{p}}$ until they scatter off the boundary or some impurity. This is similar to propagation of light in geometric optics. This is not a coincidence, as geometric optics can be derived from Maxwell's equations by using a similar gradient expansion as above [73].

To give a concrete example of the quasiclassical GF, let us consider the homogeneous BCS state. Integrating over the Gor'kov GF (24), we obtain

$$\hat{g}^{R/A}(\varepsilon) = \frac{\varepsilon \hat{\tau}_3 + i\Delta \hat{\tau}_1}{i\sqrt{\Delta^2 - (\varepsilon \pm i\delta)^2}}, \quad (80)$$

where $\sqrt{\cdot}$ refers to the principal branch of the square root function.

In terms of the quasiclassical GFs, the density of states is

$$N(\varepsilon) = \frac{N_0}{2} \text{Tr} \tau_3 [g^R(\varepsilon) - g^A(\varepsilon)] = N_0 \text{Re} \left[\frac{\varepsilon}{\sqrt{(\varepsilon + i\delta)^2 - \Delta^2}} \right], \quad (81)$$

where N_0 is the normal-state density of states at Fermi energy. In the normal state, the propagator $g^{R/A}(\varepsilon) = \pm\tau_3$ has no energy dependence. This is a consequence of the quasiclassical approximation; the information about the electron-hole asymmetry in the normal state is completely lost and the quasiclassical theory cannot describe normal state thermoelectric effects or any other effects which depend on the dimensionless ratios T_c/ε_F , T/E_F , ω/E_F , q/p_F and V/E_F , where T_c is the transition temperature and ω , q and V are the frequency, wavevector and strength of an external perturbation.[74]

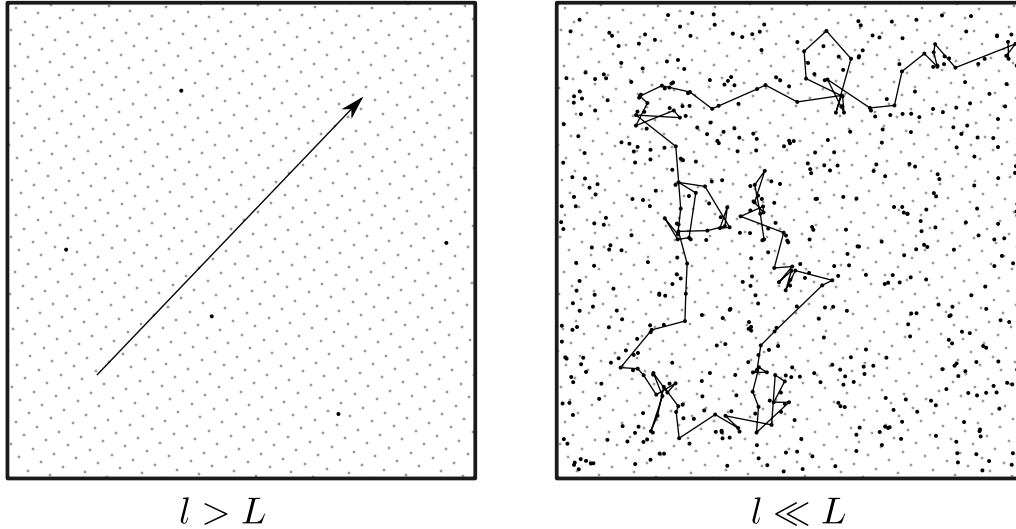


FIGURE 9 Electron motion in (a) a clean system, (b) a disordered system.

3.2.2 Usadel equation

The Eilenberger equation describes a clean superconductor in which the electrons experience a perfectly periodic lattice with Bloch wave eigenstates. Real materials are always to some extent disordered, with the perfect periodicity broken by impurity atoms and lattice defects, rendering the Bloch wave picture invalid. In the Hamiltonian, the impurities can be modeled by starting from a perfect lattice and introducing a stochastic field of randomly distributed point-like scattering centers. In Born approximation, the impurity scattering self-energy (at the Fermi surface) is

$$\check{\Sigma} = \frac{\langle \check{g} \rangle_{\theta}}{\tau_{\text{imp}}}, \quad (82)$$

where τ_{imp} is the impurity scattering rate and $\langle \cdot \rangle_{\theta}$ is an average over the momentum directions. The scattering from impurities is elastic; it randomizes the momentum direction, but does not mix states with different energies.

When the impurity scattering length $l = v_{\text{F}}\tau_{\text{imp}}$ is small compared to the other length scales of the system such as system size L , superconducting coherence length ξ_0 and spin scattering length¹ l_s , the quasiclassical propagator can be approximated by the first two spherical harmonics:

$$\check{g} = \check{g}_s + \hat{\mathbf{p}} \cdot \check{\mathbf{g}}_p + \mathcal{O}(\tau_{\text{imp}}^2) \quad (83)$$

Expanding the Eilenberger equation and the normalization condition in spherical harmonics [61] and using the assumption $\tau_{\text{imp}}^{-1} \gg \Delta_0$, one finds that the p -wave component can be expressed as the gradient of the s -wave component,

$$\check{\mathbf{g}}_p = -2l\check{g}_s \nabla \check{g}_s. \quad (84)$$

¹ Impurity scattering length has to be larger than Fermi wavelength, as otherwise the quasiclassical approximation is invalid.

Substituting this to the s -wave part of the Eilenberger equation, we find an equation of motion for $\check{g}_s = \check{g}_s(\mathbf{R}, t, t')$ (from now on we drop the subscript s) in the disordered limit:

$$D\nabla \cdot (\check{g}\nabla\check{g}) + [i\varepsilon\hat{\tau}_3 - \hat{\Delta} - \check{\Sigma}, \check{g}] = 0. \quad (85)$$

This equation is known as the Usadel equation [75], and like the Eilenberger equation, it is complemented by the normalization condition $\check{g} \circ \check{g} = \check{1}$. Unlike in the clean limit where quasiparticles move ballistically, here the quasiparticles are constantly scattering off the impurities, and the electron motion is diffusive, with diffusion constant $D = v_F^2 \tau_{\text{imp}}$ (Fig. 9b). The above equation is valid for the time-independent case.

For simplicity, we write down most of the equations for the time-independent case. However, in the publications we often consider a time-dependent drive. The Usadel equation and all the associated definitions can be translated to a time-dependent case by making the Fourier replacement

$$[i\varepsilon\hat{\tau}_3, \check{g}] \longrightarrow \hat{\tau}_3 \partial_t \check{g} + \partial_{t'} \check{g} \hat{\tau}_3, \quad (86)$$

for the energy variable in (85), and by replacing the ordinary matrix products with time-convolution products, denoted here by the \circ operator.

3.2.3 Spectral equation

Let us now consider the structure of the Usadel equation (85). The quasiclassical GF \check{g} is an 8×8 matrix in Keldysh-Nambu-spin space. The Keldysh structure is

$$\check{g} = \begin{pmatrix} \hat{g}^R & \hat{g}^K \\ 0 & \hat{g}^A \end{pmatrix}, \quad (87)$$

where $\hat{g}^{R/A/K}$ are 4×4 matrices with the Nambu-spin structure

$$\hat{g}^R(\mathbf{R}, \varepsilon) = \sum_{i,j=0}^3 g_{ij}^R(\mathbf{R}, \varepsilon) \hat{\sigma}_i \hat{\tau}_j, \quad (88)$$

The choice of the Nambu spinor [Eq. (5)] ensures that if there are no spin-dependent fields present, $g^{R/A/K}$ are proportional to the unit matrix $\hat{\sigma}_0$ in spin space. In particular, we have chosen the Nambu spinor so that the singlet pairing is in the σ_0 component.

Expanding the Keldysh matrix multiplications in Eq. (85), and picking the R component gives the spectral equation²

$$D\nabla \cdot (\hat{g}^R \nabla \hat{g}^R) + [i\varepsilon\hat{\tau}_3 - \hat{\Delta}, \hat{g}^R] = [\hat{\Sigma}^R, \hat{g}^R], \quad (89)$$

which is solved together with the normalization condition

$$(\hat{g}^R)^2 = \hat{1}. \quad (90)$$

² The correct analytical branch is obtained by replacement $\varepsilon \rightarrow \varepsilon + i\delta$, with small $\delta > 0$.

These equations determine the spectral function \hat{g}^R , and apart from the self-consistent $\Delta = \Delta[\hat{g}]$, they can be solved independently of \hat{g}^K . There is no need to solve an equation for \hat{g}^A , since one can show from the definitions (66) and (65) that $\hat{g}^A = -\hat{\tau}_3(\hat{g}^R)^\dagger\hat{\tau}_3$. Solving a differential equation (89) together with a nonlinear constraint (90) can be complicated. A common strategy is to parametrize \hat{g}^R in such a way that the normalization condition is automatically satisfied and then solve the resulting unconstrained differential equation for those parameters. We discuss the parametrization of \hat{g}^R in Sec. 3.2.10.

3.2.4 Kinetic equation

The Keldysh component of the normalization condition is

$$\hat{g}^R\hat{g}^K + \hat{g}^K\hat{g}^A = 0. \quad (91)$$

The normalization condition is automatically satisfied by introducing the distribution function \hat{f} such that

$$\hat{g}^K = \hat{g}^R\hat{f} - \hat{f}\hat{g}^A. \quad (92)$$

The distribution function is not yet uniquely defined, as one can substitute

$$\hat{f} \rightarrow \hat{f} + \hat{g}^R\hat{h} + \hat{h}\hat{g}^A, \quad (93)$$

with arbitrary \hat{h} without affecting \hat{g}^K . [76] To fix \hat{f} uniquely, we restrict it to a diagonal matrix in Nambu space[77]

$$\hat{f}(\mathbf{R}, \varepsilon) = \left(f_L + \sum_{j=1}^3 f_{Tj}\hat{\sigma}_j \right) \hat{\tau}_0 + \left(f_T + \sum_{j=1}^3 f_{Lj}\hat{\sigma}_j \right) \hat{\tau}_3, \quad (94)$$

and label the components $f_{L/Tj}$ according to the generalized Schmid-Schön notation, where L and T stand for longitudinal and transverse, respectively [63, 78, 79]. The components correspond to different non-equilibrium modes. The modes f_L , f_T are related to energy and charge accumulation, [51] and the spin-dependent modes f_{Tj} and f_{Lj} are related to spin accumulation and spin-energy accumulation, respectively.

To obtain an equation of motion for the distribution function, we define the matrix current

$$\check{\mathbf{I}} = D\check{g}\nabla\check{g}, \quad (95)$$

and write the Usadel equation in a concise form

$$\nabla \cdot \check{\mathbf{I}} = [\hat{\Lambda} + \check{\Sigma}, \check{g}] = 0, \quad (96)$$

where $\hat{\Lambda} = -i\varepsilon\hat{\tau}_3 + \hat{\Delta}$. The Keldysh component of the matrix current can be written in terms of the distribution function as

$$\hat{\mathbf{I}}^K = D \left(\nabla\hat{f} - \underbrace{g^R\nabla\hat{f}}_{I^R} g^A \right) + \underbrace{D(\hat{g}^R\nabla\hat{g}^R)}_{I^R} \hat{f} - \hat{f} \underbrace{D(\hat{g}^A\nabla\hat{g}^A)}_{I^A}, \quad (97)$$

where the first term describes the currents due to gradients of quasiparticle density, which can only exist in a non-equilibrium state. The last two terms on the other

hand can be non-zero also in equilibrium and describe the possible charge and spin supercurrents.

Taking the Keldysh component of the Usadel Eq. (85), and subtracting the supercurrent terms $\mathbf{I}^{R/A}$ from both sides using the spectral Usadel equation gives the equation

$$D \left[\nabla^2 \hat{f} - \hat{g}^R (\nabla^2 \hat{f}) \hat{g}^A \right] = \hat{g}^R (Z_H + Z_\nabla + Z_\Sigma) - (Z_H + Z_\nabla + Z_\Sigma) \hat{g}^A, \quad (98)$$

for the distribution function. The time-derivative and the order parameter, spectral gradients, and the self-energies are contained in the terms

$$Z_H = f\Lambda - \Lambda f \quad (99)$$

$$Z_\nabla = \frac{D}{2} \left[(\nabla g^R) \cdot (\nabla f) - (\nabla f) \cdot (\nabla g^A) \right], \quad (100)$$

$$Z_\Sigma = \Sigma^K - \Sigma^R f + f \Sigma^A. \quad (101)$$

In analogy to the Boltzmann equation, the equation (98) is often called the *kinetic equation*.

Let us consider what kind of physics the different terms of Eq. (98) describe. The left hand side of Eq. (98) describes the coupled diffusion of the non-equilibrium modes. [63] In the superconducting state the density of states is strongly energy-dependent and the effectiveness of diffusion depends on the quasiparticle energy. On the right hand side, the first term of $\Lambda = -i\varepsilon\tau_3 + \hat{\Delta}$ gives the time-derivative of the quasiparticle accumulation (in the time-dependent situation), whereas the Δ term describes conversion between supercurrent and quasiparticle charge currents. The spectral gradients in Z_∇ can be generated by supercurrents, and they couple the different non-equilibrium modes. The self-energy terms Z_Σ give the collision integral which relaxes the distribution function towards the equilibrium distribution.

3.2.5 Self-energies

In the publications included in this dissertation, we are interested in spin dynamics in nonequilibrium systems. To describe such systems, we need to consider some spin and energy relaxation mechanisms.

In disordered materials, the spin imbalance can relax by scattering from impurities. Depending on whether the impurities are magnetic or not, the associated self-energies are given in the first Born approximation by

$$\Sigma_{\text{sf}} = \frac{\tau_3 \boldsymbol{\sigma} \cdot \check{g} \boldsymbol{\sigma} \tau_3}{6\tau_{\text{sf}}}, \quad (102)$$

or

$$\Sigma_{\text{so}} = \frac{\boldsymbol{\sigma} \cdot \check{g} \boldsymbol{\sigma}}{6\tau_{\text{so}}}. \quad (103)$$

The former describes spin-flip relaxation due to scattering from magnetic impurities, and the latter describes Elliott-Yafet spin relaxation due to spin-orbit scattering from

a non-magnetic random impurity potential [80]. These processes are parametrized by spin-flip and spin-orbit relaxation times τ_{sf} and τ_{so} , respectively.

In the normal state, there is no difference between the two terms within the approximations used here, and one can simply define a total spin-relaxation time $\tau_{\text{sn}}^{-1} = \tau_{\text{so}}^{-1} + \tau_{\text{sf}}^{-1}$. In the superconducting state, the two spin relaxation processes act differently because the spin-orbit scattering is time-reversal invariant, but magnetic impurity potential is not. Anderson's theorem states that *s*-wave superconductivity is robust against time-reversal invariant perturbations [81], and so the spin-orbit scattering does not lower the critical temperature. Anderson's theorem does not apply to time-reversal breaking perturbations, and one finds that magnetic impurities decrease the critical temperature of the superconducting state.

In addition to the above elastic spin relaxation processes, there always exists some processes which provide inelastic relaxation, relaxing the quasiparticle distribution towards a thermal distribution. An important source of inelastic relaxation is the electron-phonon scattering, given by the self-energy [63, 71]

$$\hat{\Sigma}_{\text{e-ph}}^{R,A}(\varepsilon) = -ig_{\text{e-ph}} \int_{-\infty}^{\infty} d\omega D^K(\omega) \hat{g}^{R,A}(\varepsilon + \omega) - D^{R,A}(\omega) \hat{g}^K(\varepsilon + \omega) \quad (104)$$

$$\hat{\Sigma}_{\text{e-ph}}^K(\varepsilon) = -ig_{\text{e-ph}} \int_{-\infty}^{\infty} d\omega D^K(\omega) \hat{g}^K(\varepsilon + \omega) - D^{RA}(\omega) \hat{g}^{RA}(\varepsilon + \omega), \quad (105)$$

where $X^{RA} = X^R - X^A$, $D^{R,A} = \pm i\omega|\omega|$, $D^K = D^{RA}(\omega) \coth(\omega/2T_{\text{ph}})$, and T_{ph} is the phonon temperature.

The above phonon self-energy is often too complicated to implement in practice. A toy model for energy relaxation is given by

$$\hat{\Sigma}_{\text{ie}}^{R,A} = \pm i\Gamma \hat{\tau}_3, \quad (106)$$

$$\hat{\Sigma}_{\text{ie}}^K = 2\Gamma f^{\text{eq}}(\varepsilon) \hat{\tau}_3, \quad (107)$$

where $\Gamma > 0$ is the Dynes parameter, $f^{\text{eq}} = \tanh(\varepsilon/2T)$, and T is the bath temperature. This model gives the collision integral

$$Z_{\Sigma} = -2\Gamma(\hat{f} - f_{\text{eq}}) \hat{\tau}_3, \quad (108)$$

where Γ^{-1} is the energy relaxation rate. Apart from relaxing the quasiparticles, a finite Dynes parameter also affects the spectral properties, softening the gap edge singularity in the BCS density of states. This is often useful in when solving the Usadel equation numerically, as the sharp divergence at the gap edge can cause problems with some numerical algorithms.

3.2.6 Self-consistency equation

As before, the order parameter is determined from the self-consistency equation. The BCS self-consistency Eq. (14) generalizes to a time-dependent and spatially inhomogeneous case in terms of quasiclassical GF as

$$\begin{aligned} \Delta(\mathbf{R}, t) &= \frac{\lambda}{2} \text{Tr}[\tau_- g^K(\mathbf{R}, t, t)] \\ &= \frac{\lambda}{2} \int_{-\omega_{\text{D}}}^{\omega_{\text{D}}} \frac{d\varepsilon}{2\pi} \text{Tr}[\tau_- g^K(\mathbf{R}, \varepsilon, t)], \end{aligned} \quad (109)$$

where t is the center-of-mass time, and $\tau_- = (\tau_1 - i\tau_2)/2$. If the non-equilibrium electronic system is time-dependent, the order parameter can also oscillate.

At the weak coupling limit $\Delta_0 \ll \omega_D$, where Δ_0 is the order parameter at zero temperature in the absence of external fields, one can eliminate the dependence on the Debye frequency and the interaction constant by taking Δ_0 as a parameter instead. One way to accomplish this is to write number 1 in two ways using two different self-consistency equations:

$$\frac{\lambda}{2} \int_{-\omega_D}^{\omega_D} \frac{d\varepsilon}{2\pi} \text{Tr} \left[\tau_- \frac{g^K(\mathbf{R}, \varepsilon, t)}{\Delta(\mathbf{R}, t)} \right] = 1 = \frac{\lambda}{2} \int_{-\omega_D}^{\omega_D} \frac{d\varepsilon}{2\pi} \text{Tr} \left[\tau_- \frac{g_0^K(\varepsilon)}{\Delta_0} \right]. \quad (110)$$

The interaction constants λ and the high-energy parts of two equations cancel against each other, and we can impose a new cutoff Λ such that $\Delta \ll \Lambda \ll \omega_D$. Although Λ may initially seem like an unnecessary additional parameter, it is useful in heavy numerical applications, since now the cutoff can be chosen to be quite low ($\Lambda = 4\Delta_0$ is often good enough) without loss of accuracy. Solving for Δ , using the BCS solution for g_0^K , and taking the limit $\omega_D \rightarrow \infty$ gives a new self-consistency equation

$$\Delta = \frac{1}{C(\Delta)} \int_0^\Lambda d\varepsilon \text{Tr}[\tau_- g^K], \quad (111)$$

with the coupling constant

$$C(\Delta) = \frac{1}{2} \ln \left(\frac{\Lambda + \sqrt{\Lambda^2 - \Delta^2}}{\Delta_0} \right), \quad (112)$$

which has no reference to λ or ω_D . The above equation has good convergence properties in fixed-point iteration.

3.2.7 Observables

In quasiclassical theory, the charge, spin, energy, and spin-energy current densities can be obtained from the matrix current (95) as

$$j_i = \frac{eN_0}{4} \int d\varepsilon \text{Tr}[\hat{\tau}_3 \hat{I}_i^K], \quad j_i^k = \frac{\hbar N_0}{4} \int d\varepsilon \text{Tr}[\hat{\sigma}_k \hat{\tau}_0 \hat{I}_i^K], \quad (113)$$

$$j_{q,i} = \frac{N_0}{4} \int d\varepsilon \varepsilon \text{Tr}[\hat{\tau}_0 \hat{I}_i^K], \quad j_{q,i}^k = \frac{N_0}{4} \int d\varepsilon \varepsilon \text{Tr}[\hat{\sigma}_k \hat{\tau}_3 \hat{I}_i^K]. \quad (114)$$

The related non-equilibrium charge, spin, energy, and spin-energy accumulations are

$$\mu(\mathbf{r}, t) = - \int \frac{d\varepsilon}{16} \text{Tr}[\hat{\tau}_0 \hat{g}^K], \quad \mu_{s,k}(\mathbf{r}, t) = - \int \frac{d\varepsilon}{16} \text{Tr}[\hat{\sigma}_k \hat{\tau}_3 \delta \hat{g}^K], \quad (115)$$

$$q(\mathbf{r}, t) = - \int \frac{d\varepsilon}{16} \varepsilon \text{Tr}[\hat{\tau}_3 \delta \hat{g}^K], \quad q_{s,k}(\mathbf{r}, t) = - \int \frac{d\varepsilon}{16} \varepsilon \text{Tr}[\hat{\sigma}_k \hat{\tau}_0 \delta \hat{g}^K], \quad (116)$$

where $\delta \hat{g}^K = \hat{g}^K - \hat{g}_{\text{eq}}^K$ is the change in the Keldysh component relative to the equilibrium state. Since the quasiclassical formalism only describes the processes near the Fermi surface, it does not capture fully the possible band-shift effects due

to interactions or external fields. Thus the charge and spin densities defined above have to be corrected by non-Fermi surface contributions in some cases.

The Usadel equation written as in Eq. (96) has the form of a continuity equation, and the Nambu-diagonal components of the Usadel equation give the continuity equations for charge, heat, spin and spin-energy currents [63]. In the normal state the spectral functions are trivial ($\hat{g}^{R,A} = \pm\tau_3$) and the energy-integrated kinetic equations give e.g. the familiar charge and spin-diffusion equations

$$\partial_t \rho + \nabla \cdot \mathbf{j} = 0, \quad (117)$$

$$\partial_t S_k + \nabla \cdot \mathbf{j}_i^k = \frac{S_k}{\tau_{\text{sn}}}, \quad (118)$$

with charge and spin densities $\rho = N_0\mu$, $S_k = N_0\mu_{s,k}$ and normal state diffusion currents $j_i = D\partial_i\rho$ and $\mathbf{j}_{s,i}^k = D\partial_i S_k$. In the superconducting state, there is no such simple relation between currents (113) and accumulations (115).

3.2.8 Quasiclassical symmetries

Let us now consider the redundancy of the description that is present in the quasiclassical GFs. The retarded and advanced propagators are related to each other by definitions (65) and (66), and the definition (67) for the Keldysh propagator contains a similar symmetry relating it to itself:

$$g^A(t, t') = -\tau_3 g^R(t', t)^\dagger \tau_3, \quad (119)$$

$$g^K(t, t') = +\tau_3 g^K(t', t)^\dagger \tau_3, \quad (120)$$

where the \dagger -operator acts only on the matrix structure, and the exchange of the time coordinates is written separately. Together with the parametrization (92), the latter equation constrains the distribution function by $\hat{f}(t, t') = \hat{f}(t', t)^\dagger$.

In Nambu basis, the positive and negative energy excitations are not independent of each other, and the particle-hole redundancy (7) gives an additional constraint between positive and negative energy GFs. In time-domain this constraint is written as

$$\check{g}(t, t') = -\sigma_2 \tau_2 \check{g}(t, t')^* \sigma_2 \tau_2. \quad (121)$$

For the Fourier transformed GFs, the symmetries (119–121) give the relations

$$g^A(\varepsilon, \omega) = -\tau_3 g^R(\varepsilon, -\omega)^\dagger \tau_3, \quad g^R(\varepsilon, \omega) = -\sigma_2 \tau_2 g^R(-\varepsilon, -\omega)^* \sigma_2 \tau_2, \quad (122)$$

$$g^K(\varepsilon, \omega) = +\tau_3 g^K(\varepsilon, -\omega)^\dagger \tau_3, \quad g^K(\varepsilon, \omega) = -\sigma_2 \tau_2 g^K(-\varepsilon, -\omega)^* \sigma_2 \tau_2 \quad (123)$$

where the Fourier convention is such that $g(\varepsilon, \omega) = \int dt dt' g(t, t') e^{-i(\varepsilon-\omega/2)t+i(\varepsilon+\omega/2)t'}$, i.e. energy ε is the Fourier pair of the relative time coordinate $t-t'$, and the frequency ω is the Fourier pair of the center-of-mass time coordinate $(t+t')/2$.

The above constraints reduce the number of equations one needs to solve by a factor of 4, as the advanced GF can always be obtained from the retarded GF, the distribution function must be Hermitean, and the negative energy solutions can

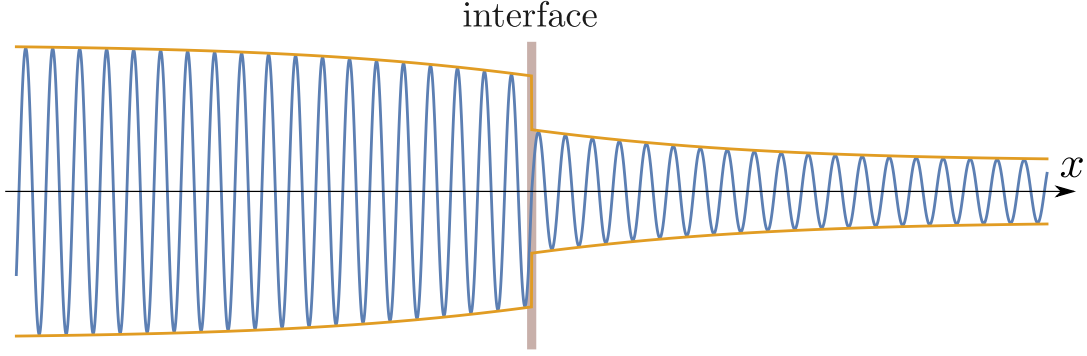


FIGURE 10 Wavefunction at an interface between two materials. Quasiclassical function (yellow) can be discontinuous, while the full wavefunction (blue) is continuous.

be obtained from the positive energy solutions.³ For the non-equilibrium modes in steady state ($\omega = 0$), the symmetries imply that the longitudinal modes f_L , f_{Lj} are odd in energy, the transverse modes f_T , f_{Tj} are even in energy, and that all the modes $f_{L/Tj}$ are real-valued.

3.2.9 Boundary conditions

As a differential equation, the Usadel equation is not fully determined without specifying the boundary conditions. In the Schrödinger equation the boundary conditions can be derived from the potential by requiring that the wavefunction is continuous. The quasiclassical GF however only measures the envelope function which can be discontinuous on quasiclassical length scales (Fig. 10). As one also has to take into account the effect of the impurity potential, the derivation of the boundary conditions for the Usadel equation is a non-trivial task. A comprehensive derivation of boundary conditions for magnetic and non-magnetic interfaces from scattering theory has been achieved in Ref. [82]. Boundary conditions have also been suggested on more phenomenological grounds [83].

Often one wants to consider transport through the interface so that the current depends on e.g. the voltage or temperature difference across the boundary. These kind of boundary conditions are encoded as *Robin boundary conditions* and can be written for the Usadel equation in the general form

$$\mathbf{n} \cdot \check{\mathbf{I}}(\mathbf{R}) = [\check{\Sigma}_{\text{bc}}(\mathbf{R}) \circledast \check{g}(\mathbf{R})], \quad (124)$$

where \mathbf{n} is the interface normal and $\mathbf{R} \in \mathcal{S}$ is a point at the interface. $\check{\Sigma}_{\text{bc}}$ is some Keldysh-Nambu-spin matrix which encodes the properties of the interface and the GFs on both sides of the interface. The commutator structure ensures that the boundary condition is compatible with the quasiclassical normalization condition.

A simple, but useful example is a tunneling interface described by Kuprianov-

³ In case of Matsubara GF, the same symmetries give a connection between negative and positive Matsubara frequencies and constrain the individual $\sigma_i \tau_j$ components of Matsubara GF so that they must be either purely real or purely imaginary.

Lukitchev boundary condition [84]

$$\check{\Sigma}_{\text{bc}} = \sigma_N \check{g}_n \quad (125)$$

where \check{g}_n is the GF on the other side of the interface, and σ_N is the normal state conductance through the interface. Boundary conditions for ferromagnetic interfaces are discussed below in Secs. 4.1.1 and 4.3.1.

3.2.10 Parametrization of the spectral functions

The retarded part of the Usadel equation is a set of coupled differential equations which have to be solved under the normalization condition $g \circ g = 1$. To simplify the solution procedure we parametrize the GF in such a way that the normalization condition is automatically satisfied and rewrite the Usadel equation for those parameters.

To find a suitable parametrization, we note that the normalization condition implies that g^R only has eigenvalues ± 1 and the particle-hole constraint implies that $\text{Tr } g^R = 0$. Thus there exists a similarity transformation U such that

$$g^R = U^{-1} \circ \tau_3 U, \quad \text{with} \quad U = \begin{pmatrix} 1 & a \\ b & 1 \end{pmatrix}, \quad (126)$$

where a and b are 2×2 spin matrices. This parametrization is known as the Riccati parametrization [69]. The diagonal elements of U have been set to unity to make the transformation unique. Expanding g^R in a and b gives

$$g^R = \begin{pmatrix} A & 0 \\ 0 & B \end{pmatrix} \circ \begin{pmatrix} 1 - a \circ b & 2a \\ 2b & -(1 - b \circ a) \end{pmatrix}, \quad (127)$$

where $A = (1 + a \circ b)^{-1}$ and $B = (1 + b \circ a)^{-1}$. We find that a and b characterize the superconducting correlations, so that in the normal state $a = b = 0$. The relative phase of a and b is related to the phase of the order parameter. For example, if $\hat{\Delta} = \Delta \tau_1$, then $a = b$.

By conjugating the retarded block of the Usadel equation with U^{-1} and using representation (126), one obtains the differential equations for the Riccati parameters

$$D \nabla^2 a = \begin{pmatrix} 1 & a \end{pmatrix} \circ (\hat{\Lambda} - \hat{\Sigma}^R) \circ \begin{pmatrix} -a \\ 1 \end{pmatrix} + D \begin{pmatrix} 0 & \partial_i a \end{pmatrix} \circ \hat{g}^R \circ \begin{pmatrix} \partial_i a \\ 0 \end{pmatrix}, \quad (128)$$

$$D \nabla^2 b = \begin{pmatrix} -b & 1 \end{pmatrix} \circ (\hat{\Lambda} - \hat{\Sigma}^R) \circ \begin{pmatrix} 1 \\ b \end{pmatrix} + D \begin{pmatrix} \partial_i b & 0 \end{pmatrix} \circ \hat{g}^R \circ \begin{pmatrix} 0 \\ \partial_i b \end{pmatrix}, \quad (129)$$

with $\Lambda = i(\varepsilon - \mathbf{h} \cdot \boldsymbol{\sigma}) \tau_3 - \hat{\Delta}$. Analogously, the boundary conditions of the form (124) can be written as

$$D \mathbf{n} \cdot \nabla a = \begin{pmatrix} 1 & a \end{pmatrix} \circ \Sigma_{\text{bc}}^R(\mathbf{x}) \circ \begin{pmatrix} -a \\ 1 \end{pmatrix}, \quad (130)$$

$$D \mathbf{n} \cdot \nabla b = \begin{pmatrix} -b & 1 \end{pmatrix} \circ \Sigma_{\text{bc}}^R(\mathbf{x}) \circ \begin{pmatrix} 1 \\ b \end{pmatrix}, \quad (131)$$

The resulting set of equations forms an 8-component second order differential equation. By writing it as a 16-component first order differential equation, it can be solved using out-of-the-box differential equation solvers. The Frobenius norm of the Riccati parameters is bounded; $0 \leq \|a\|, \|b\| \leq 1$, and typically the equations are quite well-behaved.

The Usadel equation does however contain spurious solutions. This can be seen by considering the Riccati equations for the simplest nontrivial case, a homogeneous BCS superconductor without any scattering. The equations

$$\Delta a^2 - 2i\varepsilon a - \Delta = 0, \quad \text{and} \quad \Delta b^2 - 2i\varepsilon b - \Delta = 0, \quad (132)$$

have the solutions $a, b \in (-i\varepsilon \pm \sqrt{\Delta^2 - \varepsilon^2})/\Delta$. The choice of the correct branch is done on physical grounds, as only the solution $a = b = (-i\varepsilon - \sqrt{\Delta^2 - \varepsilon^2})/\Delta$ gives a non-negative density of states. This problem of multiple branches puts some emphasis on a good choice of an initial guess for the numerical solution procedure. In energy domain the solution procedures are typically most unstable towards a non-physical solution near the DOS singularities. A finite Dynes parameter Γ can be used to round the singularities and make the numerical solution more stable.

4 SUPERCONDUCTING SPINTRONICS

Spintronics, a portmanteau of *spin* and *electronics*, is a research area studying the active manipulation of spin degrees of freedom in solid-state systems. [85] Because spin behaves in different ways in materials such as ferromagnets, antiferromagnets, topological insulators, superconductors, semiconductors, molecules and semimetals, spintronics is a very diverse field. It has many subfields which focus on specific systems, such as magnonics [86], insulatronics [87], skyrmionics [88], orbitronics [89]. In this dissertation we are interested in superconducting spintronics [63, 82, 90, 91].

Although the name “spintronics” was invented only in 1996 [85], the prehistory of spintronics goes back to the 19th century discoveries such as Faraday’s law, Lorentz force and Hall effect which demonstrate the macroscopic coupling between magnetic fields and charge currents. Since spin is not a conserved quantity like charge, many spin-transport effects only occur over length scales smaller than the spin-relaxation length of the material, and a microscopic description is necessary. An early study to consider the microscopic aspects of spin transport was the theory of electrical transport in ferromagnetic transition metals by Neville Mott in 1936. [92, 93]

The oft-quoted promise of spintronics is to try and provide faster and more energy-efficient storage, memory and logic elements for computing. [94] Spintronics emerged as a major field of study when the giant magnetoresistance effect (GMR) was discovered in 1988 by the groups led by Albert Fert and Peter Grünberg [95, 96]. Fert and Grünberg shared the 2007 Nobel Prize in physics for their discovery. In GMR the resistance of a magnetic multilayer depends strongly on the relative orientation of the magnetization. It allows magnetic memories to be read efficiently with an electrical signal, and has been utilized in magnetic random-access memories. Spintronics systems can also have other benefits, such as high sensitivity in detector elements, as discussed in Publication **III**. From the point-of-view of a theoretical physicist, we can consider spintronics as the study of all forms of angular momentum in condensed matter systems. This is a fundamental physics interesting in itself, even apart from any short-term industrial applications.

In this chapter, we consider the effects which arise from introducing superconducting elements to magnetic multilayers. One of the main effects from coupling superconducting thin films with magnetic films is the magnetic proximity effect,

which splits the spectrum of the SC into two non-degenerate spin bands. We first describe the spin splitting in the BdG framework and discuss the appropriate boundary condition with which to describe the effect in the Usadel framework. We then proceed to study some of the effects brought about by the spin splitting of the SC spectrum. As the first application, we consider a radiation detector which utilizes the thermoelectric effects between a FM and a spin-split SC.

We move on to consider the magnetization dynamics of thin film ferromagnets in the presence of superconducting contacts. Both the magnetization of the ferromagnet and the electronic spin of the superconductor are forms of angular momentum, and it can be transferred between SC and FM in the reciprocal processes known as spin-transfer torque and spin pumping. The theory of these processes is well known in the normal state, and we discuss how it is modified in the SC state. A unique effect which arises in superconductors is spin supercurrent, a coherent spin current enabled by the spin polarization of the Cooper pairs.

Finally, in a spin-split superconductor, spin dynamics is coupled to the Higgs mode, the amplitude mode of the SC order parameter. We discuss the properties of this coupling, and how it can be used to study the properties of the Higgs mode. We also discuss how this coupling is modified if there is a strong interfacial spin-orbit coupling.

4.1 Spin-splitting field in a superconductor

To understand how the Zeeman field h affects the properties of an s -wave superconductor, let us consider the normal state Hamiltonian

$$H_0 = \frac{p^2}{2m} - \mu - h\sigma_3. \quad (133)$$

In the normal state, the Zeeman field splits the two spin bands so that the Fermi momenta for the two spin species are $p_{F,\sigma} \approx p_F + \sigma h/2\mu$ (top left panel of Fig. 11).

To describe superconducting state, we use the Bogoliubov-de Gennes description of Sec. 2.1.1. In this case, the corresponding BdG Hamiltonian (6) is

$$H_{\text{BdG}} = \xi_p \tau_3 - \Delta \tau_1 - h\sigma_3, \quad (134)$$

where $\xi_p = p^2/2m - \mu$. Since $h\sigma_3$ is proportional to the unit matrix in Nambu space, the eigenvectors are the same as in the $h = 0$ case. In contrast, the eigenenergies are shifted by the Zeeman field:

$$E_{p\sigma\pm} = \pm \sqrt{\xi_p^2 + \Delta^2} + \sigma h. \quad (135)$$

The eigenenergies enter the self-consistency equation (13) only through the statistical functions. At $T = 0$ the statistical function only depends on the sign of the energies (135). If $h < \Delta$, the signs do not change from the $h = 0$ case, so the value of Δ and the structure of the ground state is unchanged. At a finite temperature the self-consistency equation is affected since now the quasiparticles on the branch with

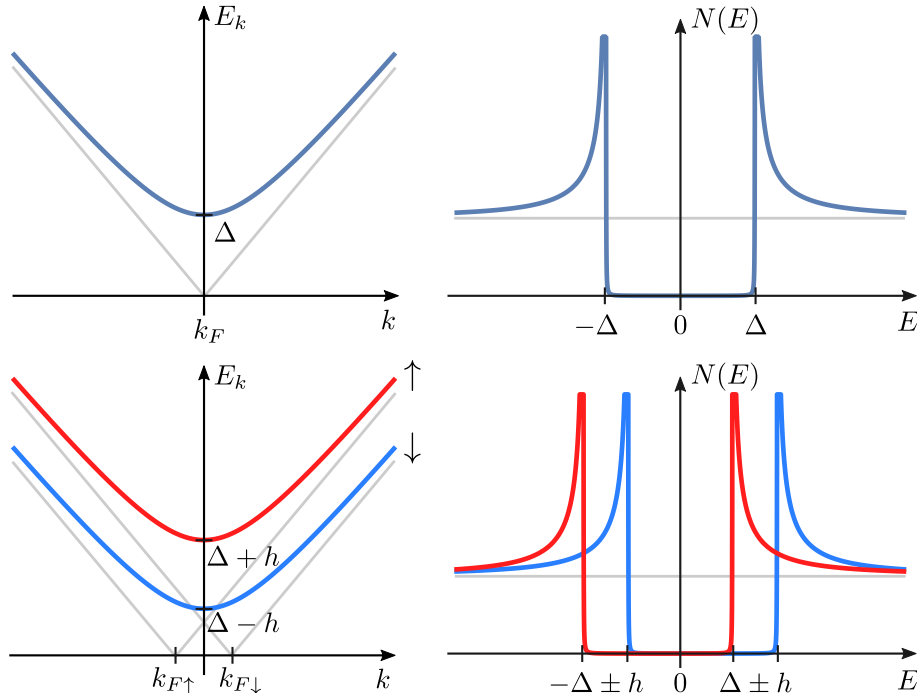


FIGURE 11 Left panel: quasiparticle excitation spectrum for a regular BCS superconductor (top) and for spin-split superconductor with exchange field h (bottom). Right panel: the respective spin-resolved densities of states. Thin grey lines indicate the normal-state spectrum and density of states.

energy $E \leq \Delta - h$ are more easily excited by the thermal processes, and the order parameter diminishes. For $\Delta < h$ signs of the energies (135) do change, and the only solution of the BdG equations at $T = 0$ is the normal state $\Delta = 0$.

The existence of a solution for the BdG equations is not a sufficient criterion for the superconducting ground state, as it only implies that the superconducting state is a local energy minimum. To determine whether the superconducting or the normal state is the global minimum, i.e., the ground state, we need to consider the free energy. At zero temperature, the free energy of the spin-split superconductor relative to the normal state is¹

$$F_s - F_n = \mathcal{V}N_0 \left(h^2 - \frac{\Delta^2}{2} \right), \quad (136)$$

where the last term is the condensation energy and the first one gives the energy penalty due to the Zeeman field. [98] From the free energy we see that the superconducting state is the ground state only for $h < h_c$, where $h_c = \Delta_0/\sqrt{2}$ is the Chandrasekhar-Clogston limit, and Δ_0 is the value of Δ at $h = 0$ and $T = 0$.

The Zeeman field splits the quasiparticle excitation spectrum into two separate spin bands, which have a well-defined spin of $\pm\hbar/2$. (Fig. 11) The spin-up quasiparticles are linear combinations of spin-up electron and spin-down hole excitations, and the spin-down quasiparticles are linear combinations of spin-down electron and

¹ This expression for the free energy is rather limited. A more general expression for SC at finite temperature, with impurity scattering self-energies and inhomogeneities has been obtained in the context of quasiclassical theory in Ref. [97].

spin-up hole excitations. If there are no spin-scattering self-energies, the spin-bands are simply shifted about the Fermi level by $\pm h$. [63] The spin-splitting affects the transport properties of the SC, as reviewed in Ref. [63].

The Zeeman field can be induced into a spin-split SC in two ways. First one is by applying an external in-plane magnetic field. If the SC is thin enough, the orbital effect from the field is negligible, and the main effect is from the Zeeman term. The problem with this approach is that to achieve sizable effects, one needs $h \lesssim \Delta/2$, which for e.g. aluminum implies a strong magnetic field of the order of 1 T. Another way is by magnetic proximity effect, which I describe below.

4.1.1 Magnetic proximity effect

Consider an interface between a metal and an insulator. By definition, there are no electronic states in the bulk of the insulator at the Fermi energy. However, near the interface, the states from the metal extend to the insulator as evanescent states, with a decay length which depends on the insulating gap. Now, if the insulator is magnetic, the insulating gap and the decay length of the evanescent states are spin-dependent.

When an electron scatters from the surface of the insulator, the up and down-spin components [where the direction is taken relative to the spin-quantization axis of the ferromagnetic insulator (FI)] acquire different phases ϕ_\uparrow and ϕ_\downarrow . If we consider only the states near Fermi energy, we can assume that the phases do not depend on energy. We are interested in the effect of the relative phase $\varphi = \phi_\uparrow - \phi_\downarrow$ between the spins, which can cause the spin states to mix when an electron scatters from the interface. To see how, let us assume that the electron is initially at an eigenstate $\sigma_x = +1$, and scatters from the metal/insulator interface: [99]

$$|+\rangle = \frac{|\uparrow\rangle + |\downarrow\rangle}{\sqrt{2}} \longrightarrow \frac{e^{i\varphi}|\uparrow\rangle + e^{-i\varphi}|\downarrow\rangle}{\sqrt{2}} \quad (137)$$

$$= \cos \varphi |+\rangle + \sin \varphi |-\rangle.$$

where $|\pm\rangle$ are the eigenstates of the σ_x operator, and we neglected the total phase $\phi_\uparrow + \phi_\downarrow$. After the scattering, we find that spin has rotated about the z -axis. The phase φ is called the spin-mixing angle, and in general it depends on the angle of incidence. [99]

In general, spin mixing causes pair-breaking: when $\varphi = \pi$, the interface is a perfect pair breaker, which suppresses Δ completely near the interface. However, here we are interested in materials for which the spin-mixing angle is small, $\varphi \ll 1$. In such materials, the pair breaking effect is negligible, and the main effect is the exchange coupling between conduction electrons of the metal and FI spins. [99].

If we are not interested in the normal state effect which has a short length scale, we may use the quasiclassical theory. In the normal state, the equilibrium effects from the interface average out within the distance $\lambda \sim 1/k_F$ from the interface. This is the length scale of the Ruderman–Kittel–Kasuya–Yosida (RKKY) interaction [100–102], which is relevant for atomically thin layers. [103] However, in the superconducting state the changes in the spectrum are mediated by the superconducting condensate

and decay at the much larger scale of the superconducting coherence length ξ . The quasiclassical theory captures the superconducting effect, but cannot be used to describe the normal state RKKY interaction.

For the Eilenberger Eq. (78), the boundary condition for the FI/SC interface is [99]

$$\check{g}(x=0, \hat{\mathbf{p}}) = \hat{S}\check{g}(x=0, \hat{\mathbf{p}})\hat{S}^\dagger, \quad (138)$$

where $\hat{\mathbf{p}}$ and $\hat{\mathbf{p}} = \hat{\mathbf{p}} - 2(\hat{\mathbf{p}} \cdot \mathbf{n})\mathbf{n}$ are the incident and reflected momentum directions, respectively, \mathbf{n} is the interface normal, and the scattering matrix $\hat{S} = \exp(i\varphi\mathbf{m} \cdot \boldsymbol{\sigma}\tau_3/2)$ describes the spin mixing. In general, the spin-mixing angle φ depends on the cosine of the incident angle $\hat{p}_n = \mathbf{n} \cdot \hat{\mathbf{p}}$. Expanding $\hat{S} \approx 1 + i\varphi\mathbf{m} \cdot \boldsymbol{\sigma}\tau_3/2$ gives a relation

$$\check{g}(\hat{\mathbf{p}}) - \check{g}(\hat{\mathbf{p}}) = i\varphi[\mathbf{m} \cdot \boldsymbol{\sigma}\tau_3, \check{g}(\hat{\mathbf{p}})], \quad (139)$$

between the incident and reflected GFs.

In the dirty limit, $\check{g}(\hat{\mathbf{p}}) \approx \check{g}_s + \hat{\mathbf{p}} \cdot \check{\mathbf{g}}_p$ is a good approximation in the bulk, but not within an impurity scattering length from the interface, where the GF can depend sharply on the momentum direction. To obtain the boundary condition for the Usadel equation, one needs to consider the process of isotropization, i.e. the averaging of the momentum direction by impurity scattering, as we get farther away from the interface. The relevant piece of information is that the angle-averaged matrix current, given in the clean limit by $\check{\mathbf{I}} = -3v_F \int \frac{d\Omega_p}{4\pi} \hat{\mathbf{p}} \check{g}(\hat{\mathbf{p}})$, and in the dirty limit by $\check{\mathbf{I}} \approx D(\check{g}_s \nabla \check{g}_s)$, is conserved in the isotropization process.[104]

Thus, calculating the matrix current in the clean limit using Eq. (139), we find the boundary condition for the Usadel equation²

$$\mathbf{n} \cdot \check{\mathbf{I}} = iJ[\mathbf{m} \cdot \boldsymbol{\sigma}\tau_3, \check{g}], \quad (140)$$

where the interfacial exchange field J is given by an angular average of the spin-mixing angle, [104, 105]

$$J = \frac{v_F}{2} \int_0^1 d\hat{p}_n \hat{p}_n \varphi(\hat{p}_n). \quad (141)$$

The effects beyond a weak spin-mixing angle can be incorporated by using the boundary conditions of Refs. [82, 104].

If the thickness of the SC is smaller than the coherence length, we can average the Usadel equation over the SC and use the boundary condition (140) to obtain the equation

$$[i(\varepsilon - \mathbf{h} \cdot \hat{\boldsymbol{\sigma}})\hat{\tau}_3 - \hat{\Delta} - \check{\Sigma}, \check{g}] = 0, \quad (142)$$

where the effective exchange field inside the SC is $\mathbf{h} = J\mathbf{m}/d$. The generalizations of this equation are used below to describe various aspects of spin-split superconductors.

² Here we again suppress the subscript of \check{g}_s .

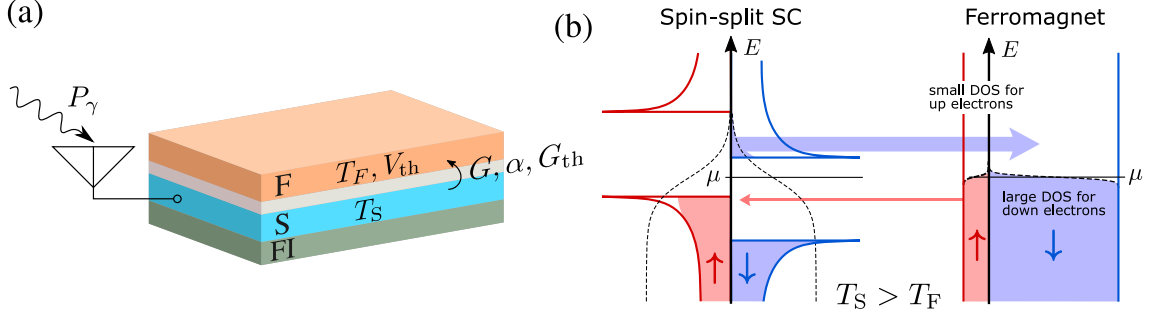


FIGURE 12 (a) Thermoelectric radiation sensor element. FI provides the exchange field for the SC, and the SC and FM are coupled by a tunnelling contact. Absorbed photon heats the SC, and the resulting temperature difference between SC and FM is converted to an electric signal (V_{th}) with the giant thermoelectric effect. (b) Semiconductor diagram for the giant thermoelectric effect in spin-split SC/FM tunnel junction. Solid lines are the densities of states for spin-up (red) and spin-down (blue) electrons, and the dashed line is the Fermi-Dirac distribution function. Spin-up and spin-down currents flow to the opposite directions. If the FM has a finite polarization at the Fermi surface, there is a net charge current through the interface. Adapted from Publication **III**.

4.1.2 Thermoelectric effects at the SC/FM interface

In Publications **III**, **V** and **VI**, we study systems in which a central element is a tunnel junction between a spin-split SC and a ferromagnetic metal (Fig. 12a). Most of the predicted phenomena are enabled by thermoelectric effects over the tunnel junction. The main thermoelectric effects are the Seebeck effect, generation of a voltage or charge current by a temperature difference, and the Peltier effect: generation of heat current from a voltage difference. These effects are related to each other by Onsager reciprocity and only exist if there is an asymmetry between the densities of states for the electron-like and the hole-like excitations.

Electron tunneling between a spin-split SC and FM can be described with the semiconductor model, [51] which gives the charge current [106]

$$I_c = \frac{G_T}{2e} \int_{-\infty}^{\infty} d\varepsilon \sum_{\sigma=\pm} N_{S,\sigma}(\varepsilon) N_{F,\sigma'}(\varepsilon) [f(\varepsilon - V - \sigma V_s, T_F) - f(\varepsilon, T_S)]. \quad (143)$$

Here, $N_{S/F,\sigma}$ are the spin resolved densities of states normalized by the Fermi level DOS per spin, $f(\varepsilon, T)$ is the Fermi distribution function, $T_{S/F}$ are the temperatures of SC and FM electrons, V is the voltage, V_s is a spin-dependent voltage, [63] and G_T the tunneling conductance. The reduced DOS of the spin-split SC is $N_{S,\sigma}(\varepsilon) = N_{\text{BCS}}(\varepsilon - \sigma h)$, where N_{BCS} is the reduced BCS DOS. The reduced DOS of the FM is $N_{F,\sigma} = (1 + P\sigma)/2$, where $P \in [-1, 1]$ is the Fermi-level spin polarization. The prefactors from the densities of states have been absorbed into G_T . Here the magnetizations of the FM and FI are collinear. The structure of the tunnel current is illustrated in Fig. 12b. A similar definition can be given for heat and spin currents. [106].

In total, the SC DOS is always electron-hole symmetric near the Fermi surface

due to the BdG symmetry (8), and thus there is no thermoelectric effect between a SC and normal metal within the quasiclassical accuracy. The introduction of the Zeeman field makes the spin-resolved densities of states highly asymmetric, but does not break the total electron-hole symmetry of the SC. The total electron-hole symmetry is only broken by connecting the spin-split SC to a FM, which has different densities of states for minority and majority spins, so that the two spin bands are weighted asymmetrically. The FM is not described by the quasiclassical theory and does not obey the BdG symmetry (8).

At linear response, the average charge, energy and spin- z currents over the FM/spin-split SC tunnel junction are given by the matrix

$$\begin{pmatrix} I_c \\ \dot{E}_S \\ I_{sz} \end{pmatrix} = \begin{pmatrix} G & P\alpha & PG \\ P\alpha & G_{\text{th}}T & \alpha \\ PG & \alpha & G \end{pmatrix} \begin{pmatrix} V \\ -\delta T/T \\ V_s/2 \end{pmatrix}, \quad (144)$$

where $\delta T = T_S - T_F$. The symmetry of the matrix is due to Onsager reciprocity [106]. The conductance G , thermal conductance G_{th} , and the thermoelectric coefficient α , are given by

$$G = -\frac{G_T}{2} \int_{-\infty}^{\infty} d\varepsilon [N_{S,+}(\varepsilon) + N_{S,-}(\varepsilon)] \frac{\partial f(\varepsilon, T)}{\partial \varepsilon}, \quad (145)$$

$$\alpha = -\frac{G_T}{2e} \int_{-\infty}^{\infty} d\varepsilon \varepsilon [N_{S,+}(\varepsilon) - N_{S,-}(\varepsilon)] \frac{\partial f(\varepsilon, T)}{\partial \varepsilon}, \quad (146)$$

$$G_{\text{th}} = -\frac{G_T}{2e^2} \int_{-\infty}^{\infty} d\varepsilon \varepsilon^2 [N_{S,+}(\varepsilon) + N_{S,-}(\varepsilon)] \frac{\partial f(\varepsilon, T)}{\partial \varepsilon}. \quad (147)$$

The conductance and thermal conductance depend on the average DOS. The thermoelectric coefficient depends on the difference between the densities of states between the two spins, since this is one of the two factors which determines the electron-hole asymmetry of the junction. The second factor is P , the Fermi-level spin polarization of the magnet.

The thermoelectric effect described above is dubbed as the *giant thermoelectric effect*, since it is huge compared to the thermoelectric effects usually observed in metals, which are of the order $k_B T/E_F$. The thermopower of the junction may exceed k_B/e , and the thermoelectric figure of merit Z_T can be larger than unity. As a heat engine, the efficiency of the junction can be made to be close to the Carnot limit.[106]

In Publication **III**, we propose that the giant thermoelectric effect can be utilized as a sensitive thermoelectric radiation detector, in which the measurable electric signal is generated by the temperature gradient across the junction due to heating from the absorbed radiation. The ongoing SUPERTED project [107] funded by European Union's Horizon 2020 research and innovation programme, aims to realize a proof of concept of this device.

4.2 Magnetization dynamics and spin pumping

In Publications **V**, **VI**, **VII**, **VIII**, and **IX** we are interested in dynamical aspects of magnetization. The dynamics can be induced by ac electromagnetic fields or ac currents, or as in some cases considered in Publication **V**, by parametric instabilities caused by dc temperature or voltage biases.

4.2.1 Landau-Lifschitz-Gilbert equation

In a strong ferromagnet, it is much easier to change the direction of the magnetization than to change its modulus $|\mathbf{M}|$. For example, a Stoner ferromagnet with an exchange field h_F has two kinds of basic magnetic excitations. First, there are single-particle Stoner excitations, which move an electron from the occupied state on one spin band to an unoccupied state on the other spin band. In the process, the total spin (magnetization) of the magnet changes by $\Delta S = \pm\hbar$. At long wavelengths $\mathbf{q} \approx 0$, these excitations occur at frequency $\omega_{\mathbf{q}=0} = 2h_F$. Second, there are spin waves, the Goldstone modes associated with spontaneously broken spin-rotation symmetry, which rotate the magnetization coherently around the equilibrium direction. In the absence of an external magnetic field, the dispersion of the long-wavelength modes is gapless.

If we consider a response to an external field with low frequency $\omega \ll h_F$ and a long wavelength, we can neglect the Stoner excitations and consider the dynamics with fixed modulus, $|\mathbf{M}(t)| = M_s$, where M_s is the saturation magnetization of the magnet. In this approximation, the magnetization direction $\mathbf{m} = \mathbf{M}/M_s$ evolves according to the Landau-Lifshitz-Gilbert (LLG) equation [108, 109]

$$\frac{d\mathbf{m}}{dt} = -\gamma(\mathbf{m} \times \mu_0\mathbf{H}) + \alpha \left(\mathbf{m} \times \frac{d\mathbf{m}}{dt} \right), \quad (148)$$

where the first term on the right-hand side describes precession in an external magnetic field $\mu_0\mathbf{H}$. The gyromagnetic ratio γ is the ratio between the magnetic moment and the angular momentum of an electron inside the ferromagnet. The second term is a phenomenological Gilbert damping term parametrized by the dimensionless Gilbert damping constant α , which relaxes the magnetization towards the equilibrium direction. A main source of Gilbert damping is spin-orbit interaction, which couples the time-dependent magnetization to the lattice dynamics.[110] Because of the cross-product structure, both terms on the right hand side conserve the modulus of magnetization.

The potential energy of a ferromagnet can also depend on the magnetization direction due to factors other than the external field. For example, there are fields due to crystalline anisotropy, and a demagnetizing field which depends on the shape of the sample. Such terms can be included into the LLG equation by replacing $\mu_0\mathbf{H}$ with the effective magnetic field

$$\mu_0\mathbf{H}_{\text{eff}} = -\nabla_{\mathbf{M}}U(\mathbf{M}), \quad (149)$$

where $U(\mathbf{M})$ is the potential energy of the magnet. The concept of the effective field can also be extended to include time-dependent fields.

4.2.2 Ferromagnetic resonance

A simple case which can be described with Eq. (148) is the ferromagnetic resonance (FMR) experiment, in which resonant absorption of a ferromagnetic film is studied. In FMR, a static magnetic field is applied in the plane of the film, and an ac field is applied perpendicular to the static field. The power absorption is measured as the field strength is swept over the resonance condition. The line shape of the power absorption reveals information about the magnetic properties of the sample.

Let us describe the FMR experiment as a linear response to an ac magnetic field. For simplicity, we neglect the anisotropy fields and the demagnetization field. Let the static field H_0 be along the z -axis, and let there be an ac field at frequency ω

$$\mathbf{B}_{\text{ac}}(t) = B_{\text{ac}}\sqrt{2} [\cos(\omega t)\mathbf{x} + \sin(\omega t)\mathbf{y}], \quad (150)$$

which is circularly polarized on x - y plane. The factor of $\sqrt{2}$ is included for later convenience.

A good basis for problems involving precession is the angular momentum basis

$$\mathbf{e}_{\pm} = \mp(\mathbf{x} \pm i\mathbf{y})/\sqrt{2}, \quad \mathbf{e}_0 = \mathbf{z}, \quad (151)$$

in which the basis vectors have the properties

$$\mathbf{e}_l^* \cdot \mathbf{e}_k = \delta_{lk}, \quad l, k \in \{\pm 1, 0\} \quad (152)$$

$$\mathbf{e}_0 \times \mathbf{e}_{\pm} = \mp i\mathbf{e}_{\pm}, \quad \mathbf{e}_+ \times \mathbf{e}_- = i\mathbf{e}_0. \quad (153)$$

The benefit of using this basis is that it preserves the rotational symmetry about the z -axis.

In linear response we assume a weak ac drive (150), which can be written in the angular momentum basis as $\mathbf{B}_{\text{ac}}(t) = \text{Re}(B_{\text{ac}}e^{-i\omega t}\mathbf{e}_+)$. Expanding \mathbf{m} in powers of H_{ac} , the magnetization has a static zeroth order component along the z -axis, and a first order component oscillating at frequency ω :

$$\mathbf{m}(t) \approx \mathbf{z} + \text{Re}(m_{\omega}e^{-i\omega t}\mathbf{e}_+). \quad (154)$$

In the angular momentum basis the LLG Eq. (148) becomes a scalar equation, which can be solved in a straightforward manner. We define the magnetic susceptibility

$$M_{\mu}(\omega) = \chi_{\mu\nu}(\omega)B_{\nu}^{\text{ac}}(\omega), \quad (155)$$

where the vector components are defined as $M_{\mu} = \mathbf{e}_{\mu}^* \cdot \mathbf{M}$. In this case, the susceptibility is diagonal, with the diagonal component

$$\chi_{++}(\omega) = \frac{\gamma M_s}{(\omega - \gamma\mu_0 H_0) + i\omega\alpha}. \quad (156)$$

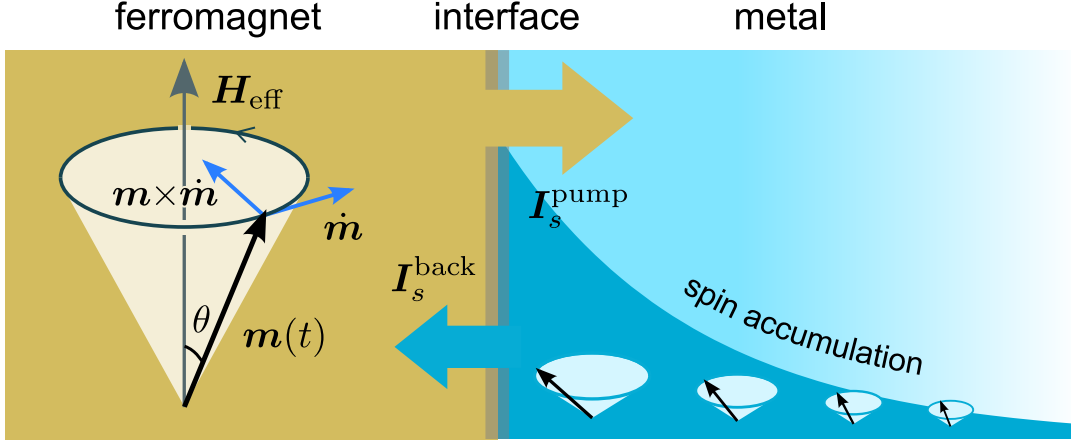


FIGURE 13 Steady precession of the magnetization, and spin pumping from ferromagnet to a metallic contact. The precession of the magnetization pumps a primary current I_s^{pump} into the metallic contact. The pumped current generates a spin accumulation near the interface, which in turn induces a back-action current I_s^{back} .

Since both the driving field and the magnetization are real-valued, the other diagonal component of the susceptibility is given by $\chi_{--}(\omega) = \chi_{++}(-\omega)^*$. In this simple case, the resonance frequency coincides with the Larmor frequency $\omega_{\text{res}} = \gamma\mu_0 H_0$. The anisotropy energies and the demagnetization field break the rotational symmetry, so that the magnetic susceptibility is no longer diagonal if they are included, and the resonance frequency is given by the Kittel formula.[111]

In FMR experiment, instead of sweeping the frequency of the applied field, one usually fixes the driving frequency ω and sweeps the external field strength to find the resonance field H_{res} . Since the linewidth is directly proportional to Gilbert damping coefficient, the FMR experiment can be used to study the spin relaxation in the material. This can be used to study the spin pumping effect, introduced below.

4.2.3 Spin pumping in the normal state

The spin pumping effect refers to the generation of dc spin current to a metallic contact (N) by an adiabatically precessing magnetization in a ferromagnet (F), as illustrated in Fig. 13. Here we assume that the contact is in the normal state. The generalization to the SC state is considered below.

In the normal state, the spin and charge currents through the F/N interface are determined by the distribution matrices in F and N near the interface, and the 2×2 conductance tensor [112, 113]

$$G^{\sigma\sigma'} = \sum_{nm} [\delta_{nm} - r_{\sigma}^{nm}(r_{\sigma'}^{nm})^*], \quad (157)$$

where r_{σ}^{nm} are the reflection coefficients in a spin-diagonal reference frame, and M is the number modes on the normal metal side of the contact. Let us for simplicity assume that F is in equilibrium, so that the charge and spin accumulations, μ_c and μ_s , are non-zero only in N. The charge current is determined by the diagonal

elements of the conductance matrix [112]

$$I_c = \frac{e}{2h} \left\{ 2(G^{\uparrow\uparrow} + G^{\downarrow\downarrow})\mu_c + (G^{\uparrow\uparrow} - G^{\downarrow\downarrow})(\boldsymbol{\mu}_s \cdot \mathbf{m}) \right\}, \quad (158)$$

where \mathbf{m} is the magnetization direction of F. The spin-quantization axis of $G^{\sigma\sigma'}$ is determined by \mathbf{m} .

Calculating the spin current requires the whole conductance matrix, and is given by [112]

$$\begin{aligned} \mathbf{I}_s^{\text{acc}} = & 2(G^{\uparrow\uparrow} - G^{\downarrow\downarrow})\mu_c \mathbf{m} + (G^{\uparrow\uparrow} + G^{\downarrow\downarrow})[\boldsymbol{\mu}_s \cdot \mathbf{m}]\mathbf{m} \\ & + G_r^{\uparrow\downarrow} \mathbf{m} \times \boldsymbol{\mu}_s \times \mathbf{m} + G_i^{\uparrow\downarrow} \boldsymbol{\mu}_s \times \mathbf{m}. \end{aligned} \quad (159)$$

The longitudinal spin current on the first line depends only on $G^{\uparrow\uparrow}$ and $G^{\downarrow\downarrow}$. In contrast, the transverse spin current on the second line is determined by the complex spin-mixing conductance $G^{\uparrow\downarrow} = (G^{\downarrow\uparrow})^*$, which has been decomposed into the real and imaginary parts $G_{r,i}^{\uparrow\downarrow}$.

Now assume that the magnetization direction \mathbf{m} is not fixed, but rotates adiabatically. One can use time-dependent scattering theory to show that the change in the magnetization direction generates a current [112]

$$\mathbf{I}_s^{\text{pump}} = G_r^{\uparrow\downarrow} \mathbf{m} \times \frac{d\mathbf{m}}{dt} + G_i^{\uparrow\downarrow} \frac{d\mathbf{m}}{dt}, \quad (160)$$

which depends on the spin-mixing conductance. The spin direction of the generated spin current is perpendicular to the instantaneous magnetization direction.

Let us assume a steady circular precession at angle θ around the z -axis,

$$\mathbf{m}(t) = \sin \theta [\cos(\omega t)\mathbf{x} + \sin(\omega t)\mathbf{y}] + \cos \theta \mathbf{z}. \quad (161)$$

Now, ‘‘pumping’’ usually refers to creation of dc currents by a periodic drive. Here we find that the current (160) indeed has a dc component

$$I_{s,z}^{\text{pump}}(\omega = 0) = G_r^{\uparrow\downarrow} \omega \sin^2 \theta, \quad (162)$$

with spin along the z -axis. In spintronics applications, spin pumping can be used to create a source of spin-polarized currents.[114]

Spin pumping is usually modified by back-action effects. The pumped spin current (160) induces a spin accumulation in N, which diffuses from the interface and relaxes according to the spin diffusion equation [115]

$$\partial_t \boldsymbol{\mu}_s = D \partial_x^2 \boldsymbol{\mu}_s - \frac{\boldsymbol{\mu}_s}{\tau_{\text{sn}}}, \quad (163)$$

which can be derived from the kinetic Eq. (98). The boundary condition

$$D \partial_x \boldsymbol{\mu}_s(x = 0) = \mathbf{I}_s^{\text{pump}} + \mathbf{I}_s^{\text{acc}}, \quad (164)$$

takes into account the spin pumping current (160) and the back-action current due to induced spin accumulation [(159)]. The back action is not simply a reduction in

the magnitude of the spin current, but it can also change its structure. For example, with purely imaginary spin-mixing conductance $G_r^{\uparrow\downarrow} = 0$, the dc part of the direct spin pumping (160) is zero. Spin diffusion away from the interface and relaxation of spin make the direction of spin accumulation lag behind the magnetization direction, which in turn generates a dc component in the back-action current. The above effect can also be considered as happening at the interface, in which case it contributes to the real part of the spin-mixing conductance.[116]

4.2.4 Spin-transfer torque

From the point of view of the ferromagnet, spin current pumped into the metallic contact shows up as a loss of angular momentum,

$$\left. \frac{d\mathbf{S}}{dt} \right|_{\text{spin current}} = -\mathbf{I}_s. \quad (165)$$

The total spin is related to the magnetization by $\mathbf{S} = -\gamma\mathbf{M}V$, where V is the volume of the ferromagnet, and the minus sign is due to the negative charge of an electron. A dc spin current implies that the magnet is steadily losing its angular momentum to the contact. To hold a steady precession, there needs to be a driving force to compensate for this loss.

To include the spin current in the LLG equation, one should project out the longitudinal current $\mathbf{I}_s \parallel \mathbf{m}$, as it does not conserve the normalization $|\mathbf{M}| = M_s$. There are physical reasons to do this as well. In an insulating ferromagnet the diagonal part of the conductance is zero, and the interfacial current (159) only has a transverse component, so the projection does nothing. In a metallic ferromagnet the interfacial current can have both longitudinal and transverse components. For a strong magnet, the relaxation time for transverse currents is very short and we can assume that they are absorbed at the interface. The longitudinal spin accumulation on the other hand has a longer relaxation time, does not necessarily vanish inside the ferromagnet, and can influence the dynamics. Here we assume that it relaxes fast towards the ‘‘equilibrium’’ value determined by the Coriolis force.

Thus, to account for the absorption of transverse spin currents in Eq. (148), we add the Slonczewski term: [117]

$$\frac{d\mathbf{m}}{dt} = -\gamma(\mathbf{m} \times \mu_0\mathbf{H}) + \alpha \left(\mathbf{m} \times \frac{d\mathbf{m}}{dt} \right) + \frac{\gamma}{V} \mathbf{m} \times \mathbf{I}_s \times \mathbf{m}, \quad (166)$$

where the action of the double cross product is to project out the longitudinal part of the spin current. Since only the transverse currents are included, the extra term is compatible with the normalization $|\mathbf{m}| = 1$. Here we have assumed that when the spin current is absorbed, all the angular momentum flows into the magnetization, and not directly to the lattice or to some other degrees of freedom.

What is the effect of this additional term on the magnetization dynamics? First of all, the added term does not need to be generated by spin pumping, but also includes situations in which the magnetization is driven by applying a spin-polarized

current through the magnet.[117] In the case of spin-pumping current it is natural to divide the transverse current into two perpendicular components

$$\mathbf{m} \times \mathbf{I}_s \times \mathbf{m} = I_f \dot{\mathbf{m}} + I_d(\mathbf{m} \times \dot{\mathbf{m}}). \quad (167)$$

The first term is a field-like current, which can be combined with the left-hand side of Eq. (166) and has the effect of renormalizing the gyromagnetic ratio. The result is a shift in the FMR resonance frequency. The second term is a damping-like current, which can be combined with the Gilbert term and gives an extra contribution to the Gilbert damping. The increase in the Gilbert damping can be observed as an increase of the FMR resonance linewidth.

A comparison with the spin pumping current, Eq. (160), shows that the real part of the spin-mixing conductance contributes to damping, whereas the imaginary part gives a field-like contribution. This is consistent with the fact that only the real part of the spin-mixing conductance generates a dc spin current, which leads to a loss of z -component of the angular momentum and a change in the precession angle θ .

4.3 Spin pumping in the superconducting state

Above consideration have been for the normal state, for which the spin diffusion can be expressed in terms of energy-integrated quantities. In the superconducting state, we cannot neglect the energy dependence as easily, and the theory is more complicated. Before going into a detailed description, let us summarize the main effects which superconductivity has on spin pumping. It is useful to consider the linear spin response of the superconductor to an exchange field at a finite frequency,

$$\mathbf{S}(\omega) = \hat{\chi}(\omega)\mathbf{h}(\omega), \quad (168)$$

where $\hat{\chi}$ is the 3×3 spin susceptibility tensor and \mathbf{h} is the dynamic exchange field. Below, we identify some processes through which a ferromagnet with dynamic magnetization interacts with the superconductor.

First, the dynamical magnetization of the ferromagnet can excite quasiparticles in SC. If the ferromagnet is a metal, the quasiparticle excitations can be tunneled between FM and SC, and if it is an insulator, the time-dependent exchange field at the interface can directly excite quasiparticles in SC. The strength of the latter process can be directly related to the imaginary part of the spin susceptibility $\text{Im} \chi^{++}(\omega)$ (Fig. 14a, bottom panel). Quasiparticle excitations are suppressed at low temperatures and at low frequencies due to the superconducting gap, so that the imaginary part of the spin susceptibility vanishes.[119–122] In most of the publications, we assume that the spin currents are created by the spin pumping effect. However, there can also be spin currents driven a temperature difference between F magnons and SC electrons. This process is considered in Publication VII.

The ferromagnet can also act as a pair-breaker and suppress Δ at the interface. This effect can also be modified by the induced spin currents,[123] or depend on the

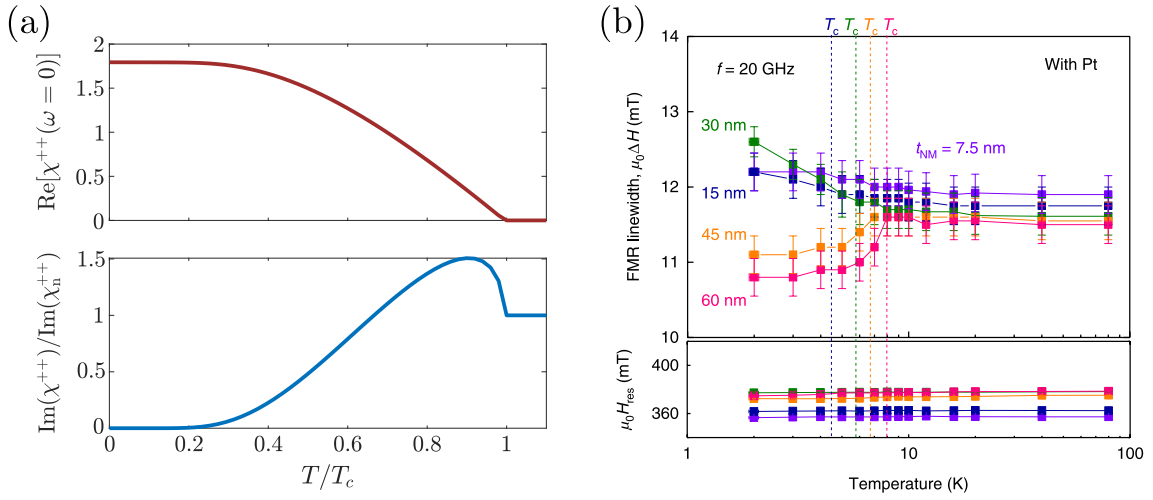


FIGURE 14 (a) Top: Real part of the spin susceptibility in the SC state as a function of temperature. The real part is associated with the magnetic proximity effect, and it vanishes in the normal state. Bottom: Imaginary part of the spin susceptibility, normalized by its normal state value. The imaginary part is associated with quasiparticle excitations, and it vanishes at low temperatures and at zero frequency. The coherence peak below T_c is due to spin-orbit scattering. Here, $\tau_{\text{so}}^{-1} = 0.2\Delta_0$ and $\Gamma = 0.01\Delta_0$, and for the imaginary part $\omega = 0.02\Delta_0$. (b) Enhanced spin transport in the superconducting state in Pt/Nb/Ni₈₀Fe₂₀/Nb/Pt multilayers. Temperature dependence of the FMR linewidth $\mu_0\Delta H$ (top) and the resonance magnetic field $\mu_0 H_{\text{res}}$ (bottom) for various Nb thicknesses. The dashed lines indicate their T_c . The samples with 45 nm and 60 nm Nb layer show the expected suppression of Gilbert damping, but the other samples show an enhancement. Panel (b) is reprinted with permission from Ref. [118], Copyright 2018 Springer Nature.

relative angle between the magnetizations in a system with multiple magnets.[124, 125] This effect has a minor role in Publication **VIII**, but is otherwise not studied in this dissertation.

A charge supercurrent flowing in a ferromagnetic weak link is accompanied by a spin current, and in systems with multiple SCs and inhomogeneous magnetization, there is a coupling between the magnetization direction and the relative superconducting phase between the elements. This coupling manifests as long-range triplet supercurrents[126, 127], pair amplitude oscillations[128], and the π -Josephson effect[129, 130]. In this dissertation, we restrict our study to systems with a single superconductor.

Finally, the magnetic proximity effect from the ferromagnet can polarize the SC.[63] The strength of the proximity effect is related to the real part of the spin susceptibility (Fig. 14a, top panel). The exchange field inside the SC follows the direction of the dynamic magnetization, and it can also excite quasiparticles in the SC. In Publication **VIII** we show that the magnetization gradients caused by the proximity effects from non-collinear sources are associated with spin supercurrents. Unlike the quasiparticle currents, the spin supercurrent is not suppressed at low temperatures, but its temperature dependence instead follows that of $\text{Re } \chi^{++}$, shown in Fig. 14a.

In FMR experiments, dc spin pumping can be identified from the increase in the effective Gilbert damping of the ferromagnet.[112] The suppression of quasiparticle excitations show as a suppression of interfacial Gilbert damping below the SC transition temperature.[119, 131] However, as shown in Fig.14b, in some experiments an increase in Gilbert damping below the transition temperature has been observed.[118, 132, 133] In Publication **VIII** we argue that in some cases this may be attributed to an increased coupling between the different layers mediated by spin supercurrents.

4.3.1 Boundary condition to a ferromagnetic metal

To derive a suitable boundary condition for the interface between a SC and a ferromagnetic metal with dynamic magnetization, let us start by considering the effect of the precessing magnetization on the conduction electrons of the ferromagnetic metal. This effect can be calculated in different ways. For example, one can make a connection with the Berry phase, and notice that the time-evolution has two terms: an ordinary dynamical phase, and a spin-dependent geometric phase which generates the spin accumulation, and ultimately the spin pumping effect[134]. Here, we use quasiclassical theory to calculate the distribution function and to complement the Berry phase description, which does not explicitly describe the relaxation processes.

The conduction electrons are described by the Hamiltonian

$$H(t) = \frac{p^2}{2m} - \mu + \mathbf{J}(t) \cdot \boldsymbol{\sigma}, \quad (169)$$

where the time-dependent exchange field is $\mathbf{J}(t) = J\mathbf{m}(t)$. For the quasiclassical theory to be applicable, the exchange field must be small compared to the Fermi energy. This requirement comes from the normalization condition which does not

allow for the two spin bands to have different densities of states at the Fermi level. The magnetization precesses circularly according to Eq. (161). We also assume that there is some coupling which provides spin relaxation with rate τ_s^{-1} and inelastic relaxation with rate $\tau_{\text{e-ph}}^{-1}$.

In the normal state, we can neglect the Nambu structure and write the kinetic equation (98) as

$$\partial_t \hat{f}(t, t') + \partial_{t'} \hat{f}(t, t') + i[\hat{f} \circledast \mathbf{J} \cdot \boldsymbol{\sigma}](t, t') = \frac{3\hat{f}(t, t') - \boldsymbol{\sigma} \cdot \hat{f}(t, t') \boldsymbol{\sigma}}{3\tau_s} + Z_{\text{e-ph}}(t, t'), \quad (170)$$

where $Z_{\text{e-ph}}$ includes inelastic relaxation. The time-dependence of $\mathbf{J}(t)$ can be removed by applying a unitary transformation $U(t) = \exp(-i\omega t \sigma_3/2)$, which takes us into a frame rotating along the magnetization. The transformed distribution function

$$\tilde{f}(t - t') = U(t) \hat{f}(t, t') U(t')^\dagger, \quad (171)$$

depends only on the relative time, and the corresponding spin accumulation is static. By applying the unitary transformation on Eq. (170), taking the spin trace, and integrating over energy, we obtain the equation

$$\tilde{\boldsymbol{\mu}}_s \times \left[J\mathbf{m}(0) - \frac{\omega \mathbf{z}}{2} \right] + \frac{\tilde{\boldsymbol{\mu}}_s - \omega \mathbf{z}}{\tau_s} = 0. \quad (172)$$

Because the form of $\boldsymbol{\sigma} \cdot \hat{f}(t, t') \boldsymbol{\sigma}$ is not invariant under the unitary transformation, the spin relaxation has an unusual form in the rotating frame. The inelastic relaxation does affect the spin accumulation, so $\tau_{\text{e-ph}}$ vanishes from this equation.

With strong exchange field $J \gg \omega, \tau_s^{-1}$, the spin accumulation can only have a longitudinal component

$$\tilde{\boldsymbol{\mu}}_s = (\omega \cos \theta) \mathbf{m}(0). \quad (173)$$

At the opposite limit of a vanishing exchange field $J = 0$, the time-dependence of the Hamiltonian (169) vanishes, and the system stays in equilibrium. In the rotating frame, the equilibrium state has a spin accumulation $\tilde{\boldsymbol{\mu}}_s^{\text{eq}} = \omega \mathbf{z}$ generated by the time-dependent unitary transformation. On the other hand, since Eq. (173) for $J \neq 0$ differs from the equilibrium value $\tilde{\boldsymbol{\mu}}_s^{\text{eq}}$, it corresponds to a finite spin accumulation in the laboratory frame. This spin accumulation drives the spin current associated with the spin pumping effect between the FM and a contact.

What is the distribution function which gives the spin accumulation (173)? Since the distribution function depends on energy and thus contains more information than the spin accumulation, the answer depends on the inelastic relaxation rate. For simplicity, we assume a fast inelastic relaxation, so that each spin band has its own thermal distribution, displaced in energy by a spin-dependent voltage:

$$\tilde{f}(\varepsilon) = \tanh \left(\frac{\varepsilon - (\omega \cos \theta/2) \mathbf{m}(0) \cdot \boldsymbol{\sigma}}{2T} \right). \quad (174)$$

The spin accumulation and the distribution function are frame-dependent quantities. The laboratory frame distribution function is obtained by making a Fourier transform of Eq. (174) and inverting the unitary transformation (171).

Now we are in the position to give the boundary condition which can describe spin pumping from a ferromagnetic metal to a SC. However, we would like to go beyond the quasiclassical limit and describe a strong ferromagnet with non-negligible Fermi surface spin polarization P . To emulate the Fermi surface spin polarization we can use the spin-filter boundary condition of Ref. [135]. It states that

$$\mathbf{n} \cdot \check{\mathbf{I}} = \kappa[\hat{\Gamma} \circ \check{g}_F \circ \hat{\Gamma} \circledast \check{g}], \quad (175)$$

where κ parametrizes the conductance of the junction, \check{g} is the quasiclassical GF of the SC at the interface, and \check{g}_F is the quasiclassical GF of the ferromagnetic metal, with components

$$g_F^R(t, t') = -g_F^A(t, t') = \tau_3 \delta(t - t'), \quad (176)$$

$$g_F^K(t, t') = 2\hat{f}(t, t'). \quad (177)$$

The distribution function characterizing \check{g}_F is hence obtained from Eqs. (171) and (174). The spin-filter matrices are $\hat{\Gamma}(t) = \mathcal{T} + \mathcal{U}\mathbf{m}(t) \cdot \boldsymbol{\sigma} \tau_3$, with $\mathcal{U}^2 + \mathcal{T}^2 = 1$, and $2\mathcal{U}\mathcal{T} = P$.

The above boundary condition is utilized in Publication **V**,³ where we consider a heterostructure of a metallic nanomagnet with a dynamic magnetization coupled with a spin-split SC. In this system, we predict a non-linear spin torque, driven either by a temperature difference or a voltage across the interface. We extend the linear response matrix (144) by including the precession frequency ω as a driving force, and the dc spin torque $\hbar\tau_z = -I_{sz}$ as a current. We derive for the interface a Keldysh action, describing the coupled charge, heat and spin transport in the presence of a precessing magnetization, which can be used to calculate the full counting statistics of the currents. We also predict a cooling effect, in which the precessing magnetization can cool either the FM or the SC.

4.3.2 Boundary condition to a ferromagnetic insulator

An interface between a ferromagnetic insulator and a superconductor can be described in the Usadel equation with the boundary condition (140), which can be directly generalized for time-dependent magnetization by replacing the ordinary products with time-convolution products:

$$\mathbf{n} \cdot \check{\mathbf{I}}(t, t') = iJ[\mathbf{m} \cdot \boldsymbol{\sigma} \tau_3 \circledast \check{g}](t, t'). \quad (178)$$

To find the spin pumping current we take a spin trace from both sides and integrate over energy. The details are given in Supplementary information Sec. I.B of Publication **VII**. The spin current is given by

$$\mathbf{I}_s(t) = JN_0[\boldsymbol{\mu}_s(t) \times \mathbf{m}(t) - \partial_t \mathbf{m}(t)], \quad (179)$$

³ In fact, we formulate the boundary condition between FM and SC in Publication **V** in a slightly different way by using the momentum-integrated GFs for ferromagnetic metal, but the final result coincides with the above quasiclassical approach.

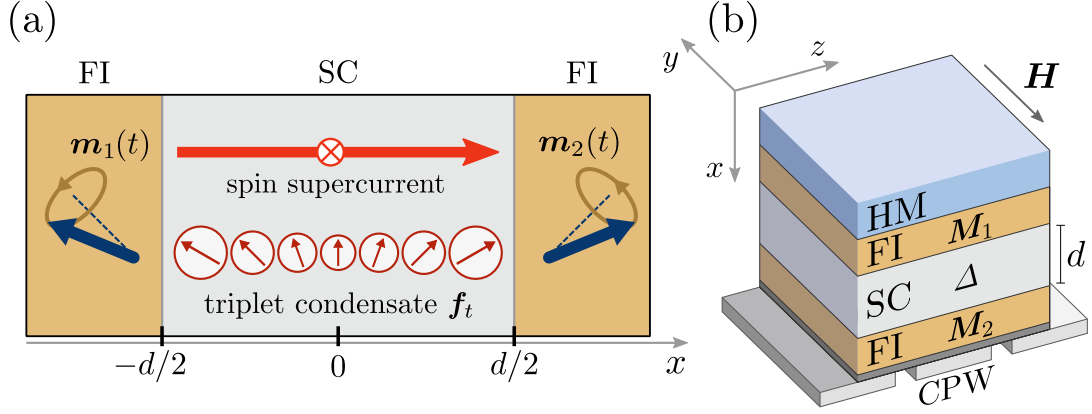


FIGURE 15 Ferromagnetic insulator/superconductor/ferromagnetic insulator trilayer. (a) Spin supercurrent mediated by the spin triplet condensate function f_t . (b) Sketch of the experimental setting for a FMR experiment. The heavy metal layer (HM) has a strong spin relaxation and controls the Gilbert damping of the second FI. Reprinted from Publication VIII, Copyright 2022 the authors.

where μ_s is the spin accumulation inside the SC near the interface. The first term describes the current due to spin accumulation, and the second one is the spin pumping current. Comparing to Eqs. (159) and (160), we can identify JN_0 with the imaginary part of the spin mixing conductance.

The boundary condition (178) is used in Publications VII, VIII and IX to study spin pumping from an insulating ferromagnet to a SC. In Publication VII the focus is not on spin pumping, but on the related spin battery effect, where a dynamic magnetization in FI induces a static spin accumulation in the SC. This effect is enhanced in the SC by several orders of magnitude relative to the normal state due to the spin-energy mixing enabled by the magnetic proximity effect. Related to this finding, we predict a giant Seebeck effect in FI/SC/FM structures, driven by the temperature bias between the FI magnons and the SC electrons.

4.3.3 Spin supercurrent

In Publication VIII we study a system in which a superconductor is sandwiched between two ferromagnetic insulators with noncollinear magnetization. (Fig. 15) This system supports a spin supercurrent, which is a dissipationless spin current.

Spin current comes in different forms. There are incoherent spin currents associated with the gradients of non-equilibrium spin accumulation, given in the normal state by

$$\mathbf{j}_s^k = D\nabla\mu_{s,k}. \quad (180)$$

These are fundamentally non-equilibrium currents, since spin accumulation vanishes in equilibrium. Then there are spin currents associated with gradients of magnetization. For example, in a Heisenberg ferromagnet with inhomogeneous equilibrium spin

density $S_k(\mathbf{x})$, there is a current

$$\mathbf{j}_s^k = K \sum_{i,j=1}^3 \epsilon_{ijk} S_i \times \nabla S_j, \quad (181)$$

where K is the exchange stiffness of the ferromagnet. This kind of currents can exist in equilibrium if the non-homogeneous magnetization is stabilized by some external forces. Since spin is not generally a conserved quantity, equilibrium spin currents have been a subject of some controversy.[136].

Superconductors can support both kinds of spin currents. The diffusive spin current is carried by quasiparticle excitations like in normal metals. At low temperatures the quasiparticles become difficult to excite and the quasiparticle currents are suppressed. The equilibrium spin currents on the other hand require a magnetization which is usually absent in a SC but can be introduced by magnetic proximity effect. If the proximity field is introduced from multiple sources which have a non-collinear magnetization, the spin-splitting field in the SC develops gradients and a spin supercurrent is induced.

In Publication **VIII** we consider spin currents in a superconducting film sandwiched between two ferromagnetic insulators (Fig. 15). Even if the two magnets are collinear in equilibrium, a FMR drive can induce a dynamically generated non-collinearity. This creates an ac spin supercurrent which couples the two magnets. We propose that this effect can explain the observed Gilbert damping increase below T_c in multilayers with ferromagnetic and superconducting elements. [118, 132, 133, 137]

4.4 Higgs mode

The superconducting order parameter is a dynamic quantity which responds to the perturbations in the electronic state in accordance with the self-consistency equation (109). In single-band s -wave superconductors, there are two collective modes related to the broken U(1) gauge symmetry. The first mode is the Nambu-Goldstone mode, the oscillation of the phase of the order parameter, which acts to restore the gauge symmetry. In a neutral superfluid, the Nambu-Goldstone mode has a linear dispersion, but in a superconductor, in which the elementary constituents of the superfluid are charged, the Coulomb interaction couples the Nambu-Goldstone mode to plasma oscillations and lifts it to the plasma frequency. The other mode is the (Anderson-)Higgs mode, the oscillation of the modulus of the order parameter. The properties of the Higgs mode are in the focus in this section. The two modes are illustrated in Fig. 16a.

The Higgs mode is analogous with the Higgs boson in electroweak theory, the unified theory of electromagnetic and weak interactions. Both superconductivity and electroweak theory are gauge theories, and the breaking of the gauge symmetry in both theories is described by the Anderson-Higgs mechanism. In superconductivity, the Anderson-Higgs mechanism explains how the photon acquires a mass inside the

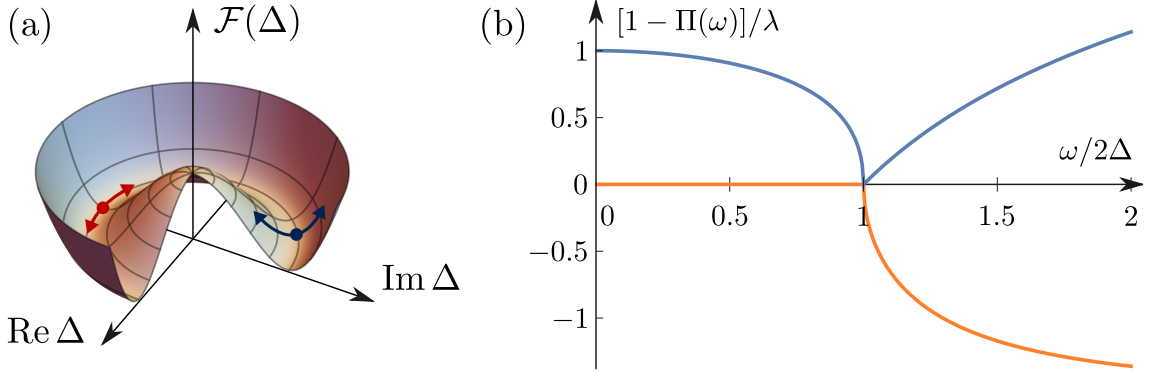


FIGURE 16 (a) Superconducting free energy with Nambu-Goldstone (red) and Anderson-Higgs (dark blue) modes generated in the symmetry breaking. (b) Polarization operator. Blue is the real part and orange is the imaginary part. The Higgs mode is at frequency $\omega = 2\Delta$.

SC (i.e. hybridizes with electrons to form a plasmon[138]). In electroweak theory, the same mechanism explains why the W and Z gauge bosons are massive but the photon remains massless. A brief history of the connection between the two theories is given by Anderson in Ref. [139]. In particle physics, the Higgs boson is of central importance, but in superconductivity the amplitude mode was largely neglected until its discovery by Littlewood and Varma in 1982.[140]

In Publications VI and IX we consider the Higgs mode at the dirty limit using the Usadel equation. Although the disorder is not essential for the existence of the Higgs mode, it does alter the coupling between the Higgs mode and the external electromagnetic field, making it easier to excite the Higgs mode with fields with a small wavevector.[105] Because Higgs mode is charge-neutral, it does not couple to electromagnetic fields linearly. Even in the dirty limit one needs nonlinear fields to excite it.

We can picture the superconductor as if it consisted of two coupled dynamical systems, the electronic system described by the Usadel equation, and the Cooper pairs described by the self-consistency equation. Let us assume that we apply some driving force at frequency ω , which perturbs the electronic system from its equilibrium configuration. In linear response, the direct perturbation of the electronic system by the force is encoded in the propagator $\check{g}_{(1)}(\varepsilon, \varepsilon - \omega)$, which enters the self-consistency equation and excites an order-parameter amplitude oscillation $\Delta^{(1)}(\omega)$. The back-action from $\Delta^{(1)}(\omega)$ perturbs the electronic system, and the electronic perturbation excites further order-parameter oscillations. The total order-parameter oscillation is

$$\begin{aligned} \Delta(\omega) &= \Delta^{(1)}(\omega) + \Pi(\omega)\Delta^{(1)}(\omega) + \Pi(\omega)^2\Delta^{(1)}(\omega) + \dots \\ &= \Pi(\omega)\Delta(\omega) + \Delta^{(1)}(\omega), \end{aligned} \quad (182)$$

where the polarization operator $\Pi(\omega)$ describes the back-action from an order-parameter oscillation to itself, mediated by the electronic system. The above equation has the solution

$$\Delta(\omega) = \frac{\Delta^{(1)}(\omega)}{1 - \Pi(\omega)}. \quad (183)$$

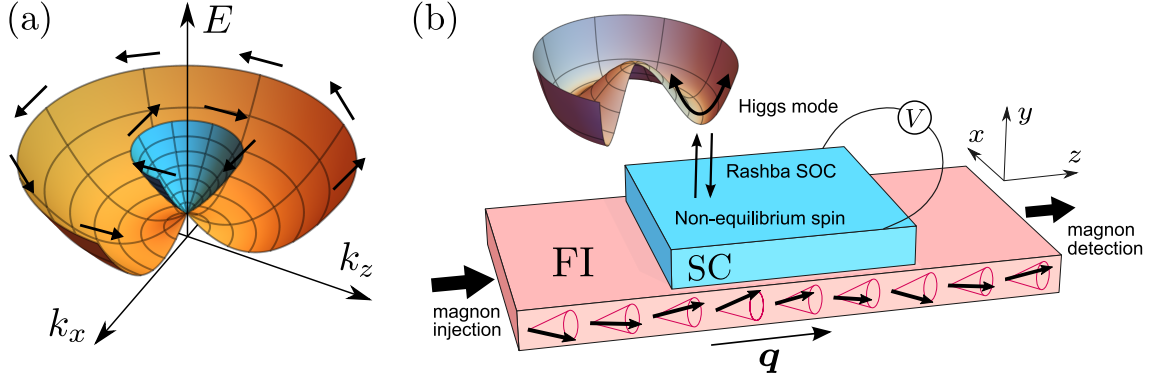


FIGURE 17 (a) Parabolic dispersion split by Rashba SOC. Arrows indicate the spin direction. (b) Device geometry for Rashba-enabled Higgs excitation by magnons. Panel (b) reprinted from Publication IX (CC BY 4.0).

The denominator diverges for $z \in \mathbb{C}$ such that $\Pi(z) = 1$. The condition $\text{Re} \Pi(\omega) = 1$ corresponds to the Higgs mode.

The polarization operator can be calculated using the Usadel equation by considering the linear response to an order parameter oscillation $\Delta(\omega)$, and substituting the solution into the self-consistency equation. In Matsubara formalism, the polarization operator can be expressed as [105]

$$\Pi(2\Omega_n) = 1 + \pi\lambda T \sum_{\omega_m} \frac{\Delta^2 + \Omega_n^2}{(\omega_m^2 - \Omega_n^2)\sqrt{\omega_m^2 + \Delta^2}}, \quad (184)$$

where Ω_n and ω_m are bosonic and fermionic Matsubara frequencies, respectively. The expression for the polarization operator for a real frequency [140] can be obtained using the analytical continuation. [105] Above, the explicit λ -dependence cancels against the λ -dependence of $\Delta^{(1)}(\omega)$. The polarization operator is shown in Fig. 16b. The Higgs mode is not a Lorentzian like a regular resonance. Mathematically it comes from the branch cut in the square root function in Eq. (184), and is instead called a pseudoresonance. [141]

In Publication VI we consider the Higgs mode in spin-split superconductors. It turns out that the spin splitting does not change the properties of the Higgs mode much. It still exists at the same frequency and remains charge neutral. However, it does now couple to a longitudinal spin, since the order parameter depends on the exchange field strength h : $\partial\Delta/\partial h \neq 0$ if $h \neq 0$. Utilizing the spin-charge coupling at a SC/FM interface allows for the conversion of the Higgs signal to a charge signal. We propose an experimental scheme in which the Higgs mode is excited by a non-linear ac electric field, and the resulting charge signal is measured.

4.5 Spin-orbit coupling

In relativistic quantum mechanics, the total angular momentum $\mathbf{J} = \mathbf{L} + \mathbf{S}$ of an electron is conserved in a spherically symmetric potential, but orbital angular

momentum $\mathbf{L} = \mathbf{r} \times \mathbf{p}$ and spin \mathbf{S} are not separately conserved. At the non-relativistic limit, this non-conservation manifests as a spin-orbit coupling (SOC)

$$H_{\text{so}} = -\frac{\hbar}{4m^2c^2} \boldsymbol{\sigma} \cdot \mathbf{p} \times (\nabla V), \quad (185)$$

where m is the electron mass, c is the speed of light, and $\mathbf{E} = -\nabla V$ is the electric field. In crystalline solids the electric potential is generated by the atomic cores, and thus the heavy elements induce larger spin-orbit fields than the light ones. The form of the spin-orbit coupling is determined by the crystal symmetry. SOC can also arise from the potential of random impurity atoms. [97] SOC arising from impurity potential is known as extrinsic SOC in contrast to a SOC arising from the crystalline potential, which is called intrinsic SOC.

A special kind of SOC arises from structural inversion asymmetry. For example at an interface between two different materials there generally are electric fields pointing towards the bulk (here we assume the interface is on the xz -plane). This gives the Rashba SOC with the Hamiltonian

$$H_{\text{Rashba}} = \alpha \boldsymbol{\sigma} \cdot (\mathbf{p} \times \mathbf{y}), \quad (186)$$

where α is the Rashba coefficient. The Rashba field splits the dispersion so that the eigenstates with $p_z = 0$ are eigenstates of σ_z , whereas eigenstates with $p_x = 0$ are eigenstates of σ_x . (Fig. 17).

In Publication **IX** we consider a thin-film superconductor interfaced with a ferromagnetic insulator. The FI induces two proximity fields inside the superconductor: the Zeeman field $\mathbf{h} = \mathbf{h}_0 + \mathbf{h}_\perp(t)$, which has a dynamic component \mathbf{h}_\perp due to magnons propagating in FI along the SC/FI interface, and the Rashba field. In the absence of the Rashba field, the magnons cannot excite the Higgs mode due to a spin-rotation symmetry about the static field \mathbf{h}_0 . With the Rashba field this symmetry is broken and the magnons can excite the Higgs mode. As shown in the Publication, the coupling to the Higgs mode modifies the spin susceptibility of the SC, which can be experimentally detected by measuring the magnon-induced voltage generated by the inverse spin Hall effect.

5 CONCLUSIONS AND SUMMARY

In this dissertation, I studied theoretically the interactions between superconductivity and magnetism in two settings: as the competition between the magnetic and superconducting orders on flat band materials, and as the interplay between the two orders on nanoelectronic hybrid structures.

In the first part of this dissertation, the emphasis was on electron-phonon superconductivity on graphene-based materials. Our results on magic-angle twisted bilayer graphene (MATBG), and other observations[49] suggest that the observed superconductivity can be explained with the conventional phonon mechanism. Although the interaction enabling superconductivity in MATBG may not be exotic, MATBG is still an exciting material, as it and the other van der Waals materials offer a uniquely controllable platform for designer quantum matter.[5] By combining layers of materials with different properties one can create systems with emergent properties and exotic physics. This field can be expected to produce further breakthroughs and calls for further studies, both theoretical and experimental.

Purely graphene-based materials also hold further promise. As the discovery of magic-angle twisted bilayer graphene shows, even after years of intense research, graphene still manages to surprise researchers. The combination of the recent discovery of superconductivity in untwisted few-layer graphene structures,[27, 28] and the earlier hints of high-temperature superconductivity in highly oriented pyrolytic graphite with large number of layers[31, 32] associated with flat bands[33] suggest that it may be possible to achieve a surprisingly high T_c in materials based purely on graphene. This would no doubt have plenty of technological uses. Whether such promise can be realized in near future depends largely on the development of fabrication techniques for van der Waals materials with many layers.

In the second part of the dissertation, I studied spintronics systems with superconducting elements. Spintronics is a promising research direction in the attempt to develop more energy-efficient memory and logic devices.[85, 142] Since the modern societies run on data processing and electronic communication, increasing energy-efficiency of information and communications technology (ICT) is at the center of the fight against the climate change. As of 2020 globally more than 10% of the generated electricity is consumed by ICT. [143, 144] Much of this

electricity is produced by burning fossil fuels, or could be used to replace them. What superconductivity also adds to spintronics are the effects related to quantum coherence, nonlocality, and entanglement.[91, 94, 145] These concepts are central for quantum computing, and thus superconducting spintronics may also provide solutions for quantum information processing.

In the overview part of the dissertation, I presented the theory of the quasiclassical superconductivity in combination with the Keldysh theory for nonequilibrium states. The initial forms of both of these theories were originally laid out in the 1960s and have since then reached a mature state. However, extensions to the quasiclassical theory are still being developed, especially with regards to magneto-electric effects enabled by spin-orbit coupling,[97, 146] which are currently only partially understood in a dynamic setting.

In the publications related to the second part, we envisioned new functionalities enabled by the magnetic proximity effect, such as a thermoelectric detector based on the giant thermoelectric effect, a cooling effect driven by the magnetic precession, a coupling between the Higgs mode of the superconductor and the spin degrees of freedom, a giant spin battery effect, and a coupling between precessional magnetic modes mediated by the spin supercurrent. These studies either suggest new experimental schemes or were motivated by recent experiments[118, 132, 133]. Although we have suggested in the publications some theoretical interpretations for these experiments, it can be said they are still only partially understood, and especially a quantitative comparison between the theory and the experimental results requires further work.

BIBLIOGRAPHY

- [1] P. Feynman Richard et al. “There is Plenty of Room at the Bottom”. *Engineering and Science, California Institute of Technology* (1960).
- [2] C. P. Toumey. “Reading Feynman into nanotechnology: A text for a new science”. *Techné: Research in Philosophy and Technology* 12.3 (2008), pp. 133–168. DOI: [10.5840/techne20081231](https://doi.org/10.5840/techne20081231).
- [3] P. M. Reis, H. M. Jaeger, and M. van Hecke. “Designer Matter: A perspective”. *Extreme Mech. Lett.* 5 (2015), pp. 25–29. ISSN: 2352-4316. DOI: <https://doi.org/10.1016/j.eml.2015.09.004>.
- [4] A. A. Khajetoorians et al. “Creating designer quantum states of matter atom-by-atom”. *Nature Rev. Phys.* 1.12 (2019), pp. 703–715. DOI: [10.1038/s42254-019-0108-5](https://doi.org/10.1038/s42254-019-0108-5).
- [5] J. L. Lado and P. Liljeroth. “Designer quantum matter in van der Waals heterostructures”. *arXiv preprint arXiv:2102.11779* (2021).
- [6] H. Kamerlingh Onnes. “The resistance of pure mercury at helium temperatures”. *Commun. Phys. Lab. Univ. Leiden* 120 (1911).
- [7] W. Meissner and R. Ochsenfeld. “Ein neuer Effekt bei Eintritt der Supraleitfähigkeit”. *Sci. Nat.* 21.44 (1933), pp. 787–788. DOI: [10.1007/BF01504252](https://doi.org/10.1007/BF01504252).
- [8] F. London and H. London. “The electromagnetic equations of the supraconductor”. *Proc. R. Soc. A* 149.866 (1935), pp. 71–88. DOI: [10.1098/rspa.1935.0048](https://doi.org/10.1098/rspa.1935.0048).
- [9] L. D. Landau and V. L. Ginzburg. “On the theory of superconductivity”. *Zh. Eksp. Teor. Fiz.* 20 (1950), p. 1064.
- [10] J. Bardeen, L. N. Cooper, and J. R. Schrieffer. “Theory of superconductivity”. *Phys. Rev.* 108.5 (1957), p. 1175. DOI: [10.1103/PhysRev.108.1175](https://doi.org/10.1103/PhysRev.108.1175).
- [11] M. Feigel’man, A. Larkin, and M. Skvortsov. “Keldysh action for disordered superconductors”. *Phys. Rev. B* 61.18 (2000), p. 12361. DOI: [10.1103/PhysRevB.61.12361](https://doi.org/10.1103/PhysRevB.61.12361).
- [12] G. Eliashberg. “Interactions between electrons and lattice vibrations in a superconductor”. *Sov. Phys. JETP* 11.3 (1960), pp. 696–702.
- [13] J. Schrieffer. *Theory of superconductivity*. New York: WA Benjamin, Inc., 1964.
- [14] F. Marsiglio. “Eliashberg theory: A short review”. *Ann. Phys.* 417 (2020). Eliashberg theory at 60: Strong-coupling superconductivity and beyond, p. 168102. ISSN: 0003-4916. DOI: <https://doi.org/10.1016/j.aop.2020.168102>.
- [15] W. Heisenberg. “Zur Theorie des Ferromagnetismus”. *Zeitschrift für Physik* 49.9-10 (1928), pp. 619–636.
- [16] E. C. Stoner. “Collective electron ferromagnetism”. *Proc. R. Soc. Lond. A* 165.922 (1938), pp. 372–414. DOI: [10.1098/rspa.1938.0066](https://doi.org/10.1098/rspa.1938.0066).

- [17] J. Jensen and A. R. Mackintosh. *Rare earth magnetism*. Clarendon Press Oxford, 1991. ISBN: 978-0198520276. URL: www.fys.ku.dk/~jjensen/REM.htm.
- [18] E. Snider et al. “Room-temperature superconductivity in a carbonaceous sulfur hydride”. *Nature* 586.7829 (2020), pp. 373–377. DOI: [10.1038/s41586-020-2801-z](https://doi.org/10.1038/s41586-020-2801-z).
- [19] T. T. Heikkilä, N. B. Kopnin, and G. E. Volovik. “Flat bands in topological media”. *JETP letters* 94.3 (2011), pp. 233–239. DOI: [10.1134/S0021364011150045](https://doi.org/10.1134/S0021364011150045).
- [20] A. H. Castro Neto et al. “The electronic properties of graphene”. *Rev. Mod. Phys.* 81.1 (2009), p. 109. DOI: [10.1103/RevModPhys.81.109](https://doi.org/10.1103/RevModPhys.81.109).
- [21] N. B. Kopnin and T. T. Heikkilä. “Surface superconductivity in rhombohedral graphite”. In: *Carbon-based new superconductors - Towards high temperature superconductivity*. Ed. by J. Haruyama. 2015. ISBN: 978-981-4303-31-6.
- [22] W. Su, J. Schrieffer, and A. J. Heeger. “Solitons in polyacetylene”. *Phys. Rev. Lett.* 42.25 (1979), p. 1698. DOI: [10.1103/PhysRevLett.42.1698](https://doi.org/10.1103/PhysRevLett.42.1698).
- [23] J. Nissinen, T. Heikkilä, and G. Volovik. “Topological polarization, dual invariants, and surface flat bands in crystalline insulators”. *Phys. Rev. B* 103.24 (2021), p. 245115. DOI: [10.1103/PhysRevB.103.245115](https://doi.org/10.1103/PhysRevB.103.245115).
- [24] T. T. Heikkilä and G. E. Volovik. “Flat bands as a route to high-temperature superconductivity in graphite”. In: *Basic Physics of Functionalized Graphite*. Ed. by P. D. Esquinazi. Cham: Springer International Publishing, 2016, pp. 123–143. ISBN: 978-3-319-39355-1. DOI: [10.1007/978-3-319-39355-1_6](https://doi.org/10.1007/978-3-319-39355-1_6).
- [25] Y.-Z. Chou et al. “Acoustic-phonon-mediated superconductivity in Bernal bilayer graphene” (2021). arXiv: [2110.12303](https://arxiv.org/abs/2110.12303).
- [26] P. Coleman. *Introduction to many-body physics*. Cambridge: Cambridge University Press, 2015. DOI: [10.1017/CBO9781139020916](https://doi.org/10.1017/CBO9781139020916).
- [27] H. Zhou et al. “Isospin magnetism and spin-triplet superconductivity in Bernal bilayer graphene” (2021). arXiv: [2110.11317](https://arxiv.org/abs/2110.11317).
- [28] H. Zhou et al. “Superconductivity in rhombohedral trilayer graphene”. *Nature* 598.7881 (Oct. 2021), pp. 434–438. DOI: [10.1038/s41586-021-03926-0](https://doi.org/10.1038/s41586-021-03926-0).
- [29] Y. Cao et al. “Unconventional superconductivity in magic-angle graphene superlattices”. *Nature* 556.7699 (2018), pp. 43–50. DOI: [10.1038/nature26160](https://doi.org/10.1038/nature26160).
- [30] Y. Cao et al. “Correlated insulator behaviour at half-filling in magic-angle graphene superlattices”. *Nature* 556.7699 (2018), pp. 80–84. DOI: [10.1038/nature26154](https://doi.org/10.1038/nature26154).
- [31] Y. Kopelevich et al. “Landau level quantization and possible superconducting instabilities in highly oriented pyrolytic graphite”. *Phys. Solid State* 41.12 (1999), pp. 1959–1962. DOI: [10.1134/1.1131135](https://doi.org/10.1134/1.1131135).
- [32] Y. Kopelevich et al. “Ferromagnetic-and superconducting-like behavior of graphite”. *J. Low Temp. Phys.* 119.5 (2000), pp. 691–702. DOI: [10.1023/A:1004637814008](https://doi.org/10.1023/A:1004637814008).

- [33] G. Volovik. “Graphite, graphene, and the flat band superconductivity”. *JETP Lett.* 107.8 (2018), pp. 516–517. DOI: [10.1134/S0021364018080052](https://doi.org/10.1134/S0021364018080052).
- [34] H. C. Po et al. “Origin of Mott insulating behavior and superconductivity in twisted bilayer graphene”. *Phys. Rev. X* 8 (3 Sept. 2018), p. 031089. DOI: [10.1103/PhysRevX.8.031089](https://doi.org/10.1103/PhysRevX.8.031089).
- [35] C. Xu and L. Balents. “Topological superconductivity in twisted multilayer graphene”. *Phys. Rev. Lett.* 121 (8 Aug. 2018), p. 087001. DOI: [10.1103/PhysRevLett.121.087001](https://doi.org/10.1103/PhysRevLett.121.087001).
- [36] A. Ramires and J. L. Lado. “Electrically tunable gauge fields in tiny-angle twisted bilayer graphene”. *Phys. Rev. Lett.* 121 (14 Oct. 2018), p. 146801. DOI: [10.1103/PhysRevLett.121.146801](https://doi.org/10.1103/PhysRevLett.121.146801).
- [37] C.-C. Liu et al. “Chiral spin density wave and $d + id$ superconductivity in the magic-angle-twisted bilayer graphene”. *Phys. Rev. Lett.* 121 (21 Nov. 2018), p. 217001. DOI: [10.1103/PhysRevLett.121.217001](https://doi.org/10.1103/PhysRevLett.121.217001).
- [38] S. Ray, J. Jung, and T. Das. “Wannier pairs in superconducting twisted bilayer graphene and related systems”. *Phys. Rev. B* 99.13 (2019), p. 134515. DOI: [10.1103/PhysRevB.99.134515](https://doi.org/10.1103/PhysRevB.99.134515).
- [39] T. Huang, L. Zhang, and T. Ma. “Antiferromagnetically ordered Mott insulator and $d + id$ superconductivity in twisted bilayer graphene: A quantum Monte Carlo study”. *Sci. Bull.* 64.5 (2019), pp. 310–314. DOI: [10.1016/j.scib.2019.01.026](https://doi.org/10.1016/j.scib.2019.01.026).
- [40] J. F. Dodaro et al. “Phases of a phenomenological model of twisted bilayer graphene”. *Phys. Rev. B* 98 (7 Aug. 2018), p. 075154. DOI: [10.1103/PhysRevB.98.075154](https://doi.org/10.1103/PhysRevB.98.075154).
- [41] G. Baskaran. “Theory of emergent Josephson lattice in neutral twisted bilayer graphene (moiré is different)” (2018). arXiv: [1804.00627](https://arxiv.org/abs/1804.00627).
- [42] B. Roy and V. Juričić. “Unconventional superconductivity in nearly flat bands in twisted bilayer graphene”. *Phys. Rev. B* 99.12 (2019), p. 121407. DOI: [10.1103/PhysRevB.99.121407](https://doi.org/10.1103/PhysRevB.99.121407).
- [43] H. Guo et al. “Pairing symmetry of interacting fermions on a twisted bilayer graphene superlattice”. *Phys. Rev. B* 97 (23 June 2018), p. 235453. DOI: [10.1103/PhysRevB.97.235453](https://doi.org/10.1103/PhysRevB.97.235453).
- [44] X. Lu et al. “Superconductors, orbital magnets and correlated states in magic-angle bilayer graphene”. *Nature* 574.7780 (2019), pp. 653–657. DOI: [10.1038/s41586-019-1695-0](https://doi.org/10.1038/s41586-019-1695-0).
- [45] J. M. B. Lopes dos Santos, N. M. R. Peres, and A. H. Castro Neto. “Graphene bilayer with a twist: Electronic structure”. *Phys. Rev. Lett.* 99.25 (2007), p. 256802. ISSN: 00319007. DOI: [10.1103/PhysRevLett.99.256802](https://doi.org/10.1103/PhysRevLett.99.256802).
- [46] J. M. B. Lopes dos Santos, N. M. R. Peres, and A. H. Castro Neto. “Continuum model of the twisted graphene bilayer”. *Phys. Rev. B* 86.15 (2012), p. 155449. DOI: [10.1103/PhysRevB.86.155449](https://doi.org/10.1103/PhysRevB.86.155449).

- [47] F. Wu, A. MacDonald, and I. Martin. “Theory of phonon-mediated superconductivity in twisted bilayer graphene”. *Phys. Rev. Lett.* 121.25 (2018), p. 257001. DOI: [10.1103/PhysRevLett.121.257001](https://doi.org/10.1103/PhysRevLett.121.257001).
- [48] B. Lian, Z. Wang, and B. A. Bernevig. “Twisted bilayer graphene: a phonon-driven superconductor”. *Phys. Rev. Lett.* 122 (25 June 2019), p. 257002. DOI: [10.1103/PhysRevLett.122.257002](https://doi.org/10.1103/PhysRevLett.122.257002).
- [49] P. Stepanov et al. “Untying the insulating and superconducting orders in magic-angle graphene”. *Nature* 583.7816 (2020), pp. 375–378. DOI: [10.1038/s41586-020-2459-6](https://doi.org/10.1038/s41586-020-2459-6).
- [50] M. Oh et al. “Evidence for unconventional superconductivity in twisted bilayer graphene”. *Nature* (2021), pp. 1–10. DOI: [10.1038/s41586-021-04121-x](https://doi.org/10.1038/s41586-021-04121-x).
- [51] M. Tinkham. *Introduction to Superconductivity*. Second edition. Mineola, NY: Dover Publications, 2004.
- [52] S. Peotta and P. Törmä. “Superfluidity in topologically nontrivial flat bands”. *Nat. Comm.* 6.1 (2015), pp. 1–9. DOI: [10.1038/ncomms9944](https://doi.org/10.1038/ncomms9944).
- [53] A. Julku et al. “Superfluid weight and Berezinskii-Kosterlitz-Thouless transition temperature of twisted bilayer graphene”. *Phys. Rev. B* 101.6 (2020), p. 060505. DOI: [10.1103/PhysRevB.101.060505](https://doi.org/10.1103/PhysRevB.101.060505).
- [54] P. Törmä, S. Peotta, and B. A. Bernevig. “Superfluidity and quantum geometry in twisted multilayer systems” (2021). arXiv: [2111.00807](https://arxiv.org/abs/2111.00807).
- [55] V. L. Berezinskii. “Destruction of long-range order in one-dimensional and two-dimensional systems having a continuous symmetry group I. Classical systems”. *Sov. Phys. JETP* 32.3 (1971), pp. 493–500.
- [56] J. M. Kosterlitz and D. Thouless. “Long range order and metastability in two dimensional solids and superfluids. (Application of dislocation theory)”. *J. Phys., C, Solid State Phys.* 5.11 (1972), p. L124. DOI: [10.1088/0022-3719/5/11/002](https://doi.org/10.1088/0022-3719/5/11/002).
- [57] J. M. Kosterlitz and D. J. Thouless. “Ordering, metastability and phase transitions in two-dimensional systems”. *J. Phys. C: Solid State Phys.* 6.7 (1973), p. 1181.
- [58] M. Beasley, J. Mooij, and T. Orlando. “Possibility of vortex-antivortex pair dissociation in two-dimensional superconductors”. *Phys. Rev. Lett.* 42.17 (1979), p. 1165. DOI: [10.1103/PhysRevLett.42.1165](https://doi.org/10.1103/PhysRevLett.42.1165).
- [59] J. Pearl. “Current distribution in superconducting films carrying quantized fluxoids”. *Appl. Phys. Lett.* 5.4 (1964), pp. 65–66. DOI: [10.1063/1.1754056](https://doi.org/10.1063/1.1754056).
- [60] J. M. Kosterlitz and D. J. Thouless. “40 Years of Berezinskii-Kosterlitz-Thouless Theory”. In: ed. by J. V. Jos and D. J. Thouless. World Scientific, 2013. Chap. Early work on defect driven phase transitions. DOI: [10.1142/S0217979216300188](https://doi.org/10.1142/S0217979216300188).

- [61] J. Rammer and H. Smith. “Quantum field-theoretical methods in transport theory of metals”. *Rev. Mod. Phys.* 58.2 (1986), p. 323. DOI: [10.1103/RevModPhys.58.323](https://doi.org/10.1103/RevModPhys.58.323).
- [62] A. Kamenev and A. Levchenko. “Keldysh technique and non-linear σ -model”. *Adv. Phys.* (2010). DOI: [10.1080/00018730902850504](https://doi.org/10.1080/00018730902850504).
- [63] T. T. Heikkilä et al. “Thermal, electric and spin transport in superconductor/ferromagnetic-insulator structures”. *Prog. Surf. Sci.* 94.3 (2019), p. 100540. DOI: [10.1016/j.progsurf.2019.100540](https://doi.org/10.1016/j.progsurf.2019.100540).
- [64] J. Rammer. *Quantum field theory of non-equilibrium states*. Cambridge: Cambridge University Press, 2007. DOI: [10.1017/CBO9780511618956](https://doi.org/10.1017/CBO9780511618956).
- [65] G. Stefanucci and R. Van Leeuwen. *Nonequilibrium many-body theory of quantum systems: a modern introduction*. Cambridge: Cambridge University Press, 2013. DOI: [10.1017/CBO9781139023979](https://doi.org/10.1017/CBO9781139023979).
- [66] A. Kamenev. *Field theory of non-equilibrium systems*. Cambridge: Cambridge University Press, 2011.
- [67] L. Landau. “On the theory of the Fermi liquid”. *Sov. Phys. JETP* 8.1 (1959), p. 70.
- [68] A. Abrikosov, L. Gor’kov, and I. Dzyaloshinskii. *Methods of quantum field theory in statistical physics*. New York: Dover Publications, 1975.
- [69] M. Eschrig. “Distribution functions in nonequilibrium theory of superconductivity and Andreev spectroscopy in unconventional superconductors”. *Phys. Rev. B* 61 (13 Apr. 2000), pp. 9061–9076. DOI: [10.1103/PhysRevB.61.9061](https://doi.org/10.1103/PhysRevB.61.9061).
- [70] G. Eilenberger. “Transformation of Gorkov’s equation for type II superconductors into transport-like equations”. *Z. Phys* 214 (1968), p. 195. DOI: [10.1007/BF01379803](https://doi.org/10.1007/BF01379803).
- [71] G. Eliashberg. “Inelastic electron collisions and nonequilibrium stationary states in superconductors”. *Sov. Phys. JETP* 34.3 (1972), pp. 668–676.
- [72] A. Larkin and Y. Ovchinnikov. “Nonlinear conductivity of superconductors in the mixed state”. *Sov. Phys. JETP* 41.5 (1975), pp. 960–965.
- [73] K. S. Thorne and R. D. Blandford. *Modern classical physics: optics, fluids, plasmas, elasticity, relativity, and statistical physics*. Princeton: Princeton University Press, 2017. ISBN: 9780691159027.
- [74] J. W. Serene and D. Rainer. “The quasiclassical approach to superfluid ^3He ”. *Phys. Rep.* 101.4 (1983), pp. 221–311. DOI: [10.1016/0370-1573\(83\)90051-0](https://doi.org/10.1016/0370-1573(83)90051-0).
- [75] K. D. Usadel. “Magnetization of dirty superconductors near the upper critical field”. *Phys. Rev. B* 4.1 (1971), p. 99. DOI: [10.1103/PhysRevB.4.99](https://doi.org/10.1103/PhysRevB.4.99).
- [76] A. Shelankov. “On the derivation of quasiclassical equations for superconductors”. *J. Low Temp. Phys.* 60.1 (1985), pp. 29–44. DOI: [10.1007/BF00681651](https://doi.org/10.1007/BF00681651).
- [77] N. Kopnin. *Theory of nonequilibrium superconductivity*. Vol. 110. Oxford University Press, 2001.

- [78] A. Schmid and G. Schön. “Linearized kinetic equations and relaxation processes of a superconductor near T_c ”. *J. Low Temp. Phys.* 20.1 (1975), pp. 207–227. DOI: [10.1007/BF00115264](https://doi.org/10.1007/BF00115264).
- [79] A. Larkin and I. N. Ovchinnikov. “Nonlinear effects during vortex motion in superconductors”. *Zh. Eksp. Teor. Fiz.* 73 (1977), pp. 299–312.
- [80] A. Abrikosov and L. Gor’kov. “Spin-orbit interaction and the Knight shift in superconductors”. *Sov. Phys. JETP* 15 (1962), p. 752.
- [81] P. Anderson. “Theory of dirty superconductors”. *J. Phys. Chem. Solids* 11.1 (1959), pp. 26–30. ISSN: 0022-3697. DOI: [10.1016/0022-3697\(59\)90036-8](https://doi.org/10.1016/0022-3697(59)90036-8).
- [82] M. Eschrig et al. “General boundary conditions for quasiclassical theory of superconductivity in the diffusive limit: application to strongly spin-polarized systems”. *New J. Phys.* 17.8 (2015), p. 083037. DOI: [10.1088/1367-2630/17/8/083037](https://doi.org/10.1088/1367-2630/17/8/083037).
- [83] F. S. Bergeret, A. F. Volkov, and K. B. Efetov. “Spin screening of magnetic moments in superconductors”. *EPL* 66.1 (2004), p. 111. DOI: [10.1209/epl/i2004-10003-3](https://doi.org/10.1209/epl/i2004-10003-3).
- [84] M. Y. Kuprianov and V. Lukichev. “Influence of boundary transparency on the critical current of dirty SS’S structures”. *Zh. Eksp. Teor. Fiz* 94 (1988), p. 149.
- [85] I. Žutić, J. Fabian, and S. D. Sarma. “Spintronics: Fundamentals and applications”. *Rev. Mod. Phys.* 76.2 (2004), p. 323. DOI: [10.1103/RevModPhys.76.323](https://doi.org/10.1103/RevModPhys.76.323).
- [86] V. Kruglyak, S. Demokritov, and D. Grundler. “Magnonics”. *J. Phys. D: Appl. Phys.* 43.26 (2010), p. 264001. DOI: [10.1088/0022-3727/43/26/264001](https://doi.org/10.1088/0022-3727/43/26/264001).
- [87] A. Brataas et al. “Spin insulatronics”. *Phys. Rep.* 885 (2020). Spin Insulatronics, pp. 1–27. ISSN: 0370-1573. DOI: [10.1016/j.physrep.2020.08.006](https://doi.org/10.1016/j.physrep.2020.08.006).
- [88] C. Back et al. “The 2020 skyrmionics roadmap”. *J. Phys. D: Appl. Phys.* 53.36 (2020), p. 363001. DOI: [10.1088/1361-6463/ab8418](https://doi.org/10.1088/1361-6463/ab8418).
- [89] D. Go et al. “Orbitronics: orbital currents in solids”. *EPL* 135.3 (2021), p. 37001. DOI: [10.1209/0295-5075/ac2653](https://doi.org/10.1209/0295-5075/ac2653).
- [90] P. M. Tedrow, J. E. Tkaczyk, and A. Kumar. “Spin-polarized electron tunneling study of an artificially layered superconductor with internal magnetic field: EuO-Al”. *Phys. Rev. Lett.* 56.16 (1986), pp. 1746–1749. DOI: [10.1103/PhysRevLett.56.1746](https://doi.org/10.1103/PhysRevLett.56.1746).
- [91] M. Eschrig. “Spin-polarized supercurrents for spintronics”. *Phys. Today* 64.1 (2011), p. 43. DOI: [10.1063/1.3541944](https://doi.org/10.1063/1.3541944).
- [92] N. F. Mott. “The electrical conductivity of transition metals”. *Proc. R. Soc. A* 153.880 (1936), pp. 699–717. DOI: [10.1098/rspa.1936.0031](https://doi.org/10.1098/rspa.1936.0031).
- [93] N. F. Mott. “The resistance and thermoelectric properties of the transition metals”. *Proc. R. Soc. A* 156.888 (1936), pp. 368–382. DOI: [10.1098/rspa.1936.0154](https://doi.org/10.1098/rspa.1936.0154).

- [94] M. Eschrig. “Spin-polarized supercurrents for spintronics: a review of current progress”. *Rep. Prog. Phys.* 78.10 (2015), p. 104501. DOI: [10.1088/0034-4885/78/10/104501](https://doi.org/10.1088/0034-4885/78/10/104501).
- [95] M. N. Baibich et al. “Giant magnetoresistance of (001) Fe/(001) Cr magnetic superlattices”. *Phys. Rev. Lett.* 61.21 (1988), p. 2472. DOI: [10.1103/PhysRevLett.61.2472](https://doi.org/10.1103/PhysRevLett.61.2472).
- [96] G. Binasch et al. “Enhanced magnetoresistance in layered magnetic structures with antiferromagnetic interlayer exchange”. *Phys. Rev. B* 39.7 (1989), p. 4828. DOI: [10.1103/PhysRevB.39.4828](https://doi.org/10.1103/PhysRevB.39.4828).
- [97] P. Virtanen, A. Vargunin, and M. Silaev. “Quasiclassical free energy of superconductors: Disorder-driven first-order phase transition in superconductor/ferromagnetic-insulator bilayers”. *Phys. Rev. B* 101.9 (2020), p. 094507. DOI: [10.1103/PhysRevB.101.094507](https://doi.org/10.1103/PhysRevB.101.094507).
- [98] G. Sarma. “On the influence of a uniform exchange field acting on the spins of the conduction electrons in a superconductor”. *Journal of Physics and Chemistry of Solids* 24.8 (1963), pp. 1029–1032. ISSN: 0022-3697. DOI: [10.1016/0022-3697\(63\)90007-6](https://doi.org/10.1016/0022-3697(63)90007-6).
- [99] T. Tokuyasu, J. A. Sauls, and D. Rainer. “Proximity effect of a ferromagnetic insulator in contact with a superconductor”. *Phys. Rev. B* 38.13 (1988), pp. 8823–8833. DOI: [10.1103/PhysRevB.38.8823](https://doi.org/10.1103/PhysRevB.38.8823).
- [100] M. A. Ruderman and C. Kittel. “Indirect exchange coupling of nuclear magnetic moments by conduction electrons”. *Phys. Rev.* 96.1 (1954), p. 99. DOI: [10.1103/PhysRev.96.99](https://doi.org/10.1103/PhysRev.96.99).
- [101] T. Kasuya. “A theory of metallic ferro- and antiferromagnetism on Zener’s model”. *Prog. Theor. Phys.* 16.1 (1956), pp. 45–57. DOI: [10.1143/PTP.16.45](https://doi.org/10.1143/PTP.16.45).
- [102] K. Yosida. “Magnetic properties of Cu-Mn alloys”. *Phys. Rev.* 106.5 (1957), p. 893. DOI: [10.1103/PhysRev.106.893](https://doi.org/10.1103/PhysRev.106.893).
- [103] S. S. P. Parkin, N. More, and K. P. Roche. “Oscillations in exchange coupling and magnetoresistance in metallic superlattice structures: Co/Ru, Co/Cr, and Fe/Cr”. *Phys. Rev. Lett.* 64 (19 1990), pp. 2304–2307. DOI: [10.1103/PhysRevLett.64.2304](https://doi.org/10.1103/PhysRevLett.64.2304).
- [104] A. Cottet et al. “Spin-dependent boundary conditions for isotropic superconducting Green’s functions”. *Phys. Rev. B* 80.18 (2009), p. 184511. DOI: [10.1103/PhysRevB.80.184511](https://doi.org/10.1103/PhysRevB.80.184511).
- [105] M. Silaev. “Nonlinear electromagnetic response and Higgs-mode excitation in BCS superconductors with impurities”. *Phys. Rev. B* 99.22 (2019), p. 224511. DOI: [10.1103/PhysRevB.99.224511](https://doi.org/10.1103/PhysRevB.99.224511).
- [106] A. Ozaeta et al. “Huge thermoelectric effects in ferromagnet-superconductor junctions in the presence of a spin-splitting field”. *Phys. Rev. Lett.* 112 (2014), p. 057001. DOI: [10.1103/PhysRevLett.112.057001](https://doi.org/10.1103/PhysRevLett.112.057001).

- [107] *SUPERTED*. European Union’s Horizon 2020 research and innovation programme under grant agreement No. 800923. URL: <https://superted-project.eu/>.
- [108] L. Landau and E. Lifshitz. “On the theory of magnetic permeability dispersion in ferromagnetic solids”. *Sov. Phys* 8 (1935), pp. 153–166.
- [109] T. L. Gilbert. “A phenomenological theory of damping in ferromagnetic materials”. *IEEE Trans. Magn.* 40.6 (2004), pp. 3443–3449. DOI: [10.1109/TMAG.2004.836740](https://doi.org/10.1109/TMAG.2004.836740).
- [110] K. Gilmore, Y. U. Idzerda, and M. D. Stiles. “Identification of the dominant precession-damping mechanism in Fe, Co, and Ni by first-principles calculations”. *Phys. Rev. Lett.* 99 (2 2007), p. 027204. DOI: [10.1103/PhysRevLett.99.027204](https://doi.org/10.1103/PhysRevLett.99.027204).
- [111] C. Kittel. “On the theory of ferromagnetic resonance absorption”. *Phys. Rev.* 73.2 (1948), p. 155. DOI: [10.1103/PhysRev.73.155](https://doi.org/10.1103/PhysRev.73.155).
- [112] Y. Tserkovnyak et al. “Nonlocal magnetization dynamics in ferromagnetic heterostructures”. *Rev. Mod. Phys.* 77.4 (2005), pp. 1375–1421. DOI: [10.1103/RevModPhys.77.1375](https://doi.org/10.1103/RevModPhys.77.1375).
- [113] A. Brataas, G. E. Bauer, and P. J. Kelly. “Non-collinear magnetoelectronics”. *Physics Reports* 427.4 (2006), pp. 157–255. DOI: [10.1016/j.physrep.2006.01.001](https://doi.org/10.1016/j.physrep.2006.01.001).
- [114] A. Brataas et al. “Spin battery operated by ferromagnetic resonance”. *Phys. Rev. B* 66.6 (2002), p. 060404. DOI: [10.1103/PhysRevB.66.060404](https://doi.org/10.1103/PhysRevB.66.060404).
- [115] S. Zhang. “Spin Hall effect in the presence of spin diffusion”. *Phys. Rev. Lett.* 85.2 (2000), p. 393. DOI: [10.1103/PhysRevLett.85.393](https://doi.org/10.1103/PhysRevLett.85.393).
- [116] X.-P. Zhang, F. S. Bergeret, and V. N. Golovach. “Theory of spin hall magnetoresistance from a microscopic perspective”. *Nano Lett.* 19.9 (2019), pp. 6330–6337. DOI: [10.1021/acs.nanolett.9b02459](https://doi.org/10.1021/acs.nanolett.9b02459).
- [117] J. C. Slonczewski. “Current-driven excitation of magnetic multilayers”. *J. Magn. Magn. Mater.* 159.1 (1996), p. L1. DOI: [10.1016/0304-8853\(96\)00062-5](https://doi.org/10.1016/0304-8853(96)00062-5).
- [118] K.-R. Jeon et al. “Enhanced spin pumping into superconductors provides evidence for superconducting pure spin currents”. *Nat. Mater.* 17.6 (2018), p. 499. DOI: [10.1038/s41563-018-0058-9](https://doi.org/10.1038/s41563-018-0058-9).
- [119] J. P. Morten et al. “Proximity-effect–assisted decay of spin currents in superconductors”. *EPL* 84.5 (2008), p. 57008. DOI: [10.1209/0295-5075/84/57008](https://doi.org/10.1209/0295-5075/84/57008).
- [120] M. Inoue, M. Ichioka, and H. Adachi. “Spin pumping into superconductors: A new probe of spin dynamics in a superconducting thin film”. *Phys. Rev. B* 96 (2 2017), p. 024414. DOI: [10.1103/PhysRevB.96.024414](https://doi.org/10.1103/PhysRevB.96.024414).
- [121] T. Kato et al. “Microscopic theory of spin transport at the interface between a superconductor and a ferromagnetic insulator”. *Phys. Rev. B* 99.14 (2019), p. 144411. DOI: [10.1103/PhysRevB.99.144411](https://doi.org/10.1103/PhysRevB.99.144411).

- [122] M. A. Silaev. “Finite-frequency spin susceptibility and spin pumping in superconductors with spin-orbit relaxation”. *Phys. Rev. B* 102 (14 Oct. 2020), p. 144521. DOI: [10.1103/PhysRevB.102.144521](https://doi.org/10.1103/PhysRevB.102.144521).
- [123] D. Koller et al. “Suppression of superconductivity by injection of spin-polarized current”. *J. Appl. Phys.* 83.11 (1998), pp. 6774–6776. DOI: [10.1063/1.367763](https://doi.org/10.1063/1.367763).
- [124] P.-G. de Gennes. “Coupling between ferromagnets through a superconducting layer”. *Phys. Lett.* 23.1 (1966), pp. 10–11. ISSN: 0031-9163. DOI: [https://doi.org/10.1016/0031-9163\(66\)90229-0](https://doi.org/10.1016/0031-9163(66)90229-0).
- [125] Y. A. Izyumov, Y. N. Proshin, and M. G. Khusainov. “Competition between superconductivity and magnetism in FM/SC heterostructures”. *Physics-Uspekhi* 45.2 (2002), p. 109. DOI: [10.1070/PU2002v045n02ABEH001025](https://doi.org/10.1070/PU2002v045n02ABEH001025).
- [126] F. S. Bergeret, A. F. Volkov, and K. B. Efetov. “Long-range proximity effects in superconductor-ferromagnet structures”. *Phys. Rev. Lett.* 86.18 (2001), p. 4096. DOI: [10.1103/PhysRevLett.86.4096](https://doi.org/10.1103/PhysRevLett.86.4096).
- [127] A. Volkov, F. Bergeret, and K. B. Efetov. “Odd triplet superconductivity in superconductor-ferromagnet multilayered structures”. *Phys. Rev. Lett.* 90.11 (2003), p. 117006. DOI: [10.1103/PhysRevLett.90.117006](https://doi.org/10.1103/PhysRevLett.90.117006).
- [128] A. I. Buzdin, L. Bulaevskii, and S. Panyukov. “Critical-current oscillations as a function of the exchange field and thickness of the ferromagnetic metal (F) in an SFS Josephson junction”. *JETP Lett.* 35.4 (1982), pp. 178–180.
- [129] L. Bulaevskii, V. Kuzii, and A. Sobyenin. “Superconducting system with weak coupling to the current in the ground state”. *JETP Lett.* 25.7 (1977).
- [130] V. Oboznov et al. “Thickness dependence of the Josephson ground states of superconductor-ferromagnet-superconductor junctions”. *Phys. Rev. Lett.* 96.19 (2006), p. 197003. DOI: [10.1103/PhysRevLett.96.197003](https://doi.org/10.1103/PhysRevLett.96.197003).
- [131] C. Bell et al. “Spin Dynamics in a Superconductor-Ferromagnet Proximity System”. *Phys. Rev. Lett.* 100.4 (2008), p. 047002. DOI: [10.1103/PhysRevLett.100.047002](https://doi.org/10.1103/PhysRevLett.100.047002).
- [132] K.-R. Jeon et al. “Exchange-field enhancement of superconducting spin pumping”. *Phys. Rev. B* 99.2 (2019), p. 024507. DOI: [10.1103/PhysRevB.99.024507](https://doi.org/10.1103/PhysRevB.99.024507).
- [133] K.-R. Jeon et al. “Tunable pure spin supercurrents and the demonstration of their gateability in a spin-wave device”. *Phys. Rev. X* 10 (3 2020), p. 031020. DOI: [10.1103/PhysRevX.10.031020](https://doi.org/10.1103/PhysRevX.10.031020).
- [134] A. Altland and B. D. Simons. *Condensed matter field theory*. Cambridge: Cambridge university press, 2010. DOI: [10.1017/CBO9780511789984](https://doi.org/10.1017/CBO9780511789984).
- [135] F. S. Bergeret, A. Verso, and A. F. Volkov. “Electronic transport through ferromagnetic and superconducting junctions with spin-filter tunneling barriers”. *Phys. Rev. B* 86 (21 2012), p. 214516. DOI: [10.1103/PhysRevB.86.214516](https://doi.org/10.1103/PhysRevB.86.214516).
- [136] E. Sonin. “Spin currents and spin superfluidity”. *Adv. Phys.* 59.3 (2010), pp. 181–255. DOI: [10.1080/00018731003739943](https://doi.org/10.1080/00018731003739943).

- [137] K.-R. Jeon et al. “Effect of Meissner screening and trapped magnetic flux on magnetization dynamics in thick Nb/Ni₈₀Fe₂₀/Nb trilayers”. *Phys. Rev. Applied* 11.1 (2019), p. 014061. DOI: [10.1103/PhysRevApplied.11.014061](https://doi.org/10.1103/PhysRevApplied.11.014061).
- [138] P. W. Anderson. “Plasmons, gauge invariance, and mass”. *Phys. Rev.* 130.1 (1963), p. 439. DOI: [10.1103/PhysRev.130.439](https://doi.org/10.1103/PhysRev.130.439).
- [139] P. W. Anderson. “Higgs, Anderson and all that”. *Nat. Phys.* 11.2 (2015), pp. 93–93. DOI: [10.1038/nphys3247](https://doi.org/10.1038/nphys3247).
- [140] P. Littlewood and C. Varma. “Amplitude collective modes in superconductors and their coupling to charge-density waves”. *Phys. Rev. B* 26.9 (1982), p. 4883. DOI: [10.1103/PhysRevB.26.4883](https://doi.org/10.1103/PhysRevB.26.4883).
- [141] N. Tsuji and H. Aoki. “Theory of Anderson pseudospin resonance with Higgs mode in superconductors”. *Phys. Rev. B* 92 (6 2015), p. 064508. DOI: [10.1103/PhysRevB.92.064508](https://doi.org/10.1103/PhysRevB.92.064508).
- [142] J. Puebla et al. “Spintronic devices for energy-efficient data storage and energy harvesting”. *Comm. Mater.* 1.1 (2020), pp. 1–9. DOI: [10.1038/s43246-020-0022-5](https://doi.org/10.1038/s43246-020-0022-5).
- [143] A. S. Andrae and T. Edler. “On global electricity usage of communication technology: trends to 2030”. *Challenges* 6.1 (2015), pp. 117–157. DOI: [10.3390/challe6010117](https://doi.org/10.3390/challe6010117).
- [144] N. Jones. “How to stop data centres from gobbling up the world’s electricity”. *Nature* 561.7722 (2018), pp. 163–167. DOI: [10.1038/d41586-018-06610-y](https://doi.org/10.1038/d41586-018-06610-y).
- [145] J. Linder and J. W. Robinson. “Superconducting spintronics”. *Nature Phys.* 11.4 (2015), pp. 307–315. DOI: [10.1038/nphys3242](https://doi.org/10.1038/nphys3242).
- [146] P. Virtanen, F. Bergeret, and I. Tokatly. “Magnetoelectric effects in superconductors due to spin-orbit scattering: Nonlinear σ -model description”. *Phys. Rev. B* 104.6 (2021), p. 064515. DOI: [10.1103/PhysRevB.104.064515](https://doi.org/10.1103/PhysRevB.104.064515).

ORIGINAL PAPERS

I

COMPETITION OF ELECTRON-PHONON MEDIATED SUPERCONDUCTIVITY AND STONER MAGNETISM ON A FLAT BAND

by

R. Ojajarvi, T. Hyart , M.A. Silaev and T.T. Heikkilä 2018

Physical Review B **98**, 054515, doi:[10.1103/PhysRevB.98.054515](https://doi.org/10.1103/PhysRevB.98.054515)

Reproduced with permission. Copyright 2018 American Physical Society.

Competition of electron-phonon mediated superconductivity and Stoner magnetism on a flat bandRisto Ojajärvi,¹ Timo Hyart,^{1,2} Mihail A. Silaev,¹ and Tero T. Heikkilä¹¹*Department of Physics and Nanoscience Center, University of Jyväskylä, P.O. Box 35 (YFL), FI-40014 Jyväskylä, Finland*²*Institut für Theoretische Physik, Universität Leipzig, D-04103 Leipzig, Germany*

(Received 7 March 2018; revised manuscript received 21 June 2018; published 22 August 2018)

The effective attractive interaction between electrons, mediated by electron-phonon coupling, is a well-established mechanism of conventional superconductivity. In metals exhibiting a Fermi surface, the critical temperature of superconductivity is exponentially smaller than the characteristic phonon energy. Therefore, such superconductors are found only at temperatures below a few kelvin. Systems with flat energy bands have been suggested to cure the problem and provide a route to room-temperature superconductivity, but previous studies are limited to only BCS models with an effective attractive interaction. Here we generalize Eliashberg's theory of strong-coupling superconductivity to systems with flat bands and relate the mean-field critical temperature to the microscopic parameters describing electron-phonon and electron-electron interaction. We also analyze the strong-coupling corrections to the BCS results and construct the phase diagram exhibiting superconductivity and magnetic phases on an equal footing. Our results are especially relevant for novel quantum materials where electronic dispersion and interaction strength are controllable.

DOI: [10.1103/PhysRevB.98.054515](https://doi.org/10.1103/PhysRevB.98.054515)**I. INTRODUCTION**

The overarching idea in quantum materials is to design the electronic (or optical, magnetic, etc.) properties of materials to perform the desired functionality [1]. This goal is aided by generic models and concepts, such as specific lattice models that lead to certain topological phases. Often the studied models and the resulting topological phases for electronic systems are noninteracting and do not include the possibility of spontaneous symmetry breaking. However, such noninteracting models are platforms for exotic electron dispersions that provide a basis for studying symmetry-broken interacting phases. In particular, certain models support approximate flat bands [2–10], and here we consider microscopic mechanisms for symmetry-breaking phases in such systems.

We analyze the interplay of electron-phonon [11] and (screened) electron-electron interaction in providing means for a symmetry-broken phase transition, thereby coupling together works on flat-band superconductivity [2,7,10,12] with those on flat-band (Stoner) magnetism [9,13–17]. In both cases the resulting mean-field critical temperature is linearly proportional to the coupling constant [18], thus allowing for a very high critical temperature. The two types of interaction mechanisms work in opposite directions and, in the case of weak interactions, in a symmetric way. However, upon increasing the coupling strength the retarded nature of the electron-phonon interaction shows up (as opposed to the instantaneous electron-electron interaction), breaking the symmetry between the two. In particular, we generalize Eliashberg's strong-coupling theory of superconductivity [19], usually formulated for systems with a Fermi surface, for flat bands. As a result, we describe the dimensionless BCS attractive interaction [20] in terms of the electron-phonon coupling and the characteristic phonon frequency [Eq. (8)]. In addition, we provide the generalization of the well-known McMillan formula of strong-coupling superconductivity (for

Fermi surface systems) [21] to the case with flat bands in Eq. (14).

In addition to superconductivity, we consider flat-band Stoner magnetism. Because of the retarded nature of the electron-phonon interaction, the combined interaction can simultaneously have attractive and repulsive components, and thus the system can be unstable with respect to both singlet superconductivity and magnetism (see a generic strong-coupling phase diagram in Fig. 1). Often one of the phases still dominates and suppresses the other, but we find that when the critical temperatures of the phases are similar, both phases are local minima of the free energy at low temperatures. We find that their bulk coexistence and the resulting odd-frequency triplet superconducting order [22,23] are only realized as an unstable solution. On the other hand, these phases can form metastable domains inside the sample, and therefore an odd-frequency triplet order parameter can appear at the domain walls.

The structure of this paper is as follows. In Sec. II we introduce the model of surface bands with electron-phonon and Coulomb interactions. In Sec. III we formulate the Eliashberg model extension for the surface bands, describe all possible ordered states that can appear within this model, and calculate the critical temperatures of the superconducting and antiferromagnetic states. We study the competition and possible coexistence of these two types of ordering in Sec. IV. Conclusions are given in Sec. V.

II. MODEL

As a low-energy model for the flat band, we assume two sublattices coupled through an electronic Hamiltonian [3]

$$H_{el,p} = \begin{pmatrix} 0 & \varepsilon_p \\ \varepsilon_p & 0 \end{pmatrix}, \quad \text{with } \varepsilon_p = \varepsilon_0 \left(\frac{p}{p_{FB}} \right)^N, \quad (1)$$

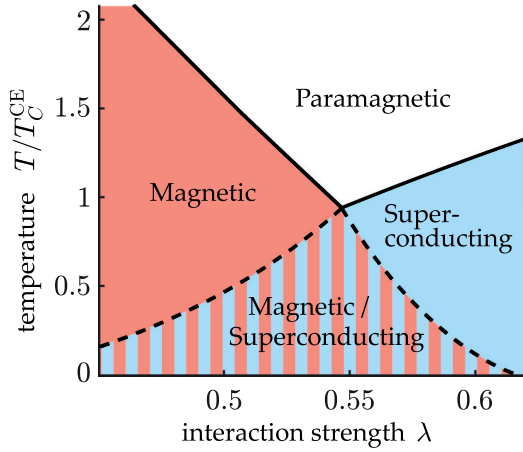


FIG. 1. Strong-coupling phase diagram for flat-band systems as a function of electron-phonon attraction λ for electron-electron repulsion $u = 0.5\omega_E$ [Eq. (8)]. T_C^{CE} is the temperature at which the T_C 's of magnetic and superconducting order coincide. In the striped region these phases can form metastable domains inside the sample. This diagram is for $N \rightarrow \infty$. For finite N the overlap region between the phases is smaller.

where an integer N parametrizes the flatness of the dispersion, and ε_0 is the energy at $p = p_{\text{FB}}$. The model is electron-hole symmetric and the two energy bands have the dispersions $\pm\varepsilon_p$. For large N , the states with low momenta, $|\mathbf{p}| < p_{\text{FB}}$, are almost at zero energy and the density of states is very high. The states with momenta larger than p_{FB} do not contribute much to the momentum integrals due to their low density of states. Therefore, the results for large N do not depend much on the momentum cutoff, as long as it is larger than p_{FB} . In our model we take the cutoff to infinity and consider only the cases $N > 2$. This is in contrast to models with isolated flat bands extending throughout the Brillouin zone. The effects discussed below in the case of large N are mostly applicable also to such models (provided they have the type of sublattice degree of freedom discussed below), as long as p_{FB} is taken as the size of the Brillouin zone. Equation (1) is approximately realized for the surface states of N -layer rhombohedrally stacked graphite. In that system the surface states delocalize into the bulk at the edges of the flat band and this gives a momentum-dependent correction in the low-energy Hamiltonian [12,24]. In the case of $N \rightarrow \infty$ the delocalization of the surface states to the bulk leads to strong amplitude mode fluctuations invalidating the mean-field theory [24]. Therefore, the theory considered in this paper is applicable to rhombohedral graphite only in the case where N is not too large.

We model the electron-electron interaction as a repulsive on-site Hubbard interaction [25] with energy U . The magnitude of U depends on the microscopic details of the system and its environment. The coupling between electrons and phonons, with strength g , creates an effective attraction between the electrons and makes the system susceptible to superconductivity [19]. We mostly consider Einstein phonons with constant energy $\omega_q = \omega_E$ and discuss generalizations in the Supplemental Material [26].

The total Hamiltonian incorporating these effects is

$$\begin{aligned}
 H = & \sum_{p,\sigma} \Psi_{p\sigma}^\dagger H_{\text{el},p} \Psi_{p,\sigma} + \sum_{q,\rho} \omega_q b_{q,\rho}^\dagger b_{q,\rho} \\
 & + \frac{U}{2\mathcal{N}} \sum_{\substack{p,k,q \\ \rho,\sigma,\sigma'}} \psi_{p+q,\sigma\rho}^\dagger \psi_{k-q,\sigma'\rho}^\dagger \psi_{k,\sigma'\rho} \psi_{p,\sigma\rho} \\
 & + \frac{g}{\sqrt{\mathcal{N}}} \sum_{p,q,\sigma,\rho} (b_{-q,\rho}^\dagger + b_{q,\rho}) \psi_{p+q,\sigma\rho}^\dagger \psi_{p,\sigma\rho}, \quad (2)
 \end{aligned}$$

where \mathcal{N} is the number of lattice points in the system and $\Psi_{p\sigma}^\dagger = (\psi_{p\sigma A}^\dagger, \psi_{p\sigma B}^\dagger)$ is a pseudospinor in sublattice space. We assume that the low-energy states on the two sublattices $\rho = A/B$ are spatially separated (e.g., localized on the two surfaces in rhombohedral graphite), so that neither the electron-electron interactions nor the phonons couple them. The only coupling between the sublattices comes from the off-diagonal dispersion relation. In the Supplemental Material we also show that the flat-band phenomenology applies to linear, graphene-like dispersion with an electronic Hamiltonian

$$H_{\text{el},p} = v_F \begin{pmatrix} 0 & p_x - ip_y \\ p_x + ip_y & 0 \end{pmatrix}, \quad (1')$$

and with an energy cutoff ε_c and Fermi velocity v_F , provided the interaction energy scales are large compared to ε_c . Hence, our results may also apply as an effective model for twisted bilayer graphene close to its “magic” angles [30].

In the theory of electron-phonon superconductivity of metals, the neglect of higher-order diagrams in the perturbation theory is typically justified with the help of the Migdal theorem [31]. In that case, the expansion parameter gets an additional factor of ω_E/E_F , where E_F is the Fermi energy. Because of the Migdal theorem, the theory of superconductivity for metals is not strictly limited to weak coupling with respect to the interaction parameter.

In the flat band, however, the chemical potential is located at the bottom of the band and there is no Fermi energy with which to compare the Debye energy. Migdal's theorem cannot be used in this case. In the intermediate case of narrow electronic bands, corrections in the higher orders of the adiabatic parameter ω_E/E_F have been studied in Refs. [32–35] and the Eliashberg theory has been found also to be in agreement with Monte Carlo results in the weak-coupling regime when $\omega_E/E_F = 1$ in Ref. [36]. We find that the diagrams beyond the mean-field approximation do not influence the self-energies significantly if the effective pairing constant introduced below in Eq. (8) is small, $\lambda \ll 1$, and $\omega_E, u \ll \varepsilon_0$. Moreover, although the mean-field theory is applied beyond its formal limits of validity in the strong-coupling regime, this theory captures the interesting possibility that the retarded nature of the electron-phonon interaction can lead to the presence of attractive and repulsive components at the same time. As a result, the system can be simultaneously unstable with respect to the appearance of both singlet superconductivity and magnetism as discussed in Sec. IV.

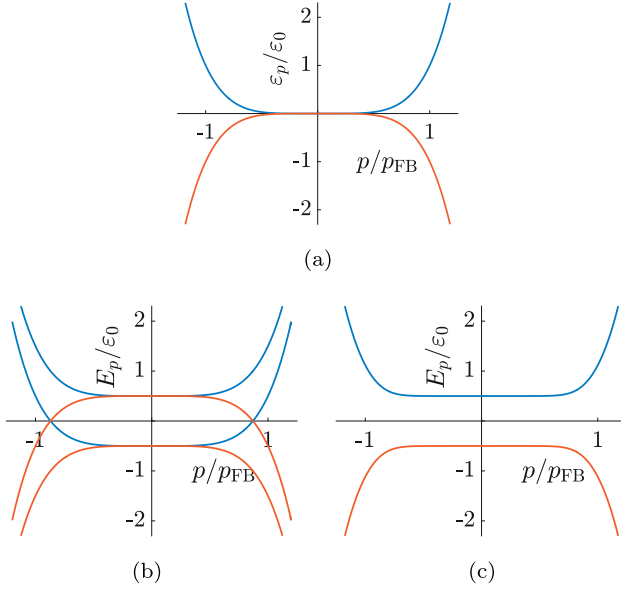


FIG. 2. Quasiparticle dispersions $E(p)$ for different kinds of symmetry breakings with $N = 5$. (a) In the noninteracting case, the spin bands are degenerate with $E(p) = \pm \epsilon(p)$. (b) For the ferromagnetic (FM) or the superconducting (SC) phase with a $\theta = \pi$ phase shift between the sublattices, one quasiparticle band is shifted up and the other down in energy. In this case, no energy gap is opened. (c) For the antiferromagnetic (AFM) or the SC phase with $\theta = 0$ an energy gap is opened and quasiparticle bands are doubly degenerate.

III. ORDERED STATES

Hamiltonian (2) allows for a number of spontaneous symmetry-breaking phases. We restrict our study to spatially homogeneous phases. Therefore, the order parameter can appear in the spin, sublattice (pseudospin), and electron-hole (Nambu) spaces. The general self-energy is

$$\Sigma(i\omega_n) = \sum_{i,j,k=0}^3 \Sigma_{ijk}(i\omega_n) \tau_i \sigma_j \rho_k, \quad (3)$$

where τ_i , σ_j , and ρ_k are the Pauli matrices in electron-hole, spin, and sublattice spaces, respectively. We characterize the different components Σ_{ijk} and determine their values within the self-consistent Hartree-Fock model. This reduces to solving a set of nonlinear integral equations, known as Eliashberg equations in the context of conventional superconductors.

To explore the possible phases of the system, we first assume that the $U(1)$ gauge symmetry is broken, but the $SU(2)$ spin-rotation symmetry is not. After fixing the overall phase of the superconducting order parameter, we are left with the self-energy $\Sigma_{000}(i\omega_n)$ and three degrees of freedom for the superconducting singlet order parameter: the magnitudes of the order parameter on the sublattices Δ_A and Δ_B and the relative phase θ . Choosing $\theta = 0$ leads to a gapped quasiparticle dispersion [Fig. 2(c)], whereas $\theta = \pi$ would imply a gapless dispersion [Fig. 2(b)]. Thus, in the case of an instantaneous interaction the total energy is minimized when $\theta = 0$ and $\Delta_A = \Delta_B$. Generalizing the above to the frequency-dependent interactions, we choose the singlet to be proportional to the

$\tau_2 \sigma_2 \rho_0$ component, whose magnitude and the functional form are obtained from the self-consistency equation. The self-energy for the fermionic Matsubara frequency ω_n is

$$\Sigma_{\text{SC}}(i\omega_n) = -i \Sigma_n^\omega \mathbb{1} + \phi_n \tau_2 \sigma_2, \quad (4)$$

where $\Sigma_n^\omega = (1 - Z_n)\omega_n$ is the frequency renormalization by the retarded interaction [19]. To simplify the equations, we define renormalized frequencies $\tilde{\omega}_n = Z_n \omega_n$. We use the symbol ϕ_n for the “bare” singlet order parameter and Δ for the maximum value of the renormalized singlet order parameter $\Delta_n \equiv \phi_n / Z_n$ related to the energy gap.

When $SU(2)$ spin-rotation symmetry is broken but $U(1)$ gauge symmetry is not, the self-energies describe the frequency renormalization and the magnetization. After fixing the direction of the magnetization on one sublattice, the relevant degrees of freedom are reduced to three similarly as in the superconducting case. These can be chosen as the magnitudes of the magnetizations in the two sublattices h_A and h_B and the relative angle φ between their directions. The quasiparticle dispersion in the magnetic case is the same as in the superconducting case if we identify $\Delta_{A,B} = h_{A,B}$ and $\theta = \pi - \varphi$ (see Fig. 2). In this case, the relative angle $\varphi = 0$ leads to a gapless quasiparticle dispersion [Fig. 2(b)], and $\varphi = \pi$ to a gapped dispersion [Fig. 2(c)]. Thus, the energy minimum is obtained with $h_A = h_B$ and $\varphi = \pi$. The stable magnetization is hence antiferromagnetic, with opposite magnetizations on the two sublattices, so that the self-energy is

$$\Sigma_{\text{AFM}}(i\omega_n) = -i \Sigma_n^\omega \mathbb{1} + h_n \tau_3 \sigma_3 \rho_3, \quad (5)$$

where h_n is the frequency-dependent exchange field. This result agrees with density functional theory (DFT) studies on rhombohedral graphite [37], and similar magnetization structure has been predicted also in the case of flat bands appearing at the zigzag edges of graphene nanoribbons [38–40]. We also note that the AFM state is insulating [see Fig. 2(c)]. If the noninteracting dispersion is completely flat at zero energy, the sublattices are uncoupled and the antiferromagnetic state is degenerate with the ferromagnetic $\varphi = 0$ state.

By calculating the Hartree-Fock self-energies, we find the self-consistency equations, from which we can determine the values of the self-energy terms. For the superconducting (SC) self-energy (4), they are

$$\phi_n = 2T \sum_{m=-\infty}^{\infty} (\lambda_{nm} - u) \int_0^\infty \frac{dp p}{p_{\text{FB}}^2} \frac{\phi_m}{\tilde{\omega}_m^2 + \epsilon_p^2 + \phi_m^2}, \quad (6)$$

$$Z_n = 1 + 2T \sum_{m=-\infty}^{\infty} \lambda_{nm} \frac{\omega_m}{\omega_n} \int_0^\infty \frac{dp p}{p_{\text{FB}}^2} \frac{Z_m}{\tilde{\omega}_m^2 + \epsilon_p^2 + \phi_m^2}, \quad (7)$$

where the interaction kernel is $\lambda_{nm} = \lambda \omega_E^3 / [\omega_E^2 + (\omega_n - \omega_m)^2]$. The functional form of the interaction kernel is determined by the phonon propagator from which it is derived. The width in frequency space is determined by the characteristic phonon frequency, which in this case is the Einstein frequency ω_E . The effective interaction constants in the flat band are

$$\lambda = \frac{g^2}{\omega_E^2} \frac{\Omega_{\text{FB}}}{\Omega_{\text{BZ}}}, \quad u = \frac{U \Omega_{\text{FB}}}{\Omega_{\text{BZ}}}, \quad (8)$$

where Ω_{FB} and Ω_{BZ} are the momentum-space areas of the flat band and of the first Brillouin zone, respectively.

For an antiferromagnet with self-energy (5), the self-consistency equations are

$$h_n = 2T \sum_{m=-\infty}^{\infty} (u - \lambda_{nm}) \int_0^{\infty} \frac{dp}{p_{\text{FB}}} \frac{p}{\tilde{\omega}_m^2 + \varepsilon_p^2 + h_m^2} h_m, \quad (9)$$

$$Z_n = 1 + 2T \sum_{m=-\infty}^{\infty} \lambda_{nm} \frac{\omega_m}{\omega_n} \int_0^{\infty} \frac{dp}{p_{\text{FB}}} \frac{p}{\tilde{\omega}_m^2 + \varepsilon_p^2 + h_m^2} Z_m. \quad (10)$$

Superconductivity and magnetism are thus symmetric with each other also on the level of the self-consistency equations, but with the roles of u and λ_{nm} switched. Tovmasyan *et al.* have shown that this duality is also broken by taking into account higher-order terms in the perturbation theory [41].

To solve the self-consistency equations (6)–(10), we truncate the Matsubara sums with a cutoff $\omega_C \sim 10\omega_E$. This causes no numerical error if we use the pseudopotential trick and simultaneously replace u with an effective value u^* , which depends on the cutoff [42]. For superconductivity (magnetism), cutting off high-energy scatterings is compensated by a reduction (increase) in the low-energy effective interaction.

After the pseudopotential trick, the solutions are found by a fixed-point iteration. The iteration is continued until all of the components have converged. The fixed-point method only finds the stable solutions; to find the unstable solutions, we used a solver based on Newton's method.

The number of parameters in Eqs. (6)–(10) can be reduced by defining new interaction constants $\tilde{\lambda} \equiv \lambda(\omega_E/\varepsilon_0)^{2/N}$ and $\tilde{u} = u\omega_E^{2/N-1}/\varepsilon^{2/N}$, so that one parameter is eliminated completely and the results become proportional to ω_E .

For weak coupling, $\lambda \ll 1$, the frequency dependence of λ_{nm} can be disregarded and we can approximate $Z \approx 1$ and $\Delta \approx \phi$. Assuming $\lambda\omega_E > u$, the superconducting gap at $T = 0$ and the critical temperature are

$$\frac{\Delta_0}{\omega_E} = \frac{1}{2} \left[\frac{(\tilde{\lambda} - \tilde{u})\sqrt{\pi}\Gamma\left(\frac{1}{2} - \frac{1}{N}\right)}{N \sin\left(\frac{\pi}{N}\right)\Gamma\left(1 - \frac{1}{N}\right)} \right]^{\frac{N}{N-2}}, \quad (11)$$

$$\frac{T_C^{\text{sc}}}{\omega_E} = \frac{1}{2\pi} \left[\frac{(\tilde{\lambda} - \tilde{u})\zeta\left(2 - \frac{2}{N}\right)\left(2^{2 - \frac{2}{N}} - 1\right)}{N \sin\left(\frac{\pi}{N}\right)} \right]^{\frac{N}{N-2}}. \quad (12)$$

These results are valid for $N > 2$ as the momentum integrals diverge without a cutoff for $N \leq 2$. Note that the $T = 0$ limit can thus be taken before the flat-band limit of large N . Analogous results have been obtained before within the BCS model in Ref. [12]. For large N , Δ_0 is linear in the coupling and its magnitude is proportional to the phonon energy scale. Hence the associated critical temperature can be very large. Relabeling $\Delta_0 \rightarrow h_0$ and $\tilde{\lambda} \leftrightarrow \tilde{u}$, we find similar equations for magnetism. Here h_0 is the magnetic order parameter at $T = 0$.

At strong coupling, the retardation matters and the results for magnetism and superconductivity diverge from each other. For superconductivity, we can improve on the weak-coupling result by including some of the corrections from the Eliashberg theory when $N \rightarrow \infty$. We still neglect the full frequency dependence, but we include the electron mass renormalization as a static factor $Z_0 = 1 + \lambda$. The order parameter at zero

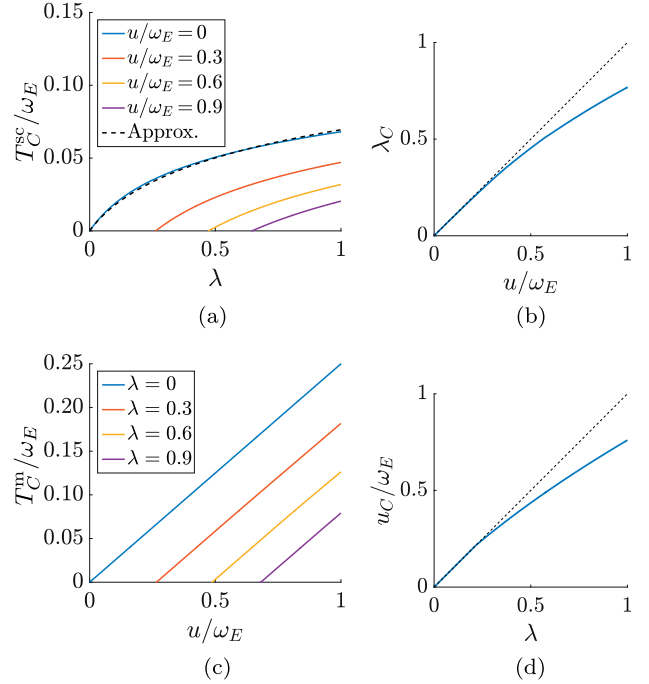


FIG. 3. Critical temperatures for superconducting and magnetic phases for $N \rightarrow \infty$. (a) Superconductivity is suppressed when $\lambda \lesssim u/\omega_E$. Above the critical point $\lambda_C(u)$, T_C^{sc} is linear in λ . With increasing λ , the electron-phonon renormalization increases and this limits the critical temperature. The dashed line is the approximation in Eq. (14). (b) Critical interaction strength for superconductivity as a function of u . When $\lambda < \lambda_C(u)$, superconductivity is suppressed. The dashed line is the instantaneous approximation. (c) Magnetism is suppressed when $u/\omega_E \lesssim \lambda$. Above the critical point $u_C(\lambda)$, T_C^{m} is linear in u . (d) Critical interaction strength for magnetism as a function of electron-phonon interaction. When $u < u_C(\lambda)$, magnetism is suppressed. The dashed line is the instantaneous approximation. In this figure, we do not take into account the possible magnetic instability of the superconducting state, or vice versa.

temperature becomes

$$\Delta_0 = \frac{\lambda\omega_E - u}{2(1 + 2\lambda)}. \quad (13)$$

In metals with a Fermi surface [43], the electron-phonon interaction renormalizes the pairing potential with the factor of $1 + \lambda$ instead of $1 + 2\lambda$ as in Eq. (13). Thus, for weak coupling, the electron-phonon renormalization is more effective in the flat band than in the usual metals. This difference is more pronounced at strong coupling, as we see next.

By linearizing Eqs. (6) and (7) with respect to ϕ , we can solve for the critical temperature [see Fig. 3(a)]. We find that when $N \rightarrow \infty$, the critical temperature scales as $T_C^{\text{sc}} \propto \lambda^{0.2}\omega_E$ for large λ . In metals [43] the asymptotic scaling goes as $T_C^{\text{sc}} \propto \lambda^{1/2}\omega_E$.

When $u \neq 0$, there is a critical point λ_C such that for $\lambda < \lambda_C$ there is no superconducting transition at any temperature. For small u/ω_E , λ_C is linearly proportional to the Coulomb interaction. For large u , λ_C increases sublinearly [see Fig. 3(b)].

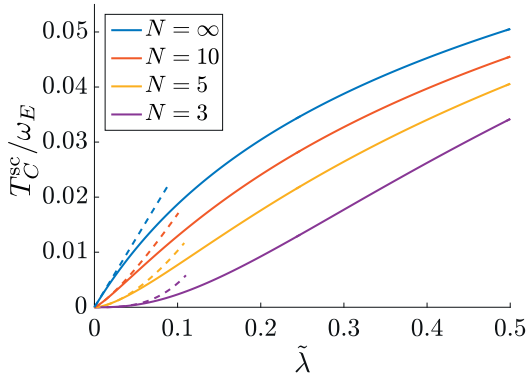


FIG. 4. Effect of finite N on critical temperature when $u = 0$. For small $\tilde{\lambda}$, the results coincide with the instantaneous approximation of Eq. (12) (shown with the dashed lines). For large $\tilde{\lambda}$, the strong-coupling corrections limit the increase in T_C^{sc} .

An approximate numerical equation for T_C^{sc} is

$$T_C^{\text{sc}} = \frac{\lambda\omega_E - u(1 - 0.3u/\omega_E)}{4(1 + 2.6\lambda^{0.8})}. \quad (14)$$

This is a flat-band analog of the McMillan equation [21], which for the conventional superconductors incorporates the Eliashberg and Coulomb corrections to T_C^{sc} . The u^2 term in the numerator accounts for the retardation correction to λ_C as in Fig. 3(b). The form of the denominator is chosen to show the $\lambda^{0.2}$ power-law behavior for large λ . The factor 2.6 is obtained by a fit in the region $\lambda < 1$ for $u = 0$. The fit is shown as the dashed line in Fig. 3(a).

The ratio Δ_0/T_C^{sc} is not constant, but depends on both N and λ . For $N \rightarrow \infty$, the ratio has the value 2 for weak coupling and increases as λ increases. For $\lambda = 1$ the ratio is 2.56. For the critical temperature at finite N , see Fig. 4.

The phenomenology of the magnetism can be understood as follows. According to the Stoner criterion, the magnetization is related to the competition between the exchange energy gain and the kinetic energy penalty from moving electrons from one spin band to another. For a flat band with $N \rightarrow \infty$, there is no kinetic energy penalty, and at zero temperature with $\lambda = 0$ even a small exchange interaction leads to a complete magnetization of the flat band. In the presence of the electron-phonon interaction the competition is between the exchange energy gain and the electron-phonon energy penalty, which coincide at $u = u_C$. If we can neglect the retardation, the total interaction in Eq. (9) is $u - \lambda\omega_E$. The flat band is completely magnetized when $u > u_C \approx \lambda\omega_E$. Due to retardation, for large λ the critical point is reduced from the linear estimate [see Fig. 3(d)].

Above, we have discussed the superconducting order parameter ϕ . The other important property of the superconducting state is the existence of a supercurrent. In the flat band the electronic group velocity vanishes and it is not immediately clear that there can be a finite supercurrent. However, the flat-band surface states of superconducting rhombohedral graphite do support a finite supercurrent [44] and similarly it is known that quantum Hall pseudospin ferromagnets can support a finite pseudospin supercurrent [16]. More generally, Peotta and Törmä [7] have shown that for a topological flat band

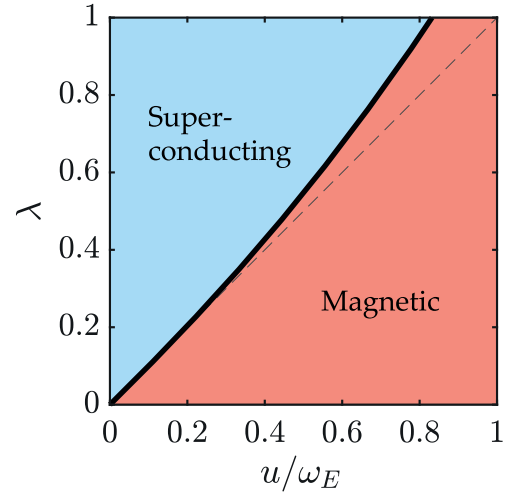


FIG. 5. Mean-field phase diagram for $N = \infty$ obtained by determining the line on which the critical temperatures for superconductivity and antiferromagnetism are equal. The thin dashed line shows the phase boundary $\lambda = u/\omega_E$ in the case of instantaneous interactions. When the energy scales of interactions are small compared to ω_E we recover the BCS results. The phase diagram for finite N looks similar but the retardation effects are weaker, so that the deviation from the BCS approximation is smaller.

there is an additional geometric contribution to the superfluid weight so that the critical current is finite. As we have not fixed the underlying topology in our model, it can be applied to topologically nontrivial flat bands.

As one can see, the Eliashberg model describes the nucleation of both the magnetic and superconducting phases which can have rather close critical temperatures as shown in Fig. 3. In the next section we consider the nonlinear problem by calculating the entire phase diagram of the ordered states to study the competition and the possible coexistence between the superconductivity and antiferromagnetism.

IV. COMPETITION BETWEEN THE PHASES

If the electron-phonon interaction is approximated as instantaneous, we can sum the two interactions together and have either a total interaction, which makes the normal state unstable to the superconducting transition ($\lambda\omega_E - u > 0$) or to the magnetic transition ($\lambda\omega_E - u < 0$), but not to both at once. On the other hand, if the electron-phonon interaction is retarded, the situation is different, as the total interaction can be attractive for low frequencies but repulsive for high frequencies. There is then a parameter range in which both phases are local minima of the free energy. This occurs when λ is large enough to overcome the suppressing effect of u in the case of superconductivity [$\lambda > \lambda_C(u)$ in Fig. 3(b)], but at the same time u is large enough to overcome the suppressing effect of λ and create a magnetic instability [$u > u_C(\lambda)$ in Fig. 3(d)].

We study the phase diagram of the system by determining the state with a higher critical temperature as a function of u and λ (Fig. 5). The phase diagram is almost symmetric with respect to SC and AFM phases except that the lack of retardation in

electron-electron repulsion favors the AFM phase for strong coupling.

Even if there is a parameter region in T , u , and λ where both SC and AFM self-consistency equations have a finite solution, it does not mean that both phases are necessarily simultaneously present. To determine the stability, we construct the coupled self-consistency equations in the case when both order parameters are nonzero and interact with each other [26]. By linearizing the coupled self-consistency equation with respect to SC, and solving the AFM part fully, the stability of the AFM phase with respect to the SC transition can be determined, and vice versa. Figure 1 shows the region in λ - T space with fixed u , where the two phases are stable. The figure shows that in the region where SC is dominant, the AFM phase is unstable near the expected second-order transition (the solid line between the magnetic and paramagnetic phases) but becomes a local minimum of free energy at lower temperatures. The same happens for superconductivity when the AFM phase dominates. The transition between SC and AFM phases is of the first order.

When discussing superconductivity in the presence of an exchange field (either induced or spontaneous), we have an additional ingredient in the self-energy, namely, the superconducting triplet order parameter [22,45], which has been discussed in the context of the Eliashberg model in Ref. [46]. The triplet is spatially isotropic, and in order to satisfy the fermionic antisymmetry, it has to be odd in frequency. It is generated in the self-energy only when there is an odd-frequency component in the interaction. In the retarded interaction, this is always satisfied. When calculating the stability of the AFM phase with respect to SC, the triplet appears in the linear order. It hence modifies the boundaries of the region where both AFM and SC phases are stable. We have taken this effect into account in Fig. 1.

Besides the competition between AFM and SC phases, we need to consider the possibility of a coexistence phase in the dashed region of Fig. 1, where both phases can show up alone. We indeed have numerically found such a coexistence solution, but tests based on fixed-point iteration revealed it to be unstable at every temperature that we checked. This finding is in accordance with a simplified model where both interaction channels are instantaneous and independent of each other [26].

However, the fact that the two phases are simultaneously local minima of the free energy suggests that this system could have domains of antiferromagnetic order coexisting with superconducting domains. Such domains would be separated by a domain wall mixing the two kinds of phases and inducing odd-frequency triplet pairing, as schematically illustrated in Fig. 6. In addition to providing a mechanism for the appearance of odd-frequency triplet pairing, the domain walls can support interesting excitations. In particular, it is known that flat-band ferromagnets can support interesting topological and domain-wall excitations in the form of different kinds of spin textures [16,47], and various combinations of spin textures and superconductivity may lead to the appearance of Majorana zero modes [48–52]. Also, alternatively to the intrinsic domain structure generation, the ferromagnetic superconductors can support different types of nonuniform magnetic order and spontaneous vortex states [53–55]. A detailed analysis of different possibilities goes beyond the scope of this paper.

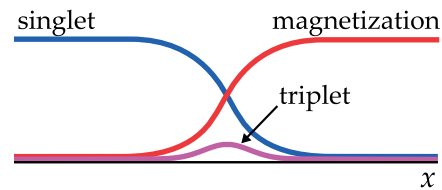


FIG. 6. Sketch of a domain wall between magnetic (red) and superconducting (blue) domains. At the domain wall a triplet component (purple) is induced.

V. CONCLUSIONS

We have proposed a simplified model of a flat-band system with a retarded electron-phonon interaction and a repulsive Hubbard interaction. For this model, we have determined the self-consistency equations in the Hartree-Fock approximation and all the possible homogeneous phases. Antiferromagnetism and superconductivity are essentially symmetric in this system, with the only difference coming from the retardation of the electron-phonon interaction. For large λ , the retardation suppresses the increase in Δ more effectively in a flat band than in metals with a Fermi surface. We find that the retardation also creates a situation in which both phases are separately local minima of the free energy, suggesting a possibility of coexisting antiferromagnetic and superconducting domains inside the sample.

Our results indicate how flat-band superconductivity can be generated from electron-phonon interaction and provides means to estimate the mean-field critical temperature when the details of the electron-phonon coupling and the screened interaction are known. The superfluid transition in low-dimensional systems occurs in the form of a Berezinskii-Kosterlitz-Thouless (BKT) transition at a temperature that is lower than the mean-field transition temperature. That the latter is nonzero is ensured by the possibility of having a nonvanishing supercurrent (see, for example, Refs. [7,10,44]) in a flat-band superconductor. Our results are of relevance in designing novel types of quantum materials for the interplay of superconducting and magnetic order, and the search for systems exhibiting exotic superconductivity with a very high critical temperature, up to room temperature. They may also shed light on recent evidence of high-temperature superconductivity in graphite interfaces [56].

Our results could also explain some of the phenomena associated with the recent experiments on bilayer graphene [30,57]. (For a more microscopic description of that case within the BCS model, see Refs. [58,59].) In the experiment, the twist angle between two superimposed graphene layers is chosen to a certain magic angle, so that the two Dirac cones in the graphene layers hybridize, forming a pair of flat bands. Our model can be adjusted to describe this situation with small changes (see the Supplemental Material [26] for details). When the chemical potential was tuned to the lower of these bands, the system became an insulator. From our point of view, this could be the insulating AFM state we describe. When the chemical potential is tuned slightly off from the flat band, a superconducting dome in the T - μ phase diagram was observed on both sides. These domes can be the s -wave SC phases

we describe here. The competition between the particle-hole (AFM) and the particle-particle (SC) channels in the presence of the chemical potential was considered by Löthman and Black-Schaffer in Ref. [8], and for a range of parameters, they reproduce a similar phase diagram near the flat band, with the AFM state at the level of the flat band and two superconducting domes with doping away from the flat band (see Fig. 2(b) in Ref. [8]). In the experiments, SC domes are only observed on the hole-doped side. The electron-doped side exhibits only insulating behavior near the flat band. One possible explanation is the difference in screening, which changes the relative magnitude of the repulsive and attractive interactions, so that

the AFM state covers the SC domes completely. However, we leave the detailed treatment of the effects of doping and screening (both intrinsic and that provided by the environment) for further work.

ACKNOWLEDGMENTS

We thank Sebastiano Peotta, Long Liang, and Päivi Törmä for helpful comments. This project was supported by the Academy of Finland Key Funding (Project No. 305256), Center of Excellence (Project No. 284594), and Research Fellow (Project No. 297439) programs.

-
- [1] B. Keimer and J. E. Moore, The physics of quantum materials, *Nat. Phys.* **13**, 1045 (2017).
- [2] V. A. Shaginyan and V. R. Khodel, Superfluidity in system with fermion condensate, *JETP Lett.* **51**, 553 (1990).
- [3] T. T. Heikkilä, N. B. Kopnin, and G. E. Volovik, Flat bands in topological media, *JETP Lett.* **94**, 233 (2011).
- [4] T. T. Heikkilä and G. E. Volovik, *Basic Physics of Functionalized Graphite* (Springer, Berlin, 2016), Chap. 6.
- [5] E. Tang and L. Fu, Strain-induced partially flat band, helical snake states and interface superconductivity in topological crystalline insulators, *Nat. Phys.* **10**, 964 (2014).
- [6] S. Matsuura, P.-Y. Chang, A. P. Schnyder, and S. Ryu, Protected boundary states in gapless topological phases, *New J. Phys.* **15**, 065001 (2013).
- [7] S. Peotta and P. Törmä, Superfluidity in topologically nontrivial flat bands, *Nat. Commun.* **6**, 8944 (2015).
- [8] T. Löthman and A. M. Black-Schaffer, Universal phase diagrams with superconducting domes for electronic flat bands, *Phys. Rev. B* **96**, 064505 (2017).
- [9] E. H. Lieb, Two Theorems on the Hubbard Model, *Phys. Rev. Lett.* **62**, 1201 (1989).
- [10] V. J. Kauppila, F. Aikebaier, and T. T. Heikkilä, Flat-band superconductivity in strained Dirac materials, *Phys. Rev. B* **93**, 214505 (2016).
- [11] H. Fröhlich, Theory of the superconducting state. I. The ground state at the absolute zero of temperature, *Phys. Rev.* **79**, 845 (1950).
- [12] N. B. Kopnin, T. T. Heikkilä, and G. E. Volovik, High-temperature surface superconductivity in topological flat-band systems, *Phys. Rev. B* **83**, 220503 (2011).
- [13] H. Tasaki, Ferromagnetism in the Hubbard Models with Degenerate Single-Electron Ground States, *Phys. Rev. Lett.* **69**, 1608 (1992).
- [14] A. Mielke and H. Tasaki, Ferromagnetism in the Hubbard model, *Commun. Math. Phys.* **158**, 341 (1993).
- [15] O. Derzhko, A. Honecker, and J. Richter, Low-temperature thermodynamics for a flat-band ferromagnet: Rigorous versus numerical results, *Phys. Rev. B* **76**, 220402 (2007).
- [16] K. Moon, H. Mori, K. Yang, S. M. Girvin, A. H. MacDonald, L. Zheng, D. Yoshioka, and S.-C. Zhang, Spontaneous interlayer coherence in double-layer quantum Hall systems: Charged vortices and Kosterlitz-Thouless phase transitions, *Phys. Rev. B* **51**, 5138 (1995).
- [17] H. A. Fertig, Energy spectrum of a layered system in a strong magnetic field, *Phys. Rev. B* **40**, 1087 (1989).
- [18] S. T. Belyaev, On the nature of the first excited states of even-even spherical nuclei, *Sov. Phys. JETP* **12**, 968 (1961).
- [19] G. M. Eliashberg, Interactions between electrons and lattice vibrations in a superconductor, *Sov. Phys. JETP* **11**, 696 (1960).
- [20] J. Bardeen, L. N. Cooper, and J. R. Schrieffer, Theory of superconductivity, *Phys. Rev.* **108**, 1175 (1957).
- [21] W. L. McMillan, Transition temperature of strong-coupled superconductors, *Phys. Rev.* **167**, 331 (1968).
- [22] V. L. Berezinskii, New model of the anisotropic phase of superfluid He-3, *JETP Lett.* **20**, 287 (1974).
- [23] M. Matsumoto, M. Koga, and H. Kusunose, Coexistence of even- and odd-frequency superconductivities under broken time-reversal symmetry, *J. Phys. Soc. Jpn.* **81**, 033702 (2012).
- [24] V. J. Kauppila, T. Hyart, and T. T. Heikkilä, Collective amplitude mode fluctuations in a flat band superconductor formed at a semimetal surface, *Phys. Rev. B* **93**, 024505 (2016).
- [25] J. Hubbard, Electron correlations in narrow energy bands, *Proc. R. Soc. London, Ser. A* **276**, 238 (1963).
- [26] See Supplemental Material at <http://link.aps.org/supplemental/10.1103/PhysRevB.98.054515> for more details. In addition to the references in the main paper, the Supplemental Information includes Refs. [27–29].
- [27] J. M. B. Lopes do Santos, N. M. R. Peres, and A. H. Castro Neto, Continuum model of the twisted graphene bilayer, *Phys. Rev. B* **86**, 155449 (2012).
- [28] E. Suárez Morell, J. D. Correa, P. Vargas, M. Pacheco, and Z. Barticevic, Flat bands in slightly twisted bilayer graphene: Tight-binding calculations, *Phys. Rev. B* **82**, 121407 (2010).
- [29] N. B. Kopnin and E. B. Sonin, BCS Superconductivity of Dirac Electrons in Graphene Layers, *Phys. Rev. Lett.* **100**, 246808 (2008).
- [30] Y. Cao, V. Fatemi, S. Fang, K. Watanabe, T. Taniguchi, E. Kaxiras, and P. Jarillo-Herrero, Unconventional superconductivity in magic-angle graphene superlattices, *Nature (London)* **556**, 43 (2018).
- [31] A. B. Migdal, Interaction between electrons and lattice vibrations in a normal metal, *Sov. Phys. JETP* **7**, 996 (1958).
- [32] C. Grimaldi, L. Pietronero, and S. Strässler, Nonadiabatic Superconductivity: Electron-Phonon Interaction Beyond Migdal's Theorem, *Phys. Rev. Lett.* **75**, 1158 (1995).
- [33] L. Pietronero, S. Strässler, and C. Grimaldi, Nonadiabatic superconductivity. I. Vertex corrections for the electron-phonon interactions, *Phys. Rev. B* **52**, 10516 (1995).
- [34] C. Grimaldi, L. Pietronero, and S. Strässler, Nonadiabatic superconductivity. II. Generalized Eliashberg equations beyond Migdal's theorem, *Phys. Rev. B* **52**, 10530 (1995).

- [35] M. Botti, E. Cappelluti, C. Grimaldi, and L. Pietronero, Nonadiabatic theory of the superconducting state, *Phys. Rev. B* **66**, 054532 (2002).
- [36] I. Esterlis, B. Nosarzewski, E. W. Huang, B. Moritz, T. P. Devereaux, D. J. Scalapino, and S. A. Kivelson, Breakdown of Migdal-Eliashberg theory: A determinant quantum Monte Carlo study, *Phys. Rev. B* **97**, 140501 (2018).
- [37] B. Pamuk, J. Baima, F. Mauri, and M. Calandra, Magnetic gap opening in rhombohedral-stacked multilayer graphene from first principles, *Phys. Rev. B* **95**, 075422 (2017).
- [38] M. Fujita, K. Wakabayashi, K. Nakada, and K. Kusakabe, Peculiar localized state at zigzag graphite edge, *J. Phys. Soc. Jpn.* **65**, 1920 (1996).
- [39] J. Fernández-Rossier, Prediction of hidden multiferroic order in graphene zigzag ribbons, *Phys. Rev. B* **77**, 075430 (2008).
- [40] Y.-W. Son, M. L. Cohen, and S. G. Louie, Half-metallic graphene nanoribbons, *Nature (London)* **444**, 347 (2006).
- [41] M. Tovmasyan, S. Peotta, P. Törmä, and S. D. Huber, Effective theory and emergent SU(2) symmetry in the flat bands of attractive Hubbard models, *Phys. Rev. B* **94**, 245149 (2016).
- [42] P. Morel and P. W. Anderson, Calculation of the superconducting state parameters with retarded electron-phonon interaction, *Phys. Rev.* **125**, 1263 (1962).
- [43] J. P. Carbotte, Properties of boson-exchange superconductors, *Rev. Mod. Phys.* **62**, 1027 (1990).
- [44] N. B. Kopnin, Surface superconductivity in multilayered rhombohedral graphene: Supercurrent, *JETP Lett.* **94**, 81 (2011).
- [45] A. Balatsky and E. Abrahams, New class of singlet superconductors which break the time reversal and parity, *Phys. Rev. B* **45**, 13125 (1992).
- [46] H. Kusunose, M. Matsumoto, and M. Koga, Strong-coupling superconductivity with mixed even-and odd-frequency pairing, *Phys. Rev. B* **85**, 174528 (2012).
- [47] D. I. Pikulin, P. G. Silvestrov, and T. Hyart, Confinement-deconfinement transition due to spontaneous symmetry breaking in quantum Hall bilayers, *Nat. Commun.* **7**, 10462 (2016).
- [48] T.-P. Choy, J. M. Edge, A. R. Akhmerov, and C. W. J. Beenakker, Majorana fermions emerging from magnetic nanoparticles on a superconductor without spin-orbit coupling, *Phys. Rev. B* **84**, 195442 (2011).
- [49] B. Braunecker and P. Simon, Interplay Between Classical Magnetic Moments and Superconductivity in Quantum One-Dimensional Conductors: Toward a Self-Sustained Topological Majorana Phase, *Phys. Rev. Lett.* **111**, 147202 (2013).
- [50] J. Klinovaja, P. Stano, A. Yazdani, and D. Loss, Topological Superconductivity and Majorana Fermions in RKKY Systems, *Phys. Rev. Lett.* **111**, 186805 (2013).
- [51] M. M. Vazifeh and M. Franz, Self-Organized Topological State with Majorana Fermions, *Phys. Rev. Lett.* **111**, 206802 (2013).
- [52] F. Pientka, L. I. Glazman, and F. von Oppen, Topological superconducting phase in helical Shiba chains, *Phys. Rev. B* **88**, 155420 (2013).
- [53] P. W. Anderson and H. Suhl, Spin alignment in the superconducting state, *Phys. Rev.* **116**, 898 (1959).
- [54] L. N. Bulaevskii, A. I. Buzdin, M. L. Kulić, and S. V. Panjukov, Coexistence of superconductivity and magnetism theoretical predictions and experimental results, *Adv. Phys.* **34**, 175 (1985).
- [55] L. Y. Vinnikov, I. S. Veshchunov, S. Y. Grebenchuk, D. S. Baranov, V. S. Stolyarov, V. V. Dremov, N. Zhou, Z. X. Shi, X. F. Xu, S. Pyon, Y. Sun, W. Jiao, G. Cao, A. A. Golubov, D. Roditchev, A. I. Buzdin, and T. Tamegai, Direct evidence of spontaneous Abrikosov vortex state in ferromagnetic superconductor $\text{EuFe}_2(\text{As}_{1-x}\text{P}_x)_2$ with $x = 0.21$, [arXiv:1709.09802](https://arxiv.org/abs/1709.09802).
- [56] C. E. Precker, P. D. Esquinazi, A. Champi, J. Barzola-Quiquia, M. Zoraghi, S. Muios-Landin, A. Setzer, W. Bühlmann, D. Spemann, J. Meijer, T. Muenster, O. Baehre, G. Kloess, and H. Beth, Identification of a possible superconducting transition above room temperature in natural graphite crystals, *New J. Phys.* **18**, 113041 (2016).
- [57] Y. Cao, V. Fatemi, A. Demir, S. Fang, S. L. Tomarken, J. Y. Luo, J. D. Sanchez-Yamagishi, K. Watanabe, T. Taniguchi, E. Kaxiras, R. C. Ashoori, and P. Jarillo-Herrero, Correlated insulator behaviour at half-filling in magic-angle graphene superlattices, *Nature (London)* **556**, 80 (2018).
- [58] T. J. Peltonen, R. Ojajärvi, and T. T. Heikkilä, Mean-field theory for superconductivity in twisted bilayer graphene, [arXiv:1805.01039](https://arxiv.org/abs/1805.01039).
- [59] F. Wu, A. H. MacDonald, and I. Martin, Theory of phonon-mediated superconductivity in twisted bilayer graphene, [arXiv:1805.08735](https://arxiv.org/abs/1805.08735).

Supplementary material to “Competition of electron-phonon mediated superconductivity and Stoner magnetism on a flat band”

Risto Ojajärvi,¹ Timo Hyart,^{1,2} Mihail A. Silaev,¹ and Tero T. Heikkilä¹

¹*Department of Physics and Nanoscience Center, University of Jyväskylä,
P.O. Box 35 (YFL), FI-40014 University of Jyväskylä, Finland*

²*Institut für Theoretische Physik, Universität Leipzig, D-04103 Leipzig, Germany*

(Dated: July 31, 2018)

NOTE ON INTERACTION CONSTANTS AND THE TIGHT BINDING MODEL

The Hamiltonian studied in the main text is derived from a tight binding model, in which the size of the system is naturally characterized by the number of lattice sites N . However, in approximating the sum over all momenta, it is more natural to use the area A of the system. The ratio A/N is the area of the real space unit cell A_c , which in turn is inversely proportional to the area of the first Brillouin zone Ω_{BZ} . For an infinite system, the momentum sum can be written in the following form.

$$\frac{1}{N} \sum_p = \frac{A}{N} \int_{\text{BZ}} \frac{d^2\mathbf{p}}{(2\pi)^2} = \frac{A_c \pi p_{\text{FB}}^2}{2\pi^2} \int_0^{p_c} \frac{dp p}{p_{\text{FB}}^2} = 2 \frac{\Omega_{\text{FB}}}{\Omega_{\text{BZ}}} \int_0^{p_c} \frac{dp p}{p_{\text{FB}}^2}, \quad (\text{S1})$$

where $\Omega_{\text{FB}} \equiv \pi p_{\text{FB}}^2$ is the area of the flat band and p_c is the momentum cutoff. We define a shorthand for the sum/integral over momenta and Matsubara frequencies

$$\sum_{\mathbf{p}, m} = 2T \sum_{\omega_m} \int_0^{p_c} \frac{dp p}{p_{\text{FB}}^2}. \quad (\text{S2})$$

We find that the effective interactions on the flat band are characterized by the constants

$$u \equiv \frac{U \Omega_{\text{FB}}}{\Omega_{\text{BZ}}}, \quad (\text{S3})$$

$$\lambda_{nm} = -\frac{g^2}{2} \frac{\Omega_{\text{FB}}}{\Omega_{\text{BZ}}} D(i\omega_m - i\omega_n) = \frac{\lambda \omega_E^3}{\omega_E^2 + (\omega_m - \omega_n)^2}, \quad \text{with} \quad \lambda \equiv \frac{g^2}{\omega_E^2} \frac{\Omega_{\text{FB}}}{\Omega_{\text{BZ}}}. \quad (\text{S4})$$

where $D(z) = -2\omega_E/(\omega_E^2 - z^2)$ is the phonon propagator. In other words, interactions are proportional to the ratio between the area of the flat band and that of the first Brillouin zone.

SELF-ENERGY COMPONENTS

In total, there are $4^3 = 64$ combinations of Pauli matrices in spin, Nambu and sublattice spaces. The ones off-diagonal in sublattice space are not possible (see below), as the interactions in the model do not couple the two sublattices. This reduces the number by a factor of 2. We are left with 16 components symmetric and 16 components antisymmetric in sublattice index ρ . Of these 32 components, the 16 components diagonal in Nambu space are associated with non-superconducting properties. The $\tau_0\sigma_0\rho_0$ -component renormalizes the frequencies in the propagator [1]. It vanishes if the interaction is instantaneous and is always present if the interaction has a nontrivial frequency structure. The $\tau_3\sigma_0\rho_0$ -component on the other hand renormalizes the chemical potential, and is usually induced by finite temperature or interaction effects. In this model it vanishes because of the electron-hole symmetry of the model at half-filling. There could in principle also be a term proportional to $\tau_0\sigma_0\rho_3$. Its effect would be to renormalize frequencies antisymmetrically in the sublattices. However, it is not induced by any of the other terms, so the only way to have it would be by spontaneous symmetry breaking. It should be odd in frequency, and this makes it vanish in the BCS limit. Even in Eliashberg theory, it is unlikely, as it is supported only by the odd-frequency part of the interaction. In this text, we do not consider this and other antisymmetric frequency renormalization components any further.

The remaining 12 components diagonal in Nambu space are due to magnetism. The magnetization direction on one sublattice is described with the three components $\sigma_i\tau_3$. We can parametrize the six degrees of freedom associated

with magnetization with the overall magnitude and the relative magnitude of the order parameter, two angles for the overall magnetization direction, and two angles for the relative direction. The six other terms of the form $\sigma_i \tau_0 \rho_j$ are spin-antisymmetric frequency renormalization components.

The 16 components off-diagonal in Nambu space are associated with superconductivity. Four of these are associated with the singlet and its phase and the sublattice: overall phase, relative phase between the sublattices, overall magnitude of the order parameter and the relative magnitude between the sublattices. The remaining 12 off-diagonal Nambu components describe the three components of the triplet and its phase and sublattice degrees of freedom. Because both the spatial and the spin parts of the triplet are symmetric, it must be odd in frequency to preserve the fermionic antisymmetry [2]. Such components are supported by the odd-frequency part of the electron-phonon interaction [3].

HARTREE-FOCK SELF-ENERGIES

Starting from the Hamiltonian and using the above definitions for the interactions, we can write the self-energies in the Hartree-Fock approximation as

$$\Sigma_{\text{H}}^{\text{c}} = -u \sum_{\mathbf{p}, m, \rho} P_{\rho} \text{Tr}[P_{\rho} G(\mathbf{p}, i\omega_m)] \quad (\text{S5})$$

$$\Sigma_{\text{F}}^{\text{c}} = u \sum_{\mathbf{p}, m, \rho} P_{\rho} G(\mathbf{p}, i\omega_m) P_{\rho} \quad (\text{S6})$$

$$\Sigma_{\text{H}}^{\text{ph}} = 0 \quad (\text{S7})$$

$$\Sigma_{\text{F}}^{\text{ph}}(i\omega_n) = - \sum_{\mathbf{p}, m, \rho} \lambda_{nm} P_{\rho} G(\mathbf{p}, i\omega_m) P_{\rho}, \quad (\text{S8})$$

where P_{ρ} is the projection operator to sublattice ρ , $\rho \in A, B$. It is immediately clear from the above expressions that the self-energy cannot have terms with A - B mixing, as the projection operators force it to be diagonal in the sublattice space. We assume that the radius of the flat band is much smaller than the maximum phonon momentum, so that the phonon cutoff does not need to be enforced in the momentum sum.

With a contact interaction, the only differences between the Hartree and Fock terms come from the sign change (from the fermionic loop in the Hartree term) and from the summation over spins. The total Coulomb self-energy is

$$\Sigma_{\sigma, \rho}^{\text{c}} = -u \sum_{\mathbf{p}, m} G_{\bar{\sigma}, \rho}(\mathbf{p}, i\omega_m). \quad (\text{S9})$$

Note that the self-energy for up spin is determined from the propagator for the down spin and vice versa.

For electron-phonon interaction we only include the Fock term. The Hartree term vanishes because there is no $p=0$ -phonon mediating the Hartree interaction.

$$\Sigma_{\sigma, \rho}^{\text{ph}}(i\omega_n) = - \sum_{\mathbf{p}, m} \lambda_{nm} G_{\sigma, \rho}(\mathbf{p}, i\omega_m). \quad (\text{S10})$$

This is written without particle-hole (Nambu) basis and must be extended to include superconductivity. For now, we consider the normal state to find what would be the stable phase if superconductivity would not be present.

The total self-energy for spin σ and surface ρ is

$$\Sigma_{\sigma, s}(i\omega_n) = - \sum_{\mathbf{p}, m} [\lambda_{nm} G_{\sigma, s}(\mathbf{p}, i\omega_m) + u G_{\bar{\sigma}, s}(\mathbf{p}, i\omega_m)]. \quad (\text{S11})$$

Below we use this to study the possibility of a pseudospin analogue of the magnetic state.

PSEUDOSPIN MAGNETISM

Let us now consider the self-energy

$$\Sigma_{\text{ps}}(i\omega_n) = -i\Sigma_n^{\omega} \mathbf{1} + h_n^{\text{ps}} \rho_3, \quad (\text{S12})$$

where h^{ps} is an analogous order parameter to ferromagnetic ordering, but with spin replaced by a pseudospin ρ (sublattice index). The propagator is

$$G^{-1}(\mathbf{p}, i\omega_n) = i\tilde{\omega}_n \mathbf{1} - \varepsilon_p \rho_1 - h_n^{\text{ps}} \rho_3, \quad (\text{S13})$$

where $\tilde{\omega}_n = \omega_n + \Sigma_n^\omega = Z\omega_n$ is the renormalized frequency.

Instead of Eq. (S11) with a complicated matrix structure, it is more useful to consider the components of the self-energy that are symmetric and antisymmetric in spin and sublattice indices σ and ρ . We get the self-consistency equations

$$-i\Sigma_n^\omega = - \sum_{\mathbf{p}, m} \lambda_{nm} \frac{1}{4} \sum_{\sigma, \rho} G_{\bar{\sigma}, \rho}(\mathbf{p}, i\omega_m) + \Delta\mu, \quad (\text{S14})$$

$$h_n^{\text{ps}} = \sum_{\mathbf{p}, m} [-u - \lambda_{nm}] \frac{1}{4} \sum_{\sigma, \rho} \rho G_{\bar{\sigma}, \rho}(\mathbf{p}, i\omega_m), \quad (\text{S15})$$

where we isolate a correction to the chemical potential as $\Delta\mu$. We assume a fixed particle number, and therefore this correction is counteracted by a shift in the chemical potential to the opposite direction and as a result, it vanishes.

In the normal state, we can write G as a 4×4 matrix. Its inverse is

$$\mathbf{G}^{-1}(\mathbf{p}, i\omega_n) = \begin{pmatrix} i\tilde{\omega}_n - h_n^{\text{ps}} & -\varepsilon_p & & \\ -\varepsilon_p & i\tilde{\omega}_n + h_n^{\text{ps}} & & \\ & & i\tilde{\omega}_n - h_n^{\text{ps}} & -\varepsilon_p \\ & & -\varepsilon_p & i\tilde{\omega}_n + h_n^{\text{ps}} \end{pmatrix}, \quad (\text{S16})$$

where the basis is chosen as $\Psi_p^\dagger = (c_{A\uparrow p}^\dagger, c_{B\uparrow p}^\dagger, c_{A\downarrow p}^\dagger, c_{B\downarrow p}^\dagger)$. The matrix can be inverted in 2×2 blocks labeled with spin:

$$\mathbf{G}_\sigma(\mathbf{p}, i\omega_n) = \frac{1}{\Omega_\sigma(\mathbf{p}, i\omega_n)} \begin{pmatrix} i\tilde{\omega}_n + h_n^{\text{ps}} & \varepsilon_p \\ \varepsilon_p & i\tilde{\omega}_n - h_n^{\text{ps}} \end{pmatrix}, \quad (\text{S17})$$

where

$$\Omega_\sigma(\mathbf{p}, i\omega_n) = (i\tilde{\omega}_n + h_n^{\text{ps}})(i\tilde{\omega}_n - h_n^{\text{ps}}) - \varepsilon_p^2 = -[\tilde{\omega}_n^2 + \varepsilon_p^2 + (h_n^{\text{ps}})^2]. \quad (\text{S18})$$

The self-consistency equations for pseudo-spin magnetism are

$$Z_n = 1 + \sum_{\mathbf{p}, m} \lambda_{nm} \frac{\omega_m}{\omega_n} \frac{Z_m}{\tilde{\omega}_m^2 + \varepsilon_p^2 + (h_m^{\text{ps}})^2} \quad (\text{S19})$$

$$h_n^{\text{ps}} = \sum_{\mathbf{p}, m} (-u - \lambda_{nm}) \frac{h_m^{\text{ps}}}{\tilde{\omega}_m^2 + \varepsilon_p^2 + (h_m^{\text{ps}})^2}. \quad (\text{S20})$$

We see from these equations that a pure pseudo-spin magnetism can be ruled out, as the interactions do not support it: both interaction terms in Eq. (S20) are negative; compare with Eqs. (S23, S35). We would need to have a repulsive electron-phonon interaction or an attractive Coulomb interaction in order to obtain a nonzero solution. The unequal form of the interactions in spin-magnetism versus pseudospin-magnetism originates from the lack of an exchange term in the electron-phonon interaction.

ANTIFERROMAGNETISM

For antiferromagnetism (AFM), the self-energy has the form

$$\Sigma_{\text{AFM}}(i\omega_n) = -i\Sigma_n^\omega \mathbf{1} + h_n \tau_3 \sigma_3, \rho_3, \quad (\text{S21})$$

where h_n is the frequency-dependent exchange field. As for the pseudospin magnetism above, the self-consistency equations for AFM are

$$Z_n = 1 + \sum_{\mathbf{p}, m} \lambda_{nm} \frac{\omega_m}{\omega_n} \frac{Z_m}{\tilde{\omega}_m^2 + \varepsilon_p^2 + h_m^2}, \quad (\text{S22})$$

$$h_n = \sum_{\mathbf{p}, m} (u - \lambda_{nm}) \frac{h_m}{\tilde{\omega}_m^2 + \varepsilon_p^2 + h_m^2}, \quad (\text{S23})$$

In contrast to Eq. (S20), the sign of u is now positive, and this makes the normal state unstable to the AFM phase. Here we take the momentum cutoff to infinity. For large N the results do not depend on the cutoff provided it is larger than p_{FB} . For $N \leq 2$ the momentum integration diverges without a cutoff, so the results below do not apply for those cases.

To numerically solve the above equations, we need to impose a cutoff ω_{max} in the Matsubara summation. To do that, we need to replace the Coulomb interaction with a modified term using the pseudopotential trick [4]. The form of the pseudopotential depends on the details of the self-consistency equation, so it has to be formulated separately for different equations. The differences are in the details, and the basic idea stays the same: in the Coulomb part of the self-energy we divide the Matsubara summation to low-energy and high-energy parts. Then we solve for the self-energy term and define a new interaction constant, which takes into account the high-energy contribution [4]. The exact form of the contribution from the high energy sum is the part which differs between different equations. We formulate equations in a form which is easy to solve numerically.

For AFM equations, we can calculate the high energy part to be

$$\begin{aligned} \alpha &= 2T \sum_{|\omega_n| > \omega_{\text{max}}} \int_0^\infty \frac{dp p}{p_{\text{FB}}^2} \frac{1}{\omega_n^2 + \varepsilon_p^2} = 2T \left(\sum_{\omega_n} - \sum_{|\omega_n| < \omega_{\text{max}}} \right) \int \frac{dp p}{p_{\text{FB}}^2} \frac{1}{\omega_n^2 + \varepsilon_p^2} \\ &= \frac{x_{\text{max}}^{2-N}}{\varepsilon_0(N-2)} + \frac{1}{\varepsilon_0} \int_0^{x_{\text{max}}} dx x^{1-N} \tanh\left(\frac{\varepsilon_0 x^N}{2T}\right) - \frac{\pi}{N \sin(\pi/N)} 2T \sum_{|\omega_n| < \omega_{\text{max}}} \frac{(\omega_n/\varepsilon_0)^{2/N}}{2\omega_n^2}, \end{aligned} \quad (\text{S24})$$

where the cutoff x_{max} is chosen so that $\varepsilon(p_{\text{FB}} x_{\text{max}}) \gg 2T$. An argument larger than 4 is already large enough in order to approximate the hyperbolic tangent by unity, so we can choose $x_c = (8T/\varepsilon_0)^{1/N}$. In total, the pseudopotential is

$$u^- = \frac{u}{1 - u\alpha}. \quad (\text{S25})$$

For a better accuracy at the strong coupling and low-temperature regime, we also include the Coulomb part of the exchange field h_c in Eq. (S24), so that α depends self-consistently on h_c . The non-self-consistent α given above is sufficient for the calculation of T_C .

With cutoff and a pseudopotential, Eqs. (S22-S23) become

$$h_n = 2T \sum_{|\omega_m| < \omega_{\text{max}}} (u^- - \lambda_{nm}) \int_0^\infty \frac{dp p}{p_{\text{FB}}^2} \frac{h_m}{\tilde{\omega}_m^2 + \varepsilon_p^2 + h_m^2}, \quad (\text{S26})$$

$$Z_n = 1 + 2T \sum_{|\omega_m| < \omega_{\text{max}}} \lambda_{nm} \frac{\omega_m}{\omega_n} \int_0^\infty \frac{dp p}{p_{\text{FB}}^2} \frac{Z_m}{\tilde{\omega}_m^2 + \varepsilon_p^2 + h_m^2}, \quad (\text{S27})$$

which can be solved numerically.

Linearized equations for solving the critical temperature

To determine the critical temperature, the self-consistency equations can be linearized with respect to h . In this case the momentum integrals can also be done analytically. We obtain

$$\begin{aligned} Z_n &= 1 + \alpha_N T \sum_{|\omega_m| < \omega_{\text{max}}} \frac{\lambda_{nm}}{\omega_n \tilde{\omega}_m} \left(\frac{\tilde{\omega}_m}{\varepsilon_0} \right)^{2/N}, \\ h_n &= \alpha_N T \sum_{|\omega_m| < \omega_{\text{max}}} [u^- - \lambda_{nm}] \frac{h_m}{\tilde{\omega}_m^2} \left(\frac{\tilde{\omega}_m}{\varepsilon_0} \right)^{2/N}, \end{aligned} \quad (\text{S28})$$

where $\alpha_N = N \sin(\pi/N)/\pi$.

If $\lambda = 0$, then $Z = 1$ and also the Matsubara summation can be done analytically. We find T_C^{m} in terms of the Riemann ζ -function,

$$T_C^{\text{m}} = \frac{1}{2\pi} \left[\frac{u \zeta(2 - \frac{2}{N}) (2^{2 - \frac{2}{N}} - 1)}{\varepsilon_0^{2/N} N \sin(\frac{\pi}{N})} \right]^{\frac{N}{N-2}}, \quad (\text{S29})$$

which approaches the value $T_C^{\text{m}} = u/4$ when $N \rightarrow \infty$.

SUPERCONDUCTIVITY

Extending the formalism to the particle-hole space to include superconductivity, we define a Nambu vector $\Psi^\dagger = (\psi_{A,\mathbf{p},\uparrow}^\dagger, \psi_{B,\mathbf{p},\uparrow}^\dagger, \psi_{A,\mathbf{p},\downarrow}^\dagger, \psi_{B,\mathbf{p},\downarrow}^\dagger, \psi_{A,-\mathbf{p},\uparrow}, \psi_{B,-\mathbf{p},\uparrow}, \psi_{A,-\mathbf{p},\downarrow}, \psi_{B,-\mathbf{p},\downarrow})$. The Feynman rules are then changed so that the interaction vertex gets an additional Nambu structure; P_ρ is replaced by $P_\rho\tau_3$. The Hartree-Fock self-energy terms are

$$\check{\Sigma}_{\text{H}}^{\text{c}} = -uP_\rho\tau_3 \text{Tr}[P_\rho\tau_3\check{G}(\mathbf{p}, i\omega_n)] \quad (\text{S30})$$

$$\check{\Sigma}_{\text{F}}^{\text{c}} = u \sum_{\mathbf{p}, m, \rho} P_\rho\tau_3\check{G}(\mathbf{p}, i\omega_m)\tau_3P_\rho \quad (\text{S31})$$

$$\check{\Sigma}_{\text{H}}^{\text{ph}} = 0 \quad (\text{S32})$$

$$\check{\Sigma}_{\text{F}}^{\text{ph}}(i\omega_n) = - \sum_{\mathbf{p}, m, \rho} \lambda_{nm}P_\rho\tau_3\check{G}(\mathbf{p}, i\omega_m)\tau_3P_\rho. \quad (\text{S33})$$

We note that the Hartree term only affects the normal-state self-energy components, and not the off-diagonal ones associated with superconductivity. Superconductivity is determined only from the Fock terms.

The order parameter is the same on both sublattices, $\phi_A = \phi_B$. In principle, the order parameter could also have a different phase and magnitude on the two surfaces, but this choice is the one with the lowest energy [5]. The self-consistency equations for the superconducting phase are

$$Z_n = 1 + 2T \sum_{\omega_m} \lambda_{nm} \frac{\omega_m}{\omega_n} \int_0^\infty \frac{dp p}{p_{\text{FB}}^2} \frac{Z_m}{\tilde{\omega}_m^2 + \varepsilon_p^2 + \phi_m^2}, \quad (\text{S34})$$

$$\phi_n = 2T \sum_{\omega_m} (\lambda_{nm} - u) \int_0^\infty \frac{dp p}{p_{\text{FB}}^2} \frac{\phi_m}{\tilde{\omega}_m^2 + \varepsilon_p^2 + \phi_m^2}. \quad (\text{S35})$$

In Eq. (S35) we can impose a Matsubara cutoff ω_{max} if we simultaneously replace u with a pseudopotential u^+ , like in Eqs. (S24, S27). Compared to the AFM case, there is a sign change in the pseudopotential,

$$u^+ = \frac{u}{1 + u\alpha}. \quad (\text{S36})$$

The interpretation of the pseudopotential is that for superconductivity, the scattering at high energies reduces the effect of interaction at lower energies, whereas for magnetism, the effect is reversed. If we remove the high-energy scattering from the theory, the interaction has to be replaced by an effective pseudopotential to account for their effect.

Correction to the critical temperature due to retardation

To obtain an approximation for the effect of the electron-phonon renormalization on superconductivity, we first solve the renormalization function Z at zero temperature by approximating the self-consistency equation as

$$Z(i\omega) = 1 + \lim_{\epsilon \rightarrow 0} \frac{\lambda}{\omega} \int \frac{d\omega'}{2\pi} \frac{\omega_E^3}{\omega_E^2 + (\omega - \omega')^2} \frac{Z_0\omega'}{(Z_0\omega')^2 + \epsilon^2}, \quad (\text{S37})$$

where $\epsilon = 0^+$ is used to regularize the integral. Inside the integral we approximate Z by its peak value $Z_0 \equiv Z(i\omega = 0)$. The integral yields

$$Z(i\omega) = 1 + \frac{\lambda\omega_E^2}{Z_0(\omega_E^2 + \omega^2)}. \quad (\text{S38})$$

For $\omega = 0$, we have $Z_0 = 1 + \lambda/Z_0$, whose solution in the first order in λ is $Z_0 = 1 + \lambda$.

Now the approximate self-consistency equation for ϕ is

$$\phi_0 = \lambda \int \frac{d\omega}{2\pi} \frac{\omega_E^3}{\omega_E^2 + \omega^2} \frac{\phi_0}{(Z\omega)^2 + \phi_0^2} \xrightarrow{\phi_0 \rightarrow 0} \frac{\lambda\omega_E}{2Z_0}. \quad (\text{S39})$$

At zero temperature, for $\Delta = \phi/Z$, we have

$$\Delta_0 = \frac{\phi_0}{Z_0} = \frac{\lambda\omega_E}{2Z_0^2} = \frac{\lambda\omega_E}{2(1+2\lambda)}. \quad (\text{S40})$$

At weak coupling, the critical temperature is half the value of Δ_0 ,

$$T_C^{\text{sc}} \approx \frac{\Delta_0}{2} = \frac{\lambda\omega_E}{4(1+2\lambda)}. \quad (\text{S41})$$

The above calculation accounts for the electron-phonon renormalization in a very crude manner. A better agreement with the numerical results is obtained by a direct fit to the numerical results. This way we obtain Eq. (15) in the main text.

Linear dispersion

An alternative to the electronic Hamiltonian with the p^N -dispersion used in the main paper is a Dirac Hamiltonian

$$H_{\text{el},p} = v_F \begin{pmatrix} 0 & p_x - ip_y \\ p_x + ip_y & 0 \end{pmatrix}, \quad (\text{S42})$$

where v_F is the Fermi velocity. The pseudospin-structure of the Hamiltonian is unchanged from Eq. (2) in the main text and it can also be considered as the $N = 1$ case of the p^N -dispersion. Unlike for the p^N -dispersion with $N > 2$ for which we can approximate the cutoff as infinite, the results for the linear dispersion are highly dependent on the cutoff. We assume a momentum cutoff p_c and approximate the Brillouin zone as being circular. The momentum cutoff corresponds to energy cutoff $\varepsilon_c = v_F p_c$.

This Hamiltonian is realized approximately in twisted bilayer graphene (TBG) when the twist angle between the two graphene layers is larger than the magic twist angle of $\theta_{\text{magic}} \approx 1.1^\circ$. TBG is only periodic in a large scale moiré superlattice, corresponding to a superlattice Brillouin zone which is small compared to graphene Brillouin zone. The lowest energy bands are described by the Hamiltonian (S42) with v_F becoming smaller and smaller as the twist angle approaches the magic angle. The rest of the Brillouin zone of the original graphene is folded into higher energy bands which we neglect. The low-energy Hamiltonian for TBG can be derived with perturbation theory when the twist angle $\theta > 1.8^\circ$ [6]. In the perturbative model, the layers are decoupled from each other. The simple perturbation expansion fails near the magic angle, but the layers remain decoupled up to the magic angle [7].

We describe TBG in terms of bare graphene, so in applying Eq. (9) of the main paper we take Ω_{FB} as the size of the superlattice Brillouin zone and Ω_{BZ} as the original Brillouin zone of graphene. In the momentum integrals the cutoff p_c is the radius of the superlattice Brillouin zone p_{FB} . The interaction constants become $\lambda = g^2/n\omega_E^2$ and $u = U/n$, where n is the ratio between the areas of the original graphene and the superlattice Brillouin zones, or equivalently the ratio between the number of lattice sites in the superlattice and the original graphene unit cells.

After doing the momentum integrals, the self-consistency equations for superconductivity become

$$\phi_n = T \sum_{m=-\infty}^{\infty} (\lambda_{nm} - u) \frac{\phi_m}{\varepsilon_c^2} \log \left[1 + \frac{\varepsilon_c^2}{\tilde{\omega}_m^2 + \phi_m^2} \right], \quad (\text{S43})$$

$$Z_n = 1 + T \sum_{m=-\infty}^{\infty} \lambda_{nm} \frac{\omega_m}{\omega_n} \frac{Z_m}{\varepsilon_c^2} \log \left[1 + \frac{\varepsilon_c^2}{\tilde{\omega}_m^2 + \phi_m^2} \right], \quad (\text{S44})$$

Again, antiferromagnetism has a similar set of equations. If we assume that $\varepsilon_c \ll \phi_0$ and $\varepsilon_c \ll \omega_E$ so that the argument of the logarithm is small for both small and large ω_m/ω_E , the logarithm can be approximated with the first order term,

$$\frac{1}{\varepsilon_c^2} \log \left[1 + \frac{\varepsilon_c^2}{\tilde{\omega}_m^2 + \phi_m^2} \right] \approx \frac{1}{\tilde{\omega}_m^2 + \phi_m^2}. \quad (\text{S45})$$

In this limit, the dependence on the cutoff energy vanishes and we recover the self-consistency equations for a completely flat band.

Unlike for the p^N dispersion, superconductivity only appears for the linear dispersion if λ is stronger than some critical value $\lambda_{C,0}$ even if $u = 0$ [8]. This is due to vanishing density of states near zero energy. This value can be found by linearizing the self-consistency equation (S43) both in ϕ and T_C^{sc} . For an interaction without retardation, we find that $\lambda_{C,0} = \varepsilon_c/\omega_E$. With $\varepsilon_c \ll \omega_E$, the phase diagram of Fig. 5 in the main paper for the linear case is the same as for $N = \infty$, except near the phase boundary, where the normal state is the ground state.

Effect of Debye dispersion

In a real material, the phonon dispersion is obviously not described by the Einstein model adopted in the text. To get an idea how much the exact phonon dispersion affects the results, we consider also the Debye model.

For the Einstein model phonons there is no momentum dependence in the interactions, and for this reason the self-energy is also independent of momentum. For Debye phonons the interaction obtains a momentum dependence through the phonon dispersion. Without calculating the full momentum dependent theory, we can estimate the effect of the dispersion by estimating the typical energy of the exchanged phonon and the average interaction constant.

The maximum phonon energy exchanged within the flat band is limited by the flat band diameter $2p_{\text{FB}}$ to be $\omega_0 = p_{\text{FB}}\omega_D/q_M$, where ω_D is the Debye energy and q_M is the maximum phonon momentum. As typically q_M is of the order of the size of the Brillouin zone, $\omega_0 \ll \omega_D$ and the energy scale is reduced. On the other hand, we find that the dimensionless interaction constant is enhanced: $\lambda \propto 1/\omega_0^2$. However, because $\Delta_0 \propto \lambda^{0.2}\omega_0$, the magnitude of Δ_0 is restricted by ω_0 and the total effect is a smaller critical temperature than with the Einstein phonons with energy ω_E equal to the Debye energy.

The above concerns interactions within one flat band. We can also consider Debye phonons in the context of two flat bands separated by the distance $pd \gg p_{\text{FB}}$ in momentum space. The momentum range of Debye phonons connecting the two parts of the Brillouin zone is limited to pd , and they can be treated as if they had a constant energy $\omega_0 = \omega_D pd/q_M$. In this case they act essentially as Einstein phonons with an effective energy scale ω_0 .

EQUATIONS FOR COMPETING MAGNETIC AND SUPERCONDUCTING PHASES

We now concentrate on the possible coexistence of antiferromagnetism and superconductivity for $N \rightarrow \infty$. The presence of AFM ($\rho_3\sigma_3\tau_3$) and the singlet superconducting order parameter ($\sigma_2\tau_2$) induces a triplet component proportional to

$$\rho_3\sigma_3\tau_3 \times \sigma_2\tau_2 \propto \rho_3\sigma_1\tau_1. \quad (\text{S46})$$

The triplet is induced into the propagator, but it also enters in the self-energy if the interactions support it. This requires that the interactions have an odd-frequency part, which is true with the retarded interaction, but not present with the instantaneous interaction.

The inverse propagator is

$$\check{G}^{-1}(i\omega_n) = i\tilde{\omega}_n\mathbb{1} - h\rho_3\sigma_3\tau_3 - \phi\sigma_2\tau_2 - id\rho_3\sigma_1\tau_1. \quad (\text{S47})$$

To invert this, we notice that the matrix separates into four 2×2 blocks. Labeling these blocks by the spin and pseudo-spin of their particle part (the hole part is associated with the opposite spin and same pseudo-spin), we can write them as

$$G_{\rho\sigma}^{-1}(i\omega_n) = \begin{pmatrix} i\tilde{\omega}_n - \rho\sigma h_n & -\sigma\phi_n + i\rho d_n \\ -\sigma\phi_n + i\rho d_n & i\tilde{\omega}_n - \rho\sigma h_n \end{pmatrix}. \quad (\text{S48})$$

The inverse of this is

$$\begin{aligned} G_{\rho\sigma}(i\omega_n) &= -\frac{(\tilde{\omega}_n^2 - h_n^2 + \phi_n^2 - d_n^2) - 2i\rho\sigma(h_n\tilde{\omega}_n + \phi_n d_n)}{(\tilde{\omega}_n^2 - h_n^2 + \phi_n^2 - d_n^2)^2 + 4(h_n\tilde{\omega}_n + \phi_n d_n)^2} \begin{pmatrix} i\tilde{\omega}_n - \rho\sigma h_n & \sigma\phi_n - i\rho d_n \\ \sigma\phi_n - i\rho d_n & i\tilde{\omega}_n - \rho\sigma h_n \end{pmatrix} \\ &\equiv -\frac{\gamma_n - i\rho\sigma\delta_n}{\zeta_n} \begin{pmatrix} i\tilde{\omega}_n - \rho\sigma h_n & \sigma\phi_n - i\rho d_n \\ \sigma\phi_n - i\rho d_n & i\tilde{\omega}_n - \rho\sigma h_n \end{pmatrix} \\ &= -\frac{i}{\zeta_n} \begin{pmatrix} \gamma_n\tilde{\omega}_n + \delta_n h_n & -\rho_n(\gamma_n d_n + \delta_n \phi_n) \\ -\rho_n(\gamma_n d_n + \delta_n \phi_n) & \gamma_n\omega_n + \delta_n h_n \end{pmatrix} + \frac{1}{\zeta_n} \begin{pmatrix} \rho\sigma(\gamma_n h_n - \delta_n \tilde{\omega}_n) & -\sigma(\gamma_n \phi_n - \delta_n d_n) \\ -\sigma(\gamma_n \phi_n - \delta_n d_n) & \rho\sigma(\gamma_n h_n - \delta_n \tilde{\omega}_n) \end{pmatrix}, \end{aligned} \quad (\text{S49})$$

where, in the last line, we have separated the odd and even frequency parts. Above, we define

$$\gamma_n = \tilde{\omega}_n^2 - h_n^2 + \phi_n^2 - d_n^2, \quad (\text{S50})$$

$$\delta_n = 2(h_n\tilde{\omega}_n + \phi_n d_n), \quad (\text{S51})$$

$$\zeta_n = \gamma_n^2 + \delta_n^2. \quad (\text{S52})$$

From these, $\tilde{\omega}$, d and δ are odd in ω_n , and the other terms are even in ω_n . The diagonal self-energies depend on the propagator for the inverted spin, and for them we add a sign change to h and ϕ .

The self-consistency equations are

$$d_n = T \sum_{|\omega_m| < \omega_{\max}} \lambda_{nm}^- \frac{\gamma_m d_m + \delta_m \phi_m}{\zeta_m}, \quad (\text{S53})$$

$$\Sigma_n^\omega = -T \sum_{|\omega_m| < \omega_{\max}} \lambda_{nm}^- \frac{\gamma_m \tilde{\omega}_m + \delta_m h_m}{\zeta_m}, \quad (\text{S54})$$

$$\phi_n = T \sum_{|\omega_m| < \omega_{\max}} [\lambda_{nm}^+ - u_c^+] \frac{\gamma_m \phi_m - \delta_m d_m}{\zeta_m}, \quad (\text{S55})$$

$$h_n = T \sum_{|\omega_m| < \omega_{\max}} [\lambda_{nm}^+ - u_c^-] \frac{\gamma_m h_m - \delta_m \tilde{\omega}_m}{\zeta_m}, \quad (\text{S56})$$

where we assume the Matsubara sum to have a cutoff which determines the values of the pseudopotential terms. The equation for Σ^ω can also be expressed in terms of Z as

$$Z_n = 1 + T \sum_{|\omega_m| < \omega_{\max}} \lambda_{nm}^- \frac{\gamma_m \tilde{\omega}_m + \delta_m h_m}{\zeta_m}. \quad (\text{S57})$$

The odd and even electron-phonon interaction kernels are

$$\lambda_{nm}^\pm = \frac{1}{2} [\lambda(\omega_n - \omega_m) \pm \lambda(\omega_n + \omega_m)] \omega_E. \quad (\text{S58})$$

The Coulomb interaction only has an even part, so it only affects the even-frequency self-energy terms, namely ϕ and h . The coexistence modifies the pseudopotentials u^\pm slightly as the high-frequency part of both order parameters has to be taken into account. It is still defined as $u^\pm = u/(1 \pm u_c \alpha_\pm)$, but now with

$$\alpha_\pm = \frac{\sinh\left(\frac{\phi_c + h_c \pm (\phi_c - h_c)}{2T}\right)}{(\phi_c + h_c \pm (\phi_c - h_c)) \left[\cosh\left(\frac{\phi_c}{T}\right) + \cosh\left(\frac{h_c}{T}\right) \right]} - T \sum_{|\omega_m| < \omega_{\max}} \frac{\omega_m^2 \mp h_c^2 \pm \phi_c^2}{(\omega_n^2 - h_c^2 + \phi_c^2)^2 + 4h_c^2 \omega_n^2}. \quad (\text{S59})$$

We solve these equations numerically to study the competition of the two phases.

A TOY MODEL FOR THE COMPETITION BETWEEN THE PHASES

To understand the phenomenology of the two co-existing order parameters, let us consider a toy model where there are two order parameters Δ and h , and two separate interaction channels, λ and u . We assume that the interactions are separate in the sense that λ only mediates superconductivity and u mediates the magnetization. For simplicity, we assume that the interactions are frequency independent so there is no triplet component and no electron-phonon renormalization term.

This model is not realized in the weak coupling as in that case the interaction channels are not separate, but have always opposing signs. The superconducting channel is mediated by the interaction with strength $\lambda\omega_E - u$ and the magnetic channel has the strength $u - \lambda\omega_E$. The channels are separate only in strong coupling, as the low interaction frequencies are attractive to superconductivity and the high frequencies for magnetism.

In the full coexistence model the dispersions for two non-equivalent bands are $E_p = \Delta \pm \sqrt{\varepsilon_p^2 + h^2}$. For $N \rightarrow \infty$ this reduces to $E_{p\sigma} = \Delta \pm h$. We take this dispersion as the starting point. For notational simplicity, we assume that $\Delta > 0$ and $h > 0$. The fields Δ and h are also included in the partition function,

$$\begin{aligned} \frac{Z}{Z_0} &= Z_0^{-1} \prod_{p \in \text{FB}, \omega_n} [\omega_n^2 + (\Delta + h)^2] \times [\omega_n^2 + (\Delta - h)^2] \times e^{-\beta\Delta^2/\lambda} \times e^{-\beta h^2/u} \\ &= \prod_{p \in \text{FB}} \cosh\left(\frac{\beta(\Delta + h)}{2}\right) \cosh\left(\frac{\beta(\Delta - h)}{2}\right) \times e^{-\beta\Delta^2/\lambda} \times e^{-\beta h^2/u}. \end{aligned} \quad (\text{S60})$$

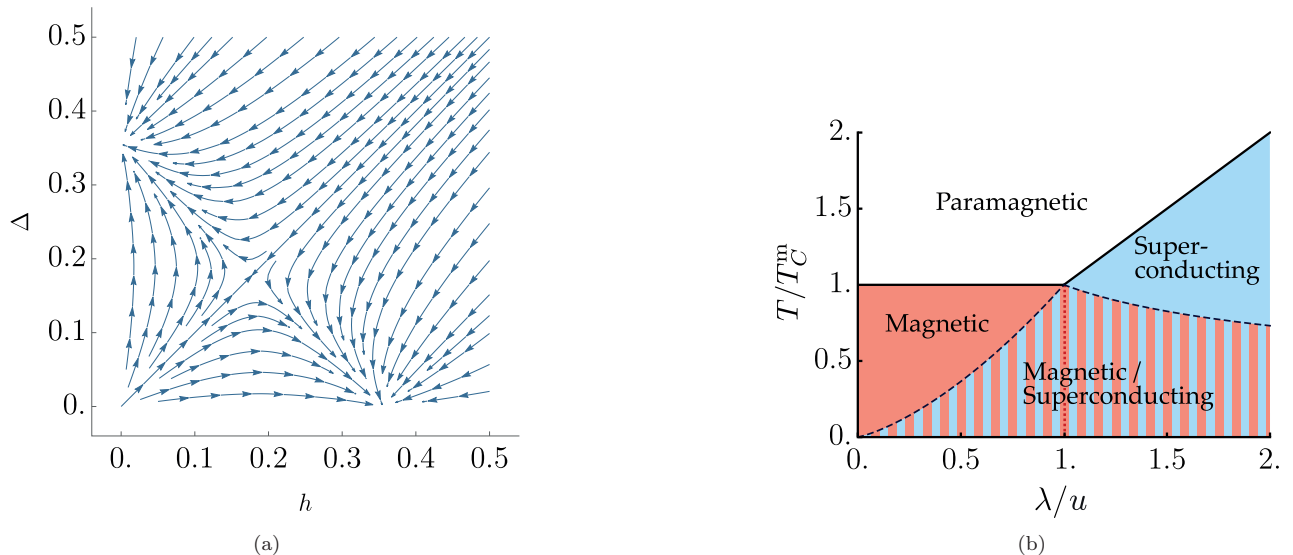


FIG. 1: (a) Stream plot of the gradient of the free energy (S61) for $\lambda = u$ at temperature $T < T_C^{\text{sc}}, T_C^{\text{m}}$. There are two local minima, which correspond to the magnetic and superconducting phases, and a saddle point which is the unstable coexistence solution. (b) Phase diagram with fixed u . When $\lambda < u$ and $T < T_C^{\text{m}}$, the thermodynamically stable state is the magnetic state and when $\lambda > u$ and $T < T_C^{\text{sc}}$ the stable state is the superconducting state. The dividing line $\lambda = u$ is marked with the red dotted line. On the striped region, both phases are possible as metastable states.

Above, the product over the Matsubara frequencies is evaluated using a standard Matsubara trick. The overall constant cancels against the normal state partition function Z_0 . The free energy relative to the normal state is

$$\begin{aligned}
 F(\Delta, h) &= -T \log \left(\frac{Z}{Z_0} \right) = C \left(\frac{\Delta^2}{\lambda} + \frac{h^2}{u} - T \log \left[\cosh \left(\frac{\Delta + h}{2T} \right) \cosh \left(\frac{\Delta - h}{2T} \right) \right] \right) \\
 &= C \left(\frac{\Delta^2}{\lambda} + \frac{h^2}{u} - T \log \left[\frac{1}{2} \cosh \left(\frac{\Delta}{T} \right) + \frac{1}{2} \cosh \left(\frac{h}{T} \right) \right] \right),
 \end{aligned} \tag{S61}$$

where the momentum sum gives the multiplicative factor $C > 0$.

The self-consistency equations are given as derivatives of the free energy with respect to fields Δ and h :

$$\Delta = \frac{\lambda}{2} \frac{\sinh(\Delta/T)}{\cosh(\Delta/T) + \cosh(h/T)}, \tag{S62}$$

$$h = \frac{u}{2} \frac{\sinh(h/T)}{\cosh(h/T) + \cosh(\Delta/T)}. \tag{S63}$$

As a check, we see that if there was no frequency dependence in the interactions, Eqs. (S55) and (S56) would give similar equations after the Matsubara summation. The difference is that in the full model with instantaneous interactions, there is effectively only one interaction constant $\lambda_{\text{eff}} = \lambda \omega_E - u$.

The self-consistency equations (S62) and (S63) for Δ and h should be solved simultaneously. At low temperatures, $T \ll h, \Delta$, we can approximate the hyperbolic functions with exponentials, and obtain

$$\Delta(T=0) = \lim_{T \rightarrow 0} \frac{\lambda}{2[1 + \exp(\frac{h-\Delta}{T})]} = \begin{cases} \Delta_0 & \text{for } h < \Delta \\ \Delta_0/2 & \text{for } h = \Delta \\ 0 & \text{for } h > \Delta, \end{cases} \tag{S64}$$

where $\Delta_0 = \lambda/2$ is the zero-temperature order parameter for $h = 0$. For h in terms of Δ , an analogous expression can be found,

$$h(T=0) = \lim_{T \rightarrow 0} \frac{u}{2[1 + \exp(\frac{\Delta-h}{T})]} = \begin{cases} h_0 & \text{for } \Delta < h \\ h_0/2 & \text{for } \Delta = h \\ 0 & \text{for } \Delta > h, \end{cases} \tag{S65}$$

with $h_0 = u/2$. At zero temperature, coexistence is only possible if $u = \lambda$ and $\Delta = h = \lambda/4$. This coexistence point is a saddle point of free energy. This is illustrated in Fig. 1a. Similar kind of solutions are also found at a finite temperature.

Assuming a second order phase transition from the normal state to a superconducting state, we can linearize (S62) with $h = 0$ to find a critical temperature $T_C^{\text{sc}} = \lambda/4$. We will see below that when $u > \lambda$ the phase transition is actually of the first order from a magnetic state to the superconducting state, but we still use the above definition for T_C^{sc} to set a temperature scale. Similarly, assuming a second order phase transition from normal state to a magnetic state, we linearize (S63) to find a critical temperature $T_C^{\text{m}} = u/4$, which we take as the definition of T_C^{m} .

Stability of the phase with lower T_C

From the free energy we see that when $\lambda < u$, the magnetic phase is stable and the superconducting phase is either metastable or unstable. When $\lambda > u$, the roles are reversed. The solution is (meta)stable if it is a local minimum of the free energy. The criterion is

$$\frac{\partial^2 F}{\partial h^2} \frac{\partial^2 F}{\partial \Delta^2} - \left(\frac{\partial^2 F}{\partial \Delta \partial h} \right)^2 > 0 \quad \text{and} \quad \frac{\partial^2 F}{\partial h^2} > 0. \quad (\text{S66})$$

When $h = 0$ or $\Delta = 0$ the cross derivatives vanish, and the stability condition becomes $\partial^2 F / \partial h^2 > 0$ and $\partial^2 F / \partial \Delta^2 > 0$.

Let us consider the (meta)stability of the superconducting phase when $0 < \lambda < u$ and $T < T_C^{\text{sc}}$, where $T_C^{\text{sc}} = \lambda/4$. The stability condition becomes

$$0 < \left. \frac{\partial^2 F}{\partial h^2} \right|_{h=0} = C \left(\frac{2}{u} - \frac{1}{T + T \cosh\left(\frac{\Delta}{T}\right)} \right). \quad (\text{S67})$$

At low temperatures, the first term in the parentheses dominates and the superconducting phase is metastable. Near T_C^{sc} the second term dominates and the superconducting phase becomes unstable against a spontaneous magnetization. In this case, $\Delta \approx 0$, and

$$\frac{2}{u} - \frac{1}{T + T \cosh\left(\frac{\Delta}{T}\right)} \approx \frac{2}{u} - \frac{1}{2T_C^{\text{sc}}} = 2 \left(\frac{1}{u} - \frac{1}{\lambda} \right) < 0. \quad (\text{S68})$$

The transition temperature T^* at which the system becomes unstable can be determined from the condition $\partial^2 F / \partial h^2 = 0$, which is equivalent to solving the magnetic critical temperature by linearizing Eq. (S62) with Δ as solved from Eq. (S63) with $h = 0$.

For $\lambda > u > 0$, the magnetic phase is the metastable one, and the equations apply after interchanging $u \leftrightarrow \lambda$, $h \leftrightarrow \Delta$ and $T_C^{\text{sc}} \leftrightarrow T_C^{\text{m}}$. The numerical solution for the transition temperature of both phases is shown in Fig. 1b as the dashed line.

Similar stability analysis can be used with the full model, except in that case the frequency dependence of the self-energy functions complicates the situation. We can however simplify the problem by projecting the order parameters on the linearized solution.

COMPETITION IN THE FULL FREQUENCY-DEPENDENT MODEL

Now we return to the full frequency-dependent Eqs. (S53)–(S56). We do for the full model the same kind of analysis as in the previous section for the toy model. As explained after (S68), the stability is determined by solving the critical temperature of the phase with higher T_C in the presence of the other order parameter.

Stability of the superconducting phase

We now consider parameters λ, u to be such that $0 < T_C^{\text{sc}} < T_C^{\text{m}}$ and determine the temperature T^* above which the superconducting phase is unstable against a magnetic instability.

To do this, we linearize Eqs. (S53)–(S56) with respect to h and d . We assume the singlet order parameter ϕ to be finite. The equations for Σ^ω and ϕ are

$$\Sigma_n^\omega = -T \sum_{|\omega_m| < \omega_{\max}} \lambda_{nm}^- \frac{\tilde{\omega}_m}{\tilde{\omega}_m^2 + \phi_m^2}, \quad (\text{S69})$$

$$\phi_n = T \sum_{|\omega_m| < \omega_{\max}} (\lambda_{nm}^+ - u^+) \frac{\phi_m}{\tilde{\omega}_m^2 + \phi_m^2}. \quad (\text{S70})$$

The equations for h and d are coupled to one 2×2 matrix,

$$\begin{bmatrix} d_n \\ h_n \end{bmatrix} = T \sum_{|\omega_m| < \omega_{\max}} \frac{1}{(\tilde{\omega}_m^2 + \phi_m^2)^2} \begin{bmatrix} \lambda_{nm}^- (\tilde{\omega}_m^2 + 3\phi_m^2) & 2\lambda_{nm}^- \phi_m \tilde{\omega}_m \\ 2(u^- - \lambda_{nm}^+) \phi_m \tilde{\omega}_m & (u^- - \lambda_{nm}^+) (\tilde{\omega}_m^2 - \phi_m^2) \end{bmatrix} \begin{bmatrix} d_m \\ h_m \end{bmatrix}. \quad (\text{S71})$$

With the high-frequency cutoff, the equation can be written as a $2M \times 2M$ matrix, where M is the number of Matsubara frequencies below the cutoff. The critical temperature T^* of this AFM/triplet phase is then determined numerically by finding the temperature at which the largest eigenvalue of the matrix becomes larger than unity [3].

Stability of the magnetic phase

Conversely, let us now consider parameters λ, u such that $0 < T_C^m < T_C^{\text{sc}}$ and determine the temperature T^* above which the magnetic phase is unstable against a superconducting instability. Now we linearize Eqs. (S53)–(S56) with respect to ϕ and d . We assume the field h to be finite. The equations for Σ^ω and h are

$$\Sigma_n^\omega = -T \sum_{|\omega_m| < \omega_{\max}} \lambda_{nm}^- \frac{\tilde{\omega}_m}{\tilde{\omega}_m^2 + h_m^2}, \quad (\text{S72})$$

$$h_n = T \sum_{|\omega_m| < \omega_{\max}} [u^- - \lambda_{nm}^+] \frac{h_m}{\tilde{\omega}_m^2 + h_m^2}. \quad (\text{S73})$$

The equations for ϕ and d are coupled, and can be written as a matrix equation

$$\begin{bmatrix} d_n \\ \phi_n \end{bmatrix} = T \sum_{|\omega_m| < \omega_{\max}} \frac{1}{(\tilde{\omega}_m^2 + h_m^2)^2} \begin{bmatrix} \lambda_{nm}^- (\tilde{\omega}_m^2 - h_m^2) & -2\lambda_{nm}^- h_m \tilde{\omega}_m \\ 2(\lambda_{nm}^+ - u^+) h_m \tilde{\omega}_m & (\lambda_{nm}^+ - u^+) (\tilde{\omega}_m^2 - h_m^2) \end{bmatrix} \begin{bmatrix} d_m \\ \phi_m \end{bmatrix} \quad (\text{S74})$$

Again, with the Matsubara cutoff, this is a matrix equation and the critical temperature T^* can be solved by searching for the temperature at which the largest eigenvalue crosses 1. The solution curve for both cases, $T_C^m < T_C^{\text{sc}}$ and $T_C^m > T_C^{\text{sc}}$, is shown as a dashed boundary line in the phase diagram, Fig. 1 in the main text.

-
- [1] Carbotte, J. Properties of boson-exchange superconductors. *Rev. Mod. Phys.* **62**, 1027 (1990).
 - [2] Berezinskii, V. New model of the anisotropic phase of superfluid He-3. *JETP Lett.* **20**, 287–289 (1974).
 - [3] Matsumoto, M., Koga, M. & Kusunose, H. Coexistence of even- and odd-frequency superconductivities under broken time-reversal symmetry. *J. Phys. Soc. Jpn.* **81**, 033702 (2012).
 - [4] Morel, P. & Anderson, P. Calculation of the superconducting state parameters with retarded electron-phonon interaction. *Phys. Rev.* **125**, 1263–1271 (1962).
 - [5] Kaupilla, V. J., Hyart, T. & Heikkilä, T. T. Collective amplitude mode fluctuations in a flat band superconductor formed at a semimetal surface. *Phys. Rev. B* **93**, 024505 (2016).
 - [6] Lopes dos Santos, J. M. B., Peres, N. M. R. & Castro Neto, A. H. Continuum model of the twisted graphene bilayer. *Phys. Rev. B* **86**, 155449 (2012).
 - [7] Suárez Morell, E., Correa, J. D., Vargas, P., Pacheco, M. & Barticevic, Z. Flat bands in slightly twisted bilayer graphene: Tight-binding calculations. *Phys. Rev. B* **82**, 121407 (2010).
 - [8] Kopnin, N. & Sonin, E. BCS superconductivity of Dirac electrons in graphene layers. *Phys. Rev. Lett.* **100**, 246808 (2008).

II

TWO TOPOLOGICALLY DISTINCT DIRAC-LINE SEMIMETAL PHASES AND TOPOLOGICAL PHASE TRANSITIONS IN RHOMBOHEDRALLY STACKED HONEYCOMB LATTICES

by

T. Hyart, R. Ojajärvi and T.T. Heikkilä 2018

Journal of Low Temperature Physics **191**, 35-48, DOI:[10.1007/s10909-017-1846-3](https://doi.org/10.1007/s10909-017-1846-3)

Reproduced with permission. Copyright 2018 Springer Nature.

Two Topologically Distinct Dirac-Line Semimetal Phases and Topological Phase Transitions in Rhombohedrally Stacked Honeycomb Lattices

T. Hyart¹  · R. Ojajarvi¹ · T. T. Heikkilä¹

Received: 15 September 2017 / Accepted: 23 December 2017 / Published online: 4 January 2018
© Springer Science+Business Media, LLC, part of Springer Nature 2018

Abstract Three-dimensional topological semimetals can support band crossings along one-dimensional curves in the momentum space (nodal lines or Dirac lines) protected by structural symmetries and topology. We consider rhombohedrally (ABC) stacked honeycomb lattices supporting Dirac lines protected by time-reversal, inversion and spin rotation symmetries. For typical band structure parameters there exists a pair of nodal lines in the momentum space extending through the whole Brillouin zone in the stacking direction. We show that these Dirac lines are topologically distinct from the usual Dirac lines which form closed loops inside the Brillouin zone. In particular, an energy gap can be opened only by first merging the Dirac lines going through the Brillouin zone in a pairwise manner so that they turn into closed loops inside the Brillouin zone, and then by shrinking these loops into points. We show that this kind of topological phase transition can occur in rhombohedrally stacked honeycomb lattices by tuning the ratio of the tunneling amplitudes in the directions perpendicular and parallel to the layers. We also discuss the properties of the surface states in the different phases of the model.

Keywords Graphite · Topological matter · Flat bands

1 Introduction

Topological materials are characterized by momentum-space topological defects, topological invariants and protected surface states [1–5]. The fully gapped topological

✉ T. Hyart
thyart@gmail.com

¹ Department of Physics and Nanoscience Center, University of Jyväskylä, P.O. Box 35 (YFL), 40014 Jyväskylä, Finland

phases have been classified in terms of the existence of various symmetries [4,5], and the variety of the different types of momentum-space topological defects is even richer in gapless systems [1,5–29]. One interesting class of three-dimensional topological semimetals is the Dirac-line (nodal line) semimetals supporting band crossings along one-dimensional curves in the momentum space. These band crossings can in principle be protected by chiral symmetry [1,5,9,13] (often an emergent or an approximate symmetry) or the structural symmetries of the systems [5,15–18,20,28,29]. From the viewpoint of topological materials the main question is what kind of topologically distinct Dirac-line semimetal phases can exist in the presence of the various structural symmetries. For example, there exists a class of nodal lines carrying a nontrivial \mathbb{Z}_2 monopole charge so that they can be created and annihilated only in pairs, whereas the nodal lines carrying a trivial \mathbb{Z}_2 monopole charge can be created and annihilated one by one [17,28,29]. In certain topological semimetals, such as Bernaly stacked graphite, there exists multiple Dirac lines which meet and merge at certain high-symmetry lines in the momentum space forming a protected triple degeneracy point of bands called nexus [19–21].

In this paper we study Dirac lines protected by time-reversal, inversion and spin rotation symmetries with the help of a general model for rhombohedrally (ABC) stacked honeycomb lattices. We show that these Dirac lines can form closed loops inside the Brillouin zone (Type A Dirac line in Fig. 1) [5,15–18] or they can extend through the whole Brillouin zone in one of the directions in the momentum space (Type B Dirac line in Fig. 1) [13] depending on the ratio of intra- and interlayer tunneling amplitudes. We show that Type A and Type B Dirac lines are topologically

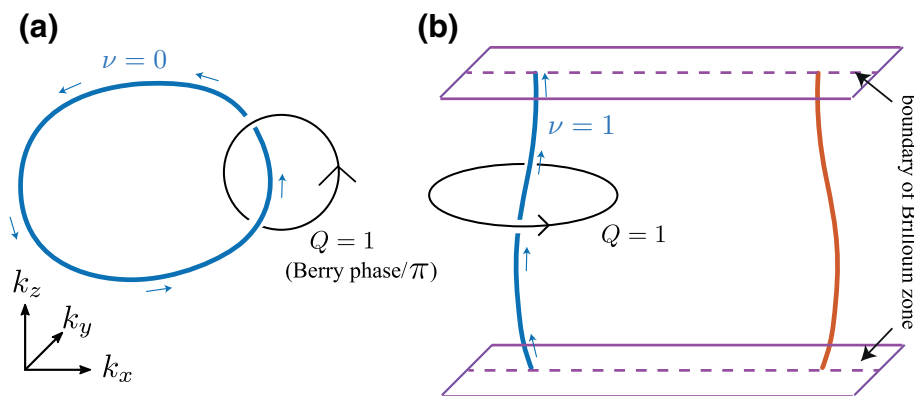


Fig. 1 Two different types of Dirac-line semimetal phases in the presence of SU(2) spin rotation, time-reversal and inversion symmetries. **a** In Type A Dirac-line semimetals the nodal lines are closed loops fully inside the Brillouin zone (blue line). Thus, they go through the full Brillouin zone $\nu = 0$ times. They carry a topological charge $Q = 1$ defined with the help of a Berry phase for a path going around the Dirac line. Type A Dirac lines can be gapped one by one. **b** In Type B Dirac-line semimetals the nodal lines extend through the whole Brillouin zone in one of the directions (blue and red curves). Thus, they go through the full Brillouin zone $\nu = 1$ times. They carry a topological charge $Q = 1$ which can be defined with the help of Berry phase, but now the radius of the closed path going around the Dirac line can be taken arbitrary large (as long as it does not go around another Dirac line). Therefore, it is possible to define a topological charge for each Type B Dirac line as an integral over a closed surface [Eq. (5)] describing their monopole-like nature: Type B Dirac lines can be gapped only by first merging them in a pairwise manner (Color figure online)

distinct. Namely, it is possible to define a topological invariant ν by counting how many times the Dirac line goes through the whole Brillouin zone, and $\nu = 0$ ($\nu = 1$) for Type A (Type B) Dirac lines (see Fig. 1). Since the Brillouin zone is a torus, ν essentially describes the winding of the Dirac line around this torus. We show that this topological difference has important consequences. Namely, it allows defining a topological charge for Type B Dirac lines describing their monopole-like nature (different from the monopole charge proposed in [17]): Type B Dirac lines are robust nodal lines which must always come in pairs. Therefore, Type A Dirac lines can be created and annihilated individually by shrinking them to a point, but Type B Dirac lines can be gapped only by first merging them in a pairwise manner so that they become Type A Dirac lines. We discuss the nature of this kind of topological phase transition in rhombohedrally stacked honeycomb lattices and depict the momentum-space structure of the surface states for the different phases of the model. We point out that the monopole-like nature and robustness of the Type B Dirac lines have been discussed also in Refs. [28,29] from different perspectives.

2 Model, Symmetries and Topological Invariants

The rhombohedral stacking of honeycomb lattices is illustrated in Fig. 2. The tight-binding model for such kind of three-dimensional system [in the sublattice space] can be written as

$$\begin{aligned}
 H(\mathbf{k}) &= \begin{pmatrix} \Theta(\mathbf{k}) & \Phi(\mathbf{k}) \\ \Phi^*(\mathbf{k}) & \Theta(\mathbf{k}) \end{pmatrix}, \\
 \Phi(\mathbf{k}) &= -\gamma_0 \sum_i e^{i\delta_i \cdot \mathbf{k}} - \gamma_1 e^{ik_z} - \gamma_3 e^{-ik_z} \sum_i e^{-i\delta_i \cdot \mathbf{k}} \\
 \Theta(\mathbf{k}) &= -\gamma_2 \sum_i e^{i\mathbf{n}_i \cdot \mathbf{k}} - \gamma_4 \left[e^{ik_z} \sum_i e^{-i\delta_i \cdot \mathbf{k}} + e^{-ik_z} \sum_i e^{i\delta_i \cdot \mathbf{k}} \right] \tag{1}
 \end{aligned}$$

The hopping parameters γ_i are illustrated in Fig. 2. The nearest-neighbor vectors δ_i inside the layers (connecting different types of sublattice atoms) are normalized so that the vectors \mathbf{n}_i connecting neighboring unit cells inside the layers (i.e., connecting the same type of sublattice atoms) have unit length. In z -direction we use the spacing between the layers as the unit length.

The important symmetries of the model are the lattice translation symmetries (guaranteeing that \mathbf{k} is a good quantum number), SU(2) spin rotation symmetry [so that we do not need to include spin degree of freedom into Hamiltonian (1)], time-reversal symmetry

$$H^*(-\mathbf{k}) = H(\mathbf{k}) \tag{2}$$

and inversion symmetry

$$\sigma_x H(-\mathbf{k}) \sigma_x = H(\mathbf{k}). \tag{3}$$

In many materials, such as graphite, spin-orbit coupling is negligible, and therefore the assumption about SU(2) spin rotation symmetry is well justified. The other

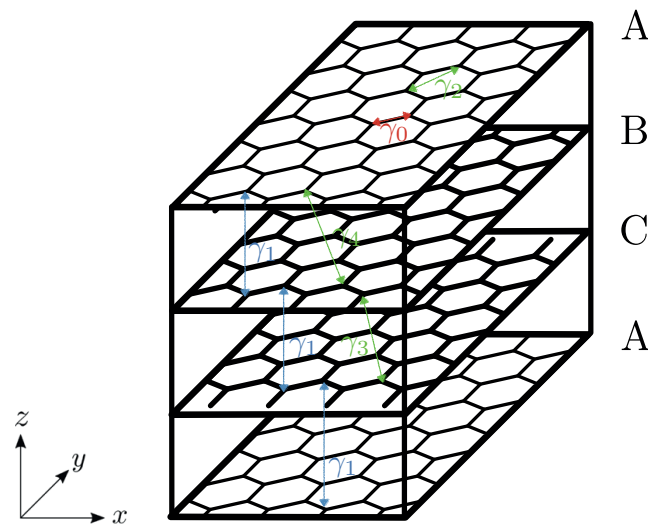


Fig. 2 Illustration of rhombohedrally stacked honeycomb lattices. The hopping amplitude γ_0 describes the nearest-neighbor hopping inside the layers. In rhombohedral stacking the layers are stacked in such a way that the nearest-neighbor interlayer hopping amplitudes γ_1 always connect one type of sublattice atom in the lower layer to the other type of sublattice atom in the upper layer. The further-neighbor hoppings γ_2 , γ_3 and γ_4 are also shown. The period in the stacking direction is three times the distance between the layers, and therefore, rhombohedral stacking is often called ABC stacking (Color figure online)

symmetries are just structural symmetries of the system, and therefore, they are satisfied independently on which hopping processes are included in the Hamiltonian. They could be broken only via a spontaneous symmetry breaking occurring due to interactions between the fermions.

It is useful to point out that if the further-neighbor hoppings are neglected $\gamma_2 = \gamma_4 = 0$, the system supports also a chiral symmetry

$$\sigma_z H(\mathbf{k}) \sigma_z = -H(\mathbf{k}). \quad (4)$$

This symmetry is valid as a good approximation in many systems, such as graphite, and it is useful in understanding the surface state spectrum of the model (see Sect. 4). The chiral symmetry can in principle also protect the existence of the Dirac lines [13]. However, in this paper we show that this approximate chiral symmetry is not necessary for the existence of the Dirac lines. The Dirac lines in this model are in fact much more robust because they are stabilized by the structural symmetries of the system.

Due to the existence of $SU(2)$, time-reversal and inversion symmetries $\sigma_x H^*(\mathbf{k}) \sigma_x = H(\mathbf{k})$, and therefore for any closed path in the momentum space the Berry phase is quantized to be $\phi = 0$ or $\phi = \pi$.¹ Moreover, it is easy to show that $\phi = \pi$ if and only if the path goes around a Dirac line. Therefore, the Dirac lines in this symmetry class carry a \mathbb{Z}_2 topological charge, which can be defined as $Q \equiv \phi/\pi$, where ϕ can be chosen to be the Berry phase for any path that goes around the Dirac line (see

¹ Berry phase ϕ depends on the convention used for the overall phase of the wavefunctions. Therefore, it is uniquely defined only up to $n2\pi$ ($n \in \mathbb{Z}$). Here, for simplicity we fix the convention for the overall phase in such a way that $0 \leq \phi < 2\pi$. This automatically fixes also a specific convention for the Berry connection $\mathcal{A}(\mathbf{k})$.

Fig. 1). Thus, the Dirac lines are stable against small perturbations. If the Dirac line forms a closed loop within the Brillouin zone (Type A Dirac line), it can be smoothly annihilated only by first shrinking it to a point so that we can no longer define a path going around it. However, there are no restrictions concerning the number of Type A Dirac lines because they can be gapped one by one in this way.

Interestingly, there exists also a topologically different type of Dirac lines in this symmetry class. Intuitively, this is easy to understand because we can visualize the Brillouin zone as a three-dimensional torus and we can define three different topological invariants for each Dirac line by counting how many times the Dirac line winds around the torus in different directions. Here, we concentrate on this kind of topological invariant ν corresponding to the stacking direction k_z . For the Type A Dirac lines, which are closed loops fully inside the Brillouin zone, $\nu = 0$. The other topologically different Dirac lines extend through the full Brillouin zone in k_z direction, so that $\nu \neq 0$ (see Fig. 1). It turns out that these Dirac lines have different properties than the ones with $\nu = 0$. In order to understand these differences we consider the Dirac lines with $\nu = 1$ shown in Fig. 1b. Similarly as above the Berry phase $\phi = \pi$ for any closed path going around the Dirac line. For each value of k_z we can now choose a path in the (k_x, k_y) -plane with arbitrary large radius (as long as it does not go around another Dirac line), and we can express the corresponding Berry phase as a line integral around that path $\phi = \oint_l \mathbf{dk} \cdot \mathcal{A}(\mathbf{k})$, where $\mathcal{A}(\mathbf{k})$ is the Berry connection (see footnote 1). Since the line integral is $\phi = \pi$ independently on k_z , we can define a new topological charge

$$Q_M = \frac{1}{2\pi^2} \int_{-\pi}^{\pi} dk_z \oint_l \mathbf{dk} \cdot \mathcal{A}(\mathbf{k}), \tag{5}$$

so that for $\nu = 1$ this topological charge is quantized to $Q_M = 1$. The difference to the earlier topological charge Q is that Q_M is expressed as a surface integral over a closed surface which encloses the whole Dirac line, and this surface can be taken arbitrarily far away from the Dirac line as long as it does not enclose any parts of other Dirac lines. (The surface is closed if one considers the momentum space as a torus so that $k_z = \pm\pi$ are the same point within the torus.) Therefore, Q_M can be considered as a topological charge calculated over a closed surface, which is different from the monopole charge proposed in Ref. [17]. Furthermore, Q_M distinguishes Type A and Type B Dirac lines since for Type A Dirac lines $Q_M = 0$. Thus, the topological charge Q_M can be used in the identification and search of Type B Dirac lines. More generally, it is related to ν because $Q_M = \nu \bmod 2$.

If we now take the path in calculation of the Berry phase to go around the full Brillouin zone in the (k_x, k_y) -plane, we find that the surface integral is always necessarily zero. Therefore, it is impossible to have only a single Dirac line with $\nu = 1$ in the Brillouin zone. This means that the existence of the charge Q_M enforces the Dirac lines to come in pairs. Therefore, these Dirac lines cannot be created and annihilated individually, and the only way to open a gap in a Type B Dirac-line semimetal is to first merge the Dirac lines in a pairwise manner. (More generally, in this symmetry class

the Dirac lines with odd ν must always come in pairs.²⁾ In Sect. 3 we illustrate this type of topological phase transition taking place as a function of γ_1/γ_0 in the model for rhombohedrally stacked honeycomb lattices [Eq. (1)].

3 Phase Diagram

Typical realization of stacked honeycomb lattices is one where the layers are loosely coupled to each other (such as graphite). In that case, the band structure parameters obey the hierarchy $\gamma_0 \gg \gamma_1 \gg \gamma_2, \gamma_3, \gamma_4$ and the model for the rhombohedrally stacked honeycomb lattices supports a pair of Dirac lines in the momentum space extending through the whole Brillouin zone in the k_z direction [13]. These Dirac spirals are centered at the K and K' points in the (k_x, k_y) -plane, so that the projection of the spiral into this plane is a circle with radius proportional to γ_1/γ_0 [see Fig. 3a, b]. As discussed in the previous section these Type B Dirac lines are protected by SU(2) spin rotation, time-reversal and inversion symmetries, and they can be gapped only by merging them in a pairwise manner. We first concentrate on the evolution of these Dirac lines with increasing γ_1/γ_0 for $\gamma_2 = \gamma_3 = \gamma_4 = 0$ and discuss the effects of the further-neighbor hoppings γ_2, γ_3 and γ_4 afterward.

The evolution of the Dirac lines with increasing γ_1/γ_0 is shown in Fig. 3. For $\gamma_1 < \gamma_0$ there exist two Type B Dirac lines (red and blue) extending through the whole Brillouin zone along the k_z direction [Fig. 3a, b]. At $\gamma_1 = \gamma_0$ there occurs a topological phase transition where the Type B Dirac lines merge in a pairwise manner and turn into Type A Dirac lines [Fig. 3c]. The merging of the Type B Dirac lines occurs at the time-reversal invariant momenta $\mathbf{k}_T^{1,2,3} = (0, 2\pi/\sqrt{3}, -2\pi/3), (\pi, \pm\pi/\sqrt{3}, \pm 2\pi/3)$. In the vicinity of these merging points at the topological phase transition ($\gamma_1 = \gamma_0$) the low-energy theory can be written as

$$H(\mathbf{k}_T^1 + \mathbf{q}) = \gamma_0 \left(q_z - \frac{2}{\sqrt{3}} q_y \right) \sigma_y + \gamma_0 \left(\frac{-3q_x^2 + q_y^2 + 6q_z^2}{12} \right) \sigma_x \quad (6)$$

This means that in the (k_x, k_y) -plane the Dirac dispersions turn into a semi-Dirac dispersion at the topological phase transition. Somewhat similar topological phase transitions where the merging of two Dirac points leads to an appearance of semi-Dirac fermions have been studied previously in various two-dimensional systems [25, 30–37] and topological phase transitions associated with merging of Weyl points have also been studied in three-dimensional systems [38–40]. Generically, at the merging transitions the dispersion turns from linear to parabolic in the direction where the

² We can generalize the argument also to the case where the system has a chiral symmetry. In this case, the Hamiltonian can be always block-off-diagonalized and the Berry phase ϕ/π in Eq. (5) can be replaced with the winding number of the determinant of the off-diagonal block of the Hamiltonian. The difference is that this new winding number does not have the same ambiguity as the Berry phase related to the shifts of $n2\pi$ ($n \in \mathbb{Z}$) and therefore Q_M becomes a \mathbb{Z} topological invariant. Because in these symmetry classes $|Q_M| = \nu$ only the Dirac lines with $\nu = 0$ can be created and annihilated individually. In the special case of 2×2 Hamiltonian with time-reversal and inversion symmetries, the Hamiltonian automatically has a chiral symmetry up to terms proportional to σ_0 . Because the terms proportional to σ_0 do not influence the existence of the Dirac lines the \mathbb{Z} topological invariant can be defined also in this case.

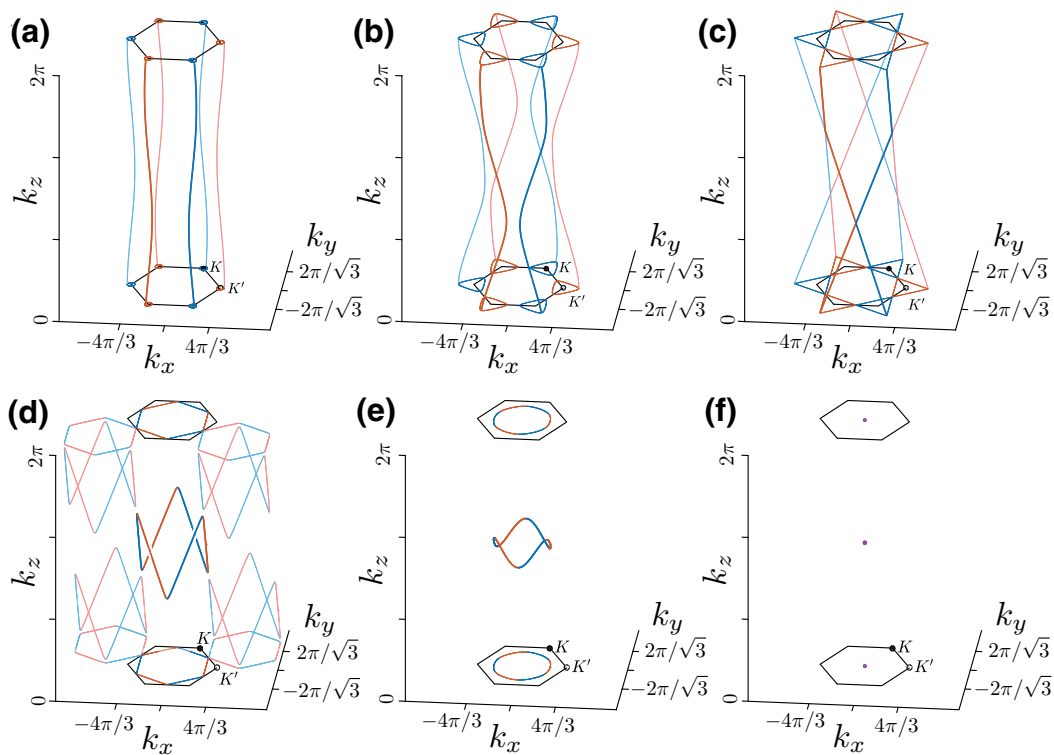


Fig. 3 Evolution of the Dirac lines in the model for rhombohedrally stacked honeycomb lattices [Eq. (1)] with increasing γ_1/γ_0 : **a** $\gamma_1/\gamma_0 = 0.3$, **b** $\gamma_1/\gamma_0 = 0.9$, **c** $\gamma_1/\gamma_0 = 1$, **d** $\gamma_1/\gamma_0 = 1.005$, **e** $\gamma_1/\gamma_0 = 1.5$, **f** $\gamma_1/\gamma_0 = 3$. **a, b** For $\gamma_1 < \gamma_0$ there exist two Type B Dirac lines (red and blue) extending through the whole Brillouin zone along the k_z direction. The light red and light blue curves show replicas of these two Dirac lines which are obtained by shifting the original Dirac lines with a reciprocal lattice vector. **c** At $\gamma_1 = \gamma_0$ there occurs a topological phase transition where the Type B Dirac lines merge in a pairwise manner and turn into Type A Dirac lines. The merging of the Type B Dirac lines occurs at the time-reversal invariant momenta $\mathbf{k}_T^{1,2,3} = (0, 2\pi/\sqrt{3}, -2\pi/3), (\pi, \pm\pi/\sqrt{3}, \pm 2\pi/3)$ (intersection points of red and blue lines). **d, e** For $\gamma_1 > \gamma_0$ the system supports a single Type A Dirac line. Replicas of this Dirac line are shown with light red and light blue curves to illustrate how this Type A Dirac line is created by merging the Type B Dirac lines. By increasing γ_1/γ_0 further, the radius of the Type A Dirac line shrinks. **f** At $\gamma_1 = 3\gamma_0$ Type A Dirac line shrinks to a point, and there occurs another topological phase transition where the system becomes fully gapped by increasing γ_1/γ_0 further. We have assumed $\gamma_3 = 0$, but this parameter only renormalizes the critical points of the topological phase transitions so that the picture stays qualitatively the same as long as $|\gamma_3| < 0.5\gamma_0$. The other further-neighbor hoppings γ_2 and γ_4 do not have any effect on the Dirac lines (Color figure online)

merging occurs. In this case the dispersions around the Dirac lines are linear in q_x before the merging ($\gamma_1 < \gamma_0$), but they turn parabolic in q_x at the transition ($\gamma_1 = \gamma_0$).

For $\gamma_0 < \gamma_1 < 3\gamma_0$ the system supports a single Type A Dirac line [Fig. 3d,e]. By increasing γ_1/γ_0 , the radius of the Type A Dirac line shrinks. At $\gamma_1 = 3\gamma_0$ the Type A Dirac line shrinks to a point at the time-reversal invariant momentum $\mathbf{k}_T^4 = (0, 0, \pi)$, and there occurs another topological phase transition where the system becomes fully gapped by increasing γ_1/γ_0 further. In the vicinity of the transition the low-energy theory can be written as

$$H(\mathbf{k}_T^4 + \mathbf{q}) = \gamma_1 q_z \sigma_y + \left(3\gamma_0 - \gamma_1 + \frac{-\gamma_0 q_x^2 - \gamma_0 q_y^2 + 2\gamma_1 q_z^2}{4} \right) \sigma_x. \quad (7)$$

This low-energy Hamiltonian describes the typical phase transition, where as a function of a parameter γ_1 the radius of Type A Dirac loop (proportional to $\sqrt{3 - \gamma_1/\gamma_0}$ for $\gamma_1 < 3\gamma_0$) shrinks to a point at the transition ($\gamma_1 = 3\gamma_0$), and then, the system becomes fully gapped by further increasing the parameter ($\gamma_1 > 3\gamma_0$). Similar transition is discussed for example in Ref. [17] for Dirac loops which do not support a monopole charge so that they can be gapped after they have been shrunk to a point.

We now discuss the effects of the further-neighbor hoppings on the transitions discussed above. The terms γ_2 and γ_4 do not have any effect on the Dirac lines or transition points except that they shift the band crossings to a finite energy. The terms proportional to γ_2 and γ_4 give rise to extra terms in low-energy Hamiltonians (6) and (7)

$$\delta H(\mathbf{q}) = (C + D_x q_x^2 + D_y q_y^2 + D_z q_z^2 + E q_y q_z) \sigma_0, \quad (8)$$

where C , D_x , D_y , D_z and E are coefficients which depend on γ_2 and γ_4 . These terms only lead to small quantitative changes in the dispersions around the band crossing points but do not affect the qualitative nature of the transitions.

The parameter γ_3 only renormalizes the critical points of the topological phase transitions, but the picture stays qualitatively the same and the transitions even occur at the same time-reversal invariant momenta $k_T^{1,2,3,4}$ as long as $|\gamma_3| < 0.5\gamma_0$. In the presence of γ_3 , the topological phase transition from Type B Dirac lines to Type A Dirac lines occurs at $\gamma_1 = \gamma_0 + \gamma_3$ and the transition from Type A Dirac line to a gapped system occurs at $\gamma_1 = 3\gamma_0 - 3\gamma_3$. Additionally, γ_3 just renormalizes the numerical coefficients in the low-energy Hamiltonians and gives rise to some unimportant cross-terms proportional to $q_y q_z$ multiplying σ_x in low-energy Hamiltonian (6). It does not lead to terms proportional to $q_x q_z$ and $q_x q_y$ because of the mirror symmetry of the structure with respect to the (y, z) -plane. In Hamiltonian (7) these cross-terms cannot arise at all because of the mirror symmetry with respect to the (y, z) -plane and rotation symmetries by $\pm 2\pi/3$ around the z -axis.

4 Surface State Spectrum

In order to compute the momentum-space structure of the surface states we follow a similar approach as in Ref. [20]. Namely, we first assume that the further-neighbor hoppings can be neglected $\gamma_2 = \gamma_3 = \gamma_4 = 0$, and discuss their effects afterward. The Hamiltonian then satisfies a chiral symmetry [Eq. (4)], which simplifies the calculation of the surface state spectrum. We start by considering the surface states at the top and bottom surfaces (Fig. 4). Because of translational invariance in the x - and y -directions k_x and k_y are good quantum numbers, and by fixing them, we get a 1D Hamiltonian $H_{k_x, k_y}(k_z)$, which depends only on k_z . Because of the chiral symmetry the 1D Hamiltonians $H_{k_x, k_y}(k_z)$ have well-defined topological invariants. To calculate this topological invariant, we first notice that the Hamiltonian can be written in a block-off-diagonal form

$$H(\mathbf{k}) = \begin{pmatrix} 0 & \Phi(\mathbf{k}) \\ \Phi^*(\mathbf{k}) & 0 \end{pmatrix}. \quad (9)$$

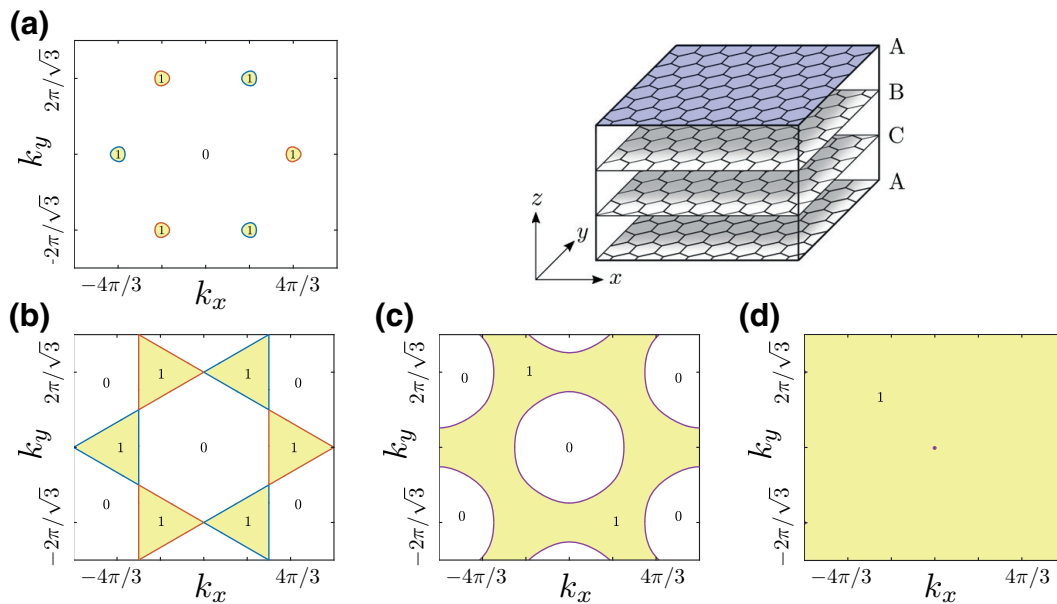


Fig. 4 $W(k_x, k_y)$ for $\gamma_2 = \gamma_3 = \gamma_4 = 0$ and various values of γ_1/γ_0 : **a** $\gamma_1/\gamma_0 = 0.3$, **b** $\gamma_1/\gamma_0 = 1$, **c** $\gamma_1/\gamma_0 = 1.5$, **d** $\gamma_1/\gamma_0 = 3$. $|W(k_x, k_y)|$ determines the number of zero-energy surface states at the top and bottom surfaces. The transitions between different values of W occur at the momenta of the projected Dirac lines so that the surface states form flat bands in regions of (k_x, k_y) bounded by the projected Dirac lines. **a** For $\gamma_1 < \gamma_0$, there exist two Type B Dirac lines and the flat bands are formed inside the regions bounded by each of them separately (regions bounded by red and blue lines). **b** At $\gamma_1 = \gamma_0$ there occurs a topological phase transition where Type B Dirac lines merge in a pairwise manner and turn into Type A Dirac lines. This merging transition shows up as a unification of the regions of the flat bands [Fig. 4b]. **c** For $\gamma_1 > \gamma_0$ the system supports a single Type A Dirac line. The flat band is now formed everywhere outside the region bounded by its projection. **d** At $\gamma_1 = 3\gamma_0$, the Type A Dirac line shrinks to a point and surface flat bands now appear at all momenta (k_x, k_y) except this point $(k_x, k_y) = \mathbf{0}$ (Color figure online)

The topological invariant can then be defined as a winding number

$$W(k_x, k_y) = -\frac{i}{2\pi} \int \frac{dz(k_z)}{z}, \quad z = \frac{\Phi(\mathbf{k})}{|\Phi(\mathbf{k})|}, \tag{10}$$

where the integration is over the 1D Brillouin zone in k_z direction. $W(k_x, k_y)$ is well defined whenever there are no gap closings as a function of k_z , and in these cases $|W(k_x, k_y)|$ determines the number of zero-energy surface states for each k_x and k_y . Therefore, the winding number and the number of topologically protected zero-energy states can only change at the momenta of the projected Dirac lines. By computing $W(k_x, k_y)$ for various values of γ_1/γ_0 we arrive at a flat band (zero energy) spectrum in the regions of the (k_x, k_y) with $W \neq 0$ in Fig. 4. For $\gamma_1 < \gamma_0$ the flat bands are formed inside the regions bounded by each of the Type B Dirac lines separately [Fig. 4a] as discussed in Refs. [13, 14]. At $\gamma_1 = \gamma_0$ the Type B Dirac lines merge in a pairwise manner and turn into Type A Dirac lines, and this shows up as a unification of the regions of the flat bands [Fig. 4b]. Similar merging of flat band surface states in a rhombohedral multilayer graphene-like system has been considered earlier as a function of an increasing anisotropy in the intra-layer hopping parameters [41]. Interestingly, for $\gamma_1 > \gamma_0$ the flat band is formed everywhere outside the region

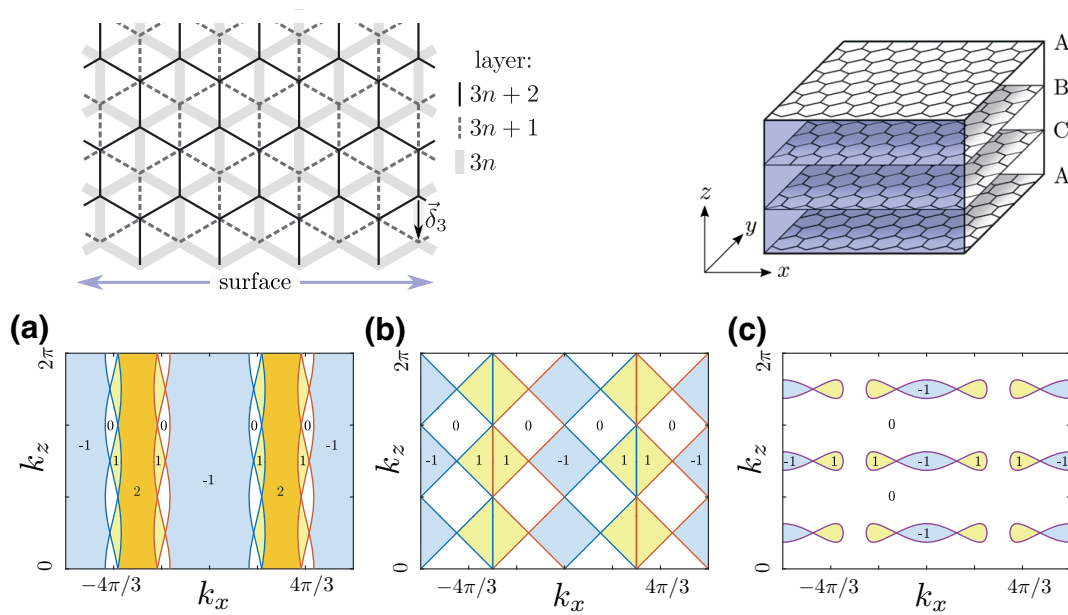


Fig. 5 Winding number $W(k_x, k_z)$ for $\gamma_2 = \gamma_3 = \gamma_4 = 0$ and various values of γ_1/γ_0 : **a** $\gamma_1/\gamma_0 = 0.3$, **b** $\gamma_1/\gamma_0 = 1$, **c** $\gamma_1/\gamma_0 = 1.5$. $|W(k_x, k_z)|$ determines the number of zero-energy surface states at the side surface with the specific surface termination shown in the figure both from above and from a three-dimensional perspective. For $\gamma_1 < \gamma_0$ there are regions in the momentum space with more than one surface flat band $|W(k_x, k_z)| > 1$. Such regions are possible because the period of the surface in the z -direction is three times the distance between the layers, so that there exist three different projections of each of the bulk Dirac lines in the (k_x, k_z) -plane (red and blue lines). After the merging transition ($\gamma_1 > \gamma_0$) the Type A Dirac line gives rise to regions with $W(k_x, k_z) = 1$ and $W(k_x, k_z) = -1$. The different signs of $W(k_x, k_z)$ indicate that the surface states are localized in the different sublattices. By increasing γ_1/γ_0 , the regions of the flat bands shrink and they disappear at $\gamma_1 = 3\gamma_0$ (Color figure online)

bounded by the projected Type A Dirac line [Fig. 4c], and therefore when the Type A Dirac line has shrunk to a point at $\gamma_1 = 3\gamma_0$ the surface flat bands appear at all momenta (k_x, k_y) except this point $(k_x, k_y) = \mathbf{0}$ [Fig. 4d]. For $\gamma_1 > 3\gamma_0$ the system is fully gapped, but the zero-energy surface flat bands still appear at all momenta and they are completely detached from the bulk bands. This type of surface flat bands have been found previously in two-dimensional systems [42].

We can now use a similar procedure to compute the momentum-space structure of the surface states at the side surfaces. This way we obtain that $W(k_y, k_z) = 0$ for all values of k_y and k_z , which means that there are no surface flat bands at the surface perpendicular to the x -direction. This result is analogous to the earlier finding that there are no flat bands at the armchair edge in graphene [9]. (The surface perpendicular to the x -direction consists of a stack of armchair edges.) On the other hand, for the surface perpendicular to the y -direction we find regions with $W(k_x, k_z) \neq 0$ indicating the existence of flat bands. The momentum-space structure flat bands for various values of γ_1/γ_0 are shown in Fig. 5. Importantly, for $\gamma_1 < \gamma_0$ there exist also regions in the momentum space with more than one surface flat band $|W(k_x, k_z)| > 1$. Such regions are possible because the period at the surface in the z -direction is three times the distance between the layers, and therefore, there are three different projections of each of the bulk Dirac lines in the (k_x, k_z) -plane (see Fig. 5). The detailed momentum-space structure of the flat bands for $\gamma_1 < \gamma_0$ can be understood by noticing that the surface

perpendicular to the y -direction contains a periodic sequence of stacks with two zigzag edges and one bearded edge (see Fig. 5). Therefore, by utilizing the results found in Ref. [9], we can interpret our numerical results in such a way that the two zigzag edges essentially give rise to the two flat bands in the region with $W(k_x, k_z) = 2$ and the bearded edge is responsible for the region with $W(k_x, k_z) = -1$ in Fig. 5a. The different signs of $W(k_x, k_z)$ indicate that the surface states are localized in the different sublattices. After the merging transition ($\gamma_1 > \gamma_0$) the Type A Dirac line gives rise to regions with $W(k_x, k_z) = 1$ and $W(k_x, k_z) = -1$, indicating that there still exists surface states localized in the different sublattices. By increasing γ_1/γ_0 , the regions of the flat bands shrink and they disappear at the topological phase transition where the system becomes gapped ($\gamma_1 = 3\gamma_0$). The detailed momentum-space structure of the flat bands depends on exact surface termination similarly as in the case of graphene [9]. The only generic property of the surface states, which is independent of the surface termination, is that the surface flat bands are always bounded in the momentum space by the projected Dirac lines.

The effects of the further-neighbor hoppings on the surface states can be computed quantitatively similarly as in Ref. [20] for the case of Bernal graphite. Here, we only discuss these effects qualitatively. The term proportional to γ_3 obeys chiral symmetry. Therefore, the same procedure of calculation of $W(k_x, k_y)$ and $W(k_x, k_z)$ can be repeated also for $\gamma_3 \neq 0$. Because for $|\gamma_3| < 0.5\gamma_0$ all the transitions stay qualitatively similar, the only effect of γ_3 in this regime is a small modification of the shape of the projected Dirac lines, so that the boundaries of the regions where the flat bands appear are slightly modified. On the other hand, the parameters γ_2 and γ_4 break the chiral symmetry and cause the Dirac lines to appear at finite energy. Similarly as found in Ref. [20] for the case of Bernal graphite, the terms breaking the chiral symmetry also modify the dispersions of the surface states, so that they turn the flat bands into drumhead surface states which are bounded by the projected Dirac lines both in energy and in momentum. In the region in between the Dirac lines, the surface states are no longer flat and their dispersions are determined by the terms proportional to γ_2 and γ_4 [43]. If these parameters are small, the surface bands are still approximately flat.

5 Summary and Discussion

We have shown that in the presence of time-reversal, inversion and spin rotation symmetries there can exist two different types of Dirac lines depending on whether the Dirac lines form closed loops fully inside the Brillouin zone (Type A Dirac lines) or they extend through the whole Brillouin zone in one of the directions (Type B Dirac lines). In the case of Type B Dirac lines, an energy gap can be opened only by first merging the Type B Dirac lines in a pairwise manner so that they turn into Type A Dirac lines, and then by shrinking these loops into points. We show that this kind of topological phase transition can occur in rhombohedrally stacked honeycomb lattices by tuning the ratio of the tunneling amplitudes. We have also discussed the properties of the surface states in the different phases of the model.

The Dirac-line semimetals considered in this paper are particularly interesting because of the possible symmetry-broken states at the surface triggered by the large

density of states caused by the topologically protected approximately flat bands. These symmetry-broken states may for example lead to realization of high-temperature superconductors or interesting magnetic orders [44–46]. Moreover, they are expected to be exotic states of matter since they cannot be described with a mean field theory [47].

Rhombohedral graphite has been studied also experimentally, and evidence of the surface flat bands has been reported [48, 49]. Moreover, the accumulated experimental evidence (e.g., sharp drop of resistance as a function of temperature and Josephson-like I-V characteristic) for graphite samples indicates the existence of high-temperature granular superconductivity which is localized at internal interfaces [50–54]. Nevertheless, a development of a consistent and comprehensive theory for all graphite experiments is a difficult and unsolved problem. In particular, the recent experiments for rhombohedral graphite were interpreted as evidence of a bulk energy gap $E_{\text{gap}} \sim 100$ meV for rhombohedral graphite [55]. In the light of the theory developed in this paper this observation is mysterious. Namely, according to the theory the rhombohedral graphite should be a Type B Dirac-line semimetal protected by the lattice translation, time-reversal, inversion and spin rotation symmetries. Moreover, the only way to open an energy gap in the presence of these symmetries (in a mean field theory description) is to merge the two Type B Dirac lines with each other, which requires a huge perturbation on the order of γ_0 . Since this is not feasible in rhombohedral graphite, the only possible explanation (assuming high-quality crystal structure so that the symmetries are not explicitly broken) would be that this bulk energy gap is due to interaction effects. Strong interactions could in principle either lead to a spontaneous symmetry breaking in the bulk destroying the protection of the Dirac lines or to a strongly correlated state which cannot be described with a mean field theory. In both cases the opening of an energy gap is in principle possible. Moreover, such kind of strong interaction effects is in principle possible. According to a simple theoretical estimate the Hubbard U parameter in graphite can be $U \sim 6$ eV [56], whereas γ_0 is typically assumed to be $\gamma_0 \sim 2.8$ eV [57].

In addition to the relevance of our theory for the rhombohedral graphite, we have made explicit predictions concerning the topological phase transition between Type B and Type A Dirac-line semimetals. These transitions could be realized experimentally in systems where the lattice potential can be controlled, so one essentially needs a three-dimensional generalizations of the type of two-dimensional systems where the merging transition of Dirac points has already been observed [33–36].

Acknowledgements We thank G. E. Volovik, T. Bzdusek and A. Bouhon for fruitful discussions and comments. This work was supported by the Academy of Finland Centre of Excellence and Key Funding programs (Project Nos. 284594 and 305256).

References

1. G.E. Volovik, *The Universe in a Helium Droplet* (Oxford University Press, Oxford, 2003)
2. M.Z. Hasan, C.L. Kane, *Rev. Mod. Phys.* **82**, 3045 (2010)
3. X.-L. Qi, S.-C. Zhang, *Rev. Mod. Phys.* **83**, 1057 (2011)
4. A.P. Schnyder, S. Ryu, A. Furusaki, A.W.W. Ludwig, *Phys. Rev. B* **78**, 195125 (2008)
5. C.-K. Chiu, J.C.Y. Teo, A.P. Schnyder, S. Ryu, *Rev. Mod. Phys.* **88**, 035005 (2016)
6. J.W. McClure, *Phys. Rev.* **108**, 612 (1957)

7. H.B. Nielsen, M. Ninomiya, *Phys. Lett. B* **130**, 389 (1983)
8. G.E. Volovik, *JETP Lett.* **46**, 98 (1987)
9. S. Ryu, Y. Hatsugai, *Phys. Rev. Lett.* **89**, 077002 (2002)
10. P. Horava, *Phys. Rev. Lett.* **95**, 016405 (2005)
11. G.P. Mikitik, YuV Sharlai, *Phys. Rev. B* **73**, 235112 (2006)
12. G.P. Mikitik, YuV Sharlai, *Low Temp. Phys.* **34**, 794 (2008)
13. T.T. Heikkilä, G.E. Volovik, *JETP Lett.* **93**, 59 (2011)
14. T.T. Heikkilä, N.B. Kopnin, G.E. Volovik, *JETP Lett.* **94**, 233 (2011)
15. A.A. Burkov, M.D. Hook, L. Balents, *Phys. Rev. B* **84**, 235126 (2011)
16. Y. Kim, B.J. Wieder, C.L. Kane, A.M. Rappe, *Phys. Rev. Lett.* **115**, 036806 (2015)
17. C. Fang, Y. Chen, H.-Y. Kee, L. Fu, *Phys. Rev. B* **92**, 081201(R) (2015)
18. Y.-H. Chan, C.-K. Chiu, M.Y. Chou, A.P. Schnyder, *Phys. Rev. B* **93**, 205132 (2016)
19. T.T. Heikkilä, G.E. Volovik, *New J. Phys.* **17**, 093019 (2015)
20. T. Hyart, T.T. Heikkilä, *Phys. Rev. B* **93**, 235147 (2016)
21. Z. Zhu, G.W. Winkler, Q. Wu, J. Li, A.A. Soluyanov, *Phys. Rev. X* **6**, 031003 (2016)
22. B. Bradlyn, J. Cano, Z. Wang, M.G. Vergniory, C. Felser, R.J. Cava, B.A. Bernevig, *Science* **353**, aaf5037 (2016)
23. T. Bzdusek, Q. Wu, A. Rüegg, M. Sigrist, A.A. Soluyanov, *Nature* **538**, 75 (2016)
24. M. Ezawa, *Phys. Rev. Lett.* **116**, 127202 (2016)
25. M. Horsdal, T. Hyart, *SciPost Phys.* **3**, 041 (2017)
26. Z. Yan, R. Bi, H. Shen, L. Lu, S.-C. Zhang, Z. Wang, *Phys. Rev. B* **96**, 041103(R) (2017)
27. M. Ezawa, *Phys. Rev. B* **96**, 041202(R) (2017)
28. T. Bzdusek, M. Sigrist, *Phys. Rev. B* **96**, 155105 (2017)
29. A. Bouhon, A.M. Black-Schaffer, [arXiv:1710.04871](https://arxiv.org/abs/1710.04871) (2017)
30. Y. Hasegawa, R. Konno, H. Nakano, M. Kohmoto, *Phys. Rev. B* **74**, 033413 (2006)
31. S. Katayama, A. Kobayashi, Y. Suzumura, *J. Phys. Soc. Jpn.* **75**, 054705 (2006)
32. G. Montambaux, F. Piéchon, J.-N. Fuchs, M.O. Goerbig, *Phys. Rev. B* **80**, 153412 (2009)
33. L. Tarruell, D. Greif, T. Uehlinger, G. Jotzu, T. Esslinger, *Nature* **483**, 302 (2012)
34. M. Bellec, U. Kuhl, G. Montambaux, F. Mortessagne, *Phys. Rev. Lett.* **110**, 033902 (2013)
35. M.C. Rechtsman, Y. Plotnik, J.M. Zeuner, D. Song, Z. Chen, A. Szameit, M. Segev, *Phys. Rev. Lett.* **111**, 103901 (2013)
36. L. Duca, T. Li, M. Reitter, I. Bloch, M. Schleier-Smith, U. Schneider, *Science* **347**, 288 (2015)
37. J. Kim, S.S. Baik, S.H. Ryu, Y. Sohn, S. Park, B.-G. Park, J. Denlinger, Y. Yi, H.J. Choi, K.S. Kim, *Science* **349**, 723 (2015)
38. G.E. Volovik, *Lect. Notes Phys.* **718**, 31 (2007)
39. S. Murakami, *New J. Phys.* **9**, 356 (2007)
40. S. Murakami, S.-I. Kuga, *Phys. Rev. B* **78**, 165313 (2008)
41. A.A. Zyuzin, V.A. Zyuzin, *JETP Lett.* **102**, 113 (2015)
42. M. Ezawa, *New J. Phys.* **16**, 115004 (2014)
43. N.B. Kopnin, M. Ijäs, A. Harju, T.T. Heikkilä, *Phys. Rev. B* **87**, 140503(R) (2013)
44. N.B. Kopnin, T.T. Heikkilä, G.E. Volovik, *Phys. Rev. B* **83**, 220503(R) (2011)
45. B. Pamuk, J. Baima, F. Mauri, M. Calandra, *Phys. Rev. B* **95**, 075422 (2017)
46. T. Löthman, A.M. Black-Schaffer, *Phys. Rev. B* **96**, 064505 (2017)
47. V.J. Kauppila, T. Hyart, T.T. Heikkilä, *Phys. Rev. B* **93**, 024505 (2016)
48. D. Pierucci, H. Sediri, M. Hajlaoui, J.-C. Girard, T. Brumme, M. Calandra, E. Velez-Fort, G. Patriarche, M.G. Silly, G. Ferro, V. Soulière, M. Marangolo, F. Sirotti, F. Mauri, A. Ouerghi, *ACS Nano* **9**, 5432 (2015)
49. Y. Henni, H.P. Ojeda Collado, K. Nogajewski, M.R. Molas, G. Usaj, C.A. Balseiro, M. Orlita, M. Potemski, C. Faugeras, *Nano Lett.* **16**, 3710 (2016)
50. P. Esquinazi, N. Garcia, J. Barzola-Quiquia, P. Rödiger, K. Schindler, J.-L. Yao, M. Ziese, *Phys. Rev. B* **78**, 134516 (2008)
51. T. Scheike, W. Böhlmann, P. Esquinazi, J. Barzola-Quiquia, A. Ballestar, A. Setzer, *Adv. Mater.* **24**, 5826 (2012)
52. A. Ballestar, J. Barzola-Quiquia, T. Scheike, P. Esquinazi, *New J. Phys.* **15**, 023024 (2013)
53. C.E. Precker, P.D. Esquinazi, A. Champi, J. Barzola-Quiquia, M. Zoraghi, S. Muinos-Landin, A. Setzer, W. Böhlmann, D. Spemann, J. Meijer, T. Muenster, O. Baehre, G. Kloess, H. Beth, *New J. Phys.* **18**, 113041 (2016)

-
54. M. Stiller, P.D. Esquinazi, C.E. Precker, J. Barzola-Quiquia, [arXiv:1705.09909](https://arxiv.org/abs/1705.09909) (2017)
 55. M. Zoraghi, J. Barzola-Quiquia, M. Stiller, A. Setzer, P. Esquinazi, G.H. Kloess, T. Muenster, T. Lühmann, I. Estrela-Lopis, *Phys. Rev. B* **95**, 045308 (2017)
 56. A.L. Tchougreeff, R. Hoffmann, *J. Phys. Chem.* **96**, 8993 (1992)
 57. A.H. Castro Neto, F. Guinea, N.M.R. Peres, K.S. Novoselov, A.K. Geim, *Rev. Mod. Phys.* **81**, 109 (2009)

III

THERMOELECTRIC RADIATION DETECTOR BASED ON SUPERCONDUCTOR-FERROMAGNET SYSTEMS

by

T.T. Heikkilä, R. Ojajärvi, I.J. Maasilta, E. Strambini, F. Giazotto, and
F.S. Bergeret 2018

Physical Review Applied **10**, 034053, DOI:[10.1103/PhysRevApplied.10.034053](https://doi.org/10.1103/PhysRevApplied.10.034053)

Reproduced with permission. Copyright 2018 American Physical Society.

Thermoelectric Radiation Detector Based on Superconductor-Ferromagnet Systems

T. T. Heikkilä,^{1,*} R. Ojajarvi,¹ I. J. Maasilta,¹ E. Strambini,² F. Giazotto,² and F. S. Bergeret^{3,4}

¹*Department of Physics and Nanoscience Center, University of Jyväskylä, P.O. Box 35, FI-40014 University of Jyväskylä, Finland*

²*NEST, Istituto Nanoscienze-CNR and Scuola Normale Superiore, 56127 Pisa, Italy*

³*Centro de Física de Materiales, Centro Mixto CSIC-UPV/EHU, Paseo Manuel de Lardizabal 5, 20018 San Sebastián, Spain*

⁴*Donostia International Physics Center, Paseo Manuel de Lardizabal 4, 20018 San Sebastián, Spain*



(Received 29 September 2017; revised manuscript received 23 April 2018; published 25 September 2018)

We suggest an ultrasensitive detector of electromagnetic fields exploiting the giant thermoelectric effect recently found in superconductor-ferromagnet hybrid structures. Compared with other types of superconducting detectors where the detected signal is based on variations of the detector impedance, the thermoelectric detector has the advantage of requiring no external driving fields. This is especially relevant in multipixel detectors, where the number of bias lines and the heating induced by them are an issue. We propose different material combinations to implement the detector and provide a detailed analysis of its sensitivity and speed. In particular, we perform a proper noise analysis that includes the cross correlation between heat and charge current noise and thereby describes also thermoelectric detectors with a large thermoelectric figure of merit.

DOI: [10.1103/PhysRevApplied.10.034053](https://doi.org/10.1103/PhysRevApplied.10.034053)

I. INTRODUCTION

Some of the most accurate sensors of wideband electromagnetic radiation are based on superconducting films. Such sensors, in particular the transition-edge sensor (TES), are used in a wide variety of applications requiring extremely high sensitivity. Those applications include detection of the cosmic microwave background [1–3] and other tasks in astrophysics [4], generic-purpose terahertz-radiation sensing used, for example, in security imaging [5], gamma-ray spectroscopy of nuclear materials [6], and analysis of materials by detection of fluorescent x-rays excited by ion beams [7], short laser-driven x-ray pulses [8], or synchrotrons [6]. Many of these applications would benefit from the addition of more pixels (i.e., more sensors) to increase the collection efficiency, detection bandwidth, or the spatial or angular resolution. However, operating large arrays of TESs can be problematic as each pixel requires a bias line. This can be cumbersome in the presence of thousands of pixels, even with advanced multiplexing techniques [6]. Moreover, the bias lines tend to carry heat into the system especially by radiation, reducing, for example, its overall noise performance. In addition, a TES always dissipates power at the pixel, giving constraints on the cryogenic design for large arrays. One alternative

is the kinetic inductance detector (KID) [9–11] and its variants [12,13], the most common being the type with passive frequency-domain multiplexing using superconducting microwave resonators [14]. With such a device, a single pair of coaxial cables can be used to probe a large array of pixels, but the probe power is, by necessity, also partially dissipated at the detectors.

Both the TES and the KID are based on the measurement of an impedance of the sensor (i.e., response to a probe signal). It would generally be beneficial if one could get rid of the probe signal altogether, so that the measured signal would result directly from the radiation coupled to the detector. This is what happens in thermoelectric detection [15–17], where the temperature rise caused by the absorption of radiation is converted into an electric voltage or current that can then be detected. Such thermoelectric detectors have been discussed before, but they have not been considered for ultrasensitive low-temperature detectors for the simple reason that thermoelectric effects are typically extremely weak at low temperatures. On the other hand, at high temperatures, where such thermoelectric effects would be strong enough, the thermal noise hampers the device sensitivity.

We suggest overcoming these problems in a *superconductor-ferromagnet thermoelectric detector* (SFTED) [18] by exploiting the newly discovered giant thermoelectric effect that occurs in superconductor-

*tero.t.heikkila@jyu.fi

ferromagnet heterostructures [19–22] for radiation sensing. As this thermoelectric effect can be realized with close to Carnot efficiency [19,22] even at subkelvin temperatures, the resulting detector can have a large signal-to-noise ratio, and a noise-equivalent power (NEP) rivaling those of the best TESs and KIDs without the burden of having to use additional bias lines for probing the sensor, and with zero (for ideal amplification) or at most very small nonsignal power dissipation at the sensor location. The only part of the system where external power is needed is in the detection of the thermoelectric currents (i.e., at the amplifier), which can be taken far from the active sensing region.

Recently the use of superconductor-ferromagnet structures in thermometry has been discussed [23]. Despite some similarities, thermometers and radiation detectors have quite different requirements regarding their sensitivity. In particular, the sensitivity of radiation detectors is typically dictated by the temperature-fluctuation noise, which is not an issue as such for thermometers. In this paper we concentrate on finding and optimizing the relevant figures of merit for radiation detection, and hence we cannot benefit much from the results in thermometry.

For concreteness, we consider the detector realization depicted in Fig. 1. The sensor element (i.e., one pixel of a possible detector array) is formed from a thin-film superconductor–ferromagnetic insulator bilayer coupled to superconducting antennas via a clean (Andreev) contact. This bilayer is further connected, via a tunnel junction (magnetic or normal) to a ferromagnetic electrode [24]. The current injected into the ferromagnetic electrode or the voltage generated across the tunnel junction is detected by a superconducting-quantum-interference-device (SQUID) current amplifier or a field-effect transistor, respectively. In what follows, we describe conditions for measuring radiation in the far-IR region, in which case it can be coupled to the detector via antennas. Alternatively, the detector could be used for measuring radiation at higher frequencies (such as x-ray frequencies), in which case the system should be connected to an additional, larger absorber element.

We consider the radiation to be directed to the detector via a superconducting antenna (not shown in Fig. 1) that is coupled via a clean (Andreev) contact to the active superconductor–ferromagnetic insulator region (absorber). To prevent heat leaking from the absorber, the superconductor used in the antenna should be fabricated from a material with a higher superconducting gap Δ_A than the one used in the absorber, Δ . One possible combination could be a Nb antenna and an Al absorber. For optimal quantum efficiency, the normal-state resistance of the absorber (seen by radiation at frequencies higher than Δ/h , where h is Planck’s constant) should be matched to the specific impedance of the antenna, typically somewhat below the vacuum impedance. For an Al film thickness of 10 nm, a typical sheet resistance is 5–10 Ω . Hence, a

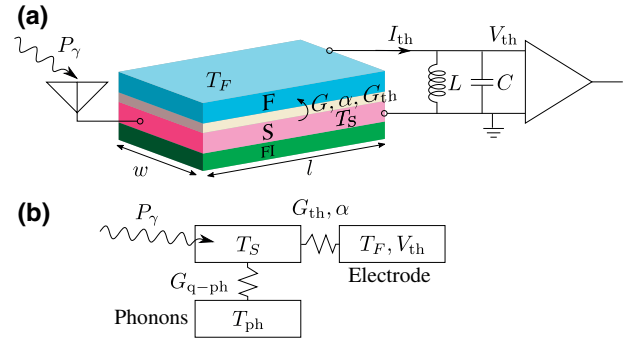


FIG. 1. (a) The thermoelectric detector, where a temperature difference $T_S - T_F$ drives a thermoelectric current I_{th} and/or a thermovoltage V_{th} across a spin-polarized junction. The latter is composed of either a normal insulator and a ferromagnetic electrode (F) or a ferromagnetic insulator (FI) and a normal metal electrode. (b) Heat balance: incoming radiation power heats up the quasiparticles in the spin-split superconductor (S), and the amount of heating depends on the heat conductances to the main heat baths.

1- μm -wide film with length $l = 10 \mu\text{m}$ would have resistance $R_Y = 50\text{--}100 \Omega$ seen by the radiation, thereby matching well with typical antennas. In what follows, we hence choose an absorber region of this size. Reducing (increasing) the width and length while keeping their ratio constant would result in the same quantum efficiency but decreased (increased) noise and dynamic range.

The absorber superconductor is placed in contact with a ferromagnetic insulator that exerts a magnetic proximity effect on the former, resulting in a spin-splitting exchange field h inside the superconductor. In Al, large induced spin-splitting fields have been detected by contacting it, for example, with EuS [25] or EuO [26]. At low temperatures compared with the superconductor critical temperature T_C , the exchange field does not have a major effect on the order parameter Δ [27,28]. However, it results in a strong (and opposite) electron-hole asymmetry in each spin component in the direction specified by the magnetization of the ferromagnetic insulator. This asymmetry can be used to generate a thermoelectric signal if the superconductor is connected via a spin filter to another electrode [19,22]. This spin filtering is provided here by the ferromagnetic electrode and is quantified by the normal-state spin polarization $P = (G_\uparrow - G_\downarrow)/(G_\uparrow + G_\downarrow) \in [-1, 1]$, where G_σ is the normal-state conductance of the superconductor-ferromagnet contact for spin channel σ . In what follows, we also characterize this contact via its spin-averaged normal-state conductance G_T . In practice, oxide contacts with ferromagnetic metals such as Ni, Co, or Fe have $P \sim 0.1\text{--}0.45$ [29,30], whereas use of ferromagnetic insulator contacts may lead to polarizations exceeding $P \sim 0.9$ [31]. The precise value of G_T for a given area of the junction can be controlled by the thickness of the tunnel junction.

II. NOISE-EQUIVALENT POWER OF A THERMOELECTRIC DETECTOR

We first consider a generic thermoelectric element working as a radiation sensor and analyze its figures of merit, in particular the NEP and the thermal time constant τ_T , both defined in detail below. As the radiation with power P_γ is absorbed in the absorber, it first creates a strong nonequilibrium state of the quasiparticles. This nonequilibrium state relaxes via (i) quasiparticle-quasiparticle collisions, (ii) spurious processes such as quasiparticle-phonon relaxation, and (iii) the escape of the quasiparticles to the (ferromagnetic) electrode. The last process yields the detected signal. Moreover, some of the excitations may escape as quasiparticles to the antenna. We assume that relaxation via quasiparticle-quasiparticle collisions dominates so that the quasiparticles thermalize between themselves before escaping to the antenna, and therefore in what follows we disregard escape of excitations as quasiparticles to the antenna. As a result of this chain of events, the quasiparticles in the absorber heat up to temperature $T_S = T + \Delta T$ determined from a heat-balance equation [32]:

$$C_h \frac{d\Delta T}{dt} = P_\gamma - G_{\text{th}}^{\text{tot}} \Delta T + \alpha V_{\text{th}}, \quad (1)$$

where C_h is the heat capacity of the absorber and $G_{\text{th}}^{\text{tot}} = G_{q\text{-ph}} + G_{\text{th}}$, where $G_{q\text{-ph}}$ and G_{th} denote the heat conductances from quasiparticles to the phonons and to the ferromagnetic electrode, respectively. In the linear regime we assume that both reside at the bath temperature T . The last term results from the Peltier heat current driven by the induced thermovoltage across the superconductor-ferromagnet junction, and it is proportional to the temperature difference ΔT . We assume that the detector operates at low powers P_γ so that these linear response relations are sufficient. The detector characteristics depend strongly on the chosen T .

The induced temperature difference (in the frequency domain) $\Delta T = (P_\gamma + \alpha V_{\text{th}})/(i\omega C_h + G_{q\text{-ph}} + G_{\text{th}})$ drives a thermoelectric current $I_{\text{th}} = \alpha \Delta T/T - G V_{\text{th}}$ into the ferromagnet and ultimately to an amplifier. To focus on detector performance limits first, we disregard the back-action noise from the amplifier, and consider the amplifier only as a reactive element: either a capacitor or an inductor, corresponding to a field-effect transistor or SQUID amplifier, respectively. Therefore, the thermoelectric current equals $V_{\text{th}}[i\omega C + 1/(i\omega L)]$ across the amplifier with capacitance C and inductance L in parallel. One can obtain the practical limits of voltage (current) measurements by considering $\omega \neq 0$ and taking the limit $L \rightarrow \infty$ ($C \rightarrow \infty$). From these relations we can obtain the voltage and current responsivities:

$$\lambda_V \equiv \frac{V_{\text{th}}}{P_\gamma} = \frac{\alpha}{Y_{\text{th}}^{\text{tot}} Y^{\text{tot}} T - \alpha^2}, \quad \lambda_I \equiv \frac{I_L}{P_\gamma} = \frac{\lambda_V}{i\omega L}, \quad (2)$$

where I_L is the current across the inductor. The relevant responsivity depends on the choice of the amplifier. Here $Y_{\text{th}}^{\text{tot}} = i\omega C_h + G_{\text{th}}^{\text{tot}}$ and $Y^{\text{tot}} = G + i\omega C + 1/(i\omega L)$ are the thermal and electrical admittances, respectively. Note that $ZT(\omega) = \alpha \lambda_V$ is a finite-frequency generalization of the usual thermoelectric figure of merit.

We next consider the temperature fluctuation δT , voltage noise ΔV across the capacitor, and current noise ΔI_L across the inductor. These are driven by the three intrinsic noise sources: the charge and heat current noises δI and $\delta \dot{Q}_J$ across the thermoelectric junction and the heat current noise $\delta \dot{Q}_{q\text{-ph}}$ for the quasiparticle-phonon process. The heat balance equation and the Kirchoff law for the noise terms read

$$Y_{\text{th}}^{\text{tot}} \delta T = \delta \dot{Q}_{q\text{-ph}} + \delta \dot{Q}_J + \alpha \Delta V, \quad (3a)$$

$$Y^{\text{tot}} \Delta V = \delta I + \alpha \delta T/T. \quad (3b)$$

Solving these yields

$$\Delta V = \lambda_V (\delta \dot{Q}_{q\text{-ph}} + \delta \dot{Q}_J + Y_{\text{th}}^{\text{tot}} T \delta I / \alpha) \quad (4)$$

and $\Delta I_L = \Delta V/(i\omega L)$. To find the second-order correlator of these noise terms, we assume that the intrinsic correlators satisfy

$$\langle \delta I^2 \rangle = 4k_B T G, \quad (5a)$$

$$\langle \delta \dot{Q}_J^2 \rangle = 4k_B T^2 G_{\text{th}}, \quad (5b)$$

$$\langle \delta I \delta \dot{Q}_J \rangle = -4k_B T \alpha, \quad (5c)$$

$$\langle \delta \dot{Q}_{q\text{-ph}}^2 \rangle = 4k_B T^2 G_{q\text{-ph}}. \quad (5d)$$

These result from the fluctuation-dissipation theorem for the individual contacts. In particular, the cross-noise term is important for strong thermoelectric response, and was not taken into account before; it was, for example, disregarded in Ref. [16]. The total voltage-noise spectral density is (note that this is the symmetrized voltage-noise correlator, and therefore one needs to take the absolute value squared)

$$S_V = \langle \Delta V^2 \rangle = |\lambda_V|^2 4k_B T^2 \frac{G_{\text{th}}^{\text{tot}} (GTG_{\text{th}}^{\text{tot}} - \alpha^2) + \omega^2 C_h GT}{\alpha^2}. \quad (6)$$

The term in parentheses is positive semidefinite due to the thermoelectric stability condition $\alpha^2 \leq GTG_{\text{th}}^{\text{tot}}$ valid for all thermoelectric systems. The current-noise spectral density

across the inductor, S_I , has the same form as S_V in Eq. (6), but where λ_V is replaced by λ_I .

The square of the NEP P_{ne}^2 is the power spectral density for which the induced-thermoelectric-voltage spectral density across the capacitor equals S_V , or for which the thermoelectric current spectral density across the inductor equals S_I . These yield the same results, $S_V/|\lambda_V|^2 = S_I/|\lambda_I|^2$,

$$P_{\text{ne}}^2 \equiv \frac{S_V}{|\lambda_V|^2} = 4k_B T^2 \frac{G_{\text{th}}^{\text{tot}}(GTG_{\text{th}}^{\text{tot}} - \alpha^2) + \omega^2 C_h^2 GT}{\alpha^2}. \quad (7)$$

This may be written in a more tractable form by use of the zero-frequency thermoelectric figure of merit $zT = \alpha^2/(G_{\text{th}}^{\text{tot}}GT - \alpha^2)$ [33] and the thermal time constant $\tau_T = C_h/G_{\text{th}}^{\text{tot}}$:

$$P_{\text{ne}}^2 = \frac{4k_B T^2 [1 + \omega^2 \tau_T^2 (1 + zT)] G_{\text{th}}^{\text{tot}}}{zT}. \quad (8)$$

The zero-frequency thermoelectric NEP thus equals the usual thermal bolometer NEP [34] from the thermal fluctuation noise divided by the square root of the figure of merit. Moreover, the thermal time constant determining the frequency band for the detection is increased by the factor $\sqrt{1 + zT}$.

Above discussion disregards the contribution from the amplifier noise. This is discussed separately below.

The NEP written above can be optimized, as typically the overall level of the thermoelectric junction conductance can be chosen almost at will, and the coefficients α and G_{th} scale with the same prefactor. In the sensor discussed here, this means optimizing the normal-state conductance of the thermoelectric junction. On the other hand, for a given absorber volume Ω , the thermal conductance of the spurious process $G_{q\text{-ph}}$ cannot be affected much. Therefore, choosing a too small junction conductance results in a poor thermoelectric figure of merit zT , whereas increasing the junction conductance increases the thermal fluctuation noise and the Johnson-Nyquist current noise of the junction. In addition, a high junction conductance may lead to a heating of the normal-metal (ferromagnetic) electrode, thereby reducing the temperature gradient across the junction, and the associated thermoelectric effects. In what follows we assume that this electrode is thick enough so that its heating can be disregarded. For zero-frequency NEP, the optimum is obtained with conductance $G_{\text{th}}/G_{\text{ph}} = \sqrt{1 + zT_i}$, where $zT_i = \alpha^2/(G_{\text{th}}GT - \alpha^2)$ is the intrinsic figure of merit of the junction (not including the heat conductance to the phonons). With this choice, the optimal NEP of the thermoelectric detector is

$$P_{\text{ne,opt}}^2 = \frac{4G_{q\text{-ph}}k_B T^2 (1 + \sqrt{1 + zT_i})^2}{zT_i}. \quad (9)$$

It hence reaches the limit set by the thermal fluctuation noise of the spurious process for $zT_i \rightarrow \infty$.

The above discussion holds for arbitrary thermoelectric sensors of the type depicted in Fig. 1(b). However, typically strong thermoelectric effects are found only above room temperature, which renders the thermal fluctuation noise very large. The combination of a spin-split superconductor with a spin-polarized contact circumvents this problem, leading to large thermoelectric response even at subkelvin temperatures. In the following, we analyze this system in more detail.

III. SUPERCONDUCTOR-FERROMAGNET THERMOELECTRIC RADIATION DETECTOR

First, following Ref. [19], we write the thermoelectric coefficients of the spin-polarized junction between the spin-split superconductor and the nonsuperconducting contact as

$$G = G_T \int_{-\infty}^{\infty} dE \frac{N_0(E)}{4k_B T \cosh^2\left(\frac{E}{2k_B T}\right)}, \quad (10a)$$

$$G_{\text{th}} = \frac{G_T}{e^2} \int_{-\infty}^{\infty} dE \frac{E^2 N_0(E)}{4k_B T^2 \cosh^2\left(\frac{E}{2k_B T}\right)}, \quad (10b)$$

$$\alpha = \frac{G_T}{2e} P \int_{-\infty}^{\infty} dE \frac{E N_z(E)}{4k_B T \cosh^2\left(\frac{E}{2k_B T}\right)}. \quad (10c)$$

Here G_T is the normal-state electrical conductance of the junction, and $N_0(E) = (N_{\uparrow} + N_{\downarrow})/2$ and $N_z = N_{\uparrow} - N_{\downarrow}$ are the spin-averaged and the spin-difference density of states (DOS) of the superconductor, normalized to the normal-state DOS ν_F at the Fermi level. They are obtained from $N_{\uparrow/\downarrow} = N_S(E \mp h)$, with $N_S(E) = \text{Re}[|E + i\Gamma|/\sqrt{(E + i\Gamma)^2 - \Delta^2}]$, where h is the spin-splitting field and $\Gamma \ll \Delta$ describes pair-breaking effects inside the superconductor. Analytic approximations for Eq. (10) are detailed in Ref. [19].

The heat capacity of the absorber with volume Ω is obtained from

$$\begin{aligned} C_h &= \frac{d}{dT} \left(\nu_F \Omega \int_{-\infty}^{\infty} dE E N_0(E) f_{\text{eq}}(E) \right) \\ &= \frac{\nu_F}{4k_B T^2} \int_{-\infty}^{\infty} \frac{E^2 N_0(E)}{\cosh^2\left(\frac{E}{2k_B T}\right)} = \frac{\nu_F \Omega e^2}{G_T} G_{\text{th}}. \end{aligned} \quad (11)$$

The thermal time constant of the junction, C_h/G_{th} , hence remains independent of superconductivity or spin splitting.

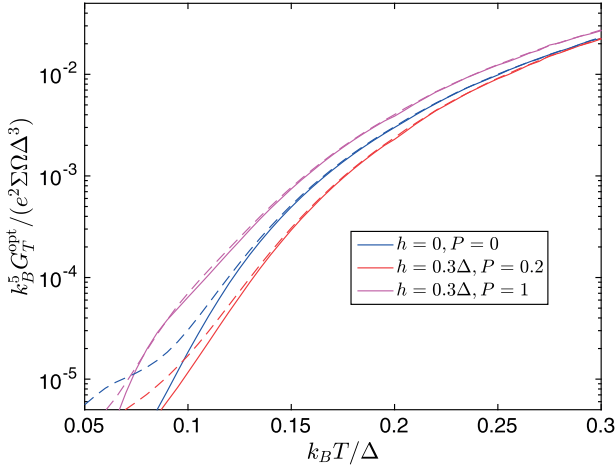


FIG. 2. Optimal normal-state tunnel conductance G_T of the thermoelectric junction. For Al of volume 10^{-19} m^3 , a value of 1 corresponds to $G_T^{-1} = 20 \text{ } \Omega$. At the lowest temperatures the results depend strongly on the value of the broadening parameter Γ used in the numerics. The solid lines are calculated with $\Gamma = 10^{-4} \Delta$ and the dashed lines are calculated with $\Gamma = 10^{-3} \Delta$.

The electron-phonon heat conductance of a spin-split superconductor in the pure limit can be obtained from [35]

$$G_{e\text{-ph}} = \frac{\Sigma \Omega}{96 \zeta(5) k_B^5 T^2} \int_{-\infty}^{\infty} dE E \int_{-\infty}^{\infty} d\omega \times \omega^2 |\omega| L_{E, E+\omega} F_{E, \omega}, \quad (12)$$

with

$$F_{E, \omega} = -\frac{1}{2} \left[\sinh\left(\frac{\omega}{2T}\right) \cosh\left(\frac{E}{2T}\right) \cosh\left(\frac{E+\omega}{2T}\right) \right]^{-1}, \quad (13)$$

$L_{E, E'} = (1/2) \sum_{\sigma=\pm} N_{\sigma}(E) N_{\sigma}(E') \{1 - \Delta^2 / [(E + \sigma h)(E' + \sigma h)]\}$, and $\sigma = \pm$ for spin \uparrow / \downarrow . Here Σ is the material-dependent electron-phonon coupling constant (for typical values, see Ref. [34]), $\Omega = wld$ is the volume of the superconductor island, and $\zeta(x)$ is the Riemann zeta function.

In the low-temperature limit $k_B T \ll \Delta - |h|$, the electron-phonon heat conductance can be approximated as

$$G_{e\text{-ph}} = \frac{\Sigma \Omega}{96 \zeta(5)} T^4 [\cosh \tilde{h} e^{-\tilde{\Delta}} f_1(\tilde{\Delta}) + \pi \tilde{\Delta}^5 e^{-2\tilde{\Delta}} f_2(\tilde{\Delta})], \quad (14)$$

where $\tilde{h} = h/k_B T$ and $\tilde{\Delta} = \Delta/k_B T$. The function f_1 can be approximated with an expansion $f_1(\tilde{\Delta}) = \sum_{n=1}^{\infty} C_n / \tilde{\Delta}^n$ with coefficients $C_0 \approx 440$, $C_1 \approx -500$, $C_2 \approx 1400$, and $C_3 \approx -4700$. An expansion for f_2 is $f_2(\tilde{\Delta}) = \sum_{n=1}^{\infty} B_n / \tilde{\Delta}^n$ with coefficients $B_0 = 64$, $B_1 = 144$, and $B_2 = 258$. The derivation of Eq. (14) is presented in the Appendix.

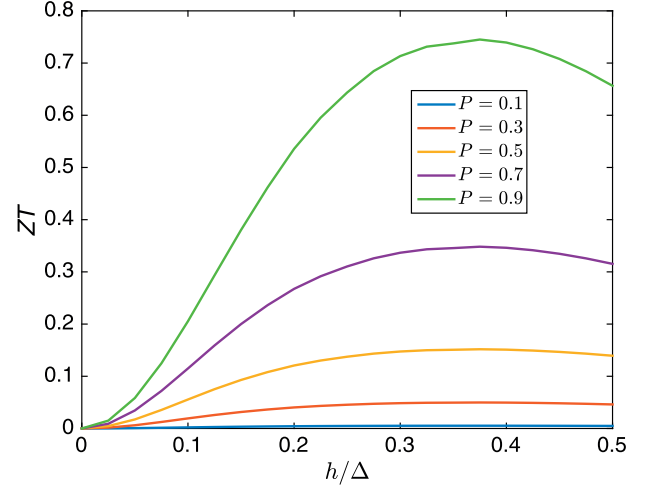


FIG. 3. Thermoelectric figure of merit as a function of the exchange field for junctions with different polarizations P at temperature $T = 0.1 \Delta / k_B$, with $G_T = 5 \times 10^{-4} e^2 \Sigma \Omega \Delta^3$ and $\Gamma = 10^{-3} \Delta$.

In the following, we use the above formulas to discuss the behavior of the SFTED. For this, we evaluate the above integrals numerically to obtain predictions of the optimal junction conductance, the thermoelectric figure of merit zT , the total NEP, and the time constant. The optimal normal-state junction conductance G_T is plotted as a function of temperature in Fig. 2. As the electron-phonon heat conductance dies out faster than the junction heat conductance at low temperatures, the optimal G_T also depends strongly on temperature. Note that for an Al absorber with electron-phonon coupling constant $\Sigma = 0.3 \times 10^9 \text{ W/m}^3 \text{ K}^5$, volume $\Omega = 10^{-19} \text{ m}^3$, and $\Delta = 200 \text{ } \mu\text{eV}$, the dimensionless parameter $k_B^5 G_T / (e^2 \Sigma \Omega \Delta^3) = G_T \times 20 \text{ } \Omega$. The optimal normal-state resistance of the junction is thus within the range from $20 \text{ k}\Omega$ to $20 \text{ M}\Omega$. Moreover, since both G_T and $\Sigma \Omega$ depend on the area of the absorber, the real optimizable parameters are the absorber film thickness and the junction conductance per unit area. In what follows, we use $G_T = 5 \times 10^{-4} e^2 \Sigma \Omega \Delta^3$, corresponding to a junction resistance of $40 \text{ k}\Omega$, optimal roughly at $T \approx 0.1 \Delta / k_B \sim 200 \text{ mK}$. This corresponds to a resistance times unit area of $400 \text{ k}\Omega \text{ } \mu\text{m}^2$, which is quite easily reached with AlO_2 tunnel junctions [36], but would be somewhat challenging for spin-filter EuS barriers, ranging typically between 10 and $1000 \text{ M}\Omega \text{ } \mu\text{m}^2$ [25].

On the other hand, the thermoelectric figure of merit zT depends strongly on the detector polarization. We show this by plotting zT for the parameters indicated above as a function of the exchange field at $T = 0.1 \Delta / k_B$ in Fig. 3. Because of the presence of the electron-phonon process acting as an extra heat channel, the figure of merit does not exceed unity.

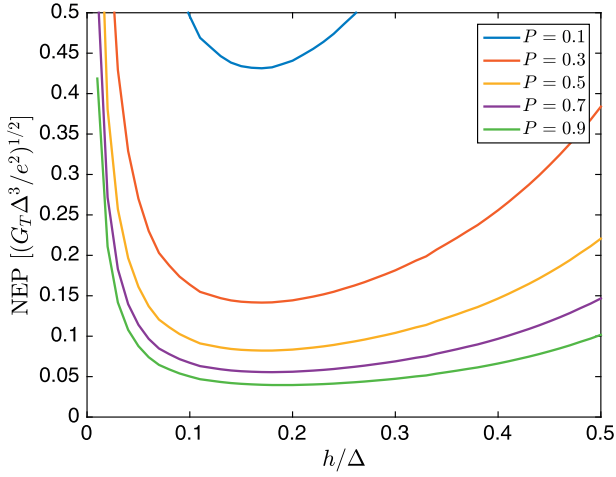


FIG. 4. Zero-frequency NEP as a function of the exchange field for junctions with different polarizations P at temperature $T = 0.1\Delta/k_B$, with $G_T = 5 \times 10^{-4} e^2 \Sigma \Omega \Delta^3$ and $\Gamma = 10^{-3} \Delta$. For the parameters considered in this paper, $\sqrt{G_T \Delta^3 / e^2} \approx 10^{-18} \text{ W}/\sqrt{\text{Hz}}$.

The most interesting characteristic of any detector is its sensitivity, in this case the NEP. We plot this as a function of exchange field in Fig. 4 and as a function of temperature in Fig. 5. The NEP is normalized to $\sqrt{G_T \Delta^3 / e^2}$, which corresponds to approximately $10^{-18} \text{ W}/\sqrt{\text{Hz}}$ for the parameters chosen. The dashed line in Fig. 5 indicates the $\text{NEP}_{\text{bolometer}} = 4G_{q\text{-ph}} T^2$ obtained for a TES with the same absorber volume at the corresponding temperature, with its heat conductance limited by electron-phonon coupling (i.e., a hot-electron TES [37]). In Fig. 4 that reference value is exactly unity for the parameters chosen. As the TES operates in the dissipative regime at the transition, the normal-state value for $G_{q\text{-ph}}$ must be used. Moreover, this estimate disregards the bias-induced heating, which sets the operating temperature higher than the bath temperature, and extra noise sources often found in TES realizations. We find that a SFTED can reach similar or better values than such a TES even with quite modest values of the junction polarization at low temperatures. Note that these results depend a bit on the precise value of the junction conductance—with a higher conductance, NEP at higher temperatures would be lower (see Fig. 2), and vice versa.

In practice, the most-sensitive TES bolometers to date have been fabricated from suspended structures where the thermal conductance to the bath is limited by phonon transport, achieving NEP on the order of $1 \times 10^{-19} \text{ W}/\sqrt{\text{Hz}}$ [38,39] at T_c of around 100 mK. On the basis of Fig. 5, the SFTED is also predicted to reach a lower NEP than that.

For completeness, we show the behavior of the thermal time constant $\tau^* = \tau_T \sqrt{1 + zT}$ as a function of temperature in Fig. 6. It is given in the units of $\tau_0 = \nu_F \Omega e^2 / G_T$.

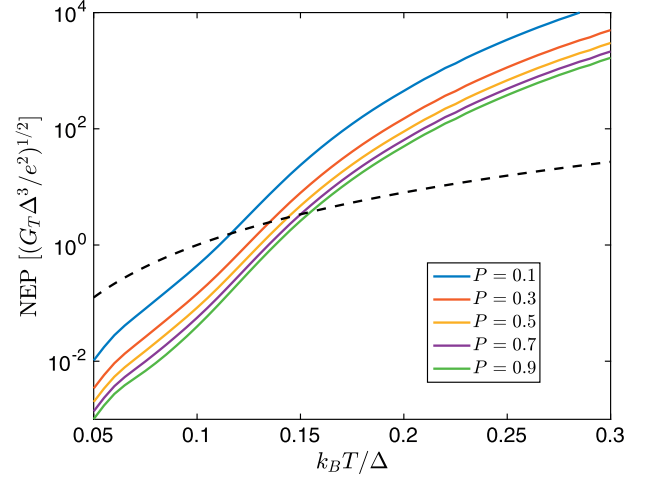


FIG. 5. Zero-frequency NEP as a function of the temperature for junctions with different polarizations P with exchange field $h = 0.2\Delta$, with $G_T = 5 \times 10^{-4} e^2 \Sigma \Omega \Delta^3$ and $\Gamma = 10^{-3} \Delta$. For the parameters considered in this paper, $\sqrt{G_T \Delta^3 / e^2} \approx 10^{-18} \text{ W}/\sqrt{\text{Hz}}$. The dashed line shows the thermal-fluctuation-noise $\text{NEP} = \sqrt{20 \Sigma \Omega T^6}$ for a TES of the same volume.

For $\nu_F = 10^{47} \text{ J}^{-1} \text{ m}^{-3}$, $\Omega = 10^{-19} \text{ m}^3$, and $G_T^{-1} = 2 \text{ M}\Omega$, $\tau_0 \approx 0.1 \text{ ms}$. At low temperatures, the tunnel junction dominates the heat conductance, and $\tau^* \approx \tau_0$. In this case zT is also appreciable, and slightly modifies τ^* . On the other hand, at high temperatures electron-phonon heat conduction takes over, and the detector becomes faster. To illustrate this crossover, we show the time constant for two different values of G_T .

The above results are obtained by disregarding spin relaxation. Aluminum is a light material, and therefore the spin-orbit scattering in it is typically quite weak, and the spin relaxation is dominated by spin-flip scattering. The typical spin relaxation times τ_{sr} in Al are on the order of 100 ps [40], and therefore $\hbar/(\tau_{sr} \Delta) \sim 0.03$, and the model disregarding spin relaxation is more or less justified. However, spin-flip scattering in the presence of exchange field yields a nonzero DOS inside the superconducting gap, and eventually leads to pair breaking [22]. Above, such effects are taken into account with the parameter Γ . For heavier materials, such as Nb, spin relaxation is caused by spin-orbit scattering, and the thermoelectric effects become weaker. Therefore, use of such heavier materials, for example, to increase the operation temperature of the thermoelectric detector beyond the critical temperature of Al, would require further analysis of the effects of spin relaxation.

A. Contribution of amplifier noise

In the preceding analysis we disregard the noise due to the voltage or current measurement. We can include it

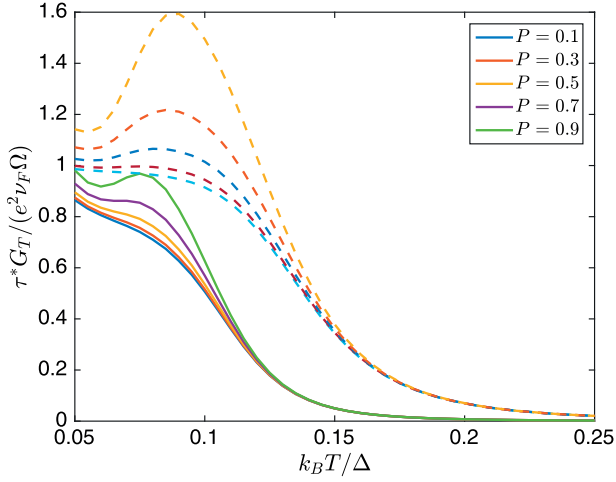


FIG. 6. Temperature dependence of the detector time constant τ^* determining the (angular) frequency bandwidth $1/\tau^*$ where the NEP is low. We chose $h = 0.2\Delta$. The solid lines are calculated with $G_T = 5 \times 10^{-4} e^2 \Sigma \Omega \Delta^3$, whereas the dashed lines correspond to 10 times larger conductance. For the former, $\tau_0 \approx 0.1$ ms, and for the latter, $\tau_0 \approx 0.01$ ms.

by assuming an added voltage-noise spectral density S_V^A or current-noise spectral density S_I^A for the amplifier used for voltage or current measurement. In the case of voltage measurements, the amplifier adds to NEP the contribution (for $\omega = 0$, for simplicity)

$$P_{\text{ne},A,V}^2 = \frac{S_V^A G T G_{\text{th}}^{\text{tot}}}{zT(1+zT)}, \quad (15)$$

whereas in the case of current measurement the contribution is

$$P_{\text{ne},A,I}^2 = \frac{S_I^A (1+zT) G_{\text{th}}^{\text{tot}} T}{G z T}. \quad (16)$$

We can hence see that the relative contribution from the voltage amplifier to the overall NEP decreases as the thermoelectric junction resistance increases. On the other hand, in the case of current measurement, the amplifier contribution becomes independent of the junction resistance when $G_{\text{th}}^{\text{tot}}$ is dominated by the junction heat conductance. Another way to estimate the contribution of amplifier noise is by dividing the corresponding NEPs by the total thermoelectric NEP from Eq. (8) (at $\omega = 0$). We hence get

$$r_V \equiv \frac{P_{\text{ne},A,V}^2}{P_{\text{ne}}^2} = \frac{S_V^A}{4k_B T} \frac{G}{(1+zT)}, \quad (17a)$$

$$r_I \equiv \frac{P_{\text{ne},A,I}^2}{P_{\text{ne}}^2} = \frac{S_I^A}{4k_B T} \frac{(1+zT)}{G}. \quad (17b)$$

A typical good voltage preamplifier for low-frequency measurements has a voltage noise on the order of $\sqrt{S_V} = 1.5$ nV/ $\sqrt{\text{Hz}}$ at room temperature and $\sqrt{S_V} = 0.3$ nV/ $\sqrt{\text{Hz}}$ at cryogenic temperatures [41]. Together with the normal-state tunnel conductance used above, and the Δ for Al, the latter value yields the relative NEP for voltage measurements as $r_V \approx G\Delta / (G_T k_B T)(1+zT)^{-1}$. This is much below unity in the entire relevant temperature range ($k_B T \ll \Delta$) due to the exponential suppression of G . On the other hand, a very good current amplifier can have an added noise of $\sqrt{S_I} = 0.5$ fA/ $\sqrt{\text{Hz}}$. With that value we get $r_I \approx 10^{-4} \Delta / (k_B T) \times (1+zT)G_T / G$. This exceeds unity below $k_B T \approx 0.1\Delta$ (the precise value depends on the exchange field chosen), and the current measurement accuracy starts limiting the thermoelectric detector NEP for $T \lesssim 0.1\Delta / k_B$. This difference between the two types of measurements originates from the fact that the thermoelectric voltage can be on the order of the temperature difference itself due to the thermopower on the order of k_B/e , whereas the thermoelectric current is exponentially suppressed [19] and hence harder to measure. However, ultimately at very low temperatures the voltage measurement also becomes harder as it requires the voltmeter impedance to far exceed that of the junction, and this condition becomes harder to meet at low temperatures.

Typical absolute-thermometer-based radiation detectors operating at the bath temperature (i.e., in contrast to, for example, a TES, where the bias sets the operating point above bath temperature) suffer from chip temperature fluctuations due to fluctuations in the cooling power. However, a thermoelectric detector measures a temperature difference ΔT instead of the absolute temperature. Because the chip temperature fluctuations affect both the temperature of the absorber and that of the measurement electrode, they do not affect ΔT (to the lowest order). This is an added benefit for TEDs in comparison with detectors based on resistance or inductance measurements.

IV. CONCLUSIONS

Thermoelectric radiation detection is not a new concept [15]. However, most of the previously studied thermoelectric detectors have relied on using semiconducting thermoelectric materials, operating at and above room temperature T_{RT} . Because the spurious heat-conduction processes have heat conductance that scales at least as approximately T^3 (typical phonon heat conductivity [34]), the corresponding NEP is $(T_{\text{RT}}/T)^{5/2} \sim 10^{15/2}$ times larger than that considered here (this estimate assumes the Debye temperature exceeds room temperature, but it should in any case be taken as indicative). On the other hand, quantum-dot structures may exhibit strong thermoelectric effects even at low temperatures [42]. In contrast to the superconductor-ferromagnet structure considered here, in those devices the thermoelectric effects are single-channel

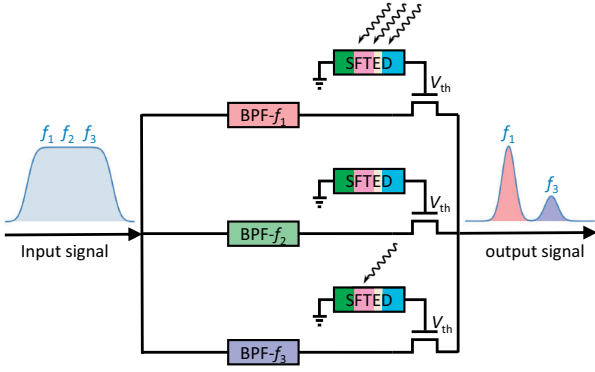


FIG. 7. One possible scheme for frequency-domain multiplexing of the thermoelectric detectors. Here a broadband electromagnetic wave, or a frequency comb, is divided into different frequency components via narrow-band-pass filters (BPFs), and directed through field-effect transistors whose conductance is modulated by the voltage from the detectors. As a result, the output spectrum contains pixel-specific information about the absorbed radiation power.

phenomena, and therefore it may be difficult to make the electronic thermal conduction dominate over the spurious heat-conduction channels.

In this paper, we show how a combination of superconducting and magnetic materials can be used to construct a low-temperature radiation detector relying on the thermoelectric effect and thereby not requiring extra bias power to be applied to the device. The proposed device thus differs qualitatively from the other previously known superconducting detectors such as TES and KID. The lack of the need to have extra bias power leads to simpler designs of arrays of such detectors, and helps in maintaining the low operating temperatures required for ultrasensitive operation. In addition, ultrasensitive TES bolometers necessarily have a very low tolerance for excess power loading, as the device can be saturated and pushed out of the transition region with it. For the detectors discussed here, there is no such abrupt effect, although excess power could lead to performance degradation due to overheating. Nevertheless, because of the lack of the bias lines, novel multiplexing strategies may need to be designed. We present one possible scheme in Fig. 7. There the output looks quite similar to that of frequency-multiplexed TES or KID read-out schemes, but the possible heating effects in the (dissipative) field-effect transistors can be engineered far apart from the pixels absorbing the radiation. Nevertheless, the optimal multiplexing strategies are a topic for further research.

ACKNOWLEDGMENTS

This project was supported by the Academy of Finland via its Key Funding Project (Grant No. 305256),

the Center of Excellence program (Grant No. 284594), and Grants No. 298667 and 317118; the European Union Seventh Framework Programme (ERC Grant No. 615187-COMANCHE) and the Horizon 2020 research and innovation programme (Grant No. 800923-SUPERTEED); the Tuscany Region under the FARFAS 2014 project SCIADRO, and the Spanish Ministerio de Economía, Industria y Competitividad (Grants No. FIS2014-55987-P and No. FIS2017-82804-P).

APPENDIX: ELECTRON-PHONON HEAT CONDUCTANCE

We calculate the electron-phonon heat conductance coefficient G_{e-ph} beginning from Eq. (12). We first extract the temperature-dependent prefactor by scaling all the quantities with dimensions of energy by temperature; for example, $\tilde{E} = E/k_B T$. The scaled quantities are dimensionless and are denoted with a tilde over the variable. We then change the integration variables to $x = \tilde{E}$ and $y = \tilde{E} + \tilde{\omega}$. We obtain

$$G_{e-ph} = \frac{\Sigma \Omega T^4}{96 \zeta(5)} \sum_{\sigma=\pm} \frac{I^\sigma}{4}, \quad (\text{A1})$$

where

$$I^\sigma = \iint dx dy \text{sgn}[(x + \sigma \tilde{h})(y + \sigma \tilde{h})] \times \frac{x|x-y|^3 \left[(x + \sigma \tilde{h})(y + \sigma \tilde{h}) - \tilde{\Delta}^2 \right] 4e^{-(|x|+|y|)/2}}{\sqrt{([x + \sigma \tilde{h}]^2 - \tilde{\Delta}^2)([y + \sigma \tilde{h}]^2 - \tilde{\Delta}^2)}} \frac{\sinh \frac{x-y}{2}}{2}. \quad (\text{A2})$$

Above, both x and y are integrated from $-\infty$ to $+\infty$, excluding the region $[-\tilde{\Delta} - \sigma \tilde{h}, \tilde{\Delta} - \sigma \tilde{h}]$, in which the spin-split DOS vanishes. We also assume that $\tilde{\Delta} - \tilde{h} \gg k_B T$ so that we can make an approximation

$$\cosh x \approx \frac{e^{|x|}}{2}, \quad x > \tilde{\Delta} - \tilde{h}, \quad (\text{A3})$$

and similarly for $\cosh y$.

The integral is divided into four separate quadrants by the gaps in the DOS. The integral over the quadrant n for the spin σ is I_n^σ . Because the integrand of Eq. (A2) is symmetric with respect to simultaneous inversion of x , y , and σ , the contributions from the opposing quadrants are equal:

$$I = \frac{1}{4} \sum_{n=1}^4 \sum_{\sigma=\pm} I_n^\sigma = \frac{1}{2} \sum_{\sigma=\pm} (I_1^\sigma + I_2^\sigma). \quad (\text{A4})$$

We calculate the integral over the first quadrant. This part of the integral represents scattering processes, for which

$x, y > 0$. Physically, this means that, the interacting quasiparticles are both particlelike. By shifting the integration limits, we get

$$\begin{aligned}
 I_1^\sigma &= \int_{\tilde{\Delta}-\sigma\tilde{h}}^{\infty} dx \int_{\tilde{\Delta}-\sigma\tilde{h}}^{\infty} dy \\
 &\times \frac{x|x-y|^3 \left[(x+\sigma h)(y+\sigma h) - \tilde{\Delta}^2 \right]}{\sqrt{[(x+\sigma h)^2 - \tilde{\Delta}^2][(y+\sigma h)^2 - \tilde{\Delta}^2]}} \frac{8}{e^x - e^y} \\
 &= \int_0^{\infty} dx \int_0^{\infty} dy \\
 &\times \frac{(x+\tilde{\Delta}-\sigma\tilde{h})|x-y|^3 \left[xy + (x+y)\tilde{\Delta} \right]}{(e^x - e^y)\sqrt{xy(x+2\tilde{\Delta})(y+2\tilde{\Delta})}} 8e^{-\tilde{\Delta}+\sigma\tilde{h}}.
 \end{aligned} \tag{A5}$$

Above, we have \tilde{h} dependence in two places: in the exponential outside the integral and as a linear term in the numerator. However, the parts of the numerator that are symmetric with respect to exchange $x \leftrightarrow y$ do not contribute to the integral. Therefore, we can write the integral as

$$\begin{aligned}
 I_1^\sigma &= e^{-\tilde{\Delta}+\sigma\tilde{h}} \int_0^{\infty} dx \int_0^{\infty} dy \\
 &\times \frac{8x^2|x-y|^3(y+\tilde{\Delta})}{(e^x - e^y)\sqrt{xy(x+2\tilde{\Delta})(y+2\tilde{\Delta})}} \\
 &= e^{-\tilde{\Delta}+\sigma\tilde{h}} f_1(\tilde{\Delta}),
 \end{aligned} \tag{A6}$$

where $f_1(\tilde{\Delta})$ is a monotonically increasing function with values $f_1(2) \approx 326$ and $\lim_{\tilde{\Delta} \rightarrow \infty} f_1(\tilde{\Delta}) \approx 438$. We can perform a Taylor expansion $f_1(\tilde{\Delta}) = \sum_{n=0}^{\infty} C_n/\tilde{\Delta}^n$ by first expanding the integrand into series in $\tilde{\Delta}^{-1}$ and then integrating separately for each term. The first few coefficients are $C_0 \approx 440$, $C_1 \approx -500$, $C_2 \approx 1400$, and $C_3 \approx -4700$.

Doing the sum over the spins, we find the contribution from the first quadrant:

$$I_1 = \sum_{\sigma=\pm} I_1^\sigma = 2 \cosh \tilde{h} e^{-\tilde{\Delta}} f_1(\tilde{\Delta}). \tag{A7}$$

The second quadrant describes the contribution from the recombination processes, for which one quasiparticle is holelike ($x < 0$) and the other is particlelike ($y > 0$):

$$I_2^\sigma = - \int_{-\infty}^{-\tilde{\Delta}-\sigma\tilde{h}} dx \int_{\tilde{\Delta}-\sigma\tilde{h}}^{\infty} dy \frac{8e^x}{e^x - e^y}$$

$$\begin{aligned}
 &\times \frac{x(x-y)^3 \left[(x+\sigma h)(y+\sigma h) - \tilde{\Delta}^2 \right]}{\sqrt{[(x+\sigma h)^2 - \tilde{\Delta}^2][(y+\sigma h)^2 - \tilde{\Delta}^2]}} \\
 &= \int_0^{\infty} dx \int_0^{\infty} dy \frac{(x+y+2\tilde{\Delta})^3 \left[xy + (x+y)\tilde{\Delta} + 2\tilde{\Delta}^2 \right]}{\sqrt{xy(2\tilde{\Delta}+x)(2\tilde{\Delta}+y)}} \\
 &\times 8(x+\tilde{\Delta}+\sigma\tilde{h})e^{-x-y}e^{-2\tilde{\Delta}},
 \end{aligned} \tag{A8}$$

where we approximate $e^{2\Delta+x+y} - 1 \approx e^{2\Delta+x+y}$. Above, the exchange field $\sigma\tilde{h}$ appears only as a linear term. If we sum over the two spin directions, terms odd in σ cancel and we can write I_2 in the form

$$I_2 = \sum_{\sigma} I_2^\sigma = 2\pi \tilde{\Delta}^5 e^{-2\tilde{\Delta}} f_2(\tilde{\Delta}). \tag{A9}$$

Within the approximation given by Eq. (A3), the exchange field does not modify the contribution from the recombination processes.

The function f_2 is defined as

$$\begin{aligned}
 f_2(\tilde{\Delta}) &= \int_0^{\infty} dx \int_0^{\infty} dy \\
 &\times \frac{(x+y+2\tilde{\Delta})^3 \left[xy + (x+y)\tilde{\Delta} + 2\tilde{\Delta}^2 \right]}{\pi \tilde{\Delta}^5 \sqrt{xy(2\tilde{\Delta}+x)(2\tilde{\Delta}+y)}} \\
 &\times 8e^{-x-y}(x+\tilde{\Delta}).
 \end{aligned} \tag{A10}$$

The function f_2 is a monotonically decreasing function with values $f_2(4) \approx 123$ and $\lim_{\tilde{\Delta} \rightarrow \infty} f_2(\tilde{\Delta}) = 64$. An expansion $f_2(\tilde{\Delta}) = \sum_{n=0}^{\infty} B_n/\tilde{\Delta}^n$ is obtained by first expanding the integrand asymptotically at $\tilde{\Delta} = \infty$ and then calculating the integral term by term. The first few coefficients are $B_0 = 64$, $B_1 = 144$, $B_2 = 258$, and $B_3 = 693/2$.

By combining Eqs. (A1), (A4), (A7), and (A9), we find the electron-phonon heat conductance for a spin-split superconductor: Eq. (14). At low temperatures, when $\tilde{\Delta} \gg 1$, scattering processes dominate the heat conductance. The two processes become of the same order of magnitude when $k_B T \approx 0.1\tilde{\Delta}$. At high temperatures, recombination processes dominate.

-
- [1] D. Hanson, S. Hoover, A. Crites, P. Ade, K. Aird, J. Austermann, J. Beall, A. Bender, B. Benson, and L. Bleem *et al.*, Detection of B-Mode Polarization in the Cosmic Microwave Background with Data from the South Pole Telescope, *Phys. Rev. Lett.* **111**, 141301 (2013).
 [2] P. Ade, Y. Akiba, A. Anthony, K. Arnold, M. Atlas, D. Barron, D. Boettger, J. Borrill, S. Chapman, and Y. Chinone

- et al.*, A measurement of the cosmic microwave background b-mode polarization power spectrum at subdegree scales with polarbear, *Astrophys. J.* **794**, 171 (2014).
- [3] M. Madhavacheril, N. Sehgal, R. Allison, N. Battaglia, J. R. Bond, E. Calabrese, J. Caligiuri, K. Coughlin, D. Crichton, and R. Datta *et al.*, Evidence of Lensing of the Cosmic Microwave Background by Dark Matter Halos, *Phys. Rev. Lett.* **114**, 151302 (2015).
- [4] D. Farrah, K. E. Smith, D. Ardila, C. M. Bradford, M. Dipirro, C. Ferkinhoff, J. Glenn, P. Goldsmith, D. Leisawitz, and T. Nikola *et al.*, Far-infrared instrumentation and technology development for the next decade, arXiv:1709.02389.
- [5] M. K. A. Luukanen, R. Appleby, and N. Salmon, in Millimeter-Wave and Terahertz Imaging in Security Applications, *Terahertz Spectroscopy and Imaging*, edited by K. E. Peiponen, A. Zeitler and M. Kuwata-Gonokami (Springer, Berlin Heidelberg, 2013), Chap., p. 491.
- [6] J. N. Ullom and D. A. Bennett, Review of superconducting transition-edge sensors for x-ray and gamma-ray spectroscopy, *Supercond. Sci. Technol.* **28**, 084003 (2015).
- [7] M. Palosaari, M. Käyhkö, K. Kinnunen, M. Laitinen, J. Julin, J. Malm, T. Sajavaara, W. Doriese, J. Fowler, and C. Reintsema *et al.*, Broadband Ultrahigh-Resolution Spectroscopy of Particle-Induced X Rays: Extending the Limits of Nondestructive Analysis, *Phys. Rev. Appl.* **6**, 024002 (2016).
- [8] L. Miaja-Avila, G. C. O'Neil, Y. I. Joe, B. K. Alpert, N. H. Damrauer, W. B. Doriese, S. M. Fatur, J. W. Fowler, G. C. Hilton, and R. Jimenez *et al.*, Ultrafast Time-Resolved Hard X-Ray Emission Spectroscopy on a Tabletop, *Phys. Rev. X* **6**, 031047 (2016).
- [9] E. N. Grossman, D. G. McDonald, and J. Sauvageau, Far-infrared kinetic-inductance detectors, *IEEE Trans. Magn.* **27**, 2677 (1991).
- [10] N. Bluzer and M. G. Forrester, Superconducting quantum detectors, *Opt. Eng.* **33**, 697 (1994).
- [11] A. Sergeev, V. Mitin, and B. Karasik, Ultrasensitive hot-electron kinetic-inductance detectors operating well below the superconducting transition, *Appl. Phys. Lett.* **80**, 817 (2002).
- [12] F. Giazotto, T. T. Heikkilä, G. P. Pepe, P. Helistö, A. Luukanen, and J. P. Pekola, Ultrasensitive proximity Josephson sensor with kinetic inductance readout, *Appl. Phys. Lett.* **92**, 162507 (2008).
- [13] J. Govenius, R. Lake, K. Tan, and M. Möttönen, Detection of Zeptojoule Microwave Pulses Using Electrothermal Feedback in Proximity-Induced Josephson Junctions, *Phys. Rev. Lett.* **117**, 030802 (2016).
- [14] P. K. Day, H. G. LeDuc, B. A. Mazin, A. Vayonakis, and J. Zmuidzinas, A broadband superconducting detector suitable for use in large arrays, *Nature* **425**, 817 (2003).
- [15] R. C. Jones, The ultimate sensitivity of radiation detectors, *JOSA* **37**, 879 (1947).
- [16] A. Varpula, A. V. Timofeev, A. Shchepetov, K. Grigoras, J. Hassel, J. Ahopelto, M. Ylilammi, and M. Prunnila, Thermoelectric thermal detectors based on ultra-thin heavily doped single-crystal silicon membranes, *Appl. Phys. Lett.* **110**, 262101 (2017).
- [17] D. V. Vechten, K. Wood, G. Fritz, A. Gyulamiryan, V. Nikogosoyan, N. Giordano, T. Jacobs, and A. Gulian, Thermoelectric single-photon detectors: Isotropic seebeck sensors, in *Eighteenth International Conference on Thermo-electrics*, IEEE, Baltimore, (1999).
- [18] Patent pending, filing number IT 102017000107007.
- [19] A. Ozaeta, P. Virtanen, F. Bergeret, and T. Heikkilä, Predicted Very Large Thermoelectric Effect in Ferromagnet-Superconductor Junctions in the Presence of a Spin-Splitting Magnetic Field, *Phys. Rev. Lett.* **112**, 057001 (2014).
- [20] P. Machon, M. Eschrig, and W. Belzig, Nonlocal Thermoelectric Effects and Nonlocal Onsager Relations in a Three-Terminal Proximity-Coupled Superconductor-Ferromagnet Device, *Phys. Rev. Lett.* **110**, 047002 (2013).
- [21] S. Kolenda, M. J. Wolf, and D. Beckmann, Observation of Thermoelectric Currents in High-Field Superconductor-Ferromagnet Tunnel Junctions, *Phys. Rev. Lett.* **116**, 097001 (2016).
- [22] F. S. Bergeret, M. Silaev, P. Virtanen, and T. T. Heikkilä, Nonequilibrium effects in superconductors with a spin-splitting field, arXiv:1706.08245.
- [23] F. Giazotto, P. Solinas, A. Braggio, and F. Bergeret, Ferromagnetic-Insulator-Based Superconducting Junctions as Sensitive Electron Thermometers, *Phys. Rev. Appl.* **4**, 044016 (2015).
- [24] The system presented in Fig. 1 is perhaps the simplest realization that does not require an external magnetic field. Alternatively, the upper superconductor-insulator-ferromagnet part could be replaced by either superconductor-ferromagnetic insulator-normal metal or superconductor-ferromagnetic insulator-superconductor, where the ferromagnetic insulator would act as the spin filter. In that case it would also be possible to remove the lower ferromagnetic insulator.
- [25] J. Moodera, X. Hao, G. Gibson, and R. Meservey, Electron-Spin Polarization in Tunnel Junctions in Zero Applied Field with Ferromagnetic Eus Barriers, *Phys. Rev. Lett.* **61**, 637 (1988).
- [26] P. Tedrow, J. Tkaczyk, and A. Kumar, Spin-Polarized Electron Tunneling Study of an Artificially Layered Superconductor with Internal Magnetic Field: Euo-al, *Phys. Rev. Lett.* **56**, 1746 (1986).
- [27] A. M. Clogston, Upper Limit for the Critical Field in Hard Superconductors, *Phys. Rev. Lett.* **9**, 266 (1962).
- [28] J. Alexander, T. Orlando, D. Rainer, and P. Tedrow, Theory of fermi-liquid effects in high-field tunneling, *Phys. Rev. B* **31**, 5811 (1985).
- [29] R. Meservey and P. Tedrow, Spin-polarized electron tunneling, *Phys. Rep.* **238**, 173 (1994).
- [30] J. S. Moodera and R. H. Meservey, in *Magneto-electronics*, edited by M. Johnson (Academic Press, San Diego, 2004), p. 151.
- [31] J. S. Moodera, T. S. Santos, and T. Nagahama, The phenomena of spin-filter tunnelling, *J. Phys. Condens. Matter* **19**, 165202 (2007).
- [32] We choose the convention where the heat currents are into the absorber, and charge currents are out of it. Alternative conventions lead to some sign changes in the equations.
- [33] Note that zT is not the zero-frequency limit of ZT , but should be considered as a definition.
- [34] F. Giazotto, T. T. Heikkilä, A. Luukanen, A. M. Savin, and J. P. Pekola, Opportunities for mesoscopies in thermometry

- and refrigeration: Physics and applications, *Rev. Mod. Phys.* **78**, 217 (2006).
- [35] P. Virtanen, T. Heikkilä, and F. Bergeret, Stimulated quasi-particles in spin-split superconductors, *Phys. Rev. B* **93**, 014512 (2016).
- [36] E. Strambini, V. Golovach, G. De Simoni, J. Moodera, F. Bergeret, and F. Giazotto, Revealing the magnetic proximity effect in eus/al bilayers through superconducting tunneling spectroscopy, *Phys. Rev. Mater.* **1**, 054402 (2017).
- [37] B. S. Karasik and R. Cantor, Demonstration of high optical sensitivity in far-infrared hot-electron bolometer, *Appl. Phys. Lett.* **98**, 193503 (2011).
- [38] A. D. Beyer, M. Kenyon, P. Echternach, B. Bumble, M. Runyan, T. Chui, C. Bradford, W. Holmes, and J. Bock, in *Millimeter, Submillimeter, and Far-Infrared Detectors and Instrumentation for Astronomy VI* (International Society for Optics and Photonics, 2012), Vol. 8452, p. 84520G.
- [39] T. Suzuki, P. Khosropanah, M. Ridder, R. Hijmering, J. Gao, H. Akamatsu, L. Gottardi, J. van der Kuur, and B. Jackson, Development of ultra-low-noise tes bolometer arrays, *J. Low Temp. Phys.* **184**, 52 (2016).
- [40] N. Poli, J. P. Morten, M. Urech, A. Brataas, D. B. Haviland, and V. Korenivski, Spin Injection and Relaxation in a Mesoscopic Superconductor, *Phys. Rev. Lett.* **100**, 136601 (2008).
- [41] N. Beev and M. Kiviranta, Fully differential cryogenic transistor amplifier, *Cryogenics* **57**, 129 (2013).
- [42] A. Svilans, M. Leijnse, and H. Linke, Experiments on the thermoelectric properties of quantum dots, *C. R. Phys.* **17**, 1096 (2016).

IV

MEAN-FIELD THEORY FOR SUPERCONDUCTIVITY IN TWISTED BILAYER GRAPHENE

by

T.J. Peltonen, R. Ojajärvi, and T.T. Heikkilä 2018


Physical Review B **98**, 220504(R), DOI:[10.1103/PhysRevB.98.220504](https://doi.org/10.1103/PhysRevB.98.220504)

Reproduced with permission. Copyright 2018 American Physical Society.

Mean-field theory for superconductivity in twisted bilayer graphene

Teemu J. Peltonen, Risto Ojajarvi, and Tero T. Heikkilä

Department of Physics and Nanoscience Center, University of Jyväskylä, P.O. Box 35 (YFL), FI-40014 University of Jyväskylä, Finland

 (Received 11 May 2018; published 10 December 2018)

Recent experiments show how a bilayer graphene twisted around a certain magic angle becomes superconducting as it is doped into a region with approximate flat bands. We investigate the mean-field s -wave superconducting state in such a system and show how the state evolves as the twist angle is tuned, and as a function of the doping level. We argue that part of the experimental findings could well be understood to result from an attractive electron-electron interaction mediated by electron-phonon coupling, but the flat-band nature of the excitation spectrum also makes the superconductivity quite unusual. For example, as the flat-band states are highly localized around certain spots in the structure, also the superconducting order parameter becomes strongly inhomogeneous.

DOI: [10.1103/PhysRevB.98.220504](https://doi.org/10.1103/PhysRevB.98.220504)

I. INTRODUCTION

Experiments on strongly doped graphene [1–4] have shown that with proper preparations, graphene can be driven to the superconducting state. Such experiments indicate that the lack of superconductivity in undoped graphene is not necessarily due to a lack of an (effective) attractive electron-electron interaction with strength λ that would drive graphene to be superconducting, but rather the small density of states (DOS) close to the Dirac point. Technically, in contrast to the Cooper instability for metals taking place with arbitrarily small λ , superconductivity in an electron system with a massless Dirac dispersion $\epsilon_p^2 = v_F^2 p^2$ and an energy cutoff ϵ_c has a quantum critical point [5] $\lambda_c = \pi \hbar^2 v_F^2 / (2\epsilon_c)$ such that for $\lambda < \lambda_c$, mean-field superconductivity does not show up at any temperature. From this perspective, doping to a potential μ leads to an increased DOS, and thereby to a nonvanishing critical temperature $T_c \approx |\mu| \exp[-(\lambda_c/\lambda - 1)\epsilon_c/|\mu| - 1]$. An alternative approach would be to change the spectrum and increase the density of states close to the Dirac point. The extreme limit would be an approximately flat band of size Ω_{FB} , where the group velocity tends to zero. In such systems the critical temperature is a linear function of the coupling strength [6,7], $T_c = \lambda \Omega_{\text{FB}} / \pi^2$, and a quite high T_c can be expected even without extra doping [8–13].

Recent observations [14] of superconductivity in twisted bilayer graphene [TBG, see Fig. 1(a)] take place in systems where theoretical studies have predicted the occurrence of asymptotically flat bands [15–25]. There have been many suggestions of an unconventional superconducting state both for regular graphene [26,27] and for TBG [24,28–36], typically directly related with the Coulomb interaction, and in some cases related with nonlocal interactions. Here, we study the mean-field theory of superconductivity in such systems, starting instead from the hypothesis that the observations could be explained with the conventional electron-phonon mechanism from the flat-band perspective [37]. This hypothesis is justified on the grounds that the relative strength and the screening of attractive and repulsive interactions are

uncertain. Furthermore, phonon-mediated attraction is considered a viable mechanism for the observed superconductivity on doped graphene [1–4,38].

In particular, we use the model of Refs. [15,20] for the spectrum of the twisted bilayer, add an on-site (leading to s -wave superconductivity) attractive interaction of strength λ , and evaluate the mean-field order parameter profile. We find that the order parameter, and along with it the mean-field critical temperature, have a similar nonmonotonous behavior with respect to the twist angle as in the experiments. We also predict the behavior of the density of states in the superconducting state, resulting from the peculiarities of the flat-band eigenstates and from the position dependence of the superconducting order parameter [Fig. 1(b)]. Even if our pairing interaction is quite simple, the resulting energy-dependent density

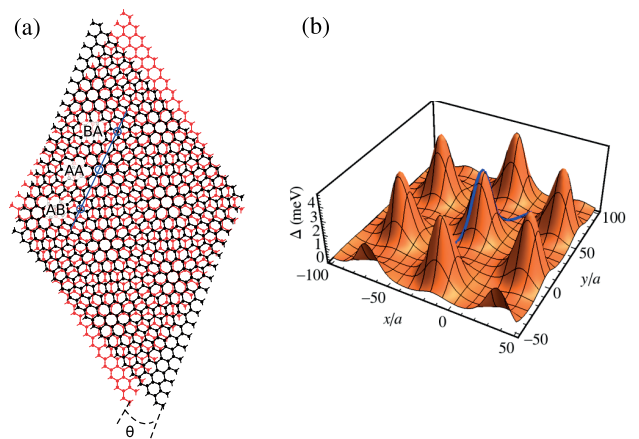


FIG. 1. (a) Twisted bilayer graphene and its moiré superlattice. The upper layer is rotated by an angle θ relative to the lower layer. (b) Position dependence of the self-consistent Δ , shown here at $T = 0$ for the magic angle $\theta = 0.96^\circ$ and $\lambda = 5 \text{ eV } a^2$. In both figures also a line passing through high-symmetry points with AB, AA, and BA stacking is shown.

of states is quite unusual. In addition, we show how doping away from the flat band eventually destroys superconductivity.

II. NORMAL STATE

We describe the normal state of TBG with the model of Refs. [15,20]. With this model, we can describe the twist angles θ at which the lattices L and L^θ of the two graphene layers are commensurate, so that the system as a whole is periodic in the moiré superlattice SL . Here, we study only the simple commensurate structures, characterized by a single rotation parameter $m \in \mathbb{N}$, for which the rotation angle is given by

$$\cos(\theta) = \frac{3m^2 + 3m + 1/2}{3m^2 + 3m + 1}. \quad (1)$$

$$\mathcal{H}_{\rho k}(\mathbf{G}, \mathbf{G}') = \begin{pmatrix} [\hbar v_F \boldsymbol{\sigma}^\rho \cdot (\mathbf{k} + \mathbf{G} + \rho \Delta \mathbf{K}/2) - \mu] \delta_{\mathbf{G}, \mathbf{G}'} & t_\perp^\rho(\mathbf{G} - \mathbf{G}') \\ t_\perp^\rho(\mathbf{G}' - \mathbf{G})^\dagger & [\hbar v_F \boldsymbol{\sigma}_\theta^\rho \cdot (\mathbf{k} + \mathbf{G} - \rho \Delta \mathbf{K}/2) - \mu] \delta_{\mathbf{G}, \mathbf{G}'} \end{pmatrix}, \quad (2)$$

where the matrix structure corresponds to the layer structure and $\rho \in \{+, -\}$ is the valley index with $+$ corresponding to \mathbf{K} and $-$ to $\mathbf{K}' = -\mathbf{K}$. Furthermore, each entry is a 2×2 matrix due to the sublattice structure in graphene. The diagonal terms in Eq. (2) describe the Dirac dispersion in the two layers and are diagonal also in \mathbf{G} . Here, $\boldsymbol{\sigma}^\rho = (\rho \sigma_x, \rho \sigma_y)$. For the second layer we include the rotation θ so that $\boldsymbol{\sigma}_\theta^\rho = e^{+i\theta \sigma_z/2} \boldsymbol{\sigma}^\rho e^{-i\theta \sigma_z/2}$. $\Delta \mathbf{K} = \mathbf{K}^\theta - \mathbf{K}$ is the relative shift of the Dirac cones between the layers. The coordinates correspond to those of layer 1 as measured from the \mathbf{K} point, but shifted with a vector $+\Delta \mathbf{K}/2$ for layer 1 and $-\Delta \mathbf{K}/2$ for layer 2. With this choice, the relative momentum \mathbf{k} on both layers corresponds to the same absolute momentum. Furthermore, μ is the chemical potential describing the effect of doping, here taken to be equal in both layers.

The off-diagonal terms in the Hamiltonian describe the coupling between the two layers. The matrix element at valley ρ between a state in sublattice α in layer 1 and a state in sublattice β in layer 2 is

$$t_\perp^{\rho, \alpha\beta}(\mathbf{G}) = \frac{1}{N} \sum_{\mathbf{r}} e^{-i\mathbf{G} \cdot (\mathbf{r} + \delta_{\alpha\beta} \delta_1)} e^{i\rho \mathbf{K}^\theta \cdot \delta^{\alpha\beta}(\mathbf{r})} t_\perp[\delta^{\alpha\beta}(\mathbf{r})], \quad (3)$$

where $\delta^{\alpha\beta}(\mathbf{r})$ is the horizontal displacement vector between the site at \mathbf{r} , sublattice α in layer 1, and the nearest neighbor at sublattice β in layer 2. δ_1 denotes one of the nearest-neighbor vectors connecting the graphene A and B sublattices. The sum is over the graphene A sublattice sites in the superlattice unit cell, and N denotes the number of these sites. For the interlayer hopping energy $t_\perp(\delta)$ we use the same Slater-Koster parametrization as in Ref. [15]. Furthermore, we approximate the interlayer coupling by only including the matrix elements with $\mathbf{G} \in \{0, -\mathbf{G}_1, -\mathbf{G}_1 - \mathbf{G}_2\}$ (valley \mathbf{K}) or $\mathbf{G} \in \{0, \mathbf{G}_1, \mathbf{G}_1 + \mathbf{G}_2\}$ (valley \mathbf{K}'), since they are an order of magnitude larger than the rest.

For $\theta \approx 1^\circ$, the electronic dispersion becomes almost flat [19] and the group velocity $d\epsilon_p/dp$ tends towards zero. In Fig. 2 we plot the resulting normal-state dispersion

According to Ref. [20], these structures approximate arbitrary commensurate structures. The primitive vectors of the superlattice SL are given by $\mathbf{t}_1 = m\mathbf{a}_1 + (m+1)\mathbf{a}_2$, $\mathbf{t}_2 = -(m+1)\mathbf{a}_1 + (2m+1)\mathbf{a}_2$, and the primitive vectors of the reciprocal superlattice SL^* are $\mathbf{G}_1 = \frac{4\pi}{3|\mathbf{t}_1|^2}[(3m+1)\mathbf{a}_1 + \mathbf{a}_2]$, $\mathbf{G}_2 = \frac{4\pi}{3|\mathbf{t}_1|^2}[-(3m+2)\mathbf{a}_1 + (3m+1)\mathbf{a}_2]$, where the lattice constant of the superlattice is $|\mathbf{t}_1| = \sqrt{3m^2 + 3m + 1}a$ and the graphene lattice primitive vectors are $\mathbf{a}_1 = (1, \sqrt{3})a/2$ and $\mathbf{a}_2 = (-1, \sqrt{3})a/2$ with a the lattice constant [15]. In the following, we assume that $\mathbf{G} \in SL^*$ belongs to the reciprocal superlattice, $\mathbf{k} \in \mathbb{R}^2/SL^*$ to the first Brillouin zone of the superlattice, and also that the corresponding sums and integrals are restricted to these sets.

In the normal state, TBG is described by a low-energy effective Hamiltonian [15]

[Figs. 2(a)–2(c)] and the (local and total) density of states [Figs. 2(d)–2(i)] close to this “magic” angle. The exact value of this magic angle depends on the details of the hopping model. In our case it is around 0.96° , i.e., somewhat lower than what was found in Ref. [19]. However, the qualitative behavior of the local density of states (LDOS) is rather similar to the previous models. In particular, there are two closely spaced DOS peaks signifying the flattening of the bands. The local density of states is plotted along the line shown in Fig. 1, including three high-symmetry points with AB, AA, and BA stacking. These correspond to $r = -1/3, 0$, and $1/3$, respectively.

III. SUPERCONDUCTING STATE

We assume that there is a local attractive interaction $\lambda_{\sigma_1 \sigma_2}(\mathbf{r}_1, \mathbf{r}_2) = \delta_{\sigma_1 \sigma_2} \delta(\mathbf{r}_1 - \mathbf{r}_2) \lambda$ with strength λ , which results [7] in an order parameter $\Delta_{\alpha i}(\mathbf{r})$ depending only on the center-of-mass coordinate \mathbf{r} (and sublattice α and layer i). On the other hand, the classification of the order parameter symmetries to s, d, f , etc., is based only on the relative coordinate $\mathbf{r}_1 - \mathbf{r}_2$, which in our model is always zero. Thus the symmetry is purely s wave.

We do not consider the specific nature of the pairing interaction and for the purposes of this Rapid Communication it can be mediated by phonons or other bosonic modes. This model disregards the retardation effects due to such a mechanism, but is a valid approximation to the more general Eliashberg approach for weak coupling [39,40]. That theory also shows that a direct Coulomb interaction, typically modeled via the Hubbard model, is less effective in reducing Δ than what could be naively expected, and should be included in the low-energy self-consistency equation as a Coulomb pseudopotential [7,40,41] $u^* = u/(1 + u\alpha)$, where $u = Ua^2$, U is the Hubbard interaction constant, and α is a constant measuring the amount of renormalization due to the high-energy bands above the electron-phonon cutoff frequency

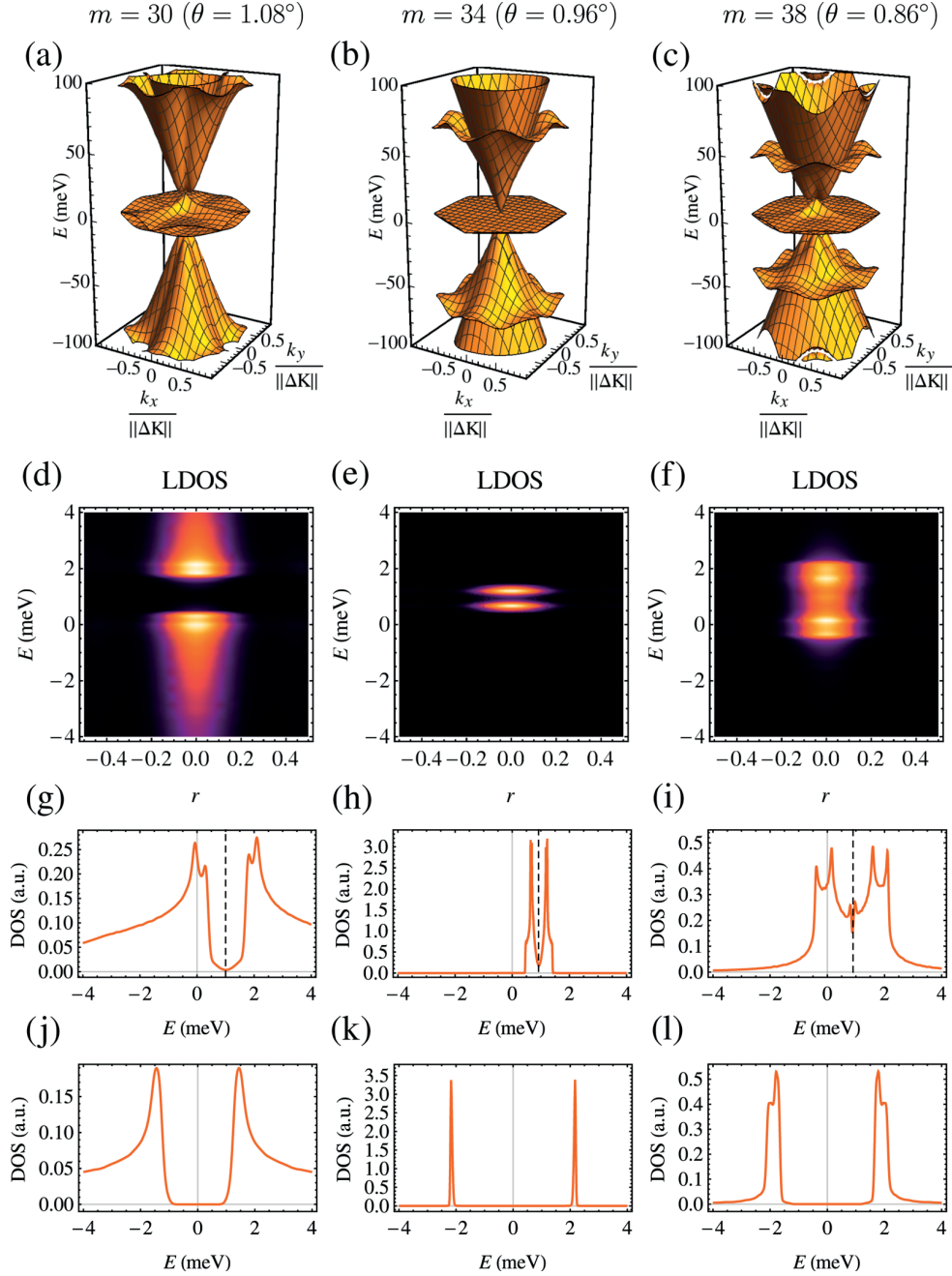


FIG. 2. (a)–(c) Normal-state dispersion, (d)–(f) local, and (g)–(i) total density of states for three different angles near the magic angle $\theta = 0.96^\circ$ in the normal state. The bottom row (j)–(l) shows the corresponding total density of states in the superconducting state, in the case $T = 0$ and $\lambda = 5 \text{ eV } \text{\AA}^2$ and when doped to the point μ_0 marked as a dashed line in (g)–(i).

ω_D . For TBG we find from a simplified model [7] $\alpha \approx 0.2 \text{ eV}^{-1} \text{\AA}^{-2}$. Thus, a combination of electron-phonon and Coulomb interactions leads to an effective interaction strength $\lambda_{\text{eff}} = \lambda - u^*$. As long as $\lambda_{\text{eff}} > 0$, there is a possibility for a superconducting state even if $u > \lambda$. For example, for $U = 5 \text{ eV}$, $u^* = 2.5 \text{ eV } \text{\AA}^2$ is in the same regime as the value of λ_{eff} in Figs. 3–5. Note that in what follows, we refer to this λ_{eff} simply as λ .

Within a mean-field theory in the Cooper channel we find a self-consistency equation for a local superconducting order

parameter [7]. Assuming that this order parameter shares the periodicity of the moiré superlattice, we find the self-consistency equation

$$\Delta_{\alpha i}(\mathbf{G}) = \lambda \sum_{\rho, b} \sum_{\mathbf{G}'} \int \frac{d\mathbf{k}}{(2\pi)^2} \tanh\left(\frac{E_{\rho b \mathbf{k}}}{2k_B T}\right) \times u_{\rho b \mathbf{k}, \alpha i}(\mathbf{G}') v_{\rho b \mathbf{k}, \alpha i}^*(\mathbf{G}' - \mathbf{G}), \quad (4)$$

where the band sum b is calculated over the positive energy bands, $\alpha \in \{A, B\}$ is the sublattice index, $i \in \{1, 2\}$ is the

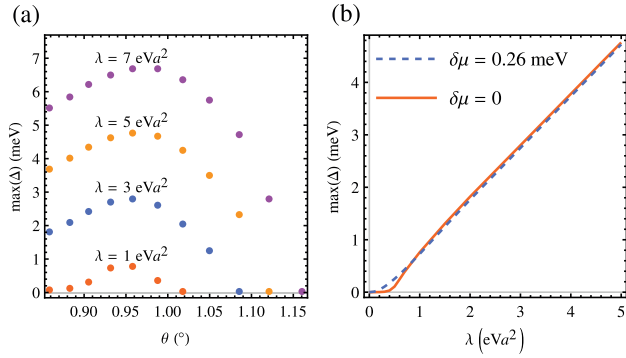


FIG. 3. Maximum of the position-dependent superconducting order parameter $\Delta(\mathbf{r})$ at $T = 0$ as a function of (a) the rotation angle and (b) the coupling strength for $\theta = 0.96^\circ$. In (b) we also show how doping to the DOS peak affects the small- λ behavior.

layer index, and $u_{\rho bk}$ and $v_{\rho bk}$ are the eigenvectors of the Bogoliubov–de Gennes equation,

$$\sum_{\mathbf{G}'} \begin{pmatrix} \mathcal{H}_{\rho k}(\mathbf{G}, \mathbf{G}') & \Delta(\mathbf{G} - \mathbf{G}') \\ \Delta^*(\mathbf{G}' - \mathbf{G}) & -\mathcal{H}_{\rho k}(\mathbf{G}, \mathbf{G}') \end{pmatrix} \begin{pmatrix} u_{\rho bk}(\mathbf{G}') \\ v_{\rho bk}(\mathbf{G}') \end{pmatrix} = E_{\rho bk} \begin{pmatrix} u_{\rho bk}(\mathbf{G}) \\ v_{\rho bk}(\mathbf{G}) \end{pmatrix}. \quad (5)$$

We solve this self-consistent order parameter with a few values of the interaction constant λ and for a few different twist angles θ close to the magic angle. We include in the sum the energy levels closest to zero energy. We have checked that the results are not sensitive to the value of the energy cutoff, which we implement as a cutoff in the b and \mathbf{G} sums. For comparison between different angles, we measure the chemical potential from μ_0 , corresponding to the charge neutrality and marked in Figs. 2(g)–2(i) with a dashed line, by writing $\mu = \mu_0 + \delta\mu$. The chemical potential shift μ_0 is caused by the interlayer coupling. Unless otherwise stated, all the results concern the behavior at $\delta\mu = 0$. The resulting total density of states is plotted in Figs. 2(j)–2(k), to allow for a comparison to the normal state. The corresponding local density of states (not shown) has the same localized structure as in the normal state, but the energy dependence is modified similarly as the total DOS. The effect of finite temperature on the superconducting DOS and LDOS happens solely via $\Delta(T)$, which is calculated below.

The maximum of the position-dependent Δ , which according to numerics is equal in both layers and sublattices, is plotted in Fig. 3(a) for different values of the twist angle and for four different coupling strengths. The precise angle for the maximum depends a bit on the chosen coupling strength. Moreover, $\max(\Delta)$ is almost a linear function of λ [see Fig. 3(b)], as appropriate for a flat-band superconductor [6]. This linearity is even more pronounced when the system is doped to the DOS peak at $\delta\mu \approx 0.26$ meV. Far from the magic angle, the Fermi speed $v_F(\theta)$ increases so that the chosen λ is below the critical value λ_c . This is why Δ vanishes for angles $\theta \gtrsim 1.1^\circ$.

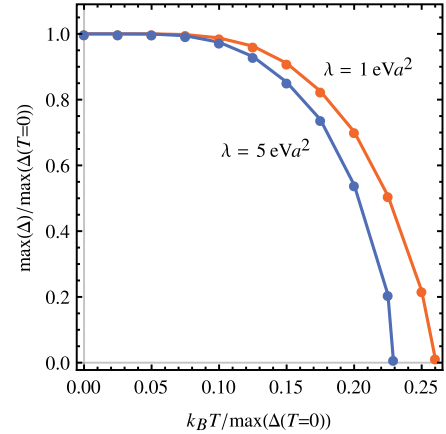


FIG. 4. $\max(\Delta)$ as a function of temperature in the case $\theta = 0.96^\circ$ for two values of λ , showing the approximate linear relation $k_B T_c \approx 0.25 \max[\Delta(T=0)]$ for the critical temperature. The dots are the calculated values and the lines are a guide to the eye.

We can analyze the resulting magnitude of Δ based on a flat-band result (assuming a position-independent Δ and $E_{\rho bk} \approx \Delta$ for an extreme flat band) according to which [7] $\Delta = \lambda \Omega_{\text{FB}} / \pi^2$, where $\Omega_{\text{FB}} \approx \Omega_{\text{moiré}} = 8\pi^2 / (\sqrt{3} |\mathbf{t}_1|^2)$. This yields $\Delta = 1.3 \times 10^{-3} \lambda / a^2$ for $m = 34$ corresponding to the magic angle. For comparison, a linear fit to the linear region in Fig. 3(b) gives $\max(\Delta) = -0.2 \text{ meV} + 1.0 \times 10^{-3} \lambda / a^2$. The magnitude hence agrees very well with this simple model. Note that the precise values of these parameters especially for small λ depend on the exact value of doping as shown below.

In Fig. 4 we show the temperature dependence of Δ for $m = 34$, from which we may infer the approximate linear relation $k_B T_c \approx 0.25 \max[\Delta(T=0)]$ for the critical temperature. The prefactor is somewhat lower than for an extreme flat band with a constant Δ , for which [7] $k_B T_c = \Delta/2$. The difference is most likely explained by the nonvanishing bandwidth and the position-dependent Δ of our model. The maximum critical temperatures for the models calculated in Fig. 3(a) range from 3 to about 20 K. The lower end of these values, calculated with $\lambda = 1 \text{ eV } a^2$, is thus quite close to that found in Ref. [14].

We stress that the above result is the mean-field critical temperature; the observed resistance transition is most likely rather a Berezinskii-Kosterlitz-Thouless (BKT) transition [42,43]. Therefore, the mean-field T_c gives an upper bound for the measured transition temperature. Furthermore, even the BKT transition temperature can be calculated from the mean-field superfluid weight [44]. The mean-field results are also relevant in that the DOS and LDOS can be experimentally measured by tunneling experiments and this depends on the structure and magnitude of mean-field Δ at temperatures below the BKT transition. Note that despite the flatness of the bands, the supercurrent can be nonvanishing in the case when the eigenstate Wannier functions overlap [45], as is the case for TBG.

Besides θ dependence, we can check how doping away from the center of the two DOS peaks affects the superconducting state. In Fig. 5(a) we plot the order parameter

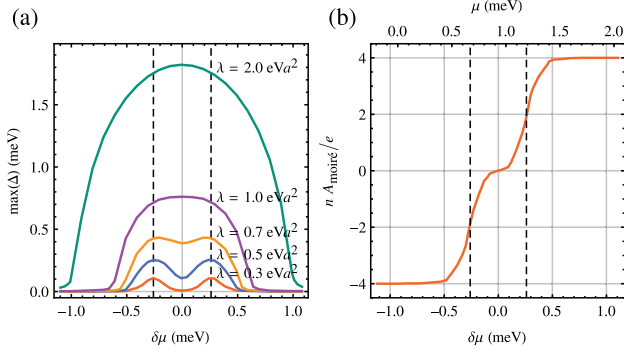


FIG. 5. Effects of electrostatic doping $\mu = \mu_0 + \delta\mu$ for $\theta = 0.96^\circ$. (a) $\max(\Delta)$ vs chemical potential for various values of λ at $T = 0$. (b) Charge density in the normal state at $T = 0$ as a function of chemical potential. The units of the charge density n are $e/A_{\text{moiré}}$, where e is the electron charge and $A_{\text{moiré}}$ is the area of the moiré unit cell. In both figures the vertical dashed lines mark the location of the DOS peaks at $\delta\mu \approx \pm 0.26$ meV.

$\max[\Delta(\delta\mu)]$ for different values of the doping $\delta\mu$ as measured from the charge neutrality point. Close to the magic angle, for $\lambda \gtrsim 1$ eV a^2 the energy scale of superconductivity exceeds that of the normal-state dispersion, and hence the only effect of the doping is to move away from the flat-band regime, suppressing superconductivity [46]. For smaller values of λ , $\max(\Delta)$ is smaller than the bandwidth, and hence doping to the DOS peaks enhances superconductivity. Especially for $\lambda \lesssim 0.3$ eV a^2 there are separate superconducting domes with doping levels close to the DOS peaks, which resembles the phase diagram in Ref. [14] for hole ($n < 0$) doping, apart from the insulating state at $n \approx -2e/A_{\text{moiré}}$. For electron doping ($n > 0$), superconductivity is absent in the experiment, whereas our model is electron-hole symmetric. Since Ref. [14] uses charge density n as a unit for the doping level while our theory is formulated in terms of the chemical potential μ , for easier comparison we show the dependence between the charge density [7] and chemical potential in Fig. 5(b). From the figure we find that the DOS peaks correspond to approximately ± 2 extra electrons per moiré unit cell.

IV. CONCLUSIONS

Concluding, we find that a BCS-type mean-field model with a relatively weak attractive interaction constant possibly even due to electron-phonon coupling can explain the occurrence of superconductivity in twisted bilayer graphene. We also make a number of predictions concerning the mean-field superconducting state, in particular, the density of states and

doping dependence. Our results form hence a checkpoint for further studies, that use a simplified picture of the TBG flat-band states or consider mechanisms beyond the one in this Rapid Communication. Our results could also have relevance in explaining the observations of superconductivity in twisted interfaces of graphite [47–49].

Our mean-field theory fails to explain the insulator state [50] found experimentally in TBG at $n \approx \pm 2e/A_{\text{moiré}}$ as well as the lack of superconductivity for electron doping [14,51]. However, the latter of these cannot be seen as a drawback of our model as in another experiment [52] some samples were found to be superconducting also on the electron-doped side, and thus it clearly depends on the samples and on the experimental setup. Regarding the insulator phase, it is plausible that the mean-field theory fails when the doping level corresponds to an integer number of electrons per superlattice unit cell. The biggest discrepancy is, however, most likely caused by the possible dependence of λ_{eff} on the charge density, because the effect of the Coulomb interaction depends on charge screening. Within the flat-band model of Ref. [40], the case $\lambda_{\text{eff}} > 0$ corresponds to a superconducting state, whereas for $\lambda_{\text{eff}} < 0$ an insulating antiferromagnetic state is realized. Thus, by taking the chemical potential dependence of λ_{eff} into account, it may be possible to describe both superconducting and insulating phases found in the experiment [14]. A detailed description would require generalizing Refs. [40,53] to the TBG case.

We point out that our simple BCS model disregards the strain effects in moiré bands, as well as the possible dependence of the interaction constant on the twist angle and doping level. Whereas such mechanisms may play a role in TBG, we believe that the simplest BCS-type mean-field superconductivity should also be considered as a viable effective model of the observations. Nevertheless, even in this case superconductivity would be highly exceptional, for example, because it can be so strongly controlled by electrostatic doping.

Note added. Recently, we became aware of Ref. [54], which addressed a similar BCS-type model as here, obtaining consistent results with this Rapid Communication. In addition to local interactions leading to s -wave superconductivity, they considered also nonlocal interactions opening the possibility to d -wave superconductivity. They found out that without including Coulomb repulsion the s -wave channel is more stable, having a higher T_c .

ACKNOWLEDGMENTS

This project was supported by Academy of Finland Key Project funding, and the Center of Excellence program (Projects No. 305256 and No. 284594). We acknowledge grants of computer capacity from the Finnish Grid and Cloud Infrastructure (persistent identifier urn:nbn:fi:research-infras-2016072533).

[1] B. M. Ludbrook, G. Levy, P. Nigge, M. Zonno, M. Schneider, D. J. Dvorak, C. N. Veenstra, S. Zhdanovich, D.

Wong, P. Dosanjh *et al.*, *Proc. Natl. Acad. Sci. U.S.A.* **112**, 11795 (2015).

- [2] A. P. Tiwari, S. Shin, E. Hwang, S.-G. Jung, T. Park, and H. Lee, *J. Phys.: Condens. Matter* **29**, 445701 (2017).
- [3] J. Chapman, Y. Su, C. A. Howard, D. Kundys, A. N. Grigorenko, F. Guinea, A. K. Geim, I. V. Grigorieva, and R. R. Nair, *Sci. Rep.* **6**, 23254 (2016).
- [4] S. Ichinokura, K. Sugawara, A. Takayama, T. Takahashi, and S. Hasegawa, *ACS Nano* **10**, 2761 (2016).
- [5] N. B. Kopnin and E. B. Sonin, *Phys. Rev. Lett.* **100**, 246808 (2008).
- [6] T. T. Heikkilä, N. B. Kopnin, and G. E. Volovik, *JETP Lett.* **94**, 233 (2011).
- [7] See Supplemental Material at <http://link.aps.org/supplemental/10.1103/PhysRevB.98.220504> for details of the derivation of the self-consistency equation, for the definition of the charge density, for a simplified model of the flat-band superconducting state, and for a calculation of the Coulomb pseudopotential, which includes Refs. [55,56].
- [8] V. A. Khodel' and V. R. Shaginyan, *Pis'ma Zh. Eksp. Teor. Fiz.* **51**, 488 (1990) [*JETP Lett.* **51**, 553 (1990)].
- [9] N. B. Kopnin, T. T. Heikkilä, and G. E. Volovik, *Phys. Rev. B* **83**, 220503(R) (2011).
- [10] E. Tang and L. Fu, *Nat. Phys.* **10**, 964 (2014).
- [11] V. J. Kauppila, F. Aikebaier, and T. T. Heikkilä, *Phys. Rev. B* **93**, 214505 (2016).
- [12] T. T. Heikkilä and G. E. Volovik, in *Basic Physics of Functionalized Graphite*, edited by P. D. Esquinazi (Springer, Berlin, 2016), pp. 123–143.
- [13] T. Löthman and A. M. Black-Schaffer, *Phys. Rev. B* **96**, 064505 (2017).
- [14] Y. Cao, V. Fatemi, S. Fang, K. Watanabe, T. Taniguchi, E. Kaxiras, and P. Jarillo-Herrero, *Nature (London)* **556**, 43 (2018).
- [15] J. M. B. Lopes dos Santos, N. M. R. Peres, and A. H. Castro Neto, *Phys. Rev. Lett.* **99**, 256802 (2007).
- [16] E. Suárez Morell, J. D. Correa, P. Vargas, M. Pacheco, and Z. Barticevic, *Phys. Rev. B* **82**, 121407(R) (2010).
- [17] E. J. Mele, *Phys. Rev. B* **81**, 161405(R) (2010).
- [18] E. J. Mele, *Phys. Rev. B* **84**, 235439 (2011).
- [19] R. Bistritzer and A. H. MacDonald, *Proc. Natl. Acad. Sci. U.S.A.* **108**, 12233 (2011).
- [20] J. M. B. Lopes dos Santos, N. M. R. Peres, and A. H. Castro Neto, *Phys. Rev. B* **86**, 155449 (2012).
- [21] A. K. Geim and I. V. Grigorieva, *Nature (London)* **499**, 419 (2013).
- [22] D. Weckbecker, S. Shallcross, M. Fleischmann, N. Ray, S. Sharma, and O. Pankratov, *Phys. Rev. B* **93**, 035452 (2016).
- [23] S. Fang and E. Kaxiras, *Phys. Rev. B* **93**, 235153 (2016).
- [24] A. Ramirez and J. L. Lado, *Phys. Rev. Lett.* **121**, 146801 (2018).
- [25] N. N. T. Nam and M. Koshino, *Phys. Rev. B* **96**, 075311 (2017).
- [26] B. Uchoa and A. H. Castro Neto, *Phys. Rev. Lett.* **98**, 146801 (2007).
- [27] R. Nandkishore, L. S. Levitov, and A. V. Chubukov, *Nat. Phys.* **8**, 158 (2012).
- [28] H. C. Po, L. Zou, A. Vishwanath, and T. Senthil, *Phys. Rev. X* **8**, 031089 (2018).
- [29] C. Xu and L. Balents, *Phys. Rev. Lett.* **121**, 087001 (2018).
- [30] C.-C. Liu, L.-D. Zhang, W.-Q. Chen, and F. Yang, *Phys. Rev. Lett.* **121**, 217001 (2018).
- [31] S. Ray and T. Das, [arXiv:1804.09674](https://arxiv.org/abs/1804.09674).
- [32] T. Huang, L. Zhang, and T. Ma, [arXiv:1804.06096](https://arxiv.org/abs/1804.06096).
- [33] J. F. Dodaro, S. A. Kivelson, Y. Schattner, X. Q. Sun, and C. Wang, *Phys. Rev. B* **98**, 075154 (2018).
- [34] G. Baskaran, [arXiv:1804.00627](https://arxiv.org/abs/1804.00627).
- [35] B. Roy and V. Juričić, [arXiv:1803.11190](https://arxiv.org/abs/1803.11190).
- [36] H. Guo, X. Zhu, S. Feng, and R. T. Scalettar, *Phys. Rev. B* **97**, 235453 (2018).
- [37] G. E. Volovik, *JETP Lett.* **107**, 516 (2018).
- [38] G. Profeta, M. Calandra, and F. Mauri, *Nat. Phys.* **8**, 131 (2012).
- [39] G. M. Éliashberg, *Zh. Eksp. Teor. Fiz.* **38**, 966 (1960) [*Sov. Phys. JETP* **11**, 696 (1960)].
- [40] R. Ojajärvi, T. Hyart, M. A. Silaev, and T. T. Heikkilä, *Phys. Rev. B* **98**, 054515 (2018).
- [41] P. Morel and P. Anderson, *Phys. Rev.* **125**, 1263 (1962).
- [42] V. L. Berezinskii, *Zh. Eksp. Teor. Fiz.* **61**, 1144 (1971) [*Sov. Phys. JETP* **34**, 610 (1972)].
- [43] J. M. Kosterlitz and D. J. Thouless, *J. Phys. C: Solid State Phys.* **6**, 1181 (1973).
- [44] A. Julku, L. Liang, and P. Törmä, *New J. Phys.* **20**, 085004 (2018).
- [45] S. Peotta and P. Törmä, *Nat. Commun.* **6**, 8944 (2015).
- [46] N. B. Kopnin and T. T. Heikkilä, in *Carbon-based Superconductors: Towards High- T_c Superconductivity*, edited by J. Haruyama (CRC Press, Boca Raton, FL, 2014), Chap. 9.
- [47] P. Esquinazi, *Pap. Phys.* **5**, 050007 (2013).
- [48] A. Ballestar, J. Barzola-Quiquia, T. Scheike, and P. Esquinazi, *New J. Phys.* **15**, 023024 (2013).
- [49] M. Stiller, P. D. Esquinazi, J. Barzola-Quiquia, and C. E. Precker, *J. Low Temp. Phys.* **191**, 105 (2018).
- [50] B. Padhi, C. Setty, and P. W. Phillips, *Nano Lett.* **18**, 6175 (2018).
- [51] Y. Cao, V. Fatemi, A. Demir, S. Fang, S. L. Tomarken, J. Y. Luo, J. D. Sanchez-Yamagishi, K. Watanabe, T. Taniguchi, E. Kaxiras, and P. Jarillo-Herrero, *Nature (London)* **556**, 80 (2018).
- [52] M. Yankowitz, S. Chen, H. Polshyn, K. Watanabe, T. Taniguchi, D. Graf, A. F. Young, and C. R. Dean, [arXiv:1808.07865](https://arxiv.org/abs/1808.07865).
- [53] E. H. Hwang, R. Sensarma, and S. Das Sarma, *Phys. Rev. B* **82**, 195406 (2010).
- [54] F. Wu, A. H. MacDonald, and I. Martin, [arXiv:1805.08735](https://arxiv.org/abs/1805.08735).
- [55] A. H. Castro Neto, F. Guinea, N. M. R. Peres, K. S. Novoselov, and A. K. Geim, *Rev. Mod. Phys.* **81**, 109 (2009).
- [56] D. K. Efetov and P. Kim, *Phys. Rev. Lett.* **105**, 256805 (2010).

Mean-field theory for superconductivity in twisted bilayer graphene: supplementary information

Teemu J. Peltonen,¹ Risto Ojajärvi,¹ and Tero T. Heikkilä¹

¹*Department of Physics and Nanoscience Center, University of Jyväskylä,
P.O. Box 35 (YFL), FI-40014 University of Jyväskylä, Finland*

(Dated: November 14, 2018)

Here we present the details of calculating the self-consistent order parameter of the twisted bilayer graphene. We also derive an expression that relates the charge density to the dispersion that we calculate. In addition, we present a simplified model which connects a given dispersion relation to the value of the superconducting gap. In particular, this shows why pristine graphene needs to be very strongly doped to find any signs of superconductivity, whereas a system with an approximate flat band of the size of the first Brillouin zone of the moiré superlattice can show superconductivity with the observed critical temperature even for quite weak effective attractive interaction. We furthermore present a way to include the Coulomb interactions by calculating the Coulomb pseudopotential in a simplified model.

I. DERIVATION OF THE SELF-CONSISTENCY EQUATION

The Hamiltonian for a local attractive interaction of strength $\lambda > 0$ is

$$H_{\text{int}} = -\frac{\lambda}{2} \sum_{\sigma, \alpha, i} \int d\mathbf{r} \psi_{\sigma, \alpha i}^{\dagger}(\mathbf{r}) \psi_{\bar{\sigma}, \alpha i}^{\dagger}(\mathbf{r}) \psi_{\bar{\sigma}, \alpha i}(\mathbf{r}) \psi_{\sigma, \alpha i}(\mathbf{r}), \quad (\text{S1})$$

where $\psi_{\sigma, \alpha i}(\mathbf{r})$ is the annihilation operator for spin σ at position \mathbf{r} , layer $i \in \{1, 2\}$, and sublattice $\alpha \in \{A, B\}$. Doing the mean field approximation in the Cooper channel, assuming only intervalley coupling, and transforming to the valley operators by $\psi_{\sigma, \alpha i}(\mathbf{r}) = \sum_{\rho} e^{i\rho \mathbf{K} \cdot \mathbf{r}} \psi_{\sigma \rho, \alpha i}(\mathbf{r})$ the interaction Hamiltonian becomes

$$H_{\text{int}} = \frac{1}{2} \sum_{\sigma, \rho, \alpha, i} \int d\mathbf{r} \Delta_{\sigma, \alpha i}(\mathbf{r}) \psi_{\sigma \rho, \alpha i}^{\dagger}(\mathbf{r}) \psi_{\bar{\sigma} \bar{\rho}, \alpha i}^{\dagger}(\mathbf{r}) + \text{h.c.} + \frac{1}{2\lambda} \sum_{\sigma, \alpha, i} \int d\mathbf{r} |\Delta_{\sigma, \alpha i}(\mathbf{r})|^2, \quad (\text{S2})$$

where the local superconducting order parameter is $\Delta_{\sigma, \alpha i}(\mathbf{r}) = -\lambda \sum_{\rho} \langle \psi_{\bar{\sigma} \bar{\rho}, \alpha i}(\mathbf{r}) \psi_{\sigma \rho, \alpha i}(\mathbf{r}) \rangle$. Then by moving to the Nambu space and doing the Bogoliubov transformation we find that the self-consistency equation for the up-spin $\Delta_{\alpha i} := \Delta_{\uparrow, \alpha i}$ becomes

$$\Delta_{\alpha i}(\mathbf{r}) = \lambda \sum_{\rho, b} \int \frac{d\mathbf{k}}{(2\pi)^2} \tanh\left(\frac{E_{\rho b \mathbf{k}}}{2k_B T}\right) u_{\rho b \mathbf{k}, \alpha i}(\mathbf{r}) v_{\rho b \mathbf{k}, \alpha i}^*(\mathbf{r}), \quad (\text{S3})$$

where $u_{\rho b \mathbf{k}, \alpha i}$ is the (α, i) -component of the spinor $u_{\rho b \mathbf{k}}$ and the b sum goes over the positive energy bands. The spinors $u_{\rho b \mathbf{k}}$ and $v_{\rho b \mathbf{k}}$ are determined by solving the Bogoliubov–de Gennes equation

$$\begin{pmatrix} \mathcal{H}_{\rho}(\mathbf{r}) & \Delta(\mathbf{r}) \\ \Delta^*(\mathbf{r}) & -\mathcal{H}_{\rho}(\mathbf{r}) \end{pmatrix} \begin{pmatrix} u_{\rho b \mathbf{k}}(\mathbf{r}) \\ v_{\rho b \mathbf{k}}(\mathbf{r}) \end{pmatrix} = E_{\rho b \mathbf{k}} \begin{pmatrix} u_{\rho b \mathbf{k}}(\mathbf{r}) \\ v_{\rho b \mathbf{k}}(\mathbf{r}) \end{pmatrix}, \quad (\text{S4})$$

where Δ is a diagonal 4 by 4 matrix including the components $\Delta_{\alpha i}$. Substituting the Bloch wave expansion

$$\begin{pmatrix} u_{\rho b \mathbf{k}}(\mathbf{r}) \\ v_{\rho b \mathbf{k}}(\mathbf{r}) \end{pmatrix} = e^{i\mathbf{k} \cdot \mathbf{r}} \sum_{\mathbf{G}'} e^{i\mathbf{G}' \cdot \mathbf{r}} \begin{pmatrix} u_{\rho b \mathbf{k}}(\mathbf{G}') \\ v_{\rho b \mathbf{k}}(\mathbf{G}') \end{pmatrix} \quad (\text{S5})$$

for the eigenstates into Eq. (S4) and assuming $\Delta(\mathbf{r})$ to be periodic in the superlattice, we find the Fourier space Bogoliubov–de Gennes equation [Eq. (5) in the main text] and the Fourier space version of the self-consistency equation [Eq. (4) in the main text].

II. CHARGE DENSITY

The non-coupled system of twisted bilayer graphene is charge neutral at the chemical potential $\mu = 0$. The charge density due to the electrons at that potential is

$$n_0 = \frac{2e}{V} \sum_{b \in B, \mathbf{k}} f_0(\epsilon_{0,b\mathbf{k}}) = \frac{2e}{V} \sum_{b \in \Omega, \mathbf{k}} f_0(\epsilon_{0,b\mathbf{k}}) + n_{\text{high}}, \quad \text{with} \quad n_{\text{high}} = \frac{2e}{V} \sum_{b \in B \setminus \Omega, \mathbf{k}} f_0(\epsilon_{0,b\mathbf{k}}) \quad (\text{S6})$$

where e is the electron charge and the factor of 2 comes from the spin. We formulate the calculation so that the \mathbf{k} -sum goes over the superlattice Brillouin zone L_{BK}^*/SL^* , B is the set of bands and $\epsilon_{0,b\mathbf{k}}$ is the non-interacting dispersion. f_0 is the Fermi-Dirac distribution function at zero temperature. In the second step we introduce a cutoff by dividing the sum over the bands into two terms; to a sum over a set of low-energy bands Ω and to a sum over high-energy bands $B \setminus \Omega$.

In the presence of interlayer coupling, (normal state) dispersion changes to $\epsilon_{b\mathbf{k}}$. The number of bands stays constant and if the interactions, temperature and chemical potential are small compared to the energy of the lowest energy band (in absolute value) of $B \setminus \Omega$ in the non-interacting case, the index set B can be chosen so that the bands in $B \setminus \Omega$ that were full (empty) in the non-interacting case, are still full (empty) in the interacting case. The interacting charge density is

$$\tilde{n}(\mu) = \frac{2e}{V} \sum_{b \in B, \mathbf{k}} f(\epsilon_{b\mathbf{k}} - \mu) = \frac{2e}{V} \sum_{b \in \Omega, \mathbf{k}} f(\epsilon_{b\mathbf{k}} - \mu) + n_{\text{high}}, \quad (\text{S7})$$

where f is the Fermi-Dirac distribution at temperature T and n_{high} has the the same value as in Eq. (S6). The above has been formulated in the non-linearized theory. To calculate the excess charge relative to the charge neutrality point in the linearized theory, we split the bands between the two valleys and find

$$n(\mu) := \tilde{n}(\mu) - n_0 = \frac{2e}{V} \sum_{\rho, b \in \Omega, \mathbf{k}} [f(\epsilon_{\rho b\mathbf{k}} - \mu) - f_0(\epsilon_{0,\rho b\mathbf{k}})] = 2e \sum_{\rho, b \in \Omega} \int \frac{d\mathbf{k}}{(2\pi)^2} [f(\epsilon_{\rho b\mathbf{k}} - \mu) - f_0(\epsilon_{0,\rho b\mathbf{k}})], \quad (\text{S8})$$

where n is the excess charge density and Ω is now the set of bands in one valley.

The charge neutrality point μ^* is determined from the equation $n(\mu^*) = 0$. It is shown for different twist angles in Figs. 2(g-i) of the main text, and is always located in the middle between the two DOS peaks.

III. SIMPLIFIED MODEL OF THE SUPERCONDUCTING STATE

The notion of weak or absent electron-phonon mediated superconductivity in pristine graphene is widely known. Here we reconcile this notion with our results claiming that a quite simple BCS-style model could describe the observations of superconductivity in twisted bilayer graphene. These results are not new, but we follow especially the treatments in Refs. 1 and 2 and adopt to the notation of the main paper, along with some estimates.

We start from the generic self-consistency equation for the mean-field order parameter Δ . If Δ is position independent, the Bogoliubov-de Gennes equation can be solved to yield

$$\Delta = 4\lambda \int^{k_c} \frac{d\mathbf{k}}{(2\pi)^2} \frac{\Delta}{E_{\mathbf{k}}} \tanh\left(\frac{E_{\mathbf{k}}}{2k_B T}\right), \quad (\text{S9})$$

where the prefactor 4 comes from summation over the valley and band indices, where in the band sum we include only the doubly degenerate lowest positive energy band. The cutoff k_c is specified more below. We moreover assume that $E_{\mathbf{k}} = \sqrt{\epsilon_{\mathbf{k}}^2 + \Delta^2}$. Here and below, without loss of generality we assume $\Delta = |\Delta| \geq 0$. Our idea is to solve the self-consistency equation in three cases: (i) at the Dirac point for a Dirac dispersion $\epsilon_{\mathbf{k}}^2 = \hbar^2 v_F^2 k^2$, (ii) for a Dirac dispersion at non-zero doping μ , i.e., $\epsilon_{\mathbf{k}}^2 = (\hbar v_F k - \mu)^2$, and (iii) for a flat band with and without doping, $\epsilon_{\mathbf{k}} \approx \mu$ for $\mathbf{k} \in \Omega_{\text{FB}}$. In each case we have the normal-state solution $\Delta = 0$, which we exclude by dividing both sides in Eq. (S9) by Δ .

Note that Eq. (S9) *does not* represent the full self-consistency equation solved in the main text. Rather, we use it here simply to provide estimates of the behavior of Δ in various limits.

A. Linear dispersion, no doping

Far away from the magic angle, the twisted bilayer behaves as if the two graphene layers would be almost uncoupled. This means that the low-energy dispersion exhibits two separate copies of the graphene Dirac dispersion. Inserting an ultraviolet energy cutoff $\epsilon_c = \hbar v_F k_c$ and performing the integral for the $T = 0$ gap function, the self-consistency equation goes to the form

$$\frac{\pi \hbar^2 v_F^2}{2\lambda} = -\Delta + \sqrt{\Delta^2 + \epsilon_c^2} \quad (\text{S10})$$

or

$$\Delta = \frac{\pi \hbar^2 v_F^2}{4} \frac{\lambda^2 - \lambda_c^2}{\lambda \lambda_c^2}, \quad (\text{S11})$$

where $\lambda_c = \pi \hbar^2 v_F^2 / (2\epsilon_c)$. Since $\Delta \geq 0$, this solution makes sense only if $\lambda > \lambda_c$, and otherwise the only possible solution is the normal state $\Delta = 0$.

In pristine graphene, the critical interaction strength can be written also in terms of the nearest-neighbour hopping term³ $\gamma_0 \approx 3 \text{ eV}$. Namely, within a nearest-neighbour tight-binding model the Fermi speed of graphene is $v_F = \sqrt{3}\gamma_0 a / (2\hbar)$, where a is the graphene lattice constant. We hence get

$$\lambda_c = \frac{3\pi}{8} \frac{\gamma_0}{\epsilon_c} \gamma_0 a^2. \quad (\text{S12})$$

If the attractive interaction results from electron–phonon coupling, a typical cutoff energy could be of the order of the Debye energy⁴ 200 meV. In this case $\lambda_c \approx 50 \text{ eV} a^2$, 5 to 50 times larger than the values of λ used in our work. 100 to 200 meV is also the range of the maximum cutoff energy that we have used in our numerical results when including the contribution from higher bands. Even if the cutoff ϵ_c would be of the order of γ_0 , the resulting λ_c would be one order of magnitude larger than the smallest λ used in our results.

B. Linear dispersion, with doping

Let us try to reconcile the observations of superconductivity in Li or Ca doped graphene with the above idea. These cases are more accurately described by⁵ within the Eliashberg theory. Here we just show in which sense doping fits into the above picture. Assuming $\epsilon_{\mathbf{k}} = \pm \hbar v_F k - \mu$ and $\Delta < \epsilon_c$, and cutting the integral at $\epsilon_{\mathbf{k}} = \epsilon_c$ the self-consistency equation at $T = 0$ becomes¹

$$\frac{\pi \hbar^2 v_F^2}{2\lambda} = \sqrt{\Delta^2 + \epsilon_c^2} - \sqrt{\Delta^2 + \mu^2} + |\mu| \ln \frac{|\mu| + \sqrt{\Delta^2 + \mu^2}}{\Delta}. \quad (\text{S13})$$

Let us assume that $\Delta \ll |\mu|, \epsilon_c$ so that we can expand the right hand side in Δ . In this case we find an analytic solution for Δ ,

$$\Delta = 2|\mu| \exp \left[-\frac{\epsilon_c}{|\mu|} \left(\frac{\lambda_c}{\lambda} - 1 \right) - 1 \right]. \quad (\text{S14})$$

Let us assume a cutoff energy $\epsilon_c = 200 \text{ meV}$ and a coupling strength $\lambda = \lambda_c / 22$ (corresponding to about $5 \text{ eV} a^2$ with the above estimates). In this case, with $\mu = 0.7 \text{ eV}$ we would get $\Delta = 1.3 \text{ meV}$. This corresponds to a critical temperature of 9 K, in the same range as the one that was measured in Li or Ca doped graphene.^{6–9}

C. Flat band estimate

Let us now make similar estimates for the flat-band case of the moiré superlattice. In this case, we assume that Δ is *larger* than the bandwidth of the lowest-energy band. Within that band, we can hence approximate $E_{\mathbf{k}} \approx \Delta$ in Eq. (S9) and at $T = 0$ the integral is over a constant function. As a result, we get

$$\Delta_{\text{FB}} = \frac{\lambda}{\pi^2} \Omega_{\text{FB}} = \frac{8\lambda}{\sqrt{3}(3m^2 + 3m + 1)a^2}, \quad (\text{S15})$$

where $\Omega_{\text{FB}} = 8\pi^2/[\sqrt{3}(3m^2 + 3m + 1)a^2]$ is the area of the first Brillouin zone of the moiré superlattice. Within the model adapted in the main text, the magic angle is around $m \approx 34$, in which case we would get $\Delta_{\text{FB}} = 1.3 \times 10^{-3} \lambda/a^2$. In Fig. 3b of the main text, the solid line has a slope of $1.0 \times 10^{-3} \lambda/a^2$, *i.e.*, very close to this simple estimate.

The temperature dependent Δ in the flat-band case is obtained by solving

$$\Delta = \Delta_{\text{FB}} \tanh\left(\frac{\Delta}{2k_B T}\right). \quad (\text{S16})$$

At the critical temperature, $\Delta \rightarrow 0$, and we can hence expand the right hand side to the linear order in $\Delta/(2k_B T_c)$. This directly yields $k_B T_c = \Delta_{\text{FB}}/2$.

In the case of a non-zero potential μ , we can use $E_{\mathbf{k}} \approx \sqrt{\mu^2 + \Delta^2}$ in the self-consistency equation. It then becomes (for $\Delta > 0$)

$$\Delta = \Delta_{\text{FB}} \frac{\Delta}{\sqrt{\mu^2 + \Delta^2}}, \text{ or } \Delta = \sqrt{\Delta_{\text{FB}}^2 - \mu^2}. \quad (\text{S17})$$

In this case superconductivity is hence suppressed when the absolute value of the chemical potential is larger than Δ_{FB} .

IV. SIMPLIFIED MODEL FOR COULOMB PSEUDOPOTENTIAL

Coulomb interaction differs from the electron–phonon interaction due to the fact that photons are almost instantaneous, whereas for phonon-mediated interaction we have to take the retardation into account. Usually in BCS theory, and also in our model, we approximate the retardation by imposing an energy cutoff at the maximum phonon frequency ω_D in the self-consistency equation. For Coulomb interaction there is no physical cutoff, and consequently, we cannot operate in purely low-energy regime. The high energy states do contribute logarithmically to Δ at low energies.

The proper way to formulate the low-energy theory with a cutoff which also applies to the Coulomb interaction, is to define a modified pseudopotential u^* which replaces the bare interaction in the self-consistency equation and takes the high-energy parts into account. If $\Delta(\mathbf{r})$ is position-dependent, the pseudopotential will be a matrix of two position coordinates $u^*(\mathbf{r}, \mathbf{r}')$. If Δ is constant in space, the pseudopotential is a scalar.

We want to consider the effect of the Hubbard interaction, described in the continuum limit by the Hamiltonian

$$H_{\text{Hubbard}} = \frac{u}{2} \sum_{\sigma, \alpha, i} \int d\mathbf{r} \psi_{\sigma, \alpha i}^\dagger(\mathbf{r}) \psi_{\bar{\sigma}, \alpha i}^\dagger(\mathbf{r}) \psi_{\bar{\sigma}, \alpha i}(\mathbf{r}) \psi_{\sigma, \alpha i}(\mathbf{r}), \quad (\text{S18})$$

where $u = Ua^2$ and U is the Hubbard parameter describing the on-site interaction in the tight-binding model. We assume that $U > 0$ so that the interaction is repulsive. The inclusion of such an interaction has multiple effects in an inhomogeneous system, but here we only consider the effect on the order parameter through the modification of the self-consistency equation.

As we are now not doing a low-energy calculation, separation into valleys is not useful and we cannot do the continuum approximation in which we assume that the graphene lattice L is duplicated infinitely many times in the superlattice. Therefore, in the following the sums and integrals are done over the sets $\mathbf{G} \in SL^*/L^*$ and $\mathbf{k} \in \mathbb{R}^2/SL^*$. The two graphene valleys are then separated from each other by a large, but finite \mathbf{G} -vector. The valley sum is thus included in the sum over \mathbf{G} and there is no valley index ρ .

For simplicity, we assume $\Delta_{\alpha i}(\mathbf{G}) = \Delta \delta_{\mathbf{G}, 0}$ so that Δ has no position dependence and is the same on both layers and sublattices. With this simplification, we can diagonalize the Hamiltonian $\mathcal{H}_{\mathbf{k}}$ and the order parameter simultaneously in the BdG equation (Eq. (5) of the main paper), which we write as

$$\begin{pmatrix} \mathcal{H}_{\mathbf{k}} & \Delta \underline{\mathbf{1}} \\ \Delta^* \underline{\mathbf{1}} & -\mathcal{H}_{\mathbf{k}} \end{pmatrix} \begin{pmatrix} \underline{u}_{\mathbf{k}b} \\ \underline{v}_{\mathbf{k}b} \end{pmatrix} = E_{\mathbf{k}b} \begin{pmatrix} \underline{u}_{\mathbf{k}b} \\ \underline{v}_{\mathbf{k}b} \end{pmatrix}, \quad (\text{S19})$$

where the underlined quantities are matrices/vectors with indices \mathbf{G}, α , and i . Let $\underline{\mathcal{G}}_{\mathbf{k}}$ be a unitary transformation which diagonalizes the normal state Hamiltonian $\mathcal{H}_{\mathbf{k}}$. Then the above equation becomes

$$\begin{pmatrix} \underline{\epsilon}_{\mathbf{k}} & \Delta \underline{\mathbf{1}} \\ \Delta^* \underline{\mathbf{1}} & -\underline{\epsilon}_{\mathbf{k}} \end{pmatrix} \begin{pmatrix} \underline{u}'_{\mathbf{k}b} \\ \underline{v}'_{\mathbf{k}b} \end{pmatrix} = E_{\mathbf{k}b} \begin{pmatrix} \underline{u}'_{\mathbf{k}b} \\ \underline{v}'_{\mathbf{k}b} \end{pmatrix}, \quad (\text{S20})$$

where $u'_{\mathbf{k}b} = \underline{\mathcal{G}}_{\mathbf{k}} u_{\mathbf{k}b}$, $v'_{\mathbf{k}b} = \underline{\mathcal{G}}_{\mathbf{k}} v_{\mathbf{k}b}$ and $\epsilon_{\mathbf{k}} = \underline{\mathcal{G}}_{\mathbf{k}} \mathcal{H}_{\mathbf{k}} \underline{\mathcal{G}}_{\mathbf{k}}^\dagger$. We now label the normal state eigenstates with band index b . With constant Δ , the positive-energy BdG eigenstates are in simple correspondence with the eigenstates (both positive and negative energy) of the normal state, and can also be labeled with the same indices. Concentrating to a single Nambu-block of the BdG-equation,

$$\begin{pmatrix} \epsilon_{\mathbf{k}b} & \Delta \\ \Delta^* & -\epsilon_{\mathbf{k}b} \end{pmatrix} \begin{pmatrix} u'_{\mathbf{k}b} \\ v'_{\mathbf{k}b} \end{pmatrix} = E_{\mathbf{k}b} \begin{pmatrix} u'_{\mathbf{k}b} \\ v'_{\mathbf{k}b} \end{pmatrix}, \quad (\text{S21})$$

we find that the eigenenergies and eigenstates assume the usual BCS form

$$E_{\mathbf{k}b} = \sqrt{\epsilon_{\mathbf{k}b}^2 + |\Delta|^2}, \quad (\text{S22})$$

$$u_{\mathbf{k}b} = \frac{e^{i\phi}}{\sqrt{2}} \left(1 + \frac{\epsilon_{\mathbf{k}b}}{E_{\mathbf{k}b}} \right)^{1/2}, \quad (\text{S23})$$

$$v_{\mathbf{k}b} = \frac{1}{\sqrt{2}} \left(1 - \frac{\epsilon_{\mathbf{k}b}}{E_{\mathbf{k}b}} \right)^{1/2}, \quad (\text{S24})$$

where $\phi = \arg(\Delta)$.

The self-consistency equation [Eq. (4) in the main text with $\mathbf{G} = 0$ and generalized to include energy-dependent interactions] can be written in the above matrix notation as

$$\Delta_{\mathbf{k}b,\alpha i} = \sum_{b'} \int \frac{d\mathbf{k}'}{(2\pi)^2} V_{\mathbf{k}\mathbf{k}'}^{bb'} \left(u_{\mathbf{k}'b'}^\dagger \underline{\Pi}_{\alpha i} v_{\mathbf{k}'b'} \right)^* \tanh\left(\frac{E_{\mathbf{k}'b'}}{2k_B T}\right), \quad (\text{S25})$$

where $\underline{\Pi}_{\alpha i}$ is the projection operator to the sublattice α and layer i . We assume that the interaction has the simplified BCS form

$$V_{\mathbf{k}\mathbf{k}'}^{bb'} = \lambda \theta(|\epsilon_{\mathbf{k}b}| - \omega_D) \theta(|\epsilon_{\mathbf{k}'b'}| - \omega_D) - u, \quad (\text{S26})$$

with electron-phonon cutoff at Debye energy ω_D .

The sum of complete set of projection operators is an identity: $\sum_{\alpha,i} \underline{\Pi}_{\alpha i} = \underline{1}$. To get rid of the projection operator, we take the average over α and i . As $\Delta_{\mathbf{k}b,\alpha i} = \Delta_{\mathbf{k}b}$, we get

$$\Delta_{\mathbf{k}b} = \frac{1}{4} \sum_{b'} \int \frac{d\mathbf{k}'}{(2\pi)^2} V_{\mathbf{k}\mathbf{k}'}^{bb'} \left(u_{\mathbf{k}'b'}^\dagger v_{\mathbf{k}'b'} \right)^* \tanh\left(\frac{E_{\mathbf{k}'b'}}{2k_B T}\right) \quad (\text{S27})$$

$$= \frac{1}{4} \sum_{b'} \int \frac{d\mathbf{k}'}{(2\pi)^2} V_{\mathbf{k}\mathbf{k}'}^{bb'} u'_{\mathbf{k}'b'} (v'_{\mathbf{k}'b'})^* \tanh\left(\frac{E_{\mathbf{k}'b'}}{2k_B T}\right). \quad (\text{S28})$$

In the second line, we did a basis transformation with the matrix $\underline{\mathcal{G}}_p^\dagger$.

We now divide $\Delta_{\mathbf{k}b} = \Delta_{\mathbf{k}b}^\lambda + \Delta^u$ into two parts, with $\Delta_{\mathbf{k}b}^\lambda$ corresponding to the λ part of the interaction in the RHS of Eq. (S28) and Δ^u corresponding to the u part of the interaction.¹⁰ The difference between the two terms is in the energy dependence. $\Delta_{\mathbf{k}b}^\lambda$ vanishes above the cutoff, but Δ^u has no energy dependence and persists at high energies. With this division, the self-consistency equation splits into two coupled equations,

$$\Delta_{\mathbf{k}b}^\lambda = \frac{\lambda}{4} \sum_{b'} \int_{|\epsilon_{\mathbf{k}'b'}| < \omega_D} \frac{d\mathbf{k}'}{(2\pi)^2} u'_{\mathbf{k}'b'} (v'_{\mathbf{k}'b'})^* \tanh\left(\frac{E_{\mathbf{k}'b'}}{2k_B T}\right) \times \theta(|\epsilon_{\mathbf{k}b}| - \omega_D), \quad (\text{S29})$$

$$\Delta^u = -\frac{u}{4} \sum_{b'} \int_{|\epsilon_{\mathbf{k}'b'}| < \omega_D} \frac{d\mathbf{k}'}{(2\pi)^2} u'_{\mathbf{k}'b'} (v'_{\mathbf{k}'b'})^* \tanh\left(\frac{E_{\mathbf{k}'b'}}{2k_B T}\right) - \frac{u}{4} \sum_{b'} \int_{|\epsilon_{\mathbf{k}'b'}| > \omega_D} \frac{d\mathbf{k}'}{(2\pi)^2} u'_{\mathbf{k}'b'} (v'_{\mathbf{k}'b'})^* \tanh\left(\frac{E_{\mathbf{k}'b'}}{2k_B T}\right). \quad (\text{S30})$$

Above, we also split the sums and integrals over the eigenstates to low and high energy parts with ω_D as the cutoff. Assuming $\omega_D \gg T, \Delta^u$, we can approximate that for high energy states

$$u'_{\mathbf{k}b} (v'_{\mathbf{k}b})^* \tanh\left(\frac{E_{\mathbf{k}b}}{2k_B T}\right) \approx \frac{\Delta^u}{2|\epsilon_{\mathbf{k}b}|}. \quad (\text{S31})$$

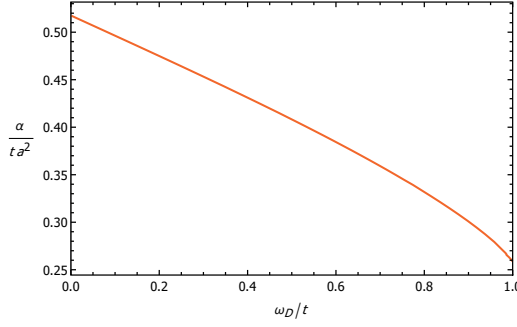


FIG. S1. Dependence of the graphene pseudopotential renormalization constant α on the electron-phonon cutoff ω_D . Pseudopotential renormalization constant of TBG can be approximated with that of graphene if $|t_\perp| \ll \omega_D$.

Inserting this into Eq. (S30), we can (partially) solve for Δ^u to obtain an equation which only refers to the low energy states,

$$\Delta^u = -\frac{u^*}{4} \sum_{b'} \int_{|\epsilon_{\mathbf{k}'b'}| < \omega_D} \frac{d\mathbf{k}'}{(2\pi)^2} u'_{\mathbf{k}'b'} (v'_{\mathbf{k}'b'})^* \tanh\left(\frac{E_{\mathbf{k}'b'}}{2k_B T}\right). \quad (\text{S32})$$

The high energy states renormalize the interaction constant, which is replaced by the Coulomb pseudopotential

$$u^* = \frac{u}{1 + u\alpha}, \quad \text{where} \quad \alpha = \frac{1}{4} \sum_b \int_{|\epsilon_{\mathbf{k}b}| > \omega_D} \frac{d\mathbf{k}}{(2\pi)^2} \frac{1}{2|\epsilon_{\mathbf{k}b}|}. \quad (\text{S33})$$

The equation for the full order parameter, including both interactions, is now

$$\Delta = \frac{\lambda_{\text{eff}}}{4} \sum_{b'} \int_{|\epsilon_{\mathbf{k}'b'}| < \omega_D} \frac{d\mathbf{k}'}{(2\pi)^2} u'_{\mathbf{k}'b'} (v'_{\mathbf{k}'b'})^* \tanh\left(\frac{E_{\mathbf{k}'b'}}{2k_B T}\right) \quad \text{with} \quad \lambda_{\text{eff}} = \lambda - u^*. \quad (\text{S34})$$

If $\Delta(\mathbf{r})$ is position dependent, the derivation becomes more complicated, and in the end, the pseudopotential becomes a matrix $u^*(\mathbf{G}, \mathbf{G}')$ instead of a scalar like above.

The pseudopotential renormalization parameter α now depends on structure of the high energy bands. It is not very sensitive to the parameters of the system and for this calculation we assume $t_\perp = 0$ so that the two graphene layers are completely independent of each other. The sums and integrals then transform as

$$\alpha = \frac{1}{4} \sum_b \int_{\mathbb{R}^2/S L^*} \int_{|\epsilon_{\mathbf{k}b}| > \omega_D} \frac{d\mathbf{k}}{(2\pi)^2} \frac{1}{2|\epsilon_{\mathbf{k}b}|} \approx \frac{1}{4} \sum_i \sum_{b \in \pm 1} \int_{\mathbb{R}^2/L^*} \int_{|\epsilon_{\mathbf{k}b}| > \omega_D} \frac{d\mathbf{k}}{(2\pi)^2} \frac{1}{2|\epsilon_{\mathbf{k}b}^0|} \quad (\text{S35})$$

where $\epsilon_{\mathbf{k}b}^0$ are the graphene eigenenergies calculated from the tight binding model with only nearest neighbour hoppings.

If approximated as above, α corresponds to the pseudopotential constant for graphene. We show the dependence on the cutoff ω_D in Fig. S1. With parameters $\omega_D = 200 \text{ meV}$ and nearest neighbour hopping $t = 3 \text{ eV}$, we find that $\alpha \approx 0.2 \text{ eV}^{-1} a^{-2}$, which holds as long as $\mu \ll \omega_D$. The maximum value for the pseudopotential is thus $u_{\text{max}}^* = 1/\alpha \approx 5 \text{ eV} a^2$, which is obtained in the limit $U \rightarrow \infty$. For $U = 5 \text{ eV}$, the effective interaction strength is reduced to half of the bare interaction strength, $u^* \approx 0.5u = 2.5 \text{ eV} a^2$.

¹ N. B. Kopnin and E. B. Sonin, *Phys. Rev. Lett.* **100**, 246808 (2008).

² N. B. Kopnin and T. T. Heikkilä, “Carbon-based Superconductors: Towards High-Tc Superconductivity,” (Taylor & Francis, 2014) Chap. 9.

³ A. H. Castro Neto, F. Guinea, N. M. R. Peres, K. S. Novoselov, and A. K. Geim, *Rev. Mod. Phys.* **81**, 109 (2009).

⁴ D. K. Efetov and P. Kim, *Phys. Rev. Lett.* **105**, 256805 (2010).

⁵ G. Profeta, M. Calandra, and F. Mauri, *Nat. Phys.* **8**, 131 (2012).

⁶ B. M. Ludbrook, G. Levy, P. Nigge, M. Zonno, M. Schneider, D. J. Dvorak, C. N. Veenstra, S. Zhdanovich, D. Wong, P. Dosanjh, *et al.*, *PNAS* **112**, 11795 (2015).

- ⁷ A. P. Tiwari, S. Shin, E. Hwang, S.-G. Jung, T. Park, and H. Lee, *J. Phys. Cond. Matt.* **29**, 445701 (2017).
- ⁸ J. Chapman, Y. Su, C. A. Howard, D. Kundys, A. N. Grigorenko, F. Guinea, A. K. Geim, I. V. Grigorieva, and R. R. Nair, *Sci. Rep.* **6**, 23254 (2016).
- ⁹ S. Ichinokura, K. Sugawara, A. Takayama, T. Takahashi, and S. Hasegawa, *ACS Nano* **10**, 2761 (2016).
- ¹⁰ P. Morel and P. Anderson, *Phys. Rev.* **125**, 1263 (1962).

V

**NONLINEAR SPIN TORQUE, PUMPING, AND COOLING IN
SUPERCONDUCTOR/FERROMAGNET SYSTEMS**

by

R. Ojajarvi, J. Manninen, T.T. Heikkilä and P. Virtanen 2020

Physical Review B **101**, 115406, DOI:[10.1103/PhysRevB.101.115406](https://doi.org/10.1103/PhysRevB.101.115406)

Reproduced with permission. Copyright 2020 American Physical Society.

Nonlinear spin torque, pumping, and cooling in superconductor/ferromagnet systemsRisto Ojajarvi ^{1,*}, Juuso Manninen ², Tero T. Heikkilä ^{1,†} and Pauli Virtanen ^{1,‡}¹*University of Jyväskylä, Department of Physics and Nanoscience Center, P.O. Box 35 (YFL), FI-40014 University of Jyväskylä, Finland*²*Aalto University, Department of Applied Physics, Low Temperature Laboratory, P.O. Box 15100, FI-00076 AALTO, Finland*

(Received 30 June 2019; revised manuscript received 19 February 2020; accepted 20 February 2020; published 5 March 2020)

We study the effects of the coupling between magnetization dynamics and the electronic degrees of freedom in a heterostructure of a metallic nanomagnet with dynamic magnetization coupled with a superconductor containing a steady spin-splitting field. We predict how this system exhibits a nonlinear spin torque, which can be driven either with a temperature difference or a voltage across the interface. We generalize this notion to arbitrary magnetization precession by deriving a Keldysh action for the interface, describing the coupled charge, heat, and spin transport in the presence of a precessing magnetization. We characterize the effect of superconductivity on the precession damping and the antidamping torques. We also predict the full nonlinear characteristic of the Onsager counterparts of the torque, showing up via pumped charge and heat currents. For the latter, we predict a spin-pumping cooling effect, where the magnetization dynamics can cool either the nanomagnet or the superconductor.

DOI: [10.1103/PhysRevB.101.115406](https://doi.org/10.1103/PhysRevB.101.115406)**I. INTRODUCTION**

The intriguing possibility to control magnetization dynamics by spin torque suggested over two decades ago [1] and its reciprocal counterpart [2,3] of spin pumping [4] have been widely studied in magnetic systems. In such systems charge and spin transport are closely linked and need to be treated on the same footing. Recently there has also been increased interest in coupling superconductors to magnets and finding out how superconductivity affects the magnetization dynamics [5–19]. On the other hand, recent work has shown that a combination of magnetic and superconducting systems results in giant thermoelectric effects [20–24] which couple charge and heat currents. These works [21,22] also imply a coupling of spin and heat. However, a general description of the implications for the magnetization dynamics, dynamical heat pumping effects, and the behavior in the nonlinear regime at energies comparable to the superconductor gap Δ , has been lacking.

In this work, we fill this gap by constructing a theory which provides a combined description of pumped charge and heat currents, spin torques, magnetization damping, voltage, and thermal bias. We consider a metallic nanomagnet F with a magnetization precessing at a rate Ω which is determined by an external magnetic field, the shape of the magnet, and the crystal anisotropy, [26] at a slowly varying angle θ to the precession axis [Fig. 1(a)]. The magnet is tunnel coupled to a superconducting electrode S that also contains a constant spin-splitting (exchange or Zeeman) field [25,27].

Main features of the problem can be understood in a tunneling model, shown schematically in Fig. 1(b). Both the spin splitting h and nonzero Ω shift the spectrum, whereas Ω generates also effective spin-dependent chemical potential shifts [28] providing a driving force which pumps the currents across the interface. The interplay of the two enables a coupling between the magnetization dynamics and the linear-response thermoelectric effect [20,21,23] originating from the spin-selective breaking of the electron-hole symmetry in the superconductor with respect to the chemical potential. As a consequence, a temperature difference between the two systems leads to a thermal spin torque, which in a suitable parameter regime yields an antidamping sufficient to obtain flipping or stable precession of the nanomagnet. The Onsager counterpart of the thermal spin torque is a Peltier-type cooling (or heating) driven by the precessing magnetization. In the nonlinear response, the precession also pumps a charge current, as already shown in [29]. We discuss the general picture for the spin-split superconductor, and, in addition to the thermomagnetic effects, find the Keldysh action [Eq. (20)] describing the stochastic properties of the S/F junction. The action allows identifying thermodynamical constraints, current noises, a spintronic fluctuation theorem, and describes the probability distribution of the magnetization direction and the spectrum of its oscillations.

The manuscript is structured as follows: We introduce a simple tunneling model in Sec. II and discuss the tunneling currents in Sec. III. Implications on magnetization dynamics are considered in Sec. IV, including thermal transport associated with the ferromagnetic resonance and physics of spin torque oscillators driven by the thermal effects. In Sec. V we focus on studying the stochastic magnetization dynamics based on a Keldysh action approach to the tunneling model, and discuss probability distributions and linewidths for the oscillators. We conclude in

*risto.m.m.ojajarvi@jyu.fi

†tero.t.heikkila@jyu.fi

‡pauli.t.virtanen@jyu.fi

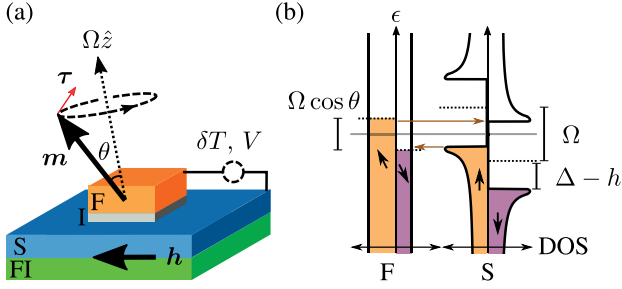


FIG. 1. (a) Schematic ferromagnetic island–superconductor tunnel junction (F/I/S) setup. The direction \mathbf{m} of magnetization in F precesses at a rate Ω at an angle θ around the axis (\hat{z}) of its effective field. Electron tunneling and intrinsic damping produces torque $\boldsymbol{\tau}$ on \mathbf{m} . The superconductor has an internal spin splitting exchange field \mathbf{h} , from external magnetic field, or a ferromagnetic insulator (FI) bilayer structure [25]. We consider also thermal and electric biasing ($\delta T, V$). (b) “Semiconductor picture” for pumping, in the frame rotating with \mathbf{m} (for $\mathbf{h} \parallel \hat{z}$). Gray solid line is the chemical potential when $\Omega = 0$. Increasing the precession frequency to $\Omega \neq 0$ shifts both the spectrum and the chemical potentials (dashed lines) by $\Omega \cos \theta$ in F and by Ω in S. The exchange field \mathbf{h} only shifts the spectrum in S.

Sec. VI. Certain details of derivations are postponed to the Appendixes.

II. TUNNELING MODEL

The main effects can be understood with a tunneling Hamiltonian description (below $\hbar = e = k_B = 1$),

$$H = H_S + \hat{R}(t)H_F\hat{R}(t)^\dagger + \sum_{jj'\sigma} W_{jj'} e^{-iVt} c_{j\sigma}^\dagger d_{j'\sigma} + \text{H.c.}, \quad (1)$$

where $c_{j\sigma}$ and $d_{j\sigma}$ are the F and S conduction electron operators and W the tunneling matrix elements for spin/momentum states $\sigma = \pm$, \mathbf{p}_j , and V is a bias voltage. The Hamiltonian H_S describes the spin-split superconductor [23], and H_F the magnet with magnetization parallel to the \hat{z} direction. The magnetization direction $\mathbf{m}(t) = (\cos \phi \sin \theta, \sin \phi \sin \theta, \cos \theta)$ is specified by a spin rotation matrix $\hat{R}(t)c_{j\sigma}\hat{R}(t)^\dagger = \sum_{\sigma'} R_{\sigma\sigma'}(t)c_{j\sigma'}$. In the frame rotating with R [28,30], assuming $\mathbf{m}(t)$ varies adiabatically so that an equilibrium electron distribution is maintained, the Berry phase $\varphi(t) = \int^t dt' \dot{\varphi}(1 - \cos \theta)$ can be absorbed (c.f. Refs. [31,32] and Appendix B) to the spin rotation,

$$R = e^{-i\phi(t)\sigma_z/2} e^{-i\theta(t)\sigma_y/2} e^{i\phi(t)\sigma_z/2} e^{-i\varphi(t)\sigma_z/2}, \quad (2)$$

where $\sigma_{x/y/z}$ are the spin matrices. Varying $\mathbf{m}(t)$ results to effective spin-dependent voltages [30] in the tunneling part. For uniform precession, they are $\Omega_{\sigma\sigma'} = (\sigma - \sigma' \cos \theta)\Omega/2$ [see Fig. 1(b)]. From the model, we can compute in leading order in W the tunneling charge, energy, and spin currents ($I_c, \dot{E}, \mathbf{I}_s$) via a standard Green function approach (see Ref. [33] and Appendix A). The assumption of local equilibrium implies that the rates of tunneling and other nonequilibrium-generating processes on the magnetic island should be small compared to electron relaxation [34–36].

Consider precession with frequency Ω around the z axis, $\phi(t) = \Omega t$ with $|\dot{\theta}| \ll \Omega$. From the above model, we find the time-averaged currents and $\hbar \bar{\tau}_z = -(\mathbf{m} \times \mathbf{I}_s \times \mathbf{m})_z$, [1,28] the z component of the time-averaged spin transfer torque:

$$\bar{I}_c = \frac{G_T}{2e} \int_{-\infty}^{\infty} d\epsilon \sum_{\sigma\sigma'} \langle \sigma | \sigma' \rangle^2 N_{S,\sigma} N_{F,\sigma'} [f_F - f_S], \quad (3)$$

$$\bar{E}_S = \frac{G_T}{2e^2} \int_{-\infty}^{\infty} d\epsilon \sum_{\sigma\sigma'} \epsilon \langle \sigma | \sigma' \rangle^2 N_{S,\sigma} N_{F,\sigma'} [f_F - f_S], \quad (4)$$

$$\bar{\tau}_z = -\frac{G_T \sin^2 \theta}{8e^2} \int_{-\infty}^{\infty} d\epsilon \sum_{\sigma\sigma'} \sigma N_{S,\sigma} N_{F,\sigma'} [f_F - f_S]. \quad (5)$$

Here, $f_F = f_0(\epsilon - V - \Omega_{\sigma\sigma'}, T_F)$, $f_S = f_0(\epsilon, T_S)$ are the Fermi distribution functions in F and S, $\langle \sigma | \sigma' \rangle^2 = (1 + \sigma\sigma' \cos \theta)/2$ the spin overlap between \mathbf{m} and the z axis, and $N_{S/F,\sigma=\pm}$ the densities of states (DOS) for up/down spins [quantization axis $\mathbf{m}(t)$ for F, and \hat{z} for S] normalized by the Fermi level DOS per spin, and G_T the tunneling conductance. Of these, Eq. (3) was previously discussed in Ref. [29] for $\mathbf{h} = 0$. Using a basic model for F and S, we have $N_{F,\sigma} = 1 + \sigma P$ and $N_{S,\sigma} = \sum_{\pm} \frac{1 \pm \sigma \hat{h} \cdot \hat{z}}{2} N_0(\epsilon \mp h)$, where $P = (v_{F,+} - v_{F,-})/(v_{F,+} + v_{F,-})$ is the spin polarization in terms of the majority/minority Fermi level DOS $v_{F,\pm}$, and $N_0(\epsilon)$ the Bardeen-Cooper-Schrieffer density of states [37]. The tunneling described by Eqs. (3)–(5) can be understood in a semiconductor picture, as shown in Fig. 1(b). The broken electron-hole symmetry around the chemical potentials for both spins in S and spin polarization in F results to thermally driven spin currents causing torques, and the rotation-induced potential shifts pump charge and heat currents.

III. TUNNELING CURRENTS

Expanding for small voltage bias V , temperature difference $\delta T = T_S - T_F$, and the precession speed Ω , the time-averaged currents are described by a linear-response matrix:

$$\begin{pmatrix} \bar{I}_c \\ \bar{E}_S \\ \bar{\tau}_z \end{pmatrix} = \begin{pmatrix} G & P\alpha \cos \theta & 0 \\ P\alpha \cos \theta & G_{\text{th}} T & \frac{\alpha}{2} \sin^2 \theta \\ 0 & -\frac{\alpha}{2} \sin^2 \theta & -\frac{G}{4} \sin^2 \theta \end{pmatrix} \begin{pmatrix} V \\ -\delta T/T \\ \Omega \end{pmatrix}, \quad (6)$$

where G and G_{th} are the linear-response electrical and thermal conductances. Here, $\alpha = -(G_T/2) \int_{-\infty}^{\infty} d\epsilon \epsilon [N_{S,+}(\epsilon) - N_{S,-}(\epsilon)] f_0'(\epsilon)$ is a thermoelectric coefficient [20,21], which originates from the exchange field h generating the electron-hole asymmetry in the superconductor. It is nonzero only when S is both superconducting and has a spin splitting $h \neq 0$. The response matrix L in Eq. (6) has the Onsager symmetry $L_{ij} = L_{ji}^{\text{tr}}$, where tr refers to time reversal, $\alpha^{\text{tr}} = -\alpha$, $P^{\text{tr}} = -P$.

The coefficient for charge pumping is here zero, unlike in the ferromagnet-ferromagnet case [30], because the spin-(anti)symmetrized DOS of S is also (anti)symmetric in energy. This also suppresses linear-response contributions to charge current from thermal magnetization fluctuations [31], which are also related to the magnon spin-Seebeck effect [3,18,31].

Importantly, the spin splitting of the superconductor enables the precession to pump energy current at linear response, and as its Onsager counterpart, there is nonzero thermal

spin torque (terms with $\alpha \neq 0$). This is made possible by the nonzero thermoelectric coefficient [20,21] driving spin currents due to a temperature difference. This effect is (in metals) parametrically larger by a factor $\varepsilon_F/\Delta \gg 1$ than that from normal-state DOS asymmetry [3,35,38] in systems with Fermi energy ε_F .

A. Symmetries

Let us now consider the joint probability P of changes δn_S and δE_S in the electron number and energy of S, and a change δm_z in the magnetization of F, during a time interval of length t_0 . It satisfies a fluctuation relation [39,40]:

$$P_{t_0}(\delta n, \delta E_S, \delta m_z) = e^{T_F^{-1}V\delta n + (T_S^{-1} - T_F^{-1})\delta E_S + T_F^{-1}\Omega S\delta m_z} \times P_{t_0}^{\text{tr}}(-\delta n, -\delta E_S, \delta m_z). \quad (7)$$

Here, we denote $\mathcal{S} = \mathcal{V}M_S/(\hbar\gamma)$ as the effective macrospin of the ferromagnetic island, \mathcal{V} and γ are the F volume and gyro-magnetic ratio, and M_S the magnetization. Moreover, P^{tr} corresponds to reversed polarizations and precession ($N_{S/F,\sigma} \mapsto N_{S/F,-\sigma}$, $\Omega \mapsto -\Omega$). The Onsager symmetry of L_{ij} in Eq. (6) is a consequence of fluctuation relations [41]. The energy transfer δE_F into the ferromagnet (generally, $\delta E_F \neq \delta E_S$) is determined by energy conservation $\delta E_F + \delta E_S = V\delta n + \Omega S\delta m_z$, which implies $\overline{\dot{E}_S} + \overline{\dot{E}_F} = \overline{I_c}V - \Omega\overline{\tau_z}$. These results arise from the symmetries of Eqs. (19) and (20) below, for the case where there is no external magnetic drive.

B. Nonlinear response

The pumped charge current is shown in Fig. 2(a), and the energy current into S in Fig. 2(b). The charge pumping is nonzero above the quasiparticle gap, $|\Omega| \gtrsim \Delta \pm h$ [29]. The heat current shows the presence of a region of cooling of either of the two leads, depending on the relative orientation of \mathbf{h} and $\Omega\hat{z}$. Nonzero h enables the N/S cooling effect to be

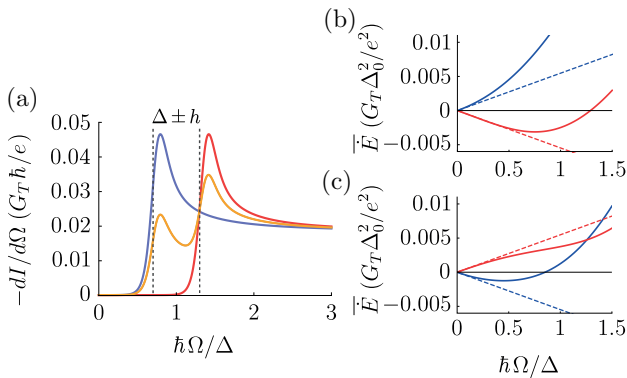


FIG. 2. (a) Pumped differential current for $T_S = T_F = 0.1 T_C$ where T_C is the critical temperature of the superconductor. Blue, yellow, and red lines are for $\mathbf{h} = -h\hat{z}$, $h\hat{x}$, $h\hat{z}$, respectively. (b) and (c) Energy current into the superconductor $\overline{\dot{E}_S}$ (blue line) and into the magnet $\overline{\dot{E}_F}$ (red line) for (b) $\mathbf{h} = -h\hat{z}$ and for (c) $\mathbf{h} = h\hat{z}$. F and S are at temperature $T = 0.6 T_C$. Dashed lines represent the linear response. In all figures, $V = 0$, $\theta = \frac{\pi}{8}$, $P = 1$, and $h = 0.3\Delta_0$, where Δ_0 is the superconductor gap at zero temperature.

present already at linear response, similarly as with voltage bias [23,42].

IV. MAGNETIZATION DYNAMICS

The Landau-Lifshitz-Gilbert-Slonczewski (LLG) equation for the tilt angle is

$$-\mathcal{S}\partial_t \cos\theta = \overline{\tau_z} - SA_0\Omega \sin^2\theta + \eta, \quad (8)$$

where the spin transfer torque $\overline{\tau_z}$ is given by Eq. (5). We include the intrinsic Gilbert damping [28] phenomenologically, and A_0 is the dimensionless damping constant. Moreover, η is a Langevin term describing the torque noise [32,39,44,45] with the correlation function $\langle \eta(t)\eta(t') \rangle = 2[D(\theta) + SA_0T] \sin^2(\theta)\delta(t-t')$; see below. Equilibrium torques are here included in the LLG effective magnetic field $\Omega\hat{z}$ (see Appendix A). We consider the limit of weak damping, where it is sufficient to consider only the equation for the z component.

A. Heat balance in ferromagnetic resonance

Let us consider a ferromagnetic resonance (FMR) [26] in a thin magnetic layer on a spin-split S, driven by a resonant circularly polarized rf magnetic field (at frequency $\omega = \Omega$), and in the case of S acting as a reservoir at a fixed temperature T . The electrical circuit is open, so that no charge flows between F and S. The FMR driving acts as a power source. We assume that a fraction $\lambda \in [0, 1]$ of the power dissipated by the intrinsic Gilbert damping heats the F electrons; the value of λ depends on into which bath(s) its microscopic mechanism dissipates the energy (see also Sec. V A below). In a steady state, the total energy current into F, the overall torque, and the charge current are zero:

$$\overline{\dot{E}_{F,\text{tot}}} = \overline{\dot{E}_F} + \lambda\overline{P_G} = 0, \quad (9)$$

$$\overline{\tau_z} + \overline{\tau_{z,\text{rf}}} + \overline{\tau_{z,G}} = 0, \quad (10)$$

$$\overline{I_c} = 0, \quad (11)$$

where $\overline{\tau_z}$ and $\overline{I_c}$ are the contributions related to the tunneling between F and S, from Eqs. (3) and (5), and $\overline{\dot{E}_F} = \overline{I_c}V - \Omega\overline{\tau_z} - \overline{\dot{E}_S}$ is found from the tunneling model via a similar calculation as in Eq. (4). Moreover, $\overline{\tau_{z,G}} = -SA_0\Omega \sin^2(\theta)$ and $\overline{P_G} = SA_0\Omega^2 \sin^2(\theta)$ are the torque due to the intrinsic damping and the rate of work done by it. At resonance, the rf drive creates a torque $\overline{\tau_{z,\text{rf}}} = \gamma\mathcal{S}(\mathbf{m} \times \mathbf{h}_{\text{rf}})_z = \gamma\mathcal{S}h_{\text{rf}} \sin\theta$, where h_{rf} is the amplitude of the rf field. From the above it follows that the power,

$$\overline{\dot{E}_S} + \overline{\dot{E}_{F,\text{tot}}} = \overline{P_{\text{rf}}} - (1-\lambda)\overline{P_G}, \quad (12)$$

is absorbed by the electron system, where $\overline{P_{\text{rf}}} = \Omega\overline{\tau_{z,\text{rf}}}$ is the total rf power absorbed at resonance [28].

Expanding Eqs. (3)–(5) in the linear order in V , $\delta T/T$, and θ^2 , but not in Ω , we find the charge and heat currents,

$$\begin{pmatrix} \overline{I_c} \\ \overline{\dot{E}_S} \\ \overline{\tau_z} \end{pmatrix} = \begin{pmatrix} G & P\alpha & P(G - \tilde{G}) \\ P\alpha & G_{\text{th}}T & \alpha + \tilde{\alpha} + \frac{\tilde{G}\Omega}{2} \\ 0 & 0 & -\tilde{G} \end{pmatrix} \begin{pmatrix} V \\ -\delta T/T \\ \frac{\Omega}{4}\theta^2 \end{pmatrix}. \quad (13)$$

Unlike the linear-response matrix in Eq. (6), the above matrix is not symmetric, as there is no Onsager reciprocity between $\bar{\tau}_z$ and θ^2 . The coefficients are

$$\tilde{\alpha} = \frac{G_T}{2} \int_{-\infty}^{\infty} d\epsilon \sum_{\sigma} \left(\epsilon - \frac{\sigma\Omega}{2} \right) N_{S,\sigma}(\epsilon) \frac{f_0(\epsilon - \sigma\Omega) - f_0(\epsilon)}{\Omega}, \quad (14)$$

$$\tilde{G} = \frac{G_T}{2} \int_{-\infty}^{\infty} d\epsilon \sum_{\sigma} \sigma N_{S,\sigma}(\epsilon) \frac{f_0(\epsilon - \sigma\Omega) - f_0(\epsilon)}{\Omega}. \quad (15)$$

These coefficients are defined so that $\lim_{\Omega \rightarrow 0} \tilde{G} = G$ and $\lim_{\Omega \rightarrow 0} \tilde{\alpha} = \alpha$, and they assume the values $\tilde{G}_{\text{normal}} = G_T$ and $\tilde{\alpha}_{\text{normal}} = 0$ in the normal state.

The torque balance (10) determines the precession angle $\theta \approx \gamma \mathcal{S} h_{\text{rf}} / (\mathcal{S} A_{\text{eff}} \Omega)$, where $\mathcal{S} A_{\text{eff}} = \mathcal{S} A_0 + \frac{\tilde{G}}{4}$. To quadratic order in h_{rf} , $\bar{E}_F = \tilde{G} \Omega^2 \theta^2 / 4 - \bar{E}_S$. Using this, and the conditions (9) and (11) for heat and charge currents, we find the FMR induced temperature difference and voltage,

$$\begin{pmatrix} V \\ -\delta T \end{pmatrix} = \begin{pmatrix} G & P\alpha \\ P\alpha & G_{\text{th}} T \end{pmatrix}^{-1} \begin{pmatrix} -\frac{P(G-\tilde{G})\Omega}{4} \\ -\frac{\alpha + \tilde{\alpha}}{4}\Omega + \left[\frac{\tilde{G}}{8} + \lambda \mathcal{S} A_0 \right] \Omega^2 \end{pmatrix} \theta^2. \quad (16)$$

The coupling between \bar{E}_S and θ^2 is of the linear order in Ω , whereas the coupling between \bar{I}_c and θ^2 , the rf power, and the magnetic dissipation are of the quadratic order in Ω . Thus, for $\Omega \ll T$ the induced temperature difference and voltage are

$$V \simeq \frac{P\alpha}{GT} \delta T, \quad \delta T \simeq \frac{\alpha}{2(G_{\text{th}} - \frac{P\alpha^2}{GT})} \Omega^2 \theta^2. \quad (17)$$

The denominator $\tilde{G}_{\text{th}} = G_{\text{th}} - \frac{P\alpha^2}{GT}$ is always positive [21]. For $\Omega \ll T$, F is refrigerated when $\alpha > 0$, which corresponds to $\mathbf{h} \cdot \hat{z} < 0$. Restoring the SI units, the magnitude of the coefficient between δT and $\Omega^2 \theta^2$ is $|\hbar\alpha / (\tilde{G}_{\text{th}} e)| \lesssim \hbar/k_B$.

At higher frequencies the magnetic dissipation, nonlinearities of $\tilde{\alpha}$ and \tilde{G} , and the coupling between charge and precession start to play a role and limit the attainable temperature difference. For $\mathcal{S} A_0 / G_T = 0.1$, the magnitude of the effect is illustrated in Fig. 3. The maximum value of A_0 for which refrigeration is possible is shown in Fig. 4 as a function of T and Ω . If $\lambda = 1$, the parameter regime is similar to that where the spin-torque driven oscillations occur (see Sec. IV B below). However, if the intrinsic damping dissipates the energy to systems different from the F conduction electrons

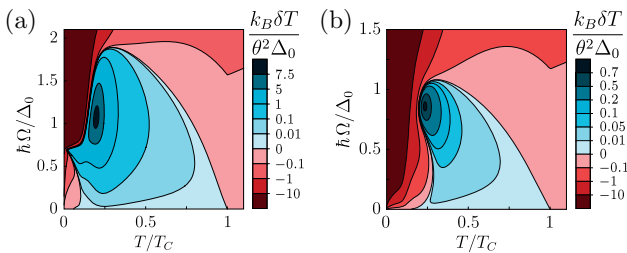


FIG. 3. Electromagnetically driven FMR induced refrigeration for $\mathbf{h} = -0.3\Delta_0\hat{z}$, $P = 1$, and $A_0 = 0.1\hbar G_T / (e^2 \mathcal{S})$. (a) For $\lambda = 0$ and (b) for $\lambda = 1$. Dynes broadening $\Gamma = 10^{-3}\Delta_0$ was assumed [43].

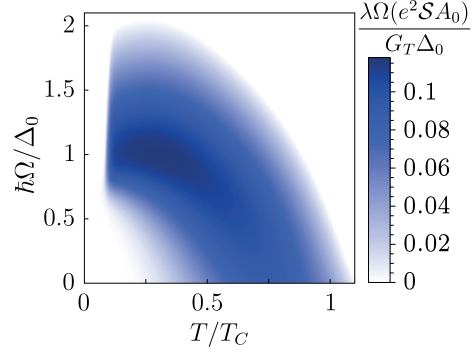


FIG. 4. Maximum intrinsic damping, expressed as $\Omega \times \lambda e^2 \mathcal{S} A_0 / (G_T \Delta_0)$, for which the system can be refrigerated, with $\mathbf{h} = -0.3\Delta_0\hat{z}$, $P = 1$, and Dynes broadening $\Gamma = 10^{-5}\Delta_0$. The maximum intrinsic damping is determined by solving A_0 from Eq. (16) with $\delta T = 0$.

($\lambda < 1$), refrigeration is easier to obtain than auto-oscillations. Therefore, measuring the temperature difference δT via the thermoelectrically induced voltage V allows for a direct study of the energy dissipation mechanism of the intrinsic Gilbert damping. Note that also in the absence of the spin splitting in S (and therefore $\alpha = 0$), it is possible to induce a nonzero voltage via FMR driving [29]. However, that generally requires higher frequencies $\Omega \lesssim \Delta$ than the case analyzed above.

If the thermoelectric coefficient is zero, F always heats up. In the normal state we have

$$\delta T_{\text{normal}} = -\frac{G_T + 8\lambda \mathcal{S} A_0}{8G_{\text{th}}} \Omega^2 \theta^2 < 0, \quad (18)$$

which shows the combined heating effect from the different sources of dissipation. However, in that case the induced voltage $V = 0$, and the temperature difference would have to be measured via some other mechanism.

B. Spin torques

The junction also exhibits a *voltage-driven spin torque*. With an exchange field such that $\mathbf{h} \cdot \hat{z} < 0$ and $\Omega \lesssim 2h$, the torque due to tunneling becomes antidamping at large voltages. When it exceeds the intrinsic damping, the $\theta = 0$ equilibrium configuration is destabilized, and a new stable steady-state configuration $\bar{\tau}_{z,\text{tot}}(\theta_*) = 0$ is established. An example of the signs of the torque and the resulting configuration is shown in Fig. 5(a): The stable angle is $\theta_* = 0$ at small voltages, after which there is a voltage range for which $0 < \theta_* < \pi$. There, the system realizes a voltage-driven spin oscillator [46,47]. At large voltages the stable angle is $\theta_* = \pi$, corresponding to a torque-driven magnetization flip.

Similarly, the *thermal torque* is shown in Fig. 5(b). Due to the nonzero linear-response coupling, it is antisymmetric in small δT , in contrast to the voltage-driven torque. Consequently, antidamping regions occur for both signs of Ω . In linear response [Eq. (6)], for temperature differences satisfying $\text{sgn}(\alpha)\delta T < \delta T_o = [1 + e^2 \mathcal{S} A_0 / (\hbar G)] P \hbar \Omega / (2e|\mathcal{S}|)$, the spin torque drives $\theta \rightarrow 0$, damping the precession. Here, $\mathcal{S} = -P\alpha / (GT)$ is the junction thermopower, which can be $|\mathcal{S}| \gtrsim k_B/e$. [21] Above the critical temperature difference $k_B \delta T_o$,

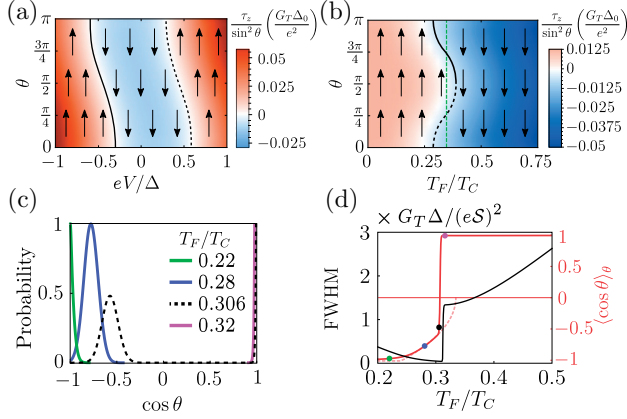


FIG. 5. (a) Torque vs angle θ and voltage V at $\Omega = 0.3\Delta/\hbar$ for $T_S = T_F = 0.5T_C$, $\mathbf{h} = -0.3\Delta_0\hat{z}$, and $P = 1$. The arrows indicate where the torque drives the angle. The solid black line indicates the stable precession angle θ_* , and the dashed line the unstable one. At $V = 0$, $\theta_* = 0$. (b) Torque vs angle and temperature difference at $\Omega = 0.5\Delta/\hbar$ for $T_S = 0.5T_C$, $\mathbf{h} = 0.3\Delta_0\hat{z}$, $P = 1$, and $V = 0$. Moreover, $S A_0 = 0$. The dashed green line indicates δT_0 . (c) Magnetization distribution normalized by its maximum value, for a thermally driven spin oscillator with $S = 100$, $T_S = 0.5T_C$, $\mathbf{h} = 0.3\Delta_0\hat{z}$, $P = 1$, $V = 0$, and $\Omega = 0.5\Delta/\hbar$. When $T_F \approx 0.31T_C$ (dashed line), the distribution is significantly bimodal. (d) Full width at half maximum (FWHM) of the dipole spectrum $S_{xx}(\omega)$ (black line) and the average magnetization (red line) with $G_T = e^2/\hbar$. The dashed line indicates θ_* and the dots correspond to (c).

the thermal spin torque drives the system away from $\theta_* = 0$ (or $\theta_* = \pi$ for $\Omega < 0$). The stable precession angle is shown in Fig. 5(b): There is a range of δT in which $\theta_* \neq 0, \pi$ and the system exhibits thermally driven [35] spin oscillations.

In Fig. 5, we neglect the effect of the intrinsic damping A_0 on the magnetization oscillations. However, it is the main obstacle in reaching auto-oscillations in FMR devices, and we estimate its effect here. For the superconducting systems, generally the effective bias $|s|\delta T$ can be at most Δ . Considering the value δT_0 given above, this results to a requirement for the resistance-area product of the S/F junction: $RA \lesssim (RA)_0 = \frac{\hbar\gamma\Delta}{e^2 A_0 M_s d_F |\Omega|} \approx 10^{-4} \Omega \mu\text{m}^2 \times \frac{1 \text{ T nm } \Delta}{\mu_0 M_s d_F A_0 |\hbar\Omega|}$, where d_F is the ferromagnet thickness. Meeting the requirement is likely challenging. Values $RA \sim 0.1 \Omega \mu\text{m}^2$ have been achieved in $\sim (100 \text{ nm})^2$ lateral size magnetic junctions [46,48]. With such RA and $\mu_0 M_s d_F = 5 \text{ T nm}$ (e.g., Co layer [46]) and $A_0 = 0.01$ [28], the condition is satisfied for $f = |\Omega|/(2\pi) < 0.02\Delta/\hbar \approx 1 \text{ GHz}$ (for Al as superconductor). The FMR refrigeration has a similar requirement but with $\Delta \mapsto \Delta/\lambda$, and hence may be easier to achieve, if the microscopic mechanism is such that $\lambda < 1$.

V. KELDYSH ACTION

To properly describe the metastable states in the magnetization precession, we need to extend the formalism. The dynamics beyond average values can be described by an effective action $S = S_0 + S_T$ for the spin including the tunneling, derived [32,34–36,39,45,49,50] by retaining the Keldysh structure [51] for the orientation of the magnetization

mean field. The action S describes the generating function of the joint probability distribution $P_{t_0}(\delta n, \delta E_S, \delta E_F, \delta m_z)$ [see Eq. (7)], with a source field $\chi, \xi_S, \xi_F, \zeta$ associated with each of the arguments. The free part reads

$$S_0 = 2S \int_{-\infty}^{\infty} dt \left[\left(\frac{\zeta}{2} + \phi^q \right) \partial_t (\cos \theta)^c - (\cos \theta)^q (\dot{\phi}^c - \Omega) \right], \quad (19)$$

where c and q denote the symmetric/antisymmetric combinations $x^{c/q} = \frac{x+\pm x}{2}$ of quantities on the two Keldysh branches (+/-), for example, $(\cos \theta)^{c/q} = \frac{1}{2} [\cos(\theta^c + \theta^q) \pm \cos(\theta^c - \theta^q)]$. Concentrating on slow perturbations around the semiclassical ($S \gg 1$) precession trajectory $\phi^c(t) = \Omega t$, the tunneling action can be expressed as $S_T \simeq -i \int_{-\infty}^{\infty} dt s_T$ with [39]

$$s_T = \frac{G_T}{2} \int_{-\infty}^{\infty} d\epsilon \sum_{\sigma\sigma'=\pm} N_{F,\sigma'} N_{S,\sigma} \left\{ \frac{\cos \theta^q + \sigma\sigma' \cos \theta^c}{2} \times [e^{i\eta_{\sigma\sigma'}} f_F(1-f_S) + e^{-i\eta_{\sigma\sigma'}} f_S(1-f_F)] - \frac{1 + \sigma\sigma'(\cos \theta)^c}{2} [f_F(1-f_S) + f_S(1-f_F)] \right\}, \quad (20)$$

where $\eta_{\sigma\sigma'} = \chi + \epsilon\xi_S - (\epsilon - V - \Omega_{\sigma\sigma'})\xi_F - 2\phi^q \frac{\Omega_{\sigma\sigma'}}{\Omega}$. Here, we have neglected terms that renormalize Ω . For computing time averages, the source fields are taken nonzero between $t = 0$ and $t = t_0$, e.g., $\chi(t) = \chi\theta(|t_0| - |t|)\theta(t \text{ sgn } t_0)$. The results (3)–(5) can be found as $\bar{I}_c = -i\partial_{\chi} s_T|_0$, $\bar{E}_S = -i\partial_{\xi_S} s_T|_0$, and $\bar{v}_z = \frac{1}{2i}\partial_{\phi^q} s_T|_0$, where $|_0$ indicates $\phi^q = \theta^q = \chi = \xi_{S/F} = 0$. Expansion around the saddle point gives Eq. (8), and the correlator characterizing the spin torque noise is $D = -\frac{1}{8}\partial_{\phi^q}^2 s_T|_0 \csc^2 \theta = -\frac{1}{8}\partial_{\theta^q}^2 s_T|_0$.

A. Intrinsic damping

We can include the phenomenological Gilbert damping term $A_0 \mathbf{m} \times \dot{\mathbf{m}}$ of the LLG equation into a corresponding term in the action, $iS_G = \int_{-\infty}^{\infty} dt s_G(t)$. With the weak-damping assumptions $\dot{\phi}^c \simeq \Omega$, $|\dot{\theta}^c| \ll |\dot{\phi}|$, the leading term in the torque is produced by $s_G \simeq -2iS A_0 \Omega \sin^2(\theta^c) \phi^q$.

Further reasoning is required for thermodynamic consistency. Let us first assume that the Gilbert damping is caused by a coupling that ultimately dissipates energy into the bath of conduction electrons in F ($\lambda = 1$). We can express the conservation of energy in conversion of magnetic energy to energy of conduction electrons as the symmetry $s_G[\xi_F + x, \phi^q + \Omega x/2] = s_G[\xi_F, \phi^q]$ for all x . In addition, to preserve the thermodynamic fluctuation relations and the second law at equilibrium, the fluctuation symmetry $s_G[\xi_F, \phi^q] = s_G[iT_F^{-1} - \xi_F, -\phi^q]$ should be fulfilled [39]. The above fixes the series expansion in ξ_F, ϕ^q, T_F^{-1} to have the form,

$$s_G[\xi_F, \phi^q] \simeq -2A_0 S \sin^2(\theta^c) \left[i\Omega \left(\phi^q - \frac{\Omega}{2} \xi_F \right) + 2T_F \left(\phi^q - \frac{\Omega}{2} \xi_F \right)^2 \right] + \dots \quad (21)$$

If the Gilbert damping dissipates energy directly to multiple baths (e.g., magnons, phonons), more terms of this form

appear, where ξ_F and T_F should be replaced by the corresponding bath variables, and only a fraction $0 \leq \lambda \leq 1$ of the total A_0 comes from conduction electrons. Including Eq. (21) in the total action $S = S_0 + S_T + S_G$ then produces, e.g., the correlation function of the Langevin noise terms in Eq. (8), and the additional term in the heat balance equation Eq. (9). These are of course possible to find also directly, by assuming the fluctuation-dissipation theorem, and reasoning about magnetic work done by the damping.

For the external rf drive, we similarly have a term $s_{\text{rf}} = 2i\mathbf{S}m^q \cdot \gamma\mathbf{h}_{\text{rf}} \simeq 2i\gamma h_{\text{rf}} \mathcal{S} \sin(\theta^c)\phi^q$, at resonance. It does not obey the above energy conservation symmetry, as power is externally provided and the mechanism generating h_{rf} is not included in the model. As a consequence, as noted in Eq. (12) $\overline{E}_{S,\text{tot}} + \overline{E}_{F,\text{tot}} \neq 0$, and the fluctuation relation (7) is modified.

B. Spin oscillator

The probability distribution of the magnetization angle θ can be obtained from Eqs. (19) and (20) [39,44], within a semiclassical method applied to $\tilde{s}_T = s_T|_{\theta^q=\chi=\xi_j=0}$ [39,51]. In this approach, at equilibrium, the fluctuation symmetry $\tilde{s}_T(\phi^q = -i\Omega/2T) = 0$ results to the Boltzmann distribution $P(\cos\theta) = Ne^{\mathcal{S}\cos(\theta)\Omega/T}$. In the nonequilibrium driven state ($V \neq 0$, $\delta T \neq 0$), the distribution deviates from this.

The probability distribution is shown in Fig. 5(c) for the thermally driven oscillator. The figure shows the spin torque-driven transition from the magnetization pointing in the direction of the magnetic field ($\cos\theta = 1$) for high T_F , to the opposite direction of the field ($\cos\theta = -1$) at low T_F . In the intermediate range $T_F \approx 0.25\text{--}0.3T_C$, the probability distribution becomes bimodal, reflecting the two locally stable configurations in Fig. 5(b): One of these corresponds to the oscillating state.

C. Emission spectrum

A driven spin oscillator produces electromagnetic emission which can be detected. [46,47] This can be characterized with the classical correlator of the magnetic dipole, whose spectrum is approximately a Lorentzian centered at frequency Ω . The classical spectrum of the magnetic dipole correlator can be written as

$$S_{\text{xx}}(\omega) = \mathcal{S}^2 \int_{-\infty}^{\infty} dt_0 e^{i\omega t_0} \langle m_x(t_0)m_x(0) \rangle, \quad (22)$$

where $m_x = \cos\phi \sin\theta$, and the average is over the driven steady state of the system. To evaluate it, the average over ϕ can be taken first, noting that $\langle \cos\phi(t_0)\cos\phi(0) \rangle_{\phi} = \frac{1}{2} \text{Re} \langle e^{i\phi(t_0)-i\phi(0)} \rangle_{\phi} = \frac{1}{2} \text{Re} \int D[\phi^c, \theta^q] e^{i\mathcal{S} e^{i\phi^c(t_0)-i\phi^c(0)}} = \frac{1}{2} \text{Re} \int D[\phi^c, \theta^q] e^{i\mathcal{S}'}$, where the exponential factor is removed by a shift $(\cos\theta)^q \mapsto (\cos\theta)^q + \text{sgn}(t_0)\theta(|t_0| - |t|)\theta(t \text{sgn } t_0)/(2\mathcal{S})$. For $\mathcal{S} \gg 1$, this results to $\mathcal{S}' - \mathcal{S} \simeq \Omega t_0 + i|t_0|\mathcal{S}^{-2}D \csc^2\theta^c =: \psi(t_0)$ so that $\langle m_x(t_0)m_x(0) \rangle_{\phi} \simeq \frac{1}{2} \sin^2\theta \text{Re} e^{i\psi(t_0)}$. Evaluating the Fourier transform, we get

$$S_{\text{xx}}(\omega) \simeq \frac{1}{2} \sum_{\pm} \langle D/[(\omega \pm \Omega)^2 + (\mathcal{S}^{-2}D \csc^2\theta^c)^2] \rangle_{\theta}. \quad (23)$$

A similar calculation is done in Ref. [44], via Langevin and Fokker-Planck approaches. The remaining average is over the steady-state distribution $P(\cos\theta)$.

The linewidth of the spectrum [black line in Fig. 5(d)] in this nonequilibrium system is a nontrivial function of the system parameters. For $T_F \approx 0.31T_C$ precession at θ_* becomes possible, and as a result the linewidth ($\propto \csc^2\theta$) narrows rapidly, becoming significantly smaller than the near-equilibrium fluctuations at $\theta \sim 0, \pi$.

VI. DISCUSSION

In this work, we explain how the thermomagnetolectric effect of a spin-split superconductor couples the magnetization in a magnetic tunnel junction to the temperature difference across it. The thermoelectric coefficient in the superconducting state is generally large, and enables a magnetic Peltier effect and thermal spin torque, with prospects for generating thermally driven oscillations detectable via spectroscopy. Superconductivity also offers possibilities to characterize and control the thermal physics via both the electric and magnetic responses or external field coupling of the magnetization.

ACKNOWLEDGMENTS

We thank A. Di Bernardo for discussions. This work was supported by Academy of Finland Project No. 317118 and No. 321982, the European Union's Horizon 2020 Research and Innovation Framework Programme under Grant No. 800923 (SUPERTED), and Jenny and Antti Wihuri Foundation.

APPENDIX A: TUNNELING CURRENTS

Calculation of the tunneling currents from the model (1) in the main text can be done with standard Green function approaches [33]. Assuming a spin and momentum-independent matrix element ($W_{jj'} = W$), the k -spin component of the spin current to S reads

$$I_s^k = \frac{G_T}{32} \int_{-\infty}^{\infty} d\epsilon \text{tr} \frac{\sigma_k}{2} [(R\check{g}_F R^\dagger)_+ \check{g}_S - \check{g}_S (R\check{g}_F R^\dagger)_-]^{K}, \quad (A1)$$

where the superscript K refers to the Keldysh component and $G_T = \pi v_F v_S |W|^2$ is the normal state tunneling conductance. The charge and energy currents can be obtained by replacing $\sigma_k/2 \mapsto \hat{\tau}_3$ and $\sigma_k/2 \mapsto \epsilon$ in Eq. (A1), respectively. Here, σ_j and $\hat{\tau}_j$ are Pauli matrices in the spin and Nambu spaces, with the basis $(\psi_\uparrow, \psi_\downarrow, -\psi_\downarrow^\dagger, \psi_\uparrow^\dagger)$, and $X_+(\epsilon, t) = \int dt' e^{i\epsilon(t-t')} X(t, t')$, $X_-(\epsilon, t) = \int dt' e^{i\epsilon(t'-t)} X(t', t)$. Moreover, $\check{g}_{F/S}(\epsilon) = \frac{2i}{\pi v_{F/S}} \hat{\tau}_3 \sum_j \check{G}_{F/S}(\epsilon, \mathbf{p}_j)$ are state-summed Keldysh Green's functions, normalized by the total density of states (DOS) $v_{F/S}$ at the Fermi level of the ferromagnet and the spin-split superconductor. The rotation matrix,

$$R = e^{-i\phi\sigma_z/2} e^{-i\theta\sigma_y/2} e^{i\psi\sigma_z/2} \times e^{-i\int^t dt' \dot{\phi}(1-\cos\theta)\sigma_z/2} e^{-iV\hat{\tau}_3 t}, \quad (A2)$$

contains the Euler angles of the time-dependent magnetization direction vector ($\mathbf{m} \cdot \boldsymbol{\sigma} = R\sigma_z R^\dagger$), a Berry phase factor, and

voltage bias V . The Berry phase appears from the Green function [31,32] of the conduction electrons in F following adiabatically the changing magnetization. For a metallic ferromagnet, $\hat{g}_F^R - \hat{g}_F^A \simeq 2 \sum_{\pm} (\hat{\tau}_3 \pm \sigma_z) \frac{v_{F,\pm}}{v_F}$ and $\hat{g}^K = [\hat{g}^R - \hat{g}^A](1 - 2f_0(\epsilon))$, where $v_{F,\uparrow/\downarrow} := v_{F,\pm}$ are the densities of states of majority/minority spins at the Fermi level and $f_0(\epsilon) = (1 + e^{\epsilon/T})^{-1}$ is the Fermi distribution function.

Evaluating Eq. (A1) for the different currents produces Eqs. (3)–(5) in the main text, with $N_{S/F,\sigma=\pm} = \frac{1}{2} \text{tr}[\frac{1+\hat{\tau}_3}{2} \frac{1+\sigma\sigma_z}{2} (\hat{g}_{S/F}^R - \hat{g}_{S/F}^A)]$.

Beyond linear response (6), we find the second-order contributions to the current and torque:

$$\delta^{(2)}\bar{I}_c = -\frac{\alpha_{2,0}^-}{2} \left[\sin^2(\theta) \left(V\Omega - \frac{P \cos \theta}{4} \Omega^2 \right) + P \cos(\theta) V^2 \right] - P \cos(\theta) \frac{A}{2} \left(\frac{\delta T}{T} \right)^2 - B \frac{\delta T}{T} V, \quad (\text{A3})$$

$$\frac{\delta^{(2)}\bar{\tau}_z}{\sin^2(\theta)} = \frac{\alpha_{2,0}^-}{4} \left[V^2 - P \cos(\theta) V\Omega + \frac{3 + \cos(\theta)}{8} \Omega^2 \right] + \frac{A}{4} \left(\frac{\delta T}{T} \right)^2 + \frac{B}{4} \frac{\delta T}{T} \Omega, \quad (\text{A4})$$

where $\alpha_{i,j}^{\mp} = -(G_T/2) \int_{-\infty}^{\infty} d\epsilon \epsilon^j [N_{S,+}(\epsilon) \mp N_{S,-}(\epsilon)] f_0^{(i)}(\epsilon)$, and $A = 2\alpha_{1,1}^- + \alpha_{2,2}^-$, $B = \alpha_{1,0}^+ + \alpha_{2,1}^+$.

For $\Omega \ll \Delta$, the onset of the voltage-driven spin oscillations [Fig. 5(a)] can be determined from Eqs. (6) and (A4) to occur at $V_o = \pm 4\sqrt{e^2 S A_{\text{eff}} \Omega / \alpha_{2,0}^-}$.

In addition to the spin transfer torque (STT) discussed in the main text, the electron transfer between F and the spin-split S generates also other torque components acting on F. This effect can be found from Eq. (A1), and appears in the torque components $\bar{\tau}_{x/y}$ perpendicular to the equilibrium magnetization \hat{z} .

In the main text, we neglect these torques, because any equilibrium torques can be absorbed to a renormalization of the effective magnetic field, and moreover, in the limit of weak damping and torques the components perpendicular to \hat{z} such that $\tau_{x/y} \ll S\Omega$ have little effect on the dynamics. In contrast, the component in the main text has a significant effect already at $\bar{\tau}_z \sim A_0 S \Omega \ll S\Omega$.

For completeness, we write here the expressions for all torques, as obtained from Eq. (A1). Equation (5) in the main text gives the dissipative contribution to τ_z . Similar contributions can be found for $\tau_{x/y}$:

$$\bar{\tau}_{x/y} = -\frac{G_T}{8} \int_{-\infty}^{\infty} d\epsilon \sum_{\sigma\sigma'} \frac{(1 + \sigma\sigma' \cos \theta)^2}{2} N_{S,x/y} \times [f_F(\epsilon - \Omega_{\sigma\sigma'} - V) - f_S(\epsilon)], \quad (\text{A5})$$

where $N_{S,0/x/y/z} = \frac{1}{2} \text{tr} \frac{1+\hat{\tau}_3}{2} \frac{\sigma_0/x/y/z}{2} (\hat{g}_S^R - \hat{g}_S^A)$.

In addition, there are two remaining contributions, the equilibrium spin torque, and a Kramers-Kronig counterpart to the density of state term. Terms of the latter type commonly appear in calculations of time-dependent response. To find it, we need $\hat{g}^{R+A} = \hat{g}^R + \hat{g}^A$. We can evaluate them, e.g., in a model with a parabolic spectrum in three dimensions, $\xi_k = k^2/(2m) - \mu$. In the superconductor, $h, \Delta \ll \mu_S$ and in

the magnet, $\Delta = 0$. Evaluating the momentum sum yields

$$\hat{g}_S^{R+A} \stackrel{\mu_S \rightarrow \infty}{\simeq} \hat{g}_{S,\text{qcl}}^R + \hat{g}_{S,\text{qcl}}^A + \hat{g}_F^{R+A} |_{h_F \rightarrow h, \mu_F \rightarrow \mu_S},$$

$$\hat{g}_F^{R+A} = 2ia \text{Re} \sqrt{-[(\epsilon - h_F \sigma_z) \hat{\tau}_3 + \mu_F] / |\mu_F|} + C. \quad (\text{A6})$$

Here $\hat{g}_{S,\text{qcl}}^{R/A}$ are quasiclassical low-energy Green functions [52], $1/a = \sum_{\pm} \sqrt{1 \pm h_F / \mu_F}$, and $h_F = \frac{v_{F\downarrow}^2 - v_{F\uparrow}^2}{v_{F\downarrow}^2 + v_{F\uparrow}^2} \mu_F$ the internal exchange field in F in the model. Moreover, C are scalars independent of ϵ, h , and Δ , and drop out from expressions for the observables here.

Neglecting terms of order $\Delta/\mu, T/\mu, \Omega/\mu$, we find the remaining terms in the spin current,

$$\mathbf{I}_S'' = \mathbf{I}_{S,\text{eq}}'' + \delta \mathbf{I}_S'', \quad (\text{A7})$$

$$\delta \mathbf{I}_S'' = -\frac{G_T}{64} \int_{-\infty}^{\infty} d\epsilon \sum_{\sigma\sigma'} \tanh \frac{\epsilon - \Omega_{\sigma\sigma'} - V}{2T_F} \times (\sigma \hat{z} + \sigma' \mathbf{m}(t)) \times \mathbf{P}(\epsilon) N_{F,\sigma'}, \quad (\text{A8})$$

where $\mathbf{P}(\epsilon) = \frac{1}{2i} \text{tr} \frac{1+\hat{\tau}_3}{2} \sigma [\hat{g}_{S,\text{qcl}}^R(\epsilon) + \hat{g}_{S,\text{qcl}}^A(\epsilon)]$. It has the symmetry $\mathbf{P}(-\epsilon) = \mathbf{P}(\epsilon)$. For a BCS superconductor, the integrand is nonzero only inside the gap, $|\epsilon \pm h| < \Delta$.

The equilibrium spin current $\mathbf{I}_{S,\text{eq}}''$ is related to the exchange coupling between F and FI mediated by the electrons in the superconductor. It can be absorbed to a small renormalization of the effective magnetic field acting on F. While its value can be calculated in the above tunneling model, the model is not sufficient for describing this non-Fermi surface term in the realistic situation. The superconducting correction $\delta \mathbf{I}_S''$ vanishes at equilibrium, but may contribute to nonequilibrium response. This torque, however, has $\bar{\tau}_z'' = 0$ and can be neglected similarly as in Eq. (A5).

APPENDIX B: ADIABATIC GREEN FUNCTION

In the tunneling calculation of Eq. (A1), an expression for the adiabatic Green function of the electrons on the ferromagnet with dynamic magnetization appears. For completeness, we discuss its meaning here. The nonequilibrium Green function for free electrons in a time-dependent exchange field, $H(t) = \sum_{n\sigma\sigma'} c_{n\sigma}^\dagger [\mathcal{H}_n(t)]_{\sigma\sigma'} c_{n\sigma'}$, $\mathcal{H}_n(t) = \epsilon_n + \mathbf{h}(t) \cdot \boldsymbol{\sigma}$, with a thermal initial state at $t=0$ is $G_n^>(t, t') = -iU_n(t, 0)(1 - \rho_n)U_n(0, t')^\dagger$, where $i\partial_t U_n(t, t') = [\epsilon_n - \mathbf{h}(t) \cdot \boldsymbol{\sigma}]U_n(t, t')$, $U(t, t) = 1$, and $\rho_n = [1 + e^{\mathcal{H}_n(0)/T}]^{-1}$. In an adiabatic approximation for $|h| \ll h^2$, $U_n(t, t') \simeq e^{-i(t-t')\epsilon_n} R(t) e^{i\varphi_n(t, t') \sigma_z / 2} R(t')^\dagger$, where $R(t) \sigma_z R(t)^\dagger = \mathbf{h}(t) \cdot \boldsymbol{\sigma}$ and $\varphi_n(t, t') = i \int_{t'}^t dt'' \text{tr} \sigma_z R(t'')^\dagger \partial_{t''} R(t'')$. In terms of Euler angles $\mathbf{h} = (\cos \phi \sin \theta, \sin \phi \sin \theta, \cos \theta)$ we write $R = e^{-i\phi \sigma_z / 2} e^{-i\theta \sigma_y / 2} e^{i\phi \sigma_x / 2} e^{-i\chi \sigma_z / 2}$. The function $\chi(t)$ is arbitrary, but U_n does not depend on it. For simplicity, we choose $\chi = \int^t dt' \dot{\phi} (1 - \cos \theta)$, which gives $\varphi_n = 0$. With this choice, the adiabatic Green function becomes

$$G_n^>(t, t') = R(t) G_{n,0}^>(t - t') R(t')^\dagger, \quad (\text{B1})$$

and the electron Berry phase appears only in the rotation matrix. This is equivalent to the ‘‘rotating frame’’ picture used in the main text and other works [28,30].

- [1] J. C. Slonczewski, *J. Magn. Magn. Mater.* **159**, L1 (1996).
- [2] M. Johnson and R. H. Silsbee, *Phys. Rev. B* **35**, 4959 (1987).
- [3] G. E. W. Bauer, E. Saitoh, and B. J. van Wees, *Nat. Mater.* **11**, 391 (2012).
- [4] Y. Tserkovnyak, A. Brataas, and G. E. W. Bauer, *Phys. Rev. B* **66**, 224403 (2002).
- [5] C. Bell, S. Milikisyants, M. Huber, and J. Aarts, *Phys. Rev. Lett.* **100**, 047002 (2008).
- [6] M. Houzet, *Phys. Rev. Lett.* **101**, 057009 (2008).
- [7] K.-R. Jeon, C. Ciccarelli, A. J. Ferguson, H. Kurebayashi, L. F. Cohen, X. Montiel, M. Eschrig, J. W. A. Robinson, and M. G. Blamire, *Nat. Mater.* **17**, 499 (2018).
- [8] Y. Yao, Q. Song, Y. Takamura, J. P. Cascales, W. Yuan, Y. Ma, Y. Yun, X. C. Xie, J. S. Moodera, and W. Han, *Phys. Rev. B* **97**, 224414 (2018).
- [9] K.-R. Jeon, C. Ciccarelli, H. Kurebayashi, L. F. Cohen, X. Montiel, M. Eschrig, T. Wagner, S. Komori, A. Srivastava, J. W. A. Robinson, and M. G. Blamire, *Phys. Rev. Applied* **11**, 014061 (2019).
- [10] K. Rogdakis, A. Sud, M. Amado, C. M. Lee, L. McKenzie-Sell, K. R. Jeon, M. Cubukcu, M. G. Blamire, J. W. A. Robinson, L. F. Cohen, and H. Kurebayashi, *Phys. Rev. Materials* **3**, 014406 (2019).
- [11] J. P. Morten, A. Brataas, G. E. W. Bauer, W. Belzig, and Y. Tserkovnyak, *EPL* **84**, 57008 (2008).
- [12] H. J. Skadsem, A. Brataas, J. Martinek, and Y. Tserkovnyak, *Phys. Rev. B* **84**, 104420 (2011).
- [13] M. Inoue, M. Ichioka, and H. Adachi, *Phys. Rev. B* **96**, 024414 (2017).
- [14] S. Teber, C. Holmqvist, and M. Fogelström, *Phys. Rev. B* **81**, 174503 (2010).
- [15] C. Richard, M. Houzet, and J. S. Meyer, *Phys. Rev. Lett.* **109**, 057002 (2012).
- [16] C. Holmqvist, M. Fogelström, and W. Belzig, *Phys. Rev. B* **90**, 014516 (2014).
- [17] H. Hammar and J. Fransson, *Phys. Rev. B* **96**, 214401 (2017).
- [18] T. Kato, Y. Ohnuma, M. Matsuo, J. Rech, T. Jonckheere, and T. Martin, *Phys. Rev. B* **99**, 144411 (2019).
- [19] P. Dutta, A. Saha, and A. M. Jayannavar, *Phys. Rev. B* **96**, 115404 (2017).
- [20] P. Machon, M. Eschrig, and W. Belzig, *Phys. Rev. Lett.* **110**, 047002 (2013).
- [21] A. Ozaeta, P. Virtanen, F. S. Bergeret, and T. T. Heikkilä, *Phys. Rev. Lett.* **112**, 057001 (2014).
- [22] M. Silaev, P. Virtanen, F. S. Bergeret, and T. T. Heikkilä, *Phys. Rev. Lett.* **114**, 167002 (2015).
- [23] F. S. Bergeret, M. Silaev, P. Virtanen, and T. T. Heikkilä, *Rev. Mod. Phys.* **90**, 041001 (2018).
- [24] T. T. Heikkilä, M. Silaev, P. Virtanen, and F. S. Bergeret, *Prog. Surf. Sci.* **94**, 100540 (2019).
- [25] P. M. Tedrow, J. E. Tkaczyk, and A. Kumar, *Phys. Rev. Lett.* **56**, 1746 (1986).
- [26] C. Kittel, *Phys. Rev.* **73**, 155 (1948).
- [27] T. Tokuyasu, J. A. Sauls, and D. Rainer, *Phys. Rev. B* **38**, 8823 (1988).
- [28] Y. Tserkovnyak, A. Brataas, G. E. W. Bauer, and B. I. Halperin, *Rev. Mod. Phys.* **77**, 1375 (2005).
- [29] M. Trif and Y. Tserkovnyak, *Phys. Rev. Lett.* **111**, 087602 (2013).
- [30] Y. Tserkovnyak, T. Moriyama, and J. Q. Xiao, *Phys. Rev. B* **78**, 020401(R) (2008).
- [31] B. Flebus, G. E. W. Bauer, R. A. Duine, and Y. Tserkovnyak, *Phys. Rev. B* **96**, 094429 (2017).
- [32] A. Shnirman, Y. Gefen, A. Saha, I. S. Burmistrov, M. N. Kiselev, and A. Altland, *Phys. Rev. Lett.* **114**, 176806 (2015).
- [33] F. S. Bergeret, A. Verso, and A. F. Volkov, *Phys. Rev. B* **86**, 214516 (2012).
- [34] T. Ludwig, I. S. Burmistrov, Y. Gefen, and A. Shnirman, *Phys. Rev. B* **95**, 075425 (2017).
- [35] T. Ludwig, I. S. Burmistrov, Y. Gefen, and A. Shnirman, *Phys. Rev. B* **99**, 045429 (2019).
- [36] T. Ludwig, I. S. Burmistrov, Y. Gefen, and A. Shnirman, *arXiv:1906.2730*.
- [37] M. Tinkham, *Introduction to Superconductivity* (Courier Corporation, North Chelmsford, 2004).
- [38] M. Hatami, G. E. W. Bauer, Q. Zhang, and P. J. Kelly, *Phys. Rev. Lett.* **99**, 066603 (2007).
- [39] P. Virtanen and T. T. Heikkilä, *Phys. Rev. Lett.* **118**, 237701 (2017).
- [40] Y. Utsumi and T. Taniguchi, *Phys. Rev. Lett.* **114**, 186601 (2015).
- [41] D. Andrieux and P. Gaspard, *J. Chem. Phys.* **121**, 6167 (2004).
- [42] F. Giazotto, T. T. Heikkilä, A. Luukanen, A. M. Savin, and J. P. Pekola, *Rev. Mod. Phys.* **78**, 217 (2006).
- [43] R. C. Dynes, J. P. Garno, G. B. Hertel, and T. P. Orlando, *Phys. Rev. Lett.* **53**, 2437 (1984).
- [44] A. L. Chudnovskiy, J. Swiebodzinski, and A. Kamenev, *Phys. Rev. Lett.* **101**, 066601 (2008).
- [45] D. M. Basko and M. G. Vavilov, *Phys. Rev. B* **79**, 064418 (2009).
- [46] S. I. Kiselev, J. C. Sankey, I. N. Krivorotov, N. C. Emley, R. J. Schoelkopf, R. A. Buhrman, and D. C. Ralph, *Nature (London)* **425**, 380 (2003).
- [47] W. H. Rippard, M. R. Pufall, S. Kaka, S. E. Russek, and T. J. Silva, *Phys. Rev. Lett.* **92**, 027201 (2004).
- [48] Y. Nagamine, H. Maehara, K. Tsunekawa, D. D. Djayaprawira, N. Watanabe, S. Yuasa, and K. Ando, *Appl. Phys. Lett.* **89**, 162507 (2006).
- [49] J. Fransson and J.-X. Zhu, *New J. Phys.* **10**, 013017 (2008).
- [50] J.-X. Zhu, Z. Nussinov, A. Shnirman, and A. V. Balatsky, *Phys. Rev. Lett.* **92**, 107001 (2004).
- [51] A. Kamenev, *Field Theory of Non-equilibrium Systems* (Cambridge University Press, Cambridge, 2011).
- [52] G. Eilenberger, *Z. Phys* **214**, 195 (1968).

VI

SPIN AND CHARGE CURRENTS DRIVEN BY THE HIGGS MODE IN HIGH-FIELD SUPERCONDUCTORS

by

M.A. Silaev, R. Ojajärvi and T.T. Heikkilä 2020

Physical Review Research **2**, 033416, DOI:[10.1103/PhysRevResearch.2.033416](https://doi.org/10.1103/PhysRevResearch.2.033416)


Reproduced with permission. Copyright 2020 American Physical Society. Published under the terms of the Creative Commons Attribution 4.0 International license.

Spin and charge currents driven by the Higgs mode in high-field superconductors

Mikhail A. Silaev,^{1,2} Risto Ojajarvi,¹ and Tero T. Heikkilä¹

¹University of Jyväskylä, Department of Physics and Nanoscience Center, P.O. Box 35 (YFL), FI-40014 University of Jyväskylä, Finland

²Moscow Institute of Physics and Technology, Dolgoprudny, Moscow Region 141700, Russia

 (Received 1 July 2019; revised 23 August 2020; accepted 25 August 2020; published 15 September 2020)

The Higgs mode in superconducting materials describes slowly decaying oscillations of the order parameter amplitude. We demonstrate that in superconductors with a built-in spin-splitting field the Higgs mode is strongly coupled to the spin degrees of freedom, allowing for the generation of time-dependent spin currents. Converting such spin currents to electric signals by spin-filtering elements provides a tool for the second-harmonic generation and the electrical detection of the Higgs mode generated by the external irradiation. The nonadiabatic spin torques generated by these spin currents allow for the magnetic detection of the Higgs mode by measuring the precession of the magnetic moment in the adjacent ferromagnet. We discuss also the reciprocal effect, which is the generation of the Higgs mode by the magnetic precession. Coupling the collective modes in superconductors to light and magnetic dynamics provides an opportunity for the study of superconducting optospintronics.

DOI: [10.1103/PhysRevResearch.2.033416](https://doi.org/10.1103/PhysRevResearch.2.033416)

I. INTRODUCTION

Oscillations of the order parameter amplitude in condensed-matter systems are often called Higgs modes (HMs) [1–5], in analogy with the Higgs boson in particle physics [6]. These collective excitations are generic for ordered states such as antiferromagnets, charge density waves [7], superfluids [8–10], cold atomic gases [11,12] and superconductors [2,13–27]. In general, one can call HMs all the possible collective modes of the order parameter, other than the Nambu-Goldstone modes [4].

Higgs modes have been observed by Raman scattering in superconductors with charge density wave order [14,15,17,28] and by the nuclear magnetic resonance in superfluid ³He [8–10]. In usual superconductors the HMs are charge neutral and thus decoupled from charge current. In such systems the observation of HMs has been facilitated by the development of low-temperature terahertz spectroscopy [18,19,24,29–32]. With this technique, HMs have been observed in NbTiN and NbN compounds [18,19]. Higgs modes have been observed indirectly as the AC linear conductance peak in current-carrying films of NbN [24] and Al [33].

Here we suggest a different mechanism allowing electrical detection of HMs due to their coupling with spin and charge degrees of freedom in high-field superconductor/ferromagnet junctions. Unusual transport properties of such systems have attracted intense attention [34–37], stimulating both experimental [38–47] and theoretical efforts [34,48–57].

The underlying physical mechanism behind the suggested electrical measurement of the HM is rooted in the strong coupling between the superconducting order parameter dynamics

and electron spins. The possibility to transmit spin signals by the order parameter excitations has been elucidated using the example of mobile topological defects, i.e., Abrikosov vortices [55,56]. Here we demonstrate that time-dependent spin currents can be generated by the collective amplitude modes in superconductors.

The structure of this paper is as follows. In Sec. II we introduce the setup and model. Section III shows the effect of the HM on AC spin and charge currents. Their use in accessing the HM either in second-harmonic generation or via the measurement of an avoided crossing between ferromagnetic resonance and HMs is discussed in Sec. IV. We conclude in Sec. V with an outlook to the range of phenomena affected by the HM.

II. SETUP AND MODEL

The generic setup that we study is shown in Fig. 1(a). Its basic element is a superconducting film placed in contact with a ferromagnetic (FM) material. An effective spin-splitting field \mathbf{h} entering as the Zeeman term in the Hamiltonian of the superconductor (SC) is induced by an external in-plane magnetic field. Alternatively, \mathbf{h} could be induced by the proximity to a ferromagnetic insulator [58–62]. The system is exposed to an external irradiation $E_\Omega e^{i\Omega t}$ which generates a time-dependent perturbation of the order parameter amplitude $\delta\Delta(t) = \Delta_{2\Omega} e^{2i\Omega t}$ through the second-order nonlinearity $\Delta_{2\Omega} \propto E_\Omega^2$ [63,64].

We model the SC/FM junction using the tunneling Hamiltonian approach [65,66], which has been used extensively to study both AC and DC tunnel currents [65,67–69],

$$H_T = \sum_{kk'\alpha} A_{k\alpha}^\dagger (\hat{\Gamma} \hat{B}_{k'})_\alpha + \text{H.c.}, \quad (1)$$

$$\hat{\Gamma} = \mathcal{T} \hat{\tau}_3 + \mathcal{U}(\mathbf{m} \cdot \hat{\sigma}). \quad (2)$$

Here $A_{k\alpha}$ ($B_{k\alpha}$) annihilates an electron with momentum k and spin α in the SC (ferromagnet), the unit vector \mathbf{m}

Published by the American Physical Society under the terms of the Creative Commons Attribution 4.0 International license. Further distribution of this work must maintain attribution to the author(s) and the published article's title, journal citation, and DOI.

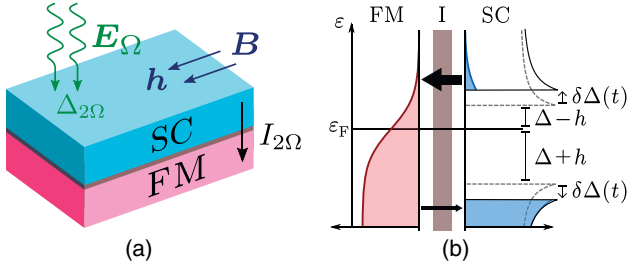


FIG. 1. (a) Setup of the superconductor/ferromagnet structure. The exchange field \mathbf{h} is induced by an external magnetic field \mathbf{B} . The double-frequency gap modulation can be excited by the external electromagnetic irradiation $\Delta_{2\Omega} \propto E_{\Omega}^2$ and is enhanced due to the coupling to the HM. (b) Semiconductor model of the current generation by a slowly varying perturbation of the order parameter amplitude $\delta\Delta(t)$. Only the spin-down band is shown. The ferromagnet has an equilibrium distribution $n_0(\varepsilon)$, while the distribution $n(\varepsilon, t)$ of the superconductor is shifted with respect to the equilibrium distribution (dashed line) by $\delta\Delta(t)$ away from the Fermi level. Due to the Zeeman shift h , the perturbation in the number of excitations is asymmetric with respect to the Fermi level ε_F . This results in net spin and charge currents flowing into the attached FM electrode through the tunnel barrier (I).

defines the spin quantization axis of the barrier, $\hat{\tau}_k$ and $\hat{\sigma}_k$ are the Pauli matrices in Nambu and spin spaces, respectively, and \mathcal{U} and \mathcal{T} are the spin-independent and spin-dependent matrix elements of the tunneling Hamiltonian, respectively [70]. The matrix tunneling current through the spin-polarized barriers can be expressed through momentum-averaged Green's functions (GFs) in the superconducting and FM electrodes $\nu_S \hat{g}_S = \hat{\tau}_3 \sum_k \langle \mathbb{T} \hat{A}_k(\tau) \hat{A}_k^\dagger(\tau') \rangle$ and $\nu_F \hat{g}_F = \hat{\tau}_3 \sum_k \langle \mathbb{T} \hat{B}_k(\tau) \hat{B}_k^\dagger(\tau') \rangle$, respectively. Here τ and τ' are imaginary times, \mathbb{T} is the time-ordering operator, and ν_S and ν_F are the normal metal densities of states on the two sides of the junction. For simplicity, we assume momentum-independent tunneling coefficients [70,71]. The time-dependent tunneling current for the general nonequilibrium state in the electrodes derived in Appendix A reads

$$\hat{I}(\tau) = i \frac{\nu_S \nu_F}{2} [\hat{g}_S \circ (\hat{\Gamma} \hat{g}_F \hat{\Gamma}) - (\hat{\Gamma} \hat{g}_F \hat{\Gamma}) \circ \hat{g}_S]_{\tau'=\tau}, \quad (3)$$

where \circ denotes time convolution. The overall tunnel current amplitude is determined by $\kappa = \nu_S \nu_F (\mathcal{T}^2 + \mathcal{U}^2)$ and the effective spin-filtering polarization is $\mathbf{P} = 2\mathcal{T}\mathcal{U}\mathbf{m}/(\mathcal{T}^2 + \mathcal{U}^2)$.

Tracing the general expression with appropriate Pauli matrices, we extract the charge current $I = e \text{Tr}(\hat{\tau}_3 \hat{I})$ and the spin current $\mathbf{I}_s = \text{Tr}(\hat{\sigma} \hat{I})$. The real-time response is obtained by the method of analytic continuation, described in Appendix B.

We assume that the electrodes are in the diffusive regime and can be described by the time-dependent Usadel equation for quasiclassical GFs. In the imaginary-time representation it has the form (we set $\hbar = 1$ here and below)

$$-i\{\hat{\tau}_3 \partial_\tau, \hat{g}\}_\tau = D \hat{\partial}_r (\hat{g} \circ \hat{\partial}_r \hat{g}) - i[\hat{\tau}_3 \hat{H}, \hat{g}]_\tau, \quad (4)$$

where D is the diffusion constant, $\hat{H} = \Delta \hat{\tau}_1 + \mathbf{h} \cdot \hat{\sigma}$, and \mathbf{h} is the exchange field. The quasiclassical GFs also satisfy the normalization condition $(\hat{g} \circ \hat{g})_{\tau, \tau'} = \delta(\tau - \tau')$. The time

derivative, convolution product, and differential superoperator in Eq. (4) are

$$\{\hat{\tau}_3 \partial_\tau, \hat{g}\}_\tau = \hat{\tau}_3 \partial_{\tau_1} \hat{g}(\tau_1, \tau_2) + \partial_{\tau_2} \hat{g}(\tau_1, \tau_2) \hat{\tau}_3, \quad (5)$$

$$(f \circ g)(\tau_1, \tau_2) = \int_0^\beta d\tau_3 f(\tau_1, \tau_3) g(\tau_3, \tau_2), \quad (6)$$

$$\hat{\partial}_r = \partial_r - \frac{ie}{c} [\hat{\tau}_3 A(\tau), \cdot], \quad (7)$$

respectively, where e is the elementary charge and c is the speed of light.

III. RESULTS

A. Qualitative description

In Fig. 1(b) we adapt the usual semiconductor picture of the tunnel current in superconductor junctions [72] to show how the time-dependent gap function creates a nonequilibrium state $n(\varepsilon, t)$ in the superconducting electrode. Due to the Zeeman shift h , this state is nonsymmetric with respect to the Fermi level ε_F and therefore produces spin current through the tunnel barrier between the SC and the adjacent normal metal. This qualitative picture is based on the time-dependent energy spectrum $E_\sigma = \sqrt{\xi_p^2 + \Delta(t)^2} + \sigma h$, with $\sigma = \pm 1$ for spin-up/down Bogoliubov quasiparticles, respectively, where ξ_p is the kinetic energy counted from the Fermi level ε_F .

For a slow time-dependent order parameter the spin-resolved perturbation of the quasiparticle distribution function can be written as $(\dot{\Delta}/\Gamma) \frac{d}{d\Delta} N_\sigma$, where the number of thermally excited states in equilibrium is $N_\sigma = \int d\xi_p n(E_\sigma(\xi_p, \Delta))$, with $n(E) = \tanh(E/2T)$. The inelastic scattering relaxation rate Γ is given by the Dynes parameter [73].

The spin-dependent perturbation of the distribution function results in the spin current

$$I_s(t) = \frac{\kappa}{\Gamma} \dot{\Delta} \frac{d}{d\Delta} (N_+ - N_-), \quad (8)$$

where κ is the effective barrier transparency. As shown below, Eq. (8) is obtained in the low-frequency limit $\Omega \ll \Gamma$ from the general result (21). The advantage of Eq. (8) is that it allows for the cartoon interpretation in terms of the semiconductor model in Fig. 1(b). However, for the most interesting case when the frequency of the $\Delta(t) \propto e^{2i\Omega t}$ oscillation is comparable to the gap $\Omega \sim \Delta$ and hence is coupled to the HM [13,16,74,75], the picture becomes more complicated and requires calculations using Eqs. (3) and (4) as described in Sec. III C.

B. Second-harmonic generation due to the broken particle-hole symmetry

Spin current generated by the HM can be converted to charge current using spin-filtering FM electrodes. In the setup shown in Fig. 1(a) the spin current is effectively converted to the charge current while passing through the spin-filtering barrier characterized by the polarization vector \mathbf{P} . The time-dependent charge current induced in this way by the order parameter amplitude oscillation is therefore qualitatively given by $I(t) \propto \mathbf{P} \cdot \mathbf{I}_s(t)$, which results in the

estimate $I(t) \propto (\mathbf{P} \cdot \mathbf{h})\partial_t \Delta$. Modulation of the order parameter amplitude can be induced, for example, by an external irradiation [63,64] $\Delta(t) \propto A^2(t)$, where $A(t)$ is the vector potential of the external field. Hence this charge current $I(t) \propto (\mathbf{P} \cdot \mathbf{h})\partial_t A^2$, being quadratic in the vector potential, demonstrates the second-harmonic generation (SHG) controlled by the superconducting order parameter.

Despite the large amount of attention to the nonlinear effects in superconductors, SHG has not been obtained before.¹ Hence only third-harmonic generation has been studied in superconductors [19,32,63,64,76]. We show below that such a kind of SHG is not prohibited by the generic symmetries of the problem, but is eliminated by the approximate symmetry of Fermi surface systems, made exact in the widely used quasiclassical approximation [77].² This additional symmetry of the GF satisfying the Usadel equation (4) is

$$\hat{g}(\mathbf{A}, \mathbf{h}, \Delta) = -\hat{\tau}_1 \hat{g}(-\mathbf{A}, \mathbf{h}, \Delta^*) \hat{\tau}_1. \quad (9)$$

The off-diagonal Nambu space Pauli matrix $\hat{\tau}_1$ interchanges the particle and hole blocks in the Hamiltonian [77], so the physical interpretation of Eq. (9) is a particle-hole symmetry. For the nonstationary charge current generated by the time-dependent vector potential this symmetry yields $I(\mathbf{A}, \Delta) = -I(-\mathbf{A}, \Delta^*)$. Further, in the absence of supercurrent or external orbital fields we can assume the order parameter to be real $\Delta = \Delta^*$. Then even the broken inversion symmetry near surfaces does not help to produce SHG in superconducting systems in contrast to the normal metal counterpart of this effect. Because of this symmetry, the direct coupling between the HM and the charge current is prohibited. However, as we see below, it allows for the spin currents driven by the HM and external field even with a nonferromagnetic barrier, that is, at $P = 0$.

The particle-hole symmetry is broken in superconducting/FM systems leading to large thermoelectric [34,78,79] and anomalous Josephson effects [77]. For real Δ the transformation (9) applied to the general tunnel current yields

$$I(\mathbf{A}, \mathbf{h}, \mathbf{P}) = -I(-\mathbf{A}, \mathbf{h}, -\mathbf{P}). \quad (10)$$

This relation allows for SHG. Because the sign of \mathbf{P} is inverted there is no longer a symmetry with respect to the mere flipping of the vector potential, $I(\mathbf{A}) \neq -I(-\mathbf{A})$. Hence, for the AC external field $A_\Omega e^{i\Omega t}$, Eq. (10) allows for the double-frequency charge current component $I_{2\Omega} e^{i2\Omega t}$ with the amplitude $I_{2\Omega} \propto |\Delta|^2 A_\Omega^2 (\mathbf{P} \cdot \mathbf{h})$ as well as the DC tunnel current [51] $I_{DC} \propto |\Delta|^2 A_\Omega A_{-\Omega} (\mathbf{P} \cdot \mathbf{h})$. The resonant SHG of spin and charge currents through the excitation of HM by electromagnetic irradiation is discussed below in Sec. III C.

C. Calculation of spin and charge currents

We assume that the superconducting electrode is driven out of equilibrium by the electromagnetic field described by the time-dependent vector potential $A_\Omega e^{i\Omega t}$. It produces

¹Here we exclude the trivial SHG which results from the third-order nonlinearity when both the oscillating and constant fields are applied.

²The Fermi surface symmetry present in the quasiclassical approximation is broken here by the spin polarization of tunneling.

the second-harmonic perturbation of the GF and tunnel current (3)

$$\hat{g}_S(\tau, \tau') = T \sum_{\omega} \hat{g}_S(\omega_+, \omega_-) e^{i\omega_+ \tau - i\omega_- \tau'}, \quad (11)$$

$$\hat{I}_{2\Omega} = i \frac{v_S v_F}{2} T \sum_{\omega} [\hat{\Gamma} \hat{g}_S \hat{\Gamma} \hat{g}_0(\omega_-) - \hat{g}_0(\omega_+) \hat{\Gamma} \hat{g}_S \hat{\Gamma}], \quad (12)$$

where $\omega_{\pm} = \omega \pm \Omega$ are the fermionic Matsubara frequencies shifted by the frequency Ω of the external field. We define $\hat{g}_S = \hat{g}_S(\omega_+, \omega_-)$ and assume that the ferromagnet is in the equilibrium state determined by the GF $\hat{g}_F(\omega) = \hat{g}_0(\omega) \equiv \text{sgn}(\omega) \hat{\tau}_3$.

There are two qualitatively different terms in the nonequilibrium GF $\hat{g}_S = \hat{g}_{AA} + \hat{g}_\Delta$. The first one is generated by the direct coupling to the external electromagnetic field. The second term is generated by the order parameter oscillations, which can be induced by either the electromagnetic field or other sources, for example, the spin current. Direct coupling to the electromagnetic field is described by the GF perturbations of second order by the vector potential.

From the Usadel equation (4) we find that the perturbation $\hat{g}_{AA}(\omega_+, \omega_-)$ satisfies the equation

$$\begin{aligned} s_+ \hat{g}_0(\omega_+) \hat{g}_{AA} - s_- \hat{g}_{AA} \hat{g}_0(\omega_-) \\ = D \left(\frac{eA_\Omega}{c} \right)^2 [\hat{g}_0(\omega_+) \hat{\tau}_3 \hat{g}_0(\omega) \hat{\tau}_3 - \hat{\tau}_3 \hat{g}_0(\omega) \hat{\tau}_3 \hat{g}_0(\omega_-)]. \end{aligned} \quad (13)$$

Expanding the normalization condition in perturbation series provides an anticommutation rule $\hat{g}_{AA} \hat{g}_0(\omega_-) = -\hat{g}_0(\omega_+) \hat{g}_{AA}$, which can be used to solve Eq. (13),

$$\hat{g}_{AA} = D \left(\frac{eA_\Omega}{c} \right)^2 \frac{\hat{\tau}_3 \hat{g}_0(\omega) \hat{\tau}_3 - \hat{g}_0(\omega_+) \hat{\tau}_3 \hat{g}_0(\omega) \hat{\tau}_3 \hat{g}_0(\omega_-)}{s_+ + s_-}, \quad (14)$$

where $s_{\pm} = \hat{s}(\omega_{\pm})$ and $\hat{s}(\omega) = \sqrt{\Delta^2 - (i\omega - \mathbf{h} \cdot \hat{\sigma})^2}$. Above, we abuse the notation slightly by writing the matrix inverse $[s_+ + s_-]^{-1}$ as a scalar division. No ambiguity is introduced as $\hat{s}(\omega)$'s commute with the terms in the numerator. Furthermore, in the final expression for the spin current (21) we shift the energy integration and remove the exchange field from the $\hat{s}(\omega)$'s, making their spin structure trivial.

Corrections to the GF induced by the time-dependent order parameter amplitude $\Delta_{2\Omega} e^{2i\Omega t}$ can be found in the form $\hat{g}_\Delta(\tau, \tau') = T \sum_{\omega} e^{i(\omega_+ \tau - \omega_- \tau')} \hat{g}_\Delta(\omega_+, \omega_-)$. From the Usadel equation (4) that $\hat{g}_\Delta(\omega_+, \omega_-)$ satisfies the equation

$$s_+ \hat{g}_0(\omega_+) \hat{g}_\Delta - s_- \hat{g}_\Delta \hat{g}_0(\omega_-) = \Delta_{2\Omega} [\hat{\tau}_2 \hat{g}_0(\omega_-) - \hat{g}_0(\omega_+) \hat{\tau}_2]. \quad (15)$$

Again using the normalization condition, the solution of this equation is given by

$$\hat{g}_\Delta = \Delta_{2\Omega} \frac{\hat{g}_0(\omega_+) \hat{\tau}_2 \hat{g}_0(\omega_-) - \hat{\tau}_2}{s_+ + s_-}. \quad (16)$$

The amplitude $\Delta_{2\Omega}$ can be found from the self-consistency equation

$$\Delta_{2\Omega} = -\lambda T \sum_{\omega} \text{Tr}[\hat{\tau}_2 (\hat{g}_{AA} + \hat{g}_\Delta)], \quad (17)$$

where we introduce the dimensionless pairing constant λ and the Pauli matrix $\hat{\tau}_2$ corresponds to the superconducting amplitude vertex.

The part which is directly produced by the irradiation provides a source of the Higgs mode

$$F_{\Delta}(2\Omega) = -\lambda T \sum_{\omega} \text{Tr}[\hat{\tau}_2 \hat{g}_{AA}]. \quad (18)$$

The other part determines the self-induced corrections to the order parameter $\tilde{\Delta}_{2\Omega} = \Pi(2\Omega)\Delta_{2\Omega}$ described by the polarization operator

$$\Pi(2\Omega) = 1 + \pi\lambda T \sum_{\omega} \text{Tr} \left[\frac{\Delta^2 + \Omega^2}{s_{-}s_{+}(s_{-} + s_{+})} \right], \quad (19)$$

where the trace is taken over the spin degree of freedom. Collecting all the contributions to the self-consistency equation (17), we get

$$\Delta_{2\Omega} = F_{\Delta}/[1 - \Pi(2\Omega)]. \quad (20)$$

This expression describes the HM excitation in the superconductor driven out of equilibrium by a continuous-wave irradiation as shown schematically in Fig. 1(a). The resonance condition corresponding to the HM is satisfied for $\Omega = \Omega^*$ when $1 - \Pi(2\Omega^*) = 0 + o(\sqrt{\Gamma})$. Hence the maximal amplitude of the order parameter oscillations is determined by the broadening parameter Γ , leading to a sharp peak in $\Delta_{2\Omega}(\Omega, T)$ for $\Omega \approx \Omega^*(T)$. In the absence of spin relaxation processes $\Omega^* = \Delta(T)$.

Using the found GF corrections (14) and (16), we calculate the spin and charge components of the tunneling current (12). The HM contribution is determined by the term \hat{g}_{Δ} . Using the procedure of analytical continuation described in Appendix B, we obtain the amplitude of real-frequency spin current $I_s(\Omega)e^{2i\Omega t}$ driven by the HM,

$$I_s(\Omega) = i\kappa\hbar\Delta_{2\Omega}\Delta \sum_{\sigma} \frac{\sigma}{h} \int \frac{d\varepsilon}{4\pi} \frac{\varepsilon[n(\varepsilon_{+}) - n(\varepsilon_{-})]}{s_{+}^R s_{-}^A (s_{+}^R + s_{-}^A)}, \quad (21)$$

where $n(\varepsilon)$ is the equilibrium distribution function. Here the spin splitting has been shifted from the spectral functions to the distribution functions, so $\varepsilon_{\pm} = \varepsilon \pm \Omega + \sigma h$ and $s^{R,A} = -i\sqrt{(\varepsilon \pm i\Gamma)^2 - \Delta^2}$. In the low-frequency limit $\Omega \ll \Gamma$ we obtain Eq. (8) when the spin current is driven by the adiabatic time dependence of Δ in accordance with the qualitative picture shown schematically in Fig. 1(b).

In the presence of the HM, which is the slowly decaying oscillations of the order parameter $\Delta(t)$ [13,16], the spin current is given by the sum of the corresponding Fourier components with the amplitudes given by (21). As a result of Eq. (21) we get slowly decaying oscillations of the spin current $I_s(t)$ which can be measured using electrical probes after the superconductor is initially driven into a nonequilibrium state by a field pulse.

Taking into account the relation (20), we obtain the SHG spin and charge currents induced by the external irradiation in accordance with the qualitative discussion in Sec. III B. The resonant behavior of the double-frequency spin current $I_s(\Omega)$ resulting from the HM mode excitation is shown in Fig. 2.

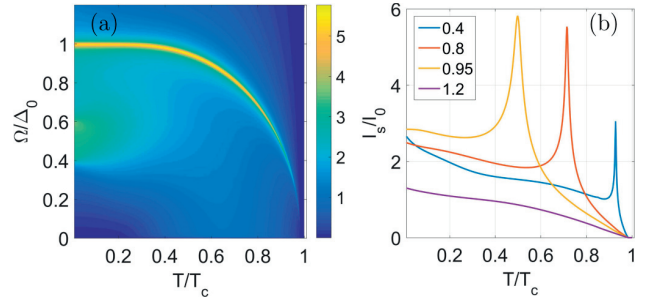


FIG. 2. Amplitude of double-frequency spin current $I_s(\Omega)e^{2i\Omega t}$ driven through the SC/ferromagnet tunnel junction by an external field $A_{\Omega}e^{i\Omega t}$. The current is normalized to $I_0 = \kappa D(eA_{\Omega}/c)^2$; T_c is the critical temperature. The sharp maximum at frequencies $\Pi(2\Omega) \approx 1$ corresponds to the resonant excitation of the Higgs mode. (a) $I_s(\Omega, T)$ and (b) $I_s(T)$ at different frequencies $\Omega/\Delta_0 = 0.4, 0.8, 0.95, 1.2$. The exchange field is $h = 0.2\Delta_0$ and the Dynes parameter $\Gamma = 0.005\Delta_0$. The peaks are at temperatures determined by $\Pi(2\Omega) \approx 1$.

IV. DISCUSSION

A. Electrical detection of the Higgs mode

The suggested effect of SHG charge current coupled to the HM can be measured, for example, in thin films of Al superconductor placed in a tunnel contact with FM iron electrodes similar to the setups used in the measurement of the nonlocal spin signals [38–40,43–47]. With $T_c = 1.6$ K and gap $\Delta_0 = 2 \times 10^{-4}$ eV, the spin-splitting field $h = 0.2\Delta_0$ can be obtained with an external in-plane magnetic field $B \approx 0.5$ T, and the polarization of this type of FM contact [44] is $P = 0.2$. With large enough area, the normal-state tunnel conductance can be similar to the experiments on stimulated superconductivity [80,81]. The electromagnetic power is characterized by the parameter $\alpha = D(eA_{\Omega}/c)^2$, which can be made as large as $\alpha = 0.1T_c$ without destroying the superconductivity [82]. For Al it yields $\alpha \approx 10^{-5}$ eV. With such parameters the charge current amplitude corresponding to Fig. 2 is $ePI_0 = 20$ nA, which is two orders of magnitude larger than the nonlocal thermoelectric current measured recently in a similar setup [47]. The maximal HM resonance frequency in Al is $2\Omega = 100$ GHz, which is within the capability of modern spectrum analysers. A 10-nA current across 50Ω corresponds to the signal amplitude -113 dBm, which means that the signal-to-noise level exceeding unity can be obtained within a 1-s measurement time with state-of-the-art high-frequency microwave spectrum analysers with a noise floor about -120 dBm/Hz.

B. Spin torques generated by the Higgs mode

If the exchange field \mathbf{h} in the SC is noncollinear with the magnetization \mathbf{m} in the ferromagnet, the HM generates a spin torque acting on \mathbf{m} . The generic system which can realize this configuration is shown in Fig. 3(a). Here the exchange field $\mathbf{h} \parallel \mathbf{m}_0$ is created by the ferromagnetic insulator layer with a fixed magnetic moment \mathbf{m}_0 [34].

The spin-transfer torque (STT) generated by the HM is shown schematically in Fig. 3(a). The polarization of the

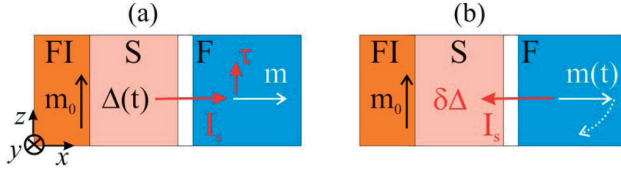


FIG. 3. Setups for studying transverse spin currents coupled to the HM in the superconductor (S). The exchange field in S is generated by the adjacent ferromagnetic insulator (FI) with magnetization m_0 . (a) The spin torque τ is generated in an adjacent ferromagnet (F) with noncollinear magnetization $\mathbf{m} \nparallel m_0$. (b) Magnetization precession $\mathbf{m}(t)$ induces the spin current \mathbf{I}_s and the spin battery effect leading to a perturbation of the order parameter amplitude $\delta\Delta$.

nonequilibrium spin current \mathbf{I}_s is determined by the direction of the exchange field \mathbf{h} . Assuming that the transverse component of the spin current is absorbed in the ferromagnet [83–87], we obtain the STT $\tau = I_s \mathbf{h}_\perp / h$, where $\mathbf{h}_\perp = \mathbf{h} - \mathbf{m}(\mathbf{m} \cdot \mathbf{h})$ is the perpendicular component of the exchange field.

The reciprocal effect shown in Fig. 3(b) is the perturbation of the gap $\delta\Delta$ by the magnetic precession. The pumped spin current [83] $\mathbf{I}_s \propto \mathbf{m} \times \dot{\mathbf{m}}$ has a longitudinal component $I_s \parallel \mathbf{h}$ which generates a time-dependent spin accumulation μ_s in the SC. In combination with the spin-splitting field \mathbf{h} , this results in [51,88]

$$\delta\Delta = \frac{\lambda\Delta}{1 - \Pi} \mu_s \partial_\Delta (N_+ - N_-), \quad (22)$$

where $1 - \Pi \propto \lambda$ is the low-frequency asymptotic of the polarization operator. This expression demonstrates the possibility to couple the order parameter amplitude with the magnetization dynamics. Thus the higher-frequency magnetization precession with $\Omega \sim \Delta$ generates the HM in the superconductor with a spin-splitting field.

This effect can be viewed as the HM-mediated transfer of the spin angular momentum from the ferromagnetic insulator to the metallic ferromagnet shown in Fig. 3(a). Oscillating STT generated by the order parameter amplitude mode can excite the ferromagnetic resonance (FMR) in the attached ferromagnet. Hybridization of the FMR and Higgs resonance should show up as the avoided crossing of the peaks in the second-harmonic response of the systems. Such an experiment will directly demonstrate the dynamical coupling of the magnetic and superconducting orders. Modification of the FMR linewidth by superconducting correlations in ferromagnet/SC structures has been observed [89–91]. In permalloy films the FMR has been measured in fields up to 0.3 T corresponding to a frequency of 20 GHz. For such a frequency the Higgs resonance in Al is expected to occur at $T \approx 0.92T_c$. Thus varying the field, one can measure the temperature-controlled hybridization of the HM and FMR mode in Al/permalloy structures within the currently accessible range of parameters.

V. CONCLUSION

We have demonstrated that spin and charge currents can be effectively generated by the collective amplitude modes of

the superconducting order parameter. Owing to the fact that the HM can be generated by external irradiation [27,92], our result paves the way for a conceptually different direction of superconducting optospintronics: the study of spin currents and spin torques generated by light interacting with superconducting materials.

We have suggested a detection scheme for the HM based on measuring resonant electric signals, either the charge current or voltage generated across the spin-polarized tunnel junction by the external field. Because these signals appear at the doubled frequency of the external field, our setup introduces a system featuring second-harmonic generation controlled by superconductivity. The suggested SHG can be studied using optical or microwave detectors [93] and the tunneling current $I_{2\Omega}$ can be detected using electrical probes. This feature of the SHG as compared to the previously known nonlinear response techniques allows for an electrical detection of the HM in superconductors.

Finally, a qualitatively similar effect should occur provided the ferromagnet is replaced by another spin-filtering element such as a semiconductor nanowire in proposed Majorana-based qubits [94–97]. The charge noise which is important in such devices [97] can cause the order parameter oscillations coupled to the splitting of Majorana zero modes. This coupling opens possibilities for many interesting effects to study.

ACKNOWLEDGMENTS

This work was supported by the Academy of Finland (Projects No. 297439 and No. 317118), Jenny and Antti Wihuri Foundation, Russian Science Foundation (Grant No. 19-19-00594), and the European Union’s Horizon 2020 research and innovation program under Grant Agreement No. 800923 (SUPERTED).

APPENDIX A: TUNNEL CURRENT

We model the spin-dependent tunneling through the SC/ferromagnet interface by the tunneling Hamiltonian (1). We calculate the tunneling current as a function of the time on the contour running along the imaginary axis from 0 to $\beta = 1/T$.

The matrix tunneling current in terms of the imaginary time functions reads

$$\hat{I}(\tau) = \frac{i}{2} \sum_k [\partial_\tau \hat{G}_S(\tau, \tau', k, k) + \partial_{\tau'} \hat{G}_S(\tau, \tau', k, k)]_{\tau=\tau'}. \quad (A1)$$

To find the perturbation we consider the contour-ordered GF

$$\hat{G}_S(\tau_1, \tau_2, k, k') = \langle \mathbb{T} \hat{S} \hat{A}_k(\tau_1) \hat{A}_{k'}^\dagger(\tau_2) \rangle, \quad (A2)$$

where \mathbb{T} is the contour-ordering operator and

$$\hat{S} \approx 1 - \int_0^\beta d\tau_3 H_T(\tau_3). \quad (A3)$$

In the interaction representation with respect to the tunneling Hamiltonian the equation of motion is

$$\partial_\tau \hat{A}_k = [\hat{A}_k, H_T] = \sum_{k'} (\hat{\Gamma}_{kk'} \hat{B}_{k'}). \quad (\text{A4})$$

Using the equation of motion we get

$$\begin{aligned} -\partial_{\tau_1} \hat{G}_S(\tau_1, \tau_2, \mathbf{k}, \mathbf{k}) &= -\sum_q \langle \mathbb{T} \hat{S} [\hat{\Gamma}_{kq} \hat{B}_q(\tau_1)] \hat{A}_k^\dagger(\tau_2) \rangle \\ &\approx \sum_q \left\langle \mathbb{T} \int_0^\beta d\tau_3 H_T(\tau_3) \hat{\Gamma}_{kq} \hat{B}_q(\tau_1) \hat{A}_k^\dagger(\tau_2) \right\rangle \\ &= \sum_{k_1, k'_1, q} \left\langle \mathbb{T} \int_0^\beta d\tau_3 \hat{B}_{k'_1}^\dagger(\tau_3) \hat{\Gamma}_{k_1 k'_1}^\dagger \hat{A}_{k_1}(\tau_3) \hat{\Gamma}_{kq} \hat{B}_q(\tau_1) \hat{A}_k^\dagger(\tau_2) \right\rangle \\ &= \sum_{k_1, k'_1, q} \int_0^\beta d\tau_3 \hat{\Gamma}_{kq} \langle \mathbb{T} \hat{B}_q(\tau_1) \hat{B}_{k'_1}^\dagger(\tau_3) \rangle \hat{\Gamma}_{k'_1 k_1} \langle \mathbb{T} \hat{A}_{k_1}(\tau_3) \hat{A}_k^\dagger(\tau_2) \rangle \\ &= \sum_{k_1, k'_1, q} \int_0^\beta d\tau_3 \hat{\Gamma}_{kq} \hat{G}_F(\tau_1, \tau_3, \mathbf{q}, \mathbf{k}'_1) \hat{\Gamma}_{k'_1 k_1} \hat{G}_S(\tau_3, \tau_2, \mathbf{k}_1, \mathbf{k}) \end{aligned} \quad (\text{A5})$$

and

$$\begin{aligned} -\partial_{\tau_2} \hat{G}_S(\tau_1, \tau_2, \mathbf{k}, \mathbf{k}) &= -\sum_q \langle \mathbb{T} \hat{S} \hat{A}_k(\tau) [\hat{\Gamma}_{kq} \hat{B}_q(\tau')]^\dagger \rangle \\ &\approx \sum_q \left\langle \mathbb{T} \int_0^\beta d\tau_3 H_T(\tau_3) \hat{A}_k(\tau_1) [\hat{\Gamma}_{kq} \hat{B}_q(\tau_2)]^\dagger \right\rangle \\ &= \sum_{k_1, k'_1, q} \left\langle \mathbb{T} \int_0^\beta d\tau_3 \hat{\Gamma}_{k_1 k'_1} \hat{B}_{k'_1}(\tau_3) \hat{A}_{k_1}^\dagger(\tau_3) \hat{A}_k(\tau_1) \hat{B}_q^\dagger(\tau_2) \hat{\Gamma}_{qk}^\dagger \right\rangle \\ &= -\sum_{k_1, k'_1, q} \int_0^\beta d\tau_3 \langle \mathbb{T} \hat{A}_k(\tau_1) \hat{A}_{k_1}^\dagger(\tau_3) \rangle \hat{\Gamma}_{k_1 k'_1} \langle \mathbb{T} \hat{B}_{k'_1}(\tau_3) \hat{B}_q^\dagger(\tau_2) \rangle \hat{\Gamma}_{qk} \\ &= -\sum_{k_1, k'_1, q} \int_0^\beta d\tau_3 \hat{G}_S(\tau_1, \tau_3, \mathbf{k}, \mathbf{k}_1) \hat{\Gamma}_{k_1 k'_1} \hat{G}_F(\tau_3, \tau_2, \mathbf{k}'_1, \mathbf{q}) \hat{\Gamma}_{qk}. \end{aligned} \quad (\text{A6})$$

Hence the matrix current is given by

$$\begin{aligned} \hat{I}(\tau) &= \frac{i}{2} \sum_{k, k_1, k'_1, q} \int_0^\beta d\tau' [\hat{G}_S(\tau, \tau', \mathbf{k}, \mathbf{k}_1) \hat{\Gamma}_{k_1 k'_1} \hat{G}_F(\tau', \tau, \mathbf{k}'_1, \mathbf{q}) \hat{\Gamma}_{qk} \\ &\quad - \hat{\Gamma}_{kq} \hat{G}_F(\tau, \tau', \mathbf{q}, \mathbf{k}_1) \hat{\Gamma}_{k_1 k'_1} \hat{G}_S(\tau', \tau, \mathbf{k}'_1, \mathbf{k})]. \end{aligned} \quad (\text{A7})$$

We assume that GFs are spatially homogeneous, so $\hat{G}_F(\tau, \tau', \mathbf{q}, \mathbf{k}_1) = \delta_{q, k_1} \hat{G}_F(\tau, \tau', \mathbf{q})$ and the matrix element is momentum independent $\hat{\Gamma}_{kk'} = \hat{\Gamma}$. Then we can introduce the quasiclassical functions $\sum_q \hat{G}_{F,S}(\tau, \tau', \mathbf{q}) = \nu_{F,S} \hat{\tau}_3 \hat{g}_{F,S}(\tau, \tau')$ to write the current as

$$\hat{I}(\tau) = i \frac{\nu_S \nu_F}{2} [\hat{g}_S \circ (\hat{\tau}_3 \hat{\Gamma} \hat{g}_F \hat{\Gamma} \hat{\tau}_3) - (\hat{\tau}_3 \hat{\Gamma} \hat{g}_F \hat{\Gamma} \hat{\tau}_3) \circ \hat{g}_S]_{\tau'=\tau}. \quad (\text{A8})$$

Taking into account that the normal metal GF \hat{g}_F commutes with $\hat{\tau}_3$, Eq. (A8) can be reduced to Eq. (3).

APPENDIX B: ANALYTICAL CONTINUATION

In order to find the real-frequency response we need to implement the analytic continuation of Eq. (12). These second-order responses are obtained by the summation of

expressions which depend on the multiple shifted fermionic frequencies such as $g(\omega_1, \omega_2, \omega_3)$. The analytic continuation of the sum by Matsubara frequencies is determined according to the general rule [98]

$$\begin{aligned} T \sum_\omega g(\omega_1, \omega_2, \omega_3) &\rightarrow \sum_{l=1}^3 \int \frac{d\varepsilon}{4\pi i} n_0(\varepsilon_l) [g(\dots, -i\varepsilon_l^R, \dots) \\ &\quad - g(\dots, -i\varepsilon_l^A, \dots)], \end{aligned} \quad (\text{B1})$$

where $n_0(\varepsilon) = \tanh(\varepsilon/2T)$ is the equilibrium distribution function. On the right-hand side of (B1) we substitute in each term $\omega_{k<l} = -i\varepsilon_k^R$ and $\omega_{k>l} = -i\varepsilon_k^A$ for $k = 1, 2, 3$, and we define $\varepsilon_k = \varepsilon + (2-k)\Omega$, $\varepsilon^R = \varepsilon + i\Gamma$, and $\varepsilon^A = \varepsilon - i\Gamma$. Here the term with $\Gamma > 0$ is added to shift the integration contour into the corresponding half plane. At the same time, Γ can be used as the Dynes parameter [73] to describe the effect of different depairing mechanisms on spectral functions in the superconductor.

We implement the analytical continuation in such a way that $s(-i\varepsilon^{R,A}) = -i\sqrt{(\varepsilon^{R,A})^2 - \Delta^2}$, assuming that the branch cuts run from (Δ, ∞) and $(-\infty, -\Delta)$. In the presence of the spin-splitting field the energy in Eq. (B1) should be shifted to $\varepsilon + \sigma h$, where $\sigma = \pm 1$ is the spin subband index.

The equilibrium GF in the imaginary frequency domain is given by $\hat{g}_0(\omega) = (\hat{\tau}_3\omega - \hat{\tau}_2\Delta)/s(\omega)$. The real-frequency continuation reads $\hat{g}_0^{R,A}(\varepsilon) = (\hat{\tau}_3\varepsilon_{R,A} - i\hat{\tau}_2\Delta)/\sqrt{(\varepsilon^{R,A})^2 - \Delta^2}$.

Example. To demonstrate the analytical continuation in practice we calculate the spin current driven by the Higgs mode. For real frequencies the spin current obtained from (A8) can be written in terms of the Keldysh component

$$\begin{aligned} I_s &= \frac{\kappa}{8\pi} \sum_{\sigma} \sigma \int d\varepsilon \text{Tr}[\hat{g}_F(\varepsilon_+)\hat{g}_S(\varepsilon) - \hat{g}_S(\varepsilon)\hat{g}_F(\varepsilon_-)]^K \\ &= \frac{\kappa}{8\pi} \sum_{\sigma} \sigma \int d\varepsilon [n(\varepsilon_+) - n(\varepsilon_-)] \text{Tr}[\hat{\tau}_3\hat{g}_S^a], \end{aligned} \quad (\text{B2})$$

where $\varepsilon_{\pm} = \varepsilon + \sigma h \pm \omega$. In deriving (B2) we used the fact that $\hat{g}_F^{R(A)} = \pm 1$ do not depend on energy. The anomalous part of the nonequilibrium GF in the superconductor is

$$\hat{g}_S^a = \Delta_{2\Omega} \frac{\hat{g}^R(\varepsilon_+)\hat{\tau}_2\hat{g}^A(\varepsilon_-) - \hat{\tau}_2}{s_+^R + s_-^A}, \quad (\text{B3})$$

where we define $s_{\pm}^{R,A} = s^{R,A}(\varepsilon_{\pm})$. Substituting the solution (B3) and using $\text{Tr}[\tau_3\hat{g}_+^R\tau_2\hat{g}_-^A] = 2i\Delta_0\varepsilon/s_+^R s_-^A$, we get

$$\begin{aligned} I_s &= i\kappa\Delta_0\Delta_{2\Omega} \sum_{\sigma} \sigma \int \frac{d\varepsilon}{4\pi} \frac{(\varepsilon + \sigma h)[n(\varepsilon_+) - n(\varepsilon_-)]}{s_+^R s_-^A (s_+^R + s_-^A)} \\ &= \frac{i\kappa\Delta_0\Delta_{2\Omega}}{(\omega + i\Gamma)} \int \frac{d\varepsilon}{16\pi} \sum_{\sigma} \sigma [n(\varepsilon_+) - n(\varepsilon_-)] \left(\frac{1}{s_+^R} - \frac{1}{s_-^A} \right), \end{aligned} \quad (\text{B4})$$

where we use $(s_+^R)^2 - (s_-^A)^2 = 4(\varepsilon + \sigma h)(\omega + i\Gamma)$. In the low-frequency limit we can substitute $n(\varepsilon_+) - n(\varepsilon_-) = 2\omega\partial_{\varepsilon}n$ and $s_+^R = -s_-^A = -i\sqrt{\varepsilon^2 - \Delta^2}$. Then the spin current can be written in the simple form

$$\begin{aligned} I_s &= \frac{\kappa}{\Gamma} \sum_{\sigma} \sigma \frac{d}{dt} \int d\xi_p n(E_{\sigma}(\xi_p, \Delta(t))) \\ &= \frac{\kappa}{\Gamma} \dot{\Delta} \frac{d}{d\Delta} (N_+ - N_-), \end{aligned} \quad (\text{B5})$$

where $E_{\sigma}(\xi_p, \Delta(t)) = \sqrt{\xi_p^2 + \Delta^2(t)} + \sigma h$ is the spectrum of Bogoliubov quasiparticles shifted by the spin-splitting field h .

- [1] C. M. Varma, Higgs boson in superconductors, *J. Low Temp. Phys.* **126**, 901 (2002).
- [2] D. Podolsky, A. Auerbach, and D. P. Arovas, Visibility of the amplitude (Higgs) mode in condensed matter, *Phys. Rev. B* **84**, 174522 (2011).
- [3] A. Pashkin and A. Leitenstorfer, Particle physics in a superconductor, *Science* **345**, 1121 (2014).
- [4] G. E. Volovik and M. A. Zubkov, Higgs bosons in particle physics and in condensed matter, *J. Low Temp. Phys.* **175**, 486 (2014).
- [5] D. Pekker and C. M. Varma, Amplitude/Higgs modes in condensed matter physics, *Annu. Rev. Condens. Matter Phys.* **6**, 269 (2015).
- [6] P. W. Higgs, Broken Symmetries and the Masses of Gauge Bosons, *Phys. Rev. Lett.* **13**, 508 (1964).
- [7] G. Grüner, The dynamics of charge-density waves, *Rev. Mod. Phys.* **60**, 1129 (1988).
- [8] D. N. Paulson, R. T. Johnson, and J. C. Wheatley, Propagation of Collisionless Sound in Normal and Extraordinary Phases of Liquid ^3He below 3 mK, *Phys. Rev. Lett.* **30**, 829 (1973).
- [9] D. T. Lawson, W. J. Gully, S. Goldstein, R. C. Richardson, and D. M. Lee, Attenuation of Zero Sound and the Low-Temperature Transitions in Liquid ^3He , *Phys. Rev. Lett.* **30**, 541 (1973).
- [10] V. V. Zavjalov, S. Autti, V. B. Eltsov, P. J. Heikkinen, and G. E. Volovik, Light Higgs channel of the resonant decay of magnon condensate in superfluid $^3\text{He-B}$, *Nat. Commun.* **7**, 10294 (2016).
- [11] U. Bissbort, S. Götze, Y. Li, J. Heinze, J. S. Krauser, M. Weinberg, C. Becker, K. Sengstock, and W. Hofstetter, Detecting the Amplitude Mode of Strongly Interacting Lattice Bosons by Bragg Scattering, *Phys. Rev. Lett.* **106**, 205303 (2011).
- [12] M. Endres, T. Fukuhara, D. Pekker, M. Cheneau, P. Schauf, C. Gross, E. Demler, S. Kuhr, and I. Bloch, The ‘Higgs’ amplitude mode at the two-dimensional superfluid/Mott insulator transition, *Nature (London)* **487**, 454 (2012).
- [13] A. F. Volkov and S. M. Kogan, Collisionless relaxation of the energy gap in superconductors, *Zh. Eksp. Teor. Fiz.* **65**, 2038 (1973) [*Sov. Phys.—JETP* **38**, 1018 (1974)].
- [14] R. Sooryakumar and M. V. Klein, Raman Scattering by Superconducting-Gap Excitations and their Coupling to Charge-Density Waves, *Phys. Rev. Lett.* **45**, 660 (1980).
- [15] P. B. Littlewood and C. M. Varma, Amplitude collective modes in superconductors and their coupling to charge-density waves, *Phys. Rev. B* **26**, 4883 (1982).
- [16] R. A. Barankov, L. S. Levitov, and B. Z. Spivak, Collective Rabi Oscillations and Solitons in a Time-Dependent BCS Pairing Problem, *Phys. Rev. Lett.* **93**, 160401 (2004).
- [17] R. Grasset, T. Cea, Y. Gallais, M. Cazayous, A. Sacuto, L. Cario, L. Benfatto, and M.-A. Méasson, Higgs-mode radiance and charge-density-wave order in 2H-NbSe₂, *Phys. Rev. B* **97**, 094502 (2018).
- [18] R. Matsunaga, Y. I. Hamada, K. Makise, Y. Uzawa, H. Terai, Z. Wang, and R. Shimano, Higgs Amplitude Mode in the BCS Superconductors Nb_{1-x}Ti_xN Induced by Terahertz Pulse Excitation, *Phys. Rev. Lett.* **111**, 057002 (2013).

- [19] R. Matsunaga, N. Tsuji, H. Fujita, A. Sugioka, K. Makise, Y. Uzawa, H. Terai, Z. Wang, H. Aoki, and R. Shimano, Light-induced collective pseudospin precession resonating with Higgs mode in a superconductor, *Science* **345**, 1145 (2014).
- [20] D. Sherman, U. S. Pracht, B. Gorshunov, S. Poran, J. Jesudasan, M. Chand, P. Raychaudhuri, M. Swanson, N. Trivedi, A. Auerbach, M. Scheffler, A. Frydman, and M. Dressel, The Higgs mode in disordered superconductors close to a quantum phase transition, *Nat. Phys.* **11**, 188 (2015).
- [21] N. Tsuji and H. Aoki, Theory of Anderson pseudospin resonance with Higgs mode in superconductors, *Phys. Rev. B* **92**, 064508 (2015).
- [22] R. Matsunaga, N. Tsuji, K. Makise, H. Terai, H. Aoki, and R. Shimano, Polarization-resolved terahertz third-harmonic generation in a single-crystal superconductor NbN: Dominance of the Higgs mode beyond the BCS approximation, *Phys. Rev. B* **96**, 020505(R) (2017).
- [23] K. Katsumi, N. Tsuji, Y. I. Hamada, R. Matsunaga, J. Schneeloch, R. D. Zhong, G. D. Gu, H. Aoki, Y. Gallais, and R. Shimano, Higgs Mode in the *d*-Wave Superconductor $\text{Bi}_2\text{Sr}_2\text{CaCu}_2\text{O}_{8+x}$ Driven by an Intense Terahertz Pulse, *Phys. Rev. Lett.* **120**, 117001 (2018).
- [24] S. Nakamura, Y. Iida, Y. Murotani, R. Matsunaga, H. Terai, and R. Shimano, Infrared Activation of the Higgs Mode by Supercurrent Injection in Superconducting NbN, *Phys. Rev. Lett.* **122**, 257001 (2019).
- [25] H. Uematsu, T. Mizushima, A. Tsuruta, S. Fujimoto, and J. A. Sauls, Chiral Higgs Mode in Nematic Superconductors, *Phys. Rev. Lett.* **123**, 237001 (2019).
- [26] A. Moor, A. F. Volkov, and K. B. Efetov, Amplitude Higgs Mode and Admittance in Superconductors with a Moving Condensate, *Phys. Rev. Lett.* **118**, 047001 (2017).
- [27] M. Silaev, Nonlinear electromagnetic response and Higgs-mode excitation in BCS superconductors with impurities, *Phys. Rev. B* **99**, 224511 (2019).
- [28] R. Grasset, Y. Gallais, A. Sacuto, M. Cazayous, S. Mañas-Valero, E. Coronado, and M.-A. Méasson, Pressure-Induced Collapse of the Charge Density Wave and Higgs Mode Visibility in 2H-TaS_2 , *Phys. Rev. Lett.* **122**, 127001 (2019).
- [29] M. Beck, M. Klammer, S. Lang, P. Leiderer, V. V. Kabanov, G. N. Gol'tsman, and J. Demsar, Energy-Gap Dynamics of Superconducting NbN Thin Films Studied by Time-Resolved Terahertz Spectroscopy, *Phys. Rev. Lett.* **107**, 177007 (2011).
- [30] M. Beck, I. Rousseau, M. Klammer, P. Leiderer, M. Mittendorff, S. Winnerl, M. Helm, G. N. Gol'tsman, and J. Demsar, Transient Increase of the Energy Gap of Superconducting NbN Thin Films Excited by Resonant Narrow-Band Terahertz Pulses, *Phys. Rev. Lett.* **110**, 267003 (2013).
- [31] R. Matsunaga and R. Shimano, Nonequilibrium BCS State Dynamics Induced by Intense Terahertz Pulses in a Superconducting NbN Film, *Phys. Rev. Lett.* **109**, 187002 (2012).
- [32] F. Giorgianni, T. Cea, C. Vicario, C. P. Hauri, W. K. Withanage, X. Xi, and L. Benfatto, Leggett mode controlled by light pulses, *Nat. Phys.* **15**, 341 (2019).
- [33] W. V. Budzinski, M. P. Garfunkel, and R. W. Markley, Magnetic field dependence of the surface resistance of pure and impure superconducting aluminum at photon energies near the energy gap, *Phys. Rev. B* **7**, 1001 (1973).
- [34] F. S. Bergeret, M. Silaev, P. Virtanen, and T. T. Heikkilä, Colloquium: Nonequilibrium effects in superconductors with a spin-splitting field, *Rev. Mod. Phys.* **90**, 041001 (2018).
- [35] T. T. Heikkilä, M. Silaev, P. Virtanen, and F. S. Bergeret, Thermal, electric and spin transport in superconductor/ferromagnetic-insulator structures, *Prog. Surf. Sci.* **94**, 100540 (2019).
- [36] D. Beckmann, Spin manipulation in nanoscale superconductors, *J. Phys.: Condens. Matter* **28**, 163001 (2016).
- [37] C. H. L. Quay and M. Aprili, Out-of-equilibrium spin transport in mesoscopic superconductors, *Philos. Trans. R. Soc. A* **376**, 20150342 (2018).
- [38] F. Hübler, M. J. Wolf, D. Beckmann, and H. v. Löhneysen, Long-Range Spin-Polarized Quasiparticle Transport in Mesoscopic Al Superconductors with a Zeeman Splitting, *Phys. Rev. Lett.* **109**, 207001 (2012).
- [39] M. J. Wolf, C. Sürgers, G. Fischer, and D. Beckmann, Spin-polarized quasiparticle transport in exchange-split superconducting aluminum on europium sulfide, *Phys. Rev. B* **90**, 144509 (2014).
- [40] M. Rouco, S. Chakraborty, F. Aikebaier, V. N. Golovach, E. Strambini, J. S. Moodera, F. Giazotto, T. T. Heikkilä, and F. S. Bergeret, Charge transport through spin-polarized tunnel junction between two spin-split superconductors, *Phys. Rev. B* **100**, 184501 (2019).
- [41] G. De Simoni, E. Strambini, J. S. Moodera, F. S. Bergeret, and F. Giazotto, Toward the absolute spin-valve effect in superconducting tunnel junctions, *Nano Lett.* **18**, 6369 (2018).
- [42] E. Strambini, V. N. Golovach, G. De Simoni, J. S. Moodera, F. S. Bergeret, and F. Giazotto, Revealing the magnetic proximity effect in EuS/Al bilayers through superconducting tunneling spectroscopy, *Phys. Rev. Mater.* **1**, 054402 (2017).
- [43] S. Kolenda, M. J. Wolf, and D. Beckmann, Observation of Thermoelectric Currents in High-Field Superconductor-Ferromagnet Tunnel Junctions, *Phys. Rev. Lett.* **116**, 097001 (2016).
- [44] M. J. Wolf, F. Hübler, S. Kolenda, H. v. Löhneysen, and D. Beckmann, Spin injection from a normal metal into a mesoscopic superconductor, *Phys. Rev. B* **87**, 024517 (2013).
- [45] C. H. L. Quay, D. Chevallier, C. Bena, and M. Aprili, Spin imbalance and spin-charge separation in a mesoscopic superconductor, *Nat. Phys.* **9**, 84 (2013).
- [46] C. H. L. Quay, C. Dutreix, D. Chevallier, C. Bena, and M. Aprili, Frequency-domain measurement of the spin-imbalance lifetime in superconductors, *Phys. Rev. B* **93**, 220501(R) (2016).
- [47] J. Heidrich and D. Beckmann, Nonlocal thermoelectric effects in high-field superconductor-ferromagnet hybrid structures, *Phys. Rev. B* **100**, 134501 (2019).
- [48] M. Silaev, P. Virtanen, F. S. Bergeret, and T. T. Heikkilä, Long-Range Spin Accumulation from Heat Injection in Mesoscopic Superconductors with Zeeman Splitting, *Phys. Rev. Lett.* **114**, 167002 (2015).
- [49] I. V. Bobkova and A. M. Bobkov, Long-range spin imbalance in mesoscopic superconductors under Zeeman splitting, *JETP Lett.* **101**, 118 (2015).
- [50] T. Krishtop, M. Houzet, and J. S. Meyer, Nonequilibrium spin transport in Zeeman-split superconductors, *Phys. Rev. B* **91**, 121407(R) (2015).

- [51] P. Virtanen, T. T. Heikkilä, and F. S. Bergeret, Stimulated quasiparticles in spin-split superconductors, *Phys. Rev. B* **93**, 014512 (2016).
- [52] F. Aikebaier, M. A. Silaev, and T. T. Heikkilä, Supercurrent-induced charge-spin conversion in spin-split superconductors, *Phys. Rev. B* **98**, 024516 (2018).
- [53] P. Virtanen, F. S. Bergeret, E. Strambini, F. Giazotto, and A. Braggio, Majorana bound states in hybrid two-dimensional Josephson junctions with ferromagnetic insulators, *Phys. Rev. B* **98**, 020501(R) (2018).
- [54] I. V. Bobkova and A. M. Bobkov, Injection of nonequilibrium quasiparticles into Zeeman-split superconductors: A way to create long-range spin imbalance, *Phys. Rev. B* **93**, 024513 (2016).
- [55] S. K. Kim, R. Myers, and Y. Tserkovnyak, Nonlocal Spin Transport Mediated by a Vortex Liquid in Superconductors, *Phys. Rev. Lett.* **121**, 187203 (2018).
- [56] A. Vargunin and M. Silaev, Flux flow spin Hall effect in type-II superconductors with spin-splitting field, *Sci. Rep.* **9**, 5914 (2019).
- [57] V. L. Vadimov, I. M. Khaymovich, and A. S. Mel'nikov, Higgs modes in proximized superconducting systems, *Phys. Rev. B* **100**, 104515 (2019).
- [58] F. S. Bergeret, A. F. Volkov, and K. B. Efetov, Enhancement of the Josephson Current by an Exchange Field in Superconductor-Ferromagnet Structures, *Phys. Rev. Lett.* **86**, 3140 (2001).
- [59] T. Tokuyasu, J. A. Sauls, and D. Rainer, Proximity effect of a ferromagnetic insulator in contact with a superconductor, *Phys. Rev. B* **38**, 8823 (1988).
- [60] A. Millis, D. Rainer, and J. A. Sauls, Quasiclassical theory of superconductivity near magnetically active interfaces, *Phys. Rev. B* **38**, 4504 (1988).
- [61] A. Cottet, D. Huertas-Hernando, W. Belzig, and Y. V. Nazarov, Spin-dependent boundary conditions for isotropic superconducting Green's functions, *Phys. Rev. B* **80**, 184511 (2009).
- [62] M. Eschrig, A. Cottet, W. Belzig, and J. Linder, General boundary conditions for quasiclassical theory of superconductivity in the diffusive limit: Application to strongly spin-polarized systems, *New J. Phys.* **17**, 083037 (2015).
- [63] L. P. Gor'kov and G. M. Éliashberg, Superconducting alloys in a strong alternating field, *Zh. Eksp. Teor. Fiz.* **56**, 1297 (1969) [*Sov. Phys.—JETP* **29**, 698 (1969)].
- [64] L. P. Gor'kov and G. M. Éliashberg, The behavior of a superconductor in a variable field, *Zh. Eksp. Teor. Fiz.* **55**, 2430 (1968) [*Sov. Phys.—JETP* **28**, 1291 (1969)].
- [65] V. Ambegaokar and A. Baratoff, Tunneling between Superconductors, *Phys. Rev. Lett.* **10**, 486 (1963).
- [66] J. Bardeen, Tunneling into Superconductors, *Phys. Rev. Lett.* **9**, 147 (1962).
- [67] U. Eckern, G. Schön, and V. Ambegaokar, Quantum dynamics of a superconducting tunnel junction, *Phys. Rev. B* **30**, 6419 (1984).
- [68] R. E. Harris, Josephson tunneling current in the presence of a time-dependent voltage, *Phys. Rev. B* **11**, 3329 (1975).
- [69] N. R. Werthamer, Nonlinear self-coupling of Josephson radiation in superconducting tunnel junctions, *Phys. Rev.* **147**, 255 (1966).
- [70] F. S. Bergeret, A. Verso, and A. F. Volkov, Electronic transport through ferromagnetic and superconducting junctions with spin-filter tunneling barriers, *Phys. Rev. B* **86**, 214516 (2012).
- [71] F. S. Bergeret, A. Verso, and A. F. Volkov, Spin-polarized Josephson and quasiparticle currents in superconducting spin-filter tunnel junctions, *Phys. Rev. B* **86**, 060506(R) (2012).
- [72] M. Tinkham, *Introduction to Superconductivity* (Courier, Chelmsford, 2004).
- [73] R. C. Dynes, J. P. Garno, G. B. Hertel, and T. P. Orlando, Tunneling Study of Superconductivity near the Metal-Insulator Transition, *Phys. Rev. Lett.* **53**, 2437 (1984).
- [74] I. O. Kulik, O. Entin-Wohlman, and R. Orbach, Pair susceptibility and mode propagation in superconductors: A microscopic approach, *J. Low Temp. Phys.* **43**, 591 (1981).
- [75] R. A. Barankov and L. S. Levitov, Synchronization in the BCS Pairing Dynamics as a Critical Phenomenon, *Phys. Rev. Lett.* **96**, 230403 (2006).
- [76] J. C. Amato and W. L. McLean, Measurement of the Superconducting Order-Parameter Relaxation Time from Harmonic Generation, *Phys. Rev. Lett.* **37**, 930 (1976).
- [77] M. A. Silaev, I. V. Tokatly, and F. S. Bergeret, Anomalous current in diffusive ferromagnetic Josephson junctions, *Phys. Rev. B* **95**, 184508 (2017).
- [78] P. Machon, M. Eschrig, and W. Belzig, Nonlocal Thermoelectric Effects and Nonlocal Onsager Relations in a Three-Terminal Proximity-Coupled Superconductor-Ferromagnet Device, *Phys. Rev. Lett.* **110**, 047002 (2013).
- [79] A. Ozaeta, P. Virtanen, F. S. Bergeret, and T. T. Heikkilä, Predicted Very Large Thermoelectric Effect in Ferromagnet-Superconductor Junctions in the Presence of a Spin-Splitting Magnetic Field, *Phys. Rev. Lett.* **112**, 057001 (2014).
- [80] T. M. Klapwijk, J. N. Van Den Bergh, and J. E. Mooij, Radiation-stimulated superconductivity, *J. Low Temp. Phys.* **26**, 385 (1977).
- [81] T. Kommers and J. Clarke, Measurement of Microwave-Enhanced Energy Gap in Superconducting Aluminum by Tunneling, *Phys. Rev. Lett.* **38**, 1091 (1977).
- [82] K. S. Tikhonov, M. A. Skvortsov, and T. M. Klapwijk, Superconductivity in the presence of microwaves: Full phase diagram, *Phys. Rev. B* **97**, 184516 (2018).
- [83] Y. Tserkovnyak, A. Brataas, G. E. W. Bauer, and B. I. Halperin, Nonlocal magnetization dynamics in ferromagnetic heterostructures, *Rev. Mod. Phys.* **77**, 1375 (2005).
- [84] J. C. Slonczewski, Current-driven excitation of magnetic multilayers, *J. Magn. Magn. Mater.* **159**, L1 (1996).
- [85] A. Brataas, Y. V. Nazarov, and G. E. W. Bauer, Finite-Element Theory of Transport in Ferromagnet-Normal Metal Systems, *Phys. Rev. Lett.* **84**, 2481 (2000).
- [86] X. Waintal, E. B. Myers, P. W. Brouwer, and D. C. Ralph, Role of spin-dependent interface scattering in generating current-induced torques in magnetic multilayers, *Phys. Rev. B* **62**, 12317 (2000).
- [87] M. D. Stiles and A. Zangwill, Anatomy of spin-transfer torque, *Phys. Rev. B* **66**, 014407 (2002).
- [88] I. V. Bobkova and A. M. Bobkov, Thermospin effects in superconducting heterostructures, *Phys. Rev. B* **96**, 104515 (2017).
- [89] C. Bell, S. Milikisyants, M. Huber, and J. Aarts, Spin Dynamics in a Superconductor-Ferromagnet Proximity System, *Phys. Rev. Lett.* **100**, 047002 (2008).
- [90] K.-R. Jeon, C. Ciccarelli, A. J. Ferguson, H. Kurebayashi, L. F. Cohen, X. Montiel, M. Eschrig, J. W. A. Robinson, and M. G. Blamire, Enhanced spin pumping into superconductors

- provides evidence for superconducting pure spin currents, *Nat. Mater.* **17**, 499 (2018).
- [91] K.-R. Jeon, C. Ciccarelli, H. Kurebayashi, L. F. Cohen, X. Montiel, M. Eschrig, S. Komori, J. W. A. Robinson, and M. G. Blamire, Exchange-field enhancement of superconducting spin pumping, *Phys. Rev. B* **99**, 024507 (2019).
- [92] Y. Murotani and R. Shimano, Nonlinear optical response of collective modes in multiband superconductors assisted by non-magnetic impurities, *Phys. Rev. B* **99**, 224510 (2019).
- [93] T. T. Heikkilä, R. Ojajärvi, I. J. Maasilta, E. Strambini, F. Giazotto, and F. S. Bergeret, Thermoelectric Radiation Detector Based on Superconductor-Ferromagnet Systems, *Phys. Rev. Appl.* **10**, 034053 (2018).
- [94] T. Hyart, B. van Heck, I. C. Fulga, M. Burrello, A. R. Akhmerov, and C. W. J. Beenakker, Flux-controlled quantum computation with Majorana fermions, *Phys. Rev. B* **88**, 035121 (2013).
- [95] T. Karzig, C. Knapp, R. M. Lutchyn, P. Bonderson, M. B. Hastings, C. Nayak, J. Alicea, K. Flensberg, S. Plugge, Y. Oreg, C. M. Marcus, and M. H. Freedman, Scalable designs for quasiparticle-poisoning-protected topological quantum computation with Majorana zero modes, *Phys. Rev. B* **95**, 235305 (2017).
- [96] S. Plugge, A. Rasmussen, R. Egger, and K. Flensberg, Majorana box qubits, *New J. Phys.* **19**, 012001 (2017).
- [97] C. Knapp, T. Karzig, R. M. Lutchyn, and C. Nayak, Dephasing of Majorana-based qubits, *Phys. Rev. B* **97**, 125404 (2018).
- [98] N. B. Kopnin, *Theory of Nonequilibrium Superconductivity* (Oxford University Press, Oxford, 2001).

VII

GIANT ENHANCEMENT TO SPIN BATTERY EFFECT IN SUPERCONDUCTOR/FERROMAGNETIC INSULATOR SYSTEMS

by

R. Ojajärvi, T.T. Heikkilä, P. Virtanen and M.A. Silaev 2021

Physical Review B **103**, 224524, DOI:[10.1103/PhysRevB.103.224524](https://doi.org/10.1103/PhysRevB.103.224524)

Reproduced with permission. Copyright 2021 American Physical Society.

Giant enhancement to spin battery effect in superconductor/ferromagnetic insulator systems

Risto Ojajarvi ¹, Tero T. Heikkilä ¹, P. Virtanen ¹ and M. A. Silaev^{1,2,3}

¹*Department of Physics and Nanoscience Center, University of Jyväskylä, P.O. Box 35 (YFL), FI-40014 University of Jyväskylä, Finland*

²*Moscow Institute of Physics and Technology, 141700 Dolgoprudny, Russia*

³*Institute for Physics of Microstructures, Russian Academy of Sciences, 603950 Nizhny Novgorod, GSP-105, Russia*



(Received 15 March 2021; accepted 3 June 2021; published 22 June 2021)

We develop a theory of the spin battery effect in superconductor/ferromagnetic insulator (SC/FI) systems taking into account the magnetic proximity effect. We demonstrate that the spin-energy mixing enabled by the superconductivity leads to the enhancement of spin accumulation by several orders of magnitude relative to the normal state. This finding can explain the recently observed giant inverse spin Hall effect generated by thermal magnons in the SC/FI system. We suggest a nonlocal electrical detection scheme which can directly probe the spin accumulation driven by the magnetization dynamics. We predict a giant Seebeck effect converting the magnon temperature bias into the nonlocal voltage signal. We also show how this can be used to enhance the sensitivity of magnon detection even up to the single-magnon level.

DOI: [10.1103/PhysRevB.103.224524](https://doi.org/10.1103/PhysRevB.103.224524)

Generation and detection of pure spin signals is one of the main paradigms in spintronics [1,2] and spin caloritronics [3]. Spin pumping [4–6] in ferromagnet/metal multilayers affects ferromagnetic resonance (FMR) and spin Hall magnetoresistance measurements [7,8]. Spin Seebeck effect [8,9] converts thermal nonequilibrium states into pure spin currents and can be used for the detection of magnons propagating through FI materials without electrical losses [10,11]. Pure spin current flowing from the ferromagnet into the adjacent metal leads to the buildup of spin accumulation known as the spin battery effect [5].

Recently it has been discovered [12–17] that superconductivity strongly increases spin relaxation times and lengths, which makes superconducting materials promising for spintronics [18–20]. Long-range nonequilibrium spin states created in superconductors by electrical and thermal injection of Bogoliubov quasiparticles have been intensively studied [20–28]. The question of how the weak spin relaxation in superconductors shows up in spin pumping properties have remained unexplored and is addressed in the present paper.

Most of the experimental [13,15,16,29–34] and theoretical works studying magnetization dynamics in superconductor/ferromagnet systems focus on the FMR properties [35–41] and spin torques [42,43]. Here we consider the spin battery effect [5] that is the static spin accumulation of Bogoliubov quasiparticles in a superconductor (SC) generated either by the coherent FMR drive or by the thermal magnons in the adjacent FI. Our study is motivated by the recent experiment demonstrating that magnons induce a giant inverse spin-Hall signal in the transition state of the Nb/YIG superconductor/ferromagnetic insulator system [34]. Due to the close relation between the spin Hall signal and spin density, this observation hints that the spin accumulation induced by thermal magnons is modified in a highly nontrivial way by the superconducting correlations.

The considered setup is detailed in Fig. 1(a) which shows the time-averaged quasiparticle spin accumulation ($\langle \mu_s \rangle$) generated in SC. It can be measured [12,13,15,16] in the nonlocal circuit Fig. 1(b) consisting of the spin-polarized tunnel contact with a metallic ferromagnet (FM) near FI and the distant normal metal electrode (NM). The dc voltage V_D induced into this tunnel contact in the absence of a charge current through it is [23]

$$V_D = \frac{G_{Fn}}{G_F} \mathbf{P}_D \cdot \langle \mu_s \rangle. \quad (1)$$

Here $G_F = G_{Fn} \int_0^\infty d\varepsilon N(\varepsilon) \partial_\varepsilon n_0$ is the linear local tunneling conductance and \mathbf{P}_D the spin polarization of the SC/FM junction, $N(\varepsilon)$ is the density of states in the superconductor, and $n_0 = \tanh(\varepsilon/2T)$ is the equilibrium distribution function.

In the superconducting case the information carried by the strength of the spin pumping which determines the FMR linewidth is different from that in $\langle \mu_s \rangle$. It is generally proportional to the amplitude of magnetization dynamics $\langle \mu_s \rangle \propto \langle \mathbf{m} \times \partial_t \mathbf{m} \rangle$, where $\mathbf{m}(t)$ is the unit vector of magnetization direction in FI. In superconductors, however, the proportionality constant of $\langle \mu_s \rangle$ is sensitive to the magnitude of energy relaxation time Γ^{-1} and its magnitude compared to the spin-relaxation time τ_s . In the typical case $\Gamma^{-1} \gg \tau_s$ the resulting nonlocal voltage V_D can be parametrically larger in the superconducting state than in the normal state by the factor $\sim (\Gamma \tau_s)^{-1}$. In superconductors Nb and Al these times are of the order [15,44] of $\tau_s \approx 0.1 T_c^{-1}$ in Al and $\tau_s \approx T_c^{-1}$ in Nb, while $\Gamma^{-1}(T_c) \approx 10^3 T_c^{-1}$ in both materials [45,46]. Therefore in these superconductors one can expect an enhancement of spin accumulation induced by spin pumping by the factor of $(\Gamma \tau_s)^{-1} \sim 10^2 - 10^3$ as compared to the normal state.

The origin of the very large spin accumulation in FI/SC contacts is twofold. First, magnetization dynamics results

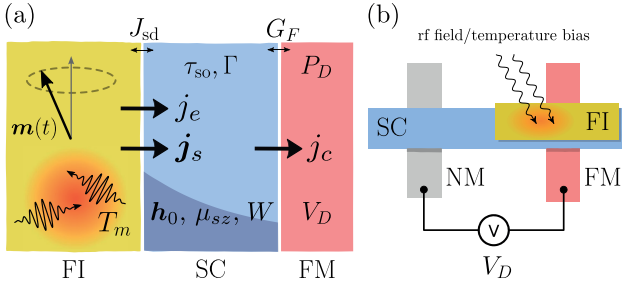


FIG. 1. Schematic FI/SC setup to measure spin accumulation induced by magnons. (a) Nonequilibrium magnon distribution in FI, generated either by a coherent FMR drive or a temperature bias, induces spin and energy currents j_s and j_e to the SC, which create spin and energy accumulations μ_s and W in SC. Proximity to FI also induces a static exchange field h_0 in the SC. The spin accumulation is converted to electrical voltage V_D in the ferromagnetic electrode (FM) with the polarization P_D . (b) Nonlocal circuit to measure magnon-induced voltage V_D .

in the energy current [4,47] $j_e = \alpha(|\partial_t \mathbf{m}|^2)$, where α is the contribution to the Gilbert damping coefficient due to the contact. Second, in superconductors the spin splitting in the Bogoliubov spectrum generated by FI through the magnetic proximity effect [20,23,48,49] leads to the strong coupling between energy and spin degrees of freedom [23]. The mechanism of converting pumped quasiparticle energy to spin accumulation via elastic spin-relaxation processes is demonstrated in Fig. 2 which shows nonequilibrium quasiparticle states on the spin-split Bogoliubov branches $E_p(p)$ for different momenta p . The spin quantization axis is determined by the Zeeman field $\mathbf{h}_0 = h_0 \mathbf{z}$ induced by the *magnetic proximity effect*, when the static magnetization direction is $\mathbf{m}_0 = \mathbf{z}$.

Energy current j_e generates spin-neutral energy accumulation W by nonequilibrium quasiparticle states shown schematically by the filled circles in Fig. 2(a). The important feature of this distribution is that both spin-up and spin-down branches have the same number of occupied states. Due to the spin splitting the spin-up and spin-down branches are filled up

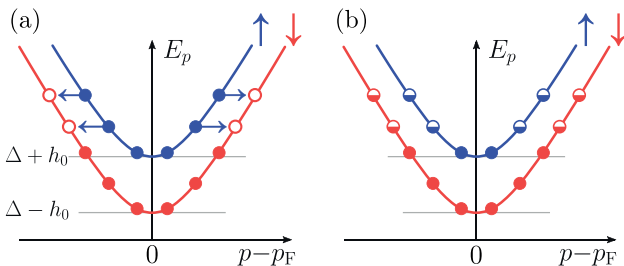


FIG. 2. Spin-split Bogoliubov spectrum in SC and its occupation driven by magnons. (a) State with pure energy accumulation W and no spin accumulation. Horizontal arrows represent elastic spin scattering. (b) Elastically relaxed state. Elastic relaxation produces spin accumulation μ_{sz} from energy accumulation W . The full/half-filled/empty circles represent occupied/partially filled/unoccupied states. The effect depends on the asymmetry between spin-resolved density of states $N_\uparrow(\epsilon)$ and $N_\downarrow(\epsilon)$ and is therefore absent in the normal state.

to different energy levels. The resulting population imbalance can relax due to the elastic spin scattering process. As a result, all spin-up and spin-down states with identical energies become equally populated. As one can see from Fig. 2, in this state the net spin accumulation is nonzero because of the energy interval $\Delta - h_0 < E_p < \Delta + h_0$ where only the spin-down states exist [50].

The energy-to-spin conversion processes can be quantified using kinetic equations together with the collision integrals corresponding to the spin-orbit or spin-flip scattering. Introducing the distribution functions $f_{\uparrow/\downarrow}$ and densities of states $N_{\uparrow/\downarrow}$ in spin-up/down subbands, normalized to $N_\uparrow + N_\downarrow = 1$ in the normal state, we obtain [51] the spectral densities for spin and energy accumulations $f_s = N_\uparrow f_\uparrow - N_\downarrow f_\downarrow$ and $f_e = \epsilon(N_\uparrow f_\uparrow + N_\downarrow f_\downarrow)$. The elastic spin-scattering collision integral is given by $\mathcal{I}_s = (f_s - \kappa_{se} f_e)/\mathcal{T}_1$, where \mathcal{T}_1 is the longitudinal spin relaxation time in the superconducting state [23] and spin-energy coupling coefficient $\kappa_{se}(\epsilon) = (N_\uparrow - N_\downarrow)/[\epsilon(N_\uparrow + N_\downarrow)]$. For weak spin splitting $h_0 \ll \Delta^2$, we can estimate $\kappa_{se} \sim h_0/(\epsilon \Delta)$, where Δ is the superconducting gap.

The spin-diffusion equation modified by the spin-energy coupling is given by

$$\partial_x \mathcal{J}_{sz} = \frac{f_s(\epsilon) - \kappa_{se} f_e}{\mathcal{T}_1}, \quad (2a)$$

$$\partial_x \mathcal{J}_e = I_{e-ph} + \Gamma f_e, \quad (2b)$$

where $\mathcal{J}_{sz}(\epsilon)$ and $\mathcal{J}_e(\epsilon)$ are the spectral densities of the time-independent spin $j_{sz} = \int d\epsilon \mathcal{J}_{sz}$ and energy $j_e = \int d\epsilon \mathcal{J}_e$ currents. The sources of these currents are determined by the boundary conditions at the FI interface with dynamical magnetization fixing the values of interfacial currents $\mathcal{J}_e(x=0) \propto \langle |\partial_t \mathbf{m}|^2 \rangle$ and $\mathcal{J}_{sz}(x=0) \propto \mathbf{z} \cdot \langle \mathbf{m} \times \partial_t \mathbf{m} \rangle$. They are obtained generalizing the theory of normal-state spin battery effect [5] for the superconducting case [51]. In the limit of small SC film thickness d the solution for spin accumulation $\mu_{sz} = (\boldsymbol{\mu}_s \cdot \mathbf{z})$ is $\mu_{sz} = -d^{-1} \int d\epsilon (\Gamma^{-1} \kappa_{se} \mathcal{J}_e + \mathcal{T}_1 \mathcal{J}_{sz})$. The first term has a large prefactor Γ^{-1} and provides the possibility of spin signal enhancement by the parameter $\kappa_{se}/(\Gamma \mathcal{T}_1)$ as compared to the normal state, where only the second term contributes. The detailed calculation [51] described below shows that both \mathcal{J}_e and \mathcal{J}_{sz} are not dramatically smaller than their normal state magnitudes down to $T \approx 0.3T_c$. Thus μ_{sz} is enhanced by the factor $\kappa_{se}/(\Gamma \mathcal{T}_1)$ at $T/T_c \approx 0.8-0.9$.

In the limit of a short elastic mean-free path, the described effects are quantified using the Keldysh-Usadel equation [39,40]

$$-\{\hat{\tau}_3 \partial_t \circ \check{g}\} + \partial_x (D \check{g} \circ \partial_x \check{g}) = [\Delta \hat{\tau}_1 + \check{\Gamma} + \check{\Sigma}_{so} \circ \check{g}] \quad (3)$$

for the quasiclassical Green's function (GF) \check{g} in 8×8 space consisting of Keldysh, Nambu, and spin indices [23]. The diffusion constant is D , the elastic spin relaxation is determined by the spin-orbit scattering self-energy $\check{\Sigma}_{so} = \boldsymbol{\sigma} \cdot \check{g} \boldsymbol{\sigma} / (6\tau_{so})$ [51], while $\check{\Gamma}$ describes the coupling to the normal reservoir to model the *inelastic relaxation* [52].

The spin splitting and pumping induced by the electron scattering at the FI interface $x=0$ are modelled by the *dynamical boundary conditions* [40,53]

$$D \check{g} \circ \partial_x \check{g}(x=0) = iJ_{sd} [\hat{\tau}_3 \hat{\boldsymbol{\sigma}} \mathbf{m} \circ \check{g}], \quad (4)$$

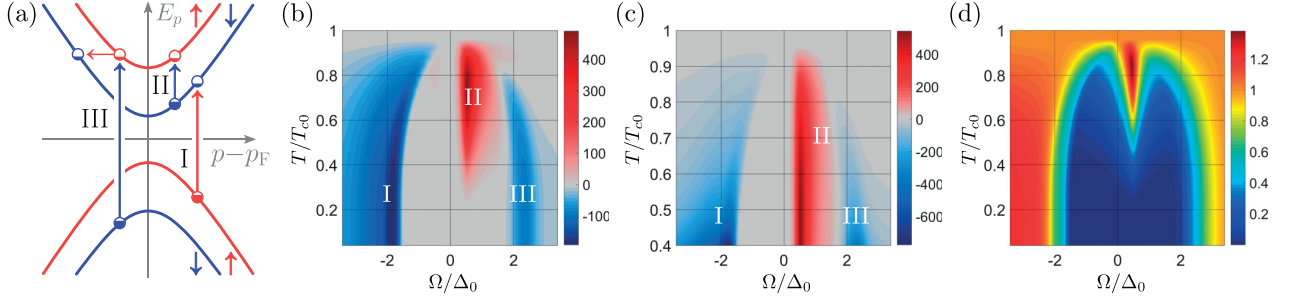


FIG. 3. (a) Quasiparticle excitation processes of the spin-split Bogoliubov spectrum. Vertical blue/red arrows are due to the absorption of a magnon with spin ± 1 . Horizontal arrows represent rapid spin relaxation. The filling of the circles shows the occupation of the states after spin relaxation. The corresponding peaks are labeled as I–III in the next panels. (b) Pumped spin accumulation $(T_{c0}/h_c^2)\mu_z(T, \Omega)$, (c) nonlocal voltage $(eT_{c0}/h_c^2)V_D(\Omega, T)$, and (d) pumped energy accumulation $W(T, \Omega)/W(T_c, \Omega)$, generated by the magnetization dynamics in the setup of Fig. 1. The parameters used for (b)–(d) are $\Gamma/T_{c0} = 10^{-3}$, $h_0/T_{c0} = 0.528$, and $\tau_{so}^{-1}/T_{c0} = 1.19$. For these parameters $T_c \approx 0.9T_{c0}$, where T_{c0} is the critical field at $h_0 = \tau_{so}^{-1} = 0$.

where we denote $[A \circ B](t_1, t_2) = \int dt A(t_1, t)B(t, t_2) - B(t_1, t)A(t, t_2)$ and similarly for the anticommutator $\{X \circ Y\}$. Here the interface is characterized by the effective exchange coupling [54] J_{sd} . Within the minimal model of the FI [53,55] it can also be expressed through the spin-mixing angle [39,40]. The longitudinal spin-relaxation time can be expressed in terms of the Green functions as $\mathcal{T}_1^{-1} = \frac{N_\uparrow + N_\downarrow}{6N_\uparrow N_\downarrow \tau_{so}} \text{Tr}[(\hat{g}_s^{RA})^2 - (\hat{g}_t^{RA})^2]$, where \hat{g}_s^{RA} and \hat{g}_t^{RA} are the singlet and triplet parts of $\hat{g}^R - \hat{g}^A = \hat{g}_s^{RA} + \hat{g}_t^{RA}$ [23].

We assume the time-dependent magnetization is $\mathbf{m}_\perp(t) = m_\Omega(\cos(\Omega t), \sin(\Omega t), 0)$ consisting of the left- and right-hand parts $\mathbf{m}_\perp(t) = m_{\Omega,l}e^{i\Omega t}(\mathbf{x} - i\mathbf{y}) + m_{-\Omega,r}e^{-i\Omega t}(\mathbf{x} + i\mathbf{y})$ with $m_{\Omega,l} = m_{-\Omega,r} = m_\Omega/2$. In general, solving Eqs. (3) and (4) to the second order in time-dependent field we obtain the stationary second-order correction to the Keldysh component of the GF $\hat{g}^K(\varepsilon) \propto m_\Omega^2$. It consists of corrections to the spectral function analogous to those induced by the electromagnetic irradiation [56,57] and of the anomalous part [58–61] \hat{g}^a which determines the stationary spin accumulation and thereby the nonlocal voltage in Eq. (1). The calculation of \hat{g}^a and its relation to the observables W , μ_{sz} and the distribution functions f_\uparrow, f_\downarrow is presented in Supplemental Material [51]. It provides the general expression for the spin accumulation

$$\mu_{sz}(\Omega, T) = \chi_{lr}(\Omega, T)m_{l,\Omega}m_{r,-\Omega}, \quad (5)$$

where χ_{lr} is the second-order spin response function.

Here we consider a superconductor film with thickness $d_S \ll \ell_{sm}, \xi_0$ small compared to the spin relaxation and coherence lengths in the superconductor. Then Eqs. (3) and (4) can be reduced [51] to the coordinate-independent Usadel equation with an effective Zeeman field $\mathbf{h} = J_{sd}\mathbf{m}/d$ so that $h_0 = J_{sd}/d$ and $h_\Omega = h_0 m_\Omega$.

The calculated dependencies of pumped spin accumulation μ_{sz} , nonlocal voltage V_D , and energy W are shown in Figs. 3(b)–3(d). One can see the clear correlation between these three quantities resulting from the strong spin-energy coupling in spin-split superconductors. The key feature of $\mu_{sz}(\Omega)$ and $V_D(\Omega)$ dependencies are the sharp peaks labeled by I and II as well as the less pronounced peak labeled by III corresponding to the different spin excitation processes shown schematically on the energy level diagram Fig. 3(a).

The excitation processes I and II create nonequilibrium quasiparticle states on the spin-down branch at the energy interval $\Delta - h_0 < E_p < \Delta + h_0$, which corresponds to the situation with spin-energy accumulation shown in Fig. 2. Such states can relax only due to the slow energy relaxation which determines the large amplitude of the peaks I and II in Figs. 3(b) and 3(c). The size of these peaks scale as $\min(\tau_s, \Delta^{-1})h_0/(\tau_s\Gamma)$ as demonstrated by the series of plots for different parameters [51]. The process III is more complicated since it requires the existence of subgap spin-up states at $[\Delta - h_0, \Delta + h_0]$ energy interval which appear due to the broadening of spin subbands by the spin relaxation. The equilibration of spin-up and spin-down populations shown by the horizontal arrow leads to $f_\uparrow = f_\downarrow$ but the spin accumulation appears due to the DOS difference $N_\downarrow > N_\uparrow$.

Results in Figs. 3(b) and 3(c) predict sizable spin and voltage signals even for low frequencies $\Omega \ll \Delta_0$. They are especially pronounced near the peak II associated with electron paramagnetic resonance frequency $\Omega \approx 2h_0$ usually reached in FMR experiments with resonance frequencies around several GHz. The excitation process II in Fig. 3(a) polarizes existing quasiparticles and therefore disappears at low temperatures $T \ll T_c$. The processes I and III exist even at $T \rightarrow 0$ since they break Cooper pairs and create spin-polarized quasiparticles out from the vacuum state. As a result peaks I and III become exponentially diverging in the voltage signal at low temperatures $T \ll T_c$ [not shown in Fig. 3(c)], $V_D \propto e^{\Delta/T}$ since the local conductance $G_F \propto e^{-\Delta/T}$ in Eq. (1).

Because of energy conservation $W(\Omega) = \alpha(\Omega)\Omega^2 m_\Omega^2/\Gamma$, where $\alpha(\Omega)$ is the frequency-dependent increase of Gilbert damping. The plot of the ratio $W(\Omega, T)/W(\Omega, T_c) = \alpha(\Omega, T)/\alpha(\Omega, T_c)$ shows the presence of the superconducting gap since the damping is generally suppressed for $\Omega < 2\Delta_0$. For temperatures somewhat below T_c there is a coherence peak [37–40] at around $\Omega \approx 2h_0$.

Next, we consider the spin accumulation driven by the stochastic magnetization corresponding to the *magnon thermal field* at temperature $T_m \neq T$ which can be controlled with the help of electrical spin injection based on the spin Hall effect [11,34]. For that we find μ_{sz} by averaging Eq. (5) over the fluctuations of magnetization. This can be done [51] by replacing the product of classical field components with the

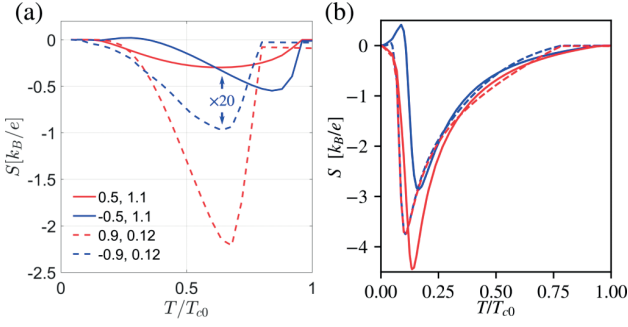


FIG. 4. Magnon Seebeck coefficient $S(T)$ in FI/SC/FM setup calculated using (a) model energy relaxation (3) with $\Gamma = 10^{-3}T_{c0}$ or (b) quasiequilibrium model (7) with electron-phonon relaxation. Red (blue) curves correspond to $(\mathbf{h}_0 \cdot \mathbf{m}_0) > (<) 0$. Blue curves in (a) are multiplied by 20 for clarity. Solid and dashed lines are for $|\mathbf{h}_0| = 0.5T_{c0}$, $\tau_{so}^{-1} = 1.1T_{c0}$ (Nb) and $|\mathbf{h}_0| = 0.9T_{c0}$, $\tau_{so}^{-1} = 0.12T_{c0}$ (Al), respectively; $P_D = 0.5$, $P_D \cdot \mathbf{h}_0 > 0$.

nonequilibrium Keldysh magnon propagator $m_{l,\Omega}m_{r,-\Omega} \rightarrow v_s \delta D^K(\Omega)$, where v_s is the volume per spin, and summing over Ω . In the stationary case $\delta D^K(\Omega) = D^{RA}(\Omega) \delta f_m(\Omega)$, where $D^{RA}(\Omega)$ and f_m are the magnon density of states and the distribution function [51]. For the thermally biased magnon state $\delta f_m(\Omega) = n_B(\Omega/T_m) - n_B(\Omega/T)$, where $n_B(\Omega/T) = \coth(\Omega/2T)$. This approach generalizes the calculation of the magnon-driven spin current [38,62,63] to that of the magnon-driven spin accumulation.

For small magnon temperature bias this spin accumulation $\mu_{sz} \propto (T - T_m)$ and the detector voltage (1) can be expressed through the linear Seebeck coefficient characterizing the conversion of magnon temperature into the electric signal in FI/SC/FM nonlocal circuit $V_D = S(T - T_m)$

$$S = P_D v_s m_M^{3/2} \frac{G_{Fn}}{e G_F} \int_0^\infty \sqrt{\Omega} \chi_{lr} \partial_T n_B d\Omega, \quad (6)$$

where v_s , the volume per unit spin in FI, determines the number of magnon modes. For YIG [64], $m_M \approx 1 \text{ eV}^{-1} \text{ \AA}^{-2}$ and [65] $v_s \approx 500 \text{ \AA}^3$. Figure 4 shows $S(T)$ for parameters qualitatively corresponding to the EuS/Al and YIG/Nb based FI/SC bilayers that have been studied recently [34,49].

The spin signals are enhanced even more due to the energy dependence of the inelastic scattering rate when the relaxation is due to the electron-phonon coupling. This can be demonstrated in the quasiequilibrium limit, assuming the rapid internal thermalization process that allows us to parametrize the distribution function by temperature T_S and the spin-dependent chemical potential shift eV_s . Then kinetic Eq. (2) can be written as the following system describing energy, spin, and charge currents at SC/FI and SC/FM interfaces

$$\begin{aligned} G_{e-ph}(T_S - T_{ph}) &= G_{me}(T_m - T_S) \\ \mathcal{V}_S v_e V_s / \tau_{sa} &= G_{ms}(T_m - T_S) \\ (G_F / G_{Fn}) V_D &= P_D V_s + \alpha_{th}(T_S - T_F). \end{aligned} \quad (7)$$

Here G_{e-ph} is the electron-phonon thermal conductance, $\alpha_{th} = e P_D \int_0^\infty (N_\uparrow - N_\downarrow) \partial_T n_0 d\varepsilon$ is the thermoelectric coefficient at the SC/FM interface [20,21], \mathcal{V}_S the superconductor

volume, v its density of states, and the energy-averaged spin relaxation rate is $\tau_{sa}^{-1} = \int_0^\infty d\varepsilon (\partial_\varepsilon n_0) \mathcal{T}_1^{-1} N_\uparrow N_\downarrow / (N_\uparrow + N_\downarrow)$. The magnon-electron conductances for spin and heat, G_{ms} and G_{me} , are expressed [51] through the linear spin susceptibility [40,66] and were previously studied in the normal state [67,68]. Further we assume that the temperature of the phonon heat bath is equal to that of the ferromagnetic metal electrode $T_F = T_S$ to obtain the electric Seebeck coefficient

$$S = \frac{G_{Fn}}{G_F} \left(\frac{P_D \tau_{sa} G_{ms}}{\mathcal{V}_S v} + \frac{\alpha_{th} G_{me}}{G_{me} + G_{e-ph}} \right). \quad (8)$$

The second term is again due to the spin-energy mixing, and it provides the dominating contribution in the superconducting state. The Seebeck coefficient is plotted in Fig. 4(b) [69]. Compared to the full nonequilibrium case [Fig. 4(a)], we find that due to the rapid decrease of the electron-phonon coupling with decreasing temperature, the signal persists to lower temperatures and is mainly limited by the Seebeck coefficient of the SC/FM junction [21].

The large value of the Seebeck coefficient converting the magnon temperature difference to an electrical voltage indicates that this device can be used as an ultrasensitive detector of propagating magnons [51], analogous to the thermoelectric detector suggested in Refs. [70,71]. The detector can have a very low noise equivalent power of the order of $NEP^2 \sim G_{th} T^2$, limited by the weak thermal conductance $G_{th} = G_{me} + G_{e-ph}$ from the superconductor to the relevant heat baths. Similar to the other nanoscale superconducting detectors [72–74], they will also have a very good energy resolution $\Delta E = NEP \sqrt{\tau_{eff}}$, provided that the thermal relaxation time τ_{eff} is not too long. With suitable setting one can then approach even the detection of single propagating magnons with frequencies of a few tens of GHz.

To conclude we have shown how the electron-hole symmetry breaking present in SC/FI bilayers mixes the spin and energy modes and leads to a giant enhancement of the spin battery effect. This leads to the large magnon-driven Seebeck effect which can be considered as a very sensitive detector of magnons. We expect this effect also to explain the giant spin-Hall signal measured in Ref. [34], but its precise description would require appending the theory with the description of the spin-Hall angle [75–77].

The mechanism of producing giant spin signals does not necessarily require superconductors, but we expect similar effects in any system exhibiting strong spin-resolved electron-hole asymmetry, such as semimetals in the presence of large exchange fields or magnetic topological insulators [78]. Such systems allow for an electrical access to the energy dissipation processes in ferromagnetic resonance or detailed studies of the magnon spectra via the heat conductance G_{me} between electrons and magnons.

We thank R. A. Duine for discussions. This work was supported by the Academy of Finland Projects 297439 and 317118, the European Union's Horizon 2020 Research and Innovation Framework Programme under Grant No. 800923 (SUPERTED), and Jenny and Antti Wihuri Foundation. The work of M.A.S. was supported by Russian Science Foundation (Grant No. 20-12-00053).

- [1] S. Wolf, D. Awschalom, R. Buhrman, J. Daughton, v. S. von Molnár, M. Roukes, A. Y. Chtchelkanova, and D. Treger, *Science* **294**, 1488 (2001).
- [2] I. Žutić, J. Fabian, and S. D. Sarma, *Rev. Mod. Phys.* **76**, 323 (2004).
- [3] G. E. W. Bauer, E. Saitoh, and B. J. van Wees, *Nat. Mater.* **11**, 391 (2012).
- [4] Y. Tserkovnyak, A. Brataas, and G. E. W. Bauer, *Phys. Rev. Lett.* **88**, 117601 (2002).
- [5] A. Brataas, Y. Tserkovnyak, G. E. W. Bauer, and B. I. Halperin, *Phys. Rev. B* **66**, 060404(R) (2002).
- [6] Y. Tserkovnyak, A. Brataas, G. E. W. Bauer, and B. I. Halperin, *Rev. Mod. Phys.* **77**, 1375 (2005).
- [7] H. Nakayama, M. Althammer, Y.-T. Chen, K. Uchida, Y. Kajiwara, D. Kikuchi, T. Ohtani, S. Geprägs, M. Opel, S. Takahashi, R. Gross, G. E. W. Bauer, S. T. B. Goennenwein, and E. Saitoh, *Phys. Rev. Lett.* **110**, 206601 (2013).
- [8] M. Weiler, M. Althammer, M. Schreier, J. Lotze, M. Pernpeintner, S. Meyer, H. Huebl, R. Gross, A. Kamra, J. Xiao, Y.-T. Chen, H. J. Jiao, G. E. W. Bauer, and S. T. B. Goennenwein, *Phys. Rev. Lett.* **111**, 176601 (2013).
- [9] K. Uchida, J. Xiao, H. Adachi, J. Ohe, S. Takahashi, J. Ieda, T. Ota, Y. Kajiwara, H. Umezawa, H. Kawai, G. E. W. Bauer, S. Maekawa, and E. Saitoh, *Nat. Mater.* **9**, 894 (2010).
- [10] A. Chumak, V. Vasyuchka, A. Serga, and B. Hillebrands, *Nat. Phys.* **11**, 453 (2015).
- [11] L. Cornelissen, J. Liu, R. Duine, J. B. Youssef, and B. van Wees, *Nat. Phys.* **11**, 1022 (2015).
- [12] H. Yang, S.-H. Yang, S. Takahashi, S. Maekawa, and S. S. Parkin, *Nat. Mater.* **9**, 586 (2010).
- [13] C. Quay, D. Chevallier, C. Bena, and M. Aprili, *Nat. Phys.* **9**, 84 (2013).
- [14] M. J. Wolf, F. Hübner, S. Kolenda, H. v. Löhneysen, and D. Beckmann, *Phys. Rev. B* **87**, 024517 (2013).
- [15] F. Hübner, M. Wolf, D. Beckmann, and H. v. Löhneysen, *Phys. Rev. Lett.* **109**, 207001 (2012).
- [16] S. Kolenda, C. Sürgers, G. Fischer, and D. Beckmann, *Phys. Rev. B* **95**, 224505 (2017).
- [17] J. Heidrich and D. Beckmann, *Phys. Rev. B* **100**, 134501 (2019).
- [18] J. Linder and J. W. Robinson, *Nat. Phys.* **11**, 307 (2015).
- [19] W. Han, S. Maekawa, and X.-C. Xie, *Nat. Mater.* **19**, 139 (2020).
- [20] F. S. Bergeret, M. Silaev, P. Virtanen, and T. T. Heikkilä, *Rev. Mod. Phys.* **90**, 041001 (2018).
- [21] A. Ozaeta, P. Virtanen, F. S. Bergeret, and T. T. Heikkilä, *Phys. Rev. Lett.* **112**, 057001 (2014).
- [22] M. Silaev, P. Virtanen, F. S. Bergeret, and T. T. Heikkilä, *Phys. Rev. Lett.* **114**, 167002 (2015).
- [23] T. T. Heikkilä, M. Silaev, P. Virtanen, and F. S. Bergeret, *Prog. Surf. Sci.* **94**, 100540 (2019).
- [24] T. Krishtop, M. Houzet, and J. S. Meyer, *Phys. Rev. B* **91**, 121407(R) (2015).
- [25] I. V. Bobkova and A. Bobkov, *JETP Lett.* **101**, 118 (2015).
- [26] I. V. Bobkova and A. M. Bobkov, *Phys. Rev. B* **96**, 104515 (2017).
- [27] P. Virtanen, T. T. Heikkilä, and F. S. Bergeret, *Phys. Rev. B* **93**, 014512 (2016).
- [28] M. Kuzmanović, B. Y. Wu, M. Weideneder, C. H. L. Quay, and M. Aprili, *Nat. Commun.* **11**, 4336 (2020).
- [29] C. Bell, S. Milikisyants, M. Huber, and J. Aarts, *Phys. Rev. Lett.* **100**, 047002 (2008).
- [30] T. Wakamura, H. Akaike, Y. Omori, Y. Niimi, S. Takahashi, A. Fujimaki, S. Maekawa, and Y. Otani, *Nat. Mater.* **14**, 675 (2015).
- [31] K.-R. Jeon, C. Ciccarelli, A. J. Ferguson, H. Kurebayashi, L. F. Cohen, X. Montiel, M. Eschrig, J. W. A. Robinson, and M. G. Blamire, *Nat. Mater.* **17**, 499 (2018).
- [32] K.-R. Jeon, X. Montiel, S. Komori, C. Ciccarelli, J. Haigh, H. Kurebayashi, L. F. Cohen, A. K. Chan, K. D. Stenning, C.-M. Lee, M. G. Blamire, and J. W. A. Robinson, *Phys. Rev. X* **10**, 031020 (2020).
- [33] I. A. Golovchanskiy, N. N. Abramov, V. S. Stolyarov, V. I. Chichkov, M. Silaev, I. V. Shchetinin, A. A. Golubov, V. V. Ryazanov, A. V. Ustinov, and M. Y. Kupriyanov, *Phys. Rev. Appl.* **14**, 024086 (2020).
- [34] K.-R. Jeon, J.-C. Jeon, X. Zhou, A. Migliorini, J. Yoon, and S. S. P. Parkin, *ACS Nano* **14**, 15874 (2020).
- [35] A. Brataas and Y. Tserkovnyak, *Phys. Rev. Lett.* **93**, 087201 (2004).
- [36] J. P. Morten, A. Brataas, G. E. W. Bauer, W. Belzig, and Y. Tserkovnyak, *Europhys. Lett.* **84**, 57008 (2008).
- [37] M. Inoue, M. Ichioka, and H. Adachi, *Phys. Rev. B* **96**, 024414 (2017).
- [38] T. Kato, Y. Ohnuma, M. Matsuo, J. Rech, T. Jonckheere, and T. Martin, *Phys. Rev. B* **99**, 144411 (2019).
- [39] M. A. Silaev, *Phys. Rev. B* **102**, 180502(R) (2020).
- [40] M. A. Silaev, *Phys. Rev. B* **102**, 144521 (2020).
- [41] M. T. Ahari and Y. Tserkovnyak, *Phys. Rev. B* **103**, L100406 (2021).
- [42] M. Trif and Y. Tserkovnyak, *Phys. Rev. Lett.* **111**, 087602 (2013).
- [43] R. Ojajarvi, J. Manninen, T. T. Heikkilä, and P. Virtanen, *Phys. Rev. B* **101**, 115406 (2020).
- [44] K.-R. Jeon, C. Ciccarelli, H. Kurebayashi, J. Wunderlich, L. F. Cohen, S. Komori, J. W. A. Robinson, and M. G. Blamire, *Phys. Rev. Appl.* **10**, 014029 (2018).
- [45] E. Gershenzon, M. Gershenzon, G. Gol'tsman, A. Lyul'kin, A. Semenov, and A. Sergeev, *Sov. Phys. JETP* **70**, 505 (1990).
- [46] T. M. Klapwijk, P. A. van der Plas, and J. E. Mooij, *Phys. Rev. B* **33**, 1474 (1986).
- [47] A. Brataas, Y. Tserkovnyak, and G. E. W. Bauer, *Phys. Rev. Lett.* **101**, 037207 (2008).
- [48] R. Meservey and P. Tedrow, *Phys. Rep.* **238**, 173 (1994).
- [49] A. Hijano, S. Ilić, M. Rouco, C. G. Orellana, M. Ilyn, C. Rogero, P. Virtanen, T. Heikkilä, S. Khorshidian, M. Spies *et al.*, *Phys. Rev. Research* **3**, 023131 (2021).
- [50] This picture is valid for weak spin relaxation with $\tau_s^{-1} \ll \Delta$. For larger τ_s^{-1} the spectrum becomes more complicated as the spin ceases to be a good quantum number. Our quasiclassical approach takes into account this spin mixing.
- [51] See Supplemental Material at <http://link.aps.org/supplemental/10.1103/PhysRevB.103.224524> for a derivation of the general relation between spin and energy currents generated by magnetization dynamics, a derivation of kinetic equations with spin-energy coupling and calculation of the anomalous parts of interfacial spin and energy currents, a derivation of the boundary conditions for Green's functions in the S/FI system with stochastic magnetization field, e.g., thermal magnons, a derivation of the second-order perturbation theory equations,

- results of such calculations for various parameters, and the comparison with the nonperturbative numerical solution of the Keldysh-Usadel equation with a time-dependent Zeeman field, and estimates for the figures of merit of the magnon detector. The Supplemental cites Refs. [79–81].
- [52] H. T. Simensen, L. G. Johnsen, J. Linder, and A. Brataas, *Phys. Rev. B* **103**, 024524 (2021).
- [53] T. Tokuyasu, J. A. Sauls, and D. Rainer, *Phys. Rev. B* **38**, 8823 (1988).
- [54] Y. Ohnuma, H. Adachi, E. Saitoh, and S. Maekawa, *Phys. Rev. B* **89**, 174417 (2014).
- [55] A. Millis, D. Rainer, and J. A. Sauls, *Phys. Rev. B* **38**, 4504 (1988).
- [56] A. V. Semenov, I. A. Devyatov, P. J. de Visser, and T. M. Klapwijk, *Phys. Rev. Lett.* **117**, 047002 (2016).
- [57] J. Linder, M. Amundsen, and J. A. Ouassou, *Sci. Rep.* **6**, 38739 (2016).
- [58] G. M. Eliashberg, *Zh. Eksp. Teor. Fiz.* **61**, 1254 (1971).
- [59] L. P. Gor'kov and N. B. Kopnin, *Sov. Phys. Usp.* **18**, 496 (1975).
- [60] A. Larkin and Y. Ovchinnikov, *Zh. Eksp. Teor. Fiz.* **73**, 299 (1977).
- [61] S. N. Artemenko and A. Volkov, *Sov. Phys. Usp.* **22**, 295 (1979).
- [62] H. Adachi, J.-I. Ohe, S. Takahashi, and S. Maekawa, *Phys. Rev. B* **83**, 094410 (2011).
- [63] H. Adachi, K.-I. Uchida, E. Saitoh, and S. Maekawa, *Rep. Prog. Phys.* **76**, 036501 (2013).
- [64] C. M. Srivastava and R. Aiyar, *J. Phys. C* **20**, 1119 (1987).
- [65] V. Cherepanov, I. Kolokolov, and V. L'vov, *Phys. Rep.* **229**, 81 (1993).
- [66] K. Maki, *Phys. Rev. B* **8**, 191 (1973).
- [67] S. A. Bender and Y. Tserkovnyak, *Phys. Rev. B* **91**, 140402(R) (2015).
- [68] L. J. Cornelissen, K. J. H. Peters, G. E. W. Bauer, R. A. Duine, and B. J. van Wees, *Phys. Rev. B* **94**, 014412 (2016).
- [69] Figure 4 assumes for simplicity that the electron-phonon coupling in Nb is the same as in Al.
- [70] T. T. Heikkilä, R. Ojajärvi, I. J. Maasilta, E. Strambini, F. Giazotto, and F. S. Bergeret, *Phys. Rev. Appl.* **10**, 034053 (2018).
- [71] S. Chakraborty and T. T. Heikkilä, *J. Appl. Phys.* **124**, 123902 (2018).
- [72] J. Govenius, R. E. Lake, K. Y. Tan, V. Pietilä, J. K. Julin, I. J. Maasilta, P. Virtanen, and M. Möttönen, *Phys. Rev. B* **90**, 064505 (2014).
- [73] J. Govenius, R. E. Lake, K. Y. Tan, and M. Möttönen, *Phys. Rev. Lett.* **117**, 030802 (2016).
- [74] R. Kokkonen, J. Govenius, V. Vesterinen, R. E. Lake, A. M. Gunyhó, K. Y. Tan, S. Simbierowicz, L. Grönberg, J. Lehtinen, M. Prunnila *et al.*, *Commun. Phys.* **2**, 124 (2019).
- [75] F. S. Bergeret and I. V. Tokatly, *Phys. Rev. B* **94**, 180502(R) (2016).
- [76] I. V. Tokatly, *Phys. Rev. B* **96**, 060502(R) (2017).
- [77] C. Huang, I. V. Tokatly, and F. S. Bergeret, *Phys. Rev. B* **98**, 144515 (2018).
- [78] M. M. Otrokov, I. I. Klimovskikh, H. Bentmann, D. Estyunin, A. Zeugner, Z. S. Aliev, S. Gaß, A. Wolter, A. Koroleva, A. M. Shikin *et al.*, *Nature (London)* **576**, 416 (2019).
- [79] R. C. Dynes, J. P. Garno, G. B. Hertel, and T. P. Orlando, *Phys. Rev. Lett.* **53**, 2437 (1984).
- [80] A. Abrikosov and L. Gor'kov, *Sov. Phys. JETP* **15**, 752 (1962).
- [81] A. Kamenev, *Field Theory of Non-Equilibrium Systems* (Cambridge University Press, Cambridge, 2011).

Giant enhancement to spin battery effect in superconductor/ferromagnetic insulator systems: Supplementary Material

Risto Ojajarvi,¹ Tero T. Heikkilä,¹ P. Virtanen,¹ and M.A. Silaev^{1,2,3}

¹*Department of Physics and Nanoscience Center, University of Jyväskylä, P.O. Box 35 (YFL), FI-40014 University of Jyväskylä, Finland*

²*Moscow Institute of Physics and Technology, Dolgoprudny, 141700 Russia*

³*Institute for Physics of Microstructures, Russian Academy of Sciences, 603950 Nizhny Novgorod, GSP-105, Russia*

I. SUPPLEMENTARY MATERIAL

Here we provide technical details of the formalism, verification of our approach by comparison with known results as well as the extended results of calculations for wide range of parameters. In Sec. IA we describe the general formalism of Keldysh-Usadel equation with the dynamical boundary conditions at the S/FI interface. In Sec. IB we show that our general formalism yields the conventional expression for the spin current with pumped and backflow terms. In Sec. IC we show that our formalism in the normal superconducting state yields the usual expression for static spin current and spin accumulation (spin battery effect).

The generalization of kinetic equations to describe spin accumulation in the superconducting spin sink are derived in Sec. ID.

In Sec. IE we describe the perturbation theory approach to solving Keldysh-Usadel equation to the second order of the driving Zeeman field to calculate the stationary spin accumulation. Here we present the extended calculation results of spin and energy accumulation as well as the non-local voltage driven by the magnetization dynamics for a wide range of parameters.

Beyond perturbation theory we have also developed the numerically exact solution of the non-stationary Keldysh-Usadel equation with the time-dependent Zeeman field. The method is described in Sec. IF.

Using the results for spin accumulation driven by the deterministic magnetic signal we can treat the case of stochastic magnetization dynamics driven by the field of thermal magnons. The approach based on the calculation of electron-magnon collision integral is presented in Sec. IG. We verify our approach by deriving the known results for the magnon-driven spin and energy currents in the normal state of FI/metal bilayer.

In Sec. IH We demonstrate that general relations between pumped spin and energy currents are valid in the superconducting state.

Section II considers the FI/SC/FM system as a magnon detector and estimates the corresponding figures of merit.

A. General formalism

We describe the superconducting film using Keldysh-Usadel equation [1] with a gradient term and without external Zeeman field

$$-\{\hat{\tau}_3 \partial_t \circ \check{g}\} + \partial_x \check{I} = [\Delta \hat{\tau}_1 + \check{\Gamma} + \check{\Sigma}_{\text{so}} \circ \check{g}]. \quad (\text{S1})$$

Here \check{g} is the quasiclassical Green's function (GF) in the 8×8 space consisting of Keldysh, Nambu and spin indices, D is the diffusion coefficient and $\check{I} = D(\check{g} \circ \partial_x \check{g})$ is the matrix current in the x -direction.[1] We assume translation invariance in the y - z plane. For double-time variables \circ is a convolution product

$$(A \circ B)(t_1, t_2) = \int dt A(t_1, t) B(t, t_2). \quad (\text{S2})$$

For single-time variables it reduces to a product

$$\begin{aligned} (a \circ B)(t_1, t_2) &= a(t_1) B(t_1, t_2), \\ (B \circ a)(t_1, t_2) &= B(t_1, t_2) a(t_2). \end{aligned} \quad (\text{S3})$$

The commutator is $[X \circ Y] = X \circ Y - Y \circ X$, and the time-derivative acts as

$$\{\hat{\tau}_3 \partial_t \circ \check{g}\}(t_1, t_2) = \hat{\tau}_3 \partial_{t_1} \check{g}(t_1, t_2) + \partial_{t_2} \check{g}(t_1, t_2) \hat{\tau}_3. \quad (\text{S4})$$

The value of the superconducting order parameter Δ is determined from the self-consistency equation

$$\Delta = \frac{\lambda}{16i} \int_{-\Omega_D}^{\Omega_D} d\varepsilon \text{Tr}[\hat{\tau}_1 \hat{g}^K(\varepsilon)]. \quad (\text{S5})$$

We assume the weak-coupling limit, so that the coupling constant λ and the high-energy cutoff Ω_D can be eliminated in favor of the transition temperature T_{c0} in the absence of pair-breaking effects.[1] We do not include the non-equilibrium correction to Δ , as it only gives a spectral correction to the GFs and does not affect the second-order perturbation theory results for the non-local voltage V_D or the energy accumulation W .

The coupling to the normal reservoir self-energy has spectral components $\hat{\Gamma}^{R,A} = \pm \Gamma \hat{\tau}_3$ and the Keldysh component $\hat{\Gamma}^K = 2\Gamma \hat{\tau}_3 n_0$ with the equilibrium distribution function in the Fourier representation $n_0(\varepsilon) = \tanh(\varepsilon/2T)$. The spectral components of this self-energy yield the frequently used Dynes[2] parameter which determines the smearing of the BCS density of states singularity. In addition, this self-energy determines the relaxation of spin-independent non-equilibrium distribution functions.

Elastic spin relaxation in the ladder approximation is determined by the spin-orbit scattering self-energy [3]

$$\check{\Sigma}_{\text{so}} = \hat{\sigma} \cdot \check{g} \hat{\sigma} / (6\tau_{\text{so}}). \quad (\text{S6})$$

The differential equation (S1) is supplemented by dynamical boundary conditions at $x=0$ describing the spin splitting and pumping induced by the electron scattering at the FI interface with time-dependent magnetization. These boundary conditions are derived from the spin-dependent scattering matrix at the FI/SC interface[4]

$$\check{I}(x=0) = iJ_{\text{sd}}[\hat{\sigma} \mathbf{m} \hat{\tau}_3 \circledast \check{g}]. \quad (\text{S7})$$

The boundary condition determines the interfacial matrix current.

B. Boundary condition for spin current

To demonstrate how the spin pumping arises in this formalism, we now derive an expression for the energy-integrated spin current generated at the interface. The Fourier transform of the Keldysh part of the matrix current is

$$\hat{I}^K(\varepsilon, \varepsilon - \Omega) = iJ_{\text{sd}} \int d\omega (\hat{m}_\omega g_{\varepsilon - \omega, \varepsilon - \Omega}^K - g_{\varepsilon, \varepsilon - \Omega + \omega}^K \hat{m}_\omega), \quad (\text{S8})$$

where $\hat{m}_\omega \equiv \int dt \tau_3 \boldsymbol{\sigma} \mathbf{m}(t) e^{-i\omega t}$. Fourier convention for double-time functions is

$$f(\varepsilon_1, \varepsilon_2) = \int dt_1 dt_2 f(t_1, t_2) e^{-i\varepsilon_1 t_1 + i\varepsilon_2 t_2}. \quad (\text{S9})$$

We extract the quasiclassical part of the energy-integrated current by imposing an energy cutoff Λ satisfying $\Delta_0, T_{c0}, \Omega \ll \Lambda \ll E_F$, so that

$$\begin{aligned} \hat{I}^K(\Omega) &= \int_{-\Lambda}^{+\Lambda} d\varepsilon \hat{I}(\varepsilon + \Omega/2, \varepsilon - \Omega/2) \\ &= iJ_{\text{sd}} \int d\omega \int_{-\Lambda}^{+\Lambda} d\varepsilon (\hat{m}_\omega g_{\varepsilon + \Omega/2 - \omega, \varepsilon - \Omega/2}^K \\ &\quad - g_{\varepsilon + \Omega/2, \varepsilon - \Omega/2 + \omega}^K \hat{m}_\omega). \end{aligned} \quad (\text{S10})$$

In terms of a matrix $\hat{n}(\omega) = \int_{-\Lambda}^{+\Lambda} d\varepsilon g_{\varepsilon - \omega/2, \varepsilon + \omega/2}^K$, the current is

$$\hat{I}^K(\Omega) = iJ_{\text{sd}} \left(\int d\omega (\hat{m}_\omega \hat{n}_{\Omega - \omega} - \hat{n}_{\Omega - \omega} \hat{m}_\omega) - 4\Omega \boldsymbol{\sigma} \mathbf{m}_\Omega \right). \quad (\text{S11})$$

The last term appears from energy shifts about the cutoff, where $g_{\varepsilon, \varepsilon - \omega}^K \approx 2 \text{sgn}(\varepsilon) \tau_3 \delta(\omega)$ does not depend on the state of the system.

Transforming to the time domain and extracting the spin-dependent part, we find the boundary condition for the spin current

$$\mathbf{j}_s(x=0) = 2J_{\text{sd}} [\boldsymbol{\mu}_s(t) \times \mathbf{m}(t) - \partial_t \mathbf{m}(t)]. \quad (\text{S12})$$

Here the spin current and the quasiclassical part of the spin accumulation are defined as

$$\mathbf{j}_s(t) = -\frac{1}{8} \int_{-\infty}^{\infty} d\varepsilon \text{Tr}[\boldsymbol{\sigma} \hat{I}^K(\varepsilon, t)], \quad (\text{S13})$$

$$\boldsymbol{\mu}_s(t) = -\frac{1}{8} \int_{-\infty}^{\infty} d\varepsilon \text{Tr}[\hat{\sigma} \tau_3 \hat{g}^K(\varepsilon, t)], \quad (\text{S14})$$

respectively, with an implicit high-energy cutoff. Above, the center-of-mass time-coordinate t is the Fourier transform of the frequency $\Omega = \varepsilon_1 - \varepsilon_2$ and $\varepsilon = (\varepsilon_1 + \varepsilon_2)/2$ as in Eq. (S9). In Eq. (S12), the latter term is the pumped spin current and the former term is the back-flow current due to spin accumulation. This expression corresponds to the general one[5] with a purely imaginary spin-mixing conductance associated with the interfacial exchange constant [6] $g_{\uparrow\downarrow} = -2iJ_{\text{sd}}/\nu$.

C. Spin diffusion in the normal state

Consider a normal metal (N) in contact with FI with time-dependent magnetization $\mathbf{m}(t)$. In the normal state Eq. (S1) is greatly simplified because we know the spectral functions $\hat{g}^{R/A} = \pm \tau_3$ and they are not perturbed by the time-dependent boundary conditions (S7). The Keldysh function is given by $\hat{g}^K = 2\tau_3 \hat{f}$ where $\hat{f} = f_L + \mathbf{f} \hat{\sigma}$. The distribution functions f_L and \mathbf{f} parametrize the energy and spin accumulations, respectively. The spin accumulation is given by

$$\boldsymbol{\mu}_s(t) = - \int_{-\infty}^{\infty} d\varepsilon \mathbf{f}(t, \varepsilon) \quad (\text{S15})$$

$$\mathbf{j}_s = D \partial_x \boldsymbol{\mu}_s \quad (\text{S16})$$

Spin diffusion equation in the normal metal, obtained from the Keldysh part of Eq. (S1), is

$$\partial_x \mathbf{j}_s = \partial_t \boldsymbol{\mu}_s + \boldsymbol{\mu}_s / \tau_s, \quad (\text{S17})$$

where τ_s^{-1} is the spin relaxation rate in the normal state. In the normal-state we can use the energy-integrated Eq. (S12) as the boundary condition for the spin current generated at the FI/N interface at $x=0$. The length of the normal metal is d and the other interface is to vacuum so that the current vanishes at $x=d$.

From the diffusion equation (S17), we find that the spin accumulation at frequency ω is determined by the spin current at $x=0$ at the same frequency,

$$\boldsymbol{\mu}_s(x, \omega) = -\mathbf{j}_s(x=0, \omega) \frac{\cosh[\kappa(x-d)]}{D\kappa \sinh(\kappa d)}, \quad (\text{S18})$$

and the boundary condition mixes the harmonics. Here the wavevector is $\kappa = \sqrt{1 + i\omega\tau_s}/\lambda_s$ with the spin diffusion length $\lambda_s = \sqrt{D\tau_s}$. We assume the FI magnetization \mathbf{m} has a circularly polarized alternating component $\mathbf{m}_\perp(t) = \text{Re}[m_\Omega(\mathbf{x} + i\mathbf{y})e^{i\Omega t}]$, with $m_\Omega^* = m_\Omega$. It drives

the alternating spin accumulation (S18) with frequency $\omega = \pm\Omega$ and for static spin accumulation with $\omega = 0$. The latter one determines the spin battery effect [5, 7]

$$\langle \boldsymbol{\mu}_s \rangle(x) = -\langle \boldsymbol{j}_s \rangle(x=0) \frac{\lambda_s \cosh[(x-d)/\lambda_s]}{D \sinh(d/\lambda_s)}, \quad (\text{S19})$$

where $\langle \dots \rangle$ denotes the time averaging.

We assume the FI magnetization \mathbf{m} has a static component $\mathbf{m}_0 = \mathbf{z}$ and a circularly polarized alternating component $\mathbf{m}_\perp(t) = \text{Re}[m_\Omega(\mathbf{x} + i\mathbf{y})e^{i\Omega t}]$, with $m_\Omega^* = m_\Omega$. Solving Eqs. (S12) and (S18), we find the linear response spin accumulation at the interface,

$$\boldsymbol{\mu}_s(x=0, \Omega) = \chi_l(\Omega) m_\Omega(\mathbf{x} + i\mathbf{y}), \quad (\text{S20})$$

$$\chi_l(\Omega) = -\frac{\Omega}{1 - i(D\kappa/2J_{sd}) \tanh(\kappa d)}. \quad (\text{S21})$$

In time-domain, $\boldsymbol{\mu}_s(t)$ is real, so the negative frequency is given by $\boldsymbol{\mu}_s(x=0, -\Omega) = \boldsymbol{\mu}_s(x=0, \Omega)^*$.

At the second order in $\mathbf{m}_\perp(t)$, the static spin current at the interface is given by the boundary condition (S12) as

$$\begin{aligned} \langle \boldsymbol{j}_s(x=0) \rangle &= J_{sd} \boldsymbol{\mu}_s(x=0, \Omega)^* \times \mathbf{m}(\Omega) + \text{c.c.} \\ &= -2J_{sd} \text{Im}[\chi_l(\Omega)] m_\Omega^2 \mathbf{z}. \end{aligned} \quad (\text{S22})$$

In the low-frequency limit $\omega\tau_s \ll 1$ we can put $\kappa = \lambda_s^{-1}$ so that combining Eqs. (S21–S22) we get the constant spin current in the conventional form [5, 7]

$$\nu \langle \boldsymbol{j}_s(x=0) \rangle = \text{Re} A_{\text{eff}}^{\uparrow\downarrow} \langle \mathbf{m} \times \partial_t \mathbf{m} \rangle \quad (\text{S23})$$

$$\frac{1}{A_{\text{eff}}^{\uparrow\downarrow}} = -\frac{\nu}{2iJ_{sd}} + \frac{\nu D}{\lambda_s} \frac{1}{\tanh(d/\lambda_s)} \quad (\text{S24})$$

Here the first term is the inverse of pure imaginary spin-mixing conductance of the FI interface $-2iJ_{sd}/\nu$ while the second term is the usual contribution from the spin relaxation in the spin sink[5] with $\nu D/\lambda_s$ is the dimensional resistance of the normal metal layer of the thickness λ_s .

In the thin-film limit $d \ll \lambda_{sd}$ and beyond the small frequency limit the susceptibility (S21) becomes

$$\chi_l(\Omega) = 2h_0\Omega/(\Omega - 2h_0 - i/\tau_s), \quad (\text{S25})$$

with the effective field $h_0 = J_{sd}/d$. It corresponds to the Bloch equation

$$\partial_t \boldsymbol{\mu}_s + 2\boldsymbol{\mu}_s \times \mathbf{h} + \boldsymbol{\mu}_s/\tau_{\text{sn}} = 2\partial_t \mathbf{h} \quad (\text{S26})$$

with $\mathbf{h} = h_0 \mathbf{m}$. Here we have electron paramagnetic resonance at $\Omega = 2h_0$.

D. Derivation of kinetic equations

The stationary non-equilibrium Keldysh function can be presented in the form

$$\hat{g}_{hh}^K = n_0(\varepsilon)(\hat{g}_{hh}^R - \hat{g}_{hh}^A) + \hat{g}_{hh}^a, \quad (\text{S27})$$

where $\hat{g}_{hh}^{R,A}$ are the corrections to the spectral function and \hat{g}_{hh}^a is the anomalous part which contains the information about non-equilibrium quasiparticles. The anomalous and spectral parts can be calculated separately.

In general, the corrections to GF satisfy the relation coming from the normalization condition

$$g_0^R g_{hh}^a + g_{hh}^a g_0^A = -g_h^R \circ g_h^a - g_h^a \circ g_h^A, \quad (\text{S28})$$

where $g_h^{R/A/a}$ are the first-order corrections and $g_{hh}^{R/A/a}$ are the second-order corrections. To derive the simplified description in terms of the stationary kinetic equations one can use a parametrization in terms of the spin-dependent distribution functions

$$\hat{g}_{hh}^a = (\hat{g}_0^R - \hat{g}_0^A)(f_L \tau_0 + f_{T3} \sigma_z). \quad (\text{S29})$$

This parametrization implies that $\hat{g}_0^R \hat{g}_{hh}^a + \hat{g}_{hh}^a \hat{g}_0^A = 0$ and therefore it is not exact. It neglects the contribution $\hat{g}_h^R \circ \hat{f}_h - \hat{f}_h \circ \hat{g}_h^A$ to the second-order correction to the anomalous function, where \hat{f}_h is the first-order correction to the distribution function. However this contribution does not contain large parts determined by the inelastic relaxation. Therefore by comparing the results given by this parametrization (S29) with the general form of g_{hh}^a we find that they coincide with good accuracy for not very small spin relaxation, that is when $\Gamma\tau_s \ll 1$. All numerical results in paper are obtained with general \hat{g}_{hh}^a as explained in Sec. IE With good accuracy we can thus parametrize the stationary anomalous GF with the help of the distribution functions.

Distribution functions satisfy stationary kinetic equations

$$\partial_x \mathcal{J}_e + \Gamma\varepsilon(Nf_L + N_z f_z) + I_{ph} = 0 \quad (\text{S30})$$

$$\partial_x \mathcal{J}_s + \mathcal{I}_{so} = 0, \quad (\text{S31})$$

where the spin-relaxation collision integral is given by

$$\mathcal{I}_{so} = \text{Tr}(\sigma_z [\Sigma_{so}, \hat{g}]^K)/4 = \tilde{\tau}_{so}^{-1} N f_{T3} \quad (\text{S32})$$

with spin relaxation time given by $\tilde{\tau}_{so}^{-1} = (1/6N\tau_{so})\text{Tr}[(g_s^{RA})^2 - (g_t^{RA})^2]$ with spin-singlet g_s^{RA} and spin-triplet g_t^{RA} parts of the difference $\hat{g}^{RA} = \hat{g}^R - \hat{g}^A$. The spectral densities of currents are given by

$$\mathcal{J}_{sz} = D_{T3} \partial_x f_L + D_L \partial_x f_{T3} \quad (\text{S33})$$

$$\mathcal{J}_e = \varepsilon(D_L \partial_x f_L + D_{T3} \partial_x f_{T3}) \quad (\text{S34})$$

with diffusion coefficients found in [8]. These kinetic equations can be rewritten in terms of the spin-up and spin-down distribution functions $f_{\uparrow/\downarrow} = f_L \pm f_{T3}$. Then we obtain the spectral densities for spin and energy accumulations $f_s = N_\uparrow f_\uparrow - N_\downarrow f_\downarrow$ and $f_e = \varepsilon(N_\uparrow f_\uparrow + N_\downarrow f_\downarrow)$. In this representation the spin-orbit scattering collision integral (S35) is given by

$$\mathcal{I}_{so} = \frac{f_s - \kappa_{se} f_e}{\mathcal{T}_1} \quad (\text{S35})$$

where $\mathcal{T}_1 = \tilde{\tau}_{so} N_\uparrow N_\downarrow / N^2$ is the longitudinal spin relaxation time and spin-energy coupling is quantified by the coefficient

$$\kappa_{se}(\varepsilon) = \frac{1}{\varepsilon} \frac{N_\uparrow - N_\downarrow}{N_\uparrow + N_\downarrow}. \quad (\text{S36})$$

Note that $\kappa_{se}(\varepsilon) \neq 0$ requires the description of the static magnetic proximity effect, i.e., the generation of the spin splitting \mathbf{h}_0 in the superconductor. The spin-diffusion equation modified by the spin-energy coupling is given by

$$\partial_x \mathcal{J}_{sz} = \frac{f_s - \kappa_{se} f_e}{\mathcal{T}_1} \quad (\text{S37a})$$

$$\partial_x \mathcal{J}_e = I_{e-ph} + \Gamma f_e, \quad (\text{S37b})$$

where $\mathcal{J}_{sz}(\varepsilon)$ and $\mathcal{J}_e(\varepsilon)$ are the spectral densities of the time-independent spin and energy currents. The sources in Eqs. (S37a–S37b) are determined by the boundary conditions for these currents at the FI/SC interface, generated by the magnetization dynamics. We obtain it from the general boundary conditions (S106–S107) by leaving only the anomalous part of the sources

$$\mathcal{J}_{sz}^{(a)}(\varepsilon) = \frac{iJ_{sd}}{8} \text{Tr}(\sigma_z [\boldsymbol{\sigma} \mathbf{m} \hat{\tau}_3 \circlearrowleft \hat{g}_h]^a)(\varepsilon) \quad (\text{S38})$$

$$\mathcal{J}_e^{(a)}(\varepsilon) = \frac{iJ_{sd}}{4} \varepsilon \text{Tr}([\boldsymbol{\sigma} \mathbf{m} \hat{\tau}_3 \circlearrowleft \hat{g}_h]^a)(\varepsilon). \quad (\text{S39})$$

The anomalous part of the boundary conditions can be calculated by subtracting the spectral part, i.e., the part independent of the nonequilibrium state of the system, from the full Keldysh component of the currents. We assume the magnetization dynamics given by $\mathbf{m}(t) = m_0 \mathbf{z} + \mathbf{m}_\perp(t)$ with rotating time-dependent component given by $\mathbf{m}_\perp(t) = m_\Omega (\cos(\Omega t), \sin(\Omega t), 0)$. It can be represented as the sum of left-hand and right-hand components with the same amplitudes $\mathbf{m}_\perp(t) = m_{\Omega,l} e^{i\Omega t} (\mathbf{x} - i\mathbf{y}) + m_{-\Omega,r} e^{-i\Omega t} (\mathbf{x} + i\mathbf{y})$ where $m_{\Omega,l} = m_{-\Omega,r} = m_\Omega/2$. This signal can be induced in the standard ferromagnetic resonance setup. The frequency Ω can be tuned by the external magnetic field.

The spectral part of the boundary conditions reads

$$\begin{aligned} \frac{i}{4} \text{Tr}(\hat{\tau}_3 \sigma_z [\boldsymbol{\sigma} \mathbf{m} \circlearrowleft \hat{g}_h]^{sp})(\varepsilon) &= m_{l,\Omega} m_{r,-\Omega} n_0(\varepsilon) \times \quad (\text{S40}) \\ &[\chi_r^{RA}(\varepsilon - \Omega, \varepsilon) - \chi_l^{RA}(\varepsilon, \varepsilon - \Omega) - \\ &\chi_l^{RA}(\varepsilon + \Omega, \varepsilon) + \chi_r^{RA}(\varepsilon, \varepsilon + \Omega)] \end{aligned}$$

With that we obtain the anomalous part

$$\begin{aligned} \frac{i}{4} \text{Tr}(\hat{\tau}_3 \sigma_z [\boldsymbol{\sigma} \mathbf{m} \circlearrowleft \hat{g}_h]^a)(\varepsilon) &= \quad (\text{S41}) \\ m_{l,\Omega} [\chi_r^K(\varepsilon - \Omega, \varepsilon) - \chi_r^{RA}(\varepsilon - \Omega, \varepsilon) n_0(\varepsilon)] \\ &- m_{r,-\Omega} [\chi_l^K(\varepsilon, \varepsilon - \Omega) - \chi_l^{RA}(\varepsilon, \varepsilon - \Omega) n_0(\varepsilon)] + \\ &m_{r,-\Omega} [\chi_l^K(\varepsilon + \Omega, \varepsilon) - \chi_l^{RA}(\varepsilon + \Omega, \varepsilon) n_0(\varepsilon)] \\ &- m_{l,\Omega} [\chi_r^K(\varepsilon, \varepsilon + \Omega) - \chi_r^{RA}(\varepsilon, \varepsilon + \Omega) n_0(\varepsilon)] \end{aligned}$$

Substituting these expressions to (S38,S39) we get the spectral densities of the anomalous parts of spin and energy currents. The examples of $\mathcal{J}_{sz}^{(a)}(\varepsilon, T)$, $\mathcal{J}_e^{(a)}(\varepsilon, T)$ functions at a given frequency of the driving magnetization are shown in Fig. 1.

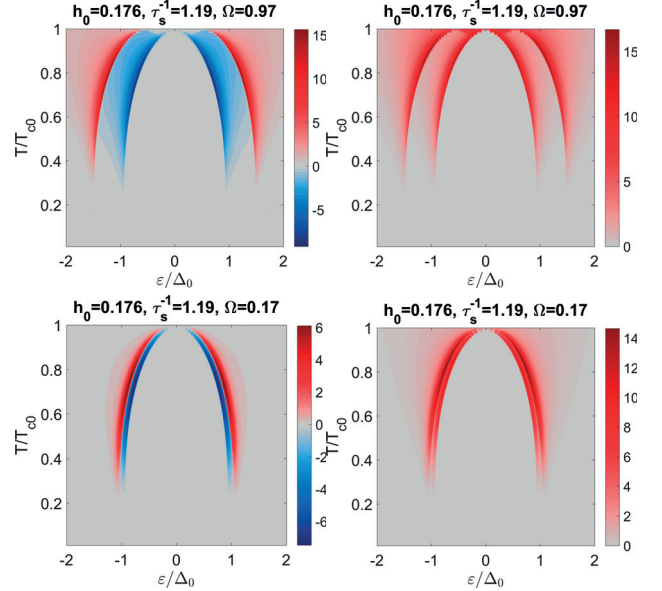


FIG. 1. Spectral densities of interfacial currents generated by the magnetization dynamics. (Left column): Energy current $\mathcal{J}_e(\varepsilon, T)$. (Right column): Spin current $\mathcal{J}_{sz}(\varepsilon, T)$. The energy-like quantities h_0, τ_s^{-1}, Ω are given in terms of T_{c0} .

E. Numerical perturbation calculations in the thin film limit

In this section we develop the perturbation theory which allows for calculating the corrections to spectral and anomalous parts of the GF in FI/SC system to the second order of the time-dependent magnetization. This calculation yields the boundary conditions for spin and energy currents which are the sources for kinetic equations discussed in Sec. ID. Besides that here we consider a general form of the anomalous function and hence can go beyond the approximation used for deriving the kinetic equations. This allows to study the limit of vanishing spin relaxation.

Integrating Eq. (S1) by thickness using boundary conditions (S7) we get the time-dependent Eilenberger equation

$$-\{\hat{\tau}_3 \partial_t \circlearrowleft \check{g}\} = [\hat{\boldsymbol{\sigma}} \mathbf{h} \hat{\tau}_3 + \Delta \hat{\tau}_1 + \check{\Gamma} + \check{\Sigma}_{so} \circlearrowleft \check{g}] \quad (\text{S42})$$

where $\hat{\sigma}_k, \hat{\tau}_k, k = 0, 1, 2, 3$ are Pauli matrices. The effective Zeeman field is $\mathbf{h} = (J_{sd}/d)\mathbf{m}$. In the presence of both the non-zero spin-splitting field \mathbf{h} and spin relaxation we can solve Eq. (S42) only numerically. Let us

write the iteration scheme for Eq. (S42) considering the time-dependent Zeeman field $\mathbf{h}(t)$ as a perturbation.

$$-\{\hat{\tau}_3 \partial_t \circ \check{g}\} = i[\sigma\tau_3 \circ \check{g}] + [h_0\sigma_z\tau_3 + \Delta\hat{\tau}_1 + \check{\Gamma} + \check{\Sigma}_s \circ \check{g}]. \quad (\text{S43})$$

Zeroth order solution is found in the form $\hat{g}_0(t_1, t_2) = \hat{g}_0(\varepsilon)e^{i\varepsilon(t_1-t_2)}$, with the Keldysh component $\hat{g}_0^K(\varepsilon) = g^{RA}n_0(\varepsilon)$. The spectral components satisfy the stationary equilibrium Eilenberger equation

$$[(h_0\sigma_z + \varepsilon \pm i\Gamma)\tau_3 + \Delta\hat{\tau}_1 + \check{\Sigma}_{\text{so}}, g_0^{R,A}] = 0 \quad (\text{S44})$$

The first-order perturbation solutions $g_h(12)e^{i\varepsilon_1 t_1 - i\varepsilon_2 t_2}$ and $g_h(21)e^{i\varepsilon_2 t_1 - i\varepsilon_1 t_2}$ where $\varepsilon_1 = \varepsilon_2 + \Omega$ are determined by

$$\begin{aligned} & [(i\varepsilon_1 + \Gamma_{\varepsilon_1})\tau_3 + \Lambda + \check{\Sigma}_0(1)]g_h(12) - \\ & g_h(12)[\tau_3(i\varepsilon_2 + \Gamma_{\varepsilon_2}) + \Lambda + \check{\Sigma}_0(2)] + \\ & \Sigma_h(12)g_0(2) - g_0(1)\Sigma_h(12) = \\ & i[\check{g}_0(1)\mathbf{h}_\Omega\sigma\tau_3 - \mathbf{h}_\Omega\sigma\tau_3\check{g}_0(2)] \end{aligned} \quad (\text{S45})$$

$$\begin{aligned} & [(i\varepsilon_2 + \Gamma_{\varepsilon_2})\tau_3 + \Lambda + \check{\Sigma}_0(2)]g_h(21) - \\ & g_h(21)[\tau_3(i\varepsilon_1 + \Gamma_{\varepsilon_1}) + \Lambda + \check{\Sigma}_0(1)] + \\ & \Sigma_h(21)g_0(1) - g_0(2)\Sigma_h(21) = \\ & i[\check{g}_0(2)\mathbf{h}_{-\Omega}\sigma\tau_3 - \mathbf{h}_{-\Omega}\sigma\tau_3\check{g}_0(1)]. \end{aligned} \quad (\text{S46})$$

Here we also denote $\Lambda = h_0\sigma_z\tau_3 + \Delta\hat{\tau}_1$.

The second order perturbation yields the stationary correction from $g_{hh}(\varepsilon)e^{i\varepsilon(t_1-t_2)}$

$$\begin{aligned} & [(i\varepsilon + \check{\Gamma})\tau_3 + \Lambda + \check{\Sigma}_0, g_{hh}] + [\Sigma_{hh}, g_0] = \\ & i[\check{g}_h(12)\mathbf{h}_{-\Omega}\sigma\tau_3 - \mathbf{h}_{-\Omega}\sigma\tau_3\check{g}_h(31)] + \\ & i[\check{g}_h(13)\mathbf{h}_\Omega\sigma\tau_3 - \mathbf{h}_\Omega\sigma\tau_3\check{g}_h(21)] - \\ & [\check{\Sigma}_h(12)g_h(21) - g_h(13)\check{\Sigma}_h(31) + \\ & \check{\Sigma}_h(13)g_h(31) - g_h(12)\check{\Sigma}_h(21)]. \end{aligned} \quad (\text{S47})$$

Here the spin-orbit terms are

$$\check{\Sigma}_h(12) = \sigma\hat{g}_h(12)\sigma/6\tau_{\text{so}} \quad (\text{S48})$$

$$\Sigma_0 = \sigma\check{g}_0\sigma/6\tau_{\text{so}}. \quad (\text{S49})$$

The linear spin response is diagonal in the circular basis. Provided that there are components $h_{l,\Omega}$, $h_{r,-\Omega}$ we can write $\boldsymbol{\mu}_s(\Omega) = \chi_l h_{l,\Omega}(\mathbf{x} + i\mathbf{y})/h_0$ and $\boldsymbol{\mu}_s(-\Omega) = \chi_r h_{r,-\Omega}(\mathbf{x} - i\mathbf{y})/h_0$. For left-hand field, $\mathbf{h}_\Omega = (1, i, 0)h_{l,\Omega}/2$, the first-order (imaginary-time) Green function solution reads

$$g_h(12) = ih_{l,\Omega}\sigma + \frac{\tau_3 - g_+(1)\tau_3 g_-(2)}{s_+(1) + s_-(2) + \frac{2}{3\tau_{\text{so}}}}. \quad (\text{S50})$$

Here $g_0(\varepsilon) = \frac{1+\sigma_s}{2}g_+(\varepsilon) + \frac{1-\sigma_s}{2}g_-(\varepsilon)$, and $g_\pm = (\omega_\pm\tau_3 + \Delta_\pm\tau_1)/s_\pm$, $\omega_\pm = -i\varepsilon \pm ih_0 + \frac{\omega_\mp}{3\tau_{\text{so}}s_\mp}$, $\Delta_\pm = \Delta + \frac{\Delta_\mp}{3\tau_{\text{so}}s_\mp}$, $s_\pm = \sqrt{\omega_\pm^2 + \Delta_\pm^2}$. The algebraic equations for ω_\pm , Δ_\pm

need to be solved numerically. The R , A components are obtained via $g_h^{R,A}(12) = g_h(1^{R,A}, 2^{R,A})$ where $\varepsilon^{R,A} = \varepsilon \pm i\Gamma$. The spin susceptibility is conveniently obtained via the analytic continuation,

$$\begin{aligned} \chi_l^K(1, 2) &= \chi_l(1^R, 2^R) \tanh \frac{\varepsilon_2}{2T} - \chi_l(1^A, 2^A) \tanh \frac{\varepsilon_1}{2T} \\ &+ \chi_l(1^R, 2^A) [\tanh \frac{\varepsilon_1}{2T} - \tanh \frac{\varepsilon_2}{2T}], \end{aligned} \quad (\text{S51})$$

where $\chi_l(12) = \frac{h_0}{8h_{l,\Omega}} \text{tr} \tau_3 \sigma_- g_h(12)$. The calculation for χ has been previously discussed in Refs. 9 and 10.

Now let us consider the equation for the rectified spin polarization $\mu_{sz} \propto \mathbf{z} \cdot (\mathbf{m}_\Omega \times \mathbf{m}_{-\Omega})$ which is given by the second-order non-linear spin response of the superconductor. We search for the correction to Keldysh function in the form

$$\hat{g}_{hh}^K = n_0(\varepsilon)(\hat{g}_{hh}^R - \hat{g}_{hh}^A) + \hat{g}_{hh}^a \quad (\text{S52})$$

where $\hat{g}_{hh}^{R,A}$ are the corrections to the spectral function and \hat{g}_{hh}^a is the anomalous part which contains the information about non-equilibrium quasiparticles. The anomalous and spectral parts can be calculated separately from Eq. (S47). We are interested in the anomalous part since it determines the non-equilibrium spin accumulation and thereby the non-local voltage in Eq. (1) of the main text

$$\boldsymbol{\mu}_s = - \int_{-\infty}^{\infty} d\varepsilon \text{Tr} [\hat{\tau}_3 \hat{\sigma} \hat{g}_{hh}^a(\varepsilon)]/8 \quad (\text{S53})$$

$$W = - \int_{-\infty}^{\infty} d\varepsilon \text{Tr} [\hat{\tau}_3 \hat{g}_{hh}^a(\varepsilon)]/4 \quad (\text{S54})$$

Using the scheme described above we calculate $\mu_{sz}(\Omega, T)$, $W(\Omega, T)$ and $V(\Omega, T)$ in the wide range of parameters. The series of calculation results for varying h_0 and τ_s are shown in Figs. 2, 3.

F. Numerical higher-order calculation in thin-film limit

Numerical calculations can be also performed beyond low-order perturbation theory. The Usadel equation in the thin-film limit can be written as

$$[\Omega(g), g] = 0, g^2 = 1, \quad (\text{S55})$$

where $\Omega = \partial_t \delta(t-t') + X$ where X is the operator on the r.h.s. of Eq. (S42). This is formally solved by

$$g = \text{sgn}(\Omega(g)), \quad (\text{S56})$$

where sgn is the sign function, defined as the analytic continuation $\text{sgn} z = \text{sgn} \text{Re} z$ of sgn from real axis to complex plane, so it extends to an operator-valued function. For finite matrices, it can be defined via the eigenvalue decomposition $X = V \text{diag}(\lambda_1, \dots, \lambda_n) V^{-1}$ as $\text{sgn}(X) = V \text{diag}(\text{sgn} \text{Re} \lambda_1, \dots, \text{sgn} \text{Re} \lambda_n) V^{-1}$.

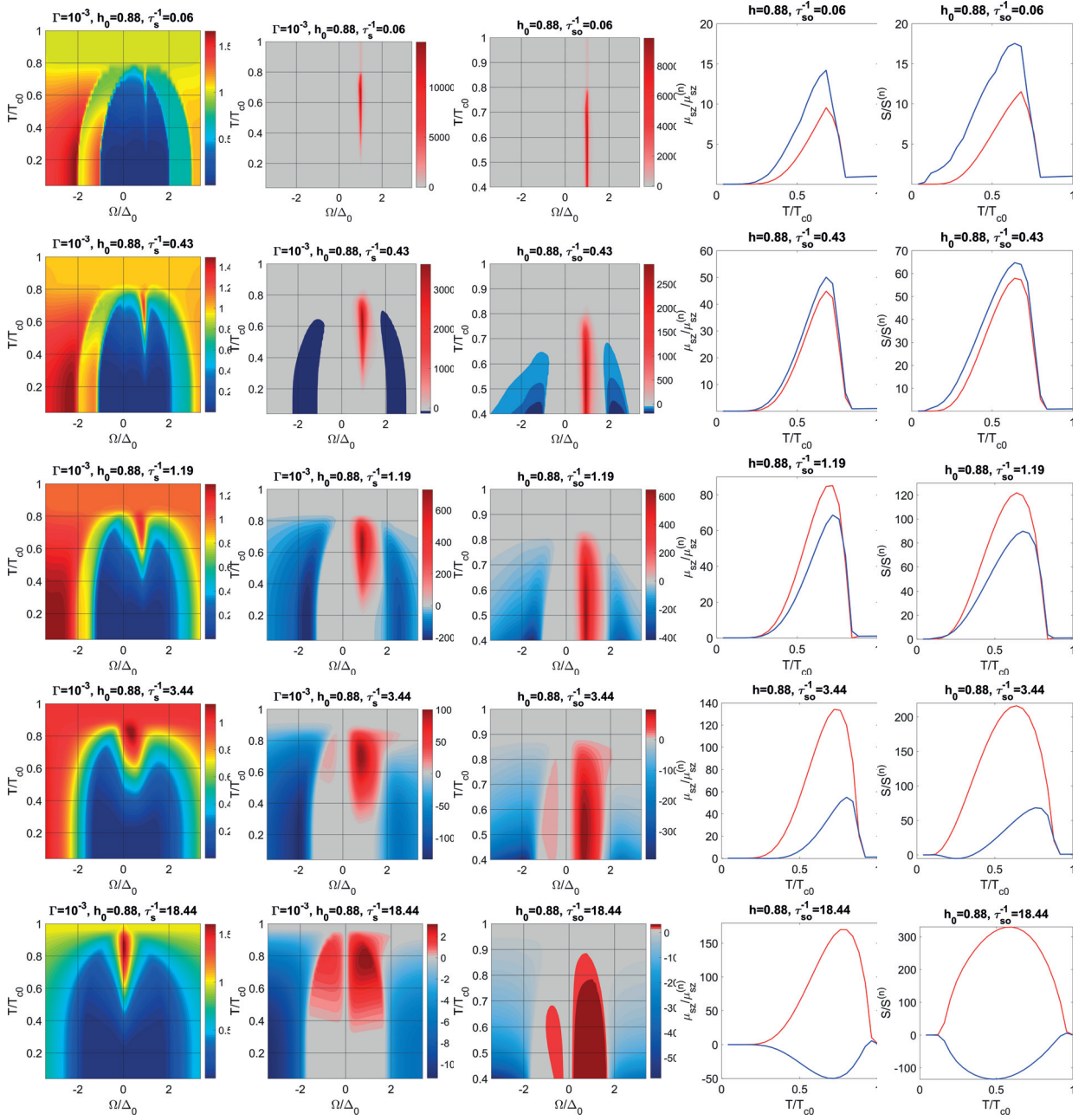


FIG. 2. (1st column): Pumped energy of the electronic system $W(T, \Omega)/W(T_c, \Omega)$. (2nd column): Pumped spin accumulation $(T_{c0}/h\Omega^2)\mu_z(T, \Omega)$. (3rd column): Non-local voltage generated by the pumped spin accumulation $(eT_{c0}/h\Omega^2)V(\Omega, T)$. (4th column): Magnon-induced spin accumulation. (5th column): nonlocal Seebeck coefficient in the FI/SC/FM bilayer. Parameters are $h_0/T_{c0} = 0.88$, energy relaxation rate $\Gamma/T_{c0} = 10^{-3}$. We consider circular polarization $h_{l,\Omega}, h_{r,-\Omega} \neq 0$. Scan over Ω, T , different values of spin relaxation.

To deal with the time convolutions, for periodic forces $\mathbf{h}(t) = \mathbf{h}(t + 2\pi\Omega^{-1})$, we can make a Green function

Floquet Ansatz,

$$g(t, t') = \int_{-\infty}^{\infty} \frac{d\omega d\omega'}{4\pi^2} e^{-i\omega t + i\omega' t'} g(\omega, \omega'), \quad (\text{S57})$$

$$g(\omega, \omega') = \sum_k g_{0,k}(\omega) 2\pi\delta(\omega - \omega' + k\Omega), \quad (\text{S58})$$

$$g_{m,n}(\omega) = g_{0,n-m}(\omega + m\Omega). \quad (\text{S59})$$

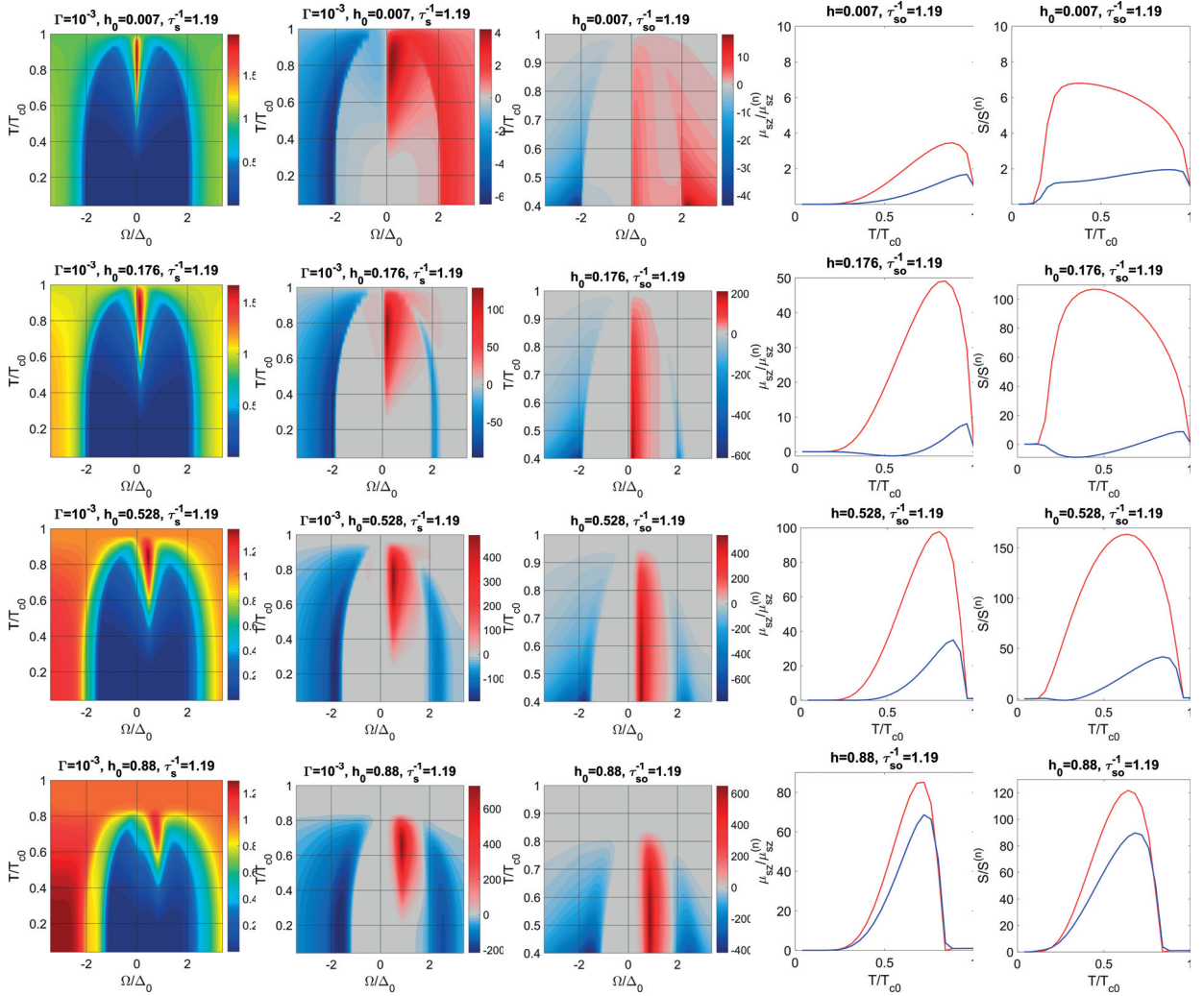


FIG. 3. (1st column): Pumped energy of electronic system $W(T, \Omega)/W(T_c, \Omega)$. (2nd column): Pumped spin accumulation $(T_{c0}/h_\Omega^2)\mu_z(T, \Omega)$. (3rd column): Non-local voltage generated by pumped spin accumulation $(eT_{c0}/h_\Omega^2)V(\Omega, T)$. (4th column): Magnon-induced spin accumulation. (5th column): nonlocal Seebeck coefficient in FI/SC/FM bilayer. Parameters are $(\tau_{so}T_{c0})^{-1} = 1.19$, energy relaxation rate $\Gamma/T_{c0} = 10^{-3}$. We consider circular polarization $h_{l,\Omega}, h_{r,-\Omega} \neq 0$. Scan over Ω, T , different values of Zeeman splitting.

One can now check that $(A \circ B)_{m,n}(\omega) = \sum_k A_{m,k}(\omega)B_{k,n}(\omega)$. Moreover, $(\epsilon)_{m,n}(E) = (E + n\omega)\delta_{m,n}$, and $(\mathbf{h})_{m,n}(E) = \int dt e^{-i(n-m)\Omega t} \mathbf{h}(t)$. We take

$$\mathbf{h} = h_0 \hat{z} + \text{Re}[h_{ac,x} e^{i\Omega t}] \hat{x} + \text{Re}[h_{ac,y} e^{i\Omega t}] \hat{y}, \quad (\text{S60})$$

$$\begin{aligned} \mathbf{h}_{m,n}(E) &= h_0 \hat{z} \delta_{m,n} + \hat{x} \frac{1}{2} (h_{ac,x} \delta_{m,n+1} + h_{ac,x}^* \delta_{m,n-1}) \\ &+ \hat{y} \frac{1}{2} (h_{ac,y} \delta_{m,n+1} + h_{ac,y}^* \delta_{m,n-1}). \end{aligned} \quad (\text{S61})$$

Hence, $\Omega \mapsto (\Omega)_{m,n}(E)$, and Eq. (S56) becomes a matrix equation. The matrix size is infinite, but when the time-

dependent perturbations are not too large, when solving for $g_{0,0}(E)$ we can limit the equations to $g_{m,n}(E)$, $|m|, |n| \leq N$ for some cutoff N . Second-order perturbation theory corresponds to $N = 1$. The iteration (S56) is reasonably convergent, and can be solved numerically in a straightforward way also for large N . However, if τ_{so} is small, Newton method is preferable.

The results are compared with the perturbation calculation of the previous section in Fig. 4. For the small excitation amplitude chosen here, results coincide.

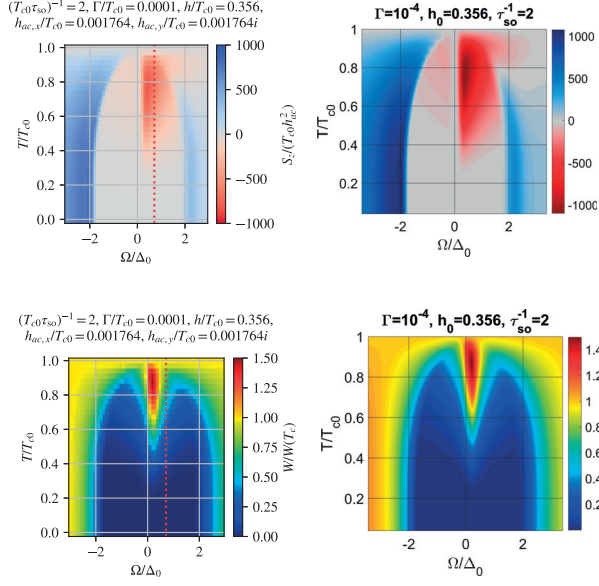


FIG. 4. Comparison of energy and spin accumulation calculated from the numerically exact solution (left panels) and second-order perturbation theory (right panels).

G. Spin pumping by the stochastic field of magnons

Here we show how to derive the electron-magnon collision integral in the case of a spin-split superconductor. The approach is relatively standard [11, 12], but the details related with superconductivity are new. We present it here for the convenience of the reader.

We can quantize time-dependent components of magnetization by introducing the bosonic creation and annihilation operators

$$H_{e-m} = \frac{1}{\sqrt{S_0}} \sum_{p, \bar{p}} \Theta_{p, \bar{p}} \hat{a}_p^\dagger \hat{\mathbf{m}} \hat{a}_{\bar{p}} \quad (\text{S62})$$

$$\hat{\mathbf{m}} = (\hat{b} \hat{\sigma}_+ + \hat{b}^\dagger \hat{\sigma}_-) \hat{\tau}_3, \quad (\text{S63})$$

where S_0 is the value of the localized spin, the matrix $\Theta_{p, \bar{p}}$ describes spin-dependent scattering at the surface and \hat{b}, \hat{b}^\dagger are the magnon field operators at the interface. They are expressed through the operators of the magnon modes in the usual way $\hat{b}(\mathbf{r}) = \sum_k \frac{e^{i\mathbf{k}\mathbf{r}}}{\sqrt{N_{FI}}} \hat{b}_k$, where N_{FI} is the number of sites in the FI.

To calculate the matrix current driven by the electron-magnon interaction (S62) we calculate the corresponding electron-magnon collision integral. We work in the interaction representation with respect to H_{em} , so that the Heisenberg equations are

$$\partial_t \hat{a}_p = i[\hat{H}_{e-m}, \hat{a}_p] = -i\Theta_{p, \bar{p}} \hat{\mathbf{m}} \hat{a}_{\bar{p}} \quad (\text{S64})$$

$$\partial_t \hat{a}_p^\dagger = i[\hat{H}_{e-m}, \hat{a}_p^\dagger] = i\Theta_{p, \bar{p}} \hat{a}_{\bar{p}}^\dagger \hat{\mathbf{m}} \quad (\text{S65})$$

The contour-ordered GF is defined as

$$\hat{G}(t_1, t_2, p, p') = \langle \mathcal{T}_c S a_p(t_1) a_{p'}^\dagger(t_2) \rangle \quad (\text{S66})$$

$$S = \mathcal{T}_c \exp(-i \int_c H_{e-m} dt) \quad (\text{S67})$$

The e-m collision integral $\hat{J}(t_1, t_2)$ is given by

$$\hat{J}(t_1, t_2) = \partial_{t_1} \hat{G}(t_1, t_2) + \partial_{t_2} \hat{G}(t_1, t_2) \quad (\text{S68})$$

Using equations of motion (S64, S65) and expanding the S-matrix $S \approx 1 - i \int_c \hat{H}_{e-m}(t) dt$ we get

$$- \partial_{t_1} \hat{G}(t_1, t_2) = \quad (\text{S69})$$

$$- \langle \mathcal{T}_c \int_c dt \hat{H}_{e-m}(t) \hat{\mathbf{m}}(t_1) \hat{\Theta}_{\bar{p}\bar{p}'} \hat{a}_{\bar{p}'}(t_1) \hat{a}_p^\dagger(t_2) \rangle =$$

$$\langle \mathcal{T}_c \int_c dt \hat{a}_{p_1}^\dagger(t) \hat{\mathbf{m}}(t) \hat{\Theta}_{\bar{p}_1} \hat{\mathbf{m}}(t_1) \hat{\Theta}_{\bar{p}'} \hat{a}_{\bar{p}'}(t_1) a_p^\dagger(t_2) \rangle =$$

$$S_0^{-1} \langle \mathcal{T}_c \int_c dt \hat{a}_{p_1}^\dagger(t) \hat{\sigma}_+ \hat{\Theta}_{\bar{p}_1} \hat{\sigma}_-(t) \hat{\Theta}_{\bar{p}'} \hat{a}_{\bar{p}'}(t_1) a_p^\dagger(t_2) \hat{b}(t) \hat{b}^\dagger(t_1) \rangle +$$

$$S_0^{-1} \langle \mathcal{T}_c \int_c dt \hat{a}_{p_1}^\dagger(t) \hat{\sigma}_- \hat{\Theta}_{\bar{p}_1} \hat{\sigma}_+(t) \hat{\Theta}_{\bar{p}'} \hat{a}_{\bar{p}'}(t_1) a_p^\dagger(t_2) \hat{b}^\dagger(t) \hat{b}(t_1) \rangle =$$

$$\int_c dt \Sigma(t_1, t, \bar{p}', \bar{p}_1) G(t, t_2, \bar{p}_1, p).$$

Here the self-energy is

$$S_0 \Sigma(t_1, t) = \quad (\text{S70})$$

$$\hat{\sigma}_- \hat{\Theta} G(t_1, t) \hat{\Theta} \hat{\sigma}_+ D^{(l)}(t, t_1) + \hat{\sigma}_+ \hat{\Theta} G(t_1, t) \hat{\Theta} \hat{\sigma}_- D^{(r)}(t, t_1)$$

where the left- and right-hand polarized magnon propagators are

$$D^{(l)}(t, t_1) = \langle \mathcal{T}_c \hat{b}(t) \hat{b}^\dagger(t_1) \rangle \quad (\text{S71})$$

$$D^{(r)}(t, t_1) = D^{(l)}(t_1, t) \quad (\text{S72})$$

Differentiating with respect to the second time variable gives

$$\partial_{t_2} \hat{G}(t_1, t_2) = \langle \mathcal{T}_c \int_c dt \hat{H}_{e-m}(t) \hat{a}_{\bar{p}}(t_1) a_p^\dagger(t_2) \hat{\Theta} \hat{\mathbf{m}}(t_2) \rangle =$$

$$\langle \mathcal{T}_c \int_c dt \hat{a}_{p_1}^\dagger(t) \hat{\mathbf{m}}(t) \hat{\Theta}_{\bar{p}_1} \hat{a}_{\bar{p}_1}(t) \hat{a}_{\bar{p}}(t_1) a_p^\dagger(t_2) \hat{\Theta} \hat{\mathbf{m}}(t_2) \rangle =$$

$$S_0^{-1} \langle \mathcal{T}_c \int_c dt \hat{a}_{\bar{p}}(t_1) a_{p_1}^\dagger(t) \hat{\sigma}_+ \hat{\Theta}_{\bar{p}_1} \hat{a}_{\bar{p}}(t) \hat{a}_{\bar{p}}(t_2) \hat{\sigma}_- \hat{\Theta} \hat{b}(t) \hat{b}^\dagger(t_2) \rangle +$$

$$S_0^{-1} \langle \mathcal{T}_c \int_c dt \hat{a}_{\bar{p}}(t_1) a_{p_1}^\dagger(t) \hat{\sigma}_- \hat{\Theta}_{\bar{p}_1} \hat{a}_{\bar{p}}(t) \hat{a}_{\bar{p}}(t_2) \hat{\Theta} \hat{\sigma}_+ \hat{b}(t) \hat{b}^\dagger(t_2) \rangle =$$

$$\int_c dt G(t_1, t, \bar{p}, p_1) \Sigma(t, t_2, \bar{p}_1, p).$$

Thus the matrix double-time current which can be considered as the electron-magnon collision integral (CI) is given by

$$\hat{J}(t_1, t_2) = \hat{G} \circ \Sigma - \Sigma \circ \hat{G}. \quad (\text{S73})$$

The self-energy can be represented as the sum of the parts associated with right- and left-hand polarized magnons $\Sigma = \Sigma^{(l)} + \Sigma^{(r)}$.

Switching to the Keldysh contour, we express the convolution product as matrix components coupling different segments of the contour, i.e.,

$$S_0 \Sigma_{11}^{(r)} = \hat{\sigma}_+ \hat{\Theta} [G_{11} D_{11}^{(r)} + G_{12} D_{21}^{(r)}] \hat{\Theta} \hat{\sigma}_- \quad (S74)$$

$$S_0 \Sigma_{22}^{(r)} = \hat{\sigma}_+ \hat{\Theta} [G_{22} D_{22}^{(r)} + G_{21} D_{12}^{(r)}] \hat{\Theta} \hat{\sigma}_- \quad (S75)$$

$$S_0 \Sigma_{12}^{(r)} = \hat{\sigma}_+ \hat{\Theta} [G_{12} D_{22}^{(r)} + G_{11} D_{12}^{(r)}] \hat{\Theta} \hat{\sigma}_- \quad (S76)$$

$$S_0 \Sigma_{21}^{(r)} = \hat{\sigma}_+ \hat{\Theta} [G_{21} D_{11}^{(r)} + G_{22} D_{21}^{(r)}] \hat{\Theta} \hat{\sigma}_- \quad (S77)$$

and

$$S_0 \Sigma_{11}^{(l)} = \hat{\sigma}_- \hat{\Theta} [G_{11} D_{11}^{(l)} + G_{12} D_{21}^{(l)}] \hat{\Theta} \hat{\sigma}_+ \quad (S78)$$

$$S_0 \Sigma_{22}^{(l)} = \hat{\sigma}_- \hat{\Theta} [G_{22} D_{22}^{(l)} + G_{21} D_{12}^{(l)}] \hat{\Theta} \hat{\sigma}_+ \quad (S79)$$

$$S_0 \Sigma_{12}^{(l)} = \hat{\sigma}_- \hat{\Theta} [G_{12} D_{22}^{(l)} + G_{11} D_{12}^{(l)}] \hat{\Theta} \hat{\sigma}_+ \quad (S80)$$

$$S_0 \Sigma_{21}^{(l)} = \hat{\sigma}_- \hat{\Theta} [G_{21} D_{11}^{(l)} + G_{22} D_{21}^{(l)}] \hat{\Theta} \hat{\sigma}_+ \quad (S81)$$

Next we use the RAK representation [12] $G \rightarrow \hat{H} \hat{G} \hat{H}$ which yields

$$S_0 \Sigma_r^R = \hat{\sigma}_+ \hat{\Theta} [D_r^R G^K + D_r^K G^R] \hat{\Theta} \hat{\sigma}_- / 2 \quad (S82)$$

$$S_0 \Sigma_r^A = \hat{\sigma}_+ \hat{\Theta} [D_r^A G^K + D_r^K G^A] \hat{\Theta} \hat{\sigma}_- / 2 \quad (S83)$$

$$S_0 \Sigma_r^K = \hat{\sigma}_+ \hat{\Theta} [D_r^K G^K + (D_r^R - D_r^A)(G^R - G^A)] \hat{\Theta} \hat{\sigma}_- / 2 \quad (S84)$$

$$S_0 \Sigma_l^R = \hat{\sigma}_- \hat{\Theta} [D_l^R G^K + D_l^K G^R] \hat{\Theta} \hat{\sigma}_+ / 2 \quad (S85)$$

$$S_0 \Sigma_l^A = \hat{\sigma}_- \hat{\Theta} [D_l^A G^K + D_l^K G^A] \hat{\Theta} \hat{\sigma}_+ / 2 \quad (S86)$$

$$S_0 \Sigma_l^K = \hat{\sigma}_- \hat{\Theta} [D_l^K G^K + (D_l^R - D_l^A)(G^R - G^A)] \hat{\Theta} \hat{\sigma}_+ / 2 \quad (S87)$$

The left- and right- handed magnon propagators are $D_{l,r}^{R/A/K} = \sum_k D_{l,r}^{R/A/K}(\Omega, \omega_k)$ where

$$D_l^{R/A/K}(\Omega, \omega_k) = D_r^{R/A/K}(\Omega, -\omega_k) \quad (S88)$$

$$D_{r/l}^K = (D_{r/l}^R - D_{r/l}^A) n_B(\Omega/T_m), \quad (S89)$$

where

$$D_r^R = (D_r^A)^* = \frac{1}{(\Omega + i\alpha) - \omega_k}. \quad (S90)$$

The dc part of the collision integral (S73) is given by the sum of two terms corresponding to the left- and right-handed magnons $\hat{J}^K = \hat{J}_l + \hat{J}_r$ where e.g.

$$S_0 \hat{J}_r = \langle [\hat{\Theta} \hat{\sigma}_+ \hat{G} \hat{\Theta} \hat{\sigma}_-, \hat{G}]^K(12) \rangle D_r^K + \quad (S91)$$

$$\hat{\sigma}_+ \hat{\Theta} G^K(1) \hat{\sigma}_- \hat{\Theta} G^K(2) D_r^R +$$

$$\hat{\sigma}_+ \hat{\Theta} G^{RA}(1) \hat{\sigma}_- \hat{\Theta} G^A(2) D_r^{RA} -$$

$$G^K(1) \hat{\sigma}_+ \hat{\Theta} G^K(2) \hat{\sigma}_- \hat{\Theta} D_r^R -$$

$$G^R(1) \hat{\sigma}_+ \hat{\Theta} G^{RA}(2) \hat{\sigma}_- \hat{\Theta} D_r^{RA}$$

where the angular brackets $\langle \dots \rangle$ denote the average by momentum and disorder.

Since only the first term in Eq. (S91) depends on the distribution of magnons and the collision integral is zero in equilibrium we can write it as $\hat{J}(\varepsilon, \Omega) = \hat{J}_r + \hat{J}_l$ where

$$S_0 \hat{J}_r(\varepsilon, \Omega) = \hat{\chi}_{rl}(\varepsilon, \Omega) \delta D_r^K(\Omega) \quad (S92)$$

$$S_0 \hat{J}_l(\varepsilon, \Omega) = \hat{\chi}_{lr}(\varepsilon, \Omega) \delta D_l^K(\Omega). \quad (S93)$$

Here we denote the response functions

$$\hat{\chi}_{rl}(\varepsilon, \Omega) = \langle [\hat{\Theta} \hat{\sigma}_+ \hat{G} \hat{\Theta} \hat{\sigma}_-, \hat{G}]^K(12) \rangle \quad (S94)$$

$$\hat{\chi}_{lr}(\varepsilon, \Omega) = \langle [\hat{\Theta} \hat{\sigma}_- \hat{G} \hat{\Theta} \hat{\sigma}_+, \hat{G}]^K(12) \rangle, \quad (S95)$$

where $G(1) = G(\varepsilon)$, $G(2) = G(\varepsilon + \Omega)$ and $\delta D_{r/l}^K$ are the non-equilibrium parts of magnon Keldysh functions. In the stationary case they can be parametrized by the magnon distribution function $\delta D_{r/l}^K(\Omega) = D_{r/l}^{RA}(\Omega) \delta f_m(\Omega)$. If the non-equilibrium is determined by the temperature difference between superconductor and magnon subsystem, the distribution function reads $\delta f_m(\Omega) = \coth(\Omega/2T_m) - \coth(\Omega/2T)$. For small damping $\alpha \ll \omega_k$ we can write $D_r^{RA} = 2i\delta(\omega_k - \Omega)$. We can sum by the magnon states to replace $D_{r/l}^{RA}$ with the density of states for magnons as

$$\frac{1}{N_{FI}} \sum_k D_r^{RA}(\omega_k) \approx \quad (S96)$$

$$i v_s D_m(\Omega) (1 + \text{Step}(\Omega)) / 2$$

where m_M is the magnon mass and $\text{Step}(x)$ is a step function, $v_s = V_{FI}/N_{FI}$ is the volume per spin, $D_m(\Omega) = m_M^{3/2} |\Omega|^{1/2}$ is the magnon density of states. To avoid extra parameters in the model, we have set the magnon gap to vanish, but it can be easily added if needed.

Using the symmetry relation $D_l^K(\Omega) = D_r^K(-\Omega)$ we can write the total current

$$\hat{J}(\varepsilon) = v_s \int_{-\infty}^{\infty} d\Omega [\hat{\chi}_{rl}(\varepsilon, \Omega) + \hat{\chi}_{lr}(\varepsilon, -\Omega)] \delta D_r^K(\Omega), \quad (S97)$$

where $v_s = V_{FI}/S_0 N_{FI}$ is the volume per spin in FI.

The correlators in Eqs. (S92–S93) can be determined by calculating the matrix currents generated by the classical time-dependent exchange field

$$\hat{J}_r^{cl}(\Omega, \varepsilon) = [\hat{\chi}_{rl}(\Omega, \varepsilon) + \hat{\chi}_{lr}(-\Omega, \varepsilon)] m_{r,\Omega} m_{l,-\Omega} \quad (S98)$$

$$\hat{J}_l^{cl}(\Omega, \varepsilon) = [\hat{\chi}_{lr}(\Omega, \varepsilon) + \hat{\chi}_{rl}(-\Omega, \varepsilon)] m_{l,\Omega} m_{r,-\Omega} \quad (S99)$$

where $m_{r/l,\Omega} = (m_{x,\Omega} \pm i m_{y,\Omega})$ are the right-hand and left-hand polarized components. The expressions for $\hat{J}_{r/l}^{cl}$ can be found using the quasiclassical equations. Then, to get the magnon-driven current we can replace the classical field amplitudes by the magnon propagators $m_{r,\Omega} m_{l,-\Omega} \rightarrow v_s \delta D_r^K / \Omega$ and $m_{l,\Omega} m_{r,-\Omega} \rightarrow v_s \delta D_l^K / \Omega$.

Using this general matrix current we can calculate spin and energy currents as $j_e = \nu \int_{-\infty}^{\infty} \mathcal{J}_e d\varepsilon$ and $j_{sz} = \nu \int_{-\infty}^{\infty} \mathcal{J}_{sz} d\varepsilon$ where the spectral densities are

$$\mathcal{J}_s(\varepsilon) = \frac{1}{8} \text{Tr}[\boldsymbol{\sigma} \hat{\tau}_3 \hat{J}(\varepsilon)] \quad (\text{S100})$$

$$\mathcal{J}_e(\varepsilon) = \frac{\varepsilon}{4} \text{Tr}[\hat{\tau}_3 \hat{J}(\varepsilon)] \quad (\text{S101})$$

As shown in the next section, these currents can be in general expressed through the linear spin susceptibility

$$j_{sz} = \nu J_{sd} \int_{-\infty}^{\infty} \text{Im}(\chi_l) \delta D_l^K d\Omega \quad (\text{S102})$$

$$j_e = \nu J_{sd} \int_{-\infty}^{\infty} \Omega \text{Im}(\chi_l) \delta D_l^K d\Omega \quad (\text{S103})$$

In the normal state and low-frequency regime we have seen in Sec. IC that $\nu J_{sd} \text{Im}\chi_l = \Omega \text{Re}A_{\text{eff}}^{\uparrow\downarrow}$. Then taking into account (S96)

$$j_{sz} = \text{Re}A_{\text{eff}}^{\uparrow\downarrow} \int_0^{\infty} \text{Im}(\chi_l) D_m(\Omega) \Omega [n_B(T_m) - n_B(T)] d\Omega \quad (\text{S104})$$

$$j_e = \text{Re}A_{\text{eff}}^{\uparrow\downarrow} \int_0^{\infty} \text{Im}(\chi_l) D_m(\Omega) \Omega^2 [n_B(T_m) - n_B(T)] d\Omega \quad (\text{S105})$$

coincides with that derived in [13, 14]. In the normal state the expression coincides with that derived in [13, 14].

H. Spin-energy pumping: general relations

For coherent magnetization precession at frequency Ω , boundary conditions for dc spin and energy currents are

$$\mathcal{J}_s(\varepsilon) = \frac{iJ_{sd}}{8} \text{Tr}[\boldsymbol{\sigma} [\boldsymbol{\sigma} \hat{\tau}_3 \hat{\rho}; \hat{g}_h]^K](\varepsilon) \quad (\text{S106})$$

$$\mathcal{J}_e(\varepsilon) = \frac{iJ_{sd}}{4} \varepsilon \text{Tr}[\boldsymbol{\sigma} \hat{\tau}_3 \hat{\rho}; \hat{g}_h]^K(\varepsilon) \quad (\text{S107})$$

The currents can be written as

$$\mathcal{J}_{sz}(\varepsilon) = (J_{sd}/2) m_{l,\Omega} m_{r,-\Omega} \times \quad (\text{S108})$$

$$\{(\chi_r^K(\varepsilon - \Omega, \varepsilon) - \chi_l^K(\varepsilon, \varepsilon - \Omega) - [\chi_l^K(\varepsilon + \Omega, \varepsilon) - \chi_r^K(\varepsilon, \varepsilon + \Omega)])\},$$

$$\mathcal{J}_e(\varepsilon) = (\varepsilon J_{sd}) m_{l,\Omega} m_{r,-\Omega} \times \quad (\text{S109})$$

$$\{(\chi_r^K(\varepsilon - \Omega, \varepsilon) - \chi_l^K(\varepsilon, \varepsilon - \Omega) + [\chi_l^K(\varepsilon + \Omega, \varepsilon) - \chi_r^K(\varepsilon, \varepsilon + \Omega)])\},$$

where we introduce the linear response functions for the Keldysh GF

$$\frac{i}{4} \text{Tr}[\hat{\sigma}_- \hat{\tau}_3 g^K(\varepsilon - \Omega, \varepsilon)] = m_{r,-\Omega} \chi_r^K(\varepsilon - \Omega, \varepsilon) \quad (\text{S110})$$

$$\frac{i}{4} \text{Tr}[\hat{\sigma}_+ \hat{\tau}_3 g^K(\varepsilon + \Omega, \varepsilon)] = m_{l,\Omega} \chi_l^K(\varepsilon + \Omega, \varepsilon), \quad (\text{S111})$$

and where $\hat{\sigma}_{\pm} = (\hat{\sigma}_x \pm i\hat{\sigma}_y)/2$.

The total energy and spin currents are defined as $j_e = \int \mathcal{J}_e d\varepsilon$ and $j_{sz} = \int \mathcal{J}_{sz} d\varepsilon$, respectively. They can be written as

$$j_{sz} = \nu J_{sd} [\chi_r(-\Omega) - \chi_l(\Omega)] m_{l,\Omega} m_{r,-\Omega}, \quad (\text{S112})$$

$$j_e = \nu J_{sd} \Omega [\chi_r(-\Omega) - \chi_l(\Omega)] m_{l,\Omega} m_{r,-\Omega}, \quad (\text{S113})$$

where we introduce

$$\chi_l(\Omega) = \int_{-\infty}^{\infty} d\varepsilon \chi_l^K(\varepsilon, \varepsilon - \Omega), \quad (\text{S114})$$

$$\chi_r(\Omega) = \int_{-\infty}^{\infty} d\varepsilon \chi_r^K(\varepsilon, \varepsilon - \Omega). \quad (\text{S115})$$

The total spin and energy currents satisfy the relation

$$j_e = \Omega j_{sz} \quad (\text{S116})$$

Using the relation $\chi_r(-\Omega) = \chi_l^*(\Omega)$ we obtain for the currents

$$j_{sz} = 2J_{sd} \text{Im}\chi_l(\Omega) m_{l,\Omega} m_{r,-\Omega}, \quad (\text{S117})$$

$$j_e = 2J_{sd} \Omega \text{Im}\chi_l(\Omega) m_{l,\Omega} m_{r,-\Omega}. \quad (\text{S118})$$

Let us establish the connection between spin current and the Gilbert damping coefficient. From the boundary condition (S12), the linearized spin current can be written as

$$j_{sl}(\Omega) = 2iJ_{sd} [\chi_l(\Omega) - \chi(0) + \Omega] m_{l,\Omega}, \quad (\text{S119})$$

where $\chi(0)$ is the *nonlinear* static spin susceptibility. Spin current can also be parametrized in terms of the damping-like and field-like components as

$$\mathbf{j}(t) = -\alpha(\mathbf{m} \times \partial_t \mathbf{m}) - (\delta\Omega/\Omega) \partial_t \mathbf{m}, \quad (\text{S120})$$

where α is the Gilbert damping coefficient and $\delta\Omega$ is the FMR frequency shift. Comparing the two expressions for the current, the coefficients in (S120) can be expressed as

$$\alpha = \frac{\text{Re}(j_{sl})}{\Omega m_{l,\Omega}} = 2J_{sd} \frac{\text{Im}(\chi_l)}{\Omega}, \quad (\text{S121})$$

$$\delta\Omega = \frac{\text{Im}(j_{sl})}{m_{l,\Omega}} = 2J_{sd} \{\text{Re}[\chi_l(\Omega) - \chi(0)] + \Omega\}. \quad (\text{S122})$$

The last term in the frequency shift drops out when comparing difference in the frequency shift between the superconducting state and the normal state. We find that the energy current can be in general written as

$$j_e = \Omega^2 \alpha(\Omega) m_{l,\Omega} m_{r,-\Omega}. \quad (\text{S123})$$

As shown in Sec. IG the magnon-driven currents are obtained by replacing the classical field amplitudes by magnon propagators $m_{r,\Omega} m_{l,-\Omega} \rightarrow v_s \delta D_r^K$ and $m_{l,\Omega} m_{r,-\Omega} \rightarrow v_s \delta D_l^K$

$$j_{sz} = 2\nu J_{sd} \int_{-\infty}^{\infty} \text{Im}(\chi_l) \delta D_l^K d\Omega \quad (\text{S124})$$

$$j_e = 2\nu J_{sd} \int_{-\infty}^{\infty} \Omega \text{Im}(\chi_l) \delta D_l^K d\Omega \quad (\text{S125})$$

For thermal magnons with small temperature bias we can write $j_{sz/e} = G_{ms/me} \delta T$, with thermal spin and heat conductances defined as

$$G_{ms} = 2\mathcal{V}_S \nu h_0 v_s m_M^{3/2} \int_0^\infty \Omega^{1/2} \text{Im}(\chi_l) \partial_T n_B d\Omega \quad (\text{S126})$$

$$G_{me} = 2\mathcal{V}_S \nu h_0 v_s m_M^{3/2} \int_0^\infty \Omega^{3/2} \text{Im}(\chi_l) \partial_T n_B d\Omega, \quad (\text{S127})$$

where ν is the density of states and \mathcal{V}_S the volume.

I. Superconductor as an ultrasensitive magnon detector

The giant magnon-induced voltage signal in the superconductor can be used to realize a bolometric or calorimetric magnon detector and an optimized device could reach single-magnon sensitivity down to tens of GHz of magnon frequencies. Assuming unit quantum efficiency, i.e., that the main damping mechanism of magnetization dynamics in the junction is provided by the coupling to the quasiparticles in the superconductor, we can then proceed analogously to the description of the thermoelectric read-out of the dissipated spin signal as in the case of thermoelectric detection of electromagnetic radiation, presented in Refs. 15 and 16. In particular, the

noise equivalent power NEP can be made of the order of the thermal fluctuation noise due to the heat contacts to the phonons and magnons. The optimum regime is one where the heat conductances G_{th} to both are of the same order of magnitude, in which case the thermal fluctuation noise is given by [15]

$$NEP_{\text{TFN}}^2 = k_B T^2 G_{\text{th}} (1 + \sqrt{1 + ZT_i})^2 / ZT_i, \quad (\text{S128})$$

where ZT_i is the intrinsic thermoelectric figure of merit of the junction. For low temperatures and not too large spin polarization P of the superconductor-ferromagnet contact, it is $ZT_i = P^2/(1 - P^2)$ [17]. On the other hand, the energy resolution in a calorimetric detection is given by [16]

$$\Delta E = NEP \sqrt{\tau_{\text{eff}}}, \quad (\text{S129})$$

where $\tau_{\text{eff}} \approx \tau_{\text{th}}$, the thermal relaxation time in the superconductor. For an Al detector at $k_B T \sim 0.2\Delta$, with a superconductor volume of 10^{-19} m^{-3} , we would then obtain $NEP \sim 10^{-19} \text{ W}/\sqrt{\text{Hz}}$ and energy resolution enough for single-magnon detection accuracy for magnons with frequency above 200 GHz. On the other hand, with 100 times smaller detector sizes, still within reach of regular sample preparation techniques, the figures of merit could be 10 times smaller, and hence a single-magnon regime could be reached with magnon frequencies above 20 GHz.

-
- [1] T. T. Heikkilä, M. Silaev, P. Virtanen, and F. S. Bergeret, *Prog. Surf. Sci.* **94**, 100540 (2019).
- [2] R. C. Dynes, J. P. Garno, G. B. Hertel, and T. P. Orlando, *Phys. Rev. Lett.* **53**, 2437 (1984).
- [3] A. Abrikosov and L. Gor'kov, *Sov. Phys. JETP* **15**, 752 (1962).
- [4] T. Tokuyasu, J. A. Sauls, and D. Rainer, *Phys. Rev. B* **38**, 8823 (1988).
- [5] Y. Tserkovnyak, A. Brataas, G. E. W. Bauer, and B. I. Halperin, *Rev. Mod. Phys.* **77**, 1375 (2005).
- [6] Y. Ohnuma, H. Adachi, E. Saitoh, and S. Maekawa, *Phys. Rev. B* **89**, 174417 (2014).
- [7] A. Brataas, Y. Tserkovnyak, G. E. W. Bauer, and B. I. Halperin, *Phys. Rev. B* **66**, 060404(R) (2002).
- [8] M. Silaev, P. Virtanen, F. S. Bergeret, and T. T. Heikkilä, *Phys. Rev. Lett.* **114**, 167002 (2015).
- [9] K. Maki, *Phys. Rev. B* **8**, 191 (1973).
- [10] M. A. Silaev, *Phys. Rev. B* **102**, 144521 (2020).
- [11] H. Adachi, K.-i. Uchida, E. Saitoh, and S. Maekawa, *Rep. Prog. Phys.* **76**, 036501 (2013).
- [12] A. Kamenev, *Field theory of non-equilibrium systems* (Cambridge University Press, 2011).
- [13] S. A. Bender and Y. Tserkovnyak, *Phys. Rev. B* **91**, 140402(R) (2015).
- [14] L. J. Cornelissen, K. J. H. Peters, G. E. W. Bauer, R. A. Duine, and B. J. van Wees, *Phys. Rev. B* **94**, 014412 (2016).
- [15] T. T. Heikkilä, R. Ojajarvi, I. J. Maasilta, E. Strambini, F. Giazotto, and F. S. Bergeret, *Phys. Rev. Appl.* **10**, 034053 (2018).
- [16] S. Chakraborty and T. T. Heikkilä, *J. Appl. Phys.* **124**, 123902 (2018).
- [17] A. Ozaeta, P. Virtanen, F. S. Bergeret, and T. T. Heikkilä, *Phys. Rev. Lett.* **112**, 057001 (2014).

VIII

DYNAMICS OF TWO FERROMAGNETIC INSULATORS COUPLED BY SUPERCONDUCTING SPIN CURRENT

by

R. Ojajärvi, F.S. Bergeret, M.A. Silaev and T.T. Heikkilä 2021

arXiv preprint, [arXiv:2107.09959](https://arxiv.org/abs/2107.09959) [cond-mat.supr-con]

Reproduced with permission. Copyright 2021 The Authors. Published in arXiv with
a non-exclusive license to distribute the article.

Dynamics of two ferromagnetic insulators coupled by superconducting spin current

Risto Ojajärvi,¹ F.S. Bergeret,^{2,3} M.A. Silaev,^{1,4,5} and Tero T. Heikkilä¹

¹*Department of Physics and Nanoscience Center, University of Jyväskylä,
P.O. Box 35 (YFL), FI-40014 University of Jyväskylä, Finland*

²*Centro de Física de Materiales (CFM-MPC), Centro Mixto CSIC-UPV/EHU,
Manuel de Lardizabal 5, E-20018 San Sebastián, Spain*

³*Donostia International Physics Center (DIPC),
Manuel de Lardizabal 4, E-20018 San Sebastián, Spain*

⁴*Moscow Institute of Physics and Technology, Dolgoprudny, 141700 Russia*

⁵*Institute for Physics of Microstructures, Russian Academy of Sciences, 603950 Nizhny Novgorod, GSP-105, Russia*

(Dated: February 21, 2022)

A conventional superconductor sandwiched between two ferromagnets can maintain coherent equilibrium spin current. This spin supercurrent results from the rotation of odd-frequency spin correlations induced in the superconductor by the magnetic proximity effect. In the absence of intrinsic magnetization, the superconductor cannot maintain multiple rotations of the triplet component but instead provides a Josephson type weak link for the spin supercurrent. We determine the analogue of the current-phase relation in various circumstances and show how it can be accessed in experiments on dynamic magnetization. In particular, concentrating on the magnetic hysteresis and the ferromagnetic resonance response, we show how the spin supercurrent affects the nonequilibrium dynamics of magnetization which depends on a competition between spin supercurrent mediated static exchange contribution and a dynamic spin pumping contribution. Depending on the outcome of this competition, a mode crossing in the system can either be an avoided crossing or mode locking.

Superconductivity is characterized by a $U(1)$ symmetry breaking complex order parameter and the dissipationless supercurrent proportional to its phase gradient. In the context of spin transport, analogous spin superfluidity has been discussed in various scenarios [1]. Recent work on coherent spin transport in multilayers containing ferromagnetic (F) and superconducting (SC) elements has opened the question of dissipationless spin transport in superconductors [2–4]. While there are notions of dissipationless or conserved spin currents in such systems [5, 6], it has remained unclear in which sense such spin currents can be observed in experiments on dynamical magnetization. Here we clarify the situation by showing how spin supercurrents (SS) naturally arise in ferromagnetic resonance (FMR) experiments involving two or more magnets, how it is linked to the gradient of the direction of the triplet order parameter, and how it mediates magnetic interactions.

What distinguishes the superconducting currents from normal persistent ones [7–9] is their robustness against disorder and interactions and the large length scales on which they occur. In F/SC systems SS depends on the magnetic proximity effect and its range is set by the coherence length of the SC.

Here we study SS in possibly the simplest superconducting system in which it can exist, namely a SC sandwiched between two ferromagnetic insulators (FI) with noncollinear magnetizations (Fig. 1). This system was considered already in the 1960s by de Gennes who showed that the SC mediates an antiferromagnetic interaction between the magnetic moments of the two FIs [10]. We demonstrate that this interaction can also be interpreted as an equilibrium spin current, and generalize it for a

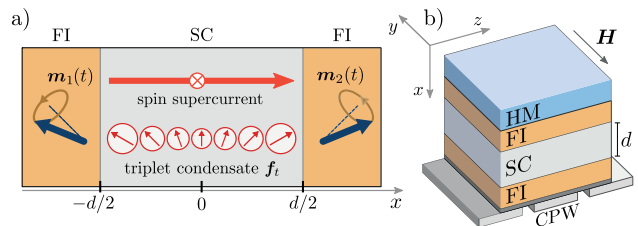


FIG. 1. a) Spin supercurrent through a superconductor with thickness d . $\mathbf{m}_1(t)$ and $\mathbf{m}_2(t)$ are the instantaneous magnetization directions of the FIs, and the direction and radius of the ‘clocks’ illustrate the spin direction and magnitude of the SC triplet condensate \mathbf{f}_t . b) Sketch of an FMR experiment. The sample is mounted on a coplanar waveguide (CPW). The static field \mathbf{H} is applied in the film plane. The additional heavy metal (HM) layer can be used to tune the Gilbert damping of the other FI.

SC with a finite length and finite spin scattering. We consider the magnetization dynamics of two FIs coupled by spin pumping and SS, and show that spin supercurrents can lead to decreased or increased damping of the FMR modes of the trilayer, as compared to unhybridized modes in the normal (N) state.

We first illustrate the concept of SS with a scheme based on the linearized Usadel equation. Consider a SC of length d coupled with two non-collinear FIs, with magnetizations on y - z plane pointing in directions \mathbf{m}_1 and \mathbf{m}_2 forming an angle ϕ . The effective exchange field at the SC/FI interface leads to a partial conversion of the conventional singlet superconducting condensate into a triplet component [11, 12]. Thus, near T_c , the Matsubara Green’s function (GF) for frequency $\omega_m > 0$ has the

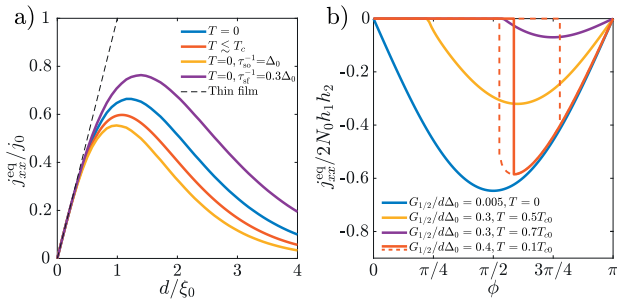


FIG. 2. a) Spin supercurrent as a function of SC thickness with fixed $h_n \ll \Delta_0$ normalized by $j_0 = h_1 h_2 \sin \phi \lim_{d \rightarrow 0} [\chi(x_1, x_2) d] \xi_0$. b) Spin current-magnetization angle relation for $d = \xi_0$ with no spin scattering. Dashed lines indicate SC/N state hysteresis.

general form

$$\hat{g} = \tau_3 + (f_s + \mathbf{f}_t \cdot \boldsymbol{\sigma})\tau_1, \quad (1)$$

where f_s and \mathbf{f}_t are the singlet and triplet condensate functions, respectively.[13] We assume translational invariance on the y - z plane. The spin supercurrent in x -direction can then be expressed as [14]

$$\begin{aligned} \mathbf{j}_x^{\text{eq}} &= \pi T \sum_{\omega_m > 0} N_0 D \mathbf{f}_t \times \partial_x \mathbf{f}_t \\ &= \pi T \sum_{\omega_m > 0} N_0 D |\mathbf{f}_t|^2 \partial_x \varphi \hat{\mathbf{x}}, \end{aligned} \quad (2)$$

where φ is the angle of \mathbf{f}_t relative to the z -axis and N_0 is the density of states at the Fermi level in the normal state. The SS arises from the coherent rotation of the triplet Cooper pairs. The vector structure of \mathbf{j}_x indicates its spin direction, and the subscript refers to the spatial direction.

The triplet condensate is determined by the Usadel equation and its boundary condition (BC)

$$D \nabla^2 \mathbf{f}_t = 2\omega_m \mathbf{f}_t, \quad (3a)$$

$$D \mathbf{n} \cdot \nabla \mathbf{f}_t|_{x=x_n} = 2iG_n \mathbf{m}_n f_s, \quad (3b)$$

where D is the diffusion constant, \mathbf{n} is the interface normal from FI to SC, and $x_{1,2} = \mp d/2$. The interface parameters G_n , which are related to the imaginary spin mixing conductances of the interfaces by $\text{Im} G_n^{\uparrow\downarrow} = G_n N_0$, determine the coupling between the singlet and triplet Cooper pairs [15, 16]. To first order in G_n , the singlet retains its bulk value $f_s = \Delta/\omega_m$. The triplet condensate leads to a spin density [17, 18]

$$\begin{aligned} \mathbf{S}(x) &= 2iN_0\pi T \sum_{\omega_m > 0} f_s \mathbf{f}_t(x) \\ &= \sum_{n=1,2} \chi(x, x_n) G_n \mathbf{m}_n. \end{aligned} \quad (4)$$

On the second line, we define the nonlocal spin susceptibility $\chi(x, x')$.

Substituting Eq. (3b) into Eq. (2), we find the SS

$$j_{xx}^{\text{eq}} = G_1 G_2 \chi(x_1, x_2) \sin \phi. \quad (5)$$

In analogy to SNS-junction, the FSF trilayer can be considered a spin Josephson junction [19, 20]. The middle layer is weak in the sense that it cannot support multiple phase windings, since there is no energy penalty for the vanishing condensate function. In order to have strong SS with a total phase winding larger than π would require the condensate to be restricted to $U(1)$ symmetry, as happens e.g. in easy-plane ferromagnets [1, 21]. Figure 2b shows the current-angle relation, which deviates from sine function at high T and at strong coupling.

As an equilibrium current, \mathbf{j}_x^{eq} is conserved through the SC.[22] Figure 2a shows its magnitude as a function of d . In the thin-film limit $d \ll \xi_0$, where ξ_0 is the SC coherence length, each interface induces a homogeneous exchange field with amplitude $h_n = G_n/d$. [23] The total exchange field is $\mathbf{h} = h_1 \mathbf{m}_1 + h_2 \mathbf{m}_2$ is limited by the Chandrasekhar-Clogston critical value $h_c = \Delta_0/\sqrt{2}$. With fixed h_n , the SS is proportional to d . When $d \rightarrow \infty$, the supercurrent vanishes as $\exp(-d/\xi_0)$. This exponential factor measures the overlap between the two proximity fields. Maximal SS is obtained when the maximum volume of SC is proximitized by both FIs at $d \approx \xi_0$.

At arbitrary temperatures and with finite spin-orbital/spin-flip scattering times $\tau_{\text{so/sf}}$, we determine the SC spin accumulation in the dirty limit from the full Usadel equation [24], using the spin-mixing BC [15, 25]

$$D \mathbf{n} \cdot \check{g} \circ \nabla \check{g}|_{x=x_n} = iG_n [\mathbf{m}_n \cdot \boldsymbol{\sigma} \tau_3 \check{g}], \quad (6)$$

where \check{g} are the 8×8 quasiclassical Green's functions in Keldysh-Nambu-Spin space and \circ -products are time-convolutions. The above BC gives Eq. (3b) as a special case. In the BC we take into account only the effective exchange field, [15] and neglect terms associated with interfacial spin relaxation and decoherence. [26–28]

By taking the trace over spin of (6), and integrating over the energy, the spin current through the n th interface is [29]

$$\mathbf{j}_{x,n}(t) = G_n [\mathbf{S}(t, x_n) \times \mathbf{m}_n(t) - N_0 \dot{\mathbf{m}}_n(t)], \quad (7)$$

where \mathbf{S} contains both the equilibrium spin density *cf.* Eq. (4) and the non-equilibrium spin accumulation. We assume that $d \gg \lambda_F$, where λ_F is Fermi wavelength, and neglect the short range Pauli paramagnetic contribution. The $\dot{\mathbf{m}}_n$ term is the spin pumping contribution, and $\mathbf{S} \times \mathbf{m}_n$ gives the equilibrium SS and the back-action due to non-equilibrium spin accumulation induced by spin pumping. [30] According to Eq. (7) there is a finite SS if the equilibrium \mathbf{S} and the magnetization of the FI are not collinear.

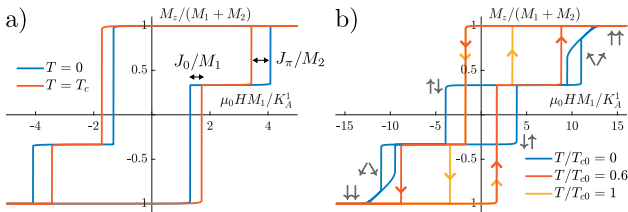


FIG. 3. Hysteresis loops for two coupled ferromagnets. a) Weak SC exchange interaction $dN_0\Delta_0^2/K_A^n = 1$. For $T = 0$ the system is always in the SC state. b) Strong exchange interaction $dN_0\Delta_0^2/K_A^n = 15$. For $T/T_c = 0.6$ the system is in the N state in P configuration, but in the SC state for AP configuration. For both panels, $M_1 = 2M_2$, $h_n = 0.3\Delta_0$, $\tau_{so/sf}^{-1} = 0$. External field is at 2° angle to the anisotropy axis.

We introduce a Stoner-Wohlfarth [31] type free energy (per interface area) to describe the effect of SS on the magnetic configuration of the FI/SC/FI trilayer

$$F(\mathbf{m}_1, \mathbf{m}_2) = \sum_{n=1,2} \left[-\mu_0 \mathbf{M}_n \cdot \mathbf{H} - K_A^n (\mathbf{m}_n \cdot \mathbf{z})^2 + K_B^n (\mathbf{m}_n \cdot \mathbf{x})^2 \right] + F_{sc}(\mathbf{m}_1 \cdot \mathbf{m}_2, \Delta), \quad (8)$$

where $|\mathbf{M}_n| = M_n$ is the FI magnetic moment per interface area. The free energy includes the Zeeman energy from external magnetic field \mathbf{H} , the SC free energy F_{sc} , and the in-plane easy axis/out-of-plane anisotropy energies $K_{A/B}^n$. In the thin-film limit, at $T = 0$ and without any spin scattering $F_{sc}(\mathbf{h}) = dN_0(|\mathbf{h}|^2 - \Delta^2/2)$. In the general case we use the SC energy functional of Ref. 32.

In a static setting, the coupling between the magnets can be described as an effective magnetic field $\mu_0 \mathbf{H}_{\text{eff},1}^{\text{sc}} = -J_\phi \mathbf{m}_2 / M_1$, which can be identified with SS via the spin-transfer torque

$$\begin{aligned} \mathbf{j}_{x,1}^{\text{eq}} &= -\mathbf{M}_1 \times \mu_0 \mathbf{H}_{\text{eff},1}^{\text{sc}} \\ &= J_\phi \mathbf{m}_1 \times \mathbf{m}_2, \end{aligned} \quad (9)$$

with exchange constant $J_\phi = dF_{sc}/d\cos\phi \geq 0$. At weak coupling Eq. (9) coincides with Eq. (5).

When the SC exchange energy is small compared to the anisotropy energies, SS modifies the coercive fields [33] (Fig. 3a). In the SC state, the coercive fields for AP-to-P switching increase by J_π/M_n , and the coercive fields for P-to-AP switching decrease by J_0/M_n relative to the N state. With a strong SS (Fig. 3b) the anisotropies cannot force the magnets into a binary parallel/antiparallel configuration space and the exchange interaction may induce a spin-flop transition, in which the two magnets collectively rotate from AP to P configuration [34].

At low temperatures the SC transition is of the first order as a function of ϕ and exhibits hysteresis (Fig. 2b). [35–38] If there is a strong uniaxial anisotropy in the FIs, it is possible to study the N-to-SC hysteresis [37,

38], as opposed to the ordinary magnetic hysteresis resulting from anisotropies. By applying the external magnetic field perpendicular to the easy axis direction, the exchange field changes continuously. If the SC transition is continuous, there is also no magnetic hysteresis. If the transition is of the first order, the N-to-SC and magnetic hysteresis become entangled. We show in the supplementary how the two can be disentangled in the magnetization curve. [24]

We now consider the dynamical effects due to SS. In contrast to most studies of F/SC hybrid structures [39, 40], we take both magnets as dynamical. We study the small-angle dynamics around the equilibrium configuration with the ansatz

$$\mathbf{m}_n(t) = \mathbf{m}_n(0) + \text{Re}[\mathbf{m}_n(\omega) \exp(-i\omega t)], \quad (10)$$

where $\mathbf{m}_n(\omega)$ is a small perturbation perpendicular to $\mathbf{m}_n(0)$. The dynamical magnetization induces a time-dependent exchange field at the SC interfaces, which in turn induces a time-dependent spin density in the SC.

The dynamics of the FI magnetizations are described by the classical Landau-Lifshitz-Gilbert (LLG) equation, supplemented by a spin current term [41]

$$\dot{\mathbf{M}}_n = -\gamma \mathbf{M}_n \times \mu_0 \mathbf{H}_{\text{eff},n}^{(0)} + \frac{\alpha_n}{M_n} (\mathbf{M}_n \times \dot{\mathbf{M}}_n) + \gamma \mathbf{j}_{x,n}, \quad (11)$$

where $\mathbf{H}_{\text{eff},n}^{(0)}$ is the effective magnetic field in the N state including the external magnetic field and anisotropy fields, γ is the gyromagnetic ratio, and α_n is the Gilbert damping coefficient, which can be controlled with an additional heavy metal layer next to the FI (Fig. 1b). The spin current is given by Eq. (7).

In a FMR experiment, the external field has a static component and a small transverse dynamic part \mathbf{H}_{rf} . The linear response to \mathbf{H}_{rf} given by LLG Eq. (11) is

$$\hat{\chi}_n^{-1}(\omega) \mathbf{M}_n(\omega) = \mu_0 \mathbf{H}_{\text{rf}}(\omega) - \mathbf{m}_n(0) \times \frac{\mathbf{j}_{x,n}(\omega)}{M_n}, \quad (12)$$

where $\hat{\chi}_n^{-1}$ are the 2×2 magnetic susceptibilities of the uncoupled magnets. [24] Since the magnets are insulating, there are no eddy currents inside the FIs and we can neglect the direct coupling between the SC and the rf field. [42, 43]

In the parallel configuration, the coupled dynamics of the two magnets is described by a matrix susceptibility

$$\hat{\chi}_{\text{tot}}^{-1}(\omega) = \begin{pmatrix} \hat{\chi}_1^{-1}(\omega) + \frac{J_0 - \delta \hat{J}_{11}(\omega)}{M_1^2} & -\frac{J_0 + \delta \hat{J}_{12}(\omega)}{M_1 M_2} \\ -\frac{J_0 + \delta \hat{J}_{21}(\omega)}{M_1 M_2} & \hat{\chi}_2^{-1}(\omega) + \frac{J_0 - \delta \hat{J}_{22}(\omega)}{M_2^2} \end{pmatrix}, \quad (13)$$

where $J_0 = -G_1 G_2 \chi(x_1, x_2)$ is the static exchange constant, and

$$\begin{aligned} \delta \hat{J}_{ij}(\omega) &= -G_i G_j [\hat{\chi}(\omega, x_i, x_j) - \chi(x_i, x_j)] \\ &\quad - N_0 G_i \omega \delta_{ij} \hat{\sigma}_3, \end{aligned} \quad (14)$$

are the dynamic corrections related to spin pumping and other finite-frequency processes. Here, $\hat{\chi}$ is the dynamic spin susceptibility, [24, 44] related to the static spin susceptibility by $\hat{\chi}(0, x_i, x_j) = \chi(x_i, x_j)\hat{1}$.

To illustrate the effect of SS on the FMR properties, we first consider a fully symmetric trilayer. In the P configuration, the eigenmodes are the acoustic and optical modes for which $\mathbf{m}_1(t) = \pm\mathbf{m}_2(t)$, respectively. [34] In the acoustic mode, the magnetizations are always parallel to each other and there is no SS [34]. The magnets are only coupled by the residual part of the susceptibility, $\chi(\omega) - \chi(0) \approx \omega\chi'(0)$. The imaginary part $\text{Im}\chi'(0)$ contributes directly to dissipation and can be included in the Gilbert damping coefficient. It describes the relaxation of quasiparticles, and vanishes at low T where quasiparticles cannot be excited due to SC gap [45]. This leads to the usual decrease of the FMR linewidth in the SC state (Fig. 4a). The real part $\text{Re}\chi'(0)$ shifts the resonance frequency.

In the optical mode the magnetizations precess out-of-phase and are strongly coupled by the SS. In this case, the effective magnetic field is shifted by $2J_0/M_n$. The resonance field difference between acoustic and optical modes at fixed frequency gives a direct measure of SS. However, measuring the optical mode can be difficult as a symmetrically applied rf field excites only the acoustic mode. Optical mode can be excited by longitudinal FMR pumping [46, 47], or by breaking the symmetry. For the optical mode the non-equilibrium spin currents pumped by the two magnets partially cancel in the SC spacer. In the thin-film limit this cancellation is exact and the dissipation in the spacer does not affect the linewidth.

In an asymmetric trilayer, SS can have a drastic effect on the linewidths of the FMR modes. For illustration, let us neglect the spin pumping and consider only the effect of SS together with the intrinsic damping of the magnets. In the N state the magnets are uncoupled, and the eigenmodes are the Kittel modes of the individual magnets with linewidths ΔH_n^0 proportional to Gilbert damping constants α_n . In the SC state, the SS hybridizes the modes so that their linewidths become weighted averages $\Delta H_n = (\Delta H_1^0 + p_n\Delta H_2^0)/(1 + p_n)$, where $p_1 = 0$ and $p_2 = \infty$ in the uncoupled system, and $p_1 \rightarrow M_1/M_2$ and $p_2 \rightarrow M_2/M_1$ in the strongly coupled system. [48] The top panel of Fig. 4b shows a numerical evaluation for the linewidth of such a system, including the spin pumping contribution. In particular, if one magnet has a lower intrinsic damping than the other magnet, the linewidth of the related mode increases below the SC transition.

The SS-mediated exchange interaction and spin pumping depend on temperature in opposite ways; spin pumping vanishes at zero temperature, whereas SS vanishes in the normal state. The competition between these two processes can be studied at a mode crossing between two FMR modes (Fig. 5), which can be engineered e.g. by having FI films with different thicknesses. In general,

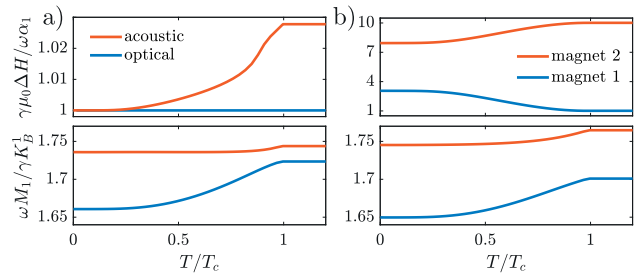


FIG. 4. Temperature dependence of linewidth (top) and resonance frequency (bottom) for a) symmetric system with $\alpha_n = 0.005$, b) asymmetric system with $\alpha_1 = 0.005$ and $\alpha_2 = 0.05$. Parameters: $K_A^n = 0$, $dN_0\Delta_0^2 = 0.1$, $\Delta_0 M_n/\gamma = 100$, $\gamma\mu_0 M_n H = 1$, in units of K_B^2 ; $h_n = 0.3\Delta_0$, $\tau_{\text{so}}^{-1} = 0.2\Delta_0$

thinner films will have stronger anisotropy fields. A mode crossing may then be seen by rotating the applied in-plane magnetic field relative to the anisotropy axis. [49]

In the N state (Fig. 5a) the magnets are only coupled by spin pumping. The dissipative component of spin pumping generated by spin relaxation in the SC layer gives rise to mode attraction. Its signature is the sudden change of the mode linewidths at the mode crossing (inset of Fig 5a) [30, 50]. In the SC state (Fig. 5b), the SS mediated exchange coupling dominates over spin pumping, creating a regular avoided crossing.

So far the dynamical properties of SS have been experimentally studied only in systems with ferromagnetic metals (FM) [2–4], and an increase in FMR linewidth below T_c has been observed in systems which include multiple FM or heavy metal layers with strong spin-orbit coupling. In some of these experiments [2], there is nominally only a single magnet, but the heavy metal layers close to the ferromagnetic instability can be magnetized by the SS-mediated magnetic proximity effect. [51]

With minor changes, our theory can describe SS-mediated coupling in FM/SC/FM trilayer. The form of the magnetic susceptibility (13) is otherwise unchanged from the insulating case, but the susceptibilities for the spin density at the interfaces are replaced by the susceptibilities for the total spin density of the FM conduction electrons, and the spin mixing conductance is replaced by the s - d coupling inside the FM. In contrast to an FI, in FM the spin current is not absorbed in a layer of atomic thickness, but penetrates into the FM at the range of $\xi_F = \sqrt{D_F/2T}$, where D_F is the diffusion coefficient of the FM. [12] The long-range triplet component [12] penetrating deep into the FM is exactly the component non-collinear to its exchange field, and the one related to SS. Because FMs support eddy currents, there is also an electromagnetic coupling between the layers. [42, 43]. Finding the magnitude of spin currents in a metallic system will be left for further work.

Despite these differences, our framework suggests that the experimentally observed enhancement below T_c is

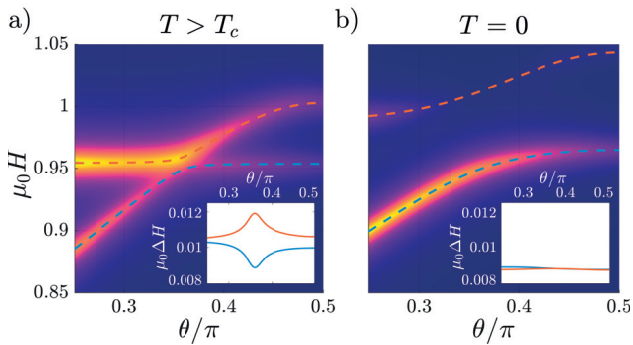


FIG. 5. Absorbed rf power as a function of external field angle θ and amplitude $\mu_0 H$ (in units of K_B^1/M_1). Dashed lines indicate the resonance fields and the insets show the linewidths. a) Mode locking in the N state is the most evident from the linewidth broadening/narrowing near the crossing. b) Avoided crossing in the SC state. The linewidths do not depend strongly on the proximity to the crossing. Parameters are as in Fig. 4a except for $\omega M_1/\gamma = 1.75$, $K_A^1 = 0.1$, $K_B^2 = 1.1$, $\Delta_0 M_n/\gamma = 10$, given in units of K_B^1 .

likely to be a result of SS-mediated hybridization between the FMR modes. In interpreting the FMR data in systems with superconducting interlayers and multiple magnets, one should not rely on the spin pumping picture with a single dynamical magnet, but instead model the magnetization dynamics of the whole structure.

Conclusions. We have studied the properties of SS in FI/SC/FI systems and shown how they can mediate damping between ferromagnetic insulators even though they, as equilibrium currents, are themselves non-dissipative. In an analogy to Josephson junctions, the SS can be characterized via the spin current - magnetization angle relation. This can be accessed by studying temperature dependent modifications to the FMR frequencies in FI/SC/FI setups.

The phenomena described here can be studied in various different FI/SC combinations, provided they can be suitably stacked or placed next to each other. The FI can be for example GdN, EuS/EuO, or ferrimagnetic YIG, which have been recently studied in combination with superconductors such as Nb, NbN or Al. [33, 52–57] Our results can be used to design magnetic resonator structures where the SS mediates a tunable coupling between the resonators.

Acknowledgements This work was supported by the Academy of Finland Project 317118, the European Union’s Horizon 2020 Research and Innovation Framework Programme under Grant No. 800923 (SUPERTEd), and Jenny and Antti Wihuri Foundation. FSB acknowledges funding by the Spanish Ministerio de Ciencia, Innovacion y Universidades (MICINN) (Project FIS2017-82804-P).

- [1] E. Sonin, *Adv. Phys.* **59**, 181 (2010).
- [2] K.-R. Jeon, C. Ciccarelli, A. J. Ferguson, H. Kurebayashi, L. F. Cohen, X. Montiel, M. Eschrig, J. W. A. Robinson, and M. G. Blamire, *Nat. Mater.* **17**, 499 (2018).
- [3] K.-R. Jeon, C. Ciccarelli, H. Kurebayashi, L. F. Cohen, X. Montiel, M. Eschrig, S. Komori, J. W. A. Robinson, and M. G. Blamire, *Phys. Rev. B* **99**, 024507 (2019).
- [4] K.-R. Jeon, X. Montiel, S. Komori, C. Ciccarelli, J. Haigh, H. Kurebayashi, L. F. Cohen, A. K. Chan, K. D. Stenning, C.-M. Lee, M. Eschrig, M. G. Blamire, and J. W. A. Robinson, *Phys. Rev. X* **10**, 031020 (2020).
- [5] S. H. Jacobsen, I. Kulagina, and J. Linder, *Sci. Rep.* **6**, 23926 (2016).
- [6] F. Aikebaier, M. A. Silaev, and T. T. Heikkilä, *Phys. Rev. B* **98**, 024516 (2018).
- [7] M. Büttiker, Y. Imry, and R. Landauer, *Phys. Lett. A* **96**, 365 (1983).
- [8] L. P. Lévy, G. Dolan, J. Dunsmuir, and H. Bouchiat, *Phys. Rev. Lett.* **64**, 2074 (1990).
- [9] A. Bleszynski-Jayich, W. Shanks, B. Peaudecerf, E. Gnossar, F. von Oppen, L. Glazman, and J. Harris, *Science* **326**, 272 (2009).
- [10] P.-G. de Gennes, *Phys. Lett.* **23**, 10 (1966).
- [11] F. S. Bergeret, A. F. Volkov, and K. B. Efetov, *Phys. Rev. Lett.* **86**, 4096 (2001).
- [12] F. S. Bergeret, A. F. Volkov, and K. B. Efetov, *Rev. Mod. Phys.* **77**, 1321 (2005).
- [13] J. Linder and A. V. Balatsky, *Rev. Mod. Phys.* **91**, 045005 (2019).
- [14] J. A. Ouassou, J. W. Robinson, and J. Linder, *Sci. Rep.* **9**, 1 (2019).
- [15] T. Tokuyasu, J. A. Sauls, and D. Rainer, *Phys. Rev. B* **38**, 8823 (1988).
- [16] D. Huertas-Hernando, Y. V. Nazarov, and W. Belzig, *Phys. Rev. Lett.* **88**, 047003 (2002).
- [17] F. S. Bergeret, A. F. Volkov, and K. B. Efetov, *Phys. Rev. B* **69**, 174504 (2004).
- [18] J. Xia, V. Shelukhin, M. Karpovski, A. Kapitulnik, and A. Palevski, *Phys. Rev. Lett.* **102**, 087004 (2009).
- [19] I. Fomin, *Physica B Condens. Matter* **169**, 153 (1991).
- [20] F. S. Nogueira and K.-H. Bennemann, *EPL* **67**, 620 (2004).
- [21] S. Takei and Y. Tserkovnyak, *Phys. Rev. Lett.* **112**, 227201 (2014).
- [22] J. A. Ouassou, A. Pal, M. Blamire, M. Eschrig, and J. Linder, *Sci. Rep.* **7**, 1 (2017).
- [23] T. T. Heikkilä, M. Silaev, P. Virtanen, and F. S. Bergeret, *Prog. Surf. Sci.* **94**, 100540 (2019).
- [24] Supplementary material at XYZ includes derivations for the thin-film spin susceptibility and the coupled magnetic susceptibility. Codes are available at gitlab.jyu.fi/jyucmt/fi-sc-fi. Refs. 35, 36, 58–62 are cited in the supplement.
- [25] M. A. Silaev, R. Ojajarvi, and T. T. Heikkilä, *Phys. Rev. Res.* **2**, 033416 (2020).
- [26] F. S. Bergeret, A. Verso, and A. F. Volkov, *Phys. Rev. B* **86**, 214516 (2012).
- [27] M. Eschrig, A. Cottet, W. Belzig, and J. Linder, *New J. Phys.* **17**, 083037 (2015).
- [28] X.-P. Zhang, F. S. Bergeret, and V. N. Golovach, *Nano*

- Lett.* **19**, 6330 (2019).
- [29] R. Ojajärvi, T. T. Heikkilä, P. Virtanen, and M. A. Silaev, *Phys. Rev. B* **103**, 224524 (2021).
- [30] Y. Tserkovnyak, A. Brataas, G. E. W. Bauer, and B. I. Halperin, *Rev. Mod. Phys.* **77**, 1375 (2005).
- [31] E. C. Stoner and E. Wohlfarth, *Philos. Trans. R. Soc. A* **240**, 599 (1948).
- [32] P. Virtanen, A. Vargunin, and M. Silaev, *Phys. Rev. B* **101**, 094507 (2020).
- [33] Y. Zhu, A. Pal, M. G. Blamire, and Z. H. Barber, *Nat. Mater.* **16**, 195 (2017).
- [34] P. Wigen, Z. Zhang, L. Zhou, M. Ye, and J. Cowen, *J. Appl. Phys.* **73**, 6338 (1993).
- [35] K. Maki and T. Tsuneto, *Prog. Theor. Phys.* **31**, 945 (1964).
- [36] P. Tedrow, R. Meservey, and B. Schwartz, *Phys. Rev. Lett.* **24**, 1004 (1970).
- [37] W. Wu and P. W. Adams, *Phys. Rev. Lett.* **74**, 610 (1995).
- [38] V. Y. Butko, P. W. Adams, and E. I. Meletis, *Phys. Rev. Lett.* **83**, 3725 (1999).
- [39] H. T. Simensen, L. G. Johnsen, J. Linder, and A. Brataas, *Phys. Rev. B* **103**, 024524 (2021).
- [40] X. Montiel and M. Eschrig, [arXiv:2106.13988](https://arxiv.org/abs/2106.13988) [cond-mat.supr-con] (2021).
- [41] J. C. Slonczewski, *J. Magn. Magn. Mater.* **159**, L1 (1996).
- [42] M. Müller, L. Liensberger, L. Flacke, H. Huebl, A. Kamra, W. Belzig, R. Gross, M. Weiler, and M. Althammer, *Phys. Rev. Lett.* **126**, 087201 (2021).
- [43] K. Kennewell, M. Kostylev, and R. Stamps, *J. Appl. Phys.* **101**, 09D107 (2007).
- [44] M. A. Silaev, *Phys. Rev. B* **102**, 144521 (2020).
- [45] J. P. Morten, A. Brataas, G. E. W. Bauer, W. Belzig, and Y. Tserkovnyak, *EPL* **84**, 57008 (2008).
- [46] Z. Zhang, L. Zhou, P. E. Wigen, and K. Ounadjela, *Phys. Rev. Lett.* **73**, 336 (1994).
- [47] J. Lindner and K. Baberschke, *J. Phys. Condens. Matter* **15**, R193 (2003).
- [48] A. Layadi, *AIP Advances* **5**, 057113 (2015).
- [49] B. Heinrich, Y. Tserkovnyak, G. Woltersdorf, A. Brataas, R. Urban, and G. E. W. Bauer, *Phys. Rev. Lett.* **90**, 187601 (2003).
- [50] Y. Tserkovnyak, *Phys. Rev. Res.* **2**, 013031 (2020).
- [51] X. Montiel and M. Eschrig, *Phys. Rev. B* **98**, 104513 (2018).
- [52] Y. Yao, Q. Song, Y. Takamura, J. P. Cascales, W. Yuan, Y. Ma, Y. Yun, X. C. Xie, J. S. Moodera, and W. Han, *Phys. Rev. B* **97**, 224414 (2018).
- [53] A. Hijano, S. Ilić, M. Rouco, C. González-Orellana, M. Ilyn, C. Rogero, P. Virtanen, T. T. Heikkilä, S. Khorshidian, M. Spies, N. Ligato, F. Giazotto, E. Strambini, and F. S. Bergeret, *Phys. Rev. Res.* **3**, 023131 (2021).
- [54] B. Li, N. Roschewsky, B. A. Assaf, M. Eich, M. Epstein-Martin, D. Heiman, M. Münzenberg, and J. S. Moodera, *Phys. Rev. Lett.* **110**, 097001 (2013).
- [55] J. P. Cascales, Y. Takamura, G. M. Stephen, D. Heiman, F. S. Bergeret, and J. S. Moodera, *Appl. Phys. Lett.* **114**, 022601 (2019).
- [56] E. Strambini, V. N. Golovach, G. De Simoni, J. S. Moodera, F. S. Bergeret, and F. Giazotto, *Phys. Rev. Mater.* **1**, 054402 (2017).
- [57] K. Rogdakis, A. Sud, M. Amado, C. M. Lee, L. McKenzie-Sell, K. R. Jeon, M. Cubukcu, M. G. Blamire, J. W. A. Robinson, L. F. Cohen, and H. Kurebayashi, *Phys. Rev. Mater.* **3**, 014406 (2019).
- [58] F. Aikebaier, P. Virtanen, and T. Heikkilä, *Phys. Rev. B* **99**, 104504 (2019).
- [59] K. D. Usadel, *Phys. Rev. B* **4**, 99 (1971).
- [60] M. Eschrig, *Phys. Rev. B* **61**, 9061 (2000).
- [61] K. Yosida, *Phys. Rev.* **110**, 769 (1958).
- [62] A. Abrikosov and L. Gor'kov, *Sov. Phys. JETP* **15**, 752 (1962).

Supplementary material

The FI/SC/FI trilayer is described by the Hamiltonian

$$H = H_{\text{SC}} + H_{\text{imp}} + \sum_{n=1,2} \left(H_{\text{FI}}^{(n)} + H_{\text{ex}}^{(n)} \right), \quad (\text{S1})$$

where H_{SC} is the BCS Hamiltonian for an s -wave superconductor, assumed infinite in y and z directions, but with a finite thickness d in the x direction. H_{imp} is the random impurity potential in the SC, containing both non-magnetic and magnetic impurities, which gives the spin-orbit and spin-flip self-energies, respectively. We assume that the elastic mean-free path is short so that the SC can be described with the quasiclassical Usadel equation.

The Hamiltonians describing the FIs and the SC/FI interfaces are[23]

$$H_{\text{FI}}^{(n)} = - \sum_{i,j} J_{ij} \mathbf{S}_i \cdot \mathbf{S}_j + H_{\text{an}}, \quad (\text{S2})$$

$$H_{\text{ex}}^{(n)} = -J_{\text{ex},n} \sum_{i \in \mathcal{I}_n} \Psi^\dagger(\mathbf{r}_i) \mathbf{S}_i \cdot \boldsymbol{\sigma} \Psi(\mathbf{r}_i), \quad (\text{S3})$$

where J_{ij} is the exchange coupling between the localized spins \mathbf{S}_i at FI lattice sites \mathbf{r}_i . H_{an} includes the possible anisotropy fields. \mathcal{I}_n is the set of spins at the interface between n th FI and the SC, and the spin-mixing conductances are related to the interfacial exchange coupling $J_{\text{ex},n}$ by $G_n = J_{\text{ex},n} S_n a$, where S_n is the local spin at the interface and a is the FI lattice constant.[23]The Nambu field operator

$$\Psi^\dagger(\mathbf{r}) = \begin{pmatrix} \psi_\uparrow^\dagger(\mathbf{r}) & \psi_\downarrow^\dagger(\mathbf{r}) & -\psi_\downarrow(\mathbf{r}) & \psi_\uparrow(\mathbf{r}) \end{pmatrix} \quad (\text{S4})$$

is chosen so that the s -wave SC order parameter is proportional to unit matrix in spin space.

Quasiclassical theory

When the elastic mean-free path is short, the SC specified by the above Hamiltonian can be described at the quasiclassical limit by using the Keldysh-Usadel equation [23, 29, 59]

$$- \{ \tau_3 \partial_t \circ \check{g} \} + \partial_x (D \check{g} \circ \partial_x \check{g}) = [\Delta \tau_1 + \check{\Sigma} \circ \check{g}] \quad (\text{S5})$$

with the boundary conditions given by Eq. (6) of the main text. Above, \check{g} is the quasiclassical Green's function (GF) in 8×8 space consisting of Keldysh, Nambu and spin indices. It obeys normalization condition $\check{g} \circ \check{g} = \delta(t, t')$. The elastic spin relaxation is determined by spin-orbit and spin-flip scattering self-energies $\check{\Sigma} = \hat{\boldsymbol{\sigma}} \cdot \check{g} \hat{\boldsymbol{\sigma}} / 6\tau_{\text{so}} + \tau_3 \hat{\boldsymbol{\sigma}} \cdot \check{g} \hat{\boldsymbol{\sigma}} \tau_3 / 6\tau_{\text{sf}}$, where $\tau_{\text{so/sf}}$ are the

scattering rates. The order parameter Δ is solved from the self-consistency equation

$$\Delta(\omega) = \frac{\lambda}{16i} \int_{-\Omega_{\text{D}}}^{\Omega_{\text{D}}} d\varepsilon \text{Tr} [\hat{\tau}_1 \hat{g}^K(\varepsilon, \varepsilon - \omega)], \quad (\text{S6})$$

where the coupling constant λ and the cutoff Ω_{D} can be eliminated in favor of SC order parameter Δ_0 at $T = 0$ in the absence of pair-breaking effects. [23].

The spin current density in x -direction and the spin density are defined as

$$\mathbf{j}_x(\omega, x) = \frac{N_0}{16} \int_{-\infty}^{\infty} d\varepsilon \text{Tr} [\boldsymbol{\sigma} D(\check{g} \circ \partial_x \check{g})(\varepsilon, \varepsilon - \omega)]^K, \quad (\text{S7})$$

$$\mathbf{S}(\omega, x) = -\frac{N_0}{8} \int_{-\infty}^{\infty} d\varepsilon \text{Tr} [\boldsymbol{\sigma} \tau_3 \hat{g}^K(\varepsilon, \varepsilon - \omega; x)]. \quad (\text{S8})$$

For the SC we use the free energy functional [32, 58]

$$F_{\text{sc}}[\hat{g}, \Delta] = N_0 \int dx \left(\frac{\Delta^2}{\lambda} - \frac{\pi T}{2} \sum_{\omega} \text{tr} \{ (\omega_n + i\mathbf{h} \cdot \boldsymbol{\sigma}) \hat{\tau}_3 \hat{g} + \Delta \tau_1 \hat{g} - \frac{D}{4} (\hat{\nabla} \hat{g})^2 + \frac{1}{12\tau_{\text{so}}} (\boldsymbol{\sigma} \hat{g}) \cdot (\boldsymbol{\sigma} \hat{g}) + \frac{1}{12\tau_{\text{sf}}} (\boldsymbol{\sigma} \hat{\tau}_3 \hat{g}) \cdot (\boldsymbol{\sigma} \hat{\tau}_3 \hat{g}) \} \right), \quad (\text{S9})$$

which is regularized by subtracting the normal state energy with $\hat{g} = \text{sgn}(\omega_n) \hat{\tau}_3$ and $\Delta = 0$.

Spin susceptibility at the thin-film limit

In equilibrium, spatially averaging over Eq. (S5) and using the BC of Eq. (6), we find an effective position-independent Usadel equation

$$[i(\varepsilon - \mathbf{h} \cdot \boldsymbol{\sigma}) \tau_3 + \Delta \tau_1 + \hat{\Sigma}, \hat{g}] = 0. \quad (\text{S10})$$

This equation is valid at the thin-film limit $d \ll \xi_0, l_{\text{sd}}$, where $l_{\text{sd}} = [D/(\tau_{\text{so}}^{-1} + \tau_{\text{sf}}^{-1})]^n$ is the normal state spin diffusion length. Equations (S6) and (S10) together with the normalization condition constitute a nonlinear group of equations which we solve numerically. In the thin-film limit we drop the spatial indices and define the static susceptibility as $\mathbf{S} = \hat{\chi}(0) \mathbf{h}$. It is related to the nonlocal susceptibility by $\hat{\chi}(0) = \lim_{d \rightarrow 0} \chi(0, x_i, x_j) d$.

Let us denote by $\chi_{\text{homog}}(\omega)$ the usual spin susceptibility to an external in-plane magnetic field [61]. It is related to the nonlocal thin-film spin susceptibility by a simple shift: $\chi(\omega) = \chi_{\text{homog}}(\omega) - N_0$. These susceptibilities vanish at different limits; $\chi_{\text{homog}}(0) = 0$ at $T = 0$ in the absence of spin scattering [62], whereas the nonlocal susceptibility vanishes in the normal state. Figure S1a shows the static spin susceptibility for $\tau_{\text{so}}^{-1} = \tau_{\text{sf}}^{-1} = 0$.

The dynamic spin susceptibility $\hat{\chi}(\omega)$ is defined as a spin response to a dynamic perturbation of the exchange field

$$\mathbf{S}(\omega, x_i) = \sum_{j=1,2} \hat{\chi}(\omega, x_i, x_j) G_j \mathbf{m}_j(\omega). \quad (\text{S11})$$

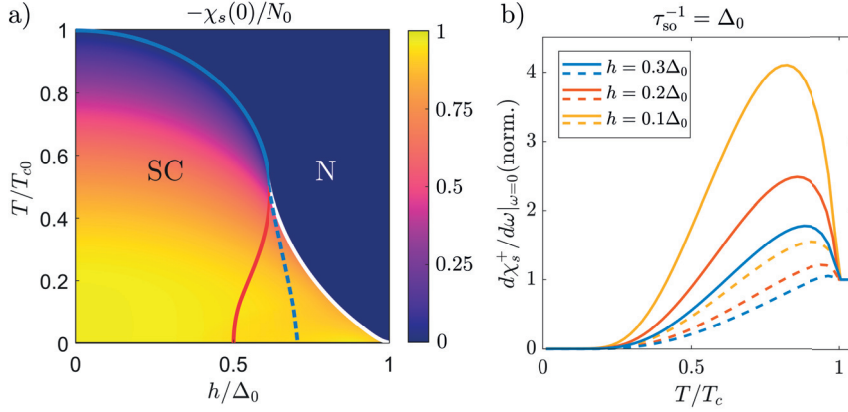


FIG. S1. a) Thin-film static spin susceptibility in the SC state without spin scattering. Overlaid lines show the phase diagram. Blue solid (dashed) line indicates a second-order (thermodynamic first order) phase transition[35]. Within the area delimited by red and white curves, both SC and normal state are (meta)stable. b) Dynamic correction for the transverse spin susceptibility. Solid and dashed lines denote the real and imaginary part, respectively. Real and imaginary parts are normalized by their normal state values given by Eq. (S22).

Generally, $\hat{\chi}$ is a 3×3 matrix. In the thin-film limit, it is diagonal in the standard circular basis

$$\mathbf{e}_{\pm} = \mp(\mathbf{x} \pm i\mathbf{y})/\sqrt{2}, \quad \mathbf{e}_z = \mathbf{z}, \quad (\text{S12})$$

where the z -axis is chosen along the static component $\mathbf{h}(0)$. The components of $\hat{\chi}$ are extracted as $\chi^{\mu\nu} = \mathbf{e}_{\mu}^{\dagger} \hat{\chi} \mathbf{e}_{\nu}$. In the parallel case, or in the thin-film limit, the susceptibilities $\hat{\chi}(\omega, x_i, x_j)$ can be simultaneously diagonalized, and we drop the second index: $\chi^{+} \equiv \chi^{++}$. We call χ^z the longitudinal susceptibility and $\chi^{+(-)}$ left(right)-handed transverse susceptibility. The longitudinal component is only induced if $\mathbf{m}_1(0)$ and $\mathbf{m}_2(0)$ are non-collinear, since only then $\mathbf{m}_1(\omega) \cdot \mathbf{m}_2(0) \neq 0$.

In the thin-film limit finite frequency transverse spin susceptibility can be obtained by solving the perturbed Usadel equation

$$\begin{aligned} & [\hat{A}(1) + \hat{\Sigma}(1)]\hat{g}(12) - \hat{g}(12)[\hat{A}(2) + \hat{\Sigma}(2)] \\ & + \hat{\Sigma}(12)\hat{g}_0(2) - \hat{g}_0(1)\hat{\Sigma}(12) \\ & = i[\hat{g}_0(1)(\mathbf{h}(\omega) \cdot \boldsymbol{\sigma})\tau_3 - (\mathbf{h}(\omega) \cdot \boldsymbol{\sigma})\tau_3\hat{g}_0(2)], \end{aligned} \quad (\text{S13})$$

where $\hat{g}_0(1)$ is the static GF at Matsubara frequency $\varepsilon_1 = i\omega_n$ and $\hat{g}(12)$ is the perturbation induced by the left polarized driving field $\mathbf{h}(\omega) = h^{+}(\omega)\mathbf{e}_{+}$, and

$$\hat{A}(\varepsilon) = -i(\varepsilon - h\sigma_3)\tau_3 + \Delta\tau_1, \quad (\text{S14})$$

$$\hat{s}(\varepsilon) = \sqrt{[\hat{A}(\varepsilon) + \hat{\Sigma}_0(\varepsilon)]^2}, \quad (\text{S15})$$

$$\hat{g}_0(\varepsilon) = \hat{s}(\varepsilon)^{-1}[\hat{A}(\varepsilon) + \hat{\Sigma}_0(\varepsilon)]. \quad (\text{S16})$$

Using the normalization condition

$$\hat{g}_0(1)^2 = 1, \quad \hat{g}_0(1)\hat{g}(12) + \hat{g}(12)\hat{g}_0(2) = 0, \quad (\text{S17})$$

and the relation

$$\begin{aligned} & \tau_3\hat{g}_0(1)\hat{g}(12)\hat{g}_0(2)\tau_3 + \hat{g}_0(1)\tau_3\hat{g}(12)\tau_3\hat{g}_0(2) \\ & = -2[g_{\uparrow 1}(1)g_{\downarrow 1}(2) - g_{\uparrow 3}(1)g_{\downarrow 3}(2)]\hat{g}(12), \end{aligned} \quad (\text{S18})$$

the solution for the Matsubara GF is found as

$$\hat{g}(12) = \frac{i[\tau_3 - \hat{g}_{\uparrow}(1)\tau_3\hat{g}_{\downarrow}(2)]\mathbf{h}(\omega) \cdot \boldsymbol{\sigma}}{s_{\uparrow}(1) + s_{\downarrow}(2) + \frac{1}{3\tau_{so}} + \frac{g_{\uparrow 1}(1)g_{\downarrow 1}(2) - g_{\uparrow 3}(1)g_{\downarrow 3}(2)}{3\tau_{sf}}}. \quad (\text{S19})$$

The energy-resolved spin susceptibility is obtained by taking the trace

$$\chi(1, 2) = -\frac{N_0}{8} \text{Tr} \left[(\mathbf{e}_{+} \cdot \boldsymbol{\sigma})^{\dagger} \tau_3 \frac{\hat{g}(12)}{h_{\omega}} \right] \quad (\text{S20})$$

The solution for real frequencies is obtained with analytical continuation

$$\begin{aligned} \chi^{+}(\omega) = \int_{-\infty}^{\infty} d\varepsilon [& \chi(1^R, 2^R)f_2 - f_1\chi(1^A, 2^A) \\ & + (f_1 - f_2)\chi(1^R, 2^A)], \end{aligned} \quad (\text{S21})$$

where $1^{R/A}$ and $2^{R/A}$ stand for the replacements $i\omega_n \rightarrow \varepsilon \pm i\Gamma$, $i\omega_m \rightarrow \varepsilon - \omega \pm i\Gamma$, $f_1 = \tanh(\varepsilon/(2T))$, $f_2 = \tanh((\varepsilon - \omega)/(2T))$, and Γ is an infinitesimally small quantity denoting the correct solution branch. In the numerical solution, we use a finite $\Gamma < 10^{-2}\Delta_0$ to broaden the BCS divergence in the density of states, which makes the numerical solution converge faster.

The solution Eq. (S19) depends on the numerically determined equilibrium GFs and thus the integral (S21) is evaluated numerically. The low-frequency corrections to the static spin susceptibility are shown in Fig. S1b. In the normal state, there are no spectral changes, and only the last term in Eq. (S21) contributes:

$$\chi_n^{+}(\omega) = \frac{2N_0\omega}{\omega - 2h + i\tau_{sn}^{-1}}, \quad (\text{S22})$$

with $\tau_{sn}^{-1} = 4(\tau_{so}^{-1} + \tau_{sf}^{-1})/3 + 2\Gamma$. We see that Γ acts as an additional mechanism for spin relaxation. In general,

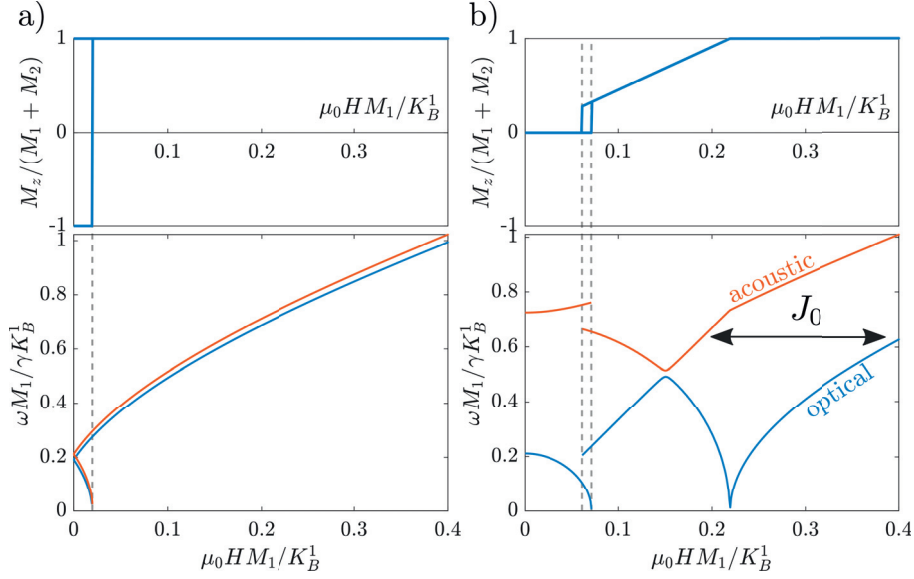


FIG. S2. FMR dispersion (bottom) and magnetic hysteresis (top) in a symmetric bilayer a) in the N state and b) in the SC state at $T = 0.01T_{c0}$. In the N state the magnets are only weakly coupled by pumped quasiparticle spin currents. In the SC state the magnets are also coupled by SS. SC is evaluated in the thin-film limit. Parameters: $dN_0\Delta_0^2 = 0.5$, $K_A^n = 0.01$, $\Delta_0 M_1/\gamma = 10^3$, in units of K_B^2 ; $h_n = 0.3\Delta_0$, $\alpha_n = 0.01$, $\tau_{so/sf} = 0$. External field is at 1° angle to the anisotropy axis.

our results depend on Γ only if the dissipation from it is comparable to dissipation from other sources ($\tau_{so/sf}$ and α_n).

For longitudinal susceptibility, there is no simple analytical solution, but the Usadel equation can be written as a 4-component matrix equation, which is solved numerically [29]. For small frequencies, the longitudinal and transverse susceptibility differ near T_c , where a small change in the modulus of \mathbf{h} can have a large effect on Δ .

Since both $\mathbf{h}(t)$ and $\mathbf{S}(t)$ are real, the left- and right-handed susceptibilities are related by $\chi^-(\omega) = \chi^+(-\omega)^*$. Also, the transverse spin susceptibility at zero frequency and the static nonlinear spin accumulation can be related to each other by considering an adiabatic rotation of the total exchange field, so that when $\hat{\chi}(0, x_i, x_j)$ for $i, j \in \{1, 2\}$ can be simultaneously diagonalized, we have

$$\mathbf{S}^{\text{eq}}(0, x_i) = \sum_{j=1,2} \chi^\pm(0, x_i, x_j) G_j \mathbf{m}_j(0). \quad (\text{S23})$$

This relation is needed to show the exact cancellation of spin supercurrents for the acoustic mode in P configuration.

Magnetic susceptibility of FI/SC/FI trilayer

In this section, we derive the non-collinear matrix susceptibility for a coupled magnetic system. To find the susceptibility, one first solves the equilibrium problem by finding a local minimum of the free energy, Eq. (8).

This determines the static magnetization directions

$$\mathbf{m}_{1/2}(0) \parallel \mathbf{H}_{\text{eff},1/2}^{(0)} - \frac{J_\phi \mathbf{m}_{2/1}(0)}{M_{1/2}}. \quad (\text{S24})$$

In LLG equation the modulus of the magnetization is fixed and there are only two degrees of freedom for each magnet. To remove the third dimension, we rotate Eq. (11) to each magnet's individual eigenbasis in which $\mathbf{m}_n(0)$ points in the z -direction and project on the x - y plane.

Identifying in Eq. (12) the parts which are proportional to $\mathbf{M}_1(\omega)$ and $\mathbf{M}_2(\omega)$, and doing the thin-film approximation $\hat{\chi}(\omega, x_i, x_j) G_j \approx \hat{\chi}(\omega) h_j$, we find the magnetic susceptibility for a non-collinear static configuration

$$\hat{\chi}_{\text{tot}}^{-1}(\omega) = \begin{pmatrix} \hat{\chi}_1^{-1}(\omega) + \frac{\hat{L}_{11}(\omega)}{M_1^2} & \frac{\hat{L}_{12}(\omega)}{M_1 M_2} \\ \frac{\hat{L}_{21}(\omega)}{M_1 M_2} & \hat{\chi}_2^{-1}(\omega) + \frac{\hat{L}_{22}(\omega)}{M_2^2} \end{pmatrix}, \quad (\text{S25a})$$

$$\chi_i^{-1}(\omega)^{++} = \frac{\omega - \gamma \mu_0 H_{\text{eff},i} - i \alpha_i \omega}{\gamma M_i}, \quad (\text{S25b})$$

$$\chi_i^{-1}(\omega)^{+-} = -K_B^i / M_i^2 \quad (\text{S25c})$$

$$\begin{aligned} \mu_0 H_{\text{eff},i} &= \mu_0 H \cos(\theta - \phi_i) \\ &+ [2K_A^i \cos(\phi_i)^2 - K_B^i] / M_i \\ &+ d\chi(0) h_1 h_2 \cos(\phi_1 - \phi_2) / M_i, \end{aligned} \quad (\text{S25d})$$

where ϕ_i (θ) is the angle between the anisotropy axis $\hat{\mathbf{z}}$ and $\mathbf{m}_i(0)$ (\mathbf{H}). We assume that the static magnetization is always in-plane. The spin currents not included

into the effective magnetic field are

$$\begin{aligned} \hat{L}_{ij}(\omega) = & -dh_i h_j \left[\hat{D}_i \hat{\chi}(\omega) \hat{D}_j^\dagger - \chi(0) \hat{\mathbf{1}}_2 \delta_{ij} \right] \\ & - dN_0 h_i \omega \delta_{ij} \hat{\sigma}_3, \end{aligned} \quad (\text{S25e})$$

where $\hat{\chi} = \text{diag}(\chi^-, \chi^z, \chi^+)$ is the spin susceptibility in the SC eigenbasis, and the 2×3 matrices $\hat{D}_n = \hat{P} \hat{D}^1(0, \phi_n - \phi_{\text{sc}}, 0)$ are a product of a projection \hat{P} to the x - y plane, and of spin-1 Wigner matrices \hat{D}^1 . ϕ_{sc} is the direction of $\mathbf{h}(0)$.

The eigenmodes are found by diagonalizing $\hat{\chi}_{\text{tot}}^{-1}(\omega)$ and finding the values of ω for which the real part of an eigenvalue vanishes. A typical dispersion for a symmetric system is shown in Fig. S2.

In parallel configuration the magnetic susceptibility can be written as Eqs. (13-14) with

$$\chi_i^{-1}(\omega)^{++} = \frac{\omega - \gamma \mu_0 H_{\text{eff},i}^{(0)} - i\alpha_i \omega}{\gamma M_i}, \quad (\text{S26a})$$

$$\chi_i^{-1}(\omega)^{+-} = -K_B^i / M_i^2 \quad (\text{S26b})$$

$$\mu_0 H_{\text{eff},i}^{(0)} = \mu_0 H + 2K_A^i / M_i - K_B^i / M_i, \quad (\text{S26c})$$

and with spin susceptibility $\hat{\chi} = \text{diag}(\chi^{++}, \chi^{--})$ which includes only the transverse components. Here we have separated the N and SC state contributions to the effective fields into $H_{\text{eff},i}^{(0)}$ and $-J/M_i$, respectively, and did not assume the thin-film limit.

Since $\mathbf{M}_n(t)$ and $\mathbf{H}_{\text{rf}}(t)$ are real, the $-+$ and $--$ components can be obtained by $\chi^{-1}(\omega)^{\mu\nu} = [\chi^{-1}(-\omega)^{\nu\mu}]^*$. The spin current $j_{xi}^\mu(\omega) = \xi_{ij}^\mu(\omega) m_j^\mu(\omega)$, where ξ is a response function, also obeys the same reality condition $\xi_{ij}^-(\omega) = [\xi_{ij}^+(-\omega)]^*$.

FMR linewidth

Here we give the definition of the FMR linewidth used in the main text. Typically in FMR experiment, rf frequency is held fixed while sweeping the external field strength H . The power of the rf drive is given by [30]

$$\begin{aligned} P/A &= \sum_{n=1,2} \langle \mathbf{H}_{\text{rf}}(t) \cdot \partial_t \mathbf{M}_n(t) \rangle \\ &= \sum_{\lambda \in \text{eigs}} \omega \text{Im} \chi_\lambda(\omega) |H_\lambda|^2, \end{aligned} \quad (\text{S27})$$

where χ_λ are the eigenvalues of the matrix susceptibility $\hat{\chi}$, and H_λ are the projections of the rf field along the corresponding eigenvector.

The linewidth is defined as the difference $\Delta H = (2/\sqrt{3})(H_{\text{min}} - H_{\text{max}})$ between the minimum and the maximum of the field derivative dP/dH . Near resonance, dP/dH is dominated by the resonant eigenmode λ and other modes can be neglected. To determine

the linewidth, we linearize the susceptibility of the resonant eigenmode, expressing it in terms of resonance field $\mu_0 H_{\text{res}}$, weight factor W and linewidth $\mu_0 \Delta H$,

$$\chi_\lambda(H)^{-1} \approx \frac{\mu_0(H - H_{\text{res}}) - i\mu_0 \Delta H}{W}. \quad (\text{S28})$$

The above parameters are defined by the equations

$$0 = \text{Re}[\chi_\lambda(H_{\text{res}})^{-1}], \quad (\text{S29a})$$

$$\frac{1}{W} = \left. \frac{d \text{Re}[\chi_\lambda(\omega)^{-1}]}{d\mu_0 H} \right|_{H=H_{\text{res}}}, \quad (\text{S29b})$$

$$\mu_0 \Delta H = -W \text{Im}[\chi_\lambda(H_{\text{res}})^{-1}]. \quad (\text{S29c})$$

In bulk ferromagnets, the field linewidth can be identified with Gilbert damping $\alpha = \gamma \mu_0 \Delta H / \omega$.

Effect of the first order SC transition on the magnetic hysteresis

At low temperatures, the transition between SC and the N state as a function of the exchange field is of the first order.[35, 36] In the phase diagram, the first order transition is accompanied by a region in which both phases are possible as metastable states, albeit only one of them is thermodynamically stable away from the phase boundary (Fig. S3a). Experimentally, the metastability shows as hysteresis or state memory when the induced exchange field is swept over the phase boundary.[37, 38]

The FI/SC/FI trilayer provides a way of probing the transition and the SC-N hysteresis via magnetization measurements. The requirement for such measurement is that it must be possible to vary the total exchange field induced into the SC continuously as a function of the external field. This requirement is met if the FIs have an in-plane easy-axis and the magnetic field is applied perpendicular to it.

The FIs individually induce the exchange fields $h_1, h_2 > 0$ into the SC. In the AP and P configurations, the total fields are $|h_1 - h_2|$ and $h_1 + h_2$, respectively. By changing the magnetization configuration, we thus sweep a horizontal segment of the phase diagram as shown in Fig. S3 for three different temperatures (blue, orange and red lines). If h_1 and h_2 are chosen properly, we cross the first order phase boundary at a low temperature (blue). Let us denote the thermodynamic transition point by h_{th} . If there is a measurable SC-N hysteresis, the N-to-SC and SC-to-N transitions occur at fields $h_{c1} < h_{\text{th}}$ and $h_{c2} > h_{\text{th}}$, respectively.

Let us then consider the magnetization in a symmetric trilayer as the external field is varied. In the normal state the magnets are uncoupled. At zero field the magnetizations lie along the anisotropy axis. Increasing the field twists the magnetizations until they point towards the external field (red dashed line in Fig. S3). The P and

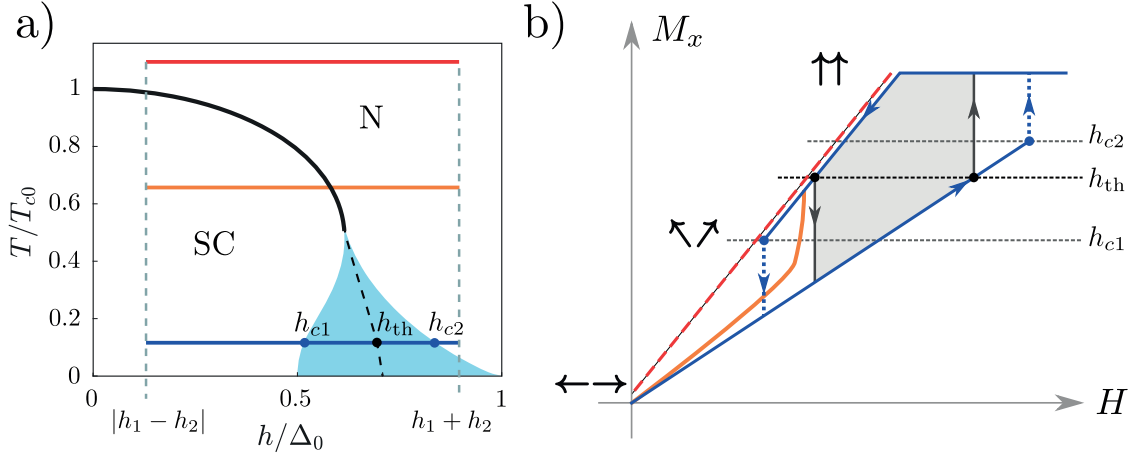


FIG. S3. Effect of the first order SC transition on the magnetic hysteresis. a) Phase diagram as a function of temperature and exchange field. Red, orange and blue lines show the range of total exchange fields, when the individual magnets induce a field of strength h_1 and h_2 . Blue shading indicated the region of metastability where both SC and N state are possible. Dashed black line indicates the thermodynamic phase transition. b) Magnetization along the external field (M_x) as a function of the field strength H . Red dashed line and the solid orange and blue lines correspond to the temperatures indicated in panel (a). Red dashed line is the high temperature (normal state) behavior. Orange line is the behavior at intermediate temperatures when the SC transition is continuous. Blue line shows the behavior at low temperatures in which the SC transition is of the first order.

AP configurations are degenerate and when the field is reduced to zero, the system may end up in either one.

The SC state on the other hand favors the AP configuration, and the slope of the magnetization curve (orange and blue lines) is lower. The first order transition (blue line) shows in the magnetization curve as hysteresis. However, the magnetic hysteresis itself is not necessarily evidence of SC-N hysteresis, but only indicates a first-order transition between SC and N states. The shaded

region in Fig. S3 is the magnetic hysteresis obtained by assuming that the SC transition always occurs when h crosses the thermodynamic field h_{th} , with no hysteresis. With this assumption, the P-to-AP and AP-to-P transitions occur in Fig. S3b at the same total magnetization, but the field strength depends on the direction of transition.

The evidence for SC-N hysteresis is the difference in the magnetization M at which the transitions occur, since there is a one-to-one correspondence between M and h .

IX

COUPLING THE HIGGS MODE AND FERROMAGNETIC RESONANCE IN SPIN-SPLIT SUPERCONDUCTORS WITH RASHBA SPIN-ORBIT COUPLING

by

Y. Lu, R. Ojajärvi, P. Virtanen, M.A. Silaev and T.T. Heikkilä 2021

arXiv preprint, [arXiv:2108.06202](https://arxiv.org/abs/2108.06202) [cond-mat.supr-con]

Reproduced with permission. Copyright 2021 The Authors. Published in arXiv under the terms of the Creative Commons Attribution 4.0 International license.

Coupling the Higgs mode and ferromagnetic resonance in spin-split superconductors with Rashba spin-orbit coupling

Yao Lu,¹ Risto Ojajärvi,¹ P. Virtanen,¹ M.A. Silaev,^{1,2,3} and Tero T. Heikkilä¹

¹*Department of Physics and Nanoscience Center, University of Jyväskylä,
P.O. Box 35 (YFL), FI-40014 University of Jyväskylä, Finland*

²*Moscow Institute of Physics and Technology, Dolgoprudny, 141700 Russia*

³*Institute for Physics of Microstructures, Russian Academy of Sciences, 603950 Nizhny Novgorod, GSP-105, Russia*
(Dated: February 21, 2022)

We show that the Higgs mode of superconductors can couple with spin dynamics in the presence of a static spin-splitting field and Rashba spin-orbit coupling. The Higgs-spin coupling dramatically modifies the spin susceptibility near the superconducting critical temperature and consequently enhances the spin pumping effect in a ferromagnetic insulator/superconductor bilayer system. We show that this effect can be detected by measuring the magnon transmission rate and the magnon-induced voltage generated by the inverse spin Hall effect.

Superconductors (SC) with broken $U(1)$ symmetry host two kinds of collective modes associated with the order parameter fluctuations: the phase mode and the amplitude mode. Coupled to a dynamical gauge field, the phase mode is lifted up to the plasma frequency [1] due to the Anderson–Higgs mechanism [2, 3]. The other collective mode in SC is the amplitude mode [4, 5] with an energy gap of 2Δ , called the Higgs mode by analogy with the Higgs boson [3] in particle physics. It was commonly believed that unlike the phase mode the Higgs mode usually does not couple linearly to any experimental probe. That is why in earlier experiments, the Higgs mode was only observed in charge-density-wave (CDW) coexisting systems [6–11]. With the advance of terahertz spectroscopy technique [12] it became possible to investigate the Higgs mode through the nonlinear light–Higgs coupling [13–17]. In these experiments, the perturbation of the order parameter is proportional to the square of the external electromagnetic field $\delta\Delta \propto E^2$, so very strong laser pulses are required.

Recently, it has been shown that in the presence of a supercurrent the Higgs resonance can actually contribute to the total admittance Y_Ω due to the linear coupling of the Higgs mode and the external electromagnetic field [18–22]. This can be understood from a symmetry argument. Suppose the external electric field is linearly polarized in the x direction $E = \hat{x}E_x e^{i\Omega t}$. The linear coupling of the Higgs mode and the external field is represented by the susceptibility $\chi_{\Delta E} = -\frac{\partial^2 S}{\partial \Delta \partial E}$ obtained from the action S describing the electron system containing the pair potential field Δ . Without a supercurrent, the system preserves the inversion symmetry (\hat{I}) and the mirror symmetry in the x direction (\hat{M}_x). On the other hand $\chi_{\Delta E}$ is odd under both these operations because E changes sign under \hat{I} and \hat{M}_x whereas Δ remains the same. Therefore $\chi_{\Delta E}$ has to vanish. In the presence of a supercurrent, the inversion symmetry and the mirror symmetry are both broken and there is no restriction for $\chi_{\Delta E_x}$ from these symmetries, so $\chi_{\Delta E}$ can be

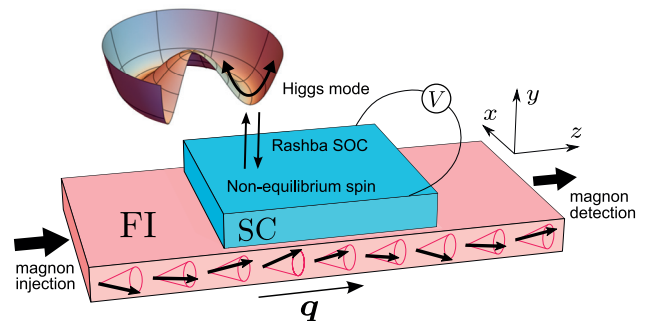


FIG. 1. System under consideration. A superconductor thin film is placed on the top of a FI with in-plane magnetization. The SC and FI are coupled via spin exchange interaction. The magnon in FI can be injected into SC in a process known as the spin pumping effect. For magnon frequency $\Omega = 2\Delta_0$ the SC Higgs mode greatly increases the spin pumping.

nonzero. This symmetry argument also explains why the Higgs mode does not couple with an external field in the direction perpendicular to the supercurrent.

Now a natural question arises: without a supercurrent does the Higgs mode couple linearly with other external probes, such as spin exchange fields? As we show in this Letter it does. The above discussion indicates that the decoupling of the Higgs mode is protected by certain symmetries. In order to couple the Higgs mode to an external field one needs to break these symmetries. Here we show how it happens in a ferromagnetic insulator (FI)/superconductor (SC) bilayer system (Fig. 1). Magnons with momentum \mathbf{q} and frequency Ω in the FI can be injected into the SC in a process known as spin pumping [23–29]. We predict that the Higgs mode in the SC couples linearly with the magnon mode in the FI in the presence of Rashba spin-orbit coupling and the magnetic proximity effect into the SC. In this system the symmetries protecting Higgs-spin decoupling are broken: in particular, the (spin) rotation symmetry and the

time-reversal symmetry. Near the critical temperature, superconductivity is suppressed and Δ_0 becomes comparable with the magnon frequency Ω . When the magnon frequency matches the Higgs frequency $\Omega_M = 2\Delta_0$, the Higgs mode is activated and the magnon absorption is hugely enhanced which can be detected through the inverse spin Hall effect (iSHE) [30–32]. This effect can possibly explain the voltage peak observed in the experiment [33].

We consider a SC/FI bilayer in which the FI and the SC are coupled via the exchange interaction as shown in Fig. 1. For simplicity, we assume that the thickness d of the SC film is much smaller than the spin relaxation length and the coherence length so that we consider it as a 2D system. The magnetization of the FI can be written as $\mathbf{m} = \mathbf{m}_0 + \mathbf{m}_\Omega$, where \mathbf{m}_0 is the static magnetization polarized in the z direction and \mathbf{m}_Ω is the dynamical component perpendicular to \mathbf{m}_0 . When magnons (spin waves) are excited in the FI, they can be injected into the SC in a process known as the spin pumping effect. The DC interface spin current flowing from the FI into the SC is polarized in the z direction and given by [34]

$$I_z = \sum_{\Omega, \mathbf{q}} -2J_{sd} \text{Im}[\tilde{\chi}_{ss}(\Omega, \mathbf{q})] m_{\Omega, \mathbf{q}}^2, \quad (1)$$

where J_{sd} is the exchange coupling strength and m_Ω is the Fourier amplitude of \mathbf{m}_Ω . $\tilde{\chi}_{ss}(\Omega, \mathbf{q})$ is the total dynamical spin susceptibility $\tilde{\chi}_{ss}(\Omega, \mathbf{q}) = S_+(\Omega, \mathbf{q})/h_+(\Omega, \mathbf{q})$, where S is the dynamical spin of the SC, \mathbf{h} is the proximity induced exchange field $\mathbf{h} = J_{sd}\mathbf{m}/d$ [35] and for a vector $\mathbf{A} = (A_x, A_y, A_z)$ the \pm component is defined as $A_\pm = A_x \pm iA_y$. One can see that for a fixed J_{sd} , the efficiency of the magnon injection is solely determined by $\tilde{\chi}_{ss}(\Omega, \mathbf{q})$. The spin susceptibility of superconductors has been extensively studied [29, 36]. However the previous theories, based on the static mean-field description, failed to explain the peak of the iSHE signal observed in the spin Seebeck experiment [33]. In this work, we start with the general partition function of the SC, $Z = \int D[\bar{\Psi}, \Psi, \bar{\Delta}, \Delta] e^{-S}$ obtained by performing the Hubbard-Stratonovich transformation. The action S is given by

$$S = \beta \sum_{K, Q} \bar{\Psi}_K (-i\omega + \epsilon_{\mathbf{k}} - \mathbf{h} \cdot \boldsymbol{\sigma}) \Psi_K + \Delta_Q \Psi_{K+Q} \Psi_{-K} + \bar{\Delta}_{-Q} \bar{\Psi}_K \bar{\Psi}_{-K-Q} + \frac{\bar{\Delta}_{-Q} \Delta_Q}{U} \quad (2)$$

Here $K = (\omega, \mathbf{k})$ and $Q = (\Omega, \mathbf{q})$ are the four-momenta of the electrons and magnons, respectively. $\omega = (2n + 1)\pi T$ and $\Omega = 2n\pi T$ are the Matsubara frequencies with $n \in Z$ and $\beta = 1/T$. $\epsilon_{\mathbf{k}}$ is the energy dispersion of the electron in the normal state, \mathbf{h} is the proximity induced exchange field, and U is the BCS interaction. In the mean-field theory, one can ignore the path integral over

Δ and replace it by its saddle point value Δ_0 which is determined by the minimization of the action $\frac{\partial S}{\partial \Delta}|_{\Delta=\Delta_0} = 0$ after integrating out the fermion fields.

To include the Higgs mode, we go beyond the mean-field theory and write the order parameter as $\Delta = \Delta_0 + \eta$, where η is the deviation of Δ from its saddle point value Δ_0 . Here we only consider the amplitude fluctuation of Δ , so η is real. Expanding the action to the second order in η and the strength of the external Zeeman field h_\pm gives $S = S_0 - S_2$ with [37]

$$S_2 = \beta \sum_Q [\eta(-Q) \ h_(-Q)] \begin{bmatrix} -\chi_{\Delta\Delta}^{-1} & \chi_{\Delta s} \\ \chi_{s\Delta} & \chi_{ss} \end{bmatrix} \begin{bmatrix} \eta(Q) \\ h_+(Q) \end{bmatrix}. \quad (3)$$

Here, all the susceptibilities are functions of Q . S_0 is the mean-field action without the external field. In usual superconductors the off-diagonal susceptibilities $\chi_{\Delta s}$ and $\chi_{s\Delta}$ vanish as required by the time-reversal symmetry and the (spin) rotation symmetry because these operations change the sign of h_+ but have no effect on η [38, 39]. In the system under consideration, the proximity induced static exchange field breaks the time-reversal symmetry and RSOC breaks the (spin) rotation symmetry. Thus the pair-spin susceptibility does not have to vanish, allowing for a nonzero Higgs–spin coupling.

Then it is straightforward to calculate the total spin susceptibility $\tilde{\chi}_{ss}$ by integrating out the η field

$$\tilde{\chi}_{ss} = \chi_{ss} - \chi_{s\Delta} \chi_{\Delta\Delta} \chi_{\Delta s}. \quad (4)$$

The imaginary part of $\chi_{\Delta\Delta}$ is sharply peak at the Higgs frequency $\Omega = 2\Delta$ dramatically modifying the total spin susceptibility.

Phenomenological theory. Before we go to the detailed calculations, we use a simple phenomenological theory to illustrate the effect of RSOC. It has been shown that RSOC can induce a Dzyaloshinskii-Moriya (DM) interaction in superconductors described by the DM free energy [40]

$$F_{DM} = \sum_i \int d\mathbf{r} |\Delta|^2 \mathbf{d}_{\alpha, i} \cdot (\mathbf{h} \times \nabla_i \mathbf{h}), \quad (5)$$

where both $\Delta = \Delta(\mathbf{r})$ and $\mathbf{h} = \mathbf{h}(\mathbf{r})$ are position dependent. $\mathbf{d}_{\alpha, i}$ is the DM vector proportional to the strength of spin-orbit coupling α . For RSOC $\mathbf{d}_\alpha \propto \alpha[\sigma_x, -\sigma_z]$, where α is the spin-orbit coupling strength and σ is the Pauli matrix acting on the spin space. To find the pair spin susceptibility we write $\Delta = \Delta_0 + \eta(t)$, $\mathbf{h} = h_0 \hat{z} + h_+(t)(\hat{x} + i\hat{y})$, where \hat{n} is the unit vector in the n direction with $n = x, y, z$, and generalize the DM free energy to the time dependent DM action. Here we consider the case where the spin wave is propagating in the z direction $h_+(t, \mathbf{r}) = \sum_{\Omega, q_z} h_+(\hat{x} + i\hat{y}) e^{i(\Omega t - q_z z)}$. Focusing on the first order terms in $\eta(t)$ and $h_+(t)$ and

Fourier transforming them to momentum and frequency space, the DM action can be written as

$$S_{DM1} = \beta \sum_{\Omega, q_z} i q_z \Delta_0 h_0 h_+ (\Omega, q_z) \eta(\Omega, q_z) \tilde{\mathbf{d}}_{\alpha, z}(\Omega, q_z) \cdot (i\hat{x} - \hat{y}), \quad (6)$$

where $\tilde{\mathbf{d}}_{\alpha, i}$ is the dynamical DM vector, which has the same finiteness and spin structure as $\mathbf{d}_{\alpha, i}$ from symmetry analysis. From the above expression, one can see that the Higgs mode couples linearly with the spin degree of freedom in the presence of RSOC.

Spin susceptibility. We adopt the quasiclassical approximation to systematically evaluate the susceptibilities. In the diffusive limit, this system can be described by the Usadel equation [18, 36, 41–45]

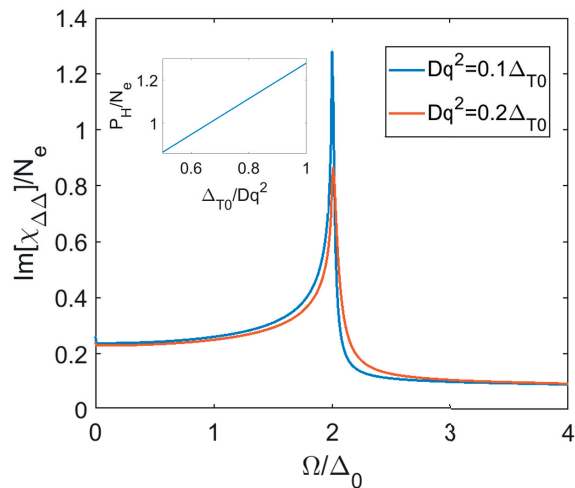


FIG. 2. Imaginary part of the pair susceptibility. This can be interpreted as the spectral weight of the Higgs mode. A significant peak emerges when the driving frequency matches the Higgs frequency $\Omega = 2\Delta_0$. The inset shows the height of the Higgs peak P_H as a function of the inverse of the momentum \mathbf{q} . Parameters: $\Delta_0 = 0.8\Delta_{T0}$, $h_0 = 0.5\Delta_{T0}$ with $\Delta_{T0} \equiv \Delta_0(T=0)$.

$$-i\{\tau_3 \partial_t, \hat{g}\} = D\tilde{\nabla}(\hat{g}\tilde{\nabla}\hat{g}) - i[H_0, \hat{g}] + [Xe^{i(\Omega t - q_z z)}, \hat{g}]. \quad (7)$$

Here \hat{g} is the quasiclassical Green function, $D = v_F \tau^2 / 3$ is the diffusion constant and τ is the disorder scattering time. $H_0 = -ih_0 \sigma_3 + \Delta_0 \tau_1$, where h_0 is the proximity induced effective static exchange field and τ_i is the Pauli matrix acting on the particle-hole space. $\tilde{\nabla} = (\tilde{\nabla}_z, \tilde{\nabla}_x)$ is the covariant derivative defined by $\tilde{\nabla}_z \cdot = \nabla_z + i\alpha[\sigma_x, \cdot]$, $\tilde{\nabla}_x \cdot = \nabla_x - i\alpha[\sigma_z, \cdot]$. The Usadel equation is supplemented by the normalization condition $\hat{g}^2 = 1$. In the quasiclassical approximation the approximate PH symmetry of the full Hamiltonian becomes ex-

act. In the linear response theory, the external oscillating field X is small and can be treated as a perturbation. Thus we can write the quasiclassical Green function as $\hat{g} = \hat{g}_0 e^{i\omega(t_1 - t_2)} + \hat{g}_X e^{i(\omega + \Omega)t_1 - i\omega t_2 - iq_z z}$, where \hat{g}_0 is the static Green function and \hat{g}_X is the perturbation of the Green function describing the response to the external field. Solving the Usadel equation we obtain the quasiclassical Green function, the anomalous Green function $F = N_e \text{Tr}[\tau_1 \hat{g}] / 4i$ and the σ_+ component of spin in the SC $\langle s \rangle = N_e \text{Tr}[\sigma_- \tau_3 \hat{g}] / 4i$, where N_e is the electron density of states at the Fermi surface and Tr is the trace. The susceptibilities can be evaluated as

$$\hat{\chi} = \begin{bmatrix} \chi_{\Delta\Delta}^{-1} & \chi_{\Delta s} \\ \chi_{s\Delta} & \chi_{ss} \end{bmatrix} = \begin{bmatrix} \frac{\partial F}{\partial \eta} + \frac{1}{U} \frac{\partial F}{\partial h_+} \\ \frac{\partial \langle s \rangle}{\partial \eta} & \frac{\partial \langle s \rangle}{\partial h_+} \end{bmatrix}. \quad (8)$$

Let us first set $X = \Delta' \tau_1$ and consider the pair susceptibility. We assume the RSOC is weak and treat α as a perturbation. At $q = 0$ and 0th order in α , we have

$$\chi_{\Delta\Delta}(i\Omega) = \left[\frac{N_e T}{2} \sum_{\omega, \sigma} \frac{4\Delta^2 + \Omega^2}{s_\sigma(\omega)(4\omega^2 - \Omega^2)} \right]^{-1}, \quad (9)$$

where $s_\sigma(\omega) = \sqrt{(\omega + i\sigma h)^2 + \Delta^2}$, with $\sigma = \pm 1$. To get the pair susceptibility as a function of real frequency, we need to perform an analytical continuation [38]. Thus $i\Omega$ is replaced by $\Omega + i0^+$. One can see that the $\chi_{\Delta\Delta}$ is peaked at the Higgs frequency $\Omega = 2\Delta$.

We numerically calculate $\chi_{\Delta\Delta}$ with finite momentum and show the results in Fig. 2 [38, 46]. One can see that the imaginary part of the inverse of the pair susceptibility exhibits a sharp peak when the driving frequency equals $2\Delta_0$. With a finite momentum, the Higgs mode is damped in the sense that the peak in the Higgs spectrum has a finite height and width.

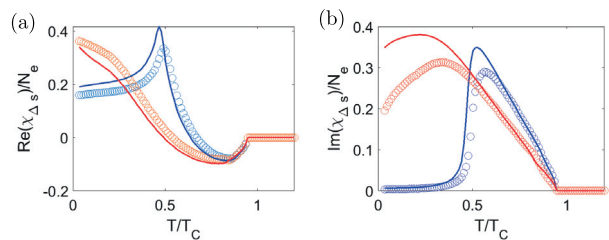


FIG. 3. Real part (a) and imaginary part (b) of pair-spin susceptibility. The solid line is the approximate result calculated from Eq. (12) and the circles show the numerical solution from Eq. (7). Parameters used here are: $\Omega = 0.8\Delta_{T0}$ for the blue lines, $\Omega = \Delta_{T0}$ for the red lines, $h_0 = 0.5\Delta_{T0}$, $Dq_z^2 = D\alpha^2 = 0.01\Delta_{T0}$.

To study the response of this system to the external exchange field we set $X = h_+ \sigma_+ \tau_3$. Again we treat α as a perturbation and write the Green function as

$$\hat{g} = \hat{g}_0 e^{i\omega(t_1 - t_2)} + (\hat{g}_{h_0} + \hat{g}_{h_\alpha}) e^{i(\omega + \Omega)t_1 - i\omega t_2 - iq_z z}, \quad (10)$$

where \hat{g}_{h0} is 0th order in α and $\hat{g}_{h\alpha}$ is first order in α . The 0th order solution in α is given by [38]

$$\hat{g}_{h0} = \hat{g}_{h00} \otimes \sigma_+ = \frac{i[\tau_3 - \hat{g}_\uparrow(1)\tau_3\hat{g}_\downarrow(2)]h_\Omega\sigma_+}{s_\uparrow(1) + s_\downarrow(2)}, \quad (11)$$

where $\hat{g}_{\uparrow/\downarrow} = \frac{(\omega \pm ih_0)\tau_3 + \Delta\tau_1}{s_{\uparrow/\downarrow}}$ and $s_{\uparrow/\downarrow} = \sqrt{(\omega \pm ih_0)^2 + \Delta^2}$. \hat{g}_{h00} is a 2×2 matrix in the particle-hole space. Without doing detailed calculations, one can immediately see that $\chi_{\Delta s}$ has to vanish without RSOC because \hat{g}_h has no σ_0 component. In this case the external exchange field cannot activate the Higgs mode. To get a finite pair-spin susceptibility we need to consider the first order terms in α which break the spin rotation symmetry. The first order solution in α yields $\hat{g}_{h\alpha} = \text{diag}(\hat{g}_{h\alpha\uparrow}, \hat{g}_{h\alpha\downarrow})$ with

$$\hat{g}_{h\alpha\uparrow/\downarrow} = 2iD\alpha \frac{\hat{g}_{0\uparrow/\downarrow} [\hat{g}_{h00}, \hat{g}_{0\uparrow/\downarrow}]}{s_{\uparrow/\downarrow}(\omega_1) + s_{\uparrow/\downarrow}(\omega_2)}. \quad (12)$$

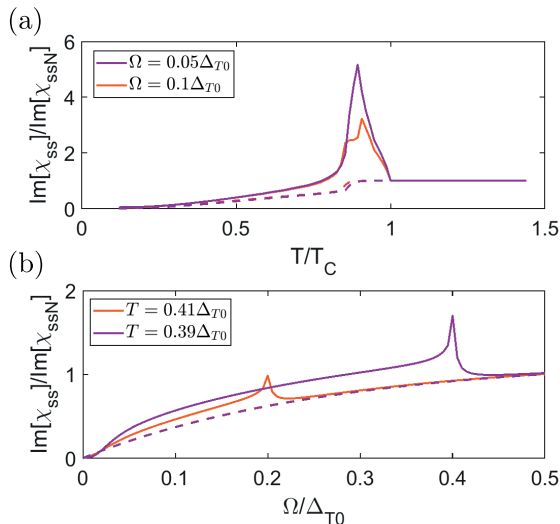


FIG. 4. (a) Total spin susceptibility as a function of temperature with a fixed frequency. (b) Total spin susceptibility as a function of frequency with a fixed temperature. The two temperatures have been chosen so that $\Delta(T_1) = 0.2\Delta_{T0}$ and $\Delta(T_2) = 0.1\Delta_{T0}$. The Higgs peak thus shows up when $\Omega = 2\Delta(T)$. The parameters used here are: $h_0 = 0.5\Delta_{T0}$, $Dq_z^2 = D\alpha^2 = 0.01\Delta_{T0}$.

Since the 0th order term does not contribute to the pair-spin susceptibility, we have $\chi_{\Delta s} = \text{Tr}[\tau_1\hat{g}_{h\alpha}]/4ih_+$. We compare this analytical result with the non-perturbative numerical solution of the Usadel equation in Fig. 3. It shows that the perturbative approach is accurate at high temperatures when $D\alpha^2 \ll \Delta_0, T$, and captures the qualitative behavior of $\chi_{\Delta s}$ also at the low temperatures. Another feature of this pair spin susceptibility is that at a lower frequency ($\Omega = 0.8\Delta_{T0}$), $\chi_{\Delta s}$ is

suppressed at low temperatures because the spin excitation is frozen by the pair gap at low temperatures. On the other hand, at higher frequency ($\Omega = \Delta_{T0}$), $\chi_{\Delta s}$ is slightly enhanced at low temperatures.

We can also get the bare spin susceptibility from \hat{g}_{h0} , $\chi_{ss} = \text{Tr}[\sigma_- \tau_3 \hat{g}_{h0}]/4ih_+$. Then it is straightforward to calculate the total spin susceptibility according to Eq. (4). The results are shown in Fig. 4. The total spin susceptibility exhibits a significant peak near critical temperature. This is a signature of the Higgs mode with the frequency $\Omega = 2\Delta_0$. The dependence of the total susceptibility on the strength of RSOC is studied in the supplementary information [38]. The details depend sensitively on the amount of disorder, as in the disordered case increasing RSOC leads to a stronger spin relaxation. We note that even though the pair-spin susceptibility is linear in momentum q_z , the magnon momentum need not be large for the detection of the Higgs mode. This is because the spectral weight of the Higgs mode is proportional to $1/q_z^2$ at the Higgs frequency, so that the height of the peak in the total spin susceptibility is independent of the magnon momentum.

Experimental detection. We propose that the Higgs mode in Rashba superconductors can be detected in the spin pumping experiment as shown in Fig. 1. Magnons in the FI with momentum \mathbf{q} and frequency Ω are injected from one side of FI and propagate in the z direction towards the other end. Due to the spin pumping effect, part of the magnons can be absorbed by the SC on top of it and converted to quasiparticles. This spin injection causes a spin current I_s flowing in the out-of-plane direction. In the presence of RSOC, I_s is converted into a charge current I_e via the iSHE $I_e = \theta_{xz}^z I_s$, where θ is the spin Hall angle [47]. When the width of the SC is smaller than the charge imbalance length the non-equilibrium charge accumulation cannot be totally relaxed resulting into a finite resistance ρ of the SC. Therefore a voltage can be measured across the SC, given by

$$V = \theta_{xz}^z \rho \sum_{\Omega, \mathbf{q}} -2J_{sd} \text{Im}[\tilde{\chi}_{ss}(\Omega, \mathbf{q})] m_\Omega^2. \quad (13)$$

Thus by tuning the temperature or the frequency of magnon, one can observe a peak in the voltage [33]. Meanwhile we can also obtain the magnon absorption rate defined as the energy of the absorbed magnons divided by time

$$W = 2\Omega \sum_{\Omega, \mathbf{q}} -2J_{sd} \text{Im}[\tilde{\chi}_{ss}(\Omega, \mathbf{q})] m_\Omega^2. \quad (14)$$

This magnon absorption rate results in a dip in the magnon transmission rate which is experimentally measurable.

Conclusion. In this Letter, we consider a FI/SC bilayer with RSOC in the bulk of the SC. Using symme-

try arguments and microscopic theory, we show that the Higgs mode in the SC couples linearly with an external exchange field. This Higgs–spin coupling hugely enhances the total spin susceptibility near a critical phase transition point, which can be detected using iSHE or via strong frequency dependent changes in the magnon transmission. Note that in this work, we consider the diffusive limit where the disorder strength is stronger than the RSOC and exchange field. However, our conclusion on Higgs–spin coupling should still be valid in the case of strong RSOC. In fact, we expect that the coupling is much stronger with strong SOC in the clean limit. In the diffusive limit, the RSOC together with disorder effectively generate spin relaxation which reduces the proximity induced exchange field suppressing the Higgs–spin coupling. On the other hand, in the clean case without disorder this effect is absent and hence the Higgs–spin coupling can be stronger. We also compare the Higgs mode in the diffusive limit and ballistic limit in the supplemental material [38].

This work was supported by Jenny and Antti Wihuri Foundation, and the Academy of Finland Project 317118 and the European Union’s Horizon 2020 Research and Innovation Framework Programme under Grant No. 800923 (SUPERTED).

-
- [1] N. Bittner, D. Einzel, L. Klam, and D. Manske, *Phys. Rev. Lett.* **115**, 227002 (2015).
- [2] P. W. Anderson, *Phys. Rev.* **130**, 439 (1963).
- [3] P. W. Higgs, *Phys. Rev. Lett.* **13**, 508 (1964).
- [4] I. Kulik, O. Entin-Wohlman, and R. Orbach, *J. Low Temp. Phys.* **43**, 591 (1981).
- [5] A. Pashkin and A. Leitenstorfer, *Science* **345**, 1121 (2014).
- [6] P. B. Littlewood and C. M. Varma, *Phys. Rev. B* **26**, 4883 (1982).
- [7] P. B. Littlewood and C. M. Varma, *Phys. Rev. Lett.* **47**, 811 (1981).
- [8] M.-A. Méasson, Y. Gallais, M. Cazayous, B. Clair, P. Rodiere, L. Cario, and A. Sacuto, *Phys. Rev. B* **89**, 060503(R) (2014).
- [9] R. Grasset, Y. Gallais, A. Sacuto, M. Cazayous, S. Mañas-Valero, E. Coronado, and M.-A. Méasson, *Phys. Rev. Lett.* **122**, 127001 (2019).
- [10] R. Grasset, T. Cea, Y. Gallais, M. Cazayous, A. Sacuto, L. Cario, L. Benfatto, and M.-A. Méasson, *Phys. Rev. B* **97**, 094502 (2018).
- [11] T. Cea and L. Benfatto, *Phys. Rev. B* **90**, 224515 (2014).
- [12] D. N. Basov, R. D. Averitt, D. vanderMarel, M. Dressel, and K. Haule, *Rev. Mod. Phys.* **83**, 471 (2011).
- [13] R. Matsunaga, Y. I. Hamada, K. Makise, Y. Uzawa, H. Terai, Z. Wang, and R. Shimano, *Phys. Rev. Lett.* **111**, 057002 (2013).
- [14] R. Matsunaga, N. Tsuji, H. Fujita, A. Sugioka, K. Makise, Y. Uzawa, H. Terai, Z. Wang, H. Aoki, and R. Shimano, *Science* **345**, 1145 (2014).
- [15] M. Beck, I. Rousseau, M. Klammer, P. Leiderer, M. Mitorff, S. Winnerl, M. Helm, G. N. Gol’tsman, and J. Demsar, *Phys. Rev. Lett.* **110**, 267003 (2013).
- [16] M. Silaev, *Phys. Rev. B* **99**, 224511 (2019).
- [17] M. A. Silaev, R. Ojajärvi, and T. T. Heikkilä, *Phys. Rev. Research* **2**, 033416 (2020).
- [18] A. Moor, A. F. Volkov, and K. B. Efetov, *Phys. Rev. Lett.* **118**, 047001 (2017).
- [19] S. Nakamura, Y. Iida, Y. Murotani, R. Matsunaga, H. Terai, and R. Shimano, *Phys. Rev. Lett.* **122**, 257001 (2019).
- [20] S. Nakamura, K. Katsumi, H. Terai, and R. Shimano, *Phys. Rev. Lett.* **125**, 097004 (2020).
- [21] M. Puviani, L. Schwarz, X.-X. Zhang, S. Kaiser, and D. Manske, *Phys. Rev. B* **101**, 220507(R) (2020).
- [22] Z. M. Raines, A. A. Allocca, M. Hafezi, and V. M. Galitski, *Phys. Rev. Research* **2**, 013143 (2020).
- [23] I. Žutić, J. Fabian, and S. Das Sarma, *Rev. Mod. Phys.* **76**, 323 (2004).
- [24] J. Linder and J. W. Robinson, *Nat. Phys.* **11**, 307 (2015).
- [25] Y. Tserkovnyak, A. Brataas, and G. E. W. Bauer, *Phys. Rev. Lett.* **88**, 117601 (2002).
- [26] E. Saitoh, M. Ueda, H. Miyajima, and G. Tatara, *Appl. Phys. Lett.* **88**, 182509 (2006).
- [27] K. Ando, S. Takahashi, J. Ieda, Y. Kajiwara, H. Nakayama, T. Yoshino, K. Harii, Y. Fujikawa, M. Matsuo, S. Maekawa, *et al.*, *J. Appl. Phys.* **109**, 103913 (2011).
- [28] Y. Tserkovnyak, A. Brataas, and G. E. W. Bauer, *Phys. Rev. B* **66**, 224403 (2002).
- [29] T. Kato, Y. Ohnuma, M. Matsuo, J. Rech, T. Jonckheere, and T. Martin, *Phys. Rev. B* **99**, 144411 (2019).
- [30] S. Takahashi and S. Maekawa, *Phys. Rev. Lett.* **88**, 116601 (2002).
- [31] S. Takahashi and S. Maekawa, *Sci. Technol. Adv. Mater.* **9**, 014105 (2008).
- [32] T. Wakamura, H. Akaike, Y. Otori, Y. Niimi, S. Takahashi, A. Fujimaki, S. Maekawa, and Y. Otani, *Nat. Mater.* **14**, 675 (2015).
- [33] K.-R. Jeon, J.-C. Jeon, X. Zhou, A. Migliorini, J. Yoon, and S. S. Parkin, *ACS Nano* **14**, 15874 (2020).
- [34] R. Ojajärvi, T. T. Heikkilä, P. Virtanen, and M. A. Silaev, *Phys. Rev. B* **103**, 224524 (2021).
- [35] T. T. Heikkilä, M. A. Silaev, P. Virtanen, and F. S. Bergeret, *Progress in Surface Science* **94**, 100540 (2019).
- [36] M. A. Silaev, *Phys. Rev. B* **102**, 144521 (2020).
- [37] T. Cea, C. Castellani, G. Seibold, and L. Benfatto, *Physical review letters* **115**, 157002 (2015).
- [38] Supplementary material includes details of the symmetry operators and derivation of the susceptibilities.
- [39] In general h_+ is inhomogeneous and the gradient of h_+ breaks the mirror symmetry locally. Thus we do not need to consider the mirror symmetry of the SC.
- [40] M. A. Silaev, D. Rabinovich, and I. Bobkova, arXiv preprint arXiv:2108.08862 (2021).
- [41] K. D. Usadel, *Phys. Rev. Lett.* **25**, 507 (1970).
- [42] W. Belzig, F. K. Wilhelm, C. Bruder, G. Schön, and A. D. Zaikin, *Superlatt. and Microstruc.* **25**, 1251 (1999).
- [43] F. S. Bergeret, A. F. Volkov, and K. B. Efetov, *Rev. Mod. Phys.* **77**, 1321 (2005).
- [44] F. S. Bergeret and I. V. Tokatly, *Phys. Rev. B* **89**, 134517 (2014).
- [45] F. S. Bergeret and I. V. Tokatly, *Phys. Rev. Lett.* **110**, 117003 (2013).
- [46] The code used to obtain the results in this manuscript

can be found at <https://gitlab.jyu.fi/jyucmt/sssc-higgs->

rashba .
[47] I. V. Tokatly, *Phys. Rev. B* **96**, 060502(R) (2017).

Supplemental material for Coupling Higgs mode and ferromagnetic resonance in spin-split superconductors with Rashba spin-orbit coupling

Yao Lu,¹ Risto Ojajarvi,¹ P. Virtanen,¹ M.A. Silaev,^{1,2,3} and Tero T. Heikkilä¹

¹*Department of Physics and Nanoscience Center, University of Jyväskylä,
P.O. Box 35 (YFL), FI-40014 University of Jyväskylä, Finland*

²*Moscow Institute of Physics and Technology, Dolgoprudny, 141700 Russia*

³*Institute for Physics of Microstructures, Russian Academy of Sciences, 603950 Nizhny Novgorod, GSP-105, Russia*

(Dated: February 21, 2022)

PACS numbers:

DETAILS OF SYMMETRY OPERATORS

Here we are most interested in the time-reversal symmetry \hat{T} , spin rotation around the z axis by 180 degrees $\hat{R}_{sz}(\pi)$, rotation (rotation in both spin and coordinate space) around the z axis by 180 degrees $\hat{R}_z(\pi)$. The symmetry operators and their effects on the Hamiltonian $H(\mathbf{k})$ are

$$\begin{aligned}\hat{T} &= i\sigma_y K \\ \hat{T}H(\mathbf{k})\hat{T}^{-1} &= H^*(-\mathbf{k}) \\ \hat{R}_{sz}(\pi) &= \sigma_z \\ \hat{R}_{sz}(\pi)H(\mathbf{k})\hat{R}_{sz}^{-1}(\pi) &= H(\mathbf{k}) \\ \hat{R}_z(\pi) &= \sigma_z \\ \hat{R}_z(\pi)H(k_x, k_y, k_z)\hat{R}_z^{-1}(\pi) &= H(-k_x, -k_y, k_z)\end{aligned}$$

where K is the complex conjugate operator and σ is the Pauli matrix acting on the spin space. These symmetry operators acting on the Zeeman and pairing terms in the Hamiltonian gives

$$\begin{aligned}\hat{O}h\sigma\hat{O}^{-1} &= -h\sigma \\ \hat{O}\eta\tau_1\hat{O}^{-1} &= \eta\tau_1,\end{aligned}\quad (S1)$$

where η is the deviation of Δ from its saddle point value Δ_0 . Here $\hat{O} = \hat{T}, \hat{R}_{sz}, \hat{R}_z$. In the main text we use these results to show that Higgs-spin coupling requires breaking all these symmetries.

CALCULATION OF PAIR SUSCEPTIBILITY

To calculate the pair susceptibility, we solve the following Usadel equation [1–7].

$$-i\{\tau_3\partial_t, \hat{g}\} = D\tilde{\nabla}(\hat{g}\nabla\hat{g}) - i[H_0, \hat{g}] + \left[Xe^{i(\Omega t - q_z z)}, \hat{g}\right], \quad (S2)$$

Here $H_0 = ih_0\sigma_3 + \Delta_0\tau_1$, where h_0 is the proximity induced effective static exchange field and τ_i is the Pauli matrix acting on particle-hole space. $\tilde{\nabla} = (\tilde{\nabla}_z, \tilde{\nabla}_x)$ is the covariant derivative defined by $\tilde{\nabla}_z \cdot = \nabla_z + i\alpha[\sigma_x, \cdot]$, $\tilde{\nabla}_x \cdot = \nabla_x - i\alpha[\sigma_x, \cdot]$. The Usadel equation is supplemented by the normalization condition $\hat{g}^2 = 1$. Here

$X = \Delta'\tau_1$. It is small compared to other energy scales and can be treated as a perturbation. Then we write the quasi-classical Green function as

$$\hat{g}(\omega_1, \omega_2) = \hat{g}_0(\omega)e^{i\omega(t_1 - t_2)} + \hat{g}_\Delta(\omega_1, \omega_2)e^{i\omega_1 t_1 - i\omega_2 t_2 - iq_z z}, \quad (S3)$$

where $\omega_1 = \omega + \Omega$ and $\omega_2 = \omega$. \hat{g}_0 is the static Green function which is 0th order in Δ' and \hat{g}_Δ is first order in Δ' . The normalization condition $\hat{g}^2 = 1$ indicates

$$\{\hat{g}_0, \hat{g}_\Delta\}_t = 0 \quad (S4)$$

The anti-commutator $\{\cdot, \cdot\}_t$ is defined by $\{A, B\}_t = A \circ B + B \circ A$, where \circ is the convolution product given by

$$(A \circ B)(t_1, t_2) = \int dt A(t_1, t)B(t, t_2) \quad (S5)$$

in time domain and

$$(A \circ B)(\omega_1, \omega_2) = \sum_\omega A(\omega_1, \omega)B(\omega, \omega_2) \quad (S6)$$

in frequency domain. Here we only consider the 0th order terms in α . The 0th order terms in Δ' give the equation for static Green function \hat{g}_0

$$[(\omega - ih_0\sigma_z)\tau_3 + \Delta_0\tau_1, \hat{g}_0] = 0. \quad (S7)$$

Solving this equation we have

$$\hat{g}_0 = \begin{bmatrix} \hat{g}_0(\omega_\uparrow) & 0 \\ 0 & \hat{g}_0(\omega_\downarrow) \end{bmatrix}, \quad (S8)$$

with

$$\hat{g}_{0\sigma} = \frac{\omega_\sigma\tau_3 + \Delta_0\tau_1}{s(\omega_\sigma)} \quad (S9)$$

where $\omega_{\uparrow/\downarrow} = \omega \pm h_0$ and $s(\omega)$ is given by

$$s(\omega) = \sqrt{\omega^2 + \Delta_0^2}. \quad (S10)$$

Next we consider the first order terms in Δ'

$$(\omega_{1\sigma}\tau_3 + \Delta_0\tau_1 + Dq_z^2)\hat{g}_\Delta(\omega_{1\sigma}, \omega_{2\sigma}) - \hat{g}_\Delta(\omega_{1\sigma}, \omega_{2\sigma})(\omega_{2,\uparrow/\downarrow}\tau_3 + \Delta_0\tau_1) = \Delta'\hat{g}_0(\omega_\sigma)\tau_1 - \Delta'\tau_1\hat{g}_0(\omega_\sigma). \quad (\text{S11})$$

Noting that

$$\omega_\sigma\tau_3 + \Delta_0\tau_1 = s(\omega_\sigma)\hat{g}_0(\omega_\sigma) \quad (\text{S12})$$

and making use of the normalization condition Eq. (S4) we obtain \hat{g}_Δ given by

$$\hat{g}_\Delta(\omega_\sigma) = \Delta' \frac{\hat{g}_0(\omega_\sigma)\tau_1 - \tau_1\hat{g}_0(\omega_\sigma)}{s(\omega_{1\sigma}) + s(\omega_{2\sigma}) + Dq_z^2} \quad (\text{S13})$$

The pair susceptibility is then given by

$$\chi_{\Delta\Delta}^{-1} = N_e T \sum_{\omega} \text{Tr}[\tau_1 \hat{g}_\Delta] / 4i\Delta' + \frac{1}{U}. \quad (\text{S14})$$

where N_e is the electron density of states at the Fermi energy in the normal state and U is the BCS interaction strength. Making use of the self-consistency equation $\frac{1}{U} = N_e T \sum_{\omega, \sigma} \frac{1}{s(\omega_\sigma)}$, we obtain

$$\chi_{\Delta\Delta}^{-1} = N_e T \sum_{\omega, \sigma = \uparrow/\downarrow} \frac{\Delta_0^2 - \omega_{1,\sigma}\omega_{2,\sigma} - s(\omega_{1,\sigma})s(\omega_{2,\sigma})}{s(\omega_{1,\sigma})s(\omega_{2,\sigma})[s(\omega_{1,\sigma}) + s(\omega_{2,\sigma}) + Dq_z^2]} + \frac{1}{s(\omega_{1,\sigma})} + \frac{1}{s(\omega_{2,\sigma})}. \quad (\text{S15})$$

In above expressions all the frequencies are Matsubara frequencies. In order to get the pair susceptibility with real frequencies, we need to perform analytical continuation according to

$$\chi^R(\Omega) = \int_{-\infty}^{\infty} d\varepsilon [\chi(\omega_1^R, \omega_2^R)f_2 - f_1\chi(\omega_1^A, \omega_2^A) + (f_1 - f_2)\chi(\omega_1^R, \omega_2^A)], \quad (\text{S16})$$

where $\omega^{R/A} = \omega \pm i0^+$ and $f(\omega) = \tanh(\omega/2T)$.

CALCULATION OF PAIR-SPIN SUSCEPTIBILITY AND THE BARE SPIN SUSCEPTIBILITY

In order to get the pair-spin susceptibility, we consider the following Usadel equation with a driven Zeeman field

$$-i\{\tau_3\partial_t, \hat{g}\} = D\tilde{\nabla}(\hat{g}\nabla\hat{g}) - i[\tau_3 H, \hat{g}] + [h_+\sigma_+\tau_3 e^{i\Omega t - iq_z z}, \hat{g}]. \quad (\text{S17})$$

Here we assume $h_+ \ll D\alpha^2 \ll Dq_z^2, T, \Delta_0, h_0$ and treat both h_Ω and α as perturbations and write the quasiclassical Green function as

$$\hat{g} = \hat{g}_0 e^{i\omega(t_1 - t_2)} + (\hat{g}_{h_0} + \hat{g}_{h\alpha}) e^{i\omega_1 t_1 - i\omega_2 t_2 - iq_z z}, \quad (\text{S18})$$

where \hat{g}_{h_0} is 0th order in α and $\hat{g}_{h\alpha}$ is first order in α . The normalization condition $\hat{g}^2 = 1$ implies

$$\begin{aligned} \hat{g}_0(\omega_1)\hat{g}_{h_0}(\omega_1, \omega_2) - \hat{g}_{h_0}(\omega_1, \omega_2)\hat{g}_0(\omega_2) &= 0 \\ \hat{g}_0(\omega_1)\hat{g}_{h\alpha}(\omega_1, \omega_2) - \hat{g}_{h\alpha}(\omega_1, \omega_2)\hat{g}_0(\omega_2) &= 0, \end{aligned} \quad (\text{S19})$$

\hat{g}_0 is given by Eq. (S9). Using the same method in the calculation of pair susceptibility, we get \hat{g}_{h_0}

$$\hat{g}_{h_0} = \hat{g}_{h_00} \otimes \sigma_+ = \frac{i[\tau_3 - \hat{g}_\uparrow(1)\tau_3\hat{g}_\downarrow(2)]h_\Omega\sigma_+}{s_\uparrow(1) + s_\downarrow(2)}. \quad (\text{S20})$$

Expanding the Usadel Eq. (S2) up to the first order in α we have

$$iD[[q_x\hat{g}_{h_0}, \sigma_1], \hat{g}_0] = K(\omega_1)\hat{g}_{h\alpha}(\omega_1, \omega_2) - \hat{g}_{h\alpha}(\omega_1, \omega_2)K(\omega_2), \quad (\text{S21})$$

where $K(\omega) = (\omega + ih_0\sigma_3)\tau_3 + \Delta_0\tau_1$. Solving this equation yields

$$\hat{g}_{h\alpha} = \begin{bmatrix} \hat{g}_{h\alpha\uparrow} & 0 \\ 0 & \hat{g}_{h\alpha\downarrow} \end{bmatrix} \quad (\text{S22})$$

with

$$\hat{g}_{h\alpha\uparrow/\downarrow} = 2iD\alpha \frac{\hat{g}_{0\uparrow/\downarrow}[\hat{g}_{h_00}, \hat{g}_{0\uparrow/\downarrow}]}{s_{\uparrow/\downarrow}(\omega_1) + s_{\uparrow/\downarrow}(\omega_2)}. \quad (\text{S23})$$

The pair-spin susceptibility is then given by

$$\chi_{\Delta s} = N_e \sum_{\omega} \text{Tr}[\tau_1 \hat{g}_{h\alpha}] / 4ih_+. \quad (\text{S24})$$

We can also get the bare spin susceptibility χ_{ss} from \hat{g}_{h_0}

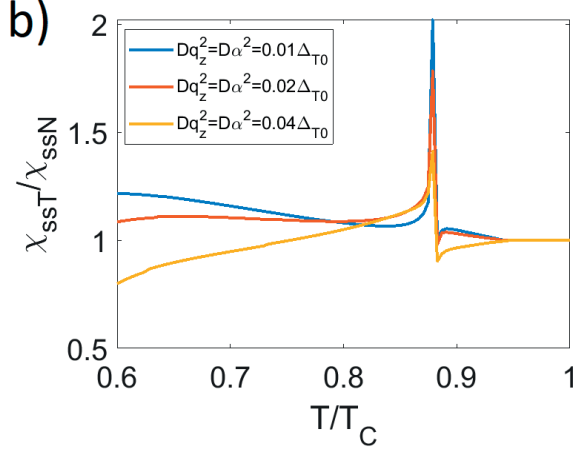


FIG. 1: The imaginary part of the total spin susceptibility as a function of temperature for different spin-orbit coupling strengths. The parameters used here are: $h_0 = 0.5\Delta_{T0}$, $\Omega = 0.4\Delta_{T0}$, where $\Delta_{T0} \equiv \Delta(T = 0)$.

$$\chi_{ss} = N_e T \sum_{\omega} \text{Tr}[\sigma_- \tau_3 \hat{g}_{h0}] / 4ih_+. \quad (\text{S25})$$

Then it is straightforward to calculate the total spin susceptibility.

$$\hat{g}_0(\omega) = \frac{\omega\tau_3 + \Delta_0\tau_1}{s(\omega)}$$

$$\hat{g}(\omega_1, \omega_2) = \Delta' \frac{\hat{g}(\omega_1)\tau_1\hat{g}(\omega_2) - \tau_1}{[s(\omega_1) + s(\omega_2)]^2 + (\mathbf{v}_F \cdot \mathbf{q})^2} [s(\omega_1) + s(\omega_2)], \quad (\text{S28})$$

where $s(\omega) = \sqrt{\omega^2 + \Delta^2}$. The pair susceptibility is then given by

$$\chi_{\Delta\Delta}^{-1} = N_e T \sum_{\omega} \text{Tr} \frac{\langle \hat{g}_{\Delta} \rangle}{4i\Delta'} + \frac{1}{s(\omega)}, \quad (\text{S29})$$

where $\langle \cdot \rangle$ denotes the direction average of \mathbf{v}_F . We evaluate the pair susceptibility by performing analytical con-

$$\text{Re}(\chi_{\Delta\Delta}^{-1}) = N_e (\Omega^2 - 4\Delta_0^2 - \frac{1}{3}v_F^2 q^2) \int d\epsilon \frac{1}{\sqrt{\epsilon^2 + \Delta^2}(\Omega^2 - 4\Delta^2 - 4\epsilon^2)}, \quad (\text{S30})$$

where $q = |\mathbf{q}|$. This expression is equivalent to Eqs. (2.28)

EFFECT OF SPIN-ORBIT COUPLING ON THE TOTAL SPIN SUSCEPTIBILITY

We numerically calculate the total spin susceptibility with different spin-orbit coupling strengths. The results are shown in Fig. 1

HIGGS MODE IN THE CLEAN LIMIT

Within the quasiclassical framework, we can also reproduce the results of Littlewood and Varma [8], but since their approach considered a clean superconductor, we need to consider the Eilenberger equation instead of the Usadel equation as in the main paper. It reads

$$-\mathbf{v}_F \cdot \nabla \hat{g} = [\omega\tau_3 + \Delta_0\tau_1, \hat{g}] + [\Delta'\tau_1 e^{i\Omega t - iq_z z}, \hat{g}], \quad (\text{S26})$$

where \mathbf{v}_F is the Fermi velocity. Again we write the Green function as

$$\hat{g}(t_1, t_2) = \hat{g}_0 e^{i\omega(t_1 - t_2)} + \hat{g}_{\Delta} e^{i(\omega + \Omega)t_1 - \omega t_2}. \quad (\text{S27})$$

Solving the Eilenberger equation in Fourier space with momentum \mathbf{q} we have

tinuation from imaginary time to real time, in which case the frequency sum becomes an integral over energy. At $\mathbf{q} = 0$, the result is Eq. (9) of the main text, which is the same both in the ballistic and diffusive limits. For non-zero momentum the total expression is cumbersome. However, we can find the Higgs mode dispersion by considering just the real part that is given by

and (2.29) in [8]. We can obtain the dispersion of the

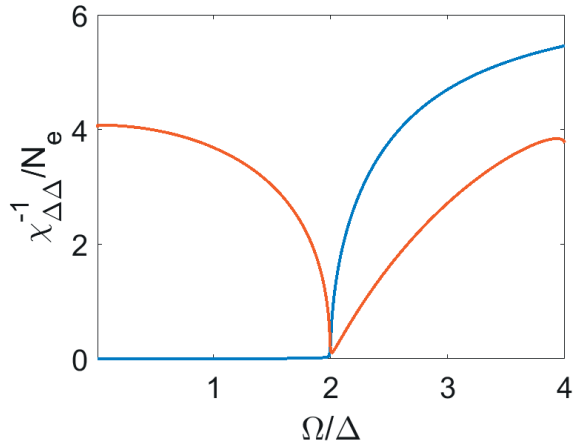


FIG. 2: Real (red) and imaginary (blue) parts of the pair susceptibility at $q = 0$.

Higgs mode from the condition $\text{Re}(\chi_{\Delta\Delta}^{-1}) = 0$. It yields

$$\Omega_H^2 = 4\Delta^2 + \frac{1}{3}v_F^2q^2. \quad (\text{S31})$$

Such a dispersion is possible to find only in the ballistic limit, whereas in the diffusive limit the Higgs peak resides at $\Omega_H^2 = 4\Delta^2$ also for finite momentum q .

To get the damping of the Higgs mode, one can follow Littlewood and Varma's method and arrive at Eq. (2.38) in their paper. Here we also show a simpler way to see the momentum dependence of the damping. In principle finite momentum may change both the damping and the frequency of the Higgs mode. However, in the clean limit the previous effect is negligible which is why the main effect of a non-zero momentum is to shift the Higgs

frequency to above 2Δ according to Eq. (S31). However, for such frequencies the damping α represented by the imaginary part of the pair susceptibility is nonzero and proportional to $\sqrt{\Omega - 2\Delta}$ even at $q = 0$ as indicated in Eq. (9) of the main paper. Inserting the dispersion $\Omega = \Omega_H(q)$ we hence get

$$\alpha \propto q. \quad (\text{S32})$$

This result is consistent with that of Littlewood and Varma. We plot the real part and the imaginary part of $\chi_{\Delta\Delta}^{-1}$ at $q_z = 0$ using Eq. 9 in the main text and the result is shown in Fig. 2.

In the diffusive case the damping of the Higgs mode behaves differently as a function of momentum. In particular, disorder leads to momentum relaxation which is why the finite momentum directly leads to damping even at $\Omega = 2\Delta$. In this case the damping is quadratic in the momentum as seen in Fig. 2 of the main paper.

-
- [1] A. Moor, A. F. Volkov, and K. B. Efetov, Phys. Rev. Lett. **118**, 047001 (2017).
 - [2] M. A. Silaev, Phys. Rev. B **102**, 144521 (2020).
 - [3] K. D. Usadel, Phys. Rev. Lett. **25**, 507 (1970).
 - [4] W. Belzig, F. K. Wilhelm, C. Bruder, G. Schön, and A. D. Zaikin, Superlatt. and Microstruc. **25**, 1251 (1999).
 - [5] F. S. Bergeret, A. F. Volkov, and K. B. Efetov, Rev. Mod. Phys. **77**, 1321 (2005).
 - [6] F. S. Bergeret and I. V. Tokatly, Phys. Rev. B **89**, 134517 (2014).
 - [7] F. S. Bergeret and I. V. Tokatly, Phys. Rev. Lett. **110**, 117003 (2013).
 - [8] P. B. Littlewood and C. M. Varma, Phys. Rev. B **26**, 4883 (1982).